Springer Series on Fluorescence 14
Series Editor: Otto S. Wolfbeis

Philip Tinnefeld
Christian Eggeling
Stefan W. Hell *Editors*

Nobel Prize® 2014

Far-Field Optical Nanoscopy

Springer

14
Springer Series on Fluorescence

Methods and Applications

Series Editor: Otto S. Wolfbeis

Springer Series on Fluorescence

Series Editor: Otto S. Wolfbeis

Recently Published and Forthcoming Volumes

Far-Field Optical Nanoscopy
Volume Editors: Philip Tinnefeld, Christian Eggeling and Stefan W. Hell
Vol. 14, 2015

Fluorescent Methods to Study Biological Membranes
Volume Editors: Y. Mély and G. Duportail
Vol. 13, 2013

Fluorescent Proteins II
Application of Fluorescent Protein Technology
Volume Editor: G. Jung
Vol. 12, 2012

Fluorescent Proteins I
From Understanding to Design
Volume Editor: G. Jung
Vol. 11, 2012

Advanced Fluorescence Reporters in Chemistry and Biology III
Applications in Sensing and Imaging
Volume Editor: A.P. Demchenko
Vol. 10, 2011

Advanced Fluorescence Reporters in Chemistry and Biology II
Molecular Constructions, Polymers and Nanoparticles
Volume Editor: A.P. Demchenko
Vol. 9, 2010

Advanced Fluorescence Reporters in Chemistry and Biology I
Fundamentals and Molecular Design
Volume Editor: A.P. Demchenko
Vol. 8, 2010

More information about this series at http://www.springer.com/series/4243

Lanthanide Luminescence
Photophysical, Analytical and Biological Aspects
Volume Editors: P. Hänninen and H. Härmä
Vol. 7, 2011

Standardization and Quality Assurance in Fluorescence Measurements II
Bioanalytical and Biomedical Applications
Volume Editor: Resch-Genger, U.
Vol. 6, 2008

Standardization and Quality Assurance in Fluorescence Measurements I
Techniques
Volume Editor: U. Resch-Genger
Vol. 5, 2008

Fluorescence of Supermolecules, Polymeres, and Nanosystems
Volume Editor: M.N. Berberan-Santos
Vol. 4, 2007

Fluorescence Spectroscopy in Biology
Volume Editor: M. Hof
Vol. 3, 2004

Fluorescence Spectroscopy, Imaging and Probes
Volume Editor: R. Kraayenhof
Vol. 2, 2002

New Trends in Fluorescence Spectroscopy
Volume Editor: B. Valeur
Vol. 1, 2001

Far-Field Optical Nanoscopy

Volume Editors:
Philip Tinnefeld
Christian Eggeling
Stefan W. Hell

With contributions by

G.P. Acuna · P.F. Aramendía · M.L. Bossi · M. Brameshuber · M.P. Bruchez · T. Cordes · G. De Cremer · D.E. De Vos · C. Eggeling · C. Forthmann · S. Gayda · A. Gietl · P.N. Hedde · S.W. Hell · J. Hofkens · B. Lalkens · S. Laurien · S.F. Lee · H.-l.D. Lee · M.D. Lew · W.E. Moerner · K. Nienhaus · G.U. Nienhaus · M.B.J. Roeffaers · M. Sauer · J.J. Schmied · G.J. Schütz · B.F. Sels · S.-H. Shim · I.H. Stein · C. Steinhauer · M.A. Thompson · P. Tinnefeld · M.H. Ulbrich · J. Vogelsang · K. Xu · D.A. Yushchenko · X. Zhuang

Springer

Volume Editors
Philip Tinnefeld
Institute of Physical and Theoretical Chemistry – NanoBioSciences
TU Braunschweig
Braunschweig
Germany

Stefan W. Hell
Department of NanoBiophotonics
Max Planck Institute for Biophysical Chemistry
Göttingen
Germany

Division of Optical Nanoscopy
German Cancer Research Center
Heidelberg
Germany

Christian Eggeling
MRC Human Immunology Unit and Wolfson Imaging Centre Oxford
Weatherall Institute of Molecular Medicine
University of Oxford
Oxford
United Kingdom

ISSN 1617-1306 ISSN 1865-1313 (electronic)
ISBN 978-3-662-45546-3 ISBN 978-3-662-45547-0 (eBook)
DOI 10.1007/978-3-662-45547-0
Springer Heidelberg New York Dordrecht London

Library of Congress Control Number: 2015930089

Printed on acid-free paper

Springer is part of Springer Science+Business Media (www.springer.com)

Series Editor

Prof. Dr. Otto S. Wolfbeis

Institute of Analytical Chemistry
Chemo- and Biosensors
University of Regensburg
93040 Regensburg
Germany
otto.wolfbeis@chemie.uni-regensburg.de

Aims and Scope

Fluorescence spectroscopy, fluorescence imaging and fluorescent probes are indispensible tools in numerous fields of modern medicine and science, including molecular biology, biophysics, biochemistry, clinical diagnosis and analytical and environmental chemistry. Applications stretch from spectroscopy and sensor technology to microscopy and imaging, to single molecule detection, to the development of novel fluorescent probes, and to proteomics and genomics. The *Springer Series on Fluorescence* aims at publishing state-of-the-art articles that can serve as invaluable tools for both practitioners and researchers being active in this highly interdisciplinary field. The carefully edited collection of papers in each volume will give continuous inspiration for new research and will point to exciting new trends.

Preface

Live-cell investigations to a great extent rely on far-field optical microscopy techniques such as wide-field, or confocal microscopy, because fluorescence detection of tagged molecules such as proteins offers large specificity and sensitivity and lens-based far-field optics allows the observation of the cellular interior with minimal invasion. Over the centuries, major efforts have been exerted to improve the resolution of far-field light microscopy, which for long meant perfecting lenses and other optical elements. The limits of this strategy became evident with the discovery of the diffraction barrier in the nineteenth century. From then onwards, it was clear that light cannot be focused to a spot smaller than about half the wavelength of light, i.e., to about 200–300 nm. This meant that molecules, such as proteins, or any other features that are closer together than this range, cannot be discerned. For example, protein distributions cannot be visualized at smaller scales in a cell. The diffraction barrier clearly impeded the applicability of far-field optical microscopy in the life sciences. Therefore, over the decades, efforts have been undertaken to overcome this major limitation, but it was not until at the end of the twentieth century that this barrier was overcome. Since then, a multitude of super-resolution far-field fluorescence microscopy or nanoscopy techniques have been developed, such as STED, GSD, RESOLFT, (f)PALM, (d)STORM, GSDIM, etc., and it has become clear that lens-based fluorescence microscopes can resolve features at the nanometer scale.

At their very basis, all current fluorescence nanoscopy techniques share the same operational principle: nearby sample molecules are no longer discerned just by the phenomenon of focusing light but by prompting them to briefly assume (at least) two different states. Usually, the (two) states that are selected for separation are a fluorescence on- and an off-state. In other words, turning molecules on and off is employed so that the signal does not stem from all molecules simultaneously. Thus, the use of two different states for molecular distinction renders nearby objects distinguishable when illuminated by the same diffraction pattern, yielding images with nanoscale resolution.

Unfortunately, even up to date, there is a lot of confusion about the basics, similarities, and differences of the various nanoscopy approaches, as well as about

their potential. Parts of these concerns are based on contingent issues such as an increased setup complexity, phototoxicity, and demands on labeling. Yet, recent years have seen major improvements, allowing the widespread onset of turn-key optical nanoscopes into open facilities of biological institutes. Here, a major drive has been the developments in lasers and optics technology but specifically also in labeling techniques.

As a matter of fact, in optical nanoscopy, fluorescent labels must fulfill two roles. First, they have to highlight the structures of interest, giving bright signal that may be distinguishable from other molecular tags. Secondly, the labels have to provide the pair of different states, say the on- and off-states required for discerning nearby molecules. Therefore, it is the symbiosis of molecular tags and optical design that makes the microscopes of today sharp and bright.

This book tackles all of the above issues. In 11 chapters distinguished scientists and leaders in the respective fields elaborate on the basics of the different nanoscopy approaches and their recent advancements, on improved labeling technology, as well as give an overview of representative applications.

The first part of the book introduces different optical nanoscopy approaches. Chapter "STED Fluorescence Nanoscopy" (by C. Eggeling and S. W. Hell) introduces STED microscopy, the earliest far-field fluorescence nanoscopy approach. The chapter describes the advances that have overcome initial system complexities, resulting in multiple applications of this technique. Chapter "Super-Resolution Imaging Through Stochastic Switching and Localization of Single Molecules: An Overview" by X. Zhuang and co-workers introduces the STORM approach, guiding the reader through the basics and selected applications of this technique and of the related approaches (f)PALM, GSDIM, etc. In chapter "A Practical Guide to dSTORM: Super-Resolution Imaging with Standard Fluorescent Probes", the approach called dSTORM by M. Sauer is presented. Similar to GSDIM or blink microscopy, the great achievement here was the investigation of how to implement any organic dye or fluorescent protein into the concept of STORM/(f)PALM, which were initially restricted to a certain class of photoswitchable dyes. Specifically, in dSTORM dedicated buffer conditions for mounting of samples have been developed.

The second part of the book focuses on the demands that optical nanoscopy has put on the fluorescence labels. Chapter "Single-Molecule Photocontrol and Nanoscopy" by W. E. Moerner and co-workers depicts the development of eYFP and novel photoactivatable organic dyes for their use in (d)STORM/(f)PALM type of nanoscopy. Chapter "Probes for Nanoscopy: Fluorescent Proteins" by U. Nienhaus and co-workers provides an overview of fluorescent proteins, with a special focus on their usage in optical nanoscopy. In chapter "Tailoring Fluorescent Labels for Far-Field Nanoscopy", D. A. Yushchenko and M. P. Bruchez highlight the advances in fluorophore development for a range of existing techniques. Emphasis is placed on the requirements these distinct methods demand from the fluorophores in order to maximize resolution, particularly in live-cell imaging. P. F. Aramendia and M. L. Bossi (chapter "Probes for Nanoscopy: Photoswitchable Fluorophores") discuss on how photochromic organic dyes can be designed to fulfill the

requirements of a suitable probe for different fluorescence nanoscopy strategies. In chapter "Far-Field Nanoscopy with Conventional Fluorophores: Photostability, Photophysics, and Transient Binding", P. Tinnefeld and his team give an overview of their work on using conventional organic fluorophores for (d)STORM/(f)PALM type nanoscopy, with a special focus on the importance and principles of photostability and blinking characteristics of these probes.

The third part gives specific developments and selected applications. In chapter "NASCA Microscopy: Super-Resolution Mapping of Chemical Reaction Centers" J. Hofkens, B.J. Roeffaers and co-workers introduce their concept of NASCA nanoscopy to visualize single chemical reaction centers with sub-diffraction resolution using special fluorogenic probe molecules. M. H. Ulbrich (chapter "Counting Molecules: Toward Quantitative Imaging") shows how single-molecule fluorescence can be used to analyze protein–protein interactions by enabling the direct visualization of protein complexes and the number and species of their constituent subunits. Finally, in chapter "In Vivo Tracking of Single Biomolecules: What Trajectories Tell Us About the Acting Forces" M. Brameshuber and G. J. Schütz introduce the reader to the concept of the tracking of single biomolecules in living cells, and how their trajectories can report on acting forces, e.g., by the underlying cytoskeleton.

Emerging nanoscopy techniques are flourishing and have started revealing exciting new biology, such as insights of the cytoskeleton, protein complexes, or virus maturation. Meanwhile, fluorescence nanoscopes are commercially available and new probes are developed at fast pace. The collection of chapters in this book can present only a glimpse on these exciting developments. The work presented, however, gives a good overview into different approaches of this interdisciplinary and rapidly developing field. Fluorescence nanoscopy involves a new physics and new chemistry to reveal new biology! We are grateful to the authors for their outstanding contributions and believe that the book will be stimulating for the community of microscope developer, microscopy users, and all interested readers.

Braunschweig, Germany — Philip Tinnefeld
Oxford, UK — Christian Eggeling
Göttingen, Germany — Stefan W. Hell

Contents

Part I
Optical Nanoscopy Techniques

STED Fluorescence Nanoscopy

Christian Eggeling and Stefan W. Hell

Abstract The turn of the twenty-first century has witnessed the advent of far-field (lens-based) fluorescence nanoscopy, a fluorescence microscopy featuring a spatial resolution down to molecular scales. Lens-based optical microscopy is a very popular technique for investigating the living cell, but the spatial resolution of its standard versions is limited to about 200 nm due to diffraction, impeding the imaging of molecular assemblies at smaller scales. Being the first of such nanoscopy techniques, STED microscopy was for a long time considered as a very complex technique, hard to apply in everyday biological research. However, recent years have seen major improvements of the STED nanoscopy approach, and STED microscopes are becoming increasingly widespread, nowadays providing turnkey sub-diffraction resolution imaging in open imaging facilities. Based on recent publications, we give a brief overview of some of the improvements that made these developments possible, a short insight into successful applications, as well as a brief comparison to other far-field fluorescence nanoscopy techniques.

Keywords Optical nanoscopy · Optical super-resolution microscopy · STED microscopy

C. Eggeling (✉)
MRC Human Immunology Unit and Wolfson Imaging Centre Oxford, Weatherall Institute of Molecular Medicine, University of Oxford, Oxford OX3 9DS, UK
e-mail: christian.eggeling@rdm.ox.ac.uk

S.W. Hell
Department of Nanobiophotonics, Max-Planck-Institute for Biophysical Chemistry, Am Fassberg 11, 37077 Göttingen, Germany

P. Tinnefeld et al. (eds.), *Far-Field Optical Nanoscopy*,
Springer Ser Fluoresc (2015) 14: 3–26, DOI 10.1007/4243_2014_75,

Contents

1 Introduction

Optical far-field microscopy such as confocal scanning microscopy is invaluable for cell biology, since it facilitates the investigation of the interior of living cells with minimal invasion. Especially the combination with fluorescence detection of tagged molecules offers unique specificity and sensitivity when imaging molecular organizations in cells [1]. However, far-field microscopy employs lenses for focusing the light in use, which comes at a major cost. Due to diffraction, light cannot be focused to an infinitely small spot, which for visible light amounts to a lower limit of about 200 nm. As a consequence of this limitation, objects of the same kind that are closer together than 200 nm cannot be discerned and details such as subcellular protein distributions can be visualized only down to about this scale [2, 3]. The nanoscale, which is the actual scale of relevance for protein distributions, remains obscured.

Following the initial demonstration and application of stimulated emission depletion (STED) microscopy, the last decade has seen a strong interest in developing far-field fluorescence nanoscopy or "super-resolution" approaches, affording a huge increase in spatial resolution. Thus, over the last decade, nanoscopy variants arose, featuring acronyms such as GSD, RESOLFT, STORM, (f)PALM, PALMIRA, GSDIM, dSTORM, etc. (see, e.g. [3–28]). In all these techniques, the features that are closer together than the diffraction barrier are discerned by getting their fluorophores transiently in two discernible states, i.e. states of different fluorescence emission characteristics, such as a dark OFF and a bright ON state. The transition between an ON and an OFF state ensures that the measured signal only stems from molecules within a region of the sample that is much smaller than 200 nm [3, 7, 9, 21, 28]; in the extreme case, it is (the region covered by) a single molecule.

Based on recent reviews and articles [21, 28–30], we here briefly review advances of STED nanoscopy which have put this technique into the position to be highly versatile for the observation of living cells, more and more finding its way into state-of-the-art optical imaging facilities in biomedical research institutes. We discuss earlier technical limitations and show how these were overcome in the course of recent development. Last but not least, we compare STED with other optical far-field nanoscopy approaches.

2 STED Nanoscopy: The Basics

STED (stimulated emission depletion) nanoscopy was proposed in 1994 [4] and first realized in 1999 and 2000 [31, 32]. It uses stimulated emission to reversibly silence fluorophores in predefined regions in the sample to facilitate separation at sub-diffraction length scales. In a typical implementation of STED nanoscopy, a laser is added to a scanning (confocal) far-field microscope, which forces excited fluorophores to their dark ground state, i.e. inhibits fluorescence emission (Fig. 1). The wavelength of this second laser is tuned to the red edge of the fluorophore's emission spectrum so that it stimulates the de-excitation of the fluorophore, i.e. causes the transition from the fluorescent ON state (the electronically excited state) to the dark OFF state (the ground state). By detecting only the spontaneous (and not the stimulated) emission, the signal that can be registered from a fluorophore is decreased and completely switched off when increasing the intensity of the STED laser above a threshold at which the optical de-excitation is nearly certain. The introduction of a wavefront-modifying optical element (phase plate) into the STED beam creates, once focused by the microscope objective, an intensity distribution which features one (or even several) local zero(es), such as a doughnut-shaped intensity distribution (Fig. 1). While this intensity pattern is still ruled by diffraction, large STED laser intensities force the area in which fluorophores are not effectively confined to the ground state to sub-diffraction scales. The observation region and thus the spatial resolution of the STED microscope are therefore tuned by the intensity of the STED laser. Scanning of the overlaid laser beams creates images with sub-diffraction resolution (Fig. 2). STED nanoscopy has achieved imaging with a spatial resolution of down to 20 nm in (living) cells and down to about 70 nm in vivo (upper brain layers of living mice) and <5 nm in solid materials (diamond crystals) [3, 28, 32–44].

3 STED Nanoscopy: Technical Concerns

To realize optically driven de-excitation from the excited ON to the OFF state, relatively large intensities of the added STED laser have to be employed (compare Fig. 1). This is because the stimulated emission process has to outperform the

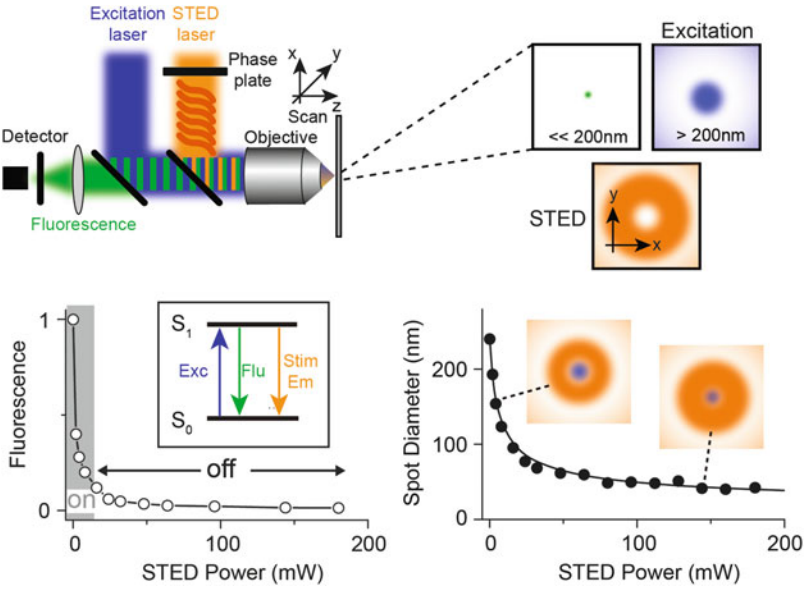

Fig. 1 Principles of STED nanoscopy. (*Upper panel*) Schematic drawing of the setup of a STED nanoscope with the microscope objective which focuses the excitation laser (*blue*) and the STED laser (*orange*), and collects the fluorescence signal (*green*) for detection, and a three-dimensional (*x*, *y*, *z*) scanning device for moving the sample relative to the laser light. The excitation laser renders an ordinary diffraction limited focal spot, while the STED laser passes through a phase plate that realizes a focal intensity distribution with a local zero, such as a doughnut-like pattern, creating an effective excitation volume much below the diffraction limit. (*Lower left panel*) When electrons are excited (Exc), the STED laser inhibits fluorescence (Flu) by de-exciting the excited state (S_1) to the ground state (S_0) via stimulated emission (Stim Em). Increasing the power of the STED laser over a certain threshold effectively precludes the occupation of the excited state S_1. (*Lower right panel*) Sub-diffraction volumes to which the occupation of the excited state and hence fluorescence emission is restricted are created by driving the STED laser intensity up, and the volume's size decreases with increasing STED laser power. Adapted from Clausen et al. [30]

usually <4-ns fast spontaneous fluorescence decay. Therefore, a concern has been that the STED laser might introduce phototoxic effects, such as photobleaching of the fluorescent labels, production of radicals, light-induced cell death, heating or optical trapping. As a consequence, STED nanoscopy was long thought to be incompatible with live-cell recordings.

Furthermore, a STED nanoscope was long considered difficult to be set up, mainly due to a complex alignment of the STED and excitation lasers, as well as the realization of the local intensity zero(s) in the focused STED beam. In addition, STED nanoscopy was originally implemented with pulsed lasers. This configuration realizes the most efficient fluorescence inhibition per given average power, since it ensures the most appropriate STED action in terms of high laser peak intensity and timing [31, 33, 35, 45]. However, this pulsed modality requires synchronization of the excitation and STED lasers and the use of complex and

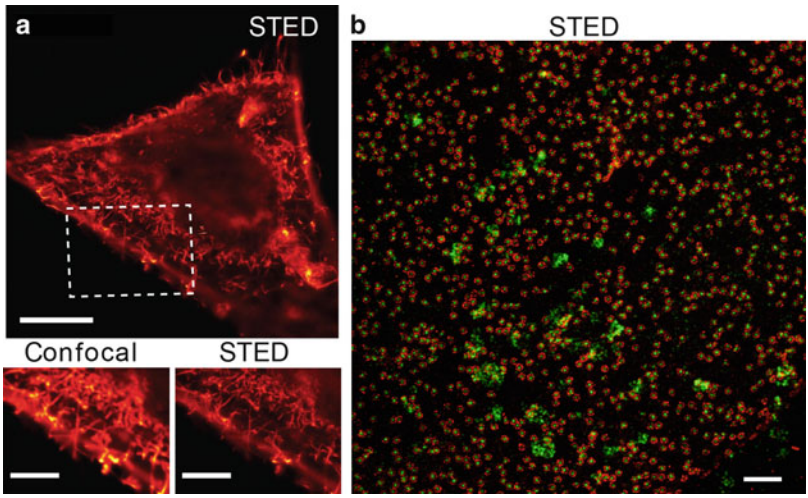

Fig. 2 STED imaging. (**a**) STED image of immunolabelled microvilli at the cell surface of fixed HeLa cells. *Scale bar*: 5 µm. (*Lower panels*) Confocal and STED close-ups of the marked area of the cell. *Scale bar*: 1 µm. Adapted from Clausen et al. [30]. (**b**) Multicolour STED image of immunolabelled subunits (peripheral transmembrane protein gp210 (*red*) and pan-FG protein (*green*) in the central pore channel) in amphibian nuclear pore complexes (NPC) of cultured *Xenopus* cells. *Scale bar*: 500 nm. Adapted from Göttfert et al. [33]

costly laser assemblies. Initially, broadly tunable mode-locked laser systems were used [31, 35]. The use of fluorescent labels such as Alexa488 and the green fluorescent protein, which are optimized for blue excitation around 488 nm, puts a demand on optimum STED wavelengths around 560–600 nm, supplied by complex laser systems such as optical parametric oscillators (OPO) pumped by a titanium–sapphire laser system [46, 47]. These issues led to the impression that STED nanoscopy could only be realized in a few laboratories.

4 STED Nanoscopy: Advancements

4.1 Laser Technology

In its early days, the preferred STED microscopy modality has been the use of ~80 MHz femtosecond pulsed Ti:Sa lasers for STED and optoelectronically triggered laser diodes for excitation. Besides an exact timing of both lasers, this requires stretching of the Ti:Sa pulses to 100–300 ps to optimize the timing and efficiency of the stimulated emission relative to the usually 80–100-ps-long excitation pulses and to minimize bias due to, for example, non-linear photobleaching via higher excited electronic states and direct excitation by the STED light [45, 48,

49]. Originally realized on custom-built setups only, this Ti:Sa-based STED modality was pursued on the first commercial systems [50–52] and in some retrofitted commercial confocal systems [30].

In a first attempt to reduce complexity and cost of the pulsed STED approach, the wavelength tunability of the STED laser was sacrificed. For example, the use of single-wavelength pico- or nanosecond laser modules allows cutting costs [53, 54], and their high pulse peak powers have facilitated imaging with spatial resolutions of $<$15 nm [33, 55]. The concomitant size reduction of the laser system has allowed the design of compact, commercially available setups [30]. Recently, pulsed lasers at wavelengths around 760–780 nm have been developed that offer another reasonable alternative to the Ti:Sa laser, since they for the first time introduce the possibility of externally triggering the STED laser's repetition rate [30]. The arise of stable and powerful white-light lasers on the other hand opened up large flexibility by offering the access to a wide wavelength range of already synchronized STED and excitation laser lines [38, 56–60]. Similarly, a 530-nm pico- or nanosecond microchip or fibre-amplified, frequency-doubled laser was coupled into a standard single-mode fibre to produce a tunable spectrum of discrete peaks between 530 nm and 620 nm via stimulated Raman scattering (SRS). This again allowed a flexible choice of STED laser wavelengths demonstrating STED nanoscopy with spatial resolution down to 20–30 nm [61–63].

A huge simplification to STED nanoscopy has been introduced by realizing it with continuous-wave (CW) lasers, making laser pulse preparation redundant [64]. Initially realized with strong argon–krypton lasers [64] or Ti:Sa lasers operating in continuous-wave (CW) mode [65, 66], CW-STED nanoscopy has now been demonstrated with compact fibre lasers [67–69] or diode-pumped solid-state (DPSS) lasers [70–72] on a commercial system [30, 39]. However, CW-STED nanoscopy lags somewhat behind its pulsed STED counterpart in performance [45]. This mainly follows from the lower instantaneous probability of stimulated de-excitation of the CW-STED modality. In the pulsed STED mode, the synchronized excitation and STED pulses realize an instantaneous and thus optimized efficiency of fluorescence ON–OFF switching, since the pulses of the STED beam reach the focal plane virtually simultaneously with or a few picoseconds after the excitation pulses so as to instantly excite and inhibit fluorescence emission, respectively. Consequently, approximately three- to fivefold higher average laser powers have to be applied for CW-STED. The exact factor depends on the repetition rate of the pulsed lasers and the fluorescence lifetime of the fluorescent label. Previous examples have reported 800 mW in the CW compared to 160 mW in the pulsed case [64, 65]. Furthermore, in the CW-STED modality, a non-negligible part of the molecules emits fluorescence before having been exposed to much of the STED light, and thus residual fluorescence outside the zero-intensity point of the STED light leads to a pedestal in the effective (sub-diffraction sized) region of observation, resulting in increased image blur [45]. A remedy to these limitations is the use of a CW-STED laser in combination with a pulsed excitation laser and a gated detection scheme [73–75]. This still avoids careful synchronization of laser pulses and allows the use of compact and less costly STED laser systems. In

addition, it eliminates aforementioned blurring and reduces the required powers of the CW-STED light. For example, only 80–150 mW of average laser power have been applied in previous gated-STED (gSTED) live-cell experiments [74]. This gSTED design has paved the way to a compact design of the STED nanoscope and a stable commercial turnkey STED nanoscope [30]. Gated detection can either be realized through an electronic trigger box, synchronizing the gating of the detectors to the pulsing of the excitation laser, by applying custom-built electronics that simply filter the electronic pulses from the fluorescence detectors according to their timing with respect to the excitation pulsing, or by software processing the acquired data [74]. The latter approach allows a straightforward optimization of the gating position, which may become especially important given that gated detection also suppresses desired signal [74, 76]. Hence, relocation of the time gating may tune acquired data, weighing the optimized STED-imaging performance against a decreased signal-to-noise ratio [76]. Optimization of gSTED nanoscopy further depends on the noise levels of the CW laser sources [77], while gated detection can also be used to remove unwanted background signal, for example, caused by the STED laser [49, 78].

4.2 Setup Complexity

Yet more compact STED setups have been created by using optimized phase plates for realizing the focal intensity distribution of the STED laser [59, 79]. For example, an approach termed easySTED uses a special phase plate that can be introduced into the combined excitation and STED laser path, which selectively modulates only the STED beam, reducing alignment requirements and mechanical drifts [59] and also providing sub-diffraction resolution images of molecular orientation [79]. Adaptive optics on the other hand offers straightforward approaches for an automated alignment and aberration–correction of especially the STED beam [80, 81].

4.3 Phototoxicity

Typical intensities of the STED laser are 1–10 MW/cm^2 at around 740–780 nm as supplied by 100–300 mW average power of an approximately 100–300-ps-long pulses of a Ti:Sa laser or 80–150 mW of 570–590-nm CW light for the gSTED modality. These intensities are much higher than those of the excitation light, whose average power is usually around 1–10 μW. Once photons are absorbed, raising molecules to higher levels, such intensities oftentimes induce toxic reactions through elevated heating or bleaching. As a consequence, laser-induced phototoxic effects are a critical concern in STED microscopy. From theory, however, the STED light per se is not absorbed by the fluorescent label or sample and thus, in

this concept, should not produce any photo-reactive and thus toxic species. Rather, stimulated emission should reduce photobleaching by shortening the time the fluorescent label spends in its excited (reactive) state (compare with Eggeling et al. [82]). Undesirably, the STED laser light is occasionally also absorbed by the excited states of the fluorophores, being – as for all types of fluorescence microscopy [83] – the main reason for photobleaching in STED microscopy [35, 63, 84, 85]. However, two approaches have shown to minimize these effects. (1) Fast scanning of the laser beams reduces the population of usually very vulnerable long-lived dark states, such as the triplet state, and minimizes further excitation and photobleaching thereof [35, 68, 86, 87]. (2) A careful choice of the STED laser wavelength was shown to minimize excited-state absorption [63, 85]. We note that the involved peak intensities are lower by two orders of magnitude than those used in two-photon microscopy [88], which is a well-established live-cell microscopy technique [89]. In addition, in two-photon microscopy, the laser light is explicitly absorbed by the fluorescent labels, introducing photobleaching reactions in the focal centre, again mainly due to excited-state absorption [82, 90]. With these considerations in mind, live-cell [47, 68, 74, 91, 92] and even in vivo [93] STED imaging using fluorescent proteins were straightforward.

4.4 Labelling

A low probability of excited-state absorption at the wavelength of the STED laser is one of the priorities when designing novel fluorescent labels optimized for STED nanoscopy. In recent years, a whole palette of fluorescent labels has been designed and tested for common live-cell STED recordings [29, 94–96], ranging from organic dyes for immuno- [29, 94] and related labelling approaches [40], as well as for single-molecule imaging [97] and specifically for gSTED microscopy [98], to fluorescent proteins [47, 52]. Unfortunately, the photostability and brightness of fluorescent proteins is oftentimes not sufficient enough. This usually is the reason for resorting to organic-dye-based live-cell tagging using, for example, the Halo, Snap or Clip and similar technologies [37, 50, 51, 99, 100]. In addition, coming along with the increased sensitivity of the nanoscopy approach, greater care should be exerted when labelling cellular samples, especially with respect to unspecific background staining [101]. In general, larger care has to be taken for accurate labelling in all optical nanoscopy techniques, since artefacts due to, for example, improper fixation in immunolabelling or unspecific binding may not be observed in confocal but may be visible in nanoscopy images, due to the improved spatial resolution in the latter [40, 102].

4.5 Multicolour Recordings

Many cell imaging applications require the use of molecule-specific tags with different fluorescence emission properties, such as well-separated emission ranges or colours. In this way, the relative sites and proximities of different molecules can be determined. The large number of fluorescent labels available for STED nanoscopy has enabled multicolour recordings (Fig. 2b). One approach for multicolour STED imaging is the use of two labels with overlapping emission spectra but with a long (Stokes) shift between the excitation and emission spectra of one of the labels. This approach allows the recording of two-colour images with only one STED laser, which serves both labels, while the use of two distinct excitation lasers realizes colour separation [30, 37, 39, 103, 104]. This avoids the supply of a multitude of additional STED lasers, one for each label, which usually comes along with a complex alignment of all laser beams and the cross-photobleaching of the more red-emitting dyes by the blue-shifted STED lasers. As a consequence, initial multicolour STED experiments using such multitude of lasers were only capable of one-time subsequent recordings of multiple colours [105, 106]. Not many long-Stokes-shifted fluorescent labels suitable for STED have been identified so far; they could be avoided by carefully choosing two ordinary dyes with normal Stokes shifts whose spectra differ by less than 60 nm [43, 44, 104, 107–110]. In this scheme, the number of distinguishable labels was increased to four by separating the emission based on emission wavelength and lifetime [111]. Similarly, two-colour STED images were recorded by applying two conversely reversible photoswitchable fluorescent proteins [112].

4.6 Dynamics

STED nanoscopy has also enabled the observation of fast molecular dynamics in living cells. Using ultrafast scanners, as usually already provided in commercial instrumentation, and acquiring a few micrometres-sized field of view only, images with down to 60-nm spatial resolution were acquired with frame rates of up to 80 Hz [113, 114]. This reveals STED as the currently fastest fluorescence nanoscopy approach. Image acquisition can be accelerated by using multiple overlaid excitation and STED spots as recently realized for up to 4 pairs of scanning excitation and STED beams [115], or even more spots using crossed standing wave pairs [116]. While the requirement in laser power puts an upper limit in the feasible number of parallel spots for STED, the use of reversible photoswitchable fluorescent labels in a STED-microscopy-like fashion requires much lower laser powers [10]. In such RESOLFT (reversible saturable optical fluorescence transitions) nanoscopy [6], the use of reversible photoswitchable fluorescent proteins has thus realized sub-diffraction live-cell recordings with 1 kW/cm^2 of laser powers only [117–119] and paved the way for using more than a 1,000 doughnuts for ultrafast

live-cell imaging of large field of views with down to 70-nm spatial resolution [120]. Similarly, lower laser intensities than in STED microscopy are needed when transiently shelving fluorescence labels into a dark state, as already theoretically introduced in 1995 [5]. Termed ground-state-depletion (GSD) nanoscopy, an experimental realization in 2007 confirmed that in principle any reversible switchable on–off state transition can be employed to achieve imaging with sub-diffraction spatial resolution [121]. As for RESOLFT, the lower laser powers required for GSD nanoscopy allowed image recordings using multiple observation spots in parallel [122]. Yet, the applicability of GSD nanoscopy for live-cell microscopy has so far been hampered due to the limited numbers of ON–OFF transitions stemming from the use of usually photolabile dark states as OFF states.

4.7 Three-Dimensional Imaging

Many applications require imaging with superior resolution along all three dimensions (x, y and z). So far, we have discussed STED nanoscopy with resolution improved along all directions in the focal plane (x, y) only. The combination of STED with an evanescent wave excitation scheme (total internal reflection, TIRF) [123, 124] may be sufficient for 3D nanoscopy of membranes or flat cells, but does not allow the investigation of intracellular structures such as the Golgi apparatus or mitochondria. TIRF microscopy confines imaging to a thin layer in the sample that is close to the surface of a medium generating the evanescent wave, but does not improve the z-resolution. STED nanoscopy using two-photon excitation enables imaging in sections with deep penetration depths [42, 44, 66, 67, 69, 125] but does not provide diffraction-unlimited 3D imaging. To that end, STED nanoscopy has been adapted with different phase plate assemblies, which directly created the desired restriction of fluorescence generation along all spatial directions [43, 58, 126–128]. The implementation of adaptive optics has allowed 3D imaging in optically more challenging specimens such as tissues [80]. Technically more complex setups have been realized using two opposing high-aperture objective lenses [103, 129–132] or by the combination with single-plane-illumination microscopy (SPIM) [133].

4.8 Beyond Imaging

STED nanoscopy also improves single-molecule-based fluorescence spectroscopy methods, improving the investigation of molecular interactions at the nanoscale. This has recently been shown by combining it with fluorescence correlation spectroscopy (FCS) [134, 135]. In such STED-FCS experiments, the fluctuating intensity data was analysed as labelled molecules moved in and out of the non-scanned observation volume. Most importantly, the unique capability of STED microscopy

to record FCS data for different sizes of the observation volume below the diffraction limit allowed disclosing heterogeneity in the observed diffusion characteristics and revealing how molecules interacted on the nanoscale [36, 136–138]. Applications of STED-FCS range from the disclosure of different diffusion modes and interaction dynamics of different lipid analogs in the plasma membrane of living cells [36, 136–141] as well as in model membranes [142], over novel insights into lipid rafts [136, 138, 140, 143, 144] and membrane protein organization and dynamics [36, 145–147], to an accurate determination of critical fluctuations of polymers [148]. Recent technological advancements in the STED-FCS approach included its combination with time-gated detection [74, 149] and fast beam scanning [144, 145, 150, 151], offering the observation of more details of spatio-temporal characteristics of molecular interactions [144, 149]. A remaining task is the setup of multicolour STED-FCS (such as the combination of fluorescence cross-correlation spectroscopy, FCCS [152], with STED), allowing on the identification of binding partners of the aforementioned molecular interactions.

5 Comparison with Other Nanoscopy Approaches

Based on the same principle for feature separation, namely, keeping all but one feature dark through molecular OFF states (Fig. 3), a different nanoscopy approach arose in 2006 and a multitude of acronyms as a result: stochastic optical reconstruction microscopy (STORM) [11], (fluorescence) photo-activated localization microscopy ((f)PALM) [12, 13], ground-state-depletion *microscopy* followed by individual molecule return (GSDIM) [17], direct STORM (dSTORM) [18] or single-molecule active-control microscopy (SMACM) [153]. This approach relies on the stochastic on and off switching of the fluorescence emission of individual labels within the diffraction limit, combined with the determination of their exact spatial positions. In contrast, STED/RESOLFT/GSD uses a deterministic switching approach where the fluorophore ON and OFF states are assumed at predefined positions (Fig. 3).

In the spatially stochastic (d)STORM/(f)PALM/GSDIM approaches, usually a large area of the sample is illuminated all at once, and the spatial distribution of labelled molecules is determined by imaging the fluorescence onto a camera. Normally, similar details that are closer together than 200 nm cannot be distinguished, since the fluorescence image of a single emitter is blurred on the camera due to diffraction. By inhibiting the fluorescence emission of most of the labels, only single molecules per diffraction area or volume are allowed to fluoresce at a given time (by random ON switching or activation), thus allowing the separation of the feature containing the ON-state molecule from their surrounding features. As the position of the ON-state molecule is random, it has to be determined after the activation, which can be accomplished from the diffraction pattern on the camera using different localization (centroid calculation) approaches. By stochastically switching on and off a representative number of individual molecules within the

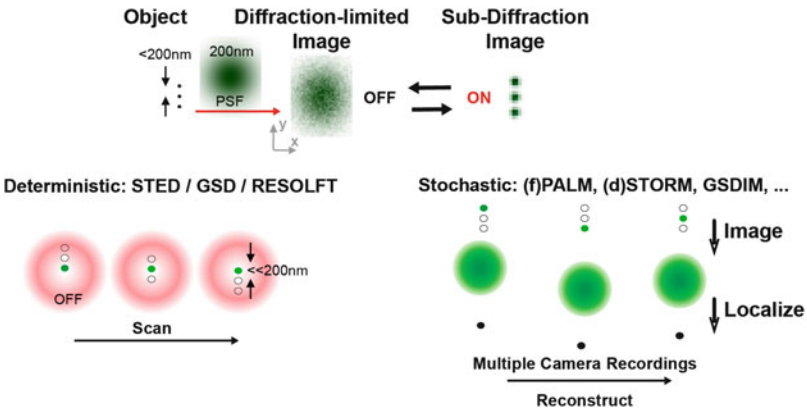

Fig. 3 Principle of different far-field fluorescence nanoscopy approaches. (*Upper panels*) Due to the diffraction of light, object details that are closer together than about 200 nm cannot be discerned when imaged with focused light (diffraction spot or point spread function PSF ~200 nm in diameter), resulting in blurred images. Sub-diffraction images are realized by switching the fluorescence ability of the fluorophores on and off either in a deterministic or stochastic manner, resulting in the ability to resolve structures <200 nm in size. (*Lower left panel*) In the usual application of deterministic methods such as STED, GSD or RESOLFT, a diffraction-limited spot of the fluorescence excitation (ON) laser beam is overlaid with a second laser beam which switches off fluorescence emission and which features at least one zero-intensity point. Consequently, the off-switching light selectively inhibits fluorescence everywhere but at the zero-intensity points, creating observation spots of nanoscopic size. Scanning fluorescence images therefore feature a considerable improvement in spatial resolution. (*Lower right panel*) Stochastic methods such as (f)PALM, (d)STORM, GSDIM, etc. are usually based on the recording of multiple wide-field images using a sensitive camera. During these recordings only single molecules within the diffraction range are allowed to fluoresce in order to facilitate separation of the features. The position of the molecules is found while the molecules are in the ON state, emitting multiple fluorescent photons and allowing the position to be determined using different localization approaches. By stochastically switching on and off all molecules during the recordings, the final image with sub-diffraction-sized spatial resolution is reconstructed from the summation of all identified molecules. Adapted from Eggeling et al. [28]

diffraction zone in subsequent camera recordings, the final image with sub-diffraction-sized spatial resolution is reconstructed from the summation of all localized spatial positions. It should be kept in mind that localization per se cannot provide sub-diffraction spatial resolution: separating object details at small distances requires a criterion to discern them from one another. Again, in these stochastic methods, the separation is accomplished by transferring the fluorophores between a fluorescent on and off state [3–5, 154–156]. This is why although it had been routinely applied for decades, specifically for spatio-temporal tracking of single isolated molecules (see, e.g. Kusumi et al. [157]), localization alone could not provide images with sub-diffraction resolution. The matters changed, though, when an OFF state was introduced for precluding fluorescence emission of molecules that are exposed to excitation light.

Both spatially stochastic and deterministic fluorescence nanoscopy approaches have their specific advantages and disadvantages with respect to photobleaching, setup complexity, imaging speed or image reconstruction. For instance, a direct image of the spatial distribution of labelled molecules is formed in the scanning approach of the deterministic STED/GSD/RESOLFT nanoscopes, whereas a reconstruction algorithm based on the identification and localization of single isolated molecules needs to be employed to create the final image in the stochastic (d) STORM/(f)PALM/GSDIM approaches. Potential bias to the latter reconstruction process may arise, for example, from a lack of knowledge of missed or repeated recordings of molecules [158, 159]. Furthermore, the concentration of ON-state molecules has to be controlled at any given point in time. Also, the determination of molecular positions may be biased for out-of-focus molecules [160, 161]. Quite a number of improvements in the identification and localization algorithms have therefore been developed over the past years, aiming at image reconstructions for more densely labelled samples and/or those having low signal-to-noise levels (see [162–176]).

Photobleaching of the fluorescent labels is an issue in deterministic-based nanoscopy, because the fluorescence ability of the fluorophores has to be switched on and off multiple times during the scanning type of recording. In stochastic-based methods, a molecule needs to be switched on and off only once, at least in principle, and then molecular bleaching is randomly distributed over the sample. Random molecular bleaching makes bleaching appear less of an issue than in the deterministic approaches where imaging breaks down when bleaching dominates. On the other hand, the image acquisition time of the stochastic (d)STORM/(f)PALM/GSDIM approaches is limited by the need to on–off cycle a sufficient number of molecules for the image reconstruction. Despite the aforementioned recent improvements in reconstruction algorithms, there may always be an uncertainty as to whether a representative number of molecules have been recorded, i.e. of when to stop the acquisition (see, e.g. Shroff et al. [158] and Small [159]). This is different for deterministic-based STED/GSD/RESOLFT approaches, where the scanning process defines the acquisition time. As pointed out before, the use of fast beam scanners has established STED/RESOLFT nanoscopy as the currently fastest sub-diffraction imaging technique available, with up to 60–80 frames per second recording times for a few μm-sized observation areas [114, 119].

Importantly, as for STED/RESOLFT the stochastic (d)STORM/(f)PALM/GSDIM approaches can straightforwardly be expanded to multiple colour recordings and improved spatial resolution along all spatial directions (e.g. [177–182]). Since they are based on the same basic principle of switching fluorescence on and off, in a number of cases, the very same sample can be used for both spatially deterministic and spatially stochastic nanoscopy [17, 118, 121]. In view of the increased sensitivity and the potential aforementioned bias, both approaches can be applied for the validation of results.

Other microscopy approaches providing higher resolution such as 4Pi microscopy [183, 184] and so-called structured illumination microscopy (SIM) [185, 186] achieve a twofold improvement in spatial resolution in the focal plane for SIM and

five- to sixfold improvement in axial resolution for 4Pi. However, their spatial resolution is still limited by diffraction, since they only push the spatial resolution to the limits of the diffraction barrier. So far, only the use of a transition between two distinguishable states, typically the use of a (transient) state in which fluorescence is not possible, has overcome these limits in a generally applicable imaging system [6, 116, 120, 129, 187–190]. The fact that these fluorescence nanoscopy or super-resolution variants oftentimes complement each other in their applications promotes research environments which can easily access a whole range of microscopes and nanoscopes, depending on their suitability for the case in hand.

6 Conclusion

In this review we have highlighted how recent developments in STED nanoscopy have fundamentally improved its use in day-to-day cellular research. It is to be expected that this will be further improved by ongoing developments in labelling, laser and optical technology, creating more and more flexible, compact and less costly experimental realizations of this nanoscale imaging technique.

References

1. Pawley JB (2006) Handbook of biological confocal microscopy, 2nd edn. Springer, New York
2. Abbe E (1873) Beiträge zur Theorie des Mikroskops und der mikroskopischen Wahrnehmung. Arch Mikrosk Anat 9:413–468
3. Hell SW (2009) Microscopy and its focal switch. Nat Methods 6(1):24–32
4. Hell SW, Wichmann J (1994) Breaking the diffraction resolution limit by stimulated-emission - stimulated-emission-depletion fluorescence microscopy. Opt Lett 19(11):780–782
5. Hell SW, Kroug M (1995) Ground-state depletion fluorescence microscopy, a concept for breaking the diffraction resolution limit. Appl Phys B 60:495–497
6. Hell SW, Jakobs S, Kastrup L (2003) Imaging and writing at the nanoscale with focused visible light through saturable optical transitions. Appl Phys A 77:859–860
7. Hell SW (2003) Toward fluorescence nanoscopy. Nat Biotechnol 21(11):1347–1355
8. Hell SW (2004) Strategy for far-field optical imaging and writing without diffraction limit. Phys Lett A 326(1–2):140–145
9. Hell SW, Dyba M, Jakobs S (2004) Concepts for nanoscale resolution in fluorescence microscopy. Curr Opin Neurobiol 14(5):599–609
10. Hofmann M, Eggeling C, Jakobs S, Hell SW (2005) Breaking the diffraction barrier in fluorescence microscopy at low light intensities by using reversibly photoswitchable proteins. Proc Natl Acad Sci U S A 102(49):17565–17569
11. Rust MJ, Bates M, Zhuang XW (2006) Sub-diffraction-limit imaging by stochastic optical reconstruction microscopy (STORM). Nat Methods 3:793–795
12. Betzig E, Patterson GH, Sougrat R, Lindwasser OW, Olenych S, Bonifacino JS, Davidson MW, Lippincott-Schwartz J, Hess HF (2006) Imaging intracellular fluorescent proteins at nanometer resolution. Science 313(5793):1642–1645

13. Hess ST, Girirajan TPK, Mason MD (2006) Ultra-high resolution imaging by fluorescence photoactivation localization microscopy. Biophys J 91(11):4258–4272
14. Hell SW (2007) Far-field optical nanoscopy. Science 316(5828):1153–1158
15. Rice JH (2007) Beyond the diffraction limit: far-field fluorescence imaging with ultrahigh resolution. Mol Biosyst 3(11):781–793
16. Egner A, Geisler C, von Middendorff C, Bock H, Wenzel D, Medda R, Andresen M, Stiel A-C, Jakobs S, Eggeling C, Schoenle A, Hell SW (2007) Fluorescence nanoscopy in whole cells by asynchronous localization of photoswitching emitters. Biophys J 93:3285–3290
17. Fölling J, Bossi M, Bock H, Medda R, Wurm CA, Hein B, Jakobs S, Eggeling C, Hell SW (2008) Fluorescence nanoscopy by ground-state depletion and single-molecule return. Nat Methods 5:943–945
18. Heilemann M, van de Linde S, Schuttpelz M, Kasper R, Seefeldt B, Mukherjee A, Tinnefeld P, Sauer M (2008) Subdiffraction-resolution fluorescence imaging with conventional fluorescent probes. Angew Chem Int Ed Engl 47:6172–6176
19. Bates M, Huang B, Zhuang XW (2008) Super-resolution microscopy by nanoscale localization of photo-switchable fluorescent probes. Curr Opin Chem Biol 12(5):505–514
20. Fernandez-Suarez M, Ting AY (2008) Fluorescent probes for super-resolution imaging in living cells. Nat Rev Mol Cell Biol 9:929–943
21. Hell S (2009) Far-field optical nanoscopy. In: Gräslund A, Rigler R, Widengren J (eds) Single molecule spectroscopy in chemistry. Springer, Berlin, pp 365–398
22. Evanko D (2009) Primer: fluorescence imaging under the diffraction limit. Nat Methods 6(1):19–20
23. Huang B, Bates M, Zhuang X (2009) Super-resolution fluorescence microscopy. Annu Rev Biochem 78:993–1016
24. Heilemann M, Dedecker P, Hofkens J, Sauer M (2009) Photoswitches: key molecules for subdiffraction-resolution fluorescence imaging and molecular quantification. Laser Photon Rev 3(1–2):180–202
25. Chi KR (2009) Super-resolution microscopy: breaking the limits. Nat Methods 6(1):15–18
26. Dempsey GT, Vaughan JC, Chen KH, Bates M, Zhuang X (2011) Evaluation of fluorophores for optimal performance in localization-based super-resolution imaging. Nat Methods 8(12):1027–1036
27. Muller T, Schumann C, Kraegeloh A (2012) STED microscopy and its applications: new insights into cellular processes on the nanoscale. Chemphyschem 13(8):1986–2000. doi:10.1002/cphc.201100986
28. Eggeling C, Willig KI, Barrantes FJ (2013) STED microscopy of living cells - new frontiers in membrane and neurobiology. J Neurochem 126(2):203–212
29. Wurm CA, Kolmakov K, Göttfert F, Ta H, Bossi M, Schill H, Berning S, Jakobs S, Donnert G, Belov VN, Hell SW (2012) Novel red fluorophores with superior performance in STED microscopy. Opt Nanoscopy 1(7):1–7
30. Clausen MP, Galiani S, Bernardino de la Serna J, Fritzsche M, Chojnacki J, Gehmlich K, Lagerholm BC, Eggeling C (2013) Pathways to optical STED microscopy. NanoBioImag 1(1):1–12
31. Klar TA, Hell SW (1999) Subdiffraction resolution in far-field fluorescence microscopy. Opt Lett 24(14):954–956
32. Klar TA, Jakobs S, Dyba M, Egner A, Hell SW (2000) Fluorescence microscopy with diffraction resolution barrier broken by stimulated emission. Proc Natl Acad Sci U S A 97:8206–8210.
33. Göttfert F, Wurm CA, Mueller V, Berning S, Cordes VC, Honigmann A, Hell SW (2013) Coaligned dual-channel STED nanoscopy and molecular diffusion analysis at 20 nm resolution. Biophys J 105:L01–L03
34. Willig KI, Rizzoli SO, Westphal V, Jahn R, Hell SW (2006) STED microscopy reveals that synaptotagmin remains clustered after synaptic vesicle exocytosis. Nature 440(7086):935–939

35. Donnert G, Keller J, Medda R, Andrei MA, Rizzoli SO, Lurmann R, Jahn R, Eggeling C, Hell SW (2006) Macromolecular-scale resolution in biological fluorescence microscopy. Proc Natl Acad Sci U S A 103(31):11440–11445
36. Eggeling C, Ringemann C, Medda R, Schwarzmann G, Sandhoff K, Polyakova S, Belov VN, Hein B, von Middendorff C, Schonle A, Hell SW (2009) Direct observation of the nanoscale dynamics of membrane lipids in a living cell. Nature 457:1159-U1121
37. Pellett PA, Sun X, Gould TJ, Rothman JE, Xu M-Q, Correa IR Jr, Bewersdorf J (2011) Two-color STED microscopy in living cells. Biomed Opt Express 2(8):2364–2371
38. Blom H, Rönnlund D, Scott L, Spicarova Z, Widengren J, Bondar A, Aperia A, Brismar H (2011) Spatial distribution of Na + -K + -ATPase in dendritic spines dissected by nanoscale superresolution STED microscopy. BMC Neurosci 12:16
39. Friedemann K, Turshatov A, Landfester K, Crespy D (2011) Characterization via two-color STED microscopy of nanostructured materials synthesized by colloid electrospinning. Langmuir 27(11):7132–7139
40. Opazo F, Levy M, Byrom M, Schaefer C, Geisler C, Groemer TW, Ellington AD, Rizzoli SO (2012) Aptamers as potential tools for super-resolution microscopy. Nat Methods 9:938–939
41. Lau L, Lee YL, Sahl SJ, Stearns T, Moerner WE (2012) STED microscopy with optimized labeling density reveals 9-fold arrangement of a centriole protein. Biophys J 102:2926–2935
42. Takasaki KT, Ding JB, Sabatini BL (2013) Live-cell superresolution imaging by pulsed STED two-photon excitation microscopy. Biophys J 104:770–777
43. Osseforth C, Moffitt JR, Schermelleh L, Michaelis J (2013) Simultaneous dual-color 3D STED microscopy. Opt Express 22(6):7028–7039
44. Bethge P, Chereau R, Avignone E, Marsicano G, Nagerl UV (2013) Two-photon excitation STED microscopy in two colors in acute brain slices. Biophys J 104:778–785
45. Leutenegger M, Eggeling C, Hell SW (2010) Analytical description of STED microscopy performance. Opt Express 18(25):26417
46. Willig KI, Kellner RR, Medda R, Hein B, Jakobs S, Hell SW (2006) Nanoscale resolution in GFP-based microscopy. Nat Methods 3(9):721–723
47. Hein B, Willig KI, Hell SW (2008) Stimulated emission depletion (sted) nanoscopy of a fluorescent protein-labeled organelle inside a living cell. Proc Natl Acad Sci U S A 105 (38):14271–14276
48. Dyba M, Hell SW (2003) Photostability of a fluorescent marker under pulsed excited-state depletion through stimulated emission. Appl Opt 42(25):5123–5129
49. Vicidomini G, Moneron G, Eggeling C, Rittweger E, Hell SW (2012) STED with wavelengths closer to the emission maximum. Opt Express 20(5):5225–5236
50. Schröder J, Benink H, Dyba M, Los GV (2008) In vivo labeling method using a genetic construct for nanoscale resolution microscopy. Biophys J 96(1):L1–L3
51. Fitzpatrick JA, Yan Q, Sieber JJ, Dyba M, Schwarz U, Szent-Gyorgyi C, Woolford CA, Berget PB, Waggoner AS, Bruchez MP (2009) STED nanoscopy in living cells using fluorogen activating proteins. Bioconjug Chem 20(10):1843–1847
52. Morozova KS, Piatkevich KD, Gould TJ, Zhang J, Bewersdorf J, Verkhusha VV (2010) Far-red fluorescent protein excitable with red lasers for flow cytometry and superresolution STED nanoscopy. Biophys J 99:L13–L15
53. Westphal V, Blanca CM, Dyba M, Kastrup L, Hell SW (2003) Laser-diode-stimulated emission depletion microscopy. Appl Phys Lett 82(18):3125–3127
54. Schrof S, Staudt T, Rittweger E, Wittenmayer N, Dresbach T, Engelhardt J, Hell SW (2011) STED nanoscopy with mass-produced laser diodes. Opt Express 19(9):8066–8072
55. Rittweger E, Han KY, Irvine SE, Eggeling C, Hell SW (2009) Sted microscopy reveals crystal colour centres with nanometric resolution. Nat Photon 3:144–147
56. Auksorius E, Boruah BR, Dunsby C, Lanigan PMP, Kennedy G, Neil MAA, French PMW (2008) Stimulated emission depletion microscopy with a supercontinuum source and fluorescence lifetime imaging. Opt Lett 33(2):113–115

57. Wildanger D, Rittweger E, Kastrup L, Hell SW (2008) STED microscopy with a supercontinuum laser source. Opt Express 16(13):9614–9621
58. Wildanger D, Medda R, Kastrup L, Hell SW (2009) A compact STED microscope providing 3D nanoscale resolution. J Microsc 236:35–43
59. Wildanger D, Bückers J, Westphal V, Hell SW, Kastrup L (2009) A STED microscope aligned by design. Opt Express 17(18):16100–16110
60. Kastrup L, Wildanger D, Rankin B, Hell SW (2010) STED microscopy with compact light sources. In: Diaspro A (ed) Nanoscopy and multidimensional optical fluorescence microscopy. Chapman & Hall/CRC, Boca Raton, pp 1–13
61. Rankin BR, Kellner RR, Hell SW (2008) Stimulated-emission-depletion microscopy with a multicolor stimulated-Raman-scattering light source. Opt Lett 33(21):2491–2493
62. Rankin BR, Hell SW (2009) STED microscopy with a MHz pulsed stimulated-Raman-scattering source. Opt Express 17(18):15679–15684
63. Rankin BR, Moneron G, Wurm CA, Nelson JC, Walter A, Schwarzer D, Schroeder J, Colon-Ramos DA, Hell SW (2011) Nanoscopy in a living multicellular organism expressing GFP. Biophys J 100:L63–L65
64. Willig KI, Harke B, Medda R, Hell SW (2007) STED microscopy with continuous wave beams. Nat Methods 4(11):915–918
65. Harke B (2008) 3D STED microscopy with pulsed and continuous wave lasers. PhD-Thesis, Georg-August-University Goettingen, Goettingen
66. Ding JB, Takasaki KT, Sabatini BL (2009) Supraresolution imaging in brain slices using stimulated-emission depletion two-photon laser scanning microscopy. Neuron 63:429–437
67. Moneron G, Hell S (2009) Two-photon excitation STED microscopy. Opt Express 17 (17):14567–14573
68. Moneron G, Medda R, Hein B, Giske A, Westphal V, Hell SW (2010) Fast STED microscopy with continuous wave fiber lasers. Opt Express 18(2):1302–1309
69. Bianchini P, Diaspro A (2012) Fast scanning STED and two-photon fluorescence excitation microscopy with continuous wave beam. J Microsc 245(3):225–228
70. Honigmann A, Eggeling C, Schulze M, Lepert A (2012) Super-resolution STED microscopy advances with yellow CW OPSL. Laser Focus World 48(1):75–79
71. Mueller V, Eggeling C, Karlsson H, von Gegerfelt D (2012) CW DPSS lasers make STED microscopy more practical. Biophotonics 19(5):30–32
72. Honigmann A, Mueller V, Fernando UP, Eggeling C, Sperling J (2013) Simplifying STED microscopy of photostable red-emitting labels. Laser+Photonics 5:40–42
73. Moffitt JR, Osseforth C, Michaelis J (2011) Time-gating improves the spatial resolution of STED microscopy. Opt Express 19(5):4242–4254
74. Vicidomini G, Moneron G, Han KY, Westphal V, Ta H, Reuss M, Engelhardt H, Eggeling C, Hell SW (2011) Sharper low-power STED nanoscopy by time gating. Nat Methods 8(7):571–573
75. Vicidomini G, Hernandez IC, d'Amora M, Zanacchi FC, Bianchini P, Diaspro A (2014) Gated CW-STED microscopy: a versatile tool for biological nanometer scale investigation. Methods 66:124–130
76. Vicidomini G, Schoenle A, Ta H, Han KY, Moneron G, Eggeling C, Hell SW (2013) STED nanoscopy with time-gated detection: theoretical and experimental aspects. PLoS One 8(1): e54421
77. Hernandez IC, d'Amora M, Diaspro A, Vicidomini G (2014) Influence of laser intensity noise on gated CW-STED microscopy. Laser Phys Lett 11:095603
78. Hernandez IC, Peres C, Zanacchi FC, d'Amora M, Christodoulou S, Bianchini P, Diaspro A, Vicidomini G (2014) A new filtering technique for removing anti-stokes emission background in gated CW-STED microscopy. J Biophotonics 7(6):376–380
79. Reuss M, Engelhardt J, Hell S (2010) Birefringent device converts a standard scanning microscope into a STED microscope that also maps molecular orientation. Opt Express 18 (2):1049–1058

80. Gould TJ, Burke D, Bewersdorf J, Booth MJ (2012) Adaptive optics enables 3D STED microscopy in aberrating specimens. Opt Express 20(19):20998
81. Gould TJ, Kromann EB, Burke D, Booth MJ, Bewersdorf J (2013) Auto-aligning stimulated emission depletion microscope using adaptive optics. Opt Lett 38(11):1860–1862
82. Eggeling C, Volkmer A, Seidel CAM (2005) Molecular photobleaching kinetics of rhodamine 6G by one- and two-photon induced confocal fluorescence microscopy. Chemphyschem 6:791–804
83. Eggeling C, Widengren J, Rigler R, Seidel CAM (1998) Photobleaching of fluorescent dyes under conditions used for single-molecule detection: evidence of two-step photolysis. Anal Chem 70:2651–2659
84. Ringemann C, Schonle A, Giske A, von Middendorff C, Hell SW, Eggeling C (2008) Enhancing fluorescence brightness: effect of reverse intersystem crossing studied by fluorescence fluctuation spectroscopy. Chemphyschem 9(9):612–624
85. Hotta J, Fron E, Dedecker P, Janssen KPF, Li C, Muellen K, Harke B, Bückers J, Hell SW, Hofkens J (2010) Spectroscopic rationale for efficient stimulated-emission depletion microscopy fluorophores. J Am Chem Soc 132(14):5021–5023
86. Donnert G, Eggeling C, Hell SW (2007) Major signal increase in fluorescence microscopy through dark-state relaxation. Nat Methods 4(1):81–86
87. Donnert G, Eggeling C, Hell SW (2009) Triplet-relaxation microscopy with bunched pulsed excitation. Photochem Photobiol 8:481–485
88. Denk W, Strickler JH, Webb WW (1990) 2-photon laser scanning fluorescence microscopy. Science 248:73–76
89. Denk W (1996) Two-photon excitation in functional biological imaging. J Biomed Opt 1:296–304
90. Dittrich PS, Schwille P (2001) Photobleaching and stabilization of fluorophores used for single-molecule analysis with one- and two-photon excitation. Appl Phys B 73:829–837
91. Nagerl UV, Willig KI, Hein B, Hell SW, Bonhoeffer T (2008) Live-cell imaging of dendritic spines by STED microscopy. Proc Natl Acad Sci U S A 105:18982–18987
92. Urban NT, Willig KI, Hell SW, Nagerl UV (2011) STED nanoscopy of actin dynamics in synapses deep inside living brain slices. Biophys J 101(5):1277–1284
93. Berning S, Willig KI, Steffens H, Dibaj P, Hell SW (2012) Nanoscopy in a living mouse brain. Science 335:551
94. Kolmakov K, Belov VN, Bierwagen J, Ringemann C, Mueller V, Eggeling C, Hell SW (2010) Red-emitting rhodamine dyes for fluorescence microscopy and nanoscopy. Chem Eur J 16(1):158–166
95. Kolmakov K, Belov VN, Wurm CA, Harke B, Leutenegger M, Eggeling C, Hell SW (2010) A versatile route to red-emitting carbopyronine dyes for optical microscopy and nanoscopy. Eur J Org Chem 2010(19):3593–3610
96. Mitronova GY, Belov VN, Bossi ML, Wurm CA, Meyer L, Medda R, Moneron G, Bretschneider S, Eggeling C, Jakobs S, Hell SW (2010) New fluorinated rhodamines for optical microscopy and nanoscopy. Chem A Eur J 16(15):4477–4488
97. Kasper R, Harke B, Forthmann C, Tinnefeld P, Hell SW, Sauer M (2010) Single-molecule STED microscopy with photostable organic fluorophores. Small 6(13):1379–1384
98. Beater S, Holzmeister P, Pibiri E, Lalkens B, Tinnefeld P (2014) Choosing dyes for cw-STED nanoscopy using self-assembled nanorulers. Phys Chem Chem Phys 16:6990–6996
99. Hein B, Willig KI, Wurm CA, Westphal V, Jakobs S, Hell SW (2010) Stimulated emission depletion nanoscopy of living cells using SNAP-tag fusion proteins. Biophys J 98:158–163
100. Lukinavicius G, Umezawa K, Olivier N, Honigmann A, Yang G, Plass T, Mueller V, Reymond L, Correa IR, Luo Z-G, Schultz C, Lemke EA, Heppenstall P, Eggeling C, Johnsson K (2013) A near-infrared fluorophore for live-cell superresolution microscopy of cellular proteins. Nat Chem 5:132–139

101. Wurm CA, Neumann D, Schmidt R, Egner A, Jakobs S (2010) Sample preparation for STED microscopy. In: Papkovsky DB (ed) Live cell imaging, Methods in molecular biology. Springer, Heidelberg, pp 185–199
102. Tanaka KAK, Suzuki KGN, Shirai YM, Shibutani ST, Miyahara MSH, Tsuboi H, Yahara M, Yoshimura A, Mayor S, Fujiwara TK, Kusumi A (2010) Membrane molecules mobile even after chemical fixation. Nat Methods 7:865–866
103. Schmidt R, Wurm CA, Jakobs S, Engelhardt J, Egner A, Hell SW (2008) Spherical nanosized focal spot unravels the interior of cells. Nat Methods 5(6):539–544
104. Dean C, Liu H, Staudt T, Stahlberg MA, Vingill S, Buckers J, Kamin D, Engelhardt J, Jackson MB, Hell SW, Chapman ER (2012) Distinct subsets of Syt-IV/BDNF vesicles are sorted to axons versus dendrites and recruited to synapses by activity. J Neurosci 32 (16):5398–5413
105. Donnert G, Keller J, Wurm CA, Rizzoli SO, Westphal V, Schoenle A, Jahn R, Jakobs S, Eggeling C, Hell SW (2007) Two-color far-field fluorescence nanoscopy. Biophys J 92(8): L67–L69
106. Meyer L, Wildanger D, Medda R, Punge A, Rizzoli SO, Donnert G, Hell SW (2008) Dual-color sted microscopy at 30-nm focal-plane resolution. Small 4(8):1095–1100
107. Neumann D, Bückers J, Kastrup L, Hell S, Jakobs S (2010) Two-color STED microscopy reveals different degrees of colocalization between hexokinase-I and the three human VDAC isoforms. PMC Biophysics 5(3):1–4
108. Opaz F, Punge A, Bückers J, Hoopmann P, Kastrup L, Hell SW, Rizzoli SO (2010) Limited intermixing of synaptic vesicle components upon vesicle recycling. Traffic 11(6):800–812
109. Reisinger E, Bresee C, Neef J, Nair R, Reuter K, Bulankina A, Nouvian R, Koch M, Bückers J, Kastrup L, Roux I, Petit C, Hell SW, Brose N, Rhee J, Kügler S, Brigande JV, Moser T (2011) Probing the functional equivalence of otoferlin and synaptotagmin 1 in exocytosis. J Neurosci 31(13):4886–4895
110. Blom H, Rönnlund D, Scott L, Spicarova Z, Rantanen V, Widengren J, Aperia A, Brismar H (2012) Nearest neighbor analysis of dopamine D1 receptors and Na1-K1-ATPases in dendritic spines dissected by STED microscopy. Microsc Res Tech 75:220–228
111. Bückers J, Wildanger D, Vicidomini G, Kastrup L, Hell SW (2011) Simultaneous multi-lifetime multi-color STED imaging for colocalization analyses. Opt Express 19(4):3130–3143
112. Willig KI, Stiel AC, Brakemann T, Jakobs S, Hell SW (2011) Dual-label STED nanoscopy of living cells using photochromism. Nano Lett 11(9):3970–3973
113. Westphal V, Lauterbach MA, Di Nicola A, Hell SW (2007) Dynamic far-field fluorescence nanoscopy. New J Phys 9:435
114. Westphal V, Rizzoli SO, Lauterbach MA, Kamin D, Jahn R, Hell SW (2008) Video-rate far-field optical nanoscopy dissects synaptic vesicle movement. Science 320(5873):246–249
115. Bingen P, Reuss M, Engelhardt J, Hell SW (2011) Parrallelized STED fluorescence nanoscopy. Opt Express 19(24):23716–23726
116. Yang B, Przybilla F, Mestre M, Trebbia J-B, Lounis B (2013) Massive parallelization of STED nanoscopy using optical lattices. Optics Expr 22(5): 5581–5589
117. Grotjohann T, Testa I, Leutenegger M, Bock H, Urban NT, Lavoie-Cardinal F, Willig KI, Eggeling C, Jakobs S, Hell SW (2011) Diffraction-unlimited all-optical imaging and writing with a photochromic GFP. Nature 478:204–208
118. Brakemann T, Stiel AC, Weber G, Andresen M, Testa I, Grotjohann T, Leutenegger M, Plessmann U, Urlaub H, Eggeling C, Wahl M, Hell SW, Jakobs S (2011) A reversibly photoswitchable GFP-like protein with fluorescence excitation decoupled from switching. Nat Biotechnol 29:942–947
119. Testa I, Urban NT, Jakobs S, Eggeling C, Willig KI, Hell SW (2012) Nanoscopy of living brain slices with low light levels. Neuron 75:992–1000
120. Chmyrov A, Keller J, Grotjohann T, Ratz M, d'Este E, Jakobs S, Eggeling C, Hell SW (2013) Nanoscopy with more than 100,000 'doughnuts'. Nat Methods 10:737–740

121. Bretschneider S, Eggeling C, Hell SW (2007) Breaking the diffraction barrier in fluorescence microscopy by optical shelving. Phys Rev Lett 98(21):218103
122. Schwentker MA (2007) Parallelized ground state depletion. University of Heidelberg, Heidelberg
123. Gould TJ, Myers JR, Bewersdorf J (2011) Total internal reflection STED microscopy. Opt Express 19(14):13351–13357
124. Leutenegger M, Ringemann C, Lasser T, Hell SW, Eggeling C (2012) Fluorescence correlation spectroscopy with a total internal reflection fluorescence STED microscope (TIRF-STED-FCS). Opt Express 20(5):5243–5263
125. Li Q, Wu SSH, Chou KC (2009) Subdiffraction-limit two-photon fluorescence microscopy for GFP-tagged cell imaging. Biophys J 97(12):3224–3228. doi:10.1016/j.bpj.2009.09.038
126. Klar TA, Jakobs S, Dyba M, Egner A, Hell SW (2000) Fluorescence microscopy with diffraction resolution barrier broken by stimulated emission. Proc Natl Acad Sci U S A 97:8206–8210
127. Harke B, Keller J, Ullal CK, Westphal V, Schoenle A, Hell SW (2008) Resolution scaling in STED microscopy. Opt Express 16(6):4154–4162
128. Harke B, Ullal CK, Keller J, Hell SW (2008) Three-dimensional nanoscopy of colloidal crystals. Nano Lett 8(5):1309–1313
129. Dyba M, Hell SW (2002) Focal spots of size lambda/23 open up far-field florescence microscopy at 33 nm axial resolution. Phys Rev Lett 88(16):163901
130. Dyba M, Jakobs S, Hell SW (2003) Immunofluorescence stimulated emission depletion microscopy. Nat Biotechnol 21(11):1303–1304
131. Hell SW, Schmidt R, Egner A (2009) Diffraction-unlimited three-dimensional optical nanoscopy with opposing lenses. Nat Photon 3:381–387
132. Schmidt R, Wurm CA, Punge A, Egner A, Jakobs S, Hell SW (2009) Mitochondrial cristae revealed with focused light. Nano Lett 9(6):2508–2510
133. Friedrich M, Gan Q, Ermolayev V, Harms GS (2011) STED-SPIM: stimulated emission depletion improves sheet illumination microscopy resolution. Biophys J 100:L43–L45
134. Kastrup L, Blom H, Eggeling C, Hell SW (2005) Fluorescence fluctuation spectroscopy in subdiffraction focal volumes. Phys Rev Lett 94:178104
135. Blom H, Kastrup L, Eggeling C (2006) Fluorescence fluctuation spectroscopy in reduced detection volumes. Curr Pharm Biotechnol 7(1):51–66
136. Eggeling C (2012) STED-FCS nanoscopy of membrane dynamics. In: Mely Y, Duportail G (eds) Fluorescent methods to study biological membranes, vol 13, Springer series on fluorescence. Springer, Berlin, pp 291–309
137. Mueller V, Honigmann A, Ringemann C, Medda R, Schwarzmann G, Eggeling C (2013) FCS in STED microscopy: studying the nanoscale of lipid membrane dynamics. In: Tetin SY (ed) Methods in enzymology, vol 591. Academic/Elsevier, Burlington, pp 1–38
138. Eggeling C, Honigmann A (2014) Molecular plasma membrane dynamics dissected by STED nanoscopy and fluorescence correlation spectroscopy (STED-FCS). In: Lidke DS, Cambi A (eds) Cell membrane nanodomains: from biochemistry to nanoscopy. CRC Press, Boca Raton
139. Ringemann C, Harke B, Middendorff CV, Medda R, Honigmann A, Wagner R, Leutenegger M, Schoenle A, Hell S, Eggeling C (2009) Exploring single-molecule dynamics with fluorescence nanoscopy. New J Phys 11:103054
140. Mueller V, Ringemann C, Honigmann A, Schwarzmann G, Medda R, Leutenegger M, Polyakova S, Belov VN, Hell SW, Eggeling C (2011) STED nanoscopy reveals molecular details of cholesterol- and cytoskeleton-modulated lipid interactions in living cells. Biophys J 101:1651–1660
141. Solanko ML, Honigmann A, Midtiby HS, Lund FW, Brewer J, Dekaris V, Bittman R, Eggeling C, Wüstner D (2013) Membrane orientation and lateral diffusion of BODIPY-cholesterol as a function of probe structure. Biophys J 105:2082–2092

142. Honigmann A, Mueller V, Hell SW, Eggeling C (2013) STED microscopy detects and quantifies liquid phase separation in lipid membranes using a new far-red emitting fluorescent phosphoglycerolipid analogue. Faraday Discuss 161:77–89
143. Sezgin E, Levental I, Grzybek M, Schwarzmann G, Mueller V, Honigmann A, Belov VN, Eggeling C, Coskun Ü, Simons K, Schwille P (2012) Partitioning, diffusion, and ligand binding of raft lipid analogs in model and cellular plasma membranes. Biochim Biophys Acta 1818:1777–1784
144. Honigmann A, Mueller V, Ta H, Schoenle A, Sezgin E, Hell SW, Eggeling C (2014) Scanning STED-FCS reveals spatio-temporal heterogeneity of lipid interaction in the plasma membrane of living cells. Nature Communications 5:5412. doi: 5410.10381/ncomms6412
145. Mueller V (2012) Nanoscale studies of membrane dynamics via STED - fluorescence correlation spectroscopy. University of Heidelberg, Heidelberg
146. Guzman C, Solman M, Ligabue A, Blazevits O, Andrade DM, Reymond L, Eggeling C, Abankwa D (2014) The efficacy of Raf kinase recruitment to the GTPase H-ras depends on H-ras membrane conformer specific nanoclustering. J Biol Chem 289(14):9519–9533
147. Saka SK, Honigmann A, Eggeling C, Hell SW, Lang T, Rizzoli SO (2014) Multi-protein assemblies underlie the mesoscale organization of the plasma membrane. Nat Commun 5:4509
148. King JT, Yu C, Wilson WL, Granick S (2014) Super-resolution study of polymer mobility fluctuations near c*. ACS Nano. doi:10.1021/nn502856t
149. Vicidomini G, Ta H, Han KY, Moneron G, Honigmann A, Hell SW, Eggeling C (2014) Spatio-temporal heterogeneity of lipid membrane dynamics revealed by gated STED-FCS, in preparation
150. Hedde PN, Dorlich RM, Blomley R, Gradl D, Oppong E, Cato ACB, Nienhaus GU (2013) Stimulated emission depletion-based raster image correlation spectroscopy reveals biomolecular dynamics in live cells. Nat Commun 4:2093
151. Bianchini P, Cardarelli F, Luca D, Diaspro A, Bizzarri R (2014) Nanoscale protein diffusion by STED-based pair correlation analysis. PLoS One 9(6):e99619
152. Schwille P, MeyerAlmes FJ, Rigler R (1997) Dual-color fluorescence cross-correlation spectroscopy for multicomponent diffusional analysis in solution. Biophys J 72(4):1878–1886
153. Biteen JS, Thompson MA, Tselentis NK, Bowman GR, Shapiro L, Moerner WE (2008) Super-resolution imaging in live caulobacter crescentus cells using photoswitchable EYFP. Nat Methods 5:947–949
154. Gordon MP, Ha T, Selvin PR (2004) Single-molecule high-resolution imaging with photobleaching. Proc Natl Acad Sci U S A 101:6462–6465
155. Qu XH, Wu D, Mets L, Scherer NF (2004) Nanometer-localized multiple single-molecule fluorescence microscopy. Proc Natl Acad Sci U S A 101(31):11298–11303
156. Lidke KA, Rieger B, Jovin TM, Heintzmann R (2005) Superresolution by localization of quantum dots using blinking statistics. Opt Express 13(18):7052–7062
157. Kusumi A, Nakada C, Ritchie K, Murase K, Suzuki K, Murakoshi H, Kasai RS, Kondo J, Fujiwara T (2005) Paradigm shift of the plasma membrane concept from the two-dimensional continuum fluid to the partitioned fluid: high-speed single-molecule tracking of membrane molecules. Annu Rev Biophys 34:351–378
158. Shroff H, Galbraith CG, Galbraith JA, Betzig E (2008) Live-cell photoactivated localization microscopy of nanoscale adhesion dynamics. Nat Methods 5(5):417–423
159. Small AR (2009) Theoretical limits on errors and acquisition rates in localizing switchable fluorophores. Biophys J 96(2):L16–L18
160. Enderlein J, Toprak E, Selvin PR (2006) Polarization effect on position accuracy of fluorophore localization. Opt Express 14(18):8111–8120
161. Engelhardt J, Keller J, Hoyer P, Reuss M, Staudt T, Hell SW (2011) Molecular orientation affects localization accuracy in superresolution far-field fluorescence microscopy. Nano Lett 11:209–213. doi:10.1021/nl103472b

162. Dertinger T, Colyer R, Iyer G, Weiss S, Enderlein J (2009) Fast, background-free, 3D super-resolution optical fluctuation imaging (SOFI). Proc Natl Acad Sci U S A 106(52):22287–22292
163. Cronin B, de Wet B, Wallace MI (2009) Lucky imaging: improved localization accuracy for single molecule imaging. Biophys J 96(7):2912–2917
164. Hedde PN, Fuchs J, Oswald F, Wiedenmann J, Nienhaus GU (2009) Online image analysis software for photoactivation localization microscopy. Nat Methods 6(10):689–690
165. Smith CS, Joseph N, Rieger B, Lidke KA (2010) Fast, single-molecule localization that achieves theoretically minimum uncertainty. Nat Methods 7(5):373–375
166. Larson DR (2010) The economy of photons. Nat Methods 7(5):357–359
167. Laurence TA, Chromy BA (2010) Efficient maximum likelihood estimator fitting of histograms. Nat Methods 5(7):338–339
168. Henriques R, Lelek M, Fornasiero EF, Valtorta F, Zimmer C, Mhlanga MM (2010) QuickPALM: 3D real-time photoactivation nanoscopy image processing in ImageJ. Nat Methods 7(5):339–340
169. Mortensen KI, Churchman SL, Spudich JA, Flyvbjerg H (2010) Optimized localization analysis for single-molecule tracking and super-resolution microscopy. Nat Methods 7 (5):377–381
170. Pertsinidis A, Zhang Y, Chu S (2010) Subnanometre single-molecule localization, registration and distance measurements. Nature 466(7306):647–651
171. Wolter S, Schuttpelz M, Tscherepanow M, van de Linde S, Heilemann M, Sauer M (2010) Real-time computation of subdiffraction-resolution fluorescence images. J Microsc 237 (1):12–22
172. Endesfelder U, van de Linde S, Wolter S, Sauer M, Heilemann M (2010) Subdiffraction-resolution fluorescence microscopy of myosin–actin motility. Chemphyschem 11(4):836–840
173. Holden SJ, Uphoff S, Kapanidis AN (2011) DAOSTORM: an algorithm for high density super-resolution microscopy. Nat Methods 8(4):279–280
174. Huang F, Schwartz SL, Byars JM, Lidke KA (2011) Simultaneous multiple-emitter fitting for single molecule super-resolution imaging. Biomed Opt Express 2(5):1377–1393
175. Jones SA, Shim S-H, He J, Zhuang X (2011) Fast, three-dimensional super-resolution imaging of live cells. Nat Methods 8(6):499–505
176. Cox S, Rosten E, Monypenny J, Jovanovic-Talisman T, Burnette DT, Lippincott-Schwartz J, Jones GE, Heintzmann R (2012) Bayesian localization microscopy reveals nanoscale podosome dynamics. Nat Methods 9(2):195–200
177. Bock H, Geisler C, Wurm CA, Von Middendorff C, Jakobs S, Schonle A, Egner A, Hell SW, Eggeling C (2007) Two-color far-field fluorescence nanoscopy based on photoswitchable emitters. Appl Phys B 88(8):161–165
178. Bates M, Huang B, Dempsey GT, Zhuang XW (2007) Multicolor super-resolution imaging with photo-switchable fluorescent probes. Science 317:1749–1753
179. Huang B, Wang WQ, Bates M, Zhuang XW (2008) Three-dimensional super-resolution imaging by stochastic optical reconstruction microscopy. Science 319:810–813
180. Juette MF, Gould TJ, Lessard MD, Mlodzianoski MJ, Nagpure BS, Bennett BT, Hess ST, Bewersdorf J (2008) Three-dimensional sub-100 nm resolution fluorescence microscopy of thick samples. Nat Methods 5(6):527–529
181. Shtengel G, Galbraith JA, Galbraith CG, Lippincott-Schwartz J, Gillette JM, Manley S, Sougrat R, Waterman CM, Kanchanawong P, Davidson MW, Fetter RD, Hess HF (2009) Interferometric fluorescent super-resolution microscopy resolves 3D cellular ultrastructure. Proc Natl Acad Sci U S A 106(9):3125–3130
182. Pavani SRP, Thompson MA, Biteen JS, Lord SJ, Liu N, Twieg RJ, Piestun R, Moerner WE (2009) Three-dimensional, single-molecule fluorescence imaging beyond the diffraction limit by using a double-helix point spread function. Proc Natl Acad Sci U S A 106 (9):2995–2999

183. Hell SW (1992) Double-scanning confocal microscope. European Patent 0491289
184. Gustafsson MGL, Agard DA, Sedat JW (1995) Sevenfold improvement of axial resolution in 3D widefield microscopy using two objective lenses. Proc Soc Photo Opt Instrum Eng 2412:147–156
185. Gustafsson MGL (2000) Surpassing the lateral resolution limit by a factor of two using structured illumination microscopy. J Microsc 198(2):82–87
186. Schermelleh L, Carlton PM, Haase S, Shao L, Winoto L, Kner P, Burke B, Cardoso MC, Agard DA, Gustafsson MGL, Leonhardt H, Sedat JW (2008) Subdiffraction multicolor imaging of the nuclear periphery with 3D structured illumination microscopy. Science 320 (5881):1332–1336
187. Heintzmann R, Jovin TM, Cremer C (2002) Saturated patterned excitation microscopy - a concept for optical resolution improvement. J Opt Soc Am A Opt Image Sci Vis 19(8):1599–1609
188. Gustafsson MGL (2005) Nonlinear structured-illumination microscopy: wide-field fluorescence imaging with theoretically unlimited resolution. Proc Natl Acad Sci U S A 102 (37):13081–13086
189. Schwentker MA, Bock H, Hofmann M, Jakobs S, Bewersdorf J, Eggeling C, Hell SW (2007) Wide-field subdiffraction RESOLFT microscopy using fluorescent protein photoswitching. Microsc Res Tech 70(3):269–280
190. Rego EH, Shao L, Macklin JJ, Winoto L, Johansson GA, Kamps-Hughes N, Davidson MW, Gustafsson MGL (2012) Nonlinear structured-illumination microscopy with a photoswitchable protein reveals cellular structures at 50-nm resolution. Proc Natl Acad Sci U S A 109(3):E135–E143

Super-Resolution Imaging Through Stochastic Switching and Localization of Single Molecules: An Overview

Ke Xu, Sang-Hee Shim, and Xiaowei Zhuang

Abstract The resolution of fluorescence microscopy had traditionally been limited to ~200–300 nm due to the diffraction of light. Recently, this resolution limit has been broken using mainly two classes of methods, one of which utilizes photoswitching of fluorophores to temporally separate the spatially overlapping images of individual molecules such that the positions of these molecules can be precisely determined. A sub-diffraction-limit image can then be reconstructed from these molecular coordinates. With relatively simple optical instrumentation and sample preparation, this class of methods has improved the spatial resolution of far-field optical microscopy by more than an order of magnitude, achieving resolutions down to sub-10 nm range for biological specimens. Three-dimensional, multicolor, and live-cell super-resolution imaging has been demonstrated. In this chapter, we provide an overview of this class of optical nanoscopy, primarily in terms of the imaging principle, the spatial/temporal resolution, the different imaging schemes, the photoswitchable probes, the applications, and future directions.

Keywords (F)PALM · diffraction limit · photoswitching · single molecule · STORM · super-resolution microscopy

---

Authors Ke Xu and Sang-Hee Shim contributed equally to this chapter

K. Xu and S.-H. Shim
Department of Chemistry and Chemical Biology, Harvard University, Cambridge, MA 02138, USA

X. Zhuang (✉)
Department of Chemistry and Chemical Biology, Howard Hughes Medical Institute, Harvard University, Cambridge, MA 02138, USA

Department of Physics, Harvard University, Cambridge, MA 02138, USA
e-mail: zhuang@chemistry.harvard.edu

P. Tinnefeld et al. (eds.), *Far-Field Optical Nanoscopy*,
Springer Ser Fluoresc (2015) 14: 27–64, DOI 10.1007/4243_2013_61,

Contents

1 Background

1.1 Optical Microscopy and the Diffraction Limit

Optical microscopy is a widely used and indispensable imaging modality in biological studies. When compared to other microscopy techniques, optical microscopy, in particular fluorescence microscopy, provides the distinct advantages of being relatively noninvasive and molecularly specific. The former advantage permits the observation of live cells, tissues, and organisms. The latter, accomplished through fluorescent labels, allows for the specific observation of molecular targets with high contrast.

However, conventional optical microscopy has a resolution limit, typically on the order of several hundred nanometers, below which the structural details of the specimen can no longer be resolved. This limit is due to the wave-like nature of light. The far-field optical image of even an idealized point object will be blurred into a finite-sized spot due to diffraction, and the size of the spot is comparable to the wavelength of the light. The intensity distribution of this spot is called the point spread function (PSF). Under optimal imaging conditions with a high numerical aperture objective, the full width at half maximum (FWHM) of PSF for visible light is 200–300 nm in the lateral dimensions and 500–800 nm in the axial dimension. Hence, objects separated by a distance smaller than the width of the PSF will have overlapping images that cannot be resolved − in other words, the width of the PSF defines the resolution limit of conventional optical microscopy.

In recent years, several methods have been developed to break this conventional resolution limit imposed by diffraction. These methods are collectively called super-resolution fluorescence microscopy. One class of methods overcomes the diffraction limit by effectively reducing the size of the PSF using specially engineered illumination patterns. Examples in this category include stimulated emission depletion (STED) microscopy, microscopy taking advantage of reversible saturable optically linear fluorescence transitions (RESOLFT), and [saturated/non-linear] structured-illumination microscopy ([S/NL]SIM), which are covered in other chapters of this book.

In this chapter, we will focus on a different approach to super-resolution imaging, which resolves overlapping PSFs by the stochastic switching and localization of individual fluorophores.

1.2 Single, Isolated Fluorophores Can Be Localized with Nanometer Precision

Although diffraction inevitably results in a PSF several hundred nanometers in size for a point source of light, the position of the point source can nonetheless be localized with nanometer precision by determining the centroid of the PSF. The shape of the PSF can be determined either theoretically or experimentally. Therefore, the centroid positions of the PSFs can be readily obtained by fitting to known functions.

The theoretical PSF of a single point source of light is an Airy disk, but a simple two-dimensional (2D) Gaussian function provides a good approximation for ease of fitting [1, 2]. The fitting can be done with a precision that depends on the number of photons collected [2]. Experimentally, localization precisions as high as ~1 nm were first demonstrated for individual beads [3]. With the advent of single-molecule imaging [4], similar localization precisions were also achieved for individual fluorescent molecules [5, 6].

However, the nanometer-scale precision achieved in the localization of individual molecules does not directly translate into a high imaging resolution for densely labeled samples. This is because when the separation between adjacent fluorescent molecules is smaller than the diffraction limit, the PSFs of these molecules will overlap substantially, preventing the precise localization of the individual molecules. Early strategies to circumvent this problem include separation by orthogonal properties [7], such as color [8–10], sequential photobleaching of individual fluorophores [11, 12], and the blinking of individual quantum dots [13, 14]. These methods were able to resolve a few fluorophores per diffraction-limited area. On the other hand, for general super-resolution imaging with resolution substantially beyond the diffraction limit, many more fluorophores (hundreds to thousands) have to be resolved within a diffraction-limited area (see also Sect. 3.2), and new strategies are required.

2 Super-Resolution Imaging Through Stochastic Switching and Localization of Single Molecules

Recently, it was realized that the otherwise overlapping PSFs from densely labeled fluorophores can be separated in the time domain by employing fluorophores that can be switched between a non-emitting (dark) state and an emitting (fluorescent) state [15–17]. In this approach, at any given instant during imaging, the majority of the labeled fluorophores in the sample are maintained in the dark state, and only a small, random subset of the fluorophores are switched to the fluorescent state, typically using a weak activation laser (Fig. 1a). The number of simultaneously emitting fluorophores is kept sufficiently low that the PSFs of individual emitting fluorophores are isolated from each other; the location of each fluorophore can then be determined with nanometer precision using centroid fitting. The emitting fluorophores are then either optically switched back into the dark state or photobleached. Subsequently, another small, random subset of the labeled fluorophores is activated into the fluorescent state, and the locations of the newly activated molecules are again recorded. Iterating this procedure over time will eventually allow the locations of all (or a sufficiently large number of) the labeled fluorophores to be mapped, from which a super-resolution image can be constructed (Fig. 1).

This general strategy of super-resolution microscopy by stochastic switching and localization of single molecules has been originally introduced as stochastic optical reconstruction microscopy (STORM) [15], photoactivated localization microscopy (PALM) [16], and fluorescence photoactivation localization microscopy (FPALM) [17]. Both photoswitchable fluorescent dyes and photoactivatable fluorescent proteins can be used for sub-diffraction-limit imaging using this strategy.

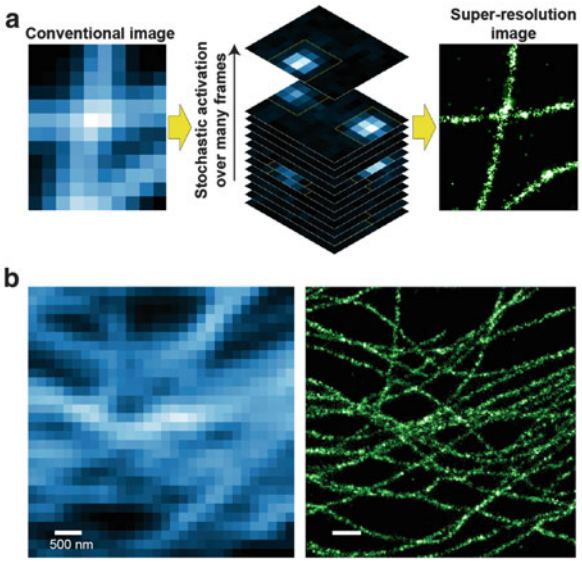

Fig. 1 The basic principles of STORM/(F)PALM. (**a**) Schematics illustrating the imaging concept. During the imaging process, only a small, optically resolvable subset of fluorophores are activated into the fluorescent state and subsequently localized with high precision at any given instant. The localized fluorophores are then switched back into the dark state and a new subset is activated. The cycle of switching and localizing repeats until a sufficient number of points are accumulated to reconstruct a super-resolution image. (**b**) Comparison of the conventional fluorescence image (*left*) of microtubules immunolabeled with Alexa 647 in a BS-C-1 cell with the STORM image (*right*) of the same area [18]. Scale bars: 500 nm. Figure adapted from reference [19]

More recently, the range of fluorescent probes that can be used for STORM/(F)PALM imaging has been substantially expanded through the realization that many conventional fluorescent dyes can in fact be photoswitched between fluorescent and dark states (a phenomenon also known as "blinking"), as demonstrated in PALMIRA (PALM with independently running acquisition) [20, 21], GSDIM (ground state depletion followed by single molecule return) [22], dSTORM (direct STORM) [23], single-molecule blinking microscopy [24], and fluorescence localization nanoscopy [25], etc. Along the same line, it is worth noting that a commonly used fluorescent protein, EYFP, can also be photoswitched between a fluorescent state and a dark state [26] and used for super-resolution imaging [27].

Photoswitching is not the only way to temperately separate overlapping images of single molecules to accomplish sub-diffraction-limit resolution. An elegant method called PAINT (points accumulation for imaging in nanoscale topography) [28] uses reversible binding of fluorescent molecules to target structures to accumulate numerous localizations and reconstruct super-resolution images. More recently, reversible binding of fluorescence quenchers has also been used to achieve the same goal [29].

Finally, due to the recent development on image analysis, the condition of well-isolated images of single molecules does not need to be rigorously satisfied for high-precision localization of individual molecules. Fluorophores with partially overlapping images can be localized using simultaneous multi-emitter fitting [30–32] and global optimization using compressed sensing [33]. Super-resolution imaging can also be accomplished by taking conventional movies and subtracting subsequent frames to reveal the transient blinking or bleaching of isolated single fluorophores using approaches called BALM (bleaching/blinking assisted localization microscopy) [34] and gSHRIMP (generalized single molecule high-resolution imaging with photobleaching) [35]). A Bayesian analysis of blinking and bleaching fluorophores (3B) [36] has been developed to model the entire fluorescence movie with an ensemble of most likely fluorophore locations. Super-resolution images can even be derived without localizing individual molecules but through correlation analysis (super-resolution optical fluctuation imaging (SOFI) [37] or nonlinear image deconvolution (decon-STORM) [38] of movie frames comprised of partially overlapping emitters. Many of these methods increase the number of molecules that can be imaged per camera frame and thereby substantially improve the imaging speed.

3 Image Resolution

3.1 Localization Precision and the Optical Resolution

The optical resolution of these molecular-localization-based super-resolution methods is ultimately determined by the precision with which each fluorophore can be localized. The theoretical limits of the localization precision are well established [2]. For a single point source, each detected photon can be viewed as an independent report of its location. As each photon is randomly distributed according to the PSF (with width Δ), a localization precision of $\sim \Delta/N^{1/2}$ can be expected when N photons are collected from the same point source. More sophisticated models also include the effects of background noise and the pixel size of the camera [2].

Experimentally, the localization precision can be determined by repeatedly measuring the position of a single fluorophore and determining the standard deviation (SD) of the localization distribution. For example, localization precisions of ~8 nm (SD) per switching cycle have been demonstrated for bright, photoswitchable dyes Cy5 and Alexa 647 [15, 18, 39]. Approximately 2x worse localization precision has been achieved with some of the dimmer dyes (e.g., Atto 488 and DyLight 750) and fluorescent proteins (e.g., tdEos and mEos2) [40, 41].

In the literature, both standard deviation (SD) and full width at half maximum (FWHM) have been used to characterize the optical resolution for localization-based super-resolution imaging methods, which potentially creates confusion in the comparison of different measurements. For Gaussian distributions, FWHM $= 2.35$ SD. FWHM is a better representation of the imaging resolution as it corresponds to

the smallest separation between two probes that can be resolved. In this chapter, we will use the FWHM value when discussing resolution.

It is also worth noting that the experimentally determined localization precision values are substantially worse (typically by twofold) than the theoretically predicted values. This indicates that the theoretical values do not faithfully represent the actual localization precision. Factors limiting the actual localization precision include camera noise, background noise, nonuniformity of the camera pixels [6], mechanical instability of the instrument, errors in data analysis, and any other imperfections of the imaging and analysis systems.

Besides the localization precision of single fluorophores, the resolvability for actual biological structures is also affected by how faithfully the labels represent the structures of interest. Any sizable label, such as antibodies (~10 nm in size) and fluorescent proteins (~4 nm in size), will substantially affect the image resolution when the resolution becomes comparable to the label size.

3.2 Localization Density and the Nyquist Resolution Limit

Super-resolution methods provide an optical resolution that sometimes approaches the distance between adjacent labels in a sample. At this level, not only does the localization precision of each label but also the label density and efficiency affect the final image resolution.

For continuous structures, the effects of labeling density can be quantified using the Nyquist-Shannon sampling criterion, which states that structural details smaller than twice that of the average label-to-label distance cannot be reliably resolved [42]. Formally, this Nyquist resolution limit can be expressed as $2/N^{1/D}$, where N is the number density of labels and D is the dimensionality of the image. To achieve Nyquist resolutions that are comparable to the optical resolution (i.e., the localization precision) of ~20 nm, a labeling density of $\sim 10^4/\mu m^2$ is required for 2D imaging. It should be noted, however, that due to the spatial inhomogeneity of biological structures, the same Nyquist resolution can often be achieved at lower *overall* localization densities, as long as the *local* localization density of the structure of interest is sufficiently high. The final image quality is affected by both the optical resolution based on localization precision and the Nyquist resolution limit determined by the label or localization density: Whichever is worse (larger in value) dominates the effective image resolution. When the two resolutions are comparable, the convolution of the two may be employed to represent the final resolution [41]. It is also worth noting that the localization density is not only limited by the label density but also by the on-off duty cycle of the photoswitchable probes, namely, the fraction of time each probe spends in the on state [40]. Because multiple probes emitting at the same time within a diffraction-limited area generate overlapping images that reduce the localization precision, fluorophores with a duty cycle of 1/N typically allow less than N molecules to be localized within a diffraction-limited area.

For super-resolution studies on the distributions of sparsely distributed molecules, the Nyquist resolution is less relevant, because the molecular structure itself does not allow a high labeling density. Nonetheless, high labeling efficiency (fraction of molecules being labeled) is still required for faithfully mapping out the underlying distribution.

4 Three-Dimensional Imaging

Most biological samples are three-dimensional (3D), and thus defining their structural details requires 3D super-resolution imaging. STORM, (F)PALM, and related methods achieve super-resolution through the localization of individual molecules; hence, to acquire 3D imaging capability entails the determination of the 3D locations of single emitting molecules. While the lateral position (x- and y-coordinates) of a fluorophore can be readily determined from the centroid of the PSF, the determination of the axial position (z-coordinate) requires additional manipulation and analysis of the PSF. Nonetheless, it can be done with a variety of methods, many of which were first developed in earlier studies for single-particle tracking and spectrally selective imaging, including fitting the shape of the PSF [43–49], interferometry [50, 51], and tilted mirrors [52].

4.1 PSF Shape-Based Methods: Astigmatism and Multifocal Plane Detection

An obvious difference between the PSFs of fluorophores with different axial positions is their apparent width. When projected onto the image plane (the camera), fluorophores right at the focal plane of the microscope produce the smallest images, whereas defocused fluorophores produce larger PSF. One could thus derive the z-information of individual molecules from the measured PSF width. The problem with directly applying this defocusing approach is that molecules above and below the focal plane have similarly broadened PSF.

To break this symmetry, 3D super-resolution imaging was first realized by the introduction of astigmatism into the imaging system [39]. Specifically, a cylindrical lens is introduced into the imaging path (Fig. 2a). As a result, the images of individual molecules become elliptical, and elongated in two orthogonal directions for molecules above and below the focal plane (Fig. 2a). The axial position of each molecule can thus be obtained from the ellipticity of the observed PSF, which in combination with the lateral positions obtained from the centroids of the PSF, leads to the 3D reconstruction of super-resolution images (Fig. 2b). The astigmatism method provides a resolution ~25 nm in xy and ~50 nm in z when imaging a bright photoswitchable fluorophore Cy5 (or its structural analog Alexa 647). Here, we

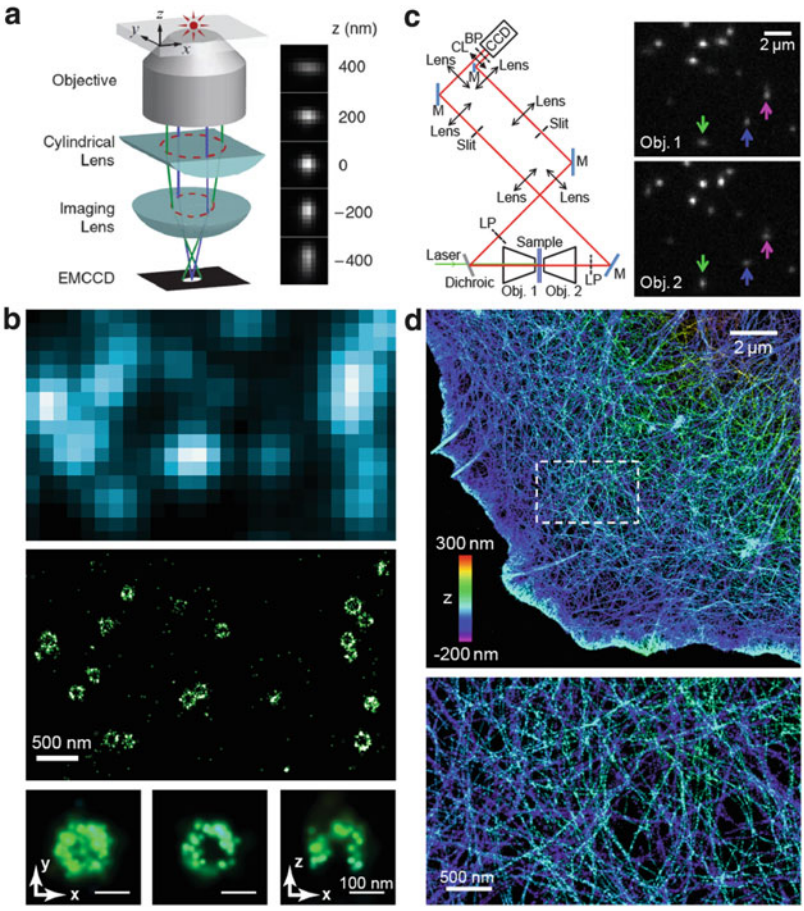

Fig. 2 Astigmatism-based three-dimensional STORM imaging. (**a**, **b**) 3D STORM imaging using a single objective. Figure adapted from reference [39]. (**a**) Schematics of the setup (*left*) and the experimentally observed images of a single fluorophore as its *z*-position was varied (*right*). A cylindrical lens is used to introduce astigmatism into the imaging system, such that elliptical images with long axes along two orthogonal directions are observed for fluorophores above and below the average focal plane. The *z*-position of each fluorophore can thus be obtained from the ellipticity of the observed image. (**b**) Conventional image (*top*) of immunolabeled clathrin-coated pits in a mammalian cell, in comparison with the corresponding 3D STORM image (*middle*) showing an *xy* cross section near the plasma membrane. *Bottom panel*: Magnified STORM images of a single clathrin-coated pit with an *xy* projection (*left*), an *xy* cross section near the plasma membrane (*center*), and an *xz* cross section cutting through the middle of the pit (*right*) (**c**, **d**) Dual-objective 3D STORM further improves image quality. Figure adapted from reference [53]. (**c**) *Left panel*: Schematic of the dual-objective setup. Two microscope objectives are placed facing each other and focused on the same spot of the sample. Astigmatism is introduced into the images collected by both objectives using a cylindrical lens. *M* mirror, *Obj.* objective, *LP* long-pass filter, *CL* cylindrical lens, *BP* band-pass filter. *Right panel*: Images of single molecules obtained from two objectives in a single frame. A molecule that appears elongated in *x* through one objective should appear elongated in *y* through the opposing objective, and vice versa

again use the FWHM values for 3D resolution as we did for 2D resolution because it is a better representation of the closest resolvable separation between objects. Using the astigmatism-based approach, a range of ~600–800 nm in z can be imaged without scanning [39]. This method remains the simplest approach to 3D super-resolution imaging.

The resolution of astigmatism-based 3D imaging can be further improved by the introduction of a second objective lens facing the first objective (Fig. 2c, d) [53]. This modification doubles the number of collected photons, provides a noise-canceling mechanism due to the anticorrelated ellipticity detected from the two objectives (Fig. 2c), and improves the mechanical stability of the setup. The combination of these effects led to a substantially improved resolution of 10 nm in xy and 20 nm in z when imaging Alexa 647 [53].

In a different defocusing approach, biplane imaging was carried out to achieve sub-diffraction-limit resolution in three dimensions by splitting the emitted fluorescence into two optical paths with different path lengths [54]. The z-positions of individual fluorophores were obtained by comparing the defocused PSF shapes at the two different image planes with the expected 3D PSF. An axial resolution of 75 nm was demonstrated when using caged fluorescein as the probe, with a ~800 nm z-imaging range without moving the sample [54].

While the use of PSF shape alone to determine the z-position can be more readily implemented with conventional optics, the z-resolution of these methods is limited to ~2x the lateral resolution due to the fact that the 3D PSF itself is wider in the axial direction than in the lateral directions. To achieve higher resolution in z, the phase information of the emitted photons can be used. Although the phase information provides a means to achieve higher z-resolution, the experimental implementation is often more complicated (Fig. 3a, c) and poses difficulties for emission-based multicolor imaging (see Sect. 5.2). We describe these phase-based approaches below.

4.2 PSF Engineering Through Fourier Optics

Phase information can be encoded into the PSF shape by the use of a predesigned phase mask (typically created using a spatial light modulator) placed at the Fourier plane of a 4-*f* imaging system (Fig. 3a). It has been shown that the PSF of individual fluorophores can be engineered to have two lobes that rotate as a function of the axial

Fig. 2 (continued) (e.g., *green* and *blue arrows*). In contrast, if two nearby molecules were mistaken for a single molecule, the images obtained through both objectives would appear elongated in the same direction along the line that connects the two molecules (e.g., *magenta arrows*). (**d**) Dual-objective 3D STORM resolves individual actin filaments in cells. *Top panel*: Dual-objective STORM image of actin (labeled with Alexa 647-phalloidin) in a COS-7 cell. *Bottom panel*: Close-up of the boxed region in the *top panel*. z-positions are color coded according to the color bar in the *top panel*

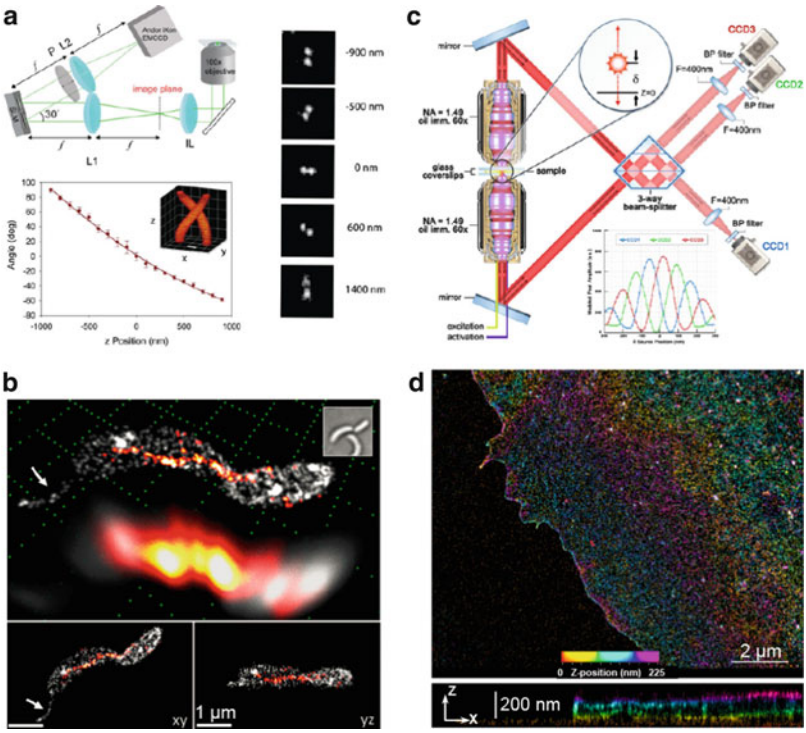

Fig. 3 Three-dimensional super-resolution imaging using double-helix PSF and single-molecule interferometry. (**a**, **b**) Double-helix PSF-based 3D imaging. (**a**) Schematics of the setup and *z*-calibration. Figure adapted from reference [55]. A spatial light modulator (SLM) loaded with a predesigned phase mask is placed at the Fourier plane of a 4-*f* imaging system, leading to two-lobe-shaped PSFs for individual fluorophores. The two lobes rotate as a function of the axial position of the fluorophore, thus providing *z*-information for each fluorophore. (**b**) Double-helix PSF 3D super-resolution imaging of CreS-eYFP (*red-orange*) and cell membrane (*gray*) in *Caulobacter crescentus*. *Top panel*: Super-resolution and diffraction-limited perspective images. *Bottom panel*: Two-dimensional isometric *xy* and *yz* projections. Figure adapted from reference [60]. (**c**, **d**) An example of the interferometry-based approach. Figure adapted from reference [57]. (**c**) Schematic of the setup. The fluorescence of individual fluorophores is collected by two objectives from opposing sides of the sample. The fluorescence photons interfere with themselves at the beam splitter, generating intensity interference patterns that are determined by the *z*-position of the fluorophore (*inset*). (**d**) Interferometry-based 3D super-resolution image of a COS-7 cell expressing the membrane protein VSVG that is fused to the photoconvertible FP, tdEos. *Bottom panel*: The *x*-*z* cross section of the boxed region in the *top panel*

position of the fluorophore (Fig. 3a) [55]. The resultant double-helix PSF (DH-PSF) therefore provides the *z*-information of each fluorophore by the orientation of the two lobes, allowing for 3D super-resolution imaging (Fig. 3b). A *z*-resolution of ~50 nm (FWHM) was demonstrated for the DCDHF dye. More recently, a PSF with a single-helix (SH-PSF) shape has also been created for 3D super-resolution imaging [56].

Compared to the defocusing approaches described above, an advantage of these helical PSF approaches is the longer z-range (~2 μm) that can be imaged without scanning the focal plane (Fig. 3a, b) [55]. A potential disadvantage of these approaches is that the PSF in these cases takes up a larger imaging area, which could limit the number of fluorophores that can be simultaneously imaged in each frame and thus lead to slower data acquisition. The use of a polarization-dependent spatial light modulator can also lead to a reduction in the number of photons collected at the camera.

4.3 Single-Molecule Interferometry

Interferometry-based single-molecule localization provides a direct way to extract phase information [57–59]. A single photon is coherent with itself; therefore, self-interference of individual photons will lead to intensity modulation of the signal from a single fluorophore. In this approach, photons emitted from individual fluorophores are collected by two objectives from opposing sides of the sample and self-interfered at a beam splitter, generating intensity modulations due to path-length differences determined by the axial position of the fluorophore (Fig. 3c). Using this approach, z-resolutions as high as ~10 nm have been demonstrated when using fluorescent proteins (Fig. 3d) [57] and organic dyes [59].

A major drawback of the interferometry-based method is the complexity in instrumentation, partly due to the short coherence length of fluorophores (a few micrometers). In its first implementation, the interferometry-based method was limited to samples thinner than ~200 nm because the interference pattern repeats itself every one-half of the emission wavelength [57]. In a subsequent work, this limitation was overcome by considering the spherical shape of the wavefront and examining the higher moments of the PSF, extending the working z-range to ~600 nm [59].

4.4 Tilted Mirrors

By projecting the axial dimension onto a lateral dimension using a tilted mirror, virtual volume super-resolution microscopy (VVSRM) determines the 3D position of single fluorescent emitters through observing the side-view mirror reflection (virtual image) alongside with the front-view real image [61]. VVSRM is capable of providing near-isotropic 3D resolution, but the requirement of sample being positioned close to (or attached to) a specialized, tilted micro-mirror potentially limits broader application of the method.

4.5 Thick Sample Imaging

Due to the relatively small depth of focus for high NA objectives (~600 nm, which essentially *defines* the axial resolution of conventional optical microscopy), most 3D localization techniques have a similar, limited working z-range of ~600–800 nm (except for the helical PSF methods). A natural way to extend the z-range is to scan the focal plane in steps smaller than ~600 nm and stack up the 3D super-resolution images acquired at each step [54, 62]. For example, by combining astigmatism-based imaging and z-scanning, whole-cell 3D super-resolution images were demonstrated with z-ranges of ~3 μm [62]

Although relatively easy to implement, a drawback to the direct application of z-scanning is that during imaging, illumination is not restricted to the volume being imaged. This leads to undesired activation and excitation of fluorophores outside the focal volume, causing increased fluorescence background and unnecessary photobleaching.

The illumination problem can be alleviated by the use of two-photon absorption, which, through nonlinear optical processes, is capable of confining the activation of fluorophores to a thin layer near the focal plane. This technique was first combined with 2D super-resolution imaging to generate 3D image stacks that only achieve super-resolution in the lateral directions [63, 64]. More recently, optical sectioning with two-photon activation was combined with astigmatism-based 3D super-resolution imaging, allowing a total imaging depth of up to ~7 μm [65].

Another way to confine the illumination axially is to use thin light sheets. In selective plane illumination microscopy (SPIM), the excitation light is shaped into a thin sheet that illuminates the sample through a separate objective placed perpendicular to the detection objective. Sheet illumination allows optical sectioning and prevents photobleaching and photoactivation outside the focal region [66]. Individual molecule localization-SPIM (IML-SPIM) was demonstrated by shaping the activation and excitation beams into collinear light sheets [67]. In combination with astigmatism for 3D localization, IML-SPIM achieved 63-nm lateral resolution and 140-nm axial resolution for thick specimens at a depth of 50–100 μm.

5 Multicolor Imaging

Multicolor imaging is one of the key advantages of fluorescence microscopy. With proper labeling, multicolor imaging allows for the visualization of different target molecules in a sample, from which the spatial relations and interactions between different molecules can be inferred. Multicolor super-resolution imaging has been accomplished using STORM, (F)PALM, and related methods by using fluorescent probes with different wavelengths of activation or emission.

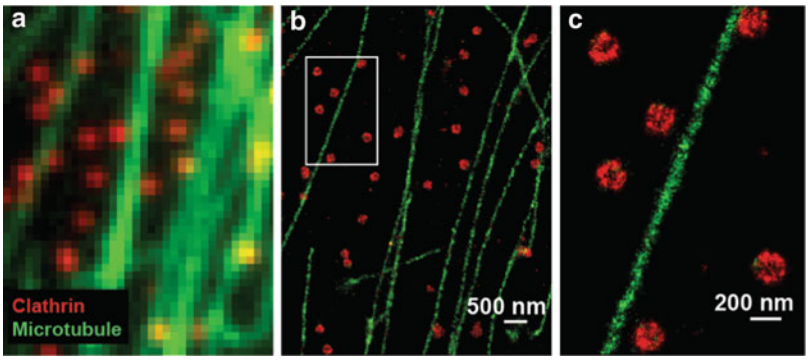

Fig. 4 Multicolor super-resolution imaging: activation-based approach. Antibodies labeled with Cy2 and Alexa 647 (*green*) and antibodies labeled with Cy3 and Alexa 647 (*red*) were used to stain the microtubules (*green*) and clathrin (*red*) in a BS-C-1 cell, respectively. Two-color imaging was achieved by alternating between two activation lasers (457 and 532 nm) and an excitation laser (657 nm). Figure adapted from reference [18]. (**a**) Conventional fluorescence image. (**b**) Corresponding STORM image. (**c**) Close-up of the boxed region in *b*

5.1 Activation-Based Multicolor Imaging

While photoswitchable dyes are typically activated to fluorescent states by illumination with ultraviolet (UV) light, the activation wavelength can be shifted into the visible range for some photoswitchable dyes by pairing them with another dye molecule that absorbs visible light. Upon absorbing light, the latter dye molecule (called an activator) can facilitate the activation of the photoswitchable dye (called a reporter). For example, by pairing the same reporter dye, Cy5, with three different activator dyes, Alexa Fluor 405, Cy2, and Cy3, the Cy5 dye can be activated into the fluorescent state when illuminated by violet, blue, or green light, respectively [18]. Multicolor imaging can thus be performed using these photoswitchable dye pairs, in which case the same reporter dye is imaged and localized in all color channels, but the different dye pairs are distinguished by the different wavelengths of light used for activation (Fig. 4) [18]. As a result, the images in different color channels are always perfectly aligned since the same optical path was used to collect the fluorescence emitted by the reporter in different dye pairs. In addition, the activation-based multicolor approach allows one to pick the best reporter dye to achieve the highest image resolution in all different color channels.

It should be noted that the light used to image the reporter dye can also directly activate the dye, albeit with a low activation rate. On the plus side, this property allows a very simple-imaging scheme for single-color super-resolution imaging with a single-color laser source and single photoswitchable reporter [68]. On the flip side, for multicolor imaging, this property leads to a drawback of relatively high color crosstalk. During imaging, activation by the imaging light results in nonspecific localizations independent of the activation light. This effect can lead to substantial

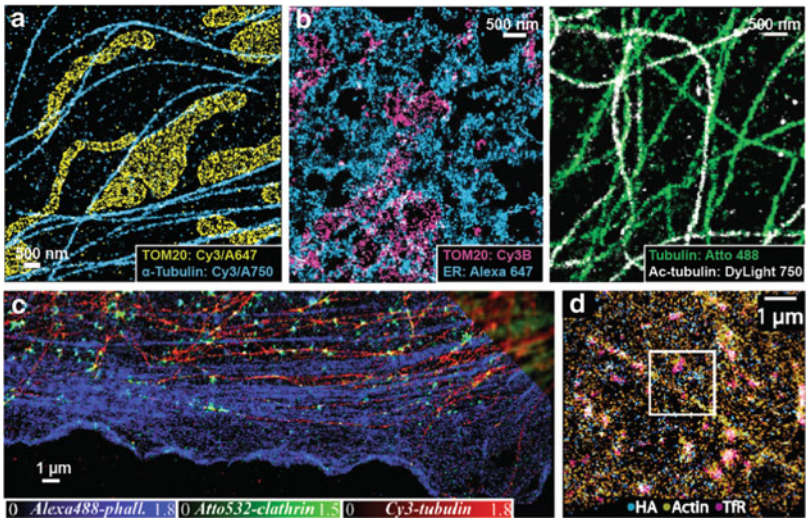

Fig. 5 Multicolor super-resolution imaging: emission-based approaches. (**a**, **b**) Examples in which emitters with well-separated emission spectra were used. (**a**) Dual-emission channel super-resolution imaging of microtubules (*cyan*) and mitochondria (*yellow*) in BS-C-1 cells immunostained with the Cy3-Alexa 750 dye pair and the Cy3-Alexa 647 dye pair, respectively. Figure adapted from reference [69]. (**b**) Four-color super-resolution image of a fixed BS-C-1 cell stained for the endoplasmic reticulum (ER), mitochondria, microtubules, and acetylated tubulin [40]. *Left panel*: Two of the four color channels, showing Alexa 647-labeled ER (*cyan*) and Cy3B-labeled mitochondria (*magenta*). *Right panel*: The other two color channels of the same image, showing Atto 488-labeled microtubules (*green*) and DyLight 750-labeled acetylated tubulin (*white*). Figure adapted from reference [40]. (**c**, **d**) Examples in which emitters with overlapping emission spectra were used and color identification was achieved through a ratiometric method. (**c**) Three-color super-resolution image of Alexa 488-phalloidin-labeled F-actin (*blue*), Atto 532-labeled clathrin (*green*), and Cy3-labeled tubulin (*red*) in a fixed PtK2 cell. Figure adapted from reference [77]. A conventional wide-field image of the upper right corner of the field of view is shown for comparison. (**d**) Three-color super-resolution image of Dendra2-hemagglutinin (*cyan*), PAmCherry1-β-actin (*yellow*), and PAmKate-transferrin receptor (*magenta*) expressed in a fixed HAb2 cell. Figure adapted from reference [74]

crosstalk (10–20 %) between different color channels [69]. Although crosstalk subtraction [70] can reduce the crosstalk to below 10 %, when imaging molecules with very different abundance, crosstalk from the high-abundance species could overwhelm the signal from the low-abundance species.

5.2 *Emission-Based Multicolor Imaging*

Multicolor imaging can also be achieved by employing photoswitchable probes (emitters) with different emission colors (Fig. 5). Emission-based multicolor super-resolution imaging has been achieved using different-colored fluorescent

proteins [71–74], different-colored organic dyes [40, 41, 75–77], or a combination of fluorescent proteins and dyes [21]. A recent comprehensive dye screen led to the identification of high-quality photoswitchable dyes in four separate spectral regions and thus four-color super-resolution imaging (Fig. 5b) [40]. Three-color super-resolution imaging has also been accomplished with fluorescent proteins (Fig. 5d) [74].

Compared to the activation-based approach, the emission-based approach provides substantially lower color crosstalk (as low as a few percent) when the probes used have well-separated emission spectra (Fig. 5a, b). In the event that the emission spectra of the different probes overlap considerably, they can still be separately identified using ratiometric methods (Fig. 5c, d), though the crosstalk in this case tends to be higher (5–20 %) [74, 75, 77].

A drawback of the emission-based multicolor approach is that multiple filter sets and/or optical paths have to be employed. Aligning the images obtained from different color channels with nanometer-scale accuracy is nontrivial, especially since chromatic aberrations (and other imperfections) are hard to eliminate completely in the imaging system. Alignment of different color channels is typically performed using fiducial markers such as fluorescent beads with a broad emission spectrum [41]. In addition, not all photoswtichable probes have the same brightness (number of photons detected per switching event). The brightest photoswitchable probes (i.e., Cy5, Alexa 647) all tend to have the same (far-red) emission wavelength [40]. As a result, one or more channels will have compromised image resolution using emission-based multicolor imaging as compared to activation-based multicolor imaging. The use of probes with different emission spectra also creates problems for interferometry-based 3D imaging, though it is possible to solve these problems with probes of overlapping spectra using a ratiometric method [59].

Finally, when activator-reporter dye pairs are used, combination of the activation-based and emission-based approaches allows imaging with a large number of colors. For example, when three reporter dyes and three activator dyes are combined, as many as nine distinct dye pairs can be constructed. Six- and seven-color super-resolution imaging has recently been demonstrated using this combinatorial approach [69, 78].

6 Live-Cell Imaging

Live-cell imaging capability is another key advantage of optical microscopy, which allows direct visualization of molecular processes in cells in real time. The substantially improved spatial resolution of optical nanoscopy opens a new window for capturing ultrastructural dynamics in vivo. A number of important factors should be considered for live-cell imaging, including labeling living cells with photoswitchable probes, the trade-off between spatial and temporal resolutions, motion blurring effect, and potential phototoxicity to live samples. We discuss these points below.

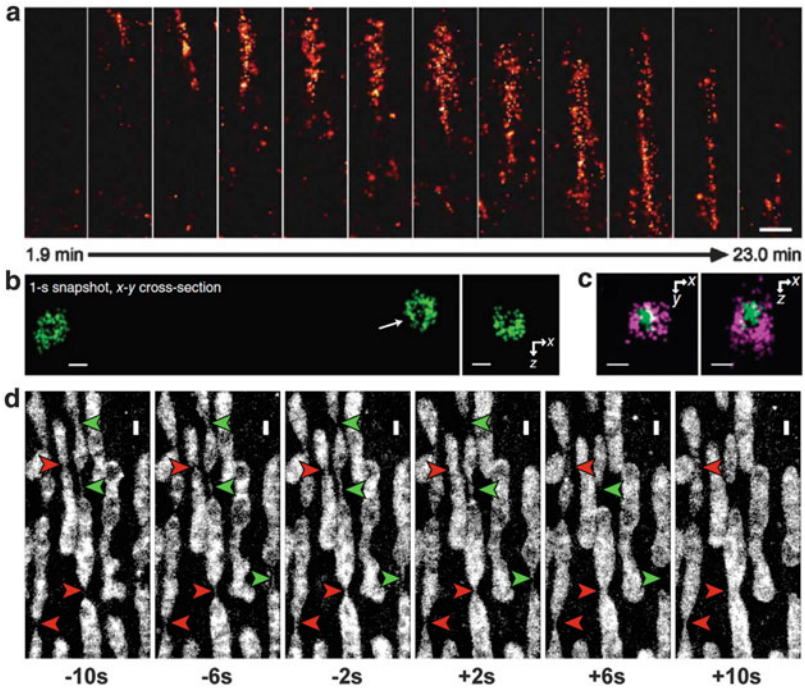

Fig. 6 Live-cell super-resolution imaging. (**a**) tdEos-tagged focal adhesion molecules imaged in 2D at 55-s time resolution in a live CHO cell. Figure adapted from reference [42]. (**b**) Alexa 647-SNAP-labeled clathrin-coated pits resolved in 3D at 1-s resolution in a live BS-C-1 cell. *Left panel*: An *x-y* cross section of clathrin-coated pits near the plasma membrane. *Right panel*: An *x-z* cross section through the middle of the coated pit indicated by the *arrow*. Figure adapted from reference [41]. (**c**) Two-color image of an Alexa 647-SNAP-labeled clathrin-coated pit (*magenta*) enclosing an Alexa 568-conjugated transferrin cluster (*green*) in a live BS-C-1 cell. *Left panel*: An *x-y* cross section near the plasma membrane. *Right panel*: An *x-z* cross section cutting through the middle of the pit. Figure adapted from reference [41]. (**d**) MitoTrackerRed-labeled mitochondria imaged at 2-s time resolution in a live BS-C-1 cell. Mitochondrial fusion (*red arrows*) and fission (*green arrows*) intermediates with tubular structures are observed with high resolution in real time. Figure adapted from reference [90]. Scale bars: (**a**) 5 μm, (**b**, **c**) 100 nm, (**d**) 500 nm

6.1 Labeling Live Cells with Photoswitchable Probes

The most straightforward method for labeling proteins in live cells with fluorescent probes is to use fluorescent proteins, which can be genetically fused to the target proteins of interest. Indeed, live-cell sub-diffraction-limit imaging using the stochastic switching was initially demonstrated with photoactivatable fluorescent proteins: PA-GFP, tdEos, or mEos2 in mammalian cells [42, 79] (Fig. 6a) and EYFP in bacteria [27]. To achieve relatively high resolution and avoid potential

artifacts due to the oligomerization tendency of fluorescent proteins, bright, monomeric proteins such as Dendra, mEos2, mEos3, PAmCherry, and PAtagRFP [73, 80–83] are preferred. On the other hand, these proteins can switch on only one to two times before photobleaching. For applications where many snapshots are required to follow the entire time course of a process, proteins with many switching cycles are required. The newly developed rsEGFP and Dreiklang, which can switch hundreds to thousands of cycles [84, 85], may be promising candidates.

Compared to fluorescent proteins, organic dyes tend to have superior brightness and faster switching rates, and thus offer higher spatial and temporal resolutions. Live-cell labeling of proteins with organic dyes, however, requires more steps than with fluorescent proteins: (1) the target protein needs to be genetically encoded with specific peptide or protein tags that can bind to or react with dyes; (2) dyes have to be delivered into live cells such that they can be attached to the specific tag. Live-cell super-resolution imaging has been demonstrated with various tags including SNAP, Halo, and trimethoprim [41, 77, 86–88]. For live-cell delivery, cell-permeable dyes are most convenient and these dyes, such as Atto 655, TMR, and OregonGreen, have been used for super-resolution imaging of living cells [77, 86, 88]. However, these dyes are not brighter (i.e., does not give more photons per switching cycle) than the above-mentioned fluorescent proteins and, hence, do not provide higher image resolution. The bright and fast switching dyes, such as Cy5 and Alexa 647, which yield ~4 times more photons than the cell-permeable dyes and fluorescent proteins in living cells, cannot spontaneously penetrate cell membrane. Nonetheless, they can be delivered into live cells by methods that temporally disrupt the cell membrane, such as electroporation, bead loading, and microinjection, providing substantially higher spatial and temporal resolution than affordable by fluorescent proteins [41] (Fig. 6b). One thing to note, however, is that switching characteristics of these cyanine dyes tend to be sensitive to their environment and the best performance often requires chemical additives such as thiols and oxygen scavengers; at low concentrations, these additives do not affect cell viability.

Small-molecule probes that directly bind to DNA or membrane can also be used for live-cell super-resolution imaging. These probes are often commercially available and easy to use. Also, the high labeling density, stemming from the small size and high affinity of these probes, improves the resolution and extends the length of time-lapse imaging. Nuclear and mitochondrial DNA were imaged in live cells with Picogreen [89]. Eight conventional membrane probes enabled live-cell imaging of the plasma membrane, mitochondria, ER, and lysosomes (Fig. 6d) [90].

Multicolor live-cell imaging has also been achieved using spectrally distinct fluorophores, either with fluorescent proteins [73] or fluorescent dyes (Fig. 6c) [41]. For fluorophores with partially overlapping spectra, ratiometric methods can be used for live-cell super-resolution imaging, again either using dyes, fluorescent proteins, or a combination between the two [74, 77, 90].

6.2 Spatial and Temporal Resolutions

In time-resolved super-resolution imaging, spatial and temporal resolutions intrinsically trade off with each other. For example, in the point scanning approaches, such as STED [91], the higher the resolution, the smaller the pixel size used on scanning and hence the slower the imaging speed. In the wide-field single-molecule-based approach, such as STORM and (F)PALM, the trade-off between spatial and temporal resolutions arises from the fact that a sufficiently large number of localizations need to be accumulated to resolve a structure at a desired Nyquist resolution (see Sect. 3.2 for definition of Nyquist resolution) [42]. Increasing the time window will result in more localizations, thereby improving the spatial resolution defined by the Nyquist criterion. Conversely, decreasing the time window for each STORM snapshot will improve the time resolution at the expense of the spatial resolution.

In live-cell studies using photoswitchable/photoactivatable fluorescent proteins, spatial resolutions of 40–70 nm have been achieved with 30–60 s time resolutions [27, 42] (Fig. 6a). Improving the time resolution may be difficult with the currently available fluorescent proteins as the number of photons detected per switching cycle tends to decrease when the excitation laser intensity was increased to accelerate the switching rate [41]. Hence, the camera frame rate used for imaging photoswitchable/photoactivatable fluorescent proteins is typically not higher than 100 Hz, beyond which the image quality deteriorates rapidly. This difficulty can be overcome with bright, fast switching fluorescent dyes, such as Alexa 647, which give a constant number of photons per switching cycle even when the off-switching rate is as fast as ~1 ms. Hence, STORM images using Alexa 647 could be recorded at the camera frame rate of 500–1,000 Hz, and cellular structures have been imaged in two dimensions with a Nyquist resolution of ~20 nm at time resolutions as high as 0.5 s [41].

For 3D imaging, substantially more localizations are required to define a structure with the same Nyquist resolution than in 2D given that the localizations are now spread across a 3D volume instead of a 2D projected area. For instance, a sphere with a 100-nm diameter would require only 80 localizations in 2D but 520 localizations in 3D to achieve a 20-nm Nyquist resolution. Hence, the temporal resolution of 3D super-resolution is typically lower than the 2D counterpart. Using Alexa 647 and astigmatism imaging, 3D super-resolution imaging has been achieved with a Nyquist resolution of 25–30 nm at 1–2-s temporal resolution (Fig. 6b) [41]. Another factor that reduces the 3D imaging speed is that the modified PSF for axial localization will cover a larger area, reducing the number of molecules that can be localized per frame, and hence the overall imaging speed. For example, the elliptically shaped PSF in astigmatism imaging [39], the isotropically expanded PSF in biplane imaging [54], and the rotating dumbbell PSF in DH-PSF imaging [55], all cover substantially larger area than the focused, circularly symmetric PSF used in 2D imaging. While the interferometry-based method [57] does not increase

the PSF size, the need to sandwich the sample between two objectives in this case considerably limits the applicability of such methods to live-cell imaging.

One way of improving the time resolution of live-cell imaging is to develop analysis methods that can fit multiple, partially overlapping PSFs simultaneously. Several analysis methods have been developed for these purposes, such as DAOSTORM [30, 32], multiple emitter fitting [31], 3B analysis [36], decon-STORM [38], and compressed sensing [33]. Such analysis methods allow for the activation of more molecules per frame, so the desired number of localizations can be collected in a smaller number of camera frames (and shorter time). SOFI [37], a super-resolution imaging method based on single-molecule fluctuation, also allows for fast live-cell super-resolution and will be described in detail in another chapter of this book.

6.3 Single-Molecule Tracking

The use of photoactivation also offers a unique opportunity to capture the dynamics of individual molecules in living cells. For example, single-particle tracking has been widely used to probe the motion (diffusion) of lipids and proteins on membranes in live cells [92]. However, to track individual molecules, the density of molecular images must be kept low enough that the images do not overlap. The low-density molecular traces make it difficult to provide both spatially and temporally resolved information about membrane diffusivity. Photoactivatable probes allow high-density single-molecule tracking in live cells by switching on an optically resolvable subset of photoactivatable probes at any time, tracking individual probes until photobleaching, and then repeating cycles of switching and tracking to accumulate a large number of trajectories [93]. Besides using photoactivation, binding/unbinding events can also be used to collect a high density of molecular trajectories on the cell surface as shown in PAINT [28, 94]. The time resolution of tracing individual molecules is limited by the camera frame rate, typically in the range of 30–1,000 Hz. The high-density map of molecular trajectories can be used to probe distinct subsets of molecules and can provide insight into spatial and temporal heterogeneities in the membrane [82, 93, 95], as well as in other systems.

6.4 Motion Blur

Unlike in fixed specimens, molecules and subcellular structures move in live cells. Their motion can effectively deteriorate spatial resolution and distort the observed structures. Two types of motions are important to consider for live-cell super-resolution imaging. The first type is the motion of probe molecules within

a camera frame (e.g., diffusion). A general rule of thumb is that, to maintain the localization precision, the probe molecule should not move by a distance larger than the localization error during a camera frame. For example, a molecule diffusing at 0.1 $\mu m^2\ s^{-1}$ on a membrane moves by 200 nm on average within 0.1 s and by 30 nm in 2 ms. Thus, a fast camera is essential for localizing fast-diffusing molecules with high precision. Additionally, the image shape of the molecule is blurred by diffusion within a camera frame, and therefore 3D imaging methods that rely on PSF shapes to obtain the axial position potentially require even faster frame rate. The plus side of molecular diffusion is that as the molecules diffuse within and map out the underlying structure, each probe molecule could contribute more than one independent localizations, which in turn improves the Nyquist resolution.

The second type of motion to consider is the motion/change of the structure itself during each super-resolution snapshot. To avoid artifacts due to this motion, the displacement/deformation of the structure during the time acquiring each snapshot should be less than the spatial resolution. Given that super-resolution methods provide higher image resolution than conventional fluorescence microscopy, and in the meantime acquires each snapshot more slowly, this paradox puts a more stringent constraint on the motion of the cellular structure.

6.5 Photo- and Chemical Toxicity

Live-cell super-resolution imaging typically requires stronger excitation light intensity than conventional microscopy. In some cases, chemical additives are also added in the imaging buffer to facilitate photoswitching of fluorophores. These conditions can affect cell viability. Red or near-infrared light is less phototoxic than blue or UV light and is thus preferred for live-cell imaging. Some photoswitchable organic dyes, including Cy5, Alexa 647, Cy7, and Alexa 750 can be imaged at far-red and near-infrared wavelengths [18, 40]. Recently, an orange-to-far-red photoswitchable fluorescent protein was also developed [96]. In addition to the imaging laser, UV or violet light is often used for activating photoswitchable dyes and fluorescent proteins. Coupling activator dyes with photoswitchable reporter dyes can help to reduce the activation intensity or to change the activation color to a less phototoxic wavelength. To prolong the lifetime of fluorophores, the imaging medium is often supplemented with oxygen and/or radical scavengers, which are also widely used for conventional live-cell imaging [97]. In addition, some organic dyes perform better in the presence of thiols or reducing/oxidizing agents. Although when added at low concentrations, these additives do not affect cell health, they have the potential to perturb the dynamics of interest and the viability of live cells at high concentrations. Hence, control experiments to test whether the imaging conditions perturb the cell viability and the dynamics under investigation are necessary.

7 Choice of Fluorescent Probes

As discussed above, the implementation of STORM, (F)PALM, and related methods depends on the stochastic switching of the fluorescent probes between the dark and emitting states. In an effort to provide general guidelines for the characterization of super-resolution probes, a recent study systematically investigated the properties of 26 organic dyes and identified several parameters as being crucial in determining the quality of the final super-resolution images: (1) photons per switching event, (2) on-off contrast ratio, (3) on-off duty cycle, and (4) number of switching cycles [40]. An ideal probe should emit a large number of photons per switching cycle and should provide high contrast between the on and off states, i.e., give bright emission in the emitting state (to maximize signal) and negligible emission in the dark state (to minimize background), so as to maximize the localization precision. It should also have a low on-off duty cycle, defined as the fraction of time that the probe spends in the on state, to maximize the number of probe molecules that can be localized per diffraction-limited volume. Together, these factors ensure a high overall image resolution when both localization precision and localization densities are considered. In addition, probes with a large number of switching cycles allow many super-resolution snapshots to be taken, which greatly benefit imaging of dynamic processes. Finally, other factors, including physical size of the probe and how the sample will be labeled with the probe, should also be taken into consideration when designing experiments.

Several subsequent chapters in this book are dedicated to probe development for nanoscopy. Here we only provide a general overview and briefly discuss the advantages and disadvantages of different types of probes for super-resolution applications.

7.1 Fluorescent Dyes vs. Fluorescent Proteins

Some photoswitchable dyes have excellent brightness (defined here as the number of photons detected per switching cycle), high contrast ratio, and low on-off duty ratio. Among the tens of synthesized dyes that have been tested, the red-absorbing (640–700 nm) dyes, Cy5, Alexa 647, and Dyomics 654 are among the best probes, each providing ~5,000 detected photons per switching cycle, exhibiting undetectable dark state fluorescence, and have an on-off duty ratio of ~0.001 or lower [40]. They consistently give higher-quality images than other probes. For multicolor imaging (see Sect. 5.2), dyes with reasonably good performance have also been identified for other spectral ranges; i.e., blue dyes Atto488 and Alexa 488; yellow dye Cy3B; and near-infrared dyes (740–805 nm) DyLight 750, Cy7, and Alexa Fluor 750 [40].

A popular way to label cellular structures with dyes is through immunofluorescence, either directly with dye-labeled primary antibodies or indirectly with labeled secondary antibodies. An advantage of the immunofluorescence scheme is that it

allows endogenous proteins to be labeled without introducing fusion proteins, which could potentially perturb the localization, function, and expression level of the target proteins. The drawbacks are that antibodies are relatively bulky (~10 nm in size) and it is difficult to label proteins in live cells with antibodies. These problems can be at least partially overcome through alternative dye-labeling methods. In hybrid fusion approaches, a specific enzyme or peptide tag is genetically fused to the protein of interest and the dye molecules are specifically attached to the tags [41, 77, 86–88, 98, 99]. In particular, short-peptide tagging methods like sortagging [100] and LplA labeling [101, 102] could be especially beneficial due to their small sizes (~1–2 nm). Target-specific small molecules can also be used to label cellular structures in some cases, e.g., phalloidin specifically labels filamentous actin [53].

Another popular type of fluorescent probes is fluorescent proteins. Compared to organic dyes, the advantage of fluorescent proteins is that they can be genetically fused to target protein of interest, offering a convenient and powerful way to label proteins in live cells. One should, however, be cautious about the potential artifacts on protein localization and function induced by fluorescent protein tags, which are ~4 nm in size and tend to oligomerize. Overexpression of the fusion proteins may also cause artifacts. The main disadvantage of fluorescent proteins is their inferior photophysical properties as compared to dyes. Fluorescent proteins are generally dimmer than organic dyes. The bright photoswitchable/photoactivable fluorescent proteins, such as Dendra2 [80], mEos2 [81], PAmCherry [73], and PAtagRFP [82] provide ~1,000 detected photons per switching cycles. The dark states of fluorescent proteins also tend to have non-negligible fluorescence, providing lower contrast ratio than switchable dyes. The on-off duty cycle of these fluorescent proteins, however, can be as low as 10^{-4}–10^{-5}, which is better than that of most organic dyes.

In addition to dyes and fluorescent proteins, quantum dots have also been used for super-resolution imaging [103].

7.2 Dye Pairs vs. Single Dyes

It has been shown that highly controllable photoswitches can be constructed when a photoswitchable reporter dye molecule (e.g., Cy5) is brought into the proximity of another activator dye molecule (e.g., Cy3) [104]. In this scheme, the reporter dye is imaged and switched off by the excitation light, while the activator dye is capable of activating the reporter when illuminated by light that matches the activator's absorption spectrum. The presence of the activator dye greatly facilitates the activation process and uniquely enables activation-based multicolor imaging, where activator dyes with different absorption spectra are used (more details of this multicolor imaging scheme are described in Sect. 5.1) [18]. For immunofluorescence imaging, antibodies can be nonspecifically labeled with both activator and reporter dyes in a single reaction step, in ways similar to labeling antibodies with a single type of dye. However, when labeling with the hybrid fusion approaches using

protein or peptide tags, covalently linked activator-reporter dye pairs are required. Such pre-linked dye pairs have been synthesized [62, 105].

The photoswitchable reporter dyes can also be directly activated through either the excitation light or an additional short-wavelength (e.g., UV to green) light [23, 68]. The major advantage of using the reporter dye alone (as opposed to dye pairs) is that a single dye can be more easily used to directly label target proteins (such as through the hybrid fusion approach) or to label small molecules. However, in the absence of an activator dye, the light intensity used to activate the reporter dye is often several orders of magnitude higher than when the activator dye is present. Strong short-wavelength illuminations, particularly UV and violet, could induce phototoxicity. Multicolor imaging with single dyes can be accomplished through the emission-based multicolor scheme. The advantages and disadvantages of the activation- and emission-based multicolor schemes are described in Sect. 5.

7.3 Reversible Photoswitchable vs. Irreversible Photoactivatable Probes

The switchable probes used for super-resolution imaging can also be categorized according to their switching properties. The reversible, *photoswitchable* probes can be switched between the emitting and dark states multiple times. An advantage of using reversible, photoswitchable probes is that each probe can be localized multiple times. This is particularly useful for live-cell studies, in which the morphological changes of structures often need to be tracked over a substantially long period. In addition, most photoswitchable probes start in an emitting state before being switched off prior to super-resolution imaging. Conventional fluorescence images can thus be obtained before super-resolution imaging is performed, which in practice is useful for locating regions of interest.

In comparison, the irreversible, *photoactivatable* probes can only be brought into the emission state once. During imaging, individual probes are activated, imaged, and permanently photobleached. As each probe can only be imaged once, these probes are less suitable for monitoring live-cell dynamics that requires many snapshots. On the other hand, the fact that each molecule only appears once makes it easier to quantify the number of molecules in a target structure. It is worth noting though, many photoactivatable fluorescent proteins that are thought to be irreversibly activated can in fact be switched on and off a few times [106, 107], and methods to account for this reversible blinking effect in protein quantification have been recently developed [95, 108, 109]. For stoichiometric quantification, one also needs to know the fraction of target molecules that are labeled and the fraction of the fluorescent labels that have matured (for fluorescent proteins) and can be photoactivated (for both fluorescent proteins and dyes).

Rather than switching between a dark state and an emitting state, *photochromic* probes switch from one emitting color to a different color (e.g., from green to red)

upon being activated by light. For example, EosFP switches from a green, pre-activation state to an orange/red, post-activation state [110]. Photochromic probes can either irreversibly or reversibly switch between two emitting states. Photochromic probes, in general, also allow for the recording of conventional fluorescence images before super-resolution imaging, e.g., in the color channel before photoswitching.

7.4 Other Probes

Beyond using photoswitchable fluorescent probes as discussed above, it is also worth mentioning that alternative strategies have also been developed. These strategies include the use of the PAINT approach [28], in which the emission of the probes is recorded when they stochastically bind to the target, and the reversible chemical quenchers [29], in which the stochastic switching of probes is realized through the reversible binding of fluorescence quenchers (Sect. 2).

8 Applications

Due to their superb resolving power and relatively simple implementation, STORM, (F)PALM, and related methods have been rapidly adopted by many labs and applied to a variety of biological systems. Here we will focus on applications in our laboratory and related studies. Interested readers can also find numerous applications in other chapters of this book.

8.1 Applications in Cell Biology

In eukaryotic cells, many well-characterized structures such as the cytoskeleton and other protein scaffolds have been reexamined with super-resolution fluorescence microscopy. These proof-of-principle systems not only demonstrated the resolving power of the technique but also gave a glimpse of its potential for novel discoveries. One application where this potential has been demonstrated is the study of clathrin-coated pits, an essential cellular structure used for receptor-mediated endocytosis. A clathrin-coated pit on the plasma membrane contains layers of receptor and adaptor proteins under the clathrin coat, forming a spherical shell with a diameter of ~100 nm. The sub-diffraction-limit morphology of clathrin-coated pits was used to demonstrate the multicolor [18], 3D [39], and live-cell [41] capabilities of STORM imaging in cells. In an in vitro model system, two membrane-curvature generating/sensing proteins, dynamin and FBP17, were found to distribute differentially on membrane tubules connecting clathrin-coated

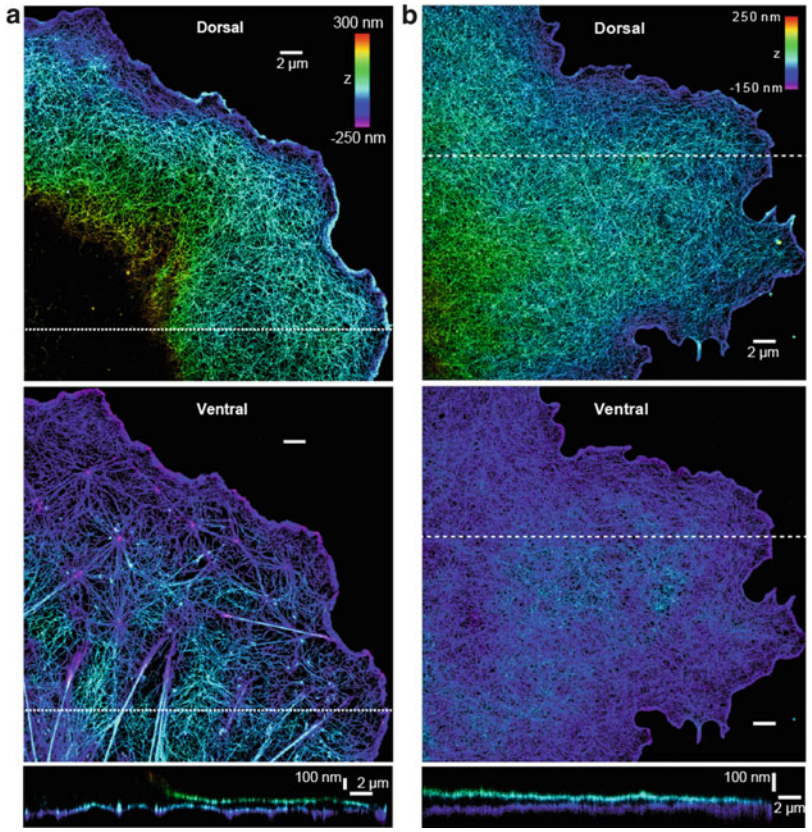

Fig. 7 STORM images of actin in sheet-like protrusions. (**a**) Dorsal (*top*) and ventral (*middle*) actin layers of a BS-C-1 cell. *Bottom panel*: Vertical cross section (500 nm wide in *y*) along the dotted lines in the *top* and *middle panels*. (**b**) Dorsal (*top*) and ventral (*middle*) actin layers of a COS-7 cell treated with blebbistatin, an inhibitor for myosin II. *Bottom panel*: Vertical cross section (500 nm wide in y) along the dashed lines in the top and middle panels. Scale bars: 2 μm (*horizontal*), 100 nm (*vertical*). Figure adapted from reference [53]

pits: While FBP17 coats the entire tubule below the clathrin-coated pit, dynamin is only located at the narrow neck region between the clathrin-coated pit and the FBP-17-coated tubule [111]. In conjunction with confocal fluorescence imaging and electron microscopy, STORM revealed an unexpected role of FBP17 in creating endocytic vesicles [111].

Actin cytoskeleton is another representative example. Dual-objective STORM resolved individual actin filaments in cells and revealed 3D ultrastructure of the actin cytoskeleton [53]. In particular, two vertically separated layers of actin networks were revealed in sheet-like cell protrusions (Fig. 7a). The two actin layers exhibited highly distinct structural organizations: The dorsal layer appeared as a consistently dense and homogeneous meshwork; the ventral layer typically formed

a web-like structure with a lower filament density and highly variable organization (Fig. 7a). This striking structural difference between the ventral and dorsal actin networks could be completely removed by inhibiting myosin II activity (Fig. 7b), suggesting an important role of myosin II in maintaining the distinct structural organization of the two actin networks.

8.2 Applications in Microbiology

In addition to eukaryotic cells, super-resolution fluorescence microscopy is also becoming an important imaging tool for investigating bacteria. Due to the very small volumes (~1 μm^3) of prokaryotic cells, it is difficult to resolve the subcellular organization of bacteria using conventional fluorescence microscopy. Ultrastructural studies have thus mostly relied on electron microscopy (EM). However, it is often difficult to resolve molecule-specific structures in EM images due to poor molecular contrast. Moreover, EM cannot be used to image live specimens and monitor dynamics. Fluorescence imaging methods with molecule-specific contrast and nanometer-scale resolution promise to change our view of bacterial cell biology by revealing how proteins are organized in bacterial cells. For example, clustered distribution of chemotaxis proteins, Tar receptor, CheY, and CheW has been observed in fixed *E. coli* cells [112]. A helical organization of MreB, an actin analog, has been observed in live *Caulobacter crescentus* [27]. The DNA-partitioning proteins, ParA and ParB, form narrow, linear polymer structures in *Caulobacter crescentus*, resembling mitotic spindles in eukaryotic cells [113]. A major nucleoid-associated protein (NAP), H-NS, forms tight clusters in the nucleoid in live *E. coli* cells, ~ 2 clusters per chromosome (Fig. 8a) [114]. This clustered distribution, highly distinct from other major NAPs (Fig. 8b), is formed due to the self-interactions between the N-terminal domain of H-NS. As a global transcriptional silencer, H-NS sequester numerous H-NS–regulated genes into these compact clusters (Fig. 8c), which serve as organization centers to organize bacterial chromosome. Other bacterial proteins, such as HU, IHF, FIS, StpA [114, 115], FtsZ [116], and SpoIIIE [117], have also been investigated using super-resolution imaging.

8.3 Applications in Neurobiology

Another exciting area into which super-resolution imaging will likely bring new breakthroughs is neurobiology. Neurons have complex, multi-scale morphologies. Many important neuronal structures have dimensions on submicron or nanometer scales. For example, axons in the neuropil can be as thin as 100 nm. Dendritic spine necks are often narrower than 100 nm. Chemical synapses, the basic functional units in the brain that mediate neurotransmitter-based communications between

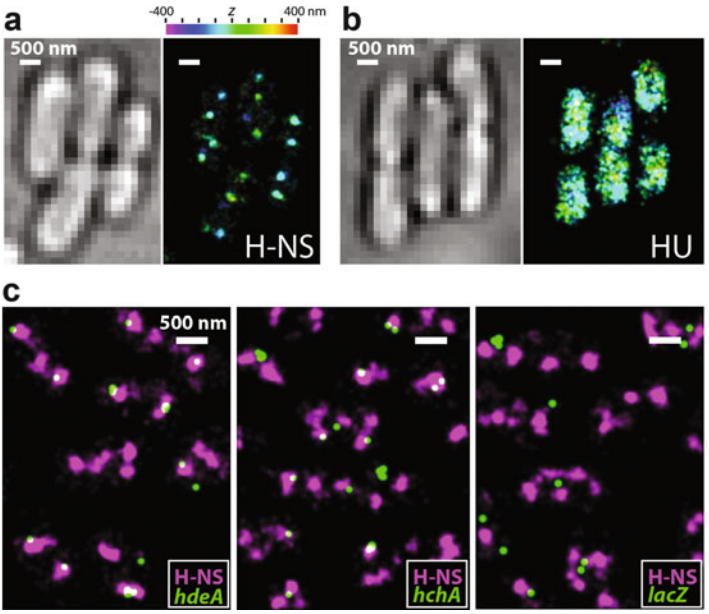

Fig. 8 STORM images of nucleoid-associated proteins in living *E. coli* cells. (**a**) H-NS forms compact clusters in the nucleosome. *Left panel*: Bright-field image of the cells. *Right panel*: 3D super-resolution image of H-NS fused with mEos2. The z-coordinates are color coded according to the color bar (*top*). (**b**) HU is scattered through the nucleoid. *Left panel*: Bright-field image of the cells. *Right panel*: 3D super-resolution image of HU fused with mEos2. (**c**) Colocalization of H-NS clusters and gene loci revealed by two-color live-cell images of mEos2-labeled H-NS (*magenta*) and eYFP-labeled gene loci (*green*). The two H-NS–regulated loci, *hdeA* (*left*) and *hchA* (*center*), were colocalized with H-NS clusters to a noticeably larger extent than did *lacZ* (*right*), which is not regulated by H-NS. Scale bars: 500 nm. Figure adapted from reference [114]

neurons and their target cells, are typically several hundred nanometers in size. Hence, both the investigations of sub-neuronal structures and the mapping of neural connectivity in the brain require imaging tools with nanometer resolution. Indeed, super-resolution fluorescence imaging has begun to provide new insights into neuronal and sub-neuronal structures. For example, multicolor 3D super-resolution imaging has been performed to determine the molecular distributions of ten protein components of the presynaptic active zone and the postsynaptic density (Fig. 9) [70]. This study has shown a laminar organization of the postsynaptic density components, PSD-95, Shank, and Homer, consistent with previous EM analysis [118] (Fig. 9i). It has also revealed a previously unknown, oriented organization of the presynaptic scaffolding proteins, Bassoon and Piccolo (Fig. 9i). Significant variations in the spatial distributions of neurotransmitter receptors have also been observed from synapse to synapse (Fig. 9f–h). Moreover, quantitative receptor composition analysis led to the discovery of a surprisingly large population of immature synapses with activity-dependent plasticity in the adult accessory olfactory bulb [70]. In a different study, high-density single-molecule tracking with

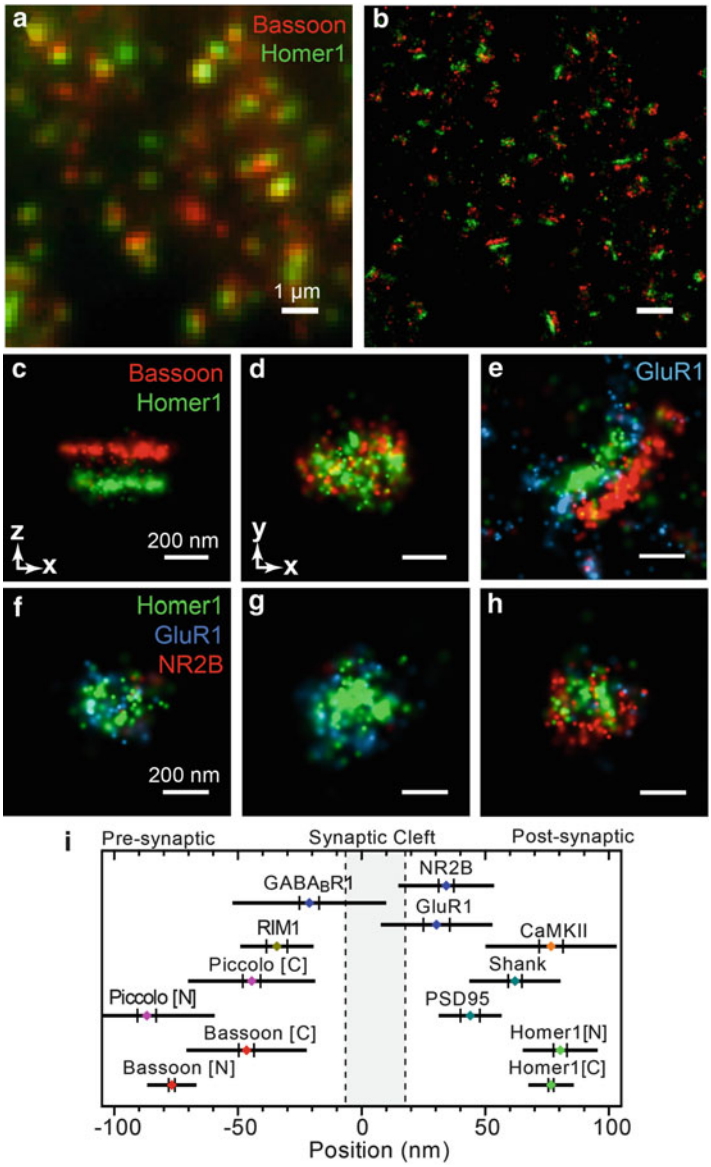

Fig. 9 STORM images of synaptic proteins in brain tissues. (**a**–**d**) STORM imaging of pre- and postsynaptic scaffolding proteins. Presynaptic protein Bassoon (*red*) and postsynaptic protein Homer1 (*green*) in the mouse main olfactory bulb were immunolabeled with Cy3-Alexa 647 and Alexa 405-Alexa 647 dye pairs. Partially overlapping puncta in a conventional image (**a**) were clearly resolved as distinct synaptic structures in the corresponding STORM image (**b**). (**c**, **d**) Well-separated elliptical disks of presynaptic scaffolds Bassoon (*red*) and postsynaptic scaffolds Homer1 (*green*) are shown in two different orientations. (**c**) A side view with the trans-synaptic axis rotated into the viewing plane. (**d**) An en face view with the trans-synaptic axis rotated

photoactivatable proteins has been used to investigate actin dynamics within dendritic spines [119]. This work has revealed a heterogeneous distribution of the actin polymerization rate as well as highly localized but spatially diverse foci of actin polymerization, indicating an active regulatory role of actin in the synapses [119].

Due to the space limit, we could only provide a glimpse of the recent applications of STORM, (F)PALM, and related imaging methods. More applications of these methods can be found in subsequent chapters of this book. The number of applications is increasing exponentially. We expect numerous new discoveries enabled by these powerful imaging approaches.

9 Concluding Remarks and Future Developments

By separating the otherwise spatially overlapping fluorescence signals from densely packed fluorophores in the time domain, STORM, (F)PALM, and related methods overcome the diffraction limit through switching and localization of individual molecules. These methods improve the spatial resolution of far-field optical microscopy by more than an order of magnitude, achieving resolutions down to the sub-10 nm range for biological specimens. The ability to perform multicolor, 3D, and live-cell imaging further enhances the versatility of these methods. Super-resolution fluorescence imaging can also be combined with other microscopy methods, such as EM [16, 120], to simultaneously exploit the respective strengths of different imaging modalities.

In principle, the image resolution of these methods can be extremely high, as long as suitable conditions could be found to allow for both maximal emission of photons and proper photoswitching (though in practice, being a fluorescence imaging modality, the image resolution may not exceed the size of the fluorescent labels). It is thus expected that the spatial resolution of these methods could become substantially better than 10 nm. In fact, a recent work has demonstrated the use of reductive caging to generate ultrabright photoactivatable fluorescent probes and improved image resolution to the single digit nanometer range [121]. We anticipate even higher resolution to be possible. Likewise, further improvement in faster switching probes, faster camera, and image analysis algorithms should also allow

Fig. 9 (continued) perpendicular to the viewing plane. (**e**) AMPA receptor subunit GluR1 (*blue*) imaged together with Bassoon (*red*) and Homer1 (*green*). A side view of a synapse is shown here. (**f–h**) Radial distributions of glutamate neurotransmitter receptors in the postsynaptic density (PSD) shown in the en face view. AMPA receptor subunit GluR1 (*blue*) and NMDA receptor subunit NR2B (*red*) were imaged together with Homer1 (*green*). (**i**) Axial positions of 13 synaptic proteins along the trans-synaptic axis. For each protein, the *colored dots* indicate the mean position, the two vertical lines represent the associated standard error, and the half-lengths of the horizontal bar denote standard deviation, derived from multiple synapses. Scale bars: 1 μm (**a–b**), 200 nm (**c–h**). Figure adapted from reference [70]

imaging with time resolutions substantially faster than 1 s. Another important frontier is in vivo imaging, which requires substantial improvement of the imaging depth of these methods in scattering tissues.

Future development of these methods will require synergy between multiple disciplines. On the optics and hardware front, careful design and/or calibration of the imaging setup [6] could lead to extraordinarily high localization precision of single molecules. Besides continued innovations in the detection paths [39, 53–57, 59, 61, 122], recent studies have shown that developments in the illumination paths are also fruitful, especially for increasing imaging depth using multi-photoactivation and sheet illumination [65, 67]. Advances in cameras (e.g., scientific CMOS) [123, 124] could also be beneficial by improving the spatiotemporal resolution and/or introducing new capabilities.

Meanwhile, developments in analysis algorithms and theoretical modeling, possibly in combination with modifications to how the experimental data are acquired, could continue to improve the performance of these super-resolution methods and further broaden their range of application. For example, for improvement of spatial resolution, maximum-likelihood fitting of single-molecule images to true PSFs has led to more optimal localization results [125, 126]. For improvement of temporal resolution, methods have been developed to analyze overlapped images of multiple fluorophores simultaneously [30–33, 36–38] (see also discussion in Sects. 2 and 6.2).

On the chemistry and chemical biology side, the design and/or screening of new photoswitchable probes [40, 84, 85, 127, 128] with superior brightness of the fluorescent state (i.e., large number of photons per switching event), higher contrast ratio between the fluorescent and dark state, lower on-off duty cycle, faster switching speed, and more switching cycles would be tremendously helpful not only for improving the spatial and temporal resolutions, but also for prolonging the observation time window and expanding the color palette. To this end, understanding the photoswitching mechanisms of the probes will be very useful [128–131]. Novel stochastic readouts other than photoswitching could further expand the palette of probes and the information content [28, 29, 132]. The development of new, live-cell-compatible labeling methods that can achieve high molecular specificity and high labeling density with small label sizes [98] would also contribute substantially to further improvement of imaging qualities.

Combining the above efforts, we anticipate that true molecular-scale resolution in living cells, tissues, and even living animals will be within reach some day. At the other end of the spectrum, engineering efforts have packaged the imaging system into a compact, easy-to-operate unit. Commercial, user-friendly, super-resolution imaging systems are becoming available through multiple companies [133, 134]. These systems could make the benefits of these imaging methods accessible to all researchers, not just those who are comfortable with building their own setups.

Acknowledgments We thank Hazen P. Babcock for help in manuscript preparation. This work is supported in part by the National Institute of Health (to X.Z.). X.Z. is a Howard Hughes Medical Institute investigator.

References

1. Guilford WH, Cheezum MK, Walker WF (2001) Quantitative comparison of algorithms for tracking single fluorescent particles. Biophys J 81(4):2378–2388
2. Thompson RE, Larson DR, Webb WW (2002) Precise nanometer localization analysis for individual fluorescent probes. Biophys J 82(5):2775–2783
3. Gelles J, Schnapp BJ, Sheetz MP (1988) Tracking kinesin-driven movements with nanometre-scale precision. Nature 331(6155):450–453
4. Moerner WE, Orrit M (1999) Illuminating single molecules in condensed matter. Science 283(5408):1670–1676
5. Yildiz A, Forkey JN, McKinney SA, Ha T, Goldman YE, Selvin PR (2003) Myosin V walks hand-over-hand: single fluorophore imaging with 1.5-nm localization. Science 300(5628):2061–2065
6. Pertsinidis A, Zhang YX, Chu S (2010) Subnanometre single-molecule localization, registration and distance measurements. Nature 466(7306):647–651
7. Betzig E (1995) Proposed method for molecular optical imaging. Opt Lett 20(3):237–239
8. Schmidt J, van Oijen AM, Kohler J, Muller M, Brakenhoff GJ (1998) 3-Dimensional super-resolution by spectrally selective imaging. Chem Phys Lett 292(1–2):183–187
9. Lacoste TD, Michalet X, Pinaud F, Chemla DS, Alivisatos AP, Weiss S (2000) Ultrahigh-resolution multicolor colocalization of single fluorescent probes. Proc Natl Acad Sci U S A 97(17):9461–9466
10. Churchman LS, Okten Z, Rock RS, Dawson JF, Spudich JA (2005) Single molecule high-resolution colocalization of Cy3 and Cy5 attached to macromolecules measures intramolecular distances through time. Proc Natl Acad Sci U S A 102(5):1419–1423
11. Gordon MP, Ha T, Selvin PR (2004) Single-molecule high-resolution imaging with photobleaching. Proc Natl Acad Sci U S A 101(17):6462–6465
12. Qu XH, Wu D, Mets L, Scherer NF (2004) Nanometer-localized multiple single-molecule fluorescence microscopy. Proc Natl Acad Sci U S A 101(31):11298–11303
13. Lidke KA, Rieger B, Jovin TM, Heintzmann R (2005) Superresolution by localization of quantum dots using blinking statistics. Opt Express 13(18):7052–7062
14. Lagerholm BC, Averett L, Weinreb GE, Jacobson K, Thompson NL (2006) Analysis method for measuring submicroscopic distances with blinking quantum dots. Biophys J 91(8):3050–3060
15. Rust MJ, Bates M, Zhuang XW (2006) Sub-diffraction-limit imaging by stochastic optical reconstruction microscopy (STORM). Nat Methods 3(10):793–795
16. Betzig E, Patterson GH, Sougrat R, Lindwasser OW, Olenych S, Bonifacino JS, Davidson MW, Lippincott-Schwartz J, Hess HF (2006) Imaging intracellular fluorescent proteins at nanometer resolution. Science 313(5793):1642–1645
17. Hess ST, Girirajan TPK, Mason MD (2006) Ultra-high resolution imaging by fluorescence photoactivation localization microscopy. Biophys J 91(11):4258–4272
18. Bates M, Huang B, Dempsey GT, Zhuang XW (2007) Multicolor super-resolution imaging with photo-switchable fluorescent probes. Science 317(5845):1749–1753
19. Huang B, Babcock H, Zhuang XW (2010) Breaking the diffraction barrier: super-resolution imaging of cells. Cell 143(7):1047–1058
20. Egner A, Geisler C, Von Middendorff C, Bock H, Wenzel D, Medda R, Andresen M, Stiel AC, Jakobs S, Eggeling C, Schonle A, Hell SW (2007) Fluorescence nanoscopy in whole cells by asynchronous localization of photoswitching emitters. Biophys J 93(9):3285–3290
21. Bock H, Geisler C, Wurm CA, Von Middendorff C, Jakobs S, Schonle A, Egner A, Hell SW, Eggeling C (2007) Two-color far-field fluorescence nanoscopy based on photoswitchable emitters. Appl Phys B-Lasers Opt 88(2):161–165
22. Folling J, Bossi M, Bock H, Medda R, Wurm CA, Hein B, Jakobs S, Eggeling C, Hell SW (2008) Fluorescence nanoscopy by ground-state depletion and single-molecule return. Nat Methods 5(11):943–945

23. Heilemann M, van de Linde S, Schuttpelz M, Kasper R, Seefeldt B, Mukherjee A, Tinnefeld P, Sauer M (2008) Subdiffraction-resolution fluorescence imaging with conventional fluorescent probes. Angew Chem-Int Edit 47(33):6172–6176
24. Vogelsang J, Cordes T, Forthmann C, Steinhauer C, Tinnefeld P (2009) Controlling the fluorescence of ordinary oxazine dyes for single-molecule switching and superresolution microscopy. Proc Natl Acad Sci U S A 106(20):8107–8112
25. Lemmer P, Gunkel M, Weiland Y, Muller P, Baddeley D, Kaufmann R, Urich A, Eipel H, Amberger R, Hausmann M, Cremer C (2009) Using conventional fluorescent markers for far-field fluorescence localization nanoscopy allows resolution in the 10-nm range. J Microsc-Oxf 235(2):163–171
26. Dickson RM, Cubitt AB, Tsien RY, Moerner WE (1997) On/off blinking and switching behaviour of single molecules of green fluorescent protein. Nature 388(6640):355–358
27. Biteen JS, Thompson MA, Tselentis NK, Bowman GR, Shapiro L, Moerner WE (2008) Super-resolution imaging in live *Caulobacter crescentus* cells using photoswitchable EYFP. Nat Methods 5(11):947–949
28. Sharonov A, Hochstrasser RM (2006) Wide-field subdiffraction imaging by accumulated binding of diffusing probes. Proc Natl Acad Sci U S A 103(50):18911–18916
29. Schwering M, Kiel A, Kurz A, Lymperopoulos K, Sprodefeld A, Kramer R, Herten DP (2011) Far-field nanoscopy with reversible chemical reactions. Angew Chem-Int Edit 50(13):2940–2945
30. Holden SJ, Uphoff S, Kapanidis AN (2011) DAOSTORM: an algorithm for high-density super-resolution microscopy. Nat Methods 8(4):279–280
31. Huang F, Schwartz SL, Byars JM, Lidke KA (2011) Simultaneous multiple-emitter fitting for single molecule super-resolution imaging. Biomed Opt Express 2(5):1377–1393
32. Babcock H, Sigal Y, Zhuang X (2012) A high-density 3D localization algorithm for stochastic optical reconstruction microscopy. Optical Nanoscopy 1(1):6
33. Zhu L, Zhang W, Elnatan D, Huang B (2012) Faster STORM using compressed sensing. Nat Methods 9(7):721–723
34. Burnette DT, Sengupta P, Dai YH, Lippincott-Schwartz J, Kachar B (2011) Bleaching/blinking assisted localization microscopy for superresolution imaging using standard fluorescent molecules. Proc Natl Acad Sci U S A 108(52):21081–21086
35. Simonson PD, Rothenberg E, Selvin PR (2011) Single-molecule-based super-resolution images in the presence of multiple fluorophores. Nano Lett 11(11):5090–5096
36. Cox S, Rosten E, Monypenny J, Jovanovic-Talisman T, Burnette DT, Lippincott-Schwartz J, Jones GE, Heintzmann R (2012) Bayesian localization microscopy reveals nanoscale podosome dynamics. Nat Methods 9(2):195–200
37. Dertinger T, Colyer R, Iyer G, Weiss S, Enderlein J (2009) Fast, background-free, 3D super-resolution optical fluctuation imaging (SOFI). Proc Natl Acad Sci U S A 106(52):22287–22292
38. Mukamel E, Babcock H, Zhuang X (2012) Statistical deconvolution for superresolution fluorescence microscopy. Biophys J 102(10):2391–2400
39. Huang B, Wang WQ, Bates M, Zhuang XW (2008) Three-dimensional super-resolution imaging by stochastic optical reconstruction microscopy. Science 319(5864):810–813
40. Dempsey GT, Vaughan JC, Chen KH, Bates M, Zhuang X (2011) Evaluation of fluorophores for optimal performance in localization-based super-resolution imaging. Nat Methods 8(12):1027–1036
41. Jones SA, Shim SH, He J, Zhuang XW (2011) Fast, three-dimensional super-resolution imaging of live cells. Nat Methods 8(6):499–505
42. Shroff H, Galbraith CG, Galbraith JA, Betzig E (2008) Live-cell photoactivated localization microscopy of nanoscale adhesion dynamics. Nat Methods 5(5):417–423
43. Kao HP, Verkman AS (1994) Tracking of single fluorescent particles in three dimensions: use of cylindrical optics to encode particle position. Biophys J 67(3):1291–1300
44. van Oijen AM, Kohler J, Schmidt J, Muller M, Brakenhoff GJ (1998) 3-Dimensional super-resolution by spectrally selective imaging. Chem Phys Lett 292(1–2):183–187

45. Speidel M, Jonas A, Florin EL (2003) Three-dimensional tracking of fluorescent nanoparticles with subnanometer precision by use of off-focus imaging. Opt Lett 28(2):69–71
46. Prabhat P, Ram S, Ward ES, Ober RJ (2006) Simultaneous imaging of several focal planes in fluorescence microscopy for the study of cellular dynamics in 3D. Proc SPIE 6090:60900L
47. Holtzer L, Meckel T, Schmidt T (2007) Nanometric three-dimensional tracking of individual quantum dots in cells. Appl Phys Lett 90(5):3
48. Toprak E, Balci H, Blehm BH, Selvin PR (2007) Three-dimensional particle tracking via bifocal imaging. Nano Lett 7(7):2043–2045
49. Pavani SRP, Piestun R (2008) Three dimensional tracking of fluorescent microparticles using a photon-limited double-helix response system. Opt Express 16(26):22048–22057
50. Braun D, Fromherz P (1998) Fluorescence interferometry of neuronal cell adhesion on microstructured silicon. Phys Rev Lett 81(23):5241–5244
51. Bilenca A, Cao J, Colice M, Ozcan A, Bouma B, Raftery L, Tearney G (2008) Fluorescence interferometry: principles and applications in biology. Ann N Y Acad Sci 1130(1):68–77
52. McMahon MD, Berglund AJ, Carmichael P, McClelland JJ, Liddle JA (2009) 3D particle trajectories observed by orthogonal tracking microscopy. ACS Nano 3(3):609–614
53. Xu K, Babcock HP, Zhuang X (2012) Dual-objective STORM reveals three-dimensional filament organization in the actin cytoskeleton. Nat Methods 9(2):185–188
54. Juette MF, Gould TJ, Lessard MD, Mlodzianoski MJ, Nagpure BS, Bennett BT, Hess ST, Bewersdorf J (2008) Three-dimensional sub-100 nm resolution fluorescence microscopy of thick samples. Nat Methods 5(6):527–529
55. Pavani SRP, Thompson MA, Biteen JS, Lord SJ, Liu N, Twieg RJ, Piestun R, Moerner WE (2009) Three-dimensional, single-molecule fluorescence imaging beyond the diffraction limit by using a double-helix point spread function. Proc Natl Acad Sci U S A 106(9):2995–2999
56. Lew MD, Lee SF, Badieirostami M, Moerner WE (2011) Corkscrew point spread function for far-field three-dimensional nanoscale localization of pointlike objects. Opt Lett 36(2):202–204
57. Shtengel G, Galbraith JA, Galbraith CG, Lippincott-Schwartz J, Gillette JM, Manley S, Sougrat R, Waterman CM, Kanchanawong P, Davidson MW, Fetter RD, Hess HF (2009) Interferometric fluorescent super-resolution microscopy resolves 3D cellular ultrastructure. Proc Natl Acad Sci U S A 106(9):3125–3130
58. Von Middendorff C, Egner A, Geisler C, Hell S, Schonle A (2008) Isotropic 3D Nanoscopy based on single emitter switching. Opt Express 16(25):20774–20788
59. Aquino D, Schonle A, Geisler C, von Middendorff C, Wurm CA, Okamura Y, Lang T, Hell SW, Egner A (2011) Two-color nanoscopy of three-dimensional volumes by 4Pi detection of stochastically switched fluorophores. Nat Methods 8(4):353–359
60. Lew MD, Lee SF, Ptacin JL, Lee MK, Twieg RJ, Shapiro L, Moerner WE (2011) Three-dimensional superresolution colocalization of intracellular protein superstructures and the cell surface in live *Caulobacter crescentus*. Proc Natl Acad Sci U S A 108(46):E1102–E1110
61. Tang JY, Akerboom J, Vaziri A, Looger LL, Shank CV (2010) Near-isotropic 3D optical nanoscopy with photon-limited chromophores. Proc Natl Acad Sci U S A 107(22):10068–10073
62. Huang B, Jones SA, Brandenburg B, Zhuang XW (2008) Whole-cell 3D STORM reveals interactions between cellular structures with nanometer-scale resolution. Nat Methods 5(12):1047–1052
63. Vaziri AVA, Tang JY, Shroff H, Shank CV (2008) Multilayer three-dimensional super resolution imaging of thick biological samples. Proc Natl Acad Sci U S A 105(51):20221–20226
64. Folling J, Belov V, Kunetsky R, Medda R, Schonle A, Egner A, Eggeling C, Bossi M, Hell SW (2007) Photochromic rhodamines provide nanoscopy with optical sectioning. Angew Chem-Int Edit 46(33):6266–6270

65. York AG, Ghitani A, Vaziri A, Davidson MW, Shroff H (2011) Confined activation and subdiffractive localization enables whole-cell PALM with genetically expressed probes. Nat Methods 8(4):327–333
66. Huisken J, Swoger J, Del Bene F, Wittbrodt J, Stelzer EH (2004) Optical sectioning deep inside live embryos by selective plane illumination microscopy. Science 305(5686):1007–1009
67. Cella Zanacchi F, Lavagnino Z, Perrone Donnorso M, Del Bue A, Furia L, Faretta M, Diaspro A (2011) Live-cell 3D super-resolution imaging in thick biological samples. Nat Methods 8(12):1047–1049
68. Zhuang XW (2009) Nano-imaging with STORM. Nat Photonics 3(7):365–367
69. Bates M, Dempsey GT, Chen KH, Zhuang X (2012) Multicolor super-resolution fluorescence imaging via multi-parameter fluorophore detection. ChemPhysChem 13(1):99–107
70. Dani A, Huang B, Bergan J, Dulac C, Zhuang XW (2010) Superresolution imaging of chemical synapses in the brain. Neuron 68(5):843–856
71. Shroff H, Galbraith CG, Galbraith JA, White H, Gillette J, Olenych S, Davidson MW, Betzig E (2007) Dual-color superresolution imaging of genetically expressed probes within individual adhesion complexes. Proc Natl Acad Sci U S A 104(51):20308–20313
72. Andresen M, Stiel AC, Folling J, Wenzel D, Schonle A, Egner A, Eggeling C, Hell SW, Jakobs S (2008) Photoswitchable fluorescent proteins enable monochromatic multilabel imaging and dual color fluorescence nanoscopy. Nat Biotechnol 26(9):1035–1040
73. Subach FV, Patterson GH, Manley S, Gillette JM, Lippincott-Schwartz J, Verkhusha VV (2009) Photoactivatable mCherry for high-resolution two-color fluorescence microscopy. Nat Methods 6(2):153–159
74. Gunewardene MS, Subach FV, Gould TJ, Penoncello GP, Gudheti MV, Verkhusha VV, Hess ST (2011) Superresolution imaging of multiple fluorescent proteins with highly overlapping emission spectra in living cells. Biophys J 101(6):1522–1528
75. Bossi M, Folling J, Belov VN, Boyarskiy VP, Medda R, Egner A, Eggeling C, Schonle A, Hell SW (2008) Multicolor far-field fluorescence nanoscopy through isolated detection of distinct molecular species. Nano Lett 8(8):2463–2468
76. van de Linde S, Endesfelder U, Mukherjee A, Schuttpelz M, Wiebusch G, Wolter S, Heilemann M, Sauer M (2009) Multicolor photoswitching microscopy for subdiffraction-resolution fluorescence imaging. Photochem Photobiol Sci 8(4):465–469
77. Testa I, Wurm CA, Medda R, Rothermel E, von Middendorf C, Folling J, Jakobs S, Schonle A, Hell SW, Eggeling C (2010) Multicolor fluorescence nanoscopy in fixed and living cells by exciting conventional fluorophores with a single wavelength. Biophys J 99(8):2686–2694
78. Lubeck E, Cai L (2012) Single-cell systems biology by super-resolution imaging and combinatorial labeling. Nat Methods 9(7):743–748
79. Hess ST, Gould TJ, Gudheti MV, Maas SA, Mills KD, Zimmerberg J (2007) Dynamic clustered distribution of hemagglutinin resolved at 40 nm in living cell membranes discriminates between raft theories. Proc Natl Acad Sci U S A 104(44):17370–17375
80. Gurskaya NG, Verkhusha VV, Shcheglov AS, Staroverov DB, Chepurnykh TV, Fradkov AF, Lukyanov S, Lukyanov KA (2006) Engineering of a monomeric green-to-red photoactivatable fluorescent protein induced by blue light. Nat Biotechnol 24(4):461–465
81. McKinney SA, Murphy CS, Hazelwood KL, Davidson MW, Looger LL (2009) A bright and photostable photoconvertible fluorescent protein. Nat Methods 6(2):131–133
82. Subach FV, Patterson GH, Renz M, Lippincott-Schwartz J, Verkhusha VV (2010) Bright monomeric photoactivatable red fluorescent protein for two-color super-resolution sptPALM of live cells. J Am Chem Soc 132(18):6481–6491
83. Zhang MS, Chang H, Zhang YD, Yu JW, Wu LJ, Ji W, Chen JJ, Liu B, Lu JZ, Liu YF, Zhang JL, Xu PY, Xu T (2012) Rational design of true monomeric and bright photoactivatable fluorescent proteins. Nat Methods 9(7):727–729
84. Grotjohann T, Testa I, Leutenegger M, Bock H, Urban NT, Lavoie-Cardinal F, Willig KI, Eggeling C, Jakobs S, Hell SW (2011) Diffraction-unlimited all-optical imaging and writing with a photochromic GFP. Nature 478(7368):204–208

85. Brakemann T, Stiel AC, Weber G, Andresen M, Testa I, Grotjohann T, Leutenegger M, Plessmann U, Urlaub H, Eggeling C, Wahl MC, Hell SW, Jakobs S (2011) A reversibly photoswitchable GFP-like protein with fluorescence excitation decoupled from switching. Nat Biotechnol 29(10):942–947
86. Wombacher R, Heidbreder M, van de Linde S, Sheetz MP, Heilemann M, Cornish VW, Sauer M (2010) Live-cell super-resolution imaging with trimethoprim conjugates. Nat Methods 7(9):717–719
87. Lee HL, Lord SJ, Iwanaga S, Zhan K, Xie H, Williams JC, Wang H, Bowman GR, Goley ED, Shapiro L, Twieg RJ, Rao J, Moerner WE (2010) Superresolution imaging of targeted proteins in fixed and living cells using photoactivatable organic fluorophores. J Am Chem Soc 132(43):15099–15101
88. Klein T, Loschberger A, Proppert S, Wolter S, van de Linde SV, Sauer M (2011) Live-cell dSTORM with SNAP-tag fusion proteins. Nat Methods 8(1):7–9
89. Benke A, Manley S (2012) Live-Cell dSTORM of Cellular DNA Based on Direct DNA Labeling. ChemBioChem 13(2):298–301
90. Shim S-H, Xia C, Zhong G, Babcock HP, Vaughan JC, Huang B, Wang X, Xu C, Bi G-Q, Zhuang X (2012) Super-resolution fluorescence imaging of organelles in live cells with photoswitchable membrane probes. Proc Nat Acad Sci U S A 109(35):13978–13983
91. Hell SW (2009) Microscopy and its focal switch. Nat Methods 6(1):24–32
92. Douglass AD, Vale RD (2005) Single-molecule microscopy reveals plasma membrane microdomains created by protein-protein networks that exclude or trap signaling molecules in T cells. Cell 121(6):937–950
93. Manley S, Gillette JM, Patterson GH, Shroff H, Hess HF, Betzig E, Lippincott-Schwartz J (2008) High-density mapping of single-molecule trajectories with photoactivated localization microscopy. Nat Methods 5(2):155–157
94. Giannone G, Hosy E, Levet F, Constals A, Schulze K, Sobolevsky AI, Rosconi MP, Gouaux E, Tampe R, Choquet D, Cognet L (2010) Dynamic superresolution imaging of endogenous proteins on living cells at ultra-high density. Biophys J 99(4):1303–1310
95. Sengupta P, Jovanovic-Talisman T, Skoko D, Renz M, Veatch SL, Lippincott-Schwartz J (2011) Probing protein heterogeneity in the plasma membrane using PALM and pair correlation analysis. Nat Methods 8(11):969–975
96. Subach OM, Patterson GH, Ting L-M, Wang Y, Condeelis JS, Verkhusha VV (2011) A photoswitchable orange-to-far-red fluorescent protein, PSmOrange. Nat Methods 8(9):771–777
97. Goldman RD, Spector DL (2005) Live cell imaging: a laboratory manual. Cold Spring Harbor Laboratory Press. Cold Spring Harbor, New York
98. Fernandez-Suarez M, Ting AY (2008) Fluorescent probes for super-resolution imaging in living cells. Nat Rev Mol Cell Biol 9(12):929–943
99. Dellagiacoma C, Lukinavicius G, Bocchio N, Banala S, Geissbuhler S, Marki I, Johnsson K, Lasser T (2010) Targeted photoswitchable probe for nanoscopy of biological structures. ChemBioChem 11(10):1361–1363
100. Popp MW, Antos JM, Grotenbreg GM, Spooner E, Ploegh HL (2007) Sortagging: a versatile method for protein labeling. Nat Chem Biol 3(11):707–708
101. Fernandez-Suarez M, Baruah H, Martinez-Hernandez L, Xie KT, Baskin JM, Bertozzi CR, Ting AY (2007) Redirecting lipoic acid ligase for cell surface protein labeling with small-molecule probes. Nat Biotechnol 25(12):1483–1487
102. Uttamapinant C, White KA, Baruah H, Thompson S, Fernandez-Suarez M, Puthenveetil S, Ting AY (2010) A fluorophore ligase for site-specific protein labeling inside living cells. Proc Natl Acad Sci U S A 107(24):10914–10919
103. Hoyer P, Staudt T, Engelhardt J, Hell SW (2011) Quantum dot blueing and blinking enables fluorescence nanoscopy. Nano Lett 11(1):245–250
104. Bates M, Blosser TR, Zhuang XW (2005) Short-range spectroscopic ruler based on a single-molecule optical switch. Phys Rev Lett 94(10):108101

105. Conley NR, Biteen JS, Moerner WE (2008) Cy3-Cy5 covalent heterodimers for single-molecule photoswitching. J Phys Chem B 112(38):11878–11880
106. Annibale P, Scarselli M, Kodiyan A, Radenovic A (2010) Photoactivatable fluorescent protein mEos2 displays repeated photoactivation after a long-lived dark state in the red photoconverted form. J Phys Chem Lett 1(9):1506–1510
107. Endesfelder U, Malkusch S, Flottmann B, Mondry J, Liguzinski P, Verveer PJ, Heilemann M (2011) Chemically induced photoswitching of fluorescent probes-a general concept for super-resolution microscopy. Molecules 16(4):3106–3118
108. Annibale P, Vanni S, Scarselli M, Rothlisberger U, Radenovic A (2011) Quantitative photo activated localization microscopy: unraveling the effects of photoblinking. PLoS One 6(7): e22678
109. Lando D, Endesfelder U, Berger H, Subramanian L, Dunne PD, McColl J, Klenerman D, Carr AM, Sauer M, Allshire RC, Heilemann M, Laue ED (2012) Quantitative single-molecule microscopy reveals that CENP-A^{Cnp1} deposition occurs during G2 in fission yeast. Open Biol 2:120078
110. Wiedenmann J, Ivanchenko S, Oswald F, Schmitt F, Rocker C, Salih A, Spindler KD, Nienhaus GU (2004) EosFP, a fluorescent marker protein with UV-inducible green-to-red fluorescence conversion. Proc Natl Acad Sci U S A 101(45):15905–15910
111. Wu M, Huang B, Graham M, Raimondi A, Heuser JE, Zhuang XW, De Camilli P (2010) Coupling between clathrin-dependent endocytic budding and F-BAR-dependent tubulation in a cell-free system. Nat Cell Biol 12(9):902–908
112. Greenfield D, McEvoy AL, Shroff H, Crooks GE, Wingreen NS, Betzig E, Liphardt J (2009) Self-organization of the *Escherichia coli* chemotaxis network imaged with super-resolution light microscopy. PLoS Biol 7(6):e1000137
113. Ptacin JL, Lee SF, Garner EC, Toro E, Eckart M, Comolli LR, Moerner W, Shapiro L (2010) A spindle-like apparatus guides bacterial chromosome segregation. Nat Cell Biol 12(8):791–798
114. Wang WQ, Li GW, Chen CY, Xie XS, Zhuang XW (2011) Chromosome organization by a nucleoid-associated protein in live bacteria. Science 333(6048):1445–1449
115. Lee SF, Thompson MA, Schwartz MA, Shapiro L, Moerner WE (2011) Super-resolution imaging of the nucleoid-associated protein HU in *Caulobacter crescentus*. Biophys J 100(7): L31–33
116. Fu G, Huang T, Buss J, Coltharp C, Hensel Z, Xiao J (2010) In vivo structure of the *E. coli* FtsZ-ring revealed by photoactivated localization microscopy (PALM). PLoS One 5(9): e12682
117. Fleming TC, Shin JY, Lee SH, Becker E, Huang KC, Bustamante C, Pogliano K (2010) Dynamic SpoIIIE assembly mediates septal membrane fission during *Bacillus subtilis* sporulation. Genes Dev 24(11):1160–1172
118. Valtschanoff JG, Weinberg RJ (2001) Laminar organization of the NMDA receptor complex within the postsynaptic density. J Neurosci 21(4):1211–1217
119. Frost NA, Shroff H, Kong HH, Betzig E, Blanpied TA (2010) Single-molecule discrimination of discrete perisynaptic and distributed sites of actin filament assembly within dendritic spines. Neuron 67(1):86–99
120. Watanabe S, Punge A, Hollopeter G, Willig KI, Hobson RJ, Davis MW, Hell SW, Jorgensen EM (2011) Protein localization in electron micrographs using fluorescence nanoscopy. Nat Methods 8(1):80–84
121. Vaughan JC, Jia S, Zhuang XW (2012) Ultrabright photoactivatable fluorophores created by reductive caging. Nat Methods 9(12):1181–1184
122. Izeddin I, El Beheiry M, Andilla J, Ciepielewski D, Darzacq X, Dahan M (2012) PSF shaping using adaptive optics for three-dimensional single-molecule super-resolution imaging and tracking. Opt Express 20(5):4957–4967
123. Baker M (2011) Faster frames, clearer pictures. Nat Methods 8(12):1005–1009

124. Huang ZL, Zhu H, Long F, Ma H, Qin L, Liu Y, Ding J, Zhang Z, Luo Q, Zeng S (2011) Localization-based super-resolution microscopy with an sCMOS camera. Opt Express 19(20):19156–19168
125. Smith CS, Joseph N, Rieger B, Lidke KA (2010) Fast, single-molecule localization that achieves theoretically minimum uncertainty. Nat Methods 7(5):373–375
126. Mortensen KI, Churchman LS, Spudich JA, Flyvbjerg H (2010) Optimized localization analysis for single-molecule tracking and super-resolution microscopy. Nat Methods 7(5):377–381
127. Lippincott-Schwartz J, Patterson GH (2009) Photoactivatable fluorescent proteins for diffraction-limited and super-resolution imaging. Trends Cell Biol 19(11):555–565
128. Vogelsang J, Steinhauer C, Forthmann C, Stein IH, Person-Skegro B, Cordes T, Tinnefeld P (2010) Make them blink: probes for super-resolution microscopy. ChemPhysChem 11(12):2475–2490
129. Dempsey GT, Bates M, Kowtoniuk WE, Liu DR, Tsien RY, Zhuang XW (2009) Photoswitching mechanism of cyanine dyes. J Am Chem Soc 131(51):18192–18193
130. Kottke T, van de Linde S, Sauer M, Kakorin S, Heilemann M (2010) Identification of the product of photoswitching of an oxazine fluorophore using Fourier transform infrared difference spectroscopy. J Phys Chem Lett 1(21):3156–3159
131. van de Linde S, Krstic I, Prisner T, Doose S, Heilemann M, Sauer M (2011) Photoinduced formation of reversible dye radicals and their impact on super-resolution imaging. Photochem Photobiol Sci 10(4):499–506
132. Roeffaers MBJ, De Cremer G, Libeert J, Ameloot R, Dedecker P, Bons AJ, Buckins M, Martens JA, Sels BF, De Vos DE, Hofkens J (2009) Super-resolution reactivity mapping of nanostructured catalyst particles. Angew Chem-Int Edit 48(49):9285–9289
133. Chi KR (2009) Microscopy: Ever-increasing resolution. Nature 462(7273):675–678
134. Baker M (2011) Bright light, better labels. Nature 478(7367):137–142

A Practical Guide to *d*STORM: Super-Resolution Imaging with Standard Fluorescent Probes

Markus Sauer

Abstract This chapter provides a comprehensive overview of how reliable structural information can be obtained from super-resolution imaging based on stochastic photoswitching of organic fluorophores in fixed and living cells. Since single-molecule-based super-resolution imaging relies critically on the labeling density, the reversibility of photoswitching, and exact fitting of the center of mass of the measured point spread functions (PSFs) of isolated fluorophores, the controlled photoswitching of organic fluorophores with minimal photobleaching are discussed in detail, with particular focus on how they influence structural information extractable. Furthermore, the mechanism of reversible photoswitching of organic fluorophores in aqueous solvents in the presence of thiols is described. Finally, representative applications of *direct* stochastic optical reconstruction microscopy (*d*STORM) are provided and consequences for live-cell super-resolution imaging with organic fluorophores with high spatiotemporal resolution is discussed.

Keywords *d*STORM · Nanoscopy · Organic fluorophores · Photoswitching · Photophysics · Super-resolution imaging

Contents

M. Sauer (✉)
Department of Biotechnology & Biophysics, Julius-Maximilans-University Würzburg, Am Hubland, 97074 Würzburg, Germany
e-mail: sauer@urz.uni-heidelberg.de

P. Tinnefeld et al. (eds.), *Far-Field Optical Nanoscopy*,
Springer Ser Fluoresc (2015) 14: 65–84, DOI 10.1007/4243_2012_41

1 Separation of Fluorescence Emission in Time

Fluorescence intermittency or blinking was one of the most surprising results of early single-molecule spectroscopy experiments [1]. Even though continuously excited, the emission of a single fluorophore behaves as a random telegraph, i.e., it shows ON/OFF switching at random times for random durations. This behavior demonstrates the observation of a single quantum system because two or more independently emitting fluorophores cannot switch OFF and ON simultaneously without synchronization. The random interruption of fluorescence emission of a single fluorophore is a direct consequence of the observation of a single quantum system with discrete fluorescent and non-fluorescent states. Blinking has often been described by a three-level system involving the singlet ground, first excited singlet, and triplet state. As long as the fluorophore is cycled between the two singlet states, it emits fluorescence photons determined by the excitation intensity and the fluorescence quantum yield. However, upon entering the triplet state via intersystem crossing, the fluorophore can no longer emit fluorescence photons until reverse intersystem crossing and repopulation of the singlet ground state, e.g., through quenching with molecular oxygen, occurs [2, 3]. With lifetimes of several microseconds under ambient conditions, i.e., much longer than typical fluorescence lifetimes of fluorophores, fluorescence trajectories of individual fluorophores thus exhibit unpredictable fluorescence intermittencies [1–4].

Fluorescence detection with high signal-to-background ratio is important for precise localization of the emission pattern of individual molecules. For negligible background noise, the localization precision depends on the number of collected photons N and on the standard deviation of the PSF (σ) and can be approximated by $\sigma/\sqrt{N}$ [5, 6]. Given the fact that it is possible to detect thousands of fluorescence photons from a single organic fluorophore before it photobleaches, localization of individual fluorophores with nanometer accuracy is feasible and has been used successfully to monitor molecular motor dynamics [7]. Because photobleaching and blinking complicate the prolonged observation of single fluorophores, different strategies have been developed to efficiently quench the relatively long-lived triplet state of fluorophores which has been identified as the starting point for different reversible and irreversible chemical reactions [8–13]. Here, the reducing and oxidizing system (ROXS) [11] constitutes the best understood and generally applicable method as it not only quenches the triplet state using, e.g., a reducing agent such as ascorbic acid through the formation of a radical anion but likewise repopulates the singlet ground state by oxidizing the radical anion with an electron acceptor (e.g., methylviologen) in a second step. Dependent on the redox properties of the fluorophore and the reducing and oxidizing agent as well as the concentrations, respectively, either reduction or oxidation proceeds first and allows the observation of very long fluorescence trajectories from individual fluorophores uninterrupted by fluorescence intermittencies [11].

On the other hand, fluorescence intermittencies can be exploited advantageously to separate fluorescence emission of two adjacent fluorophores with overlapping

PSF in time, thus enabling independent position determination (localization). Whereas STED applies deterministic photoswitching of fluorophores, i.e., a phase mask ensures that fluorophores at the rim of the laser focus are turned OFF [14, 15], single-molecule-based localization microscopy methods use the stochastic nature of fluorescence intermittencies to separate fluorescence emission of individual fluorophores in time as the central key for resolution enhancement. In 2005, Lidtke et al. [16] described how stochastic fluorescence intermittency or blinking of individual semiconductor nanocrystals, so-called quantum dots, can be exploited for resolution improvement. If the blinking processes can be assumed to be statistically independent for each emitter, information about each individual fluorophore is encoded in the form of its temporal intensity fluctuations. Hence, the light emitted by each individual nanoparticle can be identified and precisely localized. When applied to the labeling of structures, a high-resolution "image" consisting of individually localized points may be reconstructed leading to the term "pointillism" [16]. However, for precise position determination, i.e., fitting of ideal PSFs to the measured photon distributions, active (fluorescent) fluorophores have to be spaced further apart than the distance resolved by the microscope. That is, only a small subpopulation of fluorophores are allowed to be fluorescent at any time of the experiment, or, in other words, the majority of fluorophores have to reside in a non-fluorescent OFF state. This requirement is not easy to fulfill and renders super-resolution imaging with quantum dots blinking on relatively fast time scales complicated. On the other hand, quantum dot blinking appears to be ideally suited for super-resolution optical fluctuation imaging (SOFI) which is based on the analysis of temporal fluorescence fluctuations of emitters and can therefore handle also samples with higher signal densities [17].

2 Emerging Single-Molecule Based-Localization Microscopy Methods

Ultimately, the introduction of photoactivatable and photoconvertible fluorescent proteins (PA-FPs) and the controlled reversible photoswitching of organic fluorophores paved the way for super-resolution imaging of cellular structures with optical resolution approaching virtually molecular scale. The first experimental realizations of super-resolution fluorescence imaging based on precise position determination (localization) of individual isolated fluorophore signals emerged in 2006 under the denotations photoactivated localization microscopy (PALM) [18], fluorescence photoactivation localization microscopy (FPALM) [19], and stochastic optical reconstruction microscopy (STORM) [20]. While PALM and FPALM use photoactivatable or photoconvertible fluorescent proteins (PA-FPs) [21–23], STORM exploits reversible photoswitching of carbocyanine dyes such as Cy5 and Alexa Fluor 647 between an ON and OFF state in close proximity to a second activator dye (e.g., Cy3) [24]. Independently but simultaneously another

publication appeared reporting that fluorescent dyes such as Cy5 and Alexa Fluor 647 can be switched directly without a second activator dye under otherwise identical conditions [25]. In these first photoswitching reports of organic fluorophores, the addition of millimolar concentrations of β-mercaptoethylamine (MEA) and oxygen removal using an enzymatic oxygen scavenging system was described as mandatory to achieve reversible photoswitching. In 2008, super-resolution imaging with commercially available standard fluorescent probes in the presence of thiols was demonstrated and termed *direct* STORM (*d*STORM) [26]. In the same year, also other single-molecule based localization microscopy methods using standard fluorescent probes evolved, including ground state depletion microscopy followed by individual molecule return (GSDIM) [27], blink microscopy [28], and related methods [29, 30].

Microscopic methods that employ single-molecule localization randomly readout the emission of individual fluorophores. This is achieved by transferring the majority of fluorophores to a reversible OFF state and stochastic activation of individual fluorophores, e.g., upon irradiation with light of appropriate wavelength and intensity, and single-molecule fluorescence detection using a widefield fluorescence microscope equipped with a sensitive CCD camera. If the probability of activation is sufficiently low, then the majority of activated fluorophores residing in their ON state are spaced further apart than the resolution limit and their positions can be precisely localized. This cycle of photoactivation and readout is repeated to record an image stack of thousands of images. A prerequisite to minimize artifacts in data analysis is that only a single fluorophore is emitting at any time within a diffraction-limited area. A super-resolution image is finally reconstructed from all single-molecule localizations (typically several ten thousands to millions of localizations).

Even though excellent reviews have already been published highlighting the strengths and limitations of single-molecule-based localization microscopy methods [22, 23, 31–34], super-resolution imaging methods using standard fluorescent probes warrant special attention because they differ from PALM and FPALM in several important points. For example, whereas PA-FPs are relatively small and enable protein labeling efficiencies of nearly 100 %, a level impossible to achieve by chemical staining with organic fluorophores, standard organic fluorophores exhibit a higher brightness and photostability than PA-FPs [35]. The number of detectable photons of PA-FPs is typically a few hundred photons before they bleach, whereas organic fluorophores can emit more than 1,000 photons per cycle [36, 37], thus enabling a higher localization precision [5–7].

From this point of view, methods exploiting reversible photoswitching of small organic fluorophores are advantageous because organic fluorophores survive moderate excitation conditions for longer time periods (i.e., they exhibit a higher photostability), emit thousands of photons, and their photoswitching rates can be controlled by external means [25, 37, 38]. Furthermore, most ATTO and Alexa Fluor dyes spanning the entire visible spectral range can be operated as reversible photoswitches in aqueous solvents simply by adding millimolar concentrations of reducing thiols even in the presence of oxygen [37, 38]. Only in the case of

carbocyanine dyes such as Cy5, Cy5.5, Cy7, Alexa Fluor 647, Alexa Fluor 680, and Alexa Fluor 750 the reversibility of photoswitching is improved when the oxygen concentration is reduced [37]. Therefore, *d*STORM and related methods have already found broad acceptance and has been used successfully to study the number, distribution, and density of cellular or membrane proteins in fixed cells [39–43] and the in vitro dynamics of molecular motor proteins [44].

Since *d*STORM requires only the presence of millimolar concentrations of a thiol and living cells contain reducing glutathione at the appropriate concentration, live-cell *d*STORM is possible without addition of external reagents. This fact has been exploited to study the distribution and dynamics of core histone proteins in living cells applying standard fluorophores with TMP- and SNAP-tags, respectively [45, 46], in combination with real-time data analysis [47]. The finding that organic fluorophores can be photoswitched reversibly in the presence of millimolar concentrations of glutathione under physiological conditions has in fact been published already in 2008 [40] and has been used successfully also by other groups for live-cell super-resolution imaging studies with chemical tags and standard fluorophores [48, 49]. This opens the potential to combine the use of organic fluorophores and PA-FPs for multicolor super-resolution imaging experiments in living cells, profiting from orthogonal labeling strategies. The tunability of photoswitching of organic fluorophores under physiological conditions allows frame rates of 10–1,000 Hz at excitation intensities between 0.5 and 50 kW cm^{-2}, such that data acquisition takes only seconds to a few minutes.

Even though super-resolution imaging experiments using PA-FPs and standard fluorescent probes, respectively, rely basically on the same principles and can be performed under similar experimental conditions, the initial situation in super-resolution imaging experiments can be different. For example, PA-FPs are essentially non-fluorescent at the beginning of the experiment, allowing the number of fluorescent molecules, i.e., the density of fluorescent molecules, to be tightly controlled by the irradiation intensity of a 405 nm laser. In contrast, one of the key steps of single-molecule-based localization microscopy with synthetic organic fluorophores is the efficient transfer of the fluorophores to a reversible, relatively stable OFF state at the beginning of the experiment [20, 26–30, 38–47]. In other words, a bright fluorescent sample has to be turned "dim" by increasing the irradiation intensity in a way that ensures that only a sparse subset of fluorophores remain fluorescent. The challenge of the procedure is twofold because damage of the sample and photobleaching of the fluorophores has to be avoided. These considerations demonstrate that (1) a highly reliable and in case of organic fluorophores reversible photoswitching mechanism and (2) appropriate photoswitching rates (i.e., stable OFF states) are of utmost importance for super-resolution fluorescence imaging based on single-molecule localization. Finally, it has to be considered that a high localization precision does not automatically permit a high experimental structural resolution which is rather controlled by the labeling density via the Nyquist-Shannon sampling theorem [50]. Therefore, (3) highly efficient and dense labeling with photoswitchable fluorescent probes is likewise important for all super-resolution imaging methods.

3 Reliable and Reversible Photoswitching

Each super-resolution fluorescence imaging method based on localization of individual organic fluorophores starts under identical conditions: The sample – in most cases a fluorescently labeled fixed or living cell – has to be irradiated to convert the majority of fluorophores to a metastable OFF state. At any time during the following movie sequence, the density of fluorescent fluorophores has to be low enough to allow the isolated localization of individual fluorophores. In this context, the reversibility of photoswitching plays an important role. The less reversible the photoswitching process is, the more perforated the structure, e.g., microtubule filaments, will appear in the reconstructed super-resolution image. This is intuitively easy to understand because fluorophores photobleached in the first switching cycle cannot contribute to image reconstruction. In addition, inefficient labeling with fluorescent probes contributes to the appearance of perforated structures and will be addressed later.

The challenge that has to be met is twofold: First, the majority of fluorophores have to be transferred to a reversible OFF state by irradiation with light with negligible photobleaching and second, the fluorescent ON state has to be recovered stochastically ensuring that the density of fluorescent fluorophores is low enough for precise localization of individual fluorophores. GSDIM claims to switch off by depleting the molecular ground state and shelving the fluorophores in their triplet or other metastable dark states. It differs from other stochastic methods such as STORM and *d*STORM in that the organic fluorophore is not optically activated but is automatically switched on after its spontaneous return from the dark triplet state to its singlet state [31]. Spectral precision distance microscopy/spectral position determination microscopy (SPDM) argues that "reversible photobleaching" of fluorophores can be used for super-resolution imaging [51]. Blink microscopy uses the ROXS concept [11] to control ON/OFF switching of fluorophores through the addition of oxidizing and reducing agents. Instead of immediately repopulating the singlet ground state by oxidation or reduction of the metastable, reduced or oxidized species to increase the photostability and minimize fluorescence intermittencies of the fluorophores, it attempts to adjust the oxidizing and reducing efficiency to enable localization of individual fluorophores residing in their ON state [28, 52]. A very elegant method is point accumulation for imaging in nanoscale topography (PAINT) which uses transient binding of fluorescent probes to a structure as the ON state to reconstruct a super-resolved reactivity map [53]. Alternatively, single catalytic conversions of fluorogenic probes at active sites of a catalyst can be exploited to reconstruct diffraction-unlimited reactivity maps of catalytic particles (NASCA standing for "Nanometer Accuracy by Stochastic Catalytic reActions microscopy") [54].

Chronologically, the two first reports about reversible photoswitching of standard organic fluorophores appeared in 2005. They demonstrated that single carbocyanine dyes such as Cy5 can be used as efficient reversible single-molecule optical switch, whose fluorescent state after apparent photobleaching can be restored at room

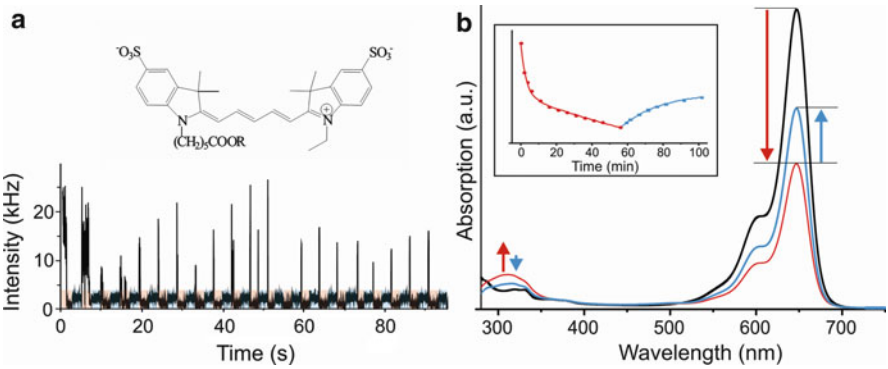

Fig. 1 (**a**) Reversible optical switching of a single biotinylated and Cy5-labeled dsDNA immobilized on a BSA/streptavidin surface in deaerated PBS, pH 7.4 in the presence of 100 mM MEA. The molecule was irradiated in a confocal fluorescence microscope at 633 nm until fluorescence ceased and then recovered by irradiation at 488 nm for 2.5 s. The underlayed color indicates the excitation wavelength (blue: 488 nm, red: 633 nm). In addition, the molecular structure of the carbocyanine dye Cy5 is given. (**b**) Ensemble switching experiment of an argon-bubbled 10^{-6} M aqueous Cy5 solution (PBS, pH 7.4, 100 mM MEA). In aqueous solvents, Cy5 exhibits an absorption and emission maximum at 649 and 670 nm, respectively. After irradiation at 647 nm (300 mW) by a defocused laser beam, the absorption decreased by 50 % at 650 nm (*red*). About 40 % of the absorption could be restored upon irradiation at 488 nm (300 mW) for 30 min (*blue*) [25]. The different switching efficiency observed at the single-molecule and ensemble level might be caused by the different experimental conditions such as different oxygen-removing efficiencies and/or different excitation intensities. Furthermore, it has to be considered that the time the fluorophore resides in the OFF state is much longer in the ensemble experiments promoting the formation of irreversible follow-up reactions

temperature upon irradiation at shorter wavelengths. Single-molecule photoswitching experiments in aqueous buffer in the presence of 100 mM MEA and oxygen scavenger demonstrated that single carbocyanine molecules can be cycled between a fluorescent and non-fluorescent state more than 100 times with a reproducibility of > 90 % at room temperature (Fig. 1) [24, 25]. This finding demonstrates that photoswitching carbocyanine dyes in the presence of thiols is highly reliable and thus a good basis for super-resolution imaging.

The underlying photoswitching mechanism is still under debate but new experiments indicate that the triplet state of carbocyanine dyes can be reduced by thiols such as MEA, and a corresponding radical anion is formed that absorbs around 500–600 nm [55]. The radical anion is relatively stable in oxygen-depleted solutions and can be transferred to the singlet ground state upon direct excitation. At the ensemble level, a follow-up reaction of photoreduction of the triplet state could involve thiol-adduct formation in the polymethine bridge of the dyes, as was recently observed by mass spectroscopy [56]. Because thiol-adducts do not absorb at ~ 500 nm, photoinduced recovery of the ON state is inefficient (Fig. 1b) and photoswitching is not as reversible as observed at the single-molecule level (Fig. 1a).

This intriguing photoswitching mechanism can be conveyed to most other standard fluorophores enabling reliable *d*STORM experiments in fixed and living cells in the presence of oxygen [37, 38, 45, 46]. The devolution of the photoswitching mechanism to most Alexa Fluor and ATTO dyes succeeds because most of the dyes belong to the class of rhodamine dyes that share similar redox reactivity, i.e., they exhibit a pronounced electron affinity. In contrast to the strongly electron-donating aromatic amines [57], relatively high concentrations (> 50 mM) of thiols such as MEA or glutathione (GSH) at pH values > 8 are required to noticeably quench the first singlet state of rhodamine dyes with a lifetime of a few nanoseconds [55]. The triplet state of rhodamine derivatives, however, exhibits lifetimes in the microsecond range in aqueous buffer [2, 3] and is therefore already quenched by millimolar concentrations of MEA and GSH at pH ~ 8. Accordingly, photoreduction of the rhodamine Alexa Fluor 488 by thiols in aqueous solutions can be described by the scheme shown in Fig. 2a. The photoreaction is initiated by intersystem crossing from the excited singlet state to the triplet state. In the presence of molecular oxygen, the triplet state is efficiently quenched via energy transfer from the dye triplet to triplet oxygen to produce singlet molecular oxygen. The thiol competes with molecular oxygen in triplet quenching, naturally present at 200–250 μM concentration in aqueous solution at room temperature, forming the thiyl and dye radical (Fig. 2).

Whereas thiyl radicals efficiently react with molecular oxygen via formation of superoxide radicals and hydrogen peroxide [58], rhodamine radical anions are more stable to oxidation and survive for several hundred milliseconds to seconds in the presence of physiological oxygen concentrations [55]. Upon removal of oxygen, rhodamine dyes can be easily trapped in their radical anion state for several hours [55]. On the other hand, thiazine and oxazine dyes such as methylene blue and ATTO 655 or ATTO 680 exhibit a higher electron affinity than rhodamine dyes [59]. Hence, the semireduced fluorophore radicals ($F^{\bullet}$) are intermediary reaction products that accept a second electron in the presence of thiols forming the corresponding fully reduced leuco-dye (FH) (Fig. 2a). The fundamental mechanism of *d*STORM, i.e., photoinduced formation of intermediate radical anions for most Alexa Fluor and ATTO dyes in aqueous solvents in the presence of millimolar thiols, can be easily demonstrated by ensemble absorption and EPR experiments [59].

To close the photoswitching cycle, the fluorescent state of the fluorophores is recovered upon oxidation by molecular oxygen (Fig. 2a). Both processes, reduction of the triplet state by thiols and oxidation of the intermediate reduced state by oxygen are facilitated upon irradiation. Excitation of the fluorescent form pumps the fluorophore into the triplet state which is reduced by the thiolate and direct excitation of the radical anion (all radical anions show a pronounced absorbance around 400 nm) [55] at, e.g., 405 nm facilitates recovery of the fluorescent form (Fig. 2b and c). Since animal cells contain oxygen as well as millimolar concentrations of GSH [60], super-resolution imaging with organic fluorophores can be performed in living cells under physiological conditions without any addition [45, 46, 48, 49].

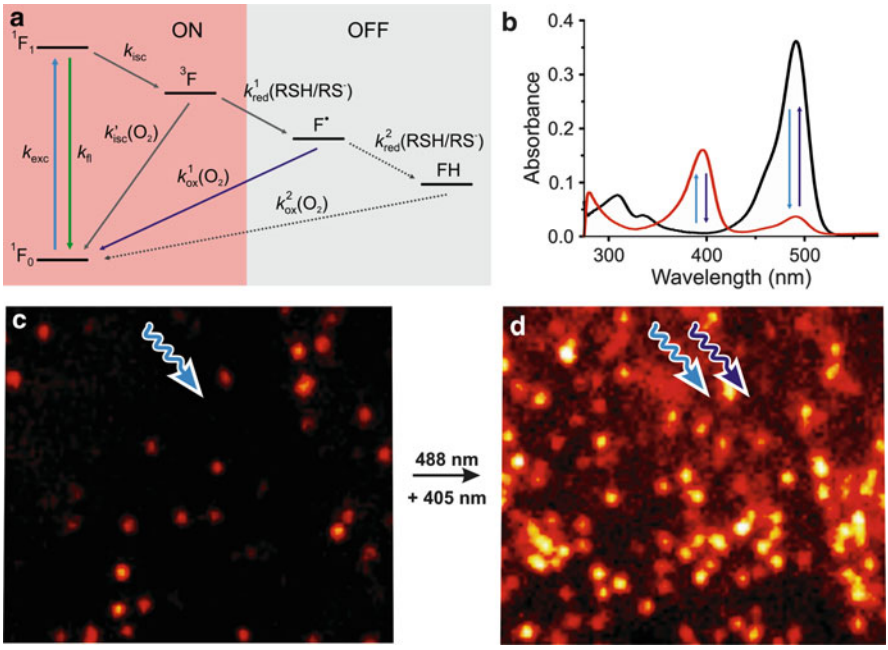

Fig. 2 (**a**) The *d*STORM reaction mechanism. Reversible photoswitching of Alexa Fluor and ATTO dyes in the presence of thiols. The fluorophore is either cycled between its singlet ground and excited state emitting fluorescence photons or can undergo intersystem crossing with rate k_{isc} upon irradiation. The triplet state (^{3}F) can react with molecular oxygen to recover the singlet ground state and produce singlet oxygen or react with the thiolate with rate $k_{red}{}^1$ to form the radical anion of the fluorophore ($F^\bullet$) and the corresponding thiyl radical. The radical anion can be oxidized by oxygen with rate $k_{ox}{}^1$ to recover the singlet ground state. Since radical anions of most rhodamine and oxazine derivatives show pronounced absorption at ~ 400 nm, irradiation at, e.g., 405 nm promotes recovery of the fluorescent form, i.e., OFF and ON switching occur photoinduced. Whereas the thiyl radicals formed react efficiently with molecular oxygen to produce superoxide radicals and hydrogen peroxides, the fluorophore radical anion is very unreactive and survives for up to several seconds even in the presence of molecular oxygen. Fluorophores like ATTO 655 and ATTO 680 accept a second electron ($k_{red}{}^2$) to the fully reduced leuco-dye (FH). Oxidation of FH with oxygen ($k_{ox}{}^2$) also recovers the ON state. (**b**) Absorption spectra of Alexa Fluor 488 in PBS, pH 7.4 in the presence of 100 mM MEA. Upon irradiation at 488 nm (*light blue*), the absorption at 488 nm decreases and the radical anion absorbing maximally around 400 nm appears. The fluorescent state is recovered spontaneously or by direct excitation of the radical anion at ~ 400 nm (*dark blue*). The stability (lifetime) of the radical anion is mainly determined by the oxygen concentration and can easily exceed several hours [55]. (**c**, **d**) The effect of direct excitation of rhodamine radical anions on the number of rhodamine dyes residing in their fluorescent ON state and *d*STORM of actin filaments in U373 cells with Alexa Fluor 488 phalloidin. Photoswitching of Alexa Fluor 488 was performed in 100 mM MEA (pH 8.0) at room temperature exciting at 488 nm with an excitation intensity of 5 kW cm^{-2} and a frame rate of 60 Hz in the absence (**c**) and presence (**d**) of additional excitation at 405 nm with 0.1 kW cm^{-2}

This finding demonstrates the important role of molecular oxygen in super-resolution imaging experiments because fluorophores (especially rhodamine and oxazine dyes) can be trapped in their reduced states (radical or leuco-dye) for up to

several hours in the absence of oxygen. Furthermore, oxygen is essential to compete with the thiol in efficient triplet state quenching.

In the absence of oxygen, the triplet state when populated by intersystem crossing would be quenched by the thiol and a relatively stable radical anion would be generated. With intersystem crossing yields of 0.2–1 %, [2, 3] single rhodamine dyes would emit at best 500 fluorescence photons before being reduced by the thiol. Hence, only ~ 25–50 photons would be detected from a single molecule assuming an overall detection efficiency of ~ 5–10 % rendering precise single-molecule localization difficult. In other words, a minimum amount of oxygen is required to recover the singlet state and to ensure the detection of enough fluorescence photons from the ON state of single emitters before they enter a stable OFF state. These findings demonstrate that the triplet state of organic fluorophores has to be considered as part of the "ON state" in super-resolution imaging based on single-molecule localization whereas the OFF state is the charged radical or leuco-dye state (Fig. 2a). Therefore, it is reasonable to assume that the reversible photoinduced generation of stable radical anions establishes the basis for reliable single-molecule-based localization microscopy.

4 Controlling Photoswitching Rates

Most commercially available organic standard fluorophores have demonstrated their applicability for super-resolution imaging, i.e., they can be switched between an OFF and ON state in the presence of thiols under physiological conditions. Starting from the green to the red wavelength range, the list comprises Alexa Fluor 488, Dy505, Rhodamine 123, ATTO 488, SNAP-Cell 505, Rhodamine 6 G, ATTO 520, Dy530, ATTO 532, Alexa Fluor 532, SNAP-Cell-TMR-Star, ATTO 565, Alexa Fluor 568, ATTO 590, Alexa Fluor 647, Cy5, Cy5.5, Cy7, ATTO 655, TMP-ATTO 655, ATTO680, ATTO 700, Alexa Fluor 680, and Alexa Fluor 750 [37]. Most of the fluorophores exhibit remarkably stable OFF states that absorb at shorter wavelengths, in the range of 350–550 nm, and survive the entire photocycle several times with only minimal photobleaching.

The detection and analysis of individual emitters from a densely labeled structure comprises that the majority of fluorophores must be non-fluorescent, while only a sparse subset of fluorophores is allowed to be fluorescent at any time. As a consequence and due to the stochastic nature of photoswitching, fluorophores used for super-resolution imaging must exhibit a long-lasting non-fluorescent OFF state, e.g., a stable radical ion or other charged intermediate state as used in the *d*STORM concept. Photo-activatable or photo-convertible fluorescent proteins as used in PALM and FPLAM generally exhibit thermally very stable OFF states and can be switched on ("activated") upon irradiation with light of specific wavelength (in most cases ~ 400 nm) and intensity. Thus, the density for single-molecule-based localization microscopy can be precisely adjusted. In contrast, organic standard fluorescent probes are fluorescent at the beginning of the experiment and have to be

converted with rate k_{off} to the OFF state to ensure single-molecule localization before the ground state is repopulated with rate k_{on}. Here the switching rates and thus the length of the ON and OFF state of a fluorophore, i.e., the lifetimes τ_{on} and τ_{off}, directly control the effective spot density and thus affect the ability to resolve a structure with a given fluorophore density [61, 62].

The ability to resolve a structure can be best described introducing the ratio of the two rates or lifetimes, respectively, $r := k_{off} / k_{on} = \tau_{off} / \tau_{on}$. An increase of this ratio enhances the ability to localize more fluorophores correctly, i.e., as individual single-molecule events. Basically, the rate ratio can be increased by shortening τ_{on} or increasing τ_{off} but it has to be considered that τ_{on} controls the maximum reasonable frame rate. Increasing excitation intensity will enforce k_{off} and thus shorten τ_{on}, whereas τ_{off} can be prolonged when no or less reactivation intensity is used or the oxidation efficiency is reduced, e.g., by depleting oxygen from the buffer by an oxygen scavenging system. OFF state lifetimes of photoswitchable synthetic fluorophores have been reported to vary from 10 to 100 ms [27, 28] to several seconds [24–26, 40, 55]. For metastable OFF states with short τ_{off}, high irradiation intensities must be applied to reduce τ_{on} and to generate a sufficient ratio r, e.g., $r = 100$ for $\tau_{on} = 1$ ms and $\tau_{off} = 100$ ms. In the case of OFF state lifetimes in the range of seconds, a sufficient high ratio r can be achieved with comparably long ON-times and corresponding low irradiation intensity, which is very important for live cell applications [46–49]. For fixed cells, however, τ_{on} can be further decreased applying higher irradiation intensities to increase r and the imaging speed (i.e., the frame rate).

Nevertheless, due to the stochastic nature of photoswitching, multi-fluorophore events can occur in single-molecule-based localization microscopy experiments (Fig. 3). In other words, there is a chance that two or more fluorophores are fluorescent at the same time within a diffraction-limited region. Consequently, the localization of the sum of the individual PSFs introduces errors or artificial localizations, respectively [61]. To avoid multi-fluorophore localizations, a photon threshold and a geometrical inspection of the PSF can be performed because it is expected that overlapping PSFs of differently localized individual emitters produce an unsymmetrical signal distribution. However, here it has to be mentioned that geometrical inspection of the PSF is inappropriate for 3D measurements where, e.g., astigmatism is used to derive axial information and fluorescence intensity is a poor parameter for quantification as each emitter might contribute differently to the resulting overlapping photon distribution. Hence, a certain fraction of false localized events is always present in super-resolved images. However, the fraction of artificial or false localization can be kept low with appropriate control of the number of fluorophores residing in the ON state and becomes higher when the photoswitching rates are set inappropriate, i.e., for low r.

Using PALM or FPALM each protein is tagged with a single PA-FP, whereas in the case of reversibly photoswitchable organic fluorophores, often multiple labeled antibodies are used as fluorescent probes. Thus, the labeling density increases and an accordingly higher ratio has to be applied to be able to resolve the structure (Fig. 3). Furthermore, it is important to mention that each fluorophore is generally

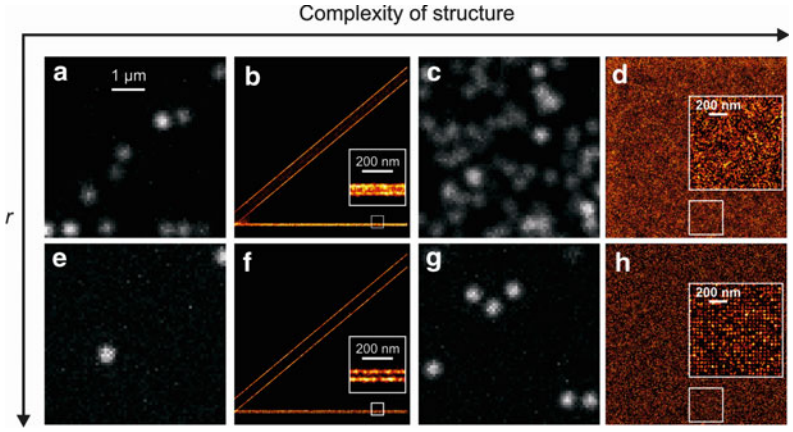

Fig. 3 Simulated data demonstrating the influence of the ratio of photoswitching rates, r, on different complexities. With increasing complexity of the imaged structure, the number of fluorophores present per area increases. The photoswitching ratio is mainly determined by the stability of the OFF state. Images shown in (**a**), (**c**), (**e**), and (**g**) are snapshots from the localization microscopy stacks from which the reconstructed super-resolution images (**b**), (**d**), (**f**), and (**h**) were generated. (**b**, **f**) show pairs of lines separated by 300 and 50 nm with a fluorophore attached every 8.5 nm, while (**d**, **h**) show a lattice with 40 nm spacing. (**a-d**) Images were simulated with $r = 250$; (**e–h**) images were simulated with $r = 3{,}000$. It becomes clear that the necessary photoswitching ratio depends strongly on the structure imaged: when the photoswitching ratio is too low (**c**, **d**), more than one fluorophore might fluoresce per diffraction-limited area and subsequent fitting of the PSF might result in false localizations and image artifacts. On the other hand, high photoswitching ratios result in a small number of localizations per image and thus prolong the acquisition time unnecessarily. Note that the density of fluorescence emissions is roughly the same for the images shown in (**a**) and (**g**), even though they are simulated for different values of r

localized multiple times. Therefore, structural information is not lost when a two- or multi-fluorophore event is recognized and discarded from further analysis because it is likely that the same fluorophore is localized again individually. In addition, even for inappropriately set photoswitching rates, a structure can be resolved as long as every fluorophore is localized individually at least once and the error-rate for discarding multi-fluorophore events (which increases with decreasing r) is kept low.

For the use of photoactivatable fluorophores in concepts like PALM or FPALM, two-spot events can occur stochastically or if the irradiation intensity for activation is set too high. Then the localization information is irretrievably lost or a false localization is made. Since the resolution is controlled by the labeling density, lost localizations decrease the achievable resolution. These considerations indicate that the density of fluorophores residing in their fluorescent state is easier to control in PALM or FPALM whereas STORM or *d*STORM exhibit the advantage that every fluorophore can be localized multiple times.

Super-resolution imaging with standard fluorescent probes in the presence of thiols offers several possibilities to vary r through fine adjustment of τ_{on} and τ_{off}

enabling super-resolved imaging of cellular structures with different complexity and fluorophore densities in fixed and living cells. While k_{off} is controlled by the singlet-state excitation intensity, the intersystem crossing yield, and the concentration of thiolate, k_{on} is determined by the radical excitation intensity and the concentration of molecular oxygen.

Using a laser with a maximum power of ~ 100 mW k_{off} can be easily controlled over 1 order of magnitude. The concentration of the reducing thiolate (RS^-) can be increased by both the concentration of thiol added and the pH (between pH 6 and 9) of the solvent and enables the adjustment of k_{off} over ~ 2 orders of magnitude [26]. On the other hand, k_{on} can be increased (at least 1 order of magnitude) by direct excitation of the radical anions at, e.g., 405 nm, whereas k_{on} can be reduced by several orders of magnitude by depleting oxygen from the buffer by an oxygen scavenging system (upon efficient removal of oxygen, the lifetime of the radical anions can approach several hours in ensemble experiments) [55]. Tuning both rates k_{off} and k_{on} allows arbitrary control of the photoswitching ratio r over several orders of magnitude. Thus, r can be adjusted to match the required conditions for super-resolution imaging of different cellular structures [61]. A suitable r is determined by the complexity of the structure but should be (as a rule of thumb) adjusted such that ~ 0.1–1.0 fluorophores are simultaneously active per μm^{-2} to ensure the localization of single emitters. For live cell *d*STORM experiments, manipulating k_{off} and k_{on} is limited to the laser intensities for both the fluorescence readout and the radical anion, respectively, whereas the excitations intensities should be kept low to avoid cellular damage. Recently [63], new algorithms appeared that facilitate the analysis of higher fluorophore densities (up to 10 molecules μm^{-2}) by fitting simultaneously overlapping PSFs with multiple model PSFs. Unfortunately, hitherto no reference sample is available that enables the experimental verification of stochastic precision, i.e., the quotient of true positive localizations to all localizations found, and recall, i.e., the quotient of the number of true positive localizations to the total number of spots that should have been localized, of commonly used super-resolution imaging algorithms [64].

Figure 4 demonstrates experimentally the influence of the photoswitching rates on the quality of the reconstructed super-resolved structure. Because both the ON and the OFF switching rates scale linearly with the readout and radical anion laser intensity, r can be easily adjusted and the same structure can be imaged multiple times with different ratios without the need for changing the chemical environment. The cellular structure (Fig. 4) was imaged with two different ratios $r_1 = 153 \pm 11$ and $r_2 = 503 \pm 37$ [61]. Both ratios allow the reconstruction of a *d*STORM image with significant improved resolution. However, crossing and adjacent filaments cannot be resolved clearly applying the lower ratio r_1, whereas with higher rate-ratio r_2 structural details become visible (Figs. 4b and c). In addition, it has to be mentioned that commercially available Alexa Fluor 647 labeled antibodies are multiple labeled (DOL ~ 3), which further reduces the rate-ratios to $r_1 \approx 50$ and $r_2 \approx 170$ as the lifetime of the OFF state of the antibody becomes three times shorter.

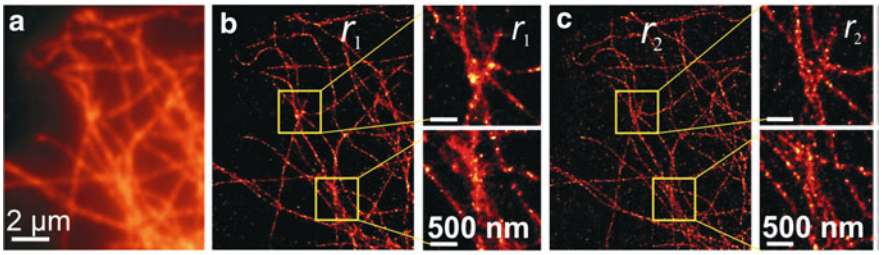

Fig. 4 *d*STORM images of the microtubule network of a COS-7 cell labeled with Alexa Fluor 647. In contrast to the wide-field fluorescence image (**a**), the *d*STORM images (**b**, **c**) clearly demonstrate superior resolution. The same microtubule network was acquired with two different photoswitching ratios of Alexa Fluor 647 (**b**) $r_1 = 153 \pm 11$ and (**c**) $r_2 = 503 \pm 37$. Considering a DOL of ~3 for the antibody, the effective ratios are $r_1 \approx 50$ and $r_2 \approx 170$. The magnified views of two insets demonstrate that a higher r affords substantially improved discrimination in areas with high labeling density

5 Efficient Fluorescence Labeling

According to information theory, the required density of fluorescent probes for super-resolution imaging has to be sufficiently high to satisfy the Nyquist-Shannon sampling theorem [50]. In essence, it states that the mean distance between neighboring localized fluorophores (the sampling interval) must be at least twice as fine as the desired resolution. For example, to resolve 20 nm structural features in one dimension, a fluorophore has to be localized at least every 10 nm (Fig. 5). Extended to a two-dimensional structure, this corresponds to a labeling density of about 10^4 fluorophores μm^{-2} and translates to 600 fluorophores present within a diffraction-limited area with a diameter of ~ 250 nm. Here FPs are advantageous because they can be genetically fused to almost any protein of interest and they are smaller than fluorophore labeled IgG antibodies typically used in *d*STORM applications with a size of ~ 8 nm. Therefore, the density of fluorophores tagging a structure is generally lower compared to endogenously expressed PA-FPs. Whereas the smallest resolvable distance between two fluorophores determines the optical resolution, the structural interpretation of localization microscopy data is determined by the labeling density. These considerations highlight the importance of efficient labeling strategies since the labeling density also determines the structural resolution attainable (Fig. 5).

Live-cell super-resolution imaging experiments require special consideration. At first sight, labeling of proteins with PA-FPs is much easier, but otherwise organic fluorophores are more photostable and exhibit more fluorescence photons. To circumvent this constraint, chemical tags have been developed as surrogate to FPs in which a genetically encoded polypeptide tag is labeled with a modular organic fluorophore [65–67]. For example, the tetracysteine tag reacts with arsenical fluorophores to form stable and highly fluorescent complexes [68]. Alternative approaches include the SNAP-tag that allows labeling of fusion proteins of human

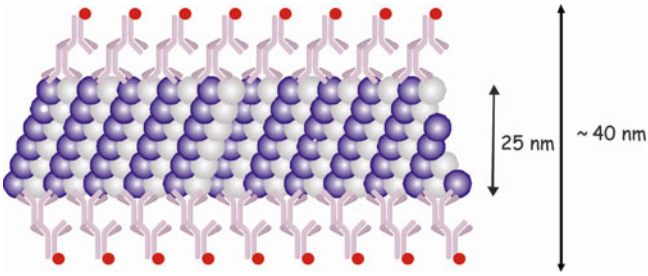

Fig. 5 High-density fluorescence labeling of cellular structures. The microtubule filament with a diameter of ~ 25 nm is labeled with primary and fluorescently labeled secondary antibodies using a standard immunocytochemistry protocol. To achieve a lateral resolution of ~ 20 nm in reconstructed super-resolution images, a fluorescent probe has to be localized every 10 nm on the target structure. The size of an IgG antibody of ~ 8 nm highlights the challenge of efficient fluorescence labeling. In addition, it has to be pointed out that the optical resolution of super-resolution imaging methods such as *d*STORM is so high that the size of IgG antibodies used to label the structure has to be considered. Therefore, microtubule filaments exhibit a diameter of 40–45 nm in reconstructed *d*STORM images [26]

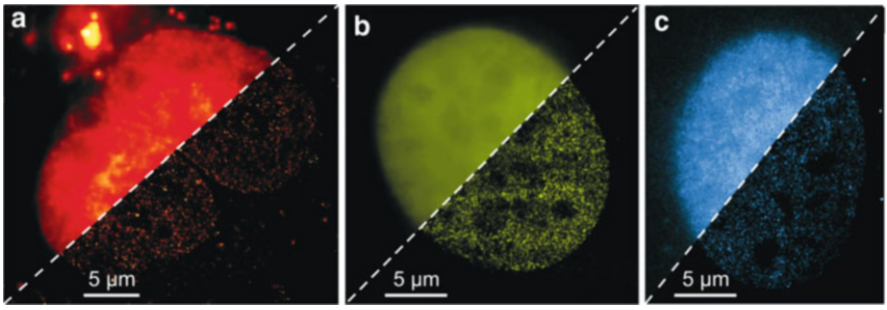

Fig. 6 Live-cell *d*STORM of core histone proteins H2B in HeLa cells using (**a**) TMP-ATTO 655 excited at 647 nm (5 kW cm^{-2}, 50 Hz frame rate), (**b**) SNAP-Cell TMR-Star excited at 532 nm (1 kW cm^{-2}, 50 Hz) and (**c**) SNAP-Cell 505 excited at 488 nm (1 kW cm^{-2}, 50 Hz) [45, 46]. Excitation of core histone proteins was performed applying a highly inclined thin illumination scheme [73]. The *d*STORM images were reconstructed from 10,000 images corresponding to an acquisition time of ~ 3 min

O^6-alkylguanine-DNA alkyltransferase (AGT) with O^6-benzylguanine derivatives [69, 70]. The trimethoprim (TMP)-tag [71, 72] is based on the high-affinity non-covalent interaction between *Escherichia coli* dihydrofolate reductase (eDHFR) and TMP. Recently, it has been shown that the TMP-tag method can be used successfully for live-cell *d*STORM with ATTO dyes achieving a resolution of ~ 20 nm [45]. On the other hand, commercial SNAP-Tag kits also use reversibly photoswitchable rhodamine fluorophores as O^6-benzylguanine conjugates such as tetramethylrhodamine (TMR) and can therefore also be used for live cell *d*STORM (Fig. 6) [46]. Because cells naturally contain the "redox cocktail" thiol (glutathione)

and oxygen at appropriate concentrations, the *d*STORM method is widely applicable for in vivo multicolor super-resolution imaging experiments also in combination with PA-FPs.

6 Accomplishment of *d*STORM Experiments

In order to perform *d*STORM experiments in fixed cells, the sample has to be embedded in aqueous buffer (e.g., PBS, pH 7.4) in the presence of 10–200 mM thiol (MEA or glutathione). For cyanine fluorophores, the application of an oxygen scavenging system significantly improves the reversibility of photoswitching. After proper sample alignment by fluorescence imaging under low excitation conditions (< 0.1 kW cm^{-2}) the excitation intensity is increased to 5–30 kW cm^{-2} until the majority of fluorophores are switched off to enable precise single-molecule localization. This step requires typically only a few seconds. Since the triplet yield and subsequent photoinduced formation of non-fluorescent reduced fluorophore intermediates depend linearly on the excitation intensity, the thiol concentration and the pH of the solvent [25, 26, 37, 55] are available as parameters to optimize the transfer of the majority of fluorophores to their non-fluorescent stable OFF state. For subsequent data acquisition, the excitation intensity is tuned to ensure that the lifetime of the ON state equals one to four times the acquisition time of the CCD camera.

For live cell *d*STORM, the excitation intensity has to be lowered to ≤ 5 kW cm^{-2} to avoid cellular damage. At higher intensities, photoinduced fluorophore and thiyl radical formation and subsequent production of reactive oxygen species is enhanced [55]. However, for fixed cells or other samples, the excitation intensity can be kept high (up to 50 kW cm^{-2}) to reduce the lifetime of the fluorescent ON state to a few milliseconds enabling frame rates of up to 1 kHz [47]. Without another irradiation wavelength for direct excitation of the reduced intermediates, the lifetime or stability of the OFF state is only controlled by the redox property of the fluorophore itself and the oxygen concentration. Independent of the laser excitation intensity, typically between 500 and 5,000 photons are detected from the ON state of most Alexa Fluor and ATTO dyes.

For the successful application of chemical tags for super-resolution imaging with organic fluorophores in living cells, several facts have to be carefully considered. First, the transfection and labeling efficiency with chemical tags varies strongly dependent on the cell type used. Therefore, the optimal substrate concentration has to be identified experimentally. Second, nonspecific adsorption of fluorescent substrates to glass surfaces, cellular membranes, and structures, respectively, can strongly increase the background signal especially when applied at high concentrations (≥ 1 μM) [37]. Low transfection efficiencies result in a high concentration of unbound fluorophore conjugates and increased nonspecific labeling because unbound fluorophore conjugates can diffuse out of cells. To minimize nonspecific adsorption effects, the cell density can be increased to effectively

reduce the interspace between cells before labeling. Alternatively, and much more efficiently, cells can be trypsinized and transferred into a new chamber well after labeling [45] or the surface can be blocked efficiently by treating the surface with the amino acid glycine prior to the experiment [46]. For live-cell *d*STORM SNAP-Cell TMR-Star, SNAP-Cell 505 and TMP-ATTO 655 work reliably (Fig. 6) [37].

If applied appropriately, super-resolution imaging with organic fluorophores enables the observation of dynamic processes in living cells that move with velocities of up to several nm s^{-1} [45]. Whether or not a dynamic process can be temporally resolved is mainly controlled by two parameters: the complexity of the structure and its labeling density and the photoswitching rates controlled by the irradiation intensity. In the cellular environment, ON state lifetimes of a few tens of milliseconds (typically 10–50 ms) require imaging frame rates of 20–100 Hz. The lifetime of the OFF state varies between several hundred milliseconds to a few seconds (0.5–10 s), corresponding to $r = 50–1{,}000$. For low labeling densities, e.g., in studies of the dynamics of filaments or protein complexes with only 10–50 fluorophores per diffraction limited area, super-resolution imaging with a speed only determined by the irradiation intensity is possible. Under these conditions, super-resolution imaging at spatial resolutions of ~ 20 nm and temporal resolutions of 0.1–1 s is possible [44, 49]. On the other hand, the temporal resolution decreases for more complex structures with high labeling densities of ≥ 300 fluorophores per diffraction-limited area unless the excitation intensity is dramatically increased.

References

1. Moerner WE, Orrit M (1999) Illuminating single molecules in condensed matter. Science 283:1670–1676
2. Sauer M, Hofkens J, Enderlein J (2011) Handbook of fluorescence spectroscopy and imaging: from single molecules to ensembles: from ensemble to single molecules. Wiley, Weilheim
3. Drexhage KH (1973) Structure and properties of laser dyes. In: Schafer FP (ed) Topics in applied physics, vol 1, Dye Lasers. Springer, Heidelberg
4. Tinnefeld P, Sauer M (2005) Branching out of single-molecule fluorescence spectroscopy: challenges for chemistry and influence on biology. Angew Chem Int Ed 44:2642–2671
5. Cheezum MK, Walker WF, Guilford WH (2001) Quantitative comparison of algorithms for tracking single fluorescent particles. Biophys J 81:2378–2388
6. Thompson RE, Larson DR, Webb WW (2002) Precise nanometer localization analysis for individual fluorescent probes. Biophys J 82:2775–2783
7. Yildiz A, Selvin PR (2005) Fluorescence imaging with one nanometer accuracy: application to molecular motors. Acc Chem Res 38:574–582
8. Zondervan R, Kulzer F, Orlinskii SB, Orrit M (2003) Photoblinking of rhodamine 6 G in poly (vinyl alcohol): radical dark state formed through the triplet. J Phys Chem A 107:6770–6776
9. Rasnik I, McKinney SA, Ha T (2006) Non-blinking and long-lasting single molecule fluorescence imaging. Nat Methods 3:891–893
10. Widengren J, Chmyrov A, Eggeling C, Löfdahl PA, Seidel CAM (2007) Strategies to improve photostabilities in ultrasensitive fluorescence spectroscopy. J Phys Chem A 111:429–440
11. Vogelsang J, Kasper R, Person B, Heilemann M, Sauer M, Tinnefeld P (2008) A reducing and oxidizing system minimizes photobleaching and blinking of fluorescent dyes. Angew Chem Int Ed 47:5465–5469

12. Orrit M (2010) Chemical and physical aspects of charge transfer in the fluorescence intermittency of single molecules and quantum dots. Photochem Photobiol Sci 9:637–642
13. Spielmann T, Blom H, Geissbuehler M, Lasser T, Widengren J (2010) Transient state monitoring by total internal reflection fluorescence microscopy. J Phys Chem B 114:4035–4046
14. Hell SW, Wichmann J (1994) Breaking the diffraction resolution limit by stimulated emission: stimulated-emission-depletion fluorescence microscopy. Opt Lett 19:780–782
15. Hell SW (2007) Far-field optical nanoscopy. Science 316:1153–1158
16. Lidke KA, Rieger B, Jovin TM, Heintzmann R (2005) Superresolution by localization of quantum dots using blinking statistics. Optics Express 13:7052–7062
17. Dertinger T, Colyer R, Iyer G, Weiss S, Enderlein J (2009) Fast, background-free, 3D super-resolution optical fluctuation imaging (SOFI). Proc Natl Acad Sci USA 106:22287–22292
18. Betzig E, Patterson GH, Sougrat R, Lindwasser OW, Olenych S, Bonifacino JS, Davidson MW, Lippincott-Schwartz J, Hess HF (2006) Imaging intracellular fluorescent proteins at nanometer resolution. Science 313:1642–1645
19. Hess ST, Girirajan TP, Mason MD (2006) Ultra-high resolution imaging by fluorescence photoactivation localization microscopy. Biophys J 91:4258–4272
20. Rust MJ, Bates B, Zhuang X (2006) Subdiffraction-limit imaging by stochastic optical reconstruction microscopy (STORM). Nat Methods 3:793–795
21. Gould TJ, Verkhusha VV, Hess ST (2009) Imaging biological structures with fluorescence photoactivation localization microscopy. Nat Protocols 4:291–308
22. Shroff H, White H, Betzig E (2008) Photoactivation localization microscopy (PALM) of adhesion complexes. Current Protocols Cell Biol 4:21.1–4.21.27
23. Ji N, Shroff H, Zhong H, Betzig E (2008) Advances in the speed and resolution of light microscopy. Current Opin Neurobiol 18:605–616
24. Bates M, Blosser TR, Zhuang X (2005) Short-range spectroscopic ruler based on a single-molecule optical switch. Phys Rev Lett 94:108101
25. Heilemann M, Margeat E, Kasper R, Sauer M, Tinnefeld P (2005) Carbocyanine dyes as efficient reversible single-molecule optical switch. J Am Chem Soc 127:3801–3806
26. Heilemann M, van de Linde S, Schüttpelz M, Kasper R, Seefeldt B, Mukherjee A, Tinnefeld P, Sauer M (2008) Subdiffraction-resolution fluorescence imaging with conventional fluorescent probes. Angew Chem Int Ed 47:6172–6176
27. Fölling J, Bossi M, Bock H, Medda R, Wurm CA, Hein B, Jakobs S, Eggeling C, Hell SW (2008) Fluorescence nanoscopy by ground-state depletion and single-molecule return. Nat Methods 5:943–945
28. Steinhauer C, Forthmann C, Vogelsang J, Tinnefeld P (2008) Superresolution microscopy on the basis of engineered dark states. J Am Chem Soc 130:16840–16841
29. Flors C, Ravarani CN, Dryden DT (2009) Super-resolution imaging of DNA labeled with intercalating dyes. ChemPhysChem 10:2201–2204
30. Baddeley D, Jayasinghe ID, Cremer C, Cannell MB, Soeller C (2009) Light-induced dark states of organic fluochromes enable 30 nm resolution imaging in standard media. Biophys J 96:L22–L24
31. Hell SW (2009) Microscopy and its focal switch. Nat Methods 6:24–32
32. Huang B, Bates M, Zhuang X (2009) Super-resolution fluorescence microscopy. Annu Rev Biochem 78:993–1016
33. Patterson G, Davidson M, Manley S, Lippincott-Schwartz J (2010) Superresolution imaging using single-molecule localization. Annu Rev Phys Chem 61:345–367
34. Galbraith CG, Galbraith JA (2011) Super-resolution microscopy at a glance. J Cell Sci 124:1607–16011
35. Shaner NC, Lin MZ, McKeown MR, Steinbach PA, Hazelwood KL, Davidson MW, Tsien RY (2008) Improving the photostability of bright monomeric orange and red fluorescent proteins. Nat Methods 5:545–551
36. Tang J, Akerboom J, Vaziri A, Looger LL, Shank SV (2010) Near-isotropic 3D optical nanoscopy with photon-limited chromophores. Proc Natl Acad Sci USA 107:10068–10073

37. van de Linde S, Löschberger A, Klein T, Heidbreder M, Heilemann M, Sauer M (2011) Direct stochastic optical reconstruction microscopy with standard fluorescent probes. Nat Protocols 6:991–1009
38. Heilemann M, van de Linde S, Mukherjee A, Sauer M (2009) Super-resolution imaging with small organic fluorophores. Angew Chem Int Ed 48:6903–6908
39. van de Linde S, Sauer M, Heilemann M (2008) Subdiffraction-resolution fluorescence imaging of proteins in the inner mitochondrial membrane with photoswitchable fluorophores. J Struct Biol 164:250–254
40. van de Linde S, Kasper R, Heilemann M, Sauer M (2008) Photoswitching microscopy with standard fluorophores. Appl Phys B 93:725–731
41. Heilemann M, Dedecker P, Hofkens J, Sauer M (2009) Photoswitches: key molecules for subdiffraction-resolution fluorescence imaging and molecular quantification. Laser Photonics Rev 3:180–202
42. van de Linde S, Mukherjee A, Schüttpelz M, Wiebusch G, Steve W, Heilemann M, Sauer M (2009) Multicolor photoswitching microscopy for subdiffraction-resolution fluorescence imaging. Photochem Photobiol Sci 8:465–469
43. Owen DM, Rentero C, Rossy J, Magenau A, Williamson D, Rodriguez M, Gaus K (2009) PALM imaging and cluster analysis of protein heterogeneity at the cell surface. J Biophotonics 3:446–454
44. Endesfelder U, van de Linde S, Wolter S, Sauer M, Heilemann M (2010) Subdiffraction-resolution fluorescence microscopy of myosin-actin motility. ChemPhysChem 11:836–840
45. Wombacher R, Heidbreder M, van de Linde S, Sheetz MP, Heilemann M, Cornish VW, Sauer M (2010) Live-cell super-resolution imaging with trimethoprim conjugates. Nat Methods 7:717–719
46. Klein T, Löschberger A, Proppert S, Wolter S, van de Linde S, Sauer M (2011) Live-cell *d*STORM with SNAP-tag fusion proteins. Nat Methods 8:7–9
47. Wolter S, Schüttpelz M, Tscherepanow M, van de Linde S, Heilemann M, Sauer M (2010) Real-time computation of subdiffraction-resolution fluorescence images. J Microscopy 237:12–22
48. Testa I, Wurm CA, Medda R, Rothermel E, von Middendorf C, Fölling J, Jakobs S, Schönle A, Hell SW, Eggeling C (2010) Multicolor fluorescence nanoscopy in fixed and living cells by exciting conventional fluorophores with a single wavelength. Biophys J 99:2686–2694
49. Jones SA, Shim SH, He J, Zhuang X (2011) Fast, three-dimensional super-resolution imaging of live cells. Nat Methods 8:499–505
50. Shannon CE (1949) Communication in the presence of noise. Proceedings of the Institute of Radio Engineers 37: 10–21.
51. Lemmer P, Gunkel M, Baddeley D, Kaufmann R, Ulrich A, Weiland Y, Reymann J, Müller P, Hausmann M, Cremer C (2008) SPDM: Light microscopy with single-molecule resolution at the nanoscale. Appl Phys B 93:1–12
52. Vogelsang J, Cordes T, Forthmann C, Steinhauer C, Tinnefeld P (2009) Controlling the fluorescence of ordinary oxazine dyes for single-molecule switching and superresolution microscopy. Proc Natl Acad Sci USA 109:8107–8112
53. Sharonov A, Hochstrasser RM (2006) Wide-field subdiffraction imaging by accumulated binding of diffusing probes. Proc Acad Sci USA 103:18911–18916
54. Roeffaers MB, De Cremer G, Libeert J, Ameloot R, Dedecker P, Bons AJ, Buckins M, Martens JA, Sels BF, De Vos DE, Hofkens J (2009) Super-resolution reactivity mapping of nanostructured catalyst particles. Angew Chem Int Ed 48:9285–9289
55. van de Linde S, Krstic I, Prisner T, Doose S, Heilemann M, Sauer M (2011) Photoinduced formation of reversible dyes radicals and their impact on super-resolution imaging. Photochem Photobiol Sci 10:499–506
56. Dempsey GT, Bates M, Kowtoniuk WE, Liu DR, Tsien RY, Zhuang X (2009) Photoswitching mechanism of cyanine dyes. J Am Chem Soc 131:18192–18193
57. Wardmann P (1989) Reduction potentials of one-electron couples involving free radicals in aqueous solution. J Phys Chem Ref Data 18:1637–1755

58. Burner U, Jantschko W, Obinger C (1999) Kinetics of oxidation of aliphatic and aromatic thiols by myeloperoxidase compounds I and II. FEBS Lett 443:290–296
59. Doose S, Neuweiler H, Sauer M (2009) Fluorescence quenching by photoinduced electron transfer: A reporter for conformational dynamics of macromolecules. ChemPhysChem 10:1389–1398
60. Sies H (1999) Glutathione and its role in the cellular functions. Free Radical Biol Med 27:916–921
61. van de Linde S, Wolter S, Heilemann M, Sauer M (2010) The effect of photoswitching kinetics and labeling densities on super-resolution fluorescence imaging. J Biotechnol 149:260–266
62. Cordes T, Strackharn M, Stahl SW, Summer W, Steinhauer C, Forthmann C, Puchner EM, Vogelsang J, Gaub HE, Tinnefeld P (2010) Resolving single-molecule assembled patterns with superresolution blink-microscopy. Nano Lett 10:645–651
63. Holden SJ, Uphoff S, Kapanidis AN (2011) DAOSTORM: an algorithm for high-density super-resolution microscopy. Nat Methods 8:279–280
64. Wolter S, Endesfelder U, van de Linde S, Heilemann M, Sauer M (2011) Measuring localization performance of super-resolution algorithms on very active samples. Optics Lett 19:7020–7033
65. Giepmans BNG, Adams SR, Ellisman MH, Tsien RY (2006) The fluorescent toolbox for assessing protein location and function. Science 312:217–224
66. Miller LW, Cornish VW (2005) Selective chemical labeling of proteins in living cells. Curr Opin Chem Biol 9:56–60
67. Johnsson N, Johnsson K (2007) Chemical tools for biomolecular imaging. ACS Chem Biol 2:31–38
68. Griffin BA, Adams SR, Tsien RY (1998) Specific covalent labeling of recombinant protein molecules inside live cells. Science 281:269–272
69. Keppler A, Gendreizig S, Gronemeyer T, Pick H, Vogel H, Johnsson K (2003) A general method for the covalent labeling of fusion proteins with small molecules in vivo. Nat Biotechnol 21:86–89
70. Keppler A, Pick H, Arrivoli C, Vogel H, Johnsson K (2004) Labeling of fusion proteins with synthetic fluorophores in live cells. Proc Natl Acad Sci USA 102:9955–9959
71. Miller LW, Cai Y, Sheetz M, Cornish VW (2005) In vivo protein labeling with trimethoprim conjugates: a flexible chemical tag. Nat Methods 2:255–257
72. Gallagher S, Sable JE, Sheetz M, Cornish VW (2009) An in vivo covalent TMP-tag based on proximity-induced reactivity. ACS Chem Biol 7:547–556
73. Tokunaga M, Imamoto N, Sakata-Sogawa K (2008) Highly inclined thin illumination enables clear single-molecule imaging in cells. Nat Methods 5:159–161

Part II
Labelling Technology for Optical Nanoscopy

Single-Molecule Photocontrol and Nanoscopy

Matthew D. Lew, Steven F. Lee, Michael A. Thompson, Hsiao-lu D. Lee, and W. E. Moerner

Abstract Fluorescence microscopy is a ubiquitous tool in biological studies, but fundamental diffraction limits its resolution to ~200 nm for visible light. To overcome this physical limit, but still retain the advantages of far-field noninvasive fluorescence imaging, single-molecule photocontrol has been utilized to achieve optical nanoscopy. Superlocalization, combined with photocontrol of single molecules, allows individual molecules to be localized to precisions of tens of nanometers as part of a larger biological structure, thereby achieving super-resolution. Photoactivation, photoswitching, and photoinduced blinking are all methods of photocontrol, and critical characterization and performance parameters of photocontrollable fluorophores are discussed. We describe two classes of small molecules for use in photoactivation (azido-dicyanomethylenedihydrofuran molecules) and photoswitching (Cy3–Cy5 covalent heterodimer) studies. Furthermore, the use of the first-reported photoswitchable fluorescent protein, enhanced yellow fluorescent protein (eYFP), is also discussed for photoswitching and for photoinduced blinking experiments. Importantly, all of these methods of photocontrol have demonstrated remarkable usefulness in super-resolution studies of structures in living cells.

M.D. Lew
Department of Chemistry, Mail Code 5080, Stanford University, Stanford, CA 94305-5080, USA

Department of Electrical Engineering, Stanford University, Stanford, CA, USA

S.F. Lee
Department of Chemistry, Mail Code 5080, Stanford University, Stanford, CA 94305-5080, USA

Department of Chemistry, University of Cambridge, Cambridge, UK

M.A. Thompson, H.-l.D. Lee, and W.E. Moerner (✉)
Department of Chemistry, Mail Code 5080, Stanford University, Stanford, CA 94305-5080, USA
e-mail: wmoerner@stanford.edu

P. Tinnefeld et al. (eds.), *Far-Field Optical Nanoscopy*,
Springer Ser Fluoresc (2015) 14: 87–110, DOI 10.1007/4243_2011_37

Keywords Photoactivation · Photoswitching · Photoinduced blinking · Single-molecule · Super-resolution microscopy

Contents

1 Introduction

Fluorescence microscopy is a powerful tool for biological studies because it can noninvasively light up different cellular structures with a wide array of labels, high signal-to-background ratio, and extremely precise, genetically encoded specificity. However, using visible light often incurs the penalty of poor spatial resolution compared to X-ray or electron microscopy. Diffraction limits the resolution of an optical microscope to roughly the optical wavelength divided by twice the numerical aperture of the imaging system, $\lambda/(2NA)$. Since the largest values of NA for state-of-the-art, highly corrected microscope objectives are in the range of 1.3–1.6, the spatial resolution of optical imaging has been limited, until recently, to ~200 nm for visible light. Various techniques for increasing resolution with far-field imaging have been reviewed in previous chapters (for a comparison of the various methods see [1–3]). Here we describe methods to achieve optical nanoscopy, otherwise refered to as super-resolution optical microscopy in the literature, by utilizing the photocontrol of single molecules to resolve structures with far better resolution than the optical diffraction limit while still using a far-field optical microscope.

Despite the variety of acronyms which have been promulgated, all of the single-molecule switching-based nanoscopy techniques can be described by the synthesis of two ideas. The first is the localization of a single molecule to nanometer precision and the second is the active control of the emitter concentration such that each active emitter is separated from its emitting neighbors by at least one diffraction-limited distance. We will now briefly introduce both ideas and how they are combined to facilitate super-resolution fluorescence imaging. The fluorescent light emitted by a single molecule appears in the image relayed by a microscope as a broad, diffraction-limited spot. Even though the spot is large (~200 nm) compared to the molecule emitting the light (1–2 nm), it is possible to localize

the molecule to nanometer precision by numerically fitting the observed PSF with a model function, such as a Gaussian or Airy shape. This principle was applied in the early days of single-molecule spectroscopy, where the fluorescence excitation signal from one molecule was used to map the size of the focused pumping laser beam [4]. Characterizing and fitting the PSF to achieve "superlocalization" or spatial localization beyond the diffraction limit is well known in many areas of science and was applied to single nanoscale fluorescent beads with many emitters [5]. Later, the superlocalization approach was applied to low-temperature single-molecule measurements [6, 7], where both spatial information and a secondary variable, detuning the wavelength of the excitation laser over time, were used to localize and distinguish between molecules within a diffraction-limited spot. (At room temperature, however, spectral broadening prevents more than just a few emitters from being discriminated by pumping wavelength.) The accuracy with which a single molecule can be localized depends fundamentally upon the signal-to-noise ratio of the single-molecule image. Since this image is generated by the Poisson process of photon detection, the most important factor affecting accuracy is the total number of photons detected above background, with a weaker dependence on the size of the detector pixels and background noise [8–10]. In addition, molecular orientation can affect single-molecule PSFs since they are dipole-like emitters and not isotropic point sources [11, 12]. In experiments where fluorescent labels are rotationally constrained during imaging, such as for small organic molecules on very short tethers, care must be taken to remove any systematic offset in calculated positions due to orientation effects [13, 14].

To move from superlocalization of spatially separated single molecules to creating a super-resolution image of a structure, it is necessary to obtain position information for at least two emitters within each resolution element according to the Nyquist–Shannon theorem [15, 16]. However, superlocalization can only be achieved if adjacent molecules are distinguishable so that they can be fitted. Consequently, it was necessary to develop a way to work with high concentrations of labels where the PSFs would normally overlap. Imaging densely labeled samples requires the use of the second idea described above, namely, active control of single emitters, which means that the experimenter must use some variables under experimental control (such as intensity, other wavelengths, buffer composition, etc.) to maintain low emitting concentration in each image. In 2006, three research groups applied direct photocontrol of single emitters to generate super-resolution images in biologically relevant systems. Photoactivated GFP fusions were used by Betzig et al. for photoactivated localization microscopy (PALM) [17] and by Hess et al. for fluorescence photoactivation localization microscopy (FPALM) [18]. Rust et al. used photoswitching produced by proximal Cy3 and Cy5 molecules in the presence of thiols for stochastic optical reconstruction microscopy (STORM) [19]. Since that time, other mechanisms have been utilized for photocontrol, including collisional flux from solution (points accumulation for imaging in nanoscale topography [PAINT] [20]), photoreactivation of eYFP [21], dark state shelving (ground state depletion microscopy followed by individual molecule return [GSDIM] [22], and blink microscopy [23]).

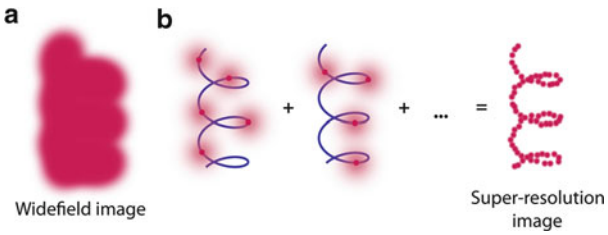

Fig. 1 Schematic showing the key idea of super-resolution imaging of a structure by photocontrol. (**a**) It is not possible to resolve the underlying structure in a conventional wide-field fluorescence image because the fluorescent labels are in high concentration and the PSF images overlap. (**b**) Using controllable fluorophores, it is possible to turn on and image a sparse subset of molecules that then can be localized with nanometer precision (*blue line* is the underlying structure being sampled). Once the first subset of molecules photobleaches, another subset is turned on and localized. This process is repeated and the resulting localizations summed to give a super-resolution image of the underlying structure (Adapted and reproduced with permission from Thompson et al. [24] copyright 2010 by Academic Press)

The basic technique for achieving super-resolution in all of these reports involves turning on only a sparse subset of all the labels present at any given time (see Fig. 1). (While the mechanism of photocontrol may differ for different fluorescent labels, active intentional control of the concentration of emitting single molecules by the experimenter is essential to achieve super-resolution. Thus these methods may generally be collectively called by the mechanism-independent term "single-molecule active-control microscopy," or SMACM.) After imaging, super-localizing, and then photobleaching a sparse group of single molecules, a new subset is turned on and the process is repeated to build up a full image of the labeled structure. The "turning on" process is random in that the members of the small subset of labels that turn on are not known in advance; thus, these methods are stochastic readout methods (in contrast to targeted readout methods such as STED, discussed in previous chapters). Over the course of data acquisition, the activated labels should sample as much of the underlying labeled structure as possible. Resolutions down to 10–30 nm have been achieved [17, 19, 25, 26], and it is this impressive improvement of resolution over diffraction-limited imaging that has caused much excitement in the field.

In this chapter, the use of photocontrol of single molecules for super-resolution microscopy will be reviewed, focusing on the authors' research. Photoactivation, photoswitching, and photoinduced blinking are all methods of photocontrol, and each offers the scientist a different pathway to maintain a low concentration for SMACM imaging. Depending upon the imaging target, each offers advantages and disadvantages. Here, we will describe two classes of small molecules for use in photoactivation and photoswitching studies. The use of the first-reported photoswitchable fluorescent protein, enhanced yellow fluorescent protein (eYFP) [27], will also be discussed both for photoswitching and photoinduced blinking experiments.

2 Characterizing Photocontrollable Fluorophores

The best emitters for photocontrolled localization-based super-resolution imaging will maximize the number of well-localized unique molecules per area per time [28]. Taking into account both localization precision [8, 9] and the Nyquist–Shannon sampling theorem [15, 16], good photoactivatable fluorophores must be bright, stable, emit many photons, densely label the sample, and have a high contrast between on and off states. In addition, the probe must be easily photoactivated to avoid cell damage from short-wavelength illumination.

One of the most important parameters for single-molecule fluorophores is the number of photons each molecule emits before photobleaching ($N_{\mathrm{tot,e}}$). Scaling inversely with $N_{\mathrm{tot,e}}$ is the photobleaching quantum yield (Φ_{B}), or the probability of bleaching with each photon absorbed (see below for equations). A very low value of Φ_{B} corresponds to not only a long-lived fluorophore but also to very high precision in localizing the fluorophore [8, 9].

Besides the number of photons emitted, fluorophore labeling density is another important variable that determines the ultimate resolution. Because super-resolution imaging by sequential localization of point sources samples the true underlying structure of interest, there are well-known restrictions on the labeling density (or spatial sampling frequency) required in order to resolve structures at a given resolution. For instance, the Nyquist–Shannon sampling theorem [15, 16, 21, 26, 28] requires that in order to resolve a structure at a resolution of x nm, the structure must be labeled at a density of 2 fluorophores per x nm. In addition, those labels must also be localized with the same average density during an imaging experiment. With such a high labeling density, the turn-on ratio (i.e., the contrast between the bright and dark states of the molecule) of the labeling fluorophore must be very high, lest the many weakly emitting "off" molecules in a diffraction-limited spot drown out the signal from the single "on" molecule.

2.1 Photobleaching and Photoconversion Quantum Yields

A useful set of characterization methods has been provided by Lord et al. [29]. First, as usual the photobleaching quantum yield may be measured on a bulk sample of the activated emitters and is defined as the probability of photobleaching per photon absorbed or the ratio of the bleaching rate R_{B} to the rate of absorbing photons R_{abs}:

$$\Phi_{\mathrm{B(P)}} = \frac{R_{\mathrm{B(P)}}}{R_{\mathrm{abs}}} = \frac{1}{\tau_{\mathrm{B(P)}} R_{\mathrm{abs}}} = \frac{1}{\tau_{\mathrm{B(P)}} \sigma_{\lambda} I_{\lambda} (\lambda / hc)}, \tag{1}$$

where $\tau_{\mathrm{B(P)}}$ is the decay constant from an exponential fit to the decay curve, the absorption cross-section σ_{λ} is related to the molar absorption coefficient ε_{λ} by the equation $\sigma_{\lambda} = 2{,}303\ \varepsilon_{\lambda}/N_{\mathrm{A}} \approx 10^{-16}\ \mathrm{cm}^2$ for good emitters, I_{λ} is the irradiance

(intensity) at the sample, λ is the excitation wavelength, h is Planck's constant, and c is the speed of light. Bulk photobleaching decay curves are often not single-exponential, and the average decay constant for a two-exponential fit, $F = \sum_{i=1}^{n=2} \alpha_i e^{(-t/\tau_i)}$, is given by

$$\bar{\tau} = f_1\tau_1 + f_2\tau_2 = \frac{\alpha_1{\tau_1}^2 + \alpha_2{\tau_2}^2}{\alpha_1\tau_1 + \alpha_2\tau_2}, \tag{2}$$

where $f_i = \alpha_i\tau_i / \sum_j \alpha_j\tau_j$. is the fractional area under the multi-exponential curve [30]. (Some other authors use $t_{90\%}$, the irradiation time in seconds for 90% conversion to product, as a more practical measure than the decay constant $\bar{\tau}$[31]; so values should be compared carefully).

Photoconversion from a precursor fluorogen to the emissive form can be monitored in bulk by measuring changes over time in absorbance or emission of the reactant or photoproduct of interest. The quantum yield of photoconversion, Φ_P, is defined in (1), where τ_P is the average decay constant from the exponential fit to the decaying absorption values of the starting material. Note that Φ_P is the probability that the starting material will react for each photon absorbed. Since the total photoreaction yield to fluorescent product is usually less than unity, only a fraction of the precursor fluorogen will become fluorescent.

2.2 *Effective Turn-on Ratio*

This section describes an experimentally convenient method for measuring a critically important parameter, the turn-on ratio of photoactivatable fluorophores, suggested by Lord et al. [29]. The goal is to measure how many times brighter an activated molecule is than the preactivated fluorogen. Recalling that resolution scales with labeling density, the single-molecule detectability limit occurs when the intensity from one bright molecule I_{on} equals the intensity from n_{off} dark fluorogens (i.e., when $I_{on} = n_{off}I_{off}$):

$$R = \frac{I_{on}}{I_{off}} = \frac{n_{off}I_{off}}{I_{off}} = n_{off}. \tag{3}$$

Assuming that every dark molecule becomes fluorescent is rarely correct (i.e., $n_{on} < n_{off}$ is the common situation). One could measure R by averaging over many single molecules; however, this procedure would select only the fluorogens that become fluorescent, and R would be artificially inflated.

Alternatively, it is more accurate to measure an effective turn-on ratio that takes into account the reaction yield. In a bulk experiment,[1] one should integrate the background-subtracted intensities over a large region before activation (S_{off}) and after activation to steady state (S_{on}). Not all copies of the fluorogen convert to the fluorescent species, as the simple ratio R assumes above; the overall reaction yield p is usually less than unity because there are often nonfluorescent photoproducts. Therefore, the total number of emitters that will turn on is the reaction yield times the number of precursor molecules: $n_{on} = pn_{off}$. The ratio of the background-subtracted signals in a bulk experiment gives the effective turn-on ratio R_{eff}, which is the experimentally relevant parameter:

$$R_{eff} = \frac{S_{on}}{S_{off}} = \frac{n_{on}I_{on}}{n_{off}I_{off}} = \frac{pn_{off}I_{on}}{n_{off}I_{off}} = p\frac{I_{on}}{I_{off}} = pR = pn_{off} = n_{on}. \quad (4)$$

Thus, R_{eff} corresponds directly to the maximum number of molecules n_{on} that one could localize in a diffraction-limited region before the aggregate signal ($n_{off}I_{off}$) from all the dark fluorogens required for that number of localizations equals the signal from one emitting molecule I_{on}.

Resolution on the order of nanometers or tens of nanometers requires a labeling density of many thousands of localizations per μm^2 and therefore turn-on ratios in the hundreds or thousands. For example, if we assume the diffraction limit to be approximately 200 nm, the area of the diffraction-limited spot is about 30,000 nm^2. If $R_{eff} = 300$, there is a maximum of 300 localizations in each diffraction-limited spot, so the distance between each localization is approximately $\sqrt{30,000 nm^2/300} = 10$ nm. The Nyquist–Shannon theorem [15, 16] requires a spatial sampling of at least twice the desired resolution, limiting the resolution to about 20 nm in two dimensions. In three dimensions, the excitation volume in z is much larger than in x and y. Therefore, much higher contrast ratios and labeling densities are required for high-resolution imaging. For more details, see the supplemental material of Shroff et al. [28].

As a side note, the measured value of R_{eff} should be considered a lower limit because any molecules already in the "on" state before activation (preactivated molecules) contribute to the signal in the frames before activation, thus lowering the measured value of the parameter. The fraction q of preactivated molecules should be kept low by protecting the fluorophore stock solution and samples from room lights and by pretreating the sample with pumping illumination to return preactivated molecules to the "off" state (prebleaching the sample). Regardless, some preactivation will inevitably occur. We can calculate the effect preactivation

[1] For bulk experiments, the fluorogens are doped into a film (e.g., polymer, gelatin, agarose) at approximately 1–2 orders of magnitude higher concentration than in single-molecule experiments, but otherwise are imaged under similar conditions. This measurement assumes that one is working in a concentration regime where the emitters are dense enough to obtain a sufficient statistical sampling of the population but separated enough to avoid self-quenching or excimer behavior.

has on measuring R_{eff} by including signal from preactivated molecules in the dark measurement:

$$R_{\text{eff,preact}} = \frac{S_{\text{on}}}{S_{\text{off,preact}}} = \frac{n_{\text{on}} I_{\text{on}}}{n_{\text{off}} I_{\text{off}} + q n_{\text{off}} I_{\text{on}}} = \frac{n_{\text{on}} I_{\text{on}}}{n_{\text{off}} I_{\text{off}} \left(1 + \frac{q n_{\text{off}} I_{\text{on}}}{n_{\text{off}} I_{\text{off}}}\right)} = \frac{pR}{1 + qR} = \frac{R_{\text{eff,true}}}{1 + qR}. \tag{5}$$

From (5), the multiplicative correction factor to convert from measured to true effective turn-on ratio is $(1 + qR)$. Even 0.1% preactivation could artificially deflate the measured value by half (assuming the $R = I_{\text{on}}/I_{\text{off}}$ of one isolated molecule is 1,000). Therefore, minimizing preactivation (or, alternatively, maximizing prebleach) before measuring the effective turn-on ratio can increase the value of R_{eff} such that it approaches the true ratio.

3 Small-Molecule Photoactivatable Fluorophores: The Azido-DCDHF Class

For several years, a collaboration between the Moerner laboratory and the laboratory of Robert J. Twieg at Kent State University has explored the properties of the dicyanomethylenedihydrofuran (DCDHF) class of molecules. Originally studied for their optical nonlinearity, the DCDHF molecules are push–pull fluorophores containing an amine electron donor covalently linked to an electron acceptor dicyanomethylenedihydrofuran group via a conjugated central core. Recently, this work produced a novel class of photoactivatable single-molecule fluorophores by replacing the amine with an azide, which is not a good electron donor. When pumping with long wavelengths, the azido fluorogenic molecules are dark because the charge-transfer optical absorption is shifted to shorter wavelengths. However, applying low-intensity blue light photochemically converts the azide to an amine and restores the donor–acceptor character, the red-shifted absorption, and the bright fluorescent emission. Such molecules thereby enable PALM-type super-resolution imaging.

Photoactivatable (or "photocaged") donor-conjugated network-acceptor (or "push–pull") chromophores can be designed by disrupting the charge transfer band [32, 33], which significantly blue shifts the absorption such that it is no longer resonant with the imaging laser. In these cases, photoactivation requires a photoreaction that converts the disrupting component to a substituent that is capable of donating electrons into the chromophore's conjugated network.

Azides are a natural choice for the disrupting substituent since they are weakly electron withdrawing [34]. Recovering fluorescence via photoconversion is possible because aryl azides are known to be photolabile. The photochemistry of aryl azides has been studied extensively [35], and the most common photoreaction reported

involves the loss of dinitrogen and rearrangement to a seven-membered azepine heterocycle, which is unlikely to act as a strong electron-donating group. Fortunately, Soundararajan and Platz [36] demonstrated that electron-withdrawing substituents on the benzene can stabilize the nitrene intermediate and promote the formation of amine and azo groups instead of rearranging to the azepine. Upon irradiation with activating light that is resonant with its blue-shifted absorption, an azido push–pull molecule should photoconvert to the fluorescent amino version since push–pull chromophores inherently contain a strong electron-withdrawing substituent.

The photoactivation of these azido fluorogens to produce fluorophores is an irreversible chemical reaction, so reversible photoswitching is not possible. This irreversible process can be a drawback in cases that require cycling between bright and dark forms, such as in STED or when using SMACM to image dynamics. However, for quantitative imaging of static structures, a probe that activates, emits millions of photons, and then disappears permanently is preferable. Otherwise, the reactivation of fluorophores causes some portions of the structure to be repeatedly localized, thus complicating the subsequent image analysis and reconstruction of the structure of interest.

Photoactivation of azido DCDHFs as well as other push–pull chromophores has been previously demonstrated [29, 37–39]. Figure 2 shows the primary

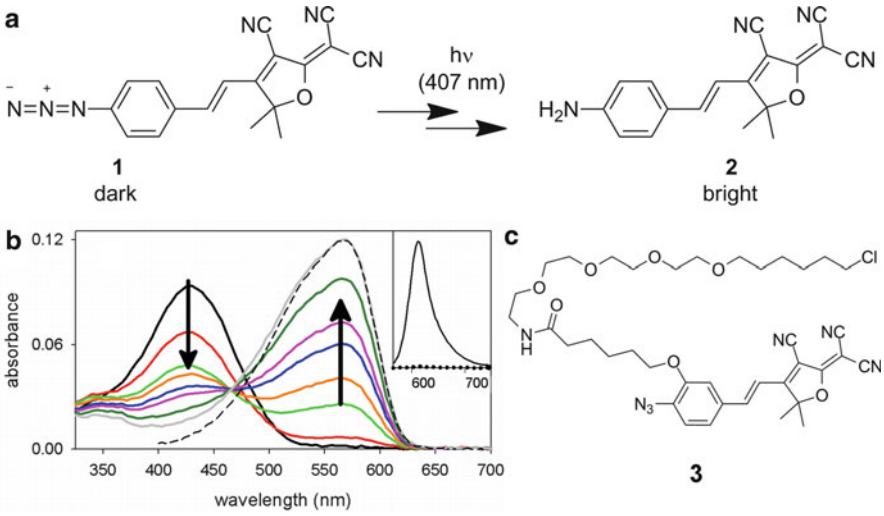

Fig. 2 Chemical structure and spectra of an azido DCDHF photoactivatable fluorogen. (**a**) Photochemical activation of the azido DCDHF fluorogen from *dark state* **1** to *bright state* **2**. (**b**) Absorption curves in ethanol (bubbled with N_2) showing photoactivation of **1** (λ_{abs} = 424 nm) over time to fluorescent product **2** (λ_{abs} = 570 nm). *Different colored* curves represent 0, 10, 90, 150, 240, 300, 480, and 1,320 s of illumination by 3.1 mW/cm^2 of diffuse 407-nm light. *Dashed line* is the absorbance of pure, synthesized **2**. (*Inset*) *Dotted line* is weak pre-activation fluorescence of **1** excited at 594 nm; *solid line* is strong post-activation fluorescence resulting from exciting **2** at 594 nm, showing >100-fold turn-on ratio. (**c**) Azido DCDHF bound to HaloTag substrate **3** for targeting to specific cellular proteins (Adapted with permission from Lord et al. [37] and Lee et al. [39]. Copyright 2008, 2010 American Chemical Society)

photoactivation reaction of an azido push–pull DCDHF fluorogen. Detailed syntheses by colleagues in the Twieg laboratory have been reported in previous papers and in supporting online material [29, 37–39]. A common trait among the azido push–pull fluorogens is their high sensitivity to photoactivating illumination (as measured by the photoconversion quantum yield Φ_P). One benefit of using azido-DCDHFs is that the photoconversion quantum yield is tunable. For instance, the subsequent addition of electron-withdrawing fluorines to the azido-phenyl group increases the photoactivation quantum yield [29]. For some fluorogens, only tens or hundreds of photons need be absorbed before the fluorogen converts to a fluorescent product. This ease of activation is important because high doses of blue or UV light can kill cells or alter phenotype. This benefit comes with the requirement that sample preparation be carried out in the dark or under red light to avoid preactivation before imaging.

Previous studies have reported that the DCDHF class of single-molecule fluorophores emits millions of photons and have low photobleaching quantum yields (Φ_B) [40, 41]. In addition, azido DCDHF fluorogens exhibit high turn-on ratios (the increase in emission from the fluorescent form compared to the dark fluorogen) of 325–1,270-fold [29]. Therefore, azido DCDHFs are attractive as photoactivatable probes for PALM. For instance, single molecules of DCDHF-V-PF4-azide immobilized in a polymer can be photoactivated and localized to less than 20 nm standard deviation in all three dimensions [38]. Azido DCDHF fluorogens can also be activated and form bright fluorophores in a live-cell environment. Figure 3 shows azido-DCDHF fluorogens activated with low amounts of

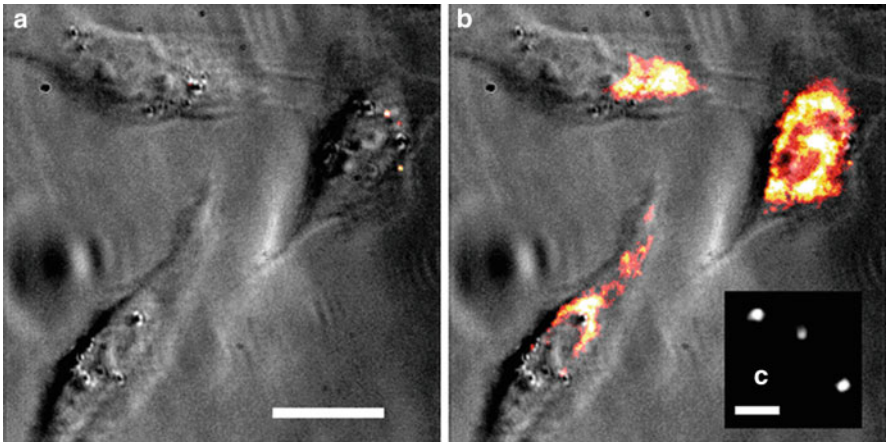

Fig. 3 Demonstration of the photoactivation of azido DCDHF in live cells. (**a**) Three CHO cells incubated with fluorogen **1** are dark before activation. (**b**) The fluorophore **2** lights up in the cells after activation with a 10-s flash of diffuse, low-irradiance (0.4 W/cm^2) 407-nm light. (False color overlay: *gray* shows the white-light transmission image and *red-yellow overlay* shows the fluorescence images, excited at 594 nm.) Scale bar: 20 μm. (**c**) Single molecules of activated **2** in a cell under higher magnification. Background was subtracted and the image was smoothed with a 1-pixel Gaussian blur. Scale bar: 800 nm (Adapted with permission from Lord et al. [37]. Copyright 2008 American Chemical Society)

blue light in live Chinese Hamster Ovary (CHO) cells. The resulting fluorophores are bright in the aqueous environment of the cell. In the data from Fig. 3, the cells were incubated with azido DCDHF fluorogens that enter the cell membrane and nonspecifically label the cell.

Targeting of azido DCDHF fluorogens to specific cellular proteins has also been demonstrated using the commercially available HaloTag approach [39]. This labeling technique requires transfecting cells to express a protein fusion composed of the protein of interest and HaloEnzyme (HaloEnz) that covalently links to the HaloTag substrate (see Fig. 4a). Thus, labeling of the target protein is achieved (i.e., a protein-HaloEnz-HaloTag-fluorophore covalent unit). Figure 4b illustrates the covalent binding of the HaloTag-DCDHF to the HaloEnzyme via the active site.

Compared with the original DCDHF-V-P-azide [37], the HaloTag-DCDHF fluorogen **3** (see Fig. 2c) exhibits similar spectral changes upon optical pumping of the aryl azide but a higher photoconversion quantum yield (see Table 1). The photoconversion was so sensitive that an additional activating blue laser was unnecessary. Instead, diffuse ambient light (e.g., the blue light emitted from a nearby liquid crystal display in a dark room) was sufficient to activate sparse sets of the fluorogen, thereby reducing the complexity of the experiment by requiring the use of only one laser. Since no blue or UV laser was necessary for activation, photodamage to samples is greatly reduced. The drawback to this sensitivity is that

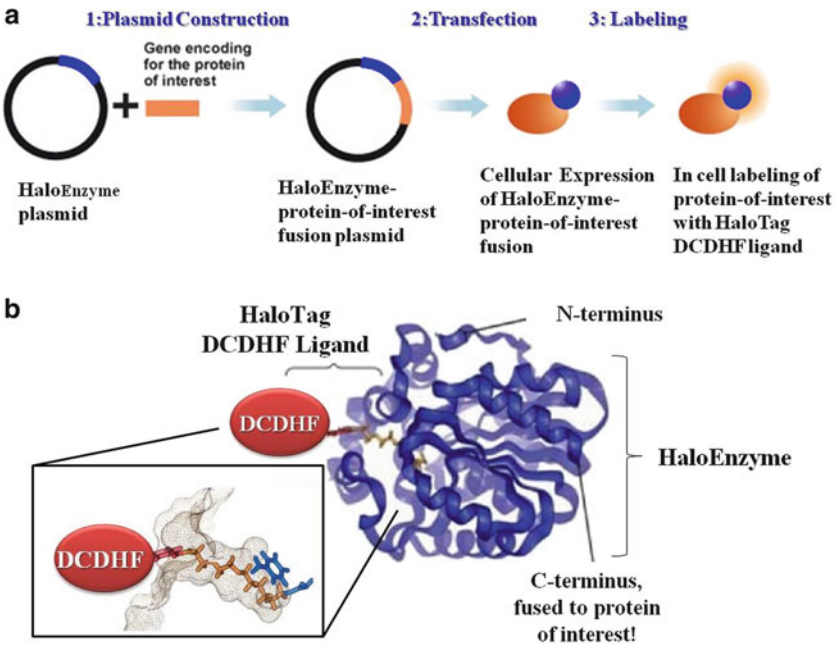

Fig. 4 Overview of HaloTag-DCDHF labeling scheme. (**a**) Flowchart of experimental procedures. (**b**) HaloTag-DCDHF fluorogen forms a covalent bond with HaloEnzyme

Table 1 Photophysical/photochemical parameters

	$\lambda_{abs,azide}$ (nm)[a]	$\lambda_{abs,amine}/\lambda_{fl,amine}$ (nm)[b]	Yield (%)[c]	Φ_P[d]
Azido-DCDHF-NHS (1)	424	570/613	65	0.0059
Azido-DCDHF-HaloTag (3)	443	572/627	~50	0.095

[a]Peak absorbance for azido fluorogen
[b]Absorbance and fluorescence peak wavelengths of the amino fluorophore
[c]Overall chemical reaction yield to the primary fluorescent amine
[d]Photoconversion quantum yield of azido fluorogens to any product (i.e., the probability of photoconverting after absorbing one photon) (Adapted with permission from Lee et al. [39]. Copyright 2010 American Chemical Society)

added precautions must be taken to prevent photoactivation of the probes before imaging (e.g., during handling and labeling).

The specificity of Azido-DCDHF-HaloTag labeling was verified in live bacterial cells and in mammalian culture [39]. For the latter case, wild-type HeLa cells and HeLa cells transfected to express HaloEnz-α-tubulin were stained live with the fluorogen, fixed, and immunostained with Alexa488-mAb to α-tubulin. Fluorescence images after photoactivation clearly demonstrate that the label was only retained in cells that expressed HaloEnz-α-tubulin. As an additional test, live CHO cells were cotransfected with HaloEnz-α-tubulin and α-tubulin-eGFP, and the fluorescent label colocalized well with the eGFP labeling (Fig. 5a, b). Finally, BS-C-1 cells were transfected with HaloEnz-α-tubulin, fixed, stained with Azido-DCDHF-HaloTag, and washed before SR imaging by PALM. Comparing diffraction-limited and super-resolution images (Fig. 5c, d), the microtubule structure is clearly imaged with a resolution beyond the optical diffraction limit.

The azido push–pull chromophores meet many of the critical requirements for high-resolution PALM-type SMACM. Several emit millions of photons before irreversibly photobleaching, are photoconverted with high quantum efficiency, exhibit high turn-on ratios, and possess moderate molar absorption coefficients and quantum yields.

4 Photoswitchable Covalent Cy3–Cy5 Heterodimers

In its original implementation, the STORM method utilized the Cy3/Cy5 photoswitching system, which requires thiol and oxygen-scavenger additives [19]. To achieve photoswitching, a Cy5 dye molecule is optically excited in the presence of a thiol until it enters into a metastable dark state. Recent mechanistic work has revealed that the dark state is an adduct of Cy5 and the thiol where the thiol has attacked the polymethine bridge of the molecule [42]. Recovery of the Cy5 fluorescent state is induced by low-intensity excitation of a proximal Cy3 fluorophore; the percentage of Cy5 emitters restored to the fluorescent state can be controlled by the intensity and duration of the Cy3 excitation pulse. The role of excitation of the Cy3 in removing the thiol and restoring Cy5 fluorescence is still

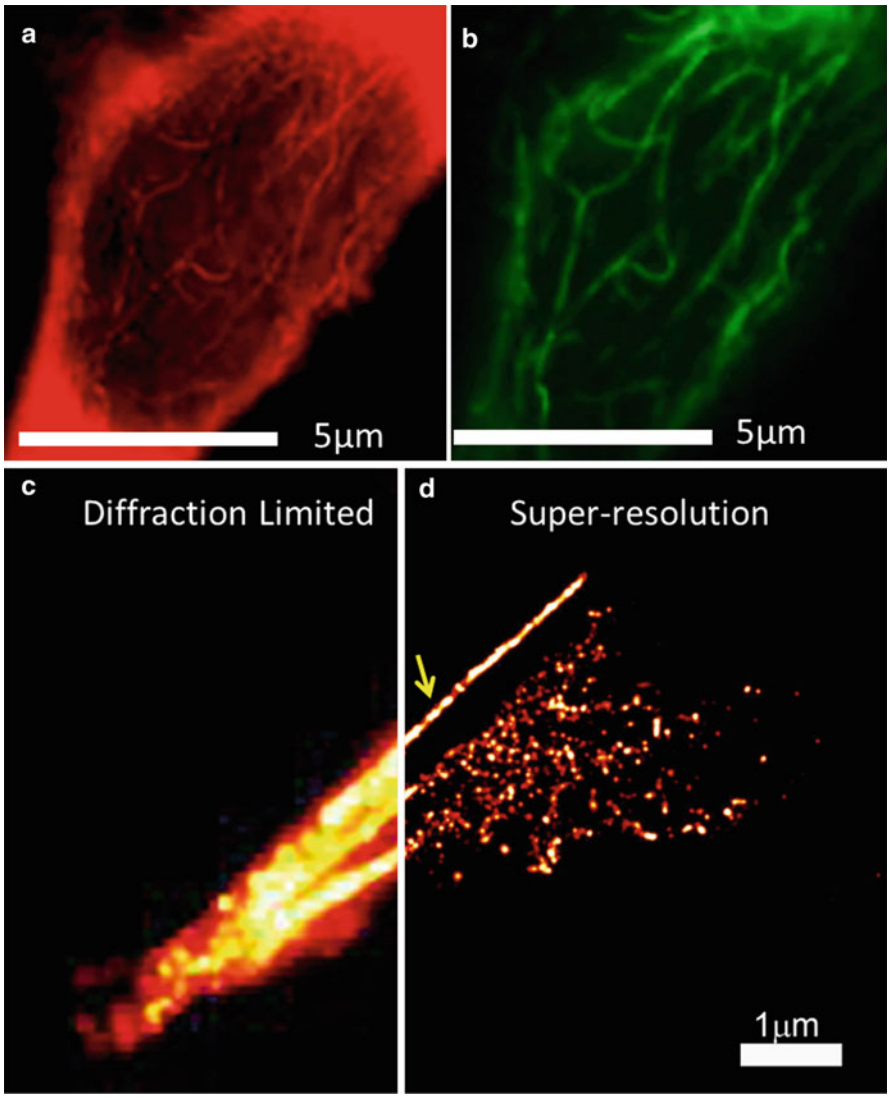

Fig.5 Evidence that the HaloTag-targeted fluorogen correctly labels specific proteins and enables SR imaging in mammalian cells. (**a**) Live CHO cells cotransfected to express both HaloEnz-α-tubulin and α-tubulin-eGFP labeled with **3** and imaged in DCDHF-V-P channel. (**b**) Cells from panel **a** imaged in the eGFP channel. (**c**) Fixed BS-C-1 cells expressing HaloEnz-α-tubulin labeled with Azido-DCDHF-HaloTag **3** imaged using conventional diffraction-limited imaging. (**d**) Same cell as panel **c** with SR imaging. Indicated microtubule measures 85 ± 15 nm fwhm (Adapted with permission from Lee et al. [39]. Copyright 2010 American Chemical Society)

unknown although local heating from nonradiative decay is a plausible mechanism. (In fact with high enough Cy5 excitation intensity, it is possible to obtain photoswitching without the attached Cy3 [43], which is used in the dSTORM process [44].) Because the

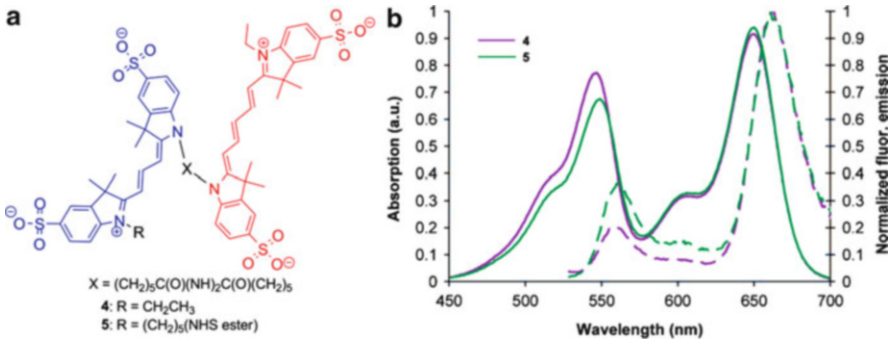

Fig. 6 Structure and spectra of covalent Cy3–Cy5 heterodimers. (**a**) Structure of Cy3–Cy5 dimer **4** and NHS ester-Cy3–Cy5 **5**. (**b**) Absorption (*solid*) and fluorescence emission (*dashed*, $\lambda_{ex} = 516$ nm) spectra of Cy3–Cy5 covalent heterodimers **4** (*purple*) and **5** (*green*) in water (3.7 μM for absorption; 37 nM for fluorescence) before photodarkening (Adapted with permission from Conley et al. [45]. Copyright 2008 American Chemical Society)

thiol is an integral part of the system, all three components, the switchable fluorophore, the activating fluorophore, and the thiol used need to be considered carefully. Since the Cy5 reporter molecule must be located within ~2 nm of the Cy3 activator molecule for efficient reactivation to occur, structures are typically labeled using heterolabeled antibodies. The labeling ratio of activator to reporter molecules on each antibody (3:1) is controlled during labeling by employing different concentrations of the reactive activator and reactive reporter fluorophores [25]. The probabilistic nature of this labeling strategy results in a poorly controlled photoswitching system that exhibits undesirable heterogeneity in switching rates. To remedy this shortcoming, Conley et al. recently reported the preparation and bulk- and single-molecule characterization of a Cy3–Cy5 covalent heterodimer [45].

As shown in Fig. 6, the absorption spectra of Cy3–Cy5 covalent heterodimers **4** and **5** contain the characteristic Cy3 and Cy5 absorbance peaks in a ratio that corresponds approximately to the molar absorptivity ratio of the two dyes (0.6:1). Optical excitation of the Cy3 in **4** or **5** produces considerable Förster resonance energy transfer (FRET), confirming the covalent linkage in each heterodimer. The fluorescence lifetime of the Cy3 donor in **4** (0.15 ± 0.03 ns) is shorter than the lifetime of monomeric Cy3 (0.254 ± 0.007 ns), whose measured value reproduces those found in the literature [46, 47]. From these data, the FRET efficiency of **4** is determined to be 0.41, where the relatively low value is possibly due to nonoptimal orientation of the transition dipoles.

To demonstrate the heterodimer, bovine serum albumin (BSA) was sparsely labeled with NHS ester–Cy3–Cy5 **5** through its lysine residues. After immobilization onto a glass cover slip, single-molecule photoswitching of **5**-labeled BSA was achieved in the presence of 2-mercaptoethanesulfonate and a glucose oxidase oxygen-scavenging system, as shown in Fig. 7a, b. The single-molecule photoswitching properties of **5** are characterized by controllable reactivation, varying "on" times, and occasional spontaneous recovery from a long-lived dark state.

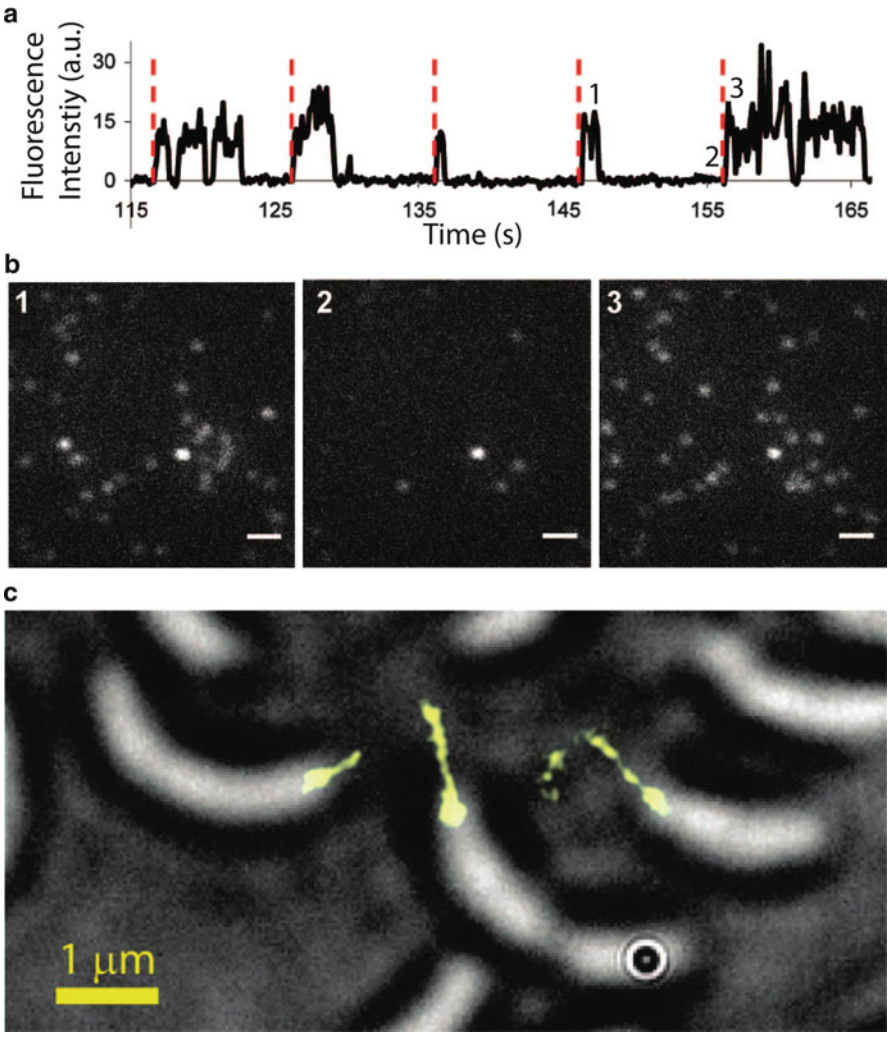

Fig. 7 Photoswitching behavior of and super-resolution imaging using the Cy3–Cy5 covalent dimer. (**a**) Representative single-molecule fluorescence time trace of **5**-labeled bovine serum albumin showing reactivation cycles 12–16, denoted by the *dashed lines*. (**b**) Fluorescence images at times 1, 2, and 3 corresponding to the times labeled in panel **a**. Scale bar, 1 μm. (**c**) Super-resolution fluorescence image of *C. crescentus* stalks with 30 nm resolution superimposed on a white-light image of the cells. The *C. crescentus* cells were incubated in 4 mM of Cy3–Cy5 NHS ester for 1 h and then washed five times before imaging to remove free fluorophores. The data were acquired over two thousand and forty eight 100-ms imaging frames with 633 nm excitation at 400 W/cm^2. After initial imaging and photobleaching of the Cy3–Cy5 dimers, the molecules were reactivated every 10 s for 0.1 s with 532-nm light at 10 W/cm^2 (Adapted and reproduced with permission from Conley et al. [45]. Copyright 2008 American Chemical Society)

The utility of **5** in SMACM super-resolution imaging was demonstrated by covalently attaching it to free amines on the surface of *Caulobacter crescentus* cells, which contain a subdiffraction-limited appendage, known as a stalk. While the stalk cannot be easily observed in white-light microscopy, it was successfully imaged with 30-nm resolution (Fig. 7c). We anticipate that Cy3–Cy5 covalent heterodimers will eventually replace more cumbersome methods for achieving Cy3/Cy5 proximity in the super-resolution imaging of biological systems; indeed, since our initial report, other reactive AlexaFluor and CyDye covalent heterodimers have been described [48].

5 Enhanced Yellow Fluorescent Protein (eYFP) as a Photoswitchable Emitter

The use of eYFP as a photoswitchable emitter vastly expands the number of biological specimens immediately available for super-resolution imaging. In most reported PALM imaging, the photoactivatable fluorescent protein has been selected from various sophisticated constructs such as PA-GFP, Dronpa, Kaede, tdEosFP, Dendra2, rsFastLime, PA-mCherry, and rsCherryRev [17, 49–52]. However, single immobilized and apparently bleached yellow FPs (S65G, S72A, T203Y or S65G, S72A, T203F) were shown to blink and reactivate with violet light more than 10 years ago [27]. The closely related eYFP (S65G, V68L, S72A, T203Y) was recently used for live-cell PALM imaging of the *C. crescentus* structural protein MreB [21], reported online the same day as a separate publication demonstrating blinking of FPs for SMACM [22]. eYFP is widely used for routine fluorescent protein fusions due to the relative absence of physiological perturbations such as agglomeration and mislocalization, and N-terminal eYFP-MreB fusions have been previously shown to be functional in *C. crescentus* and other bacteria making these eYFP-protein fusions physiologically relevant systems [53–55]. Furthermore, single-molecule imaging of eYFP-MreB with 514-nm excitation has previously shown that this fluorescent protein is a bright single-molecule emitter for live-cell imaging [56].

Figure 8 demonstrates eYFP photoreactivation in live cells [21]. Figure 8a shows a single imaging frame where the fluorescence image is superimposed over a negative-contrast white-light transmission image of the *C. crescentus* cell. Two single eYFP-MreB molecules can be identified in panel (a), which was acquired after the initial bleaching step. After further imaging with 514-nm light, all fluorophores had bleached, as observed in panel (b). eYFP reactivation was achieved after this initial bleaching step by administering a 2-s dose of 407-nm laser illumination. This pulse length, as well as the reactivation intensity of 10^3–10^4 W/cm^2, was chosen such that, at most, one eYFP molecule was reactivated in each diffraction-limited region and a different fraction of eYFP molecules was activated in each cycle of this process.

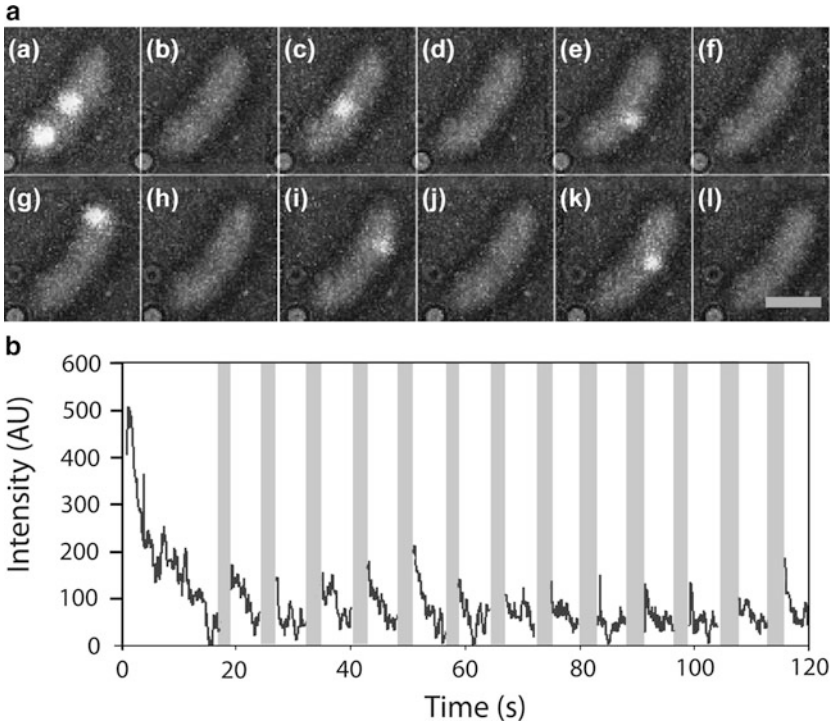

Fig. 8 Reactivation of eYFP-MreB fusions in live *C. crescentus* cells. (**a**) Single 100-ms acquisition frames showing isolated eYFP-MreB molecules (e.g., panels **a**, **c**, and **e**) upon photoactivation and no single-molecule emission (e.g., panels **b**, **d**, and **f**) after photobleaching. The spot in the *bottom left* of each image is an imaging artifact. Scale bar, 1 μm. (**b**) Bulk reactivation of a sample of 22 cells. The *gray lines* indicate 2-s pulses of 407 nm light (Adapted and reproduced with permission from Biteen et al. [21]. Copyright 2008 Nature Publishing Group)

In Fig. 8b, the total emission intensity from 22 live *C. crescentus* cells expressing eYFP-MreB is displayed as a function of time. After an initial bleaching period, flashes of 407-nm activation energy were applied between imaging cycles. These reactivation cycles were used to calculate the photoreactivation quantum yield of the eYFP fluorophore. The measured relationship between activation time and percent reactivation can be plotted and is quasi-linear. In measurements of eYFP-MreB in live *C. crescentus* cells, 370 photons are absorbed by each eYFP molecule per second of the activation pulse. From the slope of the plot, a reactivation quantum yield of 1.6×10^{-6} was found for eYFP [57]. This number is on the same order of magnitude as the activation quantum yield for PA-GFP, and only one order of magnitude smaller than the photoswitching quantum yield of the highly engineered protein, tdEos [24]. Therefore, while carefully engineered photoswitchable FPs may be optimal in certain cases, the common eYFP can also be viewed as a useful photoswitchable fluorophore for super-resolution imaging.

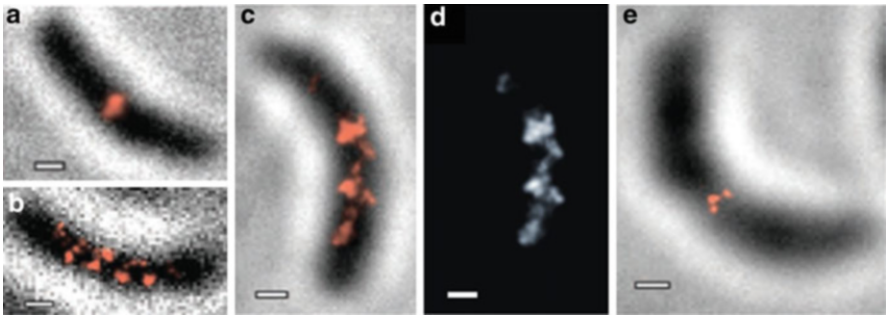

Fig. 9 Super-resolution images of MreB in live *C. crescentus* cells using standard PALM (**a**, **b**) and time-lapse imaging to obtain higher labeling density (**c**–**e**). (**a**) Image of MreB forming a midplane ring in a predivisional cell. (**b**) Banded MreB structure in a stalk cell. (**c**) Quasi-helical MreB structure at 40 nm resolution observed using time-lapse PALM. (**d**) Structure in panel **c** displayed without white-light image in order to highlight the continuity of the structure. (**e**) Time-lapse PALM image of MreB midplane ring in a predivisional cell. Scale bars, 300 nm (Adapted and reproduced with permission from Biteen et al. [21]. Copyright 2008 Nature Publishing Group)

Recently, photoswitching and single-molecule imaging of eYFP were applied to image superstructures of the bacterial actin protein MreB in live *C. crescentus* cells with sub-40-nm resolution [21]. While eYFP is used in the example shown here, the techniques and analysis can be applied to any photoswitchable or photoactivatable fluorophore. Figure 9 shows super-resolution images of the eYFP-MreB protein superstructure in *C. crescentus* [57], where Biteen et al. have identified the presence of two different structures at distinct stages in the cell cycle: a regularly spaced band-like arrangement of MreB molecules that suggests a helix in the stalked cell (Fig. 9b–d), and a ring of MreB molecules at the cell mid-plane in the predivisional cell (Fig. 9a, e). The *C. crescentus* cells are ~2 μm in length and ~0.5 μm in diameter. Since the depth of field in our system is similar to the thickness of the cells, the super-resolution images represent a 2D projection of the MreB structures. It is worth noting that these images show a much smaller field of view than most images of mammalian cells. In addition, diffraction-limited epifluorescence images of eYFP-MreB under these conditions in stalked cells showed no structure whatsoever.

6 Photoinduced Blinking of eYFP

In addition to photoswitching, eYFP has also been observed to have photoinduced blinking behavior. By using high laser irradiance, eYFP can be driven into a reversible long-lived dark state first described by Dickson et al. [27], a blinking phenomenon in small molecules and fluorescent proteins more recently referred to by some authors as GSDIM [22]. However, we will refer to this mechanism in fluorescent proteins as Super-resolution by PoweR-dependent Active Intermittency (SPRAI) [58]. A key advantage to using this mechanism, in contrast to

photoactivation and photoswitching, is that it requires the use of only one reading laser. If most of the molecules within a diffraction-limited region are pushed into the dark state by the excitation laser, the concentration of actual emitters can be maintained at the low level required for SMACM, and it is possible to image eYFP proteins individually as they return from the dark state to the bright state. SPRAI has been used in recent studies in *Caulobacter* to reveal eukaryotic-like spindle fibers that were previously thought to be a feature unique to eukaryotic cells [59] and to quantify the spatial distribution of the nucleoid-associated protein HU during different phases of the cell cycle [60].

To further characterize the power-dependent active intermittency of eYFP, the protein fusion HU2-eYFP inside living *C. crescentus* cells was pumped by a 514-nm Argon-ion laser [58, 60]. By driving the majority of molecules into transient dark states with high-intensity pumping (4–6 kW/cm^2), it was possible to image in each frame a low concentration of single eYFP that were separated by more than the diffraction limit (Fig. 10a). A careful balance of exposure time and irradiance was needed to ensure that emitting molecules were separated by more than the diffraction limit, and the majority of molecules were fluorescent for only one single imaging frame (97%) at this intensity. To verify further the presence of long-lived reversible dark states similar to those reported by Dickson et al. [27], the pumping

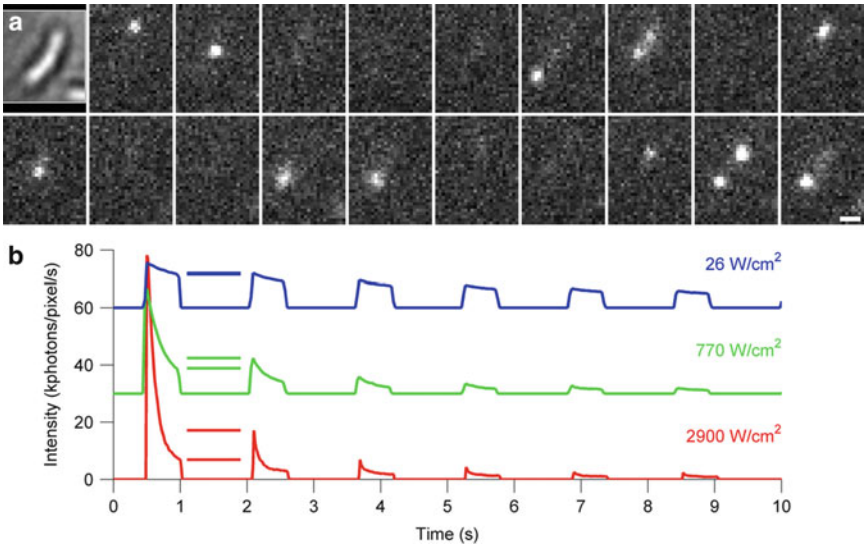

Fig. 10 Evidence of photoinduced blinking (dark state shelving) of eYFP. (**a**) White light of a single *C. crescentus* cell, followed by frames of raw data (10 ms each) showing the blinking of eYFP achieved through the use of a single 514-nm laser. Scale bar, 500 nm. (**b**) Measured intensity of bulk eYFP inside *C. crescentus* with pulsed excitation (0.5 s on time, 1 s off time) at various pump intensities (*blue*-26 W/cm^2, *green*-770 W/cm^2, *red*-2.9 kW/cm^2). The *blue* and *green curves* are shifted upward by 60 and 30 kphotons/pixel/s, respectively, to enhance readability. The emission from molecules that returned from the dark state during the first cycle is denoted by *horizontal lines* (Adapted and reproduced with permission from Lew et al. [58] and Lee et al. [60]. Copyright 2011 National Academy of Sciences and Biophysical Society)

laser was pulsed with a mechanical shutter (on time = 0.5 s, off time = 1 s). The fluorescence emission trajectory for three pumping intensities was measured (see Fig. 10b). During each pulse, some degree of irreversible photobleaching occurred (and blue light might have rescued these seemingly photobleached molecules, but blue light was not used in this case). At high pumping intensities, a portion of the eYFP population was observed to return from an inaccessible dark state, signified by a spike in fluorescence intensity after each off cycle. The fluorescence recovery increased dramatically with higher pumping intensities, as larger relative fractions of the molecules were driven into the dark state. This analysis confirms the existence of a long-lived reversible dark state in eYFP which may be populated by higher intensity pumping. Other explanations for the reactivation, including expression of new eYFP fusions or thermal reactivation of the eYFP, are unlikely to replace such a large fraction of the molecules in 1 s.

This process is particularly useful for SMACM imaging experiments in cells, and a specific application will now be described. The cell biology of nucleoid-associated proteins (NAPs) in bacteria is inadequately understood because the physical size of bacterial cells is approximately the diffraction-limited spot size for visible light. Therefore, quantitative imaging of bacterial protein distributions in standard confocal or wide-field optical microscopy is nearly impossible. Photoinduced blinking of HU2-eYFP allows localization of single HU2-eYFP molecules to 11-nm precision, thereby circumventing the diffraction limit [60]. The distribution of HU2-eYFP in *C. crescentus* was measured at three stages of its cell cycle: flagellated swarmer cell, stationary stalked cell, and predivisional cell. HU2-eYFP was observed to have an approximately uniform distribution throughout swarmer and stalked cells (see Fig. 11a, b). However, in predivisional cells clusters were often observed near the midpoint of each nascent daughter cell (see Fig. 11c). Note that the cluster in the lower part of the cell is far more visible in the super-resolution image as compared to the diffraction-limited image in the inset; this contrast illustrates a key advantage of the method. Quantitative analysis of the clustering behavior can be performed using spatial point statistics [60].

7 Summary

Single-molecule photocontrol combined with superlocalization has demonstrated outstanding usefulness for breaking the diffraction limit in optical fluorescence microscopy. It has enabled quantitative studies of localization patterns in living cells via a variety of small molecules (azido DCDHFs and Cy3–Cy5 covalent heterodimers) and fluorescent proteins (eYFP). Each method of photocontrol, including photoactivation, photoswitching, and photoinduced blinking offers the scientist a complementary pathway for studying the sample of interest, and the choice of the most appropriate technique depends upon the specific application. Combining photocontrol with cutting-edge three-dimensional imaging techniques [38, 61–65] enables examination of biological phenomena to a precision

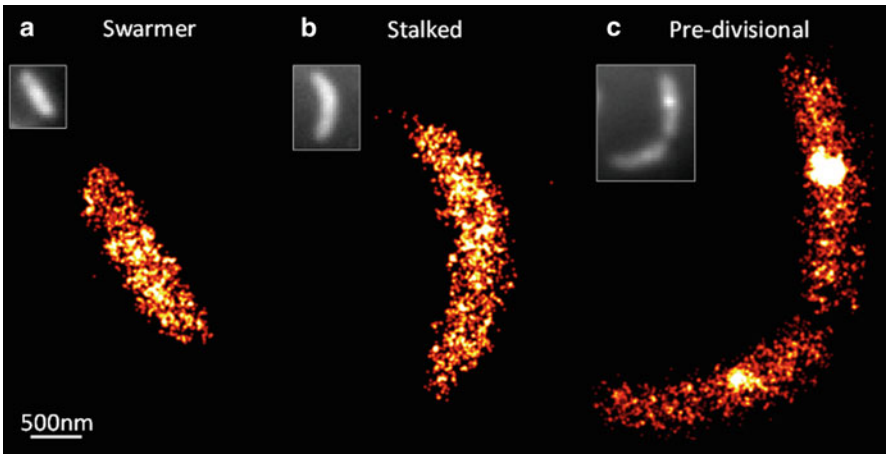

Fig. 11 Representative super-resolution imaging of HU2-eYFP at different stages in the *C. crescentus* cell cycle. (**a**) Image of a swarmer cell with corresponding diffraction-limited epifluorescence image (*inset*). (**b**) Same as panel **a** but for a stalked cell. (**c**) Significant clustering of HU2-eYFP in predivisional cells can be observed in the super-resolution image (Adapted and reproduced with permission from Lee et al. [60]. Copyright 2011 Biophysical Society)

unthinkable even a decade ago using optical microscopy. Single-molecule active control microscopy offers an unrivaled tool for achieving optical nanoscopy of living cells, and it is only a matter of time before it becomes as ubiquitous in biologists' toolboxes as fluorescence microscopy.

Acknowledgments We warmly thank former Moerner laboratory members Julie Biteen, Nick Conley, and Sam Lord for their contributions to portions of the experiments shown here and the laboratory of Prof. Lucy Shapiro and Jerod Ptacin for *C. crescentus* cell lines. The work on DCDHF molecules would not have been possible without Prof. Robert J. Twieg's group at Kent State University who synthesized the molecules. This work was supported in part by the National Institutes of Health Roadmap for Medical Research Grant No. 1P20-HG003638, and by Grant Number R01GM085437 from the National Institute of General Medical Sciences. MDL was supported in part by a National Science Foundation Graduate Research Fellowship and a 3Com Corporation Stanford Graduate Fellowship. MAT was supported in part by a National Science Foundation Graduate Research Fellowship and by a Bert and DeeDee McMurtry Stanford Graduate Fellowship.

References

1. Moerner WE (2006) Single-molecule mountains yield nanoscale images. Nat Methods 3:781–782
2. Moerner WE (2007) New directions in single-molecule imaging and analysis. Proc Natl Acad Sci USA 104:12596–12602
3. Hell SW (2007) Far-field optical nanoscopy. Science 316:1153–1158
4. Ambrose WP, Basché T, Moerner WE (1991) Detection and spectroscopy of single pentacene molecules in a p-terphenyl crystal by means of fluorescence excitation. J Chem Phys 95:7150–7163

5. Gelles J, Schnapp BJ, Sheetz MP (1988) Tracking kinesin-driven movements with nanometre-scale precision. Nature 4:450–453
6. Güttler F, Irngartinger T, Plakhotnik T et al (1994) Fluorescence microscopy of single molecules. Chem Phys Lett 217:393
7. van Oijen AM, Köhler J, Schmidt J et al (1999) Far-field fluorescence microscopy beyond the diffraction limit. J Opt Soc Am A 16:909–915
8. Thompson RE, Larson DR, Webb WW (2002) Precise nanometer localization analysis for individual fluorescent probes. Biophys J 82:2775–2783
9. Ober RJ, Ram S, Ward ES (2004) Localization accuracy in single-molecule microscopy. Biophys J 86:1185–1200
10. Michalet X, Weiss S (2006) Using photon statistics to boost microscopy resolution. Proc Natl Acad Sci USA 103:4797–4798
11. Böhmer M, Enderlein J (2003) Orientation imaging of single molecules by wide-field epifluorescence microscopy. J Opt Soc Am B 20:554–559
12. Lieb MA, Zavislan JM, Novotny L (2004) Single-molecule orientations determined by direct emission pattern imaging. J Opt Soc Am B 21:1210–1215
13. Enderlein J, Toprak E, Selvin PR (2006) Polarization effect on position accuracy of fluorophore localization. Opt Express 14:8111–8120
14. Engelhardt J, Keller J, Hoyer P et al (2011) Molecular orientation affects localization accuracy in superresolution far-field fluorescence microscopy. Nano Lett 11:209–213
15. Nyquist H (1928) Certain topics in telegraph transmission theory. Trans AIEE 47:617–644
16. Shannon CE (1949) Communication in the presence of noise. Proc IRE 37:10–21
17. Betzig E, Patterson GH, Sougrat R et al (2006) Imaging intracellular fluorescent proteins at nanometer resolution. Science 313:1642–1645
18. Hess ST, Girirajan TPK, Mason MD (2006) Ultra-high resolution imaging by fluorescence photoactivation localization microscopy. Biophys J 91:4258–4272
19. Rust MJ, Bates M, Zhuang X (2006) Sub-diffraction-limit imaging by stochastic optical reconstruction microscopy (STORM). Nat Methods 3:793–796
20. Sharonov A, Hochstrasser RM (2006) Wide-field subdiffraction imaging by accumulated binding of diffusing probes. Proc Natl Acad Sci USA 103:18911–18916
21. Biteen JS, Thompson MA, Tselentis NK et al (2008) Super-resolution imaging in live *Caulobacter crescentus* cells using photoswitchable EYFP. Nat Methods 5:947–949
22. Folling J, Bossi M, Bock H et al (2008) Fluorescence nanoscopy by ground-state depletion and single-molecule return. Nat Methods 5:943–945
23. Steinhauer C, Forthmann C, Vogelsang J et al (2008) Superresolution microscopy on the basis of engineered dark states. J Am Chem Soc 130:16840–16841
24. Thompson MA, Biteen JS, Lord SJ et al (2010) Molecules and methods for super-resolution imaging. Meth Enzymol 475:27–59
25. Bates M, Huang B, Dempsey GT et al (2007) Multicolor super-resolution imaging with photo-switchable fluorescent probes. Science 317:1749–1753
26. Shroff H, Galbraith CG, Galbraith JA et al (2007) Dual-color superresolution imaging of genetically expressed probes within individual adhesion complexes. Proc Natl Acad Sci USA 104:20308–20313
27. Dickson RM, Cubitt AB, Tsien RY et al (1997) On/Off blinking and switching behavior of single green fluorescent protein molecules. Nature 388:355–358
28. Shroff H, Galbraith CG, Galbraith JA et al (2008) Live-cell photoactivated localization microscopy of nanoscale adhesion dynamics. Nat Methods 5:417–423
29. Lord SJ, Lee H-D, Samuel R et al (2010) Azido push–pull fluorogens photoactivate to produce bright fluorescent labels. J Phys Chem B 114:14157–14167
30. Lakowicz JR (2006) Principles of fluorescence spectroscopy. Springer Science, New York
31. Adams SR, Kao JPY, Tsien RY (1989) Biologically useful chelators that take up Ca 2+ upon illumination. J Am Chem Soc 111:7957–7968

32. Doub L, Vandenbelt JM (1947) The ultraviolet absorption spectra of simple unsaturated compounds. I. Mono- and p-disubstituted benzene derivatives. J Am Chem Soc 69:2714–2723
33. Stevenson PE (1965) Effects of chemical substitution on the electronic spectra of aromatic compounds: Part I. The effects of strongly perturbing substituents on benzene. J Mol Spectrosc 15:220–256
34. Hansch C, Leo A, Taft RW (1991) A survey of Hammett substituent constants and resonance and field parameters. Chem Rev 91:165–195
35. Schriven EFV (1984) Azides and nitrenes: reactivity and utility. Anonymous Academic Press, Orlando, FL
36. Soundararajan N, Platz MS (1990) Descriptive photochemistry of polyfluorinated azide derivatives of methyl benzoate. J Org Chem 55:2034–2044
37. Lord SJ, Conley NR, Lee H-D et al (2008) A photoactivatable push−pull fluorophore for single-molecule imaging in live cells. J Am Chem Soc 130:9204–9205
38. Pavani SRP, Thompson MA, Biteen JS et al (2009) Three-dimensional, single-molecule fluorescence imaging beyond the diffraction limit by using a double-helix point spread function. Proc Natl Acad Sci USA 106:2995–2999
39. Lee H-D, Lord SJ, Iwanaga S et al (2010) Superresolution imaging of targeted proteins in fixed and living cells using photoactivatable organic fluorophores. J Am Chem Soc 132:15099–15101
40. Lord SJ, Conley NR, Lee H-D et al (2009) DCDHF fluorophores for single-molecule imaging in cells. ChemPhysChem 10:55–65
41. Willets KA, Nishimura SY, Schuck PJ et al (2005) Nonlinear optical chromophores as nanoscale emitters for single-molecule spectroscopy. Acc Chem Res 38:549–556
42. Dempsey GT, Bates M, Kowtoniuk WE et al (2009) Photoswitching mechanism of cyanine dyes. J Am Chem Soc 131:18192–18193
43. Heilemann M, Margeat E, Kasper R et al (2005) Carbocyanine dyes as efficient reversible single-molecule optical switch. J Am Chem Soc 127:3801–3806
44. Heilemann M, van de Linde S, Schüttpelz M et al (2008) Subdiffraction-resolution fluorescence imaging with conventional fluorescent probes. Angew Chem Int Ed 47:6172–6176
45. Conley NR, Biteen JS, Moerner WE (2008) Cy3–Cy5 covalent heterodimers for single-molecule photoswitching. J Phys Chem B 112:11878–11880
46. Los GV, Wood K (2007) The HaloTag: a novel technology for cell imaging and protein analysis. Methods Mol Biol 356:195–208
47. Los GV, Encell LP, McDougall MG et al (2008) HaloTag: a novel protein labeling technology for cell imaging and protein analysis. ACS Chem Biol 3:373–382
48. Huang B, Jones SA, Brandenburg B et al (2008) Whole-cell 3D STORM reveals interactions between cellular structures with nanometer-scale resolution. Nat Methods 5:1047–1052
49. Geisler C, Schönle A, von Middendorff C et al (2007) Resolution of λ/10 in fluorescence microscopy using fast single molecule photo-switching. Appl Phys A 88:223–226
50. Niu L, Yu P (2008) Investigating intracellular dynamics of FtsZ cytoskeleton with photoactivation single-molecule tracking. Biophys J 95:2009–2016
51. Stiel AC, Andresen M, Bock H et al (2008) Generation of monomeric reversibly switchable red fluorescent proteins for far-field nanoscopy. Biophys J 95(6):2989–2997
52. Subach FV, Patterson GH, Manley S et al (2009) Photoactivatable mCherry for high-resolution two-color fluorescence microscopy. Nat Methods 6:153–159
53. Carballido-López R, Errington J (2003) The bacterial cytoskeleton: in vivo dynamics of the actin-like protein Mbl of *Bacillus subtilis*. Dev Cell 4:19–28
54. Figge RM, Divakaruni AV, Gober JW (2004) MreB, the cell shape-determining bacterial actin homologue, co-ordinates cell wall morphogenesis in *Caulobacter crescentus*. Mol Microbiol 51:1321–1332
55. Gitai Z, Dye N, Shapiro L (2004) An actin-like gene can determine cell polarity in bacteria. Proc Natl Acad Sci USA 101:8643–8648

56. Kim SY, Gitai Z, Kinkhabwala A et al (2006) Single molecules of the bacterial actin MreB undergo directed treadmilling motion in *Caulobacter crescentus*. Proc Natl Acad Sci USA 103:10929–10934
57. Biteen JS, Thompson MA, Tselentis NK et al (2009) Superresolution imaging in live *Caulobacter crescentus* cells using photoswitchable enhanced yellow fluorescent protein. Proc SPIE 7185:71850I
58. Lew MD, Lee SF, Ptacin JL et al (2011) Three-dimensional superresolution colocalization of intracellular protein superstructures and the cell surface in live Caulobacter crescentus. Proc Natl Acad Sci USA 108:E1102–E1110
59. Ptacin JL, Lee SF, Garner EC et al (2010) A spindle-like apparatus guides bacterial chromosome segregation. Nat Cell Biol 12:791–798
60. Lee SF, Thompson MA, Schwartz MA et al (2011) Super-resolution imaging of the nucleoid-associated protein HU in *Caulobacter crescentus*. Biophys J 100:L31–L33
61. Donnert G, Keller J, Medda R et al (2006) Macromolecular-scale resolution in biological fluorescence microscopy. Proc Natl Acad Sci USA 103:11440–11445
62. Huang B, Wang W, Bates M et al (2008) Three-dimensional super-resolution imaging by stochastic optical reconstruction microscopy. Science 319:810–813
63. Juette MF, Gould TJ, Lessard MD et al (2008) Three-dimensional sub-100 nm resolution fluorescence microscopy of thick samples. Nat Methods 5:527–529
64. Schermelleh L, Carlton PM, Haase S et al (2008) Subdiffraction multicolor imaging of the nuclear periphery with 3D structured illumination microscopy. Science 320:1332–1336
65. Shtengel G, Galbraith JA, Galbraith CG et al (2009) Interferometric fluorescent super-resolution microscopy resolves 3D cellular ultrastructure. Proc Natl Acad Sci USA 106:3125–3130

Probes for Nanoscopy: Fluorescent Proteins

Susan Gayda, Per Niklas Hedde, Karin Nienhaus, and G. Ulrich Nienhaus

Abstract Super-resolution fluorescence microscopy (optical nanoscopy) enables molecular processes to be observed in living cells and organisms on spatial scales between 10 and 100 nm. It requires labeling of the objects under study with fluorescent markers, the emission of which can be controlled by light irradiation. Among the markers presently available, i.e., synthetic dyes, nanocrystals, and fluorescent proteins, fluorescent proteins of the GFP family have the key advantage of being genetically encodable so that they can be produced by the cells; no additional labeling steps are necessary. In recent years, these proteins have become extremely popular in the life sciences and have allowed unprecedented insights into the living cell. Here, we present an overview of this exciting protein family, with a special focus on properties that are important for using them in super-resolution fluorescence microscopy.

Keywords Fluorescent protein · Live-cell imaging · Nanoscopy · PALM · Photoactivation · SIM · STED

Contents

S. Gayda, P.N. Hedde, and K. Nienhaus
Institute of Applied Physics and Center for Functional Nanostructures, Karlsruhe Institute of Technology (KIT), Wolfgang-Gaede-Str. 1, 76131 Karlsruhe, Germany

G.U. Nienhaus (✉)
Institute of Applied Physics and Center for Functional Nanostructures, Karlsruhe Institute of Technology (KIT), Wolfgang-Gaede-Str. 1, 76131 Karlsruhe, Germany

Department of Physics, University of Illinois at Urbana-Champaign, 1110 West Green Street, Urbana, IL 61801, USA
e-mail: uli@illinois.edu

P. Tinnefeld et al. (eds.), *Far-Field Optical Nanoscopy*,
Springer Ser Fluoresc (2015) 14: 111–158, DOI 10.1007/4243_2011_34,

1 Introduction to Fluorescence Nanoscopy

Currently, our knowledge of the molecular basis of life is growing at an enormous pace. Optical microscopy is the method of choice to study biomolecular interactions and the resulting functional consequences within living cells, tissues, or organisms as they happen in space and time. It is minimally invasive; so processes can be observed over extended periods of time without introducing artifacts due to light irradiation. A key advantage of fluorescence microscopy is that biomolecules or larger structures of interest (e.g., membranes, organelles, and particular cells in an organism) can be labeled specifically; so the images reveal information on processes specific to the labeled molecules, with minimal background fluorescence from other molecules. A severe drawback of optical microscopy is its moderate resolution: due to fundamental physical laws governing wave optics, details closer than about half the wavelength of light (~200 nm) cannot be resolved [1], which precludes studies on molecular scales, unless Förster resonance energy transfer (FRET) is used, which enables probing of molecular proximities in the 1–10 nm range [2].

In recent years, however, a variety of super-resolution fluorescence microscopy techniques have cropped up, which allow processes to be observed on spatial scales

between 10 and 100 nm. Linear techniques such as confocal laser scanning microscopy (CLSM) and structured illumination microscopy (SIM) are all within the limits of wave optics and allow the lateral resolution to be improved by a factor of 2. To improve the axial resolution of the confocal microscope and, at the same time, to collect more of the incoherent photons emanating from the sample in all directions (i.e., into the entire solid angle, 4π), an interferometric arrangement of two opposing objectives has been implemented in 4Pi confocal microscopy [3]. I^5M is a related interferometric implementation in a widefield design [4].

Nonlinear techniques are capable of circumventing the resolution limitation and enable researchers to actually resolve details way beyond the diffraction limit. They all rely on fluorophores that can be switched between an on and an off state [5–7]. Two principal strategies can be distinguished: In the targeted mode, applied in stimulated emission depletion (STED), reversible saturable optical fluorescence transitions (RESOLFT) and saturated structured illumination microscopy (SSIM), a spatial light intensity distribution with points or lines of zero intensity in space switches the fluorescent markers such that a subfraction, located in a region of sub-diffraction extension, is either in the on or off state. In the stochastic switching mode, used in localization microscopy approaches such as photoactivation localization microscopy (PALM) and stochastic reconstruction microscopy (STORM), individual molecules are photoactivated, i.e., switched to the fluorescent state, randomly in space, while the surrounding molecules remain in the dark state, so that the loci of the individual emitters can be determined with high precision. In the following, we briefly introduce these super-resolution techniques and discuss the demands they place on the fluorophores.

1.1 Targeted Switching: STED, RESOLFT, and SSIM

STED microscopy [8] uses the nonlinear (switching) response of fluorophores to light irradiation. In a STED microscope, the exciting focused spot of a confocal microscope is spatially overlayed with a depletion beam that has an annular shape in the focal plane, with zero intensity in the center. Consequently, fluorophores that do not reside close to the center are efficiently deexcited by stimulated emission of photons in the direction of the depletion beam, so they do not reach the detector. Only fluorophores close to the center escape depletion and can thus spontaneously emit fluorescence photons. Therefore, the effective size of the excitation point spread function (PSF), i.e., the image of a point-like object, is smaller than the usual diffraction-limited PSF (Fig. 1). The higher the intensity of the depletion beam, the more is the fluorescence confined to the central region [6]. An image is acquired by raster scanning the excitation and depletion beams with sufficiently small step sizes, i.e., no larger than half the desired spatial resolution, across the sample.

As stimulated emission is an intrinsic physical property of all fluorophores, any fluorescent probe can, in principle, be used for STED microscopy. In practice, a

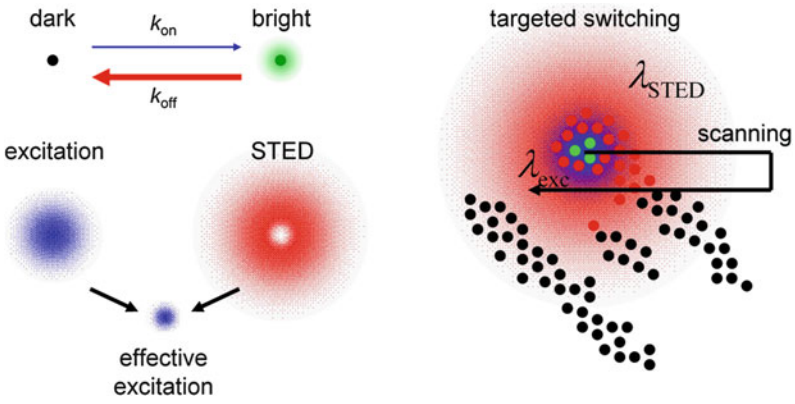

Fig. 1 Principle of STED (RESOLFT) microscopy. The fluorophores can be switched reversibly between a bright and a dark state by light irradiation. For imaging, the excitation beam is overlayed with a donut-shaped depletion beam with zero intensity in the center and scanned across the sample. Molecules close to the center emit fluorescence (*green dots*), whereas molecules further away from the center (*red dots*) are efficiently de-excited before they emit fluorescence

very good photostability is required because the fluorophores experience many excitation-depletion cycles during the scanning process. Due to the nanosecond time scale of the fluorescence decay, sufficient photon intensities, with typical laser powers in the range MW/cm^2 to GW/cm^2, are required for the depletion beam. Long fluorescence lifetimes help to decrease the power of the STED beam, and a low cross section for multiphoton and excited state absorption is advantageous as well [9]. For efficient STED, the depletion beam wavelength should match the emission spectrum, but should not overlap with the dye excitation spectrum to avoid excitation by the depletion beam. Consequently, a large Stokes shift will be advantageous.

Lately, other principles have also been used to de-excite the fluorescent markers in the wings of the excitation PSF, including pumping of the triplet state [10, 11] or exploiting the photoswitching properties of fluorophores between bright and dark states [5, 12, 13]. This generalization has been termed RESOLFT microscopy [12, 14]. Typically, very low laser powers suffice for the depletion beam because spontaneous transitions of the marker between the two states are orders of magnitude slower than the fluorescence lifetime. In RESOLFT microscopy, an ensemble of fluorophores rather than an individual one contributes to the signal associated with an individual pixel. Thus, the brightness of the individual molecule is less important than its resistance to switching fatigue because the markers have to undergo many transitions between their fluorescent and nonfluorescent states to contribute appreciably to the image.

SIM uses patterned illumination of sinusoidal shape to excite the sample and generate fluorescence with a corresponding emission pattern. Super-resolution is achieved by using high excitation intensity so that the fluorescence emission becomes saturated and, thus, is no longer proportional to the excitation power. This saturated SIM (SSIM) approach creates sharp dark regions (instead of bright

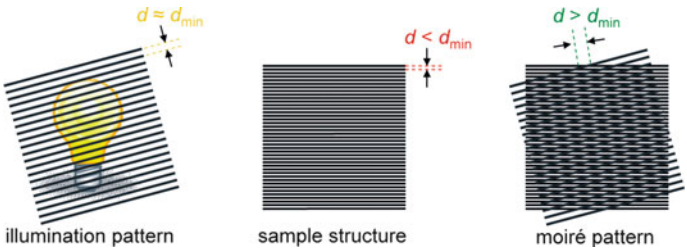

Fig. 2 Principle of SIM. The specimen features structures that are too close for being resolvable by conventional optical microscopy. A periodic pattern with a repeat distance at the diffraction limit is used for sample illumination. In the overlay of the two patterns, the unresolvable sample structures become visible as a Moiré pattern with a spatial frequency that can be resolved

regions as in STED) near the illumination pattern zeros through saturated excitation (instead of depletion) [15]. The spatial resolution scales with the level of saturation. Any fluorescent label that is compatible with conventional fluorescence imaging will work with SIM (Fig. 2). SSIM, however, relies on extremely high excitation intensities when using non-photoactivatable markers. Thus, the dyes are maintained in the chemically reactive excited state most of the time. Accordingly, this technique requires very photostable fluorophores to avoid fast photobleaching. As for RESOLFT microscopy, the intensities required can dramatically be reduced when using photoswitchers.

1.2 Stochastic Switching: Localization-Based Super-Resolution Microscopy

In conventional fluorescence microscopy, a certain density of fluorescence markers is required to faithfully image fine structures. Many fluorophores emit simultaneously; so their PSFs overlap in the resulting image and cannot be localized individually. However, if the emission properties of the fluorophores can be controlled externally by light, their individual loci can be determined with a precision well above the resolution limit. Initially, all markers are switched to their inactive (off) state. Subsequently, they are sparsely activated by a properly chosen intensity of photoactivating light, so that only a few appear in each image frame in a widefield microscope. The center of gravity of each marker's PSF can be determined with a precision that significantly exceeds the width of the PSF, which governs the resolution in standard imaging [16]. By repeated image acquisition (10–100 frames per second), a large number of frames (10^2–10^4) are collected and analyzed individually. The positions of the fluorophores within each individual image are analyzed. The final, reconstructed image is a density map depicting the spatial distribution of emitters with a resolution in the range of a few tens of nanometers (Fig. 3).

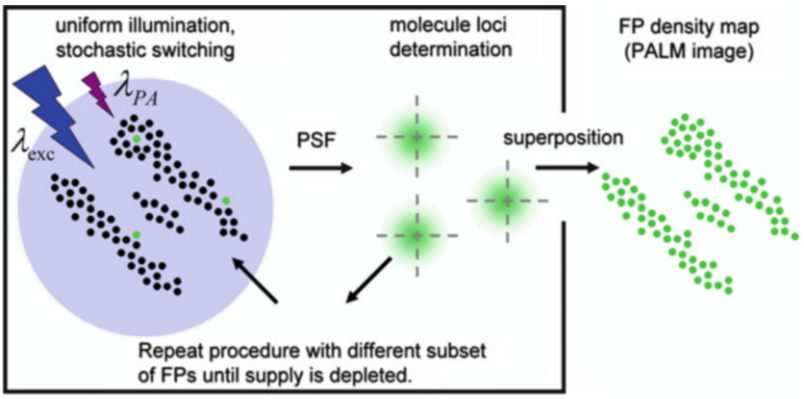

Fig. 3 Schematic depiction of localization-based super-resolution microscopy. See text for details

A variety of localization-based concepts have been developed independently and introduced with different acronyms, i.e., PALM [17], fluorescence photoactivation localization microscopy (FPALM) [18], and STORM [19]. Further developments and modifications were implemented in techniques such as PALM with independently running acquisition (PALMIRA) [20], *direct* stochastic optical reconstruction microscopy (dSTORM) [21], blink microscopy (BM) [22], PALM that relies on two-color simultaneous stroboscopic illumination (S-PALM) [23], ground state depletion microscopy followed by individual molecule return (GSDIM) [24], and points accumulation for imaging in nanoscale topography (PAINT) [25]. Super-resolution optical fluctuation imaging (SOFI) is based on temporal fluctuations of the intensity from individual emitters [26].

Localization-based microscopy is inherently a single molecule technique. The 2D localization precision depends crucially on the number of photons detected from each fluorophore [27]. Consequently, the brightness of the individual molecules is a key parameter, and, therefore, high quantum yields and high extinction coefficients are desirable. To detect single molecules despite the dense labeling of the structure under study, the fluorescent markers must possess two states, a bright state that emits fluorescence light at a certain wavelength and a dark state that either does not emit at all or not in the chosen detection window. Moreover, the fluorophores have to be photoactivatable, i.e., the fractional populations of the two states must be controllable by light. In this context, the rate coefficients for interconversion between the dark and bright states or, alternatively, the lifetimes of the fluorescent markers in one or the other state are an important issue. The lifetimes are limited by spontaneous (thermally driven) transitions, and the light-driven response to a certain intensity of photoactivating light is governed by the quantum yields associated with the transition. To avoid overlapping PSFs of single emitters, the molecules must be maintained in their dark state considerably longer than in their

bright state [28]. Therefore, spontaneous activation or light-induced activation by the imaging laser should be low. In practice, the dark state is not completely dark but has merely a reduced emission and contributes to the background fluorescence. Therefore, another important parameter is the dynamic range, i.e., the intensity ratio between the bright and dark states. The emission probability of the fluorophore in its nonfluorescent state must be sufficiently small to achieve a reasonable contrast especially at high label densities.

In contrast to STED, markers for localization microscopy are not subjected to multiple switching cycles. They have to be activated only once, subsequently emit a large number of photons for precise localization, and, to achieve a high time resolution in live-cell imaging, photobleach quickly so that the next subset of fluorophores can be activated. Reversibly photoswitchable fluorophores can be switched off after imaging and, therefore, do not require photobleaching. The rates of photobleaching (irreversible photoactivation) or deactivation (reversible photoactivation) should be balanced with the activation rate to ensure that only a small number of fluorophores emits at each point in time.

1.3 Fluorescent Probes

Fluorescence-based microscopy relies on the targeted labeling of the molecules or larger objects under study with a suitable fluorescence marker. For super-resolution microscopy, the label must allow for photoactivation (or deactivation). There are a variety of fluorophores available, including organic dyes [29], nanocrystals with size-dependent optical and physicochemical properties [30–35], and genetically encoded fluorescent proteins (FPs) [36–39]. Organic dyes are comparatively small aromatic molecules (1–2 nm) with good brightness and resistance to photobleaching. Nanocrystals also show great promise as fluorescent markers due to their excellent brightness and photostability. FPs are a family of proteins that host a chromophore within their peptide moiety.

The first FP labels used in cell biology were phycobiliproteins, i.e., photosynthetic antenna pigments from cyanobacteria [40]. Infrared FPs using the biliverdin chromophore have recently been engineered from bacterial phytochromes [41]. Most popular, however, are presently the green fluorescent protein (GFP) from the hydromedusa *Aequorea victoria* and its closely related cousins from the GFP family. They are small proteins (~3 nm) that spontaneously form a fluorescent chromophore in their interior [42]. Although the photophysical and photochemical properties of these fluorophores do not match those of synthetic dyes or nanocrystals, they have the key advantage of being genetically encodable and, therefore, can be produced by the cell itself [43]. In recent years, FPs have

revolutionized the life sciences by enabling a vast array of novel approaches to study biomolecular interactions, especially in living cells and organisms.

In the following, we summarize the structural and optical properties of proteins of the GFP family and introduce some representative members, with a particular view toward their applicability in super-resolution fluorescence microscopy.

2 Fluorescent Proteins

In 1962, Osamu Shimomura isolated the GFP of the jellyfish *A. victoria*, avGFP, from tissue extracts in his pursuit of understanding the bioluminescence of this organism [44]. He purified the protein, characterized its optical properties, and, in 1979, identified the chemical nature of the fluorophore [45]. For the ensuing 30 years, only a handful of scientists studying the luminescence of marine creatures were interested in the protein. Cloning of the avGFP gene by Prasher in 1992 [46] laid the basis for the second stage of GFP research, which started with the recombinant expression of avGFP in *Escherichia coli* and *Caenorhabditis elegans* by Martin Chalfie and collaborators [47]. This seminal work clearly proved that no other (bio)molecular component from *A. victoria* was necessary for functional expression of avGFP. Because the fluorophore forms spontaneously, avGFP can be expressed and used as a genetically encoded fluorescence marker in many different cells and organisms. It quickly became a widely used tool, and its importance was highlighted by the 2008 Nobel Prize in Chemistry, awarded to Shimomura, Chalfie, and Tsien "for the discovery and development of the green fluorescent protein, GFP" [42, 48].

In the late 1990s, proteins of the GFP family were discovered in non-bioluminescent anthozoa by Wiedenmann [49] and Lukyanov et al. [50] (Fig. 4). Recently, FPs were also found in evolutionarily distant species, including crustaceans [51], comb jellies [52], and even chordates [53]. Importantly, the long-sought orange and red FPs were identified, which are highly desirable for live-cell and tissue imaging applications because of the reduced cellular autofluorescence and scattering in the red spectral range. They also extended the color palette for multicolor labeling and FRET experiments. In recent years, so-called photoactivatable or optical highlighter FPs have emerged as powerful new tools for cellular imaging [9, 54–56]. Upon irradiation with light of specific wavelengths, these FPs can either be switched reversibly between a fluorescent and a nonfluorescent state, or their fluorescence emission intensity or color can be changed irreversibly. In recent years, photoactivatable FPs have found widespread use as "pulse chase" labels in live-cell imaging, and they have also become indispensable tools in super-resolution microscopy.

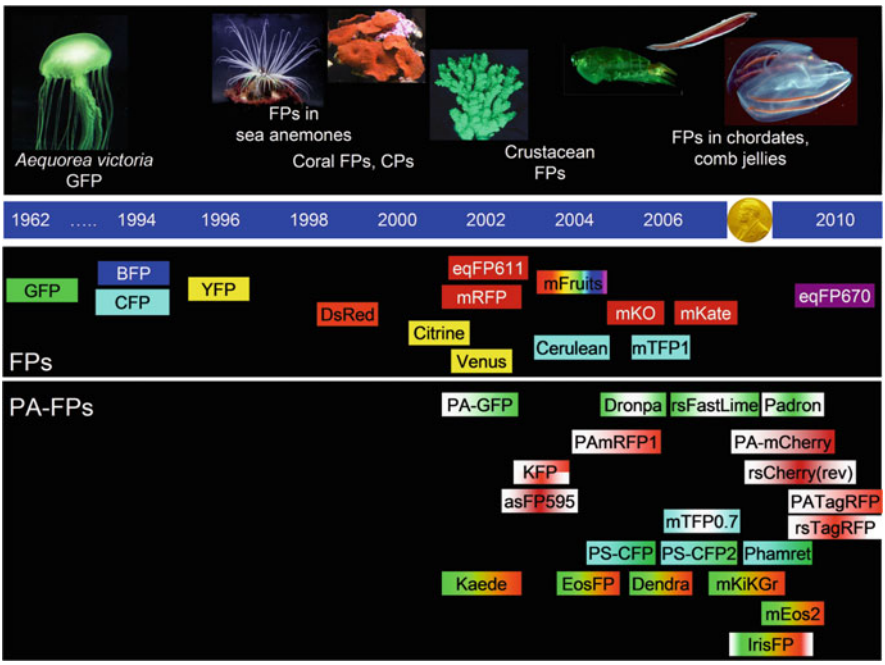

Fig. 4 The expansion of the FP tool box in time. Colors encode the emission wavelengths. Photoconvertible FPs are represented by two colors, photoswitchable FPs by three colors

3 The Molecular Structure of GFP-Like Proteins

X-ray structures of avGFP were first solved by Remington's and Phillips's groups in 1996 [57, 58]. Its polypeptide chain consists of 238 amino acid residues and folds into a rigid, 11-stranded β-can, with a central helix running along its axis (Fig. 5). The β-can is capped at either end by short helical sections and loops. The fluorescent chromophore resides close to the geometric center of the protein, anchored by the surrounding residues and structural water molecules, and held tightly in a planar conformation, which is essential for a high fluorescence quantum yield. Over the years, X-ray structures of FPs from many different species have become available. They all share the β-can, suggesting that this particular fold plays a crucial role both in the formation/maturation of the chromophore and in regulating its photophysical properties.

GFP-like proteins have a more or less pronounced tendency to oligomerize. Even avGFP, which is often viewed as monomeric, forms dimers at higher concentrations [59]. Some FPs form strongly associated dimers, e.g., GFP from the sea pansy *Renilla* [60] or phiYFP from the jellyfish *Phialidium* [51]. Natural anthozoan FPs, such as the red FP (RFP) DsRed from *Discosoma* sp., are often tightly associated tetramers (or sometimes dimers) that often can only be dissociated by harsh procedures, causing irreversible denaturation of the polypeptide chains [61–64].

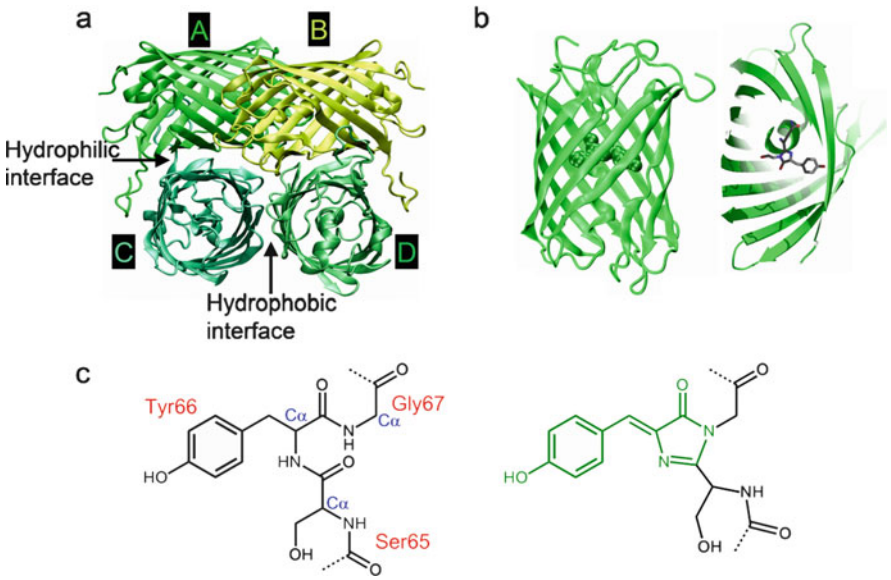

Fig. 5 Overall structure of a GFP-like protein. (**a**) Tetrameric arrangement. The protomers are denoted as *A*, *B*, *C*, *D*. (**b**) Each monomer folds into a β-can. The helix running along its axis is interrupted by the chromophore. (**c**) Chromophore-forming tripeptide and mature chromophore

The four protomers A–D are arranged as dimers of dimers, and two different interfaces between dimers, denoted by A/B (C/D) and A/C (B/D), can be distinguished (Fig. 5a) [65, 66]. The A/C interface, which is more extended than the A/B interface, is hydrophilic and stabilized by salt bridges and hydrogen bonds between polar residues and structural water molecules [64, 67]. It is further reinforced by the C-terminal end of one chain embracing the other. In the A/B interface, a cluster of hydrophobic amino acids is surrounded by polar amino acids.

4 The Chromophore Structure and Its Variations

The chromophores of all GFP-like proteins are synthesized autocatalytically from a tripeptide (in avGFP: Ser65-Tyr66-Gly67, this amino acid numbering is used throughout this chapter), requiring nothing else but molecular oxygen (Fig. 5c). In general, the first amino acid may vary, but the second and third amino acids, Tyr and Gly, are strictly conserved in nature. While Gly67 is absolutely crucial for chromophore self-synthesis, Tyr66 can be replaced, e.g., by His, Phe, or Trp [59]. The avGFP chromophore, 4-(*p*-hydroxybenzylidene)-5-imidazolinone (*p*-HBI), results from a sequential cyclization–oxidation–dehydration mechanism, with characteristic times ranging from minutes to hours. In the planar *p*-HBI chromophore, the conjugated π-electron system extends from the *p*-hydroxyphenyl ring of Tyr66

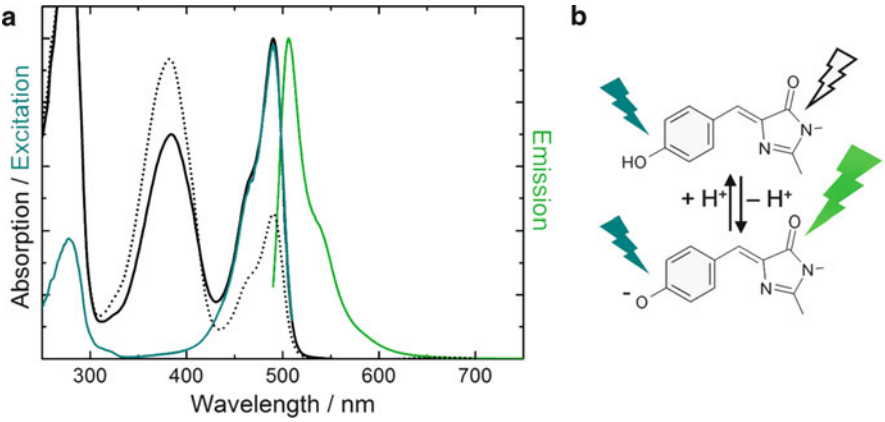

Fig. 6 (**a**) Absorption (pH 7: *solid black line*, pH 5: *dotted black line*), excitation (*dark cyan*), and emission (*green*) spectra of the GFP-like protein Dendra2. (**b**) The neutral chromophore is essentially nonfluorescent

to the imidazolinone ring (Fig. 5c). With respect to the double bond of the methene bridge (Cα–Cβ of Tyr66), both rings are arranged in a *cis* conformation.

The *p*-HBI chromophore may exist either as an anionic phenolate or a neutral hydroxyphenyl species, depending on pH and/or the local environment in its binding pocket (Fig. 6). In avGFP, the neutral form predominates; its absorption peaks at 395 nm under physiological conditions. The absorption band of the anionic chromophore peaks at 475 nm. Upon excitation in this band, the fluorescence emission is maximal at 508 nm in the green. Interestingly, excitation of the neutral chromophore also results in green emission by an anionic chromophore because, in the excited state, the phenolic proton is released and transferred to Glu222 (excited state proton transfer, ESPT), so that the anionic species forms prior to photon emission [68–70]. The equilibrium ratio of the neutral and anionic chromophores can be changed markedly by amino acid exchanges in the chromophore environment. Shifting the equilibrium toward the anionic form leads to bright, enhanced GFP (EGFP) variants [59]. Stabilization of the neutral form, by contrast, is a strategy to generate blue-fluorescent variants (in the absence of ESPT) [71].

In recent years, a number of naturally occurring chromophore modifications have been identified. In orange and red FPs such as DsRed [72] and eqFP611 [73], the single bond between the amide nitrogen and the Cα of the first chromophore-forming amino acid is oxidized to an acylimine group in-plane with the *p*-HBI chromophore (Fig. 7). Consequently, the conjugated π-electron system of the resulting 2-imino-5-(4-hydroxybenzylidene)-imidazolinone chromophore is extended, and the emission shifts bathochromically to ~600 nm. The delocalized π-electron system may extend even further to include the carbonyl group of the preceding amino acid in FPs emitting further in the red, such as mPlum (Fig. 7) [74]. In mOrange, an oxazole heterocycle is created from the side chain of Thr65, the first amino acid of the chromophore triad in this protein [75]. Likewise, the

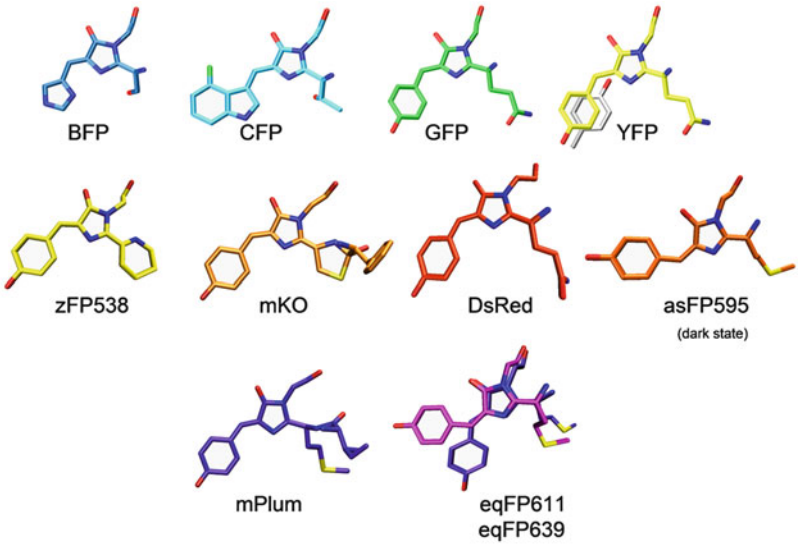

Fig. 7 Chromophore variations in GFP-like proteins

yellow zFP538 from *Zoanthus* sp. features a third heterocycle, formed by ring closure of a Lys side chain [76]. The *cis*-coplanar chromophore in mKO contains a phenolate ring, an imidazolinone, and a third 2-hydroxy-3-thiazoline ring formed by the side chain of the first amino acid in the tripeptide, Cys65 (Fig. 7) [77]. In AsRed, the mutant Ala143Ser of asFP595 from *Anemonia sulcata* [78], chromophore maturation is accompanied by a break in the polypeptide chain [79–81], and a carbonyl group, generated by hydrolysis of the intermediately formed acylimine group, extends the conjugated π-electron system of the *p*-HBI chromophore.

Color tuning may also be achieved by changing the tripeptide composition using site-directed mutagenesis. Substitution of Trp for Tyr at position 66 in the chromophore triad produces a chromophore with excitation and emission wavelengths intermediate between those of the neutral phenol (~400 nm) and anionic phenolate chromophores (~480 nm) [82]. However, accommodating the bulky indole group required a number of additional mutations to regain a reasonable brightness of these cyan FPs (CFPs) [83]. Substitution of Tyr by His shifts the emission maximum to even shorter wavelengths, generating blue-fluorescent proteins (BFPs) [82]. Verkhusha et al. generated a BFP with a neutral Tyr66, termed mTagBFP [84]. Its chromophore is a 4-(4-hydroxybenzyl)-1H-imidazole-5-ol [85], with the Cα–Cβ bond of Tyr66 fully reduced and the hydroxyphenyl ring rotated out of the chromophore plane. Introduction of the nonnatural amino acids *O*-methyltyrosine and *p*-amino-phenylalanine at position 66 resulted in blue-shifted, though weaker fluorescence than in avGFP [86]. Incorporation of the nonnatural residues 3-amino-L-tyrosine and 3-fluoro-L-tyrosine into the chromophore of the DsRed monomer caused, respectively, a 12 nm red shift and blue shift in fluorescence emission [87]. An amino-substituted variant of Trp66 turned CFP into a "gold" GFP variant [88].

In addition to the chemical alterations of the green chromophore described above, strictly photoinduced modifications may also occur, as is discussed in detail in Sect. 7.

5 Key Characteristics of Fluorescent Proteins

5.1 Oligomeric Structure and Monomerization

For a wide range of applications, the oligomeric nature of an FP is entirely irrelevant, including tissue imaging, monitoring of promoter and gene activity, and highlighting of cells and cellular organelles. However, oligomerization can be detrimental in studies involving FP fusions with other proteins because it may interfere with the function of the fusion partner [39]. Once expressed, formation of dimers or higher-order oligomers induced by the FP part of the fusion construct may produce atypical localization, or alter the normal function of the fusion partner. Moreover, if the protein of interest is also an oligomer, the fusion construct may form a network of interacting proteins, thus causing protein aggregation.

The basic strategy for overcoming oligomerization is to modify the FP amino acid sequence to include residues that disrupt the binding interfaces between the protomers, a procedure that may vary greatly in complexity depending on the nature and origin of the FP. For avGFP-based variants, dimerization can be either significantly reduced or even completely eliminated by replacing hydrophobic amino acid side chains in the dimer interface with positively charged residues at several key sequence positions [38]. For avGFP, a single mutation (Ala206Lys) was sufficient for monomerization [89]. For eqFP611, an RFP from the sea anemone *Entacmaea quadricolor*, functional dimers were obtained by single mutations in the A/B interface [90], generating the functional monomer, mRuby, required multiple rounds of random and site-directed mutagenesis [91]. To remove the interactions among the four DsRed protomers, a total of 33 amino acid replacements were necessary [92].

A different technique for generating “pseudo” monomers from dimeric FPs involves linking two copies of the FP cDNA with a short intervening DNA sequence encoding small neutral or hydrophilic amino acids (Gly, Ala, and Ser) to form so-called tandem dimers [92, 93]. Upon cellular expression, tandem FPs form intramolecular dimers that generally function as a monomer of twice the size, thus avoiding interaction with other FP molecules in solution. Tandem dimer constructs have been developed from HcRed [93], DsRed [92], and EosFP [66]. A popular tandem is tdTomato, featuring very high brightness and photostability [94]. Recently, tandem versions were also reported for Keima [95], red TurboRFP and far-red Katushka2 [96], RFP611 [91], and RFP639 [91].

Other procedures pursued to reduce FP oligomerization and aggregation include removing several basic residues from the N-terminus or simultaneous co-expression

of FP-tagged proteins with an excess of a nonfluorescent mutant of the marker protein to generate heterodimers or heterotetramers that contain only a single target polypeptide and can thus be considered pseudo-monomeric [97].

5.2 Maturation and Thermotolerance

GFP-like proteins become fluorescent only after the polypeptide chain is properly folded and the chromophore has matured, i.e., processed into its functional form. Chromophore maturation is typically the rate-limiting step for the onset of fluorescence. It may take from minutes to hours, depending on the individual FP and on environmental parameters such as oxygen concentration and temperature [73, 98, 99]. In so-called Timer FPs, the process takes even days [100–102]. Most FPs have a maturation half-life of about 1 h, which is sufficient to label cells, organelles, and proteins. FPs with fast maturation times are needed in applications such as early detection of promoter activation, monitoring proteins with short lifetimes, or observing individual translational events [103].

The wild-type form of avGFP folds fairly efficiently when expressed at or below room temperature, but its folding efficiency declines steeply at higher temperatures. However, once functional, avGFP is thermodynamically stable and fluoresces up to at least 65°C. For applications involving mammalian cell cultures, FP expression and function at 37°C is required. Codon optimization of avGFP has led to a fourfold enhancement of protein expression at 37°C [72, 104]. A number of mostly bulky amino acids in avGFP have been identified that apparently contribute to the lack of expression at higher temperature [59]. Additional protein engineering yielded "superfolder GFP," featuring improved tolerance toward circular permutation, greater resistance to chemical denaturants, and enhanced folding kinetics [105]. For some FPs, a few amino acid replacements were sufficient to enhance protein expression at 37°C, for example, the Ile57Val and Phe102Leu mutations in eqFP611 [106]. The monomeric version of EosFP (mEosFP) was optimized for use at 37°C by introducing a single point mutation, Ala69Val [107].

5.3 Molecular Brightness

For a fluorophore to be bright, it must have a high capacity to absorb photons, i.e., a high extinction coefficient at the excitation wavelength. In addition, it must have a high probability of de-excitation by photon emission, i.e., a high fluorescence quantum yield, QY. The "molecular brightness" is defined as the product of the extinction coefficient at the excitation wavelength and the QY. For easy comparison of different FPs, the relative molecular brightness has been introduced, i.e., the molecular brightness with respect to that of EGFP.

One should, however, be aware that the apparent brightness of FPs observed upon cellular expression is determined not only by the intrinsic molecular brightness, but also by parameters such as transcription and translation efficiency, mRNA and protein stability, chromophore maturation efficiency and rate, and the labeling density that can be achieved with a particular construct.

5.4 Photostability

As essentially all FP applications rely on fluorescence measurements, photostability is a key parameter for any FP, especially for long-term data acquisition, for the detection of weak fluorescence signals and for quantitative measurements such as those based on FRET. Typically, a fluorescent chromophore will emit 10^4–10^6 photons until it falls victim to permanent photodestruction. The photostability is quantified by the quantum yield of photobleaching, Φ_b, i.e., the probability of photodestruction upon photon absorption. Single molecule experiments provide a straightforward way of determining Φ_b [73].

The simplest way to compare photostabilities of FPs with similar spectral properties is to simultaneously expose them to the same excitation light. To compare FPs of different colors, it is a common practice to calculate the photobleaching half-life, i.e., the time required to reduce the initial emission to 50% [108]. To normalize the observed photobleaching time courses, the time axes are scaled with respect to the initial photon emission per chromophore [94]. This procedure, however, correlates photostability and brightness so that brighter FPs always appear more photostable because of their overall higher photon output [108].

At present, the relation between protein structure and photostability is only poorly understood. Despite its key importance, photostability has not yet received sufficient attention in FP optimization. One typically performs multiple rounds of (site-directed or random) mutagenesis, with screening for photostability after each round. Tsien and coworkers noticed the importance of residue 163 in influencing the photostability of mRFP1 variants [109]. For mTFP1, the Asn63Thr mutation was found to result in a particularly large increase in photostability [110].

5.5 pH Effects

The hydroxyphenyl moiety of the FP chromophore can either be neutral or anionic, and the ratio of the two species is governed by an equilibrium coefficient for protonation, K_a (Fig. 6). Typically, the anionic species is the fluorescent one. Green and yellow FPs usually have pK_a values in the range 5.0–7.0. Blue and far-red variants often show pK_a values below 4. Since physiological processes may involve substantial pH changes, the pH dependence of the protonation equilibrium

can considerably affect the results of quantitative experiments. However, it is also possible to use the pH dependence to monitor pH changes within live cells [111].

5.6 *Cellular Toxicity*

Aggregation of FPs within the cell may effect cytotoxicity. Link et al. [112], for example, have deliberately enhanced aggregation of avGFP by adding a special 16-peptide sequence to the C-terminus that caused paralysis upon expression in body wall muscle cells of *C. elegans*. Wild-type copGFP can form huge, needle-like crystals inside eukaryotic cells and, thereby, destroy them within hours [99]. Some FPs have the tendency to accumulate in lysosomes [113], which can merge and become potentially cytotoxic agglomerates. Interestingly, optimized codon usage significantly reduced the cytotoxicity of EosFP expressed in murine stem cells, indicating that even rather unspecific effects of overexpression may affect cytotoxicity [39].

Under illumination, FPs produce toxic reactive oxygen species (ROS) including singlet oxygen, $^1O_2$, that attacks aromatic and sulfur-containing amino acids of proteins [114]. Recently, TagRFP was shown to photosensitize $^1O_2$ with an estimated QY of 0.004 [115]. The QY is similar to that measured for the EGFP fluorophore 4-hydroxybenzylidene-1,2-dimethylimidazoline [116]. For many applications, the phototoxicity of typical FPs is low and can be ignored, which is not surprising considering that FPs evolved in organisms exposed to O_2 and plenty of sunlight.

KillerRed is a genetically encoded photosensitizer that shows an enhanced production of ROS [117]. It is orders of magnitude more phototoxic than avGFP and kills cells within minutes even under mild illumination conditions. KillerRed can also inactivate an enzyme to which it is joined in a fusion construct. In a technique termed “chromophore-assisted light inactivation” (CALI), this property is exploited to specifically inactivate the function of target proteins or organelles by selectively producing photochemical damage [118].

6 The Color Palette of Fluorescent Proteins

The color diversity of FPs covers essentially the entire visible spectrum (Table 1). In the following, we briefly summarize properties of selected monomeric FPs, ordered by increasing wavelength of their emission peaks. More elaborate overviews have been presented in several reviews [36–39, 108, 119, 120].

Table 1 Fluorescent proteins

Protein	λ_{exc}/nm	λ_{em}/nm	$\varepsilon/M^{-1}\ cm^{-1}$	QY	Rel.[a] brightness	Quaternary structure	Ref.
Sirius	355	424	15,000	0.24	0.11	Monomer	[121]
mTagBFP	399	456	52,000	0.63	0.98	Monomer	[84]
EBFP	383	447	31,000	0.18	0.17	Weak dimer	[104]
EBFP2	383	448	32,000	0.56	0.54	Weak dimer	[71]
Azurite	384	450	26,000	0.55	0.43	Weak dimer	[124]
TagCFP	458	480	37,000	0.57	0.63	Monomer	[229]
mTFP1	462	492	64,000	0.85	1.62	Monomer	[110]
ECFP	434	477	32,500	0.40	0.39	Monomer	[82,83]
Cerulian	433/451	475/503	36,000	0.57	0.62	Weak dimer	[125]
Emerald	487	509	57,500	0.68	1.19	Weak dimer	[59]
EGFP	489	509	55,000	0.60	1.00	Weak dimer	[59]
EYFP	514	527	84,000	0.61	1.55	Weak dimer	[57]
mCitrine	516	529	77,000	0.76	1.77	Monomer	[131]
Venus	515	528	92,200	0.57	1.59	Weak dimer	[98]
mOrange	548	562	71,000	0.69	1.48	Monomer	[94]
mKO	548	559	51,600	0.60	0.94	Monomer	[230]
TagRFP	555	584	100,000	0.48	1.42	Monomer	[138]
mRuby	558	605	112,000	0.35	1.20	Monomer	[91]
mRFP1	584	607	50,000	0.25	0.38	Monomer	[92]
dTomato	554	581	69,000	0.69	1.44	dimer	[94]
mStrawberry	574	596	90,000	0.29	0.79	Monomer	[94]
mCherry	587	610	72,000	0.22	0.48	Monomer	[94]
mPlum	590	649	41,000	0.10	0.12	Monomer	[140]
mKate	588	635	45,000	0.33	0.47	Monomer	[231]
mKeima	440	620	14,400	0.24	0.11	Monomer	[139]
mNeptune	599	649	57,500	0.18	0.31	Monomer	[141]
TagRFP657	611	657	34,000	0.10	0.10	Monomer	[142]

[a]Relative brightness with respect to EGFP

6.1 *Violet FPs*

The violet FP Sirius carries the Tyr66Phe mutation in the chromophore triad [121]. Sirius tolerates prolonged light exposures due to its high photostability and can be targeted to acidic organelles. However, its low brightness combined with the enhanced autofluorescence of living cells in this region of the visible spectrum and the general phototoxicity of short-wavelength light needed for Sirius excitation [122] limit its usefulness to specialized applications.

6.2 *Blue FPs*

Because of its low brightness and very poor photostability, BFP has not become a popular marker protein [83, 104]. Recently, improved variants SBFP2 [123],

Azurite [124], and EBFP2 [71] have been introduced. In the long run, His66-based BFPs may yield to BFPs such as TagBFP that carry the normal Tyr66-containing GFP-like chromophore [84].

6.3 Cyan FPs

Enhanced CFP (ECFP) has become popular for use in FRET and dual-color labeling in combination with yellow FPs [82, 83]. Directed evolution of ECFP resulted in improved variants such as Cerulean [125], super CFPs (SCFPs) [126], TagCFP, and mTurquoise [127], all characterized by enhanced brightness and/or maturation rate. Recently, the palette of CFPs was extended by a monomeric FP carrying a GFP-like chromophore, mTFP1 [110], developed from the tetrameric protein cFP484 from the soft coral *Clavilaria* sp. [50]. Its narrow emission spectrum can reduce crosstalk in multicolor and FRET experiments. However, its further red-shifted emission (Table 1) may complicate its spectral separation from yellow FPs.

6.4 Green FPs

A wide variety of monomeric GFP labels are available at present. One of the first enhanced variants developed, EGFP, already combined most of the desirable characteristics [128]. mWasabi is brighter, at the expense of some photo- and pH stability [129], and Emerald shows a higher maturation rate [130]. Superfolder GFP supports the solubility of fused proteins but may have an enhanced dimerization tendency due to the Ala206Val mutation [105]. TagGFP2 has high pH stability and fast maturation (half-time of fluorescence development at 37°C is 11 min) [84].

6.5 Yellow FPs

The bathochromic shift of the excitation and emission spectra characteristic of yellow FP (YFP) results from π-stacking of the GFP-type chromophore with Tyr203 [57]. One of the first enhanced YFPs, EYFP, is characterized by a low pH stability and high sensitivity to halide ions. Improved versions are Citrine [131], Venus [98], Topaz [132], and TagYFP [133]. One of the brightest yellow FPs known to date is YPet [134], which also demonstrates enhanced FRET with co-optimized cyan FP CyPet. However, this pair was reported to have an enhanced tendency to form homo- and heterodimers [135].

6.6 *Orange FPs*

The orange segment is represented by monomeric Kusabira Orange (mKO) [136] and mOrange [94], both developed from tetrameric anthozoan FPs. Recently, enhanced versions mKO2 and mOrange2 were introduced. However, the faster maturation of mKO2 seems to be accompanied by a lower pH stability [137], and the more photostable mOrange2 matures more slowly than its predecessor [109].

6.7 *Red FPs*

Although optimization of monomeric RFPs is still ongoing, the available variants generally satisfy the demands of most applications. Importantly, the high extinction coefficients of RFPs make them excellent FRET acceptors for yellow donors. Among the orange-red FPs, TagRFP is currently the brightest [138], followed by mStrawberry [94] and mRuby [91]. TagRFP still yields to enhanced TagRFP-T in photostability [109]. It is noteworthy that mKeima from the *Montipora* stony coral displays the largest Stokes shift among FPs reported to date, with a blue excitation peak at 440 nm and red emission peak at 620 nm [95, 139].

6.8 *Far-Red FPs*

Light of longer wavelengths can penetrate more deeply into biological tissues, and causes less background autofluorescence and less phototoxicity. These advantages, along with requirements of FRET and multicolor labeling, have spurred the development of more and more red-shifted FPs, including mRaspberry [140], mPlum [140], mKate2 [96], and mNeptune [141]. With an excitation maximum at 611 nm, TagRFP657 [142] can efficiently be excited with standard red diode lasers.

7 Photoactivatable Fluorescent Proteins

Photoactivatable FPs (PA-FPs) may undergo a variety of light-induced photoreactions, which allows their fluorescence properties to be controlled by irradiation with light of a particular wavelength. These photoreactions may be classified as irreversible (photoconversion) or reversible (photoswitching) [120].

The photoactivation properties of PA-FPs make them extremely useful for novel imaging strategies featuring higher spatial and temporal resolution (see Sects. 1 and 8). Naturally, in addition to photoactivation, PA-FPs must possess all properties expected

from conventional FPs, such as high brightness, fast and complete chromophore maturation, and monomeric character [9].

7.1 Irreversible Photoactivation: Photoconversion

Photoconversion involves a permanent photochemical modification. As a consequence, a nonfluorescent (dark) state may get permanently activated to a fluorescent (bright) state, or a bright fluorescent state is changed to a different emission wavelength (Fig. 8). Irreversibility of the photoreaction implies that its efficiency is not subject to thermodynamic equilibrium between the pre-activated and the activated states. Consequently, high fluorescence contrast ratios can be achieved. The marker proteins remain in the photoactivated state until they photobleach, which ensures a maximal photon yield per FP molecule. Experiments with photoconverting FPs are not sensitive to the expression of new proteins after photoactivation. They can, therefore, provide detailed information about protein localization, turnover, and the direction and rate of trafficking in a living cell [119]. PA-FPs that shift their emission wavelength upon photoactivation and, therefore, can be detected before and after photoconversion, are especially useful for so-called pulse chase experiments: Within a given structure, e.g., a cell or an organelle, the researcher selects a subpopulation of PA-FPs based on their initial fluorescence. This population is tagged by a brief photoconverting laser pulse that changes their color, so that these FPs can subsequently be chased over time. In contrast to color-changing PA-FPs, those that are photoconverted from a nonfluorescent to a fluorescent state cannot be observed before activation and, therefore, cannot be targeted selectively in their initial dark state. However, the dual-color emission of cyan/green and green/red PA-FPs may complicate their application in multicolor experiments.

7.1.1 Photoconversion from a Dark to a Bright Fluorescent State

Upon excitation of the neutral avGFP chromophore with UV light, transfer of a proton from the hydroxyphenyl to the imidazolinone ring (ESPT) competes with electron transfer from Glu222 to the chromophore. The electron transfer triggers decarboxylation of Glu222 [143, 144]. As a result, the hydrogen bonding network around the chromophore is modified, which, in return, causes a decrease in the chromophore's pK_a [59, 145, 146]. Consequently, the fraction of anionic, fluorescent chromophores and, concomitantly, the fluorescence intensity increases (Fig. 9). Owing to the high background fluorescence of the initial fraction of anionic chromophores, photoconversion of avGFP only results in an approximately threefold fluorescence increase. Therefore, avGFP is not suitable as a PA-FP [59, 147].

The Thr203His mutant of avGFP essentially lacks the anionic chromophore species. Consequently, predominantly neutral chromophores exist, which may

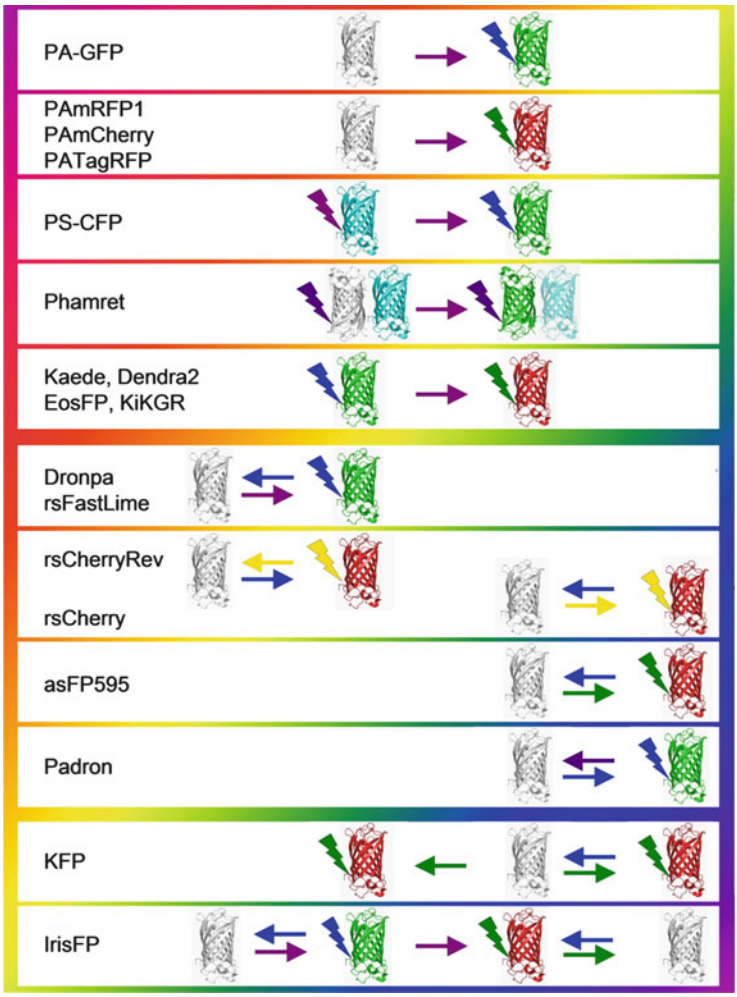

Fig. 8 Photoactivation of PA-FPs. *Arrows* are displayed in the color of the light used to induce the represented transition. Lightning bolts and β-barrels are shown in the colors of the fluorescence excitation and emission light

undergo photoconversion upon irradiation with activating light [82, 148, 149]. This variant, termed PA-GFP, was the first optical highlighter of practical use, featuring a 100-fold fluorescence enhancement upon irradiation with ~400 nm light (Table 2). Due to its monomeric nature, high contrast and high brightness of the activated form, PA-GFP has gained popularity in a variety of applications including dual-color PALM experiments [18, 150–157].

Photoactivatable monomeric RFPs (PAmRFPs) have been derived from the monomeric variant of DsRed, mRFP1 [61, 92]. They photoconvert irreversibly from a dark to a red-emitting state after illumination with violet light (Table 2).

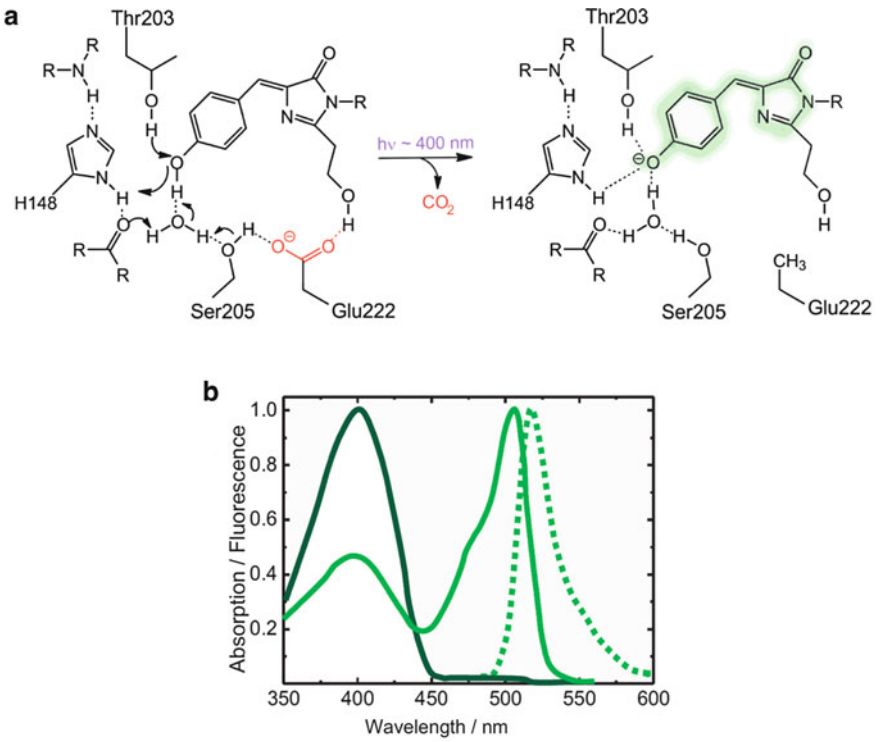

Fig. 9 (**a**) Photoactivation of PA-GFP. (**b**) Absorption spectra before (*dark green*) and after (*light green*) photoactivation and emission (*dotted*) spectrum of activated PA-GFP. For comparison, spectra have been scaled to equal amplitudes

The brightest protein among those variants is PAmRFP1. It yields a ~70-fold increase in red fluorescence upon photoactivation [158], but lacks the photostability required for single molecule-based imaging applications such as PALM [157].

The PAmCherry proteins, derived from mCherry, are advanced variants of PAmRFP1 [157]. Before photoactivation, PAmCherry markers are essentially nonfluorescent (Table 2). Illumination with violet light increases their fluorescence emission 3,000- to 5,000-fold and renders them permanently red-fluorescent [157]. All variants have been reported to display fast maturation times and excellent performance in protein fusions in live cells. PAmCherry variants, including PAmCherry1, have been used in (dual-color) localization-based super-resolution microscopy such as PALM, where PAmCherry1 appeared to be a good complement to PA-GFP [157]. Unfortunately, PAmCherry1 is not very photostable. It was observed that during data acquisition of PALM images, 80% of the initial fluorescence was lost to photobleaching within the first two to three frames [157].

X-ray structure analysis and mass spectroscopy revealed that the initial, nonfluorescent *N*-[(E)-(5-hydroxy-1H-imidazol-2-yl)methylidene]acetamide chromophore of PAmCherry1 features an *N*-acylimine group conjugated with the cyclized

Table 2 Photoactivatable fluorescent proteins

FP	State	$\lambda_{ex}/\lambda_{em}$ nm	ε M^{-1} cm^{-1}	QY	Rel. brightness	$t_{1/2\ on/off}$ s	$t_{1/2\ rec}$ min	PA[f] mode	PS mode	Ref.
PA-GFP	(Dark)	400/515	20,700	0.13	0.08			IR		[149]
	Green	504/517	17,400	0.79	0.42					
PAmRFP1		578/605	10,000	0.08	0.02					[158]
PAmCherry1		564/595	18,000	0.46	0.25			IR		[157, 202]
PATagRFP		562/595	66,000	0.38	0.76			IR		[85]
PS-CFP	Cyan	400/468	43,000	0.20	0.26			IR		[162]
	Green	490/511	47,000	0.23	0.33					
Phamret	Cyan	458/475	32,500	0.40	0.39			IR		[154]
	Green	458/517	17,400	0.79	0.42					
Kaede	Green	508/518	98,800	0.80	2.40			IR		[170]
	Red	572/580	60,400	0.33	0.60					
EosFP	Green	506/516	72,000	0.70	1.59			IR		[173]
	Red	571/581	41,000	0.62	0.80					
tdEosFP	Green	506/516	84,000	0.66	1.74			IR		[66]
	Red	569/581	33,000	0.60	0.62					
mEos2	Green	506/519	56,000	0.84	1.42			IR		[184]
	Red	573/584	46,000	0.66	0.92					
mKikGR	Green	505/515	49,000	0.69	1.02			IR		[188]
	Red	580/591	28,000	0.63	0.53					
Dendra2	Green	490/507	45,000	0.50	0.68			IR		[171]
	Red	553/573	35,000	0.55	0.58					
Padron		503/522	43,000	0.64	0.83	5.6/0.06[a]	150	R	Pos.	[205]
rsFastLime		496/518	39,000	0.77	0.91	2.6/0.03[a]	8	R	Neg.	[191]
mIrisFP	Green	486/516	47,000	0.54	0.76	8.8/6.4[b]	53	R/IR	Neg.	[107]
	Red	546/578	33,000	0.59	0.59	16.0/4.9[c]	24		Neg.	
rsCherry		572/610	81,000	n.a.	n.a.	0.05/3.0[d]	0.66	R	Pos.	[157, 202]
rsCherryRev		572/608	85,000	n.a.	n.a.	0.7/0.05[e]	0.22	R	Neg.	[157, 202]
rsTagRFP		567/585	36,800	0.11	0.12			R	Neg.	[206]

[a]Off-switching: 488 ± 5 nm, 45 mW cm^{-2}, on-switching: 405 ± 5 nm, 48 mW cm^{-2}
[b]Off-switching: 473-nm light, 30 mW cm^{-2}, on-switching: 405-nm light: 4.5 mW cm^{-2}
[c]Off-switching: 561-nm light, 6 mW cm^{-2}, on-switching: 473-nm light: 0.5 mW cm^{-2}
[d]Off-switching: 450 ± 20 nm, 4 W cm^{-2}, on-switching: 550 ± 20 nm, 4 W cm^{-2}
[e]Off-switching: 550 ± 20 nm, 4 W cm^{-2}, on-switching: 450 ± 20 nm, 4 W cm^{-2}
[f]*IR* irreversible, *R* reversible

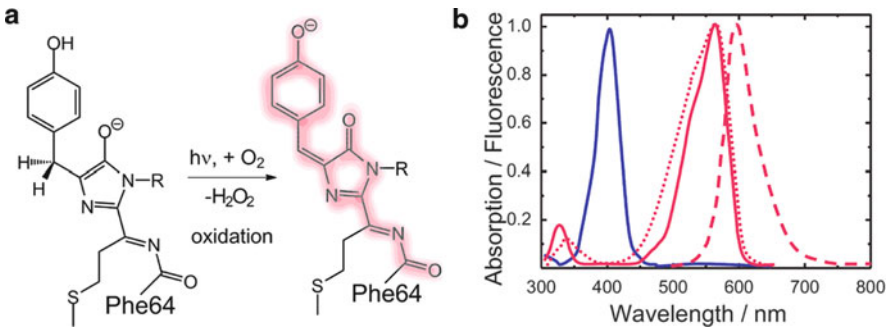

Fig. 10 Photoactivation in PAmCherry. (**a**) Light-induced modification of the chromophore. (**b**) *Blue*: absorption spectrum of PAmCherry before activation. *Red*: absorption (*solid*), excitation (*dotted*), and emission (*dashed*) spectra of activated PAmCherry

tripeptide, with a single, nonoxidized Cα–Cβ bond in the Tyr66 side chain (Fig. 10) [159]. Photoactivation leads to the oxidation of the Tyr66 Cα–Cβ bond, possibly mediated by the concurrent decarboxylation of Glu215 (Glu222 in avGP). The resulting methylene bridge extends the chromophore π-electron system toward Tyr66. In PAmCherry1, this chromophore adopts a *trans* configuration (Fig. 10).

TagRFP (Table 2, [138]) was engineered into a monomeric PA-FP, termed PATagRFP [85]. Like PAmCherry1, PATagRFP is initially dark but becomes red-fluorescent after irradiation with violet light (Table 2). PATagRFP has a high molecular brightness, excellent pH stability, and good photostability in both ensemble and single molecule applications. Moreover, the absorbance maximum of the dark state of PATagRFP is blue-shifted by ~50 nm from other PA-RFPs such as PAmCherry1 [85], which is advantageous for two-color PALM experiments. Because of this blue-shift, PATagRFP exhibits a 3.5-fold lower efficiency of "accidental" photoactivation with 488-nm light that is often used for imaging green PA-FPs such as PA-GFP.

It has been suggested that the PATagRFP dark state chromophore may represent a cyclized dehydrated aromatic α-enolate without the *N*-acylimine and without the oxidized Tyr66 C_α–C_β bond that is supposedly formed in early stages of chromophore maturation [160]. A first photoinduced oxidation reaction may then conjugate the α-enolate with the *N*-acylimine group, resulting in a chromophore similar to the initial, nonfluorescent one in PAmCherry. The second photoreaction is presumably analogous to the one in PAmCherry (Fig. 10) [157].

7.1.2 Cyan-to-Green Photoconversion

PS-CFP was originally derived from the nonfluorescent FP acGFPL [161]. Photoactivation with ~400 nm light produces a 300-fold increase in green fluorescence and a fivefold decrease in cyan fluorescence, yielding an overall 1,500-fold increase in the green-to-cyan fluorescence ratio [162]. As for PA-GFP (Fig. 9), this

effect is based on the light-induced decarboxylation of Glu215 and the concomitant deprotonation of the chromophore. The brightness of PS-CFP in both forms is relatively low (Table 2) but still sufficient for its application in pulse chase experiments [162]. An enhanced version, PS-CFP2 is twice as bright as PS-CFP and has a 2,000-fold contrast ratio. It has been shown to be suitable for dual-color PALM [163].

Phamret is a chimeric FP that consists of a PA-GFP coupled to a high-performance ECFP variant through a two-amino acid linker to form a photoactivatable tandem dimer [154]. When excited with 458-nm light, Phamret emits cyan fluorescence originating from the ECFP subunit. After photoactivation of the PA-GFP subunit by ~400 nm light, Phamret exhibits green fluorescence peaking at 520 nm upon 458-nm excitation, due to FRET between the ECFP and the activated PA-GFP. Thus, it may potentially be of use as a localization probe. A drawback of Phamret is its increased size, which could be disadvantageous in some fusion constructs.

7.1.3 Green-to-Red Photoconversion

In 1997, several GFP variants, including avGFP, avGFP S65T [82, 128], GFPmut1, 2 and 3 [82, 128, 164], and GFPuv (Clontech) [165], were reported to undergo photoconversion from a green-emitting to a red-emitting state upon irradiation with blue light [166]. The high contrast with respect to the background fluorescence allowed monitoring protein diffusion in bacteria [166] and mitochondria [167]. However, this type of photoactivation is limited to a low oxygen environment, possibly, because it is based on a photochemical reduction of the chromophore [168], so that these FPs function as PA-FPs only in facultative anaerobic organisms. EGFP was found to act as a light-induced electron donor in photochemical reactions with various electron acceptors. This process is accompanied by green-to-red photoconversion and can be observed in living cells without additional treatment [169].

Kaede [170], Dendra [171], KikGr [172], and EosFP [173] form a subgroup of photoconverting FPs that can be irreversibly switched from a green fluorescent to a red fluorescent state by ~400-nm light in the presence of oxygen. These proteins share the chromophore-forming tripeptide His65-Tyr66-Gly67 (Fig. 11).

The exact mechanism governing photoconversion is still under debate, and several hypotheses have been put forward. Initially, Mizuno et al. [174] suggested that the imidazole of His65 could become doubly protonated and thus may facilitate backbone cleavage via β-elimination, accompanied by an extension of the conjugated π-electron system [174]. Nienhaus et al. [175] proposed ESPT from the Tyr66 hydroxyl group to the His65 Nε to generate an imidazolium ion, followed by the β-elimination step in which Glu215 acts as a proton acceptor. Finally, Hayashi et al. [176] invoked a water-assisted mechanism to explain the loss of a water molecule (W1) in the red form of Kaede, which is also observed for EosFP [175]. There is, however, a general agreement that the neutral *p*-HBI chromophore is the reactive species, which loses its proton on the hydroxyphenyl oxygen upon excitation (Fig. 11), and that His65 is an essential group in the conversion mechanism,

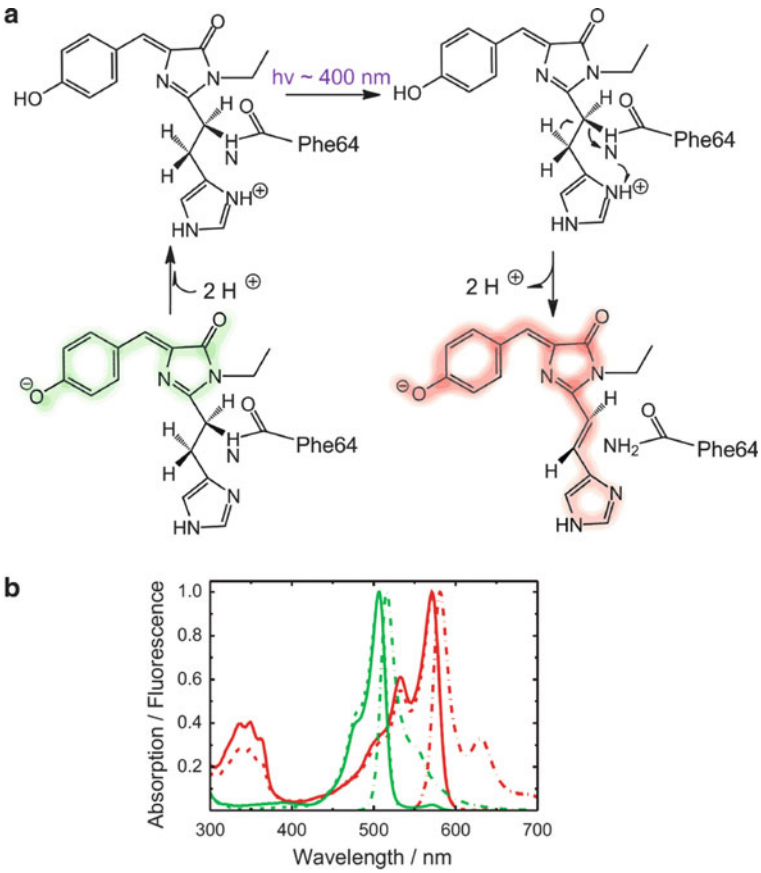

Fig. 11 (**a**) Photoconversion mechanism of EosFP. (**b**) Absorption (*solid*), excitation (*dotted*), and emission spectra (*dashed dotted*) of EosFP before (*green*) and after (*red*) photoconversion, scaled to equal amplitudes for comparison

which is underscored by the observation that photoconversion is lost in both EosFP [175] and Kaede [174] upon replacement of His65 by other amino acids [173]. Based on ground state quantum-chemical calculations on Kaede, Li et al. [177] recently suggested the stepwise occurrence of β-elimination reactions. Lelimousin et al. [178] proposed a mechanism, in which the hydroxyphenyl moiety of the chromophore remains protonated and, instead, ESPT from His65 to Phe64 promotes peptide bond cleavage.

The first FP of this class, Kaede, was isolated from the stony coral *Trachyphyllia geoffroyi* [170]. Photoconversion of Kaede yields a >2,000-fold increase in the red-to-green contrast ratio. However, Kaede is tetrameric and thus not preferable as a fusion tag [170].

Dendra2 is a monomeric variant of the tetrameric DendFP, which was isolated from *Dendronephthya* sp. [171]. The concentration of neutral green Dendra2 species is 20-fold higher at neutral pH than in EosFP, due to its higher chromophore pK_a, which leads to an enhanced green-to-red photoconversion yield [179]. In addition to the green and red anionic chromophores, and different from the other FPs in this group, the neutral red chromophore of Dendra2 fluoresces in the green spectral range [179]. Photoactivation yields a very high contrast increase, up to 4,500-fold in the red-to-green ratio [179]. Good expression of functional proteins and the enhanced photoactivation yield of Dendra2, especially with 488 nm lasers, have lead to its widespread use as a tracking tool in live-cell imaging [180, 181]. Dendra2 has been reported to perform well in sensitive fusions and to possess low cytotoxicity. However, the relatively low pH-stability of the activated red state, the high pK_a values of green and red forms, and the spectral overlap of the excitation and emission bands of the green anionic and the red neutral species may create problems in single molecule-based imaging applications such as PALM and also in pulse chase experiments.

EosFP was isolated from the stony coral *Lobophyllia hemprichii* (Table 2) [173]. Photoconversion yields a ~2,000-fold contrast ratio between the green and the red forms. EosFP has the highest photostability of all presently known PA-FPs. Although tetrameric, it has frequently been used in live-cell imaging applications including pulse chase experiments [66, 182, 183]. Two dimeric variants, d1EosFP (Val123Thr) and d2EosFP (Thr158His), were produced by random and site-directed mutagenesis [173]. Combining these mutations led to monomeric mEosFP [173], which expresses efficiently only up to 30°C [66]. To create a pseudo-monomer suitable for imaging at 37°C, two d2EosFP protomers were connected with a 16-amino acid linker to form a tandem dimer, tdEosFP [66]. This variant has proven to be a useful PA-FP for super-resolution imaging because of its high brightness and functionality as a fusion tag. Recently, the improved monomeric versions mEos2 [184] and mEosFP*thermo* [107, 185] have become available which express well at 37°C. Although not as bright as tdEosFP, these monomers are excellent tools for imaging problematic proteins that localize poorly when fused with tandem dimers [184, 186].

The photoconvertible KikGR was engineered from KikG, a protein from *Favia favus* that does not exhibit photoactivation [172]. While the tetrameric KikGR may lack some brightness in vitro, the fluorescence intensity in cells was sufficient for its application in cell migration studies [187]. The monomeric mKikGR [188] is similar to its parental protein KikGR in its spectroscopic characteristics and kinetics of photoconversion (Table 2) [189].

7.2 Reversible Photoactivation

Reversibly photoactivatable FPs can be toggled between a dark off and a bright on state by light. Therefore, they are also referred to as photoswitchable FPs. A similar

behavior was first observed in single molecule studies of avGFP mutants; the phenomenon was termed blinking at the time [190]. Photoswitching is based on an isomerization/protonation reaction of the chromophore (Fig. 12) and concomitant conformational rearrangements of amino acids in the chromophore environment [81, 191–199]. Interconversion between the energetically similar isomeric forms appears to be an intrinsic property of the chromophore [200, 201].

Under equilibrium conditions, the chromophore typically assumes the *cis* conformation, with the anionic state being the fluorescent species. Photoactivation triggers a *cis–trans* isomerization accompanied by a change of protonation state. As a result, the chromophore becomes essentially nonfluorescent. In some photoswitchers such as KFP1 and asFP595, the nonfluorescent *trans* state is thermodynamically more stable than the *cis* state, and light irradiation induces a *trans–cis* isomerization to the fluorescent *cis* state. When kept in the dark, all FPs relax within minutes to several hours to the thermodynamically more stable isomeric state. This relaxation process can be markedly enhanced by light. Note that this light has a different wavelength than that used for generating the nonequilibrium state. If illumination with the excitation light induces the transition from the on to the off state, the protein is said to exhibit a "negative switching mode." If fluorescence excitation induces an off-to-on transition, the protein exhibits a "positive switching mode" [202].

The reversibility of the photoactivation process allows repeated activation of the same fluorophore. This feature is mandatory for ensemble-based RESOLFT techniques. Concurrent photoexcitation and on-switching of positively switching FPs is especially favorable for RESOLFT microscopy as it reduces the image acquisition time. Photoswitching FPs can also be used in localization-based super-resolution approaches such as PALM. The reversibility of photoactivation allows for repeated imaging of the same sample area, which is difficult with photoconverting FPs. Photoswitching FPs featuring a negative switching mode are preferable as labels for SSIM.

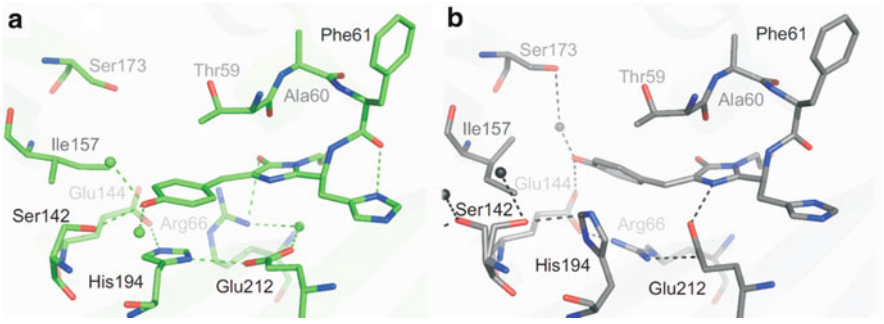

Fig. 12 Photoswitching of the green chromophore of IrisFP. (**a**) Planar, fluorescent *cis* isomer. (**b**) Nonplanar, nonfluorescent *trans* isomer

7.2.1 FPs with a Negative Switching Mode

Dronpa is a monomeric variant derived from the tetrameric FP 22G, which was isolated from the *Pectiniidae* family of stony corals [203]. Dronpa was reported to undergo ~100 times on–off cycling with a loss of 25% of the original fluorescence [203]. With its good brightness and ease of photoswitching, Dronpa has been shown to be a useful maker protein for high-resolution microscopy such as PALM [163]. Dedecker et al. [13] have used Dronpa for imaging molecules immobilized in PVA using RESOLFT microscopy.

rsFastLime is an improved variant of Dronpa with minimized steric hindrance against chromophore *cis*/*trans*-isomerization [191] and, therefore, faster switching kinetics, which may prove favorable for its application in RESOLFT microscopy. It has already been applied in PALMIRA imaging [20, 204]. bsDronpa, a random mutant of rsFastLime, can be excited efficiently with 400-nm light due to its significantly different spectral properties. It has been applied in dual-color super-resolution microscopy using Dronpa as a second label [205].

The first monomeric photoswitching FPs emitting in the red spectral range were two variants of mCherry, rsCherry (see below), and rsCherryRev [202]. In thermal equilibrium, the fluorescence signal of rsCherryRev is $<10\%$ of the maximal attainable signal; hence, the majority of the molecules resides in the off state. The poor stabilization of the on state is also obvious from the fast thermal relaxation of the bright on state back to the dark off state. The low fluorescence of nonactivated rsCherryRev in equilibrium makes it beneficial for super-resolution microscopy. In live-cell PALMIRA imaging of the endoplasmic reticulum labeled with rsCherryRev, images were obtained with ~75 nm lateral resolution [202].

A photoswitchable version of TagRFP, rsTagRFP, presents an alternative to rsCherryRev [206]. Photoswitching of rsTagRFP was used in photochromic FRET experiments, where the fluorescence intensity of the donor was modulated by light-induced "removal" and "re-provision" of the acceptor, on state rsTagRFP [206].

7.2.2 FPs with a Positive Switching Mode

The naturally occurring asFP595 (a.k.a. as asulCP) was the first photoswitchable FP reported [78]. Using this protein with RESOLFT microscopy, super-resolution images were acquired with resolutions between 50 and 100 nm in the focal plane [12]. However, due to its slow maturation, low quantum yield, contrast, and tetrameric nature, its practical use in live-cell imaging is rather limited. The kindling FP, KFP (commercially available from Evrogen as KFP1), is a variant of asFP595 that can be photoactivated reversibly to a red fluorescent state [207]. At high laser powers, photoactivation becomes irreversible.

Padron is a variant of rsFastLime that was developed by random mutagenesis [205]. In thermal equilibrium, Padron is essentially nonfluorescent (Table 2). Photoinduced switching is about as fast as for rsFastLime, but thermal relaxation of

Padron back to the off state is very slow, with a half-life of ~42 h. The dynamic range of the switchable fluorescence signal (150:1) is therefore very high, promising high contrast ratios in live-cell imaging applications.

The spectroscopic properties of rsCherry are similar to those of rsCherryRev (Table 2, Fig. 8). Its positive switching mode may be favorable, although its applicability for live-cell imaging has yet to be demonstrated [202].

7.3 PA-FPs Showing Reversible and Irreversible Photoactivation

IrisFP, a mutant of tetrameric EosFP, and its monomeric variant, mIrisFP, feature both reversible and irreversible photoactivation [107, 193]. In these PA-FPs, the chromophore can assume four different states, which are depicted schematically in Fig. 13. In their green fluorescent forms, IrisFP and mIrisFP display reversible photoswitching between a fluorescent and a nonfluorescent state [193], which involves a *cis–trans* isomerization of the chromophore [193], as for Dronpa [194] and mTFP0.7 [208]. The *trans* chromophore, which is nonplanar and essentially nonfluorescent (Fig. 12), appears to be in the protonated phenolic form, as indicated by the increased absorption at 390 nm. The isomerization transition is accompanied by substantial rearrangements of several residues in the chromophore cavity (Fig. 12) [193].

In addition, IrisFP and mIrisFP can be photoconverted irreversibly to red-emitting forms [193] by ~400 nm light. The quantum yield for driving the green-to-red transition is lower than for the *trans*-to-*cis* transition of the green form by a factor of ~240, so that the green form can be reversibly switched on and off many times before a significant green-to-red transition occurs. As for EosFP [175], the X-ray structure revealed that the chromophore environment of IrisFP is nearly unperturbed upon green-to-red photoconversion, except for backbone cleavage and dislocation of a water molecule proximal to His65 [193], as was also reported for Kaede [176]. This comparison suggests identical green-to-red photoconversion mechanisms for IrisFP and EosFP [193]. Once photoconverted to the red form, IrisFP and mIrisFP again exhibit reversible photoswitching, which involves a *cis–trans* isomerization of the chromophore as for the green form (Fig. 13). The unique combination of photoswitching and photoconversion allows more complex experimental schemes to be implemented, e.g., multistep pulse chase experiments or pulse chase experiments combined with super-resolution imaging [107].

8 Applications of FPs in Nanoscopy

All fluorescence-based imaging techniques benefit from bright fluorophores, i.e., with large extinction coefficients and fluorescence quantum yields to produce strong signals above background. Ultimately, the resolution in super-resolution optical microscopy is limited by the ability to precisely tag the structure of interest.

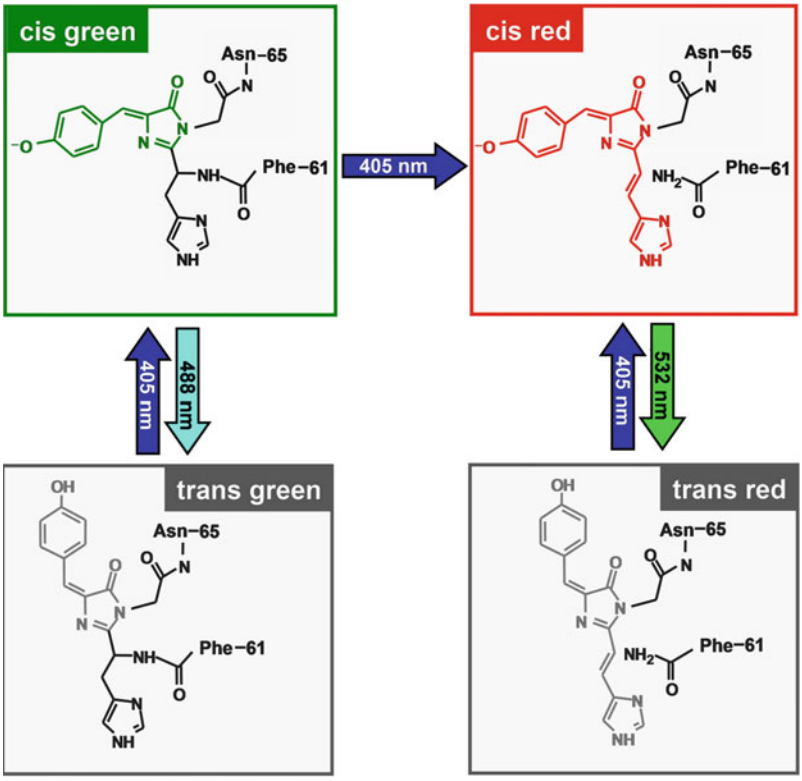

Fig. 13 Chromophore states and phototransformations in IrisFP. The four chromophore states of IrisFP are shown schematically; the photoinducible transitions are indicated by *arrows* that are colored and labeled according to the required wavelength of the activating light

Obviously, a fluorescent marker cannot reside where the labeled structure itself is located but only in close proximity. Linkers are frequently introduced to specifically attach the fluorophore to the target and, naturally, the marker has a certain size. Moreover, to image an extended structure at a specific resolution, the labeling density must be sufficiently high so that markers are separated by a distance no more than half the desired resolution (Nyquist criterion) [209]. Therefore, when using FPs as genetically encoded markers for super-resolution imaging, they should express well and mature completely to ensure that the entire fluorophore population has turned into its functional form prior to imaging.

However, too dense labeling may interfere with the processes and structures that are to be studied. Especially for live-cell studies, conditions are very demanding. Localization-based techniques require acquisition of a large number of individual camera frames for reconstruction of a high-resolution image. With current camera technology, the collection of individual frames takes at least 2 ms. Thus, acquisition of super-resolution images takes at least a few 10 s at the present time. Faster processes cannot be studied and cause blurring of the image, thereby obviating

any attempt to achieve better spatial resolution. STED microscopy of live cells at video rate has been demonstrated but is as yet confined to micron-sized regions of interest [210].

8.1 FPs in STED, RESOLFT, and SSIM

By using FPs as fluorescent labels, STED has been successfully applied to the study of a variety of biological problems. For example, YFP and Citrine were used as markers in live-cell imaging [131, 211, 212], yielding resolutions of ~50 nm (Fig. 14). FPs emitting in the far-red such as the tetrameric E2-Crimson [213] and the monomeric TagRFP657 [142] were also successfully applied in STED microscopy. Consequently, dual color STED experiments using FP labels should also be feasible. However, currently available FPs may not be the first choice as labels for STED microscopy because of their inferior photostability in comparison to fluorescent dyes.

In live-cell STED microscopy, the intensity of the depletion beam (up to 1 GW/cm^2) has to be carefully adjusted to avoid photodamage [214]. Using RESOLFT microscopy, a positively photoswitching FP (e.g., asFP595) allows depletion of the fluorescent state by off-switching with much lower intensity rather than by stimulated emission. As a matter of fact, the diffraction barrier can be broken with <1 W/cm^2 of light intensity in the depletion beam due to the slow isomerization rates of asFP595 [12]. Parallel and thus faster image acquisition can be afforded by an array of line-shaped intensity minima forming sub-diffraction-sized line-shaped regions scanned across the sample [12, 215]. The currently reported resolution of 50 nm is still restricted by switching crosstalk from the depleting light.

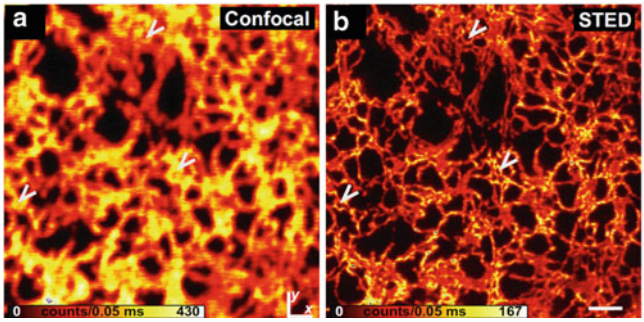

Fig. 14 Images of a live PtK2 (potoroo kidney) mammalian cell. The ER was tagged with Citrine. (**a**) Confocal image and (**b**) STED image of the same region. The *white arrows* indicate rings formed by the tubular network of the ER, which are only visible in the STED image. Scale bar, 1 μm. Reprinted from [211] with kind permission

Using a reset-dump-probe illumination scheme, negative photoswitchers such as Dronpa have also been used for RESOLFT imaging [13]. In this scheme, the FPs are first switched on by a pulse of activating light (reset). Then, the depletion beam is applied using the off-switching wavelength (dump). Only the not depleted molecules (in the center of the depletion beam) remain fluorescent and can thus be probed by a short pulse of excitation light (probe). The repetition rate of this sequence is restricted by the transition rates between the on and the off states and, therefore, the scanning speed of the method. In addition, negative photoswitchers must have a high photostability because they are excited in every reset step.

With SSIM, a lateral resolution of ~50 nm was achieved using fluorescent beads [15]. The very high laser powers used may induce radiation damage to the sample, which restricts the possible applications in live-cell imaging. Potentially, negative photoswitchable FPs could be applied in SSIM using the activation light to generate a nonlinear response. Complementary to RESOLFT imaging, the on state is saturated creating a sharp decline toward the population in the off state at the area of zero intensity. Since the lifetime of the on state is much higher than the fluorescence lifetime, much lower laser intensities are needed for a high saturation necessary for a high spatial resolution.

8.2 FPs in Localization-Based Super-Resolution Microscopy

Localization-based super-resolution microscopy has become popular in recent years for imaging both fixed and live cells. Organic dyes appear preferable to FPs for localization-based microscopy, as they are often brighter and more photostable and, thus, afford higher localization precision. For example, ~6,000 photons per label were reported per switching cycle using the Cy3–Cy5 pair of cyanine dyes [216, 217]. By comparison, tdEosFP, one of the brightest PA-FPs for PALM imaging, yields only ~2,600 photons per molecule [163], and monomeric FPs often only a few hundred photons [107]. In addition, some dyes can survive hundreds to thousands of switching cycles, whereas typical photoswitchable FPs can be activated only a few hundred times at most.

For live-cell imaging, however, PA-FPs are convenient because they can be used as a fusion construct with a particular protein under study (Fig. 15). Photoconverting FPs can be activated only once, which is entirely sufficient for localization microscopy. Taking the popular green-to-red photoconverting EosFP [66, 173, 183] as an example, we can photoconvert a few molecules to red emitters by appropriate adjustment of the 405-nm activating laser intensity. The converted molecules are registered in the red color channel of a widefield microscope with a CCD camera for 10–100 ms. A series of 10^3–10^4 image frames are collected in sequence, and the activating laser is adjusted such that photoconversion and photobleaching are balanced until the supply of fluorescent markers is depleted.

Using PA-GFP as a marker, it was shown that hemagglutinin clustered in large irregular domains ranging from several tens of nanometers to micrometers wide and

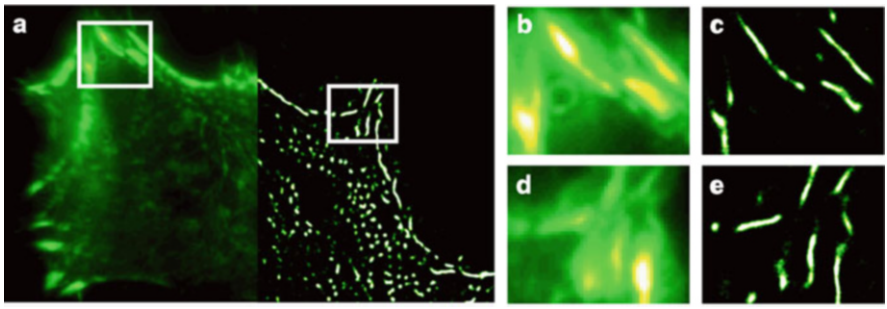

Fig. 15 (**a**) Total internal reflection microscopy (TIRFM) image (*left*) and PALM image (*right*) overlay of a live HeLa cell expressing an α-actinin–mIrisFP fusion construct. (**b**, **d**) TIRFM and (**c**, **e**) PALM close-up images of the regions marked by the white frames in (**a**)

exhibited lateral motion of <200 nm [218]. Moreover, dynamics within individual adhesion complexes was resolved [219], and temporal changes of proteins Gag and vesicular stomatitis virus glycoprotein were also shown [220]. The bacterial homolog of tubulin, Ftz, was imaged in *E. coli* using Dendra2 to reveal both stationary and mobile molecules [221]. Time-lapse images of single bacterial actin proteins in *Caulobacter crescentus* cells were obtained using photoswitchable EYFP [222]. PALM experiments using PS-CFP2 showed that TCR and Lat are expressed on separate protein islands on T-cell membranes and concatenate during activation [223]. Following single molecules, often over multiple frames prior to photobleaching, structural details as well as diffusion characteristics were uncovered [218, 220].

PA-FPs have also been successfully used in dual-color PALM experiments [163, 204, 205, 217, 224, 225]. The selection of PA-FP pairs, however, requires some additional considerations. Most currently available PA-FPs emit green fluorescence when photoactivated (e.g., PA-GFP, PS-CFP, and Dronpa) or shift their emission from green to red (e.g., KikGR, and EosFP) upon activation. Using one of each class as a dual-label pair may create problems because the green-to-red photoconverting FP molecules form a bright background prior to photoactivation that impedes isolation and localization of the PA-FP molecules that fluoresce in the green channel after photoactivation. This problem is avoided by using a photoswitching FP in combination with a photoconverting FP [163]. With the Dronpa/EosFP pair, EosFP molecules were photoactivated with 405-nm light and imaged in the red channel with 561-nm light until all EosFP molecules are bleached [163]. Later, Dronpa molecules that had become activated during imaging of EosFP molecules were deactivated by using intense 488-nm light and then registered (under weak 488 nm excitation) in the green detection channel as they slowly and spontaneously returned to their fluorescent state. When replacing Dronpa with PS-CFP2, the green background emission due to activated PS-CFP2 during imaging of EosFP is much higher than that of Dronpa. It can, however, be bleached prior to imaging the remaining population of PS-CPF2 [163].

A more straightforward approach to two-color PALM is to use green and red markers without spectral overlap, e.g., PAmCherry1 in combination with PA-GFP [157]. Both PA-FPs can be activated with 405-nm light. Of course, PAmCherry1 can also be used with other green PA-FPs, such as Dronpa, rsFastlime, and PS-CFP2. The more photostable PATagRFP was used in two-color single particle tracking PALM experiments using several PATagRFP-tagged transmembrane proteins together with a PA-GFP-tagged clathrin light chain [85].

Parallel data acquisition in two-color channels to reduce the overall acquisition time of dual-color PALM is still difficult because it requires independent photoactivation of the two labels and, concomitantly, color-specific excitation and emission detection in two channels. Interestingly, several conventional FPs not featuring an explicit photoactivation activity, such as CFP, GFP, citrine, or eYFP, exhibit long-lived dark states [149, 226, 227] and can thus be used in two-color localization microscopy (2CLM) [228]. This approach is similar to the GSDIM/dSTORM technique, where organic dyes are shelved in a metastable dark state, either the triplet state or a nonfluorescent reduced state [21, 24]. Since only an excitation laser but no additional photoactivation laser is required for each fluorophore, dual-color imaging is easily feasible using 2CLM.

The speed of PALM imaging was increased by introducing a simultaneous two-color stroboscopic illumination (S-PALM), which relies on the possibility of pulsing the laser light to match the short on-times of the FPs [23]. This approach is similar to stroboscopic photography, whereby short light flashes allow following a fast-moving object while the shutter of the camera remains open all the time. In PALMIRA, image acquisition can be accelerated significantly by matching the acquisition time with the mean duration of the photon bursts emitted by single molecules [20, 204]. Intense light is applied to drive most of the fluorophores into the dark state from which they stochastically revert to the bright state, briefly emitting a burst of photons.

The monomeric mIrisFP, with its unique combination of reversible and irreversible photoactivation, was used to study dynamical processes within live cells with a spatial resolution beyond the limits of conventional light microscopy. Specifically, a pulse-chase experiment was combined with PALM imaging to follow the movement of fusion constructs over time and at very high spatial resolution. Green mIrisFP molecules were fused to paxillin and expressed by a living cell. Subsequently, super-resolution PALM images of green mIrisFP were collected by acquiring many frames, each of which contained only a few fluorescent molecules, while the majority of IrisFP molecules remained in the off state. All molecular locations were subsequently combined in the PALM image (Fig. 15). Two small regions of the overall image are shown in Fig. 16a, f. Subsequently, a sub-ensemble of IrisFP molecules was photoconverted to the red form by irradiating a specified region of the cell with a pulse of violet light. Migration of the tagged proteins out of the conversion region into other regions of the cell was followed in time by PALM imaging, using the photoswitching capability of the red species. It is apparent that the focal adhesion imaged in Fig. 16a–d is assembled, while the one shown in

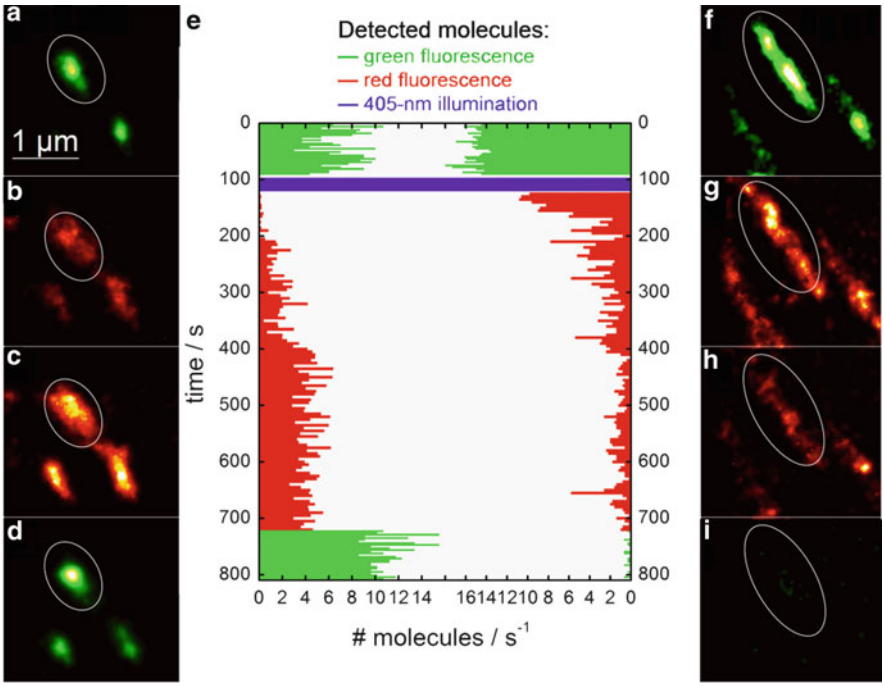

Fig. 16 Dynamics of focal adhesions of a HeLa cell expressing paxillin–mIrisFP. (**a**, **f**) PALM images (90 s, 3,000 frames of 30 ms) taken by exciting green mIrisFP. Subsequently, mIrisFP proteins (including those in the area marked in **f–i**) were photoconverted with 405-nm laser light for 30 s. (**b**, **g**) PALM images (50 ms each) acquired by exciting red mIrisFP, calculated from frames 1–6,000; (**c**, **h**) PALM images calculated from frames 6,001–12,000. (**d**, **i**) Later, PALM images (90 s, 3,000 frames of 30 ms) were again taken by exciting green mIrisFP. (**e**) Number of single-molecule bursts registered per second within individual adhesion sites marked by the *ellipses* in panels **a–d** and **f–i**, plotted as a function of time. Each bar represents an average over 100 image frames. The *violet* bars mark the period of *green*-to-*red* conversion

Fig. 16f–i is disassembled during data collection. The kinetics are shown in Fig. 16e.

9 Outlook

Fluorescence imaging has greatly contributed to advancing our understanding of molecular and cellular functions, e.g., cell adhesion, migration/motility, proliferation, and development. FPs are often preferred over other fluorescence markers because they can be genetically encoded so that the cells, tissues, or organisms produce these labels all by themselves. The remarkable photoactivation capabilities of many FP variants make them attractive for super-resolution imaging. However, currently available PA-FPs still leave much to be desired; further optimization of

their photophysical and photochemical properties will be beneficial for super-resolution imaging. Brighter, more photostable FPs would offer increased temporal resolution without sacrificing spatial resolution. Additionally, new monomeric PA-FPs of different colors will allow routine multicolor imaging at super-resolution. Higher quantum yields of the light-induced transitions and the thermal interconversion rates would also be of value for more efficient image acquisition. For the upcoming years, we look forward to the introduction of advanced PA-FPs that better serve the needs of the ever-growing optical nanoscopy community.

Acknowledgments G.U.N. was supported by the Deutsche Forschungsgemeinschaft (DFG) and the State of Baden-Württemberg through the Center for Functional Nanostructures (CFN), by DFG grant Ni 291/9 and by the Baden-Württemberg Stiftung.

References

1. Abbe E (1873) Beiträge zur Theorie des Mikroskops und der mikroskopischen Wahrnehmung. Arch Mikr Anat 9:413–468
2. Selvin PR (1995) Fluorescence resonance energy transfer. Methods Enzymol 246:300–334
3. Hell SW, Stelzer EHK (1992) Fundamental improvement of resolution with a 4Pi-confocal microscope using two-photon excitation. Opt Commun 93:277–282
4. Gustafsson MG (1999) Extended resolution fluorescence microscopy. Curr Opin Struct Biol 9 (5):627–634
5. Hell SW (2003) Toward fluorescence nanoscopy. Nat Biotechnol 21(11):1347–1355
6. Hell SW (2007) Far-field optical nanoscopy. Science 316(5828):1153–1158
7. Hell SW (2009) Microscopy and its focal switch. Nat Methods 6(1):24–32
8. Hell SW, Wichmann J (1994) Breaking the diffraction resolution limit by stimulated emission: stimulated-emission-depletion fluorescence microscopy. Opt Lett 19(11):780–782
9. Fernandez-Suarez M, Ting AY (2008) Fluorescent probes for super-resolution imaging in living cells. Nat Rev Mol Cell Biol 9(12):929–943
10. Hell SW, Kroug M (1995) Ground-state depletion fluorescence microscopy, a concept for breaking the diffraction resolution limit. Appl Phys B 60:495–497
11. Bretschneider S, Eggeling C, Hell SW (2007) Breaking the diffraction barrier in fluorescence microscopy by optical shelving. Phys Rev Lett 98(21):218103
12. Hofmann M, Eggeling C, Jakobs S, Hell SW (2005) Breaking the diffraction barrier in fluorescence microscopy at low light intensities by using reversibly photoswitchable proteins. Proc Natl Acad Sci U S A 102(49):17565–17569
13. Dedecker P, Hotta J, Flors C, Sliwa M, Uji-i H, Roeffaers MB, Ando R, Mizuno H, Miyawaki A, Hofkens J (2007) Subdiffraction imaging through the selective donut-mode depletion of thermally stable photoswitchable fluorophores: numerical analysis and application to the fluorescent protein Dronpa. J Am Chem Soc 129(51):16132–16141
14. Bossi M, Fölling J, Dyba M, Westphal V, Hell SW (2006) Breaking the diffraction resolution barrier in far-field microscopy by molecular optical bistability. New J Phys 8:275, 210 pages
15. Gustafsson MG (2005) Nonlinear structured-illumination microscopy: wide-field fluorescence imaging with theoretically unlimited resolution. Proc Natl Acad Sci U S A 102 (37):13081–13086
16. Moerner WE (2007) New directions in single-molecule imaging and analysis. Proc Natl Acad Sci U S A 104(31):12596–12602

17. Betzig E, Patterson GH, Sougrat R, Lindwasser OW, Olenych S, Bonifacino JS, Davidson MW, Lippincott-Schwartz J, Hess HF (2006) Imaging intracellular fluorescent proteins at nanometer resolution. Science 313(5793):1642–1645
18. Hess ST, Girirajan TP, Mason MD (2006) Ultra-high resolution imaging by fluorescence photoactivation localization microscopy. Biophys J 91(11):4258–4272
19. Rust MJ, Bates M, Zhuang X (2006) Sub-diffraction-limit imaging by stochastic optical reconstruction microscopy (STORM). Nat Methods 3(10):793–795
20. Egner A, Geisler C, von Middendorff C, Bock H, Wenzel D, Medda R, Andresen M, Stiel AC, Jakobs S, Eggeling C, Schonle A, Hell SW (2007) Fluorescence nanoscopy in whole cells by asynchronous localization of photoswitching emitters. Biophys J 93(9):3285–3290
21. Heilemann M, van de Linde S, Schuttpelz M, Kasper R, Seefeldt B, Mukherjee A, Tinnefeld P, Sauer M (2008) Subdiffraction-resolution fluorescence imaging with conventional fluorescent probes. Angew Chem Int Ed Engl 47(33):6172–6176
22. Vogelsang J, Cordes T, Forthmann C, Steinhauer C, Tinnefeld P (2009) Controlling the fluorescence of ordinary oxazine dyes for single-molecule switching and superresolution microscopy. Proc Natl Acad Sci U S A 106(20):8107–8112
23. Flors C, Hotta J, Uji-i H, Dedecker P, Ando R, Mizuno H, Miyawaki A, Hofkens J (2007) A stroboscopic approach for fast photoactivation-localization microscopy with Dronpa mutants. J Am Chem Soc 129(45):13970–13977
24. Folling J, Bossi M, Bock H, Medda R, Wurm CA, Hein B, Jakobs S, Eggeling C, Hell SW (2008) Fluorescence nanoscopy by ground-state depletion and single-molecule return. Nat Methods 5(11):943–945
25. Sharonov A, Hochstrasser RM (2006) Wide-field subdiffraction imaging by accumulated binding of diffusing probes. Proc Natl Acad Sci U S A 103(50):18911–18916
26. Dertinger T, Colyer R, Iyer G, Weiss S, Enderlein J (2009) Fast, background-free, 3D super-resolution optical fluctuation imaging (SOFI). Proc Natl Acad Sci U S A 106(52):22287–22292
27. Thompson RE, Larson DR, Webb WW (2002) Precise nanometer localization analysis for individual fluorescent probes. Biophys J 82(5):2775–2783
28. van de Linde S, Wolter S, Heilemann M, Sauer M (2010) The effect of photoswitching kinetics and labeling densities on super-resolution fluorescence imaging. J Biotechnol 149 (4):260–266
29. Haugland RP (2005) The handbook – a guide to fluorescent probes and labeling technologies, 10th edn. Molecular Probes, Eugene
30. Zheng J, Nicovich PR, Dickson RM (2007) Highly fluorescent noble-metal quantum dots. Annu Rev Phys Chem 58:409–431
31. Michalet X, Pinaud FF, Bentolila LA, Tsay JM, Doose S, Li JJ, Sundaresan G, Wu AM, Gambhir SS, Weiss S (2005) Quantum dots for live cells, in vivo imaging, and diagnostics. Science 307(5709):538–544
32. Fu CC, Lee HY, Chen K, Lim TS, Wu HY, Lin PK, Wei PK, Tsao PH, Chang HC, Fann W (2007) Characterization and application of single fluorescent nanodiamonds as cellular biomarkers. Proc Natl Acad Sci U S A 104(3):727–732
33. Baker SN, Baker GA (2010) Luminescent Carbon Nanodots: Emergent Nanolights. Angew Chem Int Ed Engl 49(38):6726–6744
34. Fan J, Chu PK (2010) Group IV nanoparticles: synthesis, properties, and biological applications. Small (Weinheim an der Bergstrasse, Germany) 6(19):2080–2098
35. Giljohann DA, Seferos DS, Daniel WL, Massich MD, Patel PC, Mirkin CA (2010) Gold nanoparticles for biology and medicine. Angew Chem Int Ed Engl 49(19):3280–3294
36. Shaner NC, Steinbach PA, Tsien RY (2005) A guide to choosing fluorescent proteins. Nat Methods 2(12):905–909
37. Chudakov DM, Lukyanov S, Lukyanov KA (2005) Fluorescent proteins as a toolkit for in vivo imaging. Trends Biotechnol 23(12):605–613
38. Day RN, Davidson MW (2009) The fluorescent protein palette: tools for cellular imaging. Chem Soc Rev 38(10):2887–2921
39. Wiedenmann J, Oswald F, Nienhaus GU (2009) Fluorescent proteins for live cell imaging: opportunities, limitations, and challenges. IUBMB life 61(11):1029–1042

40. Glazer AN (1989) Light guides. directional energy transfer in a photosynthetic antenna. J Biol Chem 264(1):1–4
41. Shu X, Royant A, Lin MZ, Aguilera TA, Lev-Ram V, Steinbach PA, Tsien RY (2009) Mammalian expression of infrared fluorescent proteins engineered from a bacterial phytochrome. Science 324(5928):804–807
42. Nienhaus GU (2008) The green fluorescent protein: a key tool to study chemical processes in living cells. Angew Chem Int Ed Engl 47(47):8992–8994
43. Shimomura O (2006) Discovery of green fluorescent protein. Methods Biochem Anal 47:1–13
44. Shimomura O, Johnson FH, Saiga Y (1962) Extraction, purification and properties of aequorin, a bioluminescent protein from the luminous hydromedusan, Aequorea. J Cell Comp Physiol 59:223–239
45. Shimomura O (1979) FEBS Letters 104:220–222
46. Prasher DC, Eckenrode VK, Ward WW, Prendergast FG, Cormier MJ (1992) Primary structure of the Aequorea victoria green-fluorescent protein. Gene 111(2):229–233
47. Chalfie M, Tu Y, Euskirchen G, Ward WW, Prasher DC (1994) Green fluorescent protein as a marker for gene expression. Science 263(5148):802–805
48. Tsien RY (2009) Constructing and exploiting the fluorescent protein paintbox (Nobel Lecture). Angew Chem Int Ed Engl 48(31):5612–5626
49. Wiedenmann J (1997) Die Anwendung eines fluoreszierenden Proteins und weiterer farbiger Proteine und der zugehörigen Gene aus der Artengruppe Anemonia sp. (sulcata) Pennant, (Cnidaria, Anthozoa, Actinaria) in Gentechnologie und Molekularbiologie. Offenlegungsschrift DE 197 18 640 A1, Deutsches Patent- und Markenamt, pp 1–18
50. Matz MV, Fradkov AF, Labas YA, Savitsky AP, Zaraisky AG, Markelov ML, Lukyanov SA (1999) Fluorescent proteins from nonbioluminescent Anthozoa species. Nat Biotechnol 17 (10):969–973
51. Shagin DA, Barsova EV, Yanushevich YG, Fradkov AF, Lukyanov KA, Labas YA, Semenova TN, Ugalde JA, Meyers A, Nunez JM, Widder EA, Lukyanov SA, Matz MV (2004) GFP-like proteins as ubiquitous metazoan superfamily: evolution of functional features and structural complexity. Mol Biol Evol 21(5):841–850
52. Haddock SH, Mastroianni N, Christianson LM (2010) A photoactivatable green-fluorescent protein from the phylum Ctenophora. Proc Biol Sci 277(1685):1155–1160
53. Deheyn DD, Kubokawa K, McCarthy JK, Murakami A, Porrachia M, Rouse GW, Holland ND (2007) Endogenous green fluorescent protein (GFP) in amphioxus. Biol Bull 213 (2):95–100
54. Lukyanov KA, Chudakov DM, Lukyanov S, Verkhusha VV (2005) Innovation: Photoactivatable fluorescent proteins. Nat Rev Mol Cell Biol 6(11):885–891
55. Lippincott-Schwartz J, Patterson GH (2008) Fluorescent proteins for photoactivation experiments. Methods Cell Biol 85:45–61
56. Lippincott-Schwartz J, Patterson GH (2009) Photoactivatable fluorescent proteins for diffraction-limited and super-resolution imaging. Trends Cell Biol 19(11):555–565
57. Ormö M, Cubitt AB, Kallio K, Gross LA, Tsien RY, Remington SJ (1996) Crystal structure of the Aequorea victoria green fluorescent protein. Science 273(5280):1392–1395
58. Yang F, Moss LG, Phillips GN Jr (1996) The molecular structure of green fluorescent protein. Nat Biotechnol 14(10):1246–1251
59. Tsien RY (1998) The green fluorescent protein. Annu Rev Biochem 67:509–544
60. Loening AM, Fenn TD, Gambhir SS (2007) Crystal structures of the luciferase and green fluorescent protein from Renilla reniformis. J Mol Biol 374(4):1017–1028
61. Baird GS, Zacharias DA, Tsien RY (2000) Biochemistry, mutagenesis, and oligomerization of DsRed, a red fluorescent protein from coral. Proc Natl Acad Sci U S A 97 (22):11984–11989
62. Vrzheshch PV, Akovbian NA, Varfolomeyev SD, Verkhusha VV (2000) Denaturation and partial renaturation of a tightly tetramerized DsRed protein under mildly acidic conditions. FEBS Lett 487(2):203–208

63. Wall MA, Socolich M, Ranganathan R (2000) The structural basis for red fluorescence in the tetrameric GFP homolog DsRed. Nat Struct Biol 7(12):1133–1138
64. Yarbrough D, Wachter RM, Kallio K, Matz MV, Remington SJ (2001) Refined crystal structure of DsRed, a red fluorescent protein from coral, at 2.0-Å resolution. Proc Natl Acad Sci U S A 98(2):462–467
65. Nienhaus GU, Wiedenmann J (2009) Structure, dynamics and optical properties of fluorescent proteins: perspectives for marker development. ChemPhysChem 10(9–10):1369–1379
66. Nienhaus GU, Nienhaus K, Hölzle A, Ivanchenko S, Renzi F, Oswald F, Wolff M, Schmitt F, Röcker C, Vallone B, Weidemann W, Heilker R, Nar H, Wiedenmann J (2006) Photoconvertible fluorescent protein EosFP: biophysical properties and cell biology applications. Photochem Photobiol 82(2):351–358
67. Verkhusha VV, Lukyanov KA (2004) The molecular properties and applications of Anthozoa fluorescent proteins and chromoproteins. Nat Biotechnol 22(3):289–296
68. Youvan DC, Michel-Beyerle ME (1996) Structure and fluorescence mechanism of GFP. Nat Biotechnol 14(10):1219–1220
69. Nienhaus GU (2010) The "wiggling and jiggling of atoms" leading to excited-state proton transfer in green fluorescent protein. ChemPhysChem 11(5):971–974
70. Lossau H, Kummer A, Heinecke R, Pollinger-Dammer F, Kompa C, Bieser G, Jonsson T, Silva CM, Yang MM, Youvan DC, Michel-Beyerle ME (1996) Time-resolved spectroscopy of wild-type and mutant green fluorescent proteins reveals excited state deprotonation consistent with fluorophore-protein interactions. Chem Phys 213(1–3):1–16
71. Ai HW, Shaner NC, Cheng Z, Tsien RY, Campbell RE (2007) Exploration of new chromophore structures leads to the identification of improved blue fluorescent proteins. Biochemistry 46(20):5904–5910
72. Gross LA, Baird GS, Hoffman RC, Baldridge KK, Tsien RY (2000) The structure of the chromophore within DsRed, a red fluorescent protein from coral. Proc Natl Acad Sci U S A 97(22):11990–11995
73. Wiedenmann J, Schenk A, Röcker C, Girod A, Spindler KD, Nienhaus GU (2002) A far-red fluorescent protein with fast maturation and reduced oligomerization tendency from Entacmaea quadricolor (Anthozoa, Actinaria). Proc Natl Acad Sci USA 99(18):11646–11651
74. Abbyad P, Childs W, Shi X, Boxer SG (2007) Dynamic Stokes shift in green fluorescent protein variants. Proc Natl Acad Sci U S A 104(51):20189–20194
75. Shu X, Shaner NC, Yarbrough CA, Tsien RY, Remington SJ (2006) Novel chromophores and buried charges control color in mFruits. Biochemistry 45(32):9639–9646
76. Remington SJ, Wachter RM, Yarbrough DK, Branchaud B, Anderson DC, Kallio K, Lukyanov KA (2005) zFP538, a yellow-fluorescent protein from Zoanthus, contains a novel three-ring chromophore. Biochemistry 44(1):202–212
77. Kikuchi A, Fukumura E, Karasawa S, Mizuno H, Miyawaki A, Shiro Y (2008) Structural characterization of a thiazoline-containing chromophore in an orange fluorescent protein, monomeric Kusabira Orange. Biochemistry 47(44):11573–11580
78. Lukyanov KA, Fradkov AF, Gurskaya NG, Matz MV, Labas YA, Savitsky AP, Markelov ML, Zaraisky AG, Zhao X, Fang Y, Tan W, Lukyanov SA (2000) Natural animal coloration can be determined by a nonfluorescent green fluorescent protein homolog. J Biol Chem 275 (34):25879–25882
79. Quillin ML, Anstrom DM, Shu X, O'Leary S, Kallio K, Chudakov DM, Remington SJ (2005) Kindling fluorescent protein from Anemonia sulcata: dark-state structure at 1.38 Å resolution. Biochemistry 44(15):5774–5787
80. Wilmann PG, Petersen J, Devenish RJ, Prescott M, Rossjohn J (2005) Variations on the GFP chromophore: A polypeptide fragmentation within the chromophore revealed in the 2.1-Å crystal structure of a nonfluorescent chromoprotein from Anemonia sulcata. J Biol Chem 280 (4):2401–2404

81. Andresen M, Wahl MC, Stiel AC, Grater F, Schäfer LV, Trowitzsch S, Weber G, Eggeling C, Grubmüller H, Hell SW, Jakobs S (2005) Structure and mechanism of the reversible photoswitch of a fluorescent protein. Proc Natl Acad Sci U S A 102(37):13070–13074
82. Heim R, Prasher DC, Tsien RY (1994) Wavelength mutations and posttranslational autoxidation of green fluorescent protein. Proc Natl Acad Sci U S A 91(26):12501–12504
83. Heim R, Tsien RY (1996) Engineering green fluorescent protein for improved brightness, longer wavelengths and fluorescence resonance energy transfer. Curr Biol 6(2):178–182
84. Subach OM, Gundorov IS, Yoshimura M, Subach FV, Zhang J, Gruenwald D, Souslova EA, Chudakov DM, Verkhusha VV (2008) Conversion of red fluorescent protein into a bright blue probe. Chem Biol 15(10):1116–1124
85. Subach FV, Patterson GH, Renz M, Lippincott-Schwartz J, Verkhusha VV (2010) Bright monomeric photoactivatable red fluorescent protein for two-color super-resolution sptPALM of live cells. J Am Chem Soc 132(18):6481–6491
86. Kajihara D, Hohsaka T, Sisido M (2005) Synthesis and sequence optimization of GFP mutants containing aromatic non-natural amino acids at the Tyr66 position. Protein Eng Des Sel 18(6):273–278
87. Goulding A, Shrestha S, Dria K, Hunt E, Deo SK (2008) Red fluorescent protein variants with incorporated non-natural amino acid analogues. Protein Eng Des Sel 21(2):101–106
88. Bae JH, Rubini M, Jung G, Wiegand G, Seifert MH, Azim MK, Kim JS, Zumbusch A, Holak TA, Moroder L, Huber R, Budisa N (2003) Expansion of the genetic code enables design of a novel "gold" class of green fluorescent proteins. J Mol Biol 328(5):1071–1081
89. Zacharias DA, Violin JD, Newton AC, Tsien RY (2002) Partitioning of lipid-modified monomeric GFPs into membrane microdomains of live cells. Science 296(5569):913–916
90. Wiedenmann J, Vallone B, Renzi F, Nienhaus K, Ivanchenko S, Röcker C, Nienhaus GU (2005) The red fluorescent protein eqFP611 and its genetically engineered dimeric variants. J Biomed Optics 10:014003, 014007 pages
91. Kredel S, Oswald F, Nienhaus K, Deuschle K, Röcker C, Wolff M, Heilker R, Nienhaus GU, Wiedenmann J (2009) mRuby, a bright monomeric red fluorescent protein for labeling of subcellular structures. PLoS One 4(2):e4391
92. Campbell RE, Tour O, Palmer AE, Steinbach PA, Baird GS, Zacharias DA, Tsien RY (2002) A monomeric red fluorescent protein. Proc Natl Acad Sci USA 99(12):7877–7882
93. Fradkov AF, Verkhusha VV, Staroverov DB, Bulina ME, Yanushevich YG, Martynov VI, Lukyanov S, Lukyanov KA (2002) Far-red fluorescent tag for protein labelling. Biochem J 368(1):17–21
94. Shaner NC, Campbell RE, Steinbach PA, Giepmans BN, Palmer AE, Tsien RY (2004) Improved monomeric red, orange and yellow fluorescent proteins derived from Discosoma sp. red fluorescent protein. Nat Biotechnol 22(12):1567–1572
95. Kogure T, Kawano H, Abe Y, Miyawaki A (2008) Fluorescence imaging using a fluorescent protein with a large Stokes shift. Methods 45(3):223–226
96. Shcherbo D, Murphy CS, Ermakova GV, Solovieva EA, Chepurnykh TV, Shcheglov AS, Verkhusha VV, Pletnev VZ, Hazelwood KL, Roche PM, Lukyanov S, Zaraisky AG, Davidson MW, Chudakov DM (2009) Far-red fluorescent tags for protein imaging in living tissues. Biochem J 418(3):567–574
97. Bulina ME, Verkhusha VV, Staroverov DB, Chudakov DM, Lukyanov KA (2003) Hetero-oligomeric tagging diminishes non-specific aggregation of target proteins fused with Anthozoa fluorescent proteins. Biochem J 371:109–114
98. Nagai T, Ibata K, Park ES, Kubota M, Mikoshiba K, Miyawaki A (2002) A variant of yellow fluorescent protein with fast and efficient maturation for cell-biological applications. Nat Biotechnol 20(1):87–90
99. Evdokimov AG, Pokross ME, Egorov NS, Zaraisky AG, Yampolsky IV, Merzlyak EM, Shkoporov AN, Sander I, Lukyanov KA, Chudakov DM (2006) Structural basis for the fast maturation of Arthropoda green fluorescent protein. EMBO Rep 7(10):1006–1012

100. Terskikh A, Fradkov A, Ermakova G, Zaraisky A, Tan P, Kajava AV, Zhao X, Lukyanov S, Matz M, Kim S, Weissman I, Siebert P (2000) "Fluorescent timer": protein that changes color with time. Science 290(5496):1585–1588
101. Pletnev S, Subach FV, Dauter Z, Wlodawer A, Verkhusha VV (2010) Understanding blue-to-red conversion in monomeric fluorescent timers and hydrolytic degradation of their chromophores. J Am Chem Soc 132(7):2243–2253
102. Subach FV, Subach OM, Gundorov IS, Morozova KS, Piatkevich KD, Cuervo AM, Verkhusha VV (2009) Monomeric fluorescent timers that change color from blue to red report on cellular trafficking. Nat Chem Biol 5(2):118–126
103. Yu J, Xiao J, Ren X, Lao K, Xie XS (2006) Probing gene expression in live cells, one protein molecule at a time. Science 311(5767):1600–1603
104. Yang TT, Sinai P, Green G, Kitts PA, Chen YT, Lybarger L, Chervenak R, Patterson GH, Piston DW, Kain SR (1998) Improved fluorescence and dual color detection with enhanced blue and green variants of the green fluorescent protein. J Biol Chem 273(14):8212–8216
105. Pedelacq JD, Cabantous S, Tran T, Terwilliger TC, Waldo GS (2006) Engineering and characterization of a superfolder green fluorescent protein. Nat Biotechnol 24(1):79–88
106. Kredel S, Nienhaus K, Wolff M, Oswald F, Ivanchenko S, Cymer F, Jeromin A, Michel FJ, Spindler K-D, Heilker R, Nienhaus GU, Wiedenmann J (2008) Optimized and far-red emitting variants of fluorescent protein eqFP611. Chem Biol 15:224–233
107. Fuchs J, Böhme S, Oswald F, Hedde PN, Krause M, Wiedenmann J, Nienhaus GU (2010) A photoactivatable marker protein for pulse-chase imaging with superresolution. Nat Methods 7:627–630
108. Chudakov DM, Matz MV, Lukyanov S, Lukyanov KA (2010) Fluorescent proteins and their applications in imaging living cells and tissues. Physiol Rev 90(3):1103–1163
109. Shaner NC, Lin MZ, McKeown MR, Steinbach PA, Hazelwood KL, Davidson MW, Tsien RY (2008) Improving the photostability of bright monomeric orange and red fluorescent proteins. Nat Methods 5(6):545–551
110. Ai HW, Henderson JN, Remington SJ, Campbell RE (2006) Directed evolution of a monomeric, bright and photostable version of Clavularia cyan fluorescent protein: structural characterization and applications in fluorescence imaging. Biochem J 400(3):531–540
111. Bizzarri R, Serresi M, Luin S, Beltram F (2009) Green fluorescent protein based pH indicators for in vivo use: a review. Anal Bioanal Chem 393(4):1107–1122
112. Link CD, Fonte V, Hiester B, Yerg J, Ferguson J, Csontos S, Silverman MA, Stein GH (2006) Conversion of green fluorescent protein into a toxic, aggregation-prone protein by C-terminal addition of a short peptide. J Biol Chem 281(3):1808–1816
113. Katayama H, Yamamoto A, Mizushima N, Yoshimori T, Miyawaki A (2008) GFP-like proteins stably accumulate in lysosomes. Cell Struct Funct 33(1):1–12
114. Remington SJ (2006) Fluorescent proteins: maturation, photochemistry and photophysics. Curr Opin Struct Biol 16(6):714–721
115. Ragas X, Cooper LP, White JH, Nonell S, Flors C (2011) Quantification of photosensitized singlet oxygen production by a fluorescent protein. ChemPhysChem 12(1):161–165
116. Jimenez-Banzo A, Ragas X, Abbruzzetti S, Viappiani C, Campanini B, Flors C, Nonell S (2010) Singlet oxygen photosensitisation by GFP mutants: oxygen accessibility to the chromophore. Photochem Photobiol Sci 9(10):1336–1341
117. Bulina ME, Chudakov DM, Britanova OV, Yanushevich YG, Staroverov DB, Chepurnykh TV, Merzlyak EM, Shkrob MA, Lukyanov S, Lukyanov KA (2006) A genetically encoded photosensitizer. Nat Biotechnol 24(1):95–99
118. Tour O, Meijer RM, Zacharias DA, Adams SR, Tsien RY (2003) Genetically targeted chromophore-assisted light inactivation. Nat Biotechnol 21(12):1505–1508
119. Lippincott-Schwartz J, Patterson GH (2003) Development and use of fluorescent protein markers in living cells. Science 300(5616):87–91
120. Shaner NC, Patterson GH, Davidson MW (2007) Advances in fluorescent protein technology. J Cell Sci 120(24):4247–4260

121. Tomosugi W, Matsuda T, Tani T, Nemoto T, Kotera I, Saito K, Horikawa K, Nagai T (2009) An ultramarine fluorescent protein with increased photostability and pH insensitivity. Nat Methods 6(5):351–353
122. Stephens DJ, Allan VJ (2003) Light microscopy techniques for live cell imaging. Science 300 (5616):82–86
123. Kremers GJ, Goedhart J, van den Heuvel DJ, Gerritsen HC, Gadella TW Jr (2007) Improved green and blue fluorescent proteins for expression in bacteria and mammalian cells. Biochemistry 46(12):3775–3783
124. Mena MA, Treynor TP, Mayo SL, Daugherty PS (2006) Blue fluorescent proteins with enhanced brightness and photostability from a structurally targeted library. Nat Biotechnol 24(12):1569–1571
125. Rizzo MA, Springer GH, Granada B, Piston DW (2004) An improved cyan fluorescent protein variant useful for FRET. Nat Biotechnol 22(4):445–449
126. Kremers GJ, Goedhart J, van Munster EB, Gadella TW Jr (2006) Cyan and yellow super fluorescent proteins with improved brightness, protein folding, and FRET Forster radius. Biochemistry 45(21):6570–6580
127. Goedhart J, van Weeren L, Hink MA, Vischer NO, Jalink K, Gadella TW Jr (2010) Bright cyan fluorescent protein variants identified by fluorescence lifetime screening. Nat Methods 7 (2):137–139
128. Heim R, Cubitt AB, Tsien RY (1995) Improvement of green fluorescent protein by site-directed mutations. Nature 373(6516):663–664
129. Ai HW, Olenych SG, Wong P, Davidson MW, Campbell RE (2008) Hue-shifted monomeric variants of Clavularia cyan fluorescent protein: identification of the molecular determinants of color and applications in fluorescence imaging. BMC Biol 6:13
130. Cubitt AB, Heim R, Adams SR, Boyd AE, Gross LA, Tsien RY (1995) Understanding, improving and using green fluorescent proteins. Trends Biochem Sci 20(11):448–455
131. Griesbeck O, Baird GS, Campbell RE, Zacharias DA, Tsien RY (2001) Reducing the environmental sensitivity of yellow fluorescent protein. Mechanism and applications. J Biol Chem 276(31):29188–29194
132. Cubitt AB, Woollenweber LA, Heim R (1999) Understanding structure-function relationships in the Aequorea victoria green fluorescent protein. Methods Cell Biol 58:19–30
133. Shcherbo D, Souslova EA, Goedhart J, Chepurnykh TV, Gaintzeva A, Shemiakina II, Gadella TW, Lukyanov S, Chudakov DM (2009) Practical and reliable FRET/FLIM pair of fluorescent proteins. BMC Biotechnol 9:24
134. Nguyen AW, Daugherty PS (2005) Evolutionary optimization of fluorescent proteins for intracellular FRET. Nat Biotechnol 23(3):355–360
135. Ohashi T, Galiacy SD, Briscoe G, Erickson HP (2007) An experimental study of GFP-based FRET, with application to intrinsically unstructured proteins. Protein Sci 16 (7):1429–1438
136. Karasawa S, Araki T, Nagai T, Mizuno H, Miyawaki A (2004) Cyan-emitting and orange-emitting fluorescent proteins as a donor/acceptor pair for fluorescence resonance energy transfer. Biochem J 381(1):307–312
137. Sakaue-Sawano A, Kurokawa H, Morimura T, Hanyu A, Hama H, Osawa H, Kashiwagi S, Fukami K, Miyata T, Miyoshi H, Imamura T, Ogawa M, Masai H, Miyawaki A (2008) Visualizing spatiotemporal dynamics of multicellular cell-cycle progression. Cell 132 (3):487–498
138. Merzlyak EM, Goedhart J, Shcherbo D, Bulina ME, Shcheglov AS, Fradkov AF, Gaintzeva A, Lukyanov KA, Lukyanov S, Gadella TW, Chudakov DM (2007) Bright monomeric red fluorescent protein with an extended fluorescence lifetime. Nat Methods 4(7):555–557
139. Kogure T, Karasawa S, Araki T, Saito K, Kinjo M, Miyawaki A (2006) A fluorescent variant of a protein from the stony coral Montipora facilitates dual-color single-laser fluorescence cross-correlation spectroscopy. Nat Biotechnol 24(5):577–581

140. Wang L, Jackson WC, Steinbach PA, Tsien RY (2004) Evolution of new nonantibody proteins via iterative somatic hypermutation. Proc Natl Acad Sci U S A 101 (48):16745–16749
141. Lin MZ, McKeown MR, Ng HL, Aguilera TA, Shaner NC, Campbell RE, Adams SR, Gross LA, Ma W, Alber T, Tsien RY (2009) Autofluorescent proteins with excitation in the optical window for intravital imaging in mammals. Chem Biol 16(11):1169–1179
142. Morozova KS, Piatkevich KD, Gould TJ, Zhang J, Bewersdorf J, Verkhusha VV (2010) Far-red fluorescent protein excitable with red lasers for flow cytometry and superresolution STED nanoscopy. Biophys J 99(2):L13–L15
143. van Thor JJ, Gensch T, Hellingwerf KJ, Johnson LN (2002) Phototransformation of green fluorescent protein with UV and visible light leads to decarboxylation of glutamate 222. Nat Struct Biol 9(1):37–41
144. Bell AF, Stoner-Ma D, Wachter RM, Tonge PJ (2003) Light-driven decarboxylation of wild-type green fluorescent protein. J Am Chem Soc 125(23):6919–6926
145. Chattoraj M, King BA, Bublitz GU, Boxer SG (1996) Ultra-fast excited state dynamics in green fluorescent protein: multiple states and proton transfer. Proc Natl Acad Sci USA 93 (16):8362–8367
146. Creemers TMH, Lock AJ, Subramaniam V, Jovin TM, Völker S (1999) Three photoconvertible forms of green fluorescent protein identified by spectral hole-burning. Nat Struct Biol 6(7):557–560
147. Yokoe H, Meyer T (1996) Spatial dynamics of GFP-tagged proteins investigated by local fluorescence enhancement. Nat Biotechnol 14(10):1252–1256
148. Ehrig T, O'Kane DJ, Prendergast FG (1995) Green-fluorescent protein mutants with altered fluorescence excitation spectra. FEBS Lett 367(2):163–166
149. Patterson GH, Lippincott-Schwartz J (2002) A photoactivatable GFP for selective photolabeling of proteins and cells. Science 297(5588):1873–1877
150. Chen Y, MacDonald PJ, Skinner JP, Patterson GH, Muller JD (2006) Probing nucleocytoplasmic transport by two-photon activation of PA-GFP. Microsc Res Tech 69 (3):220–226
151. Demarco IA, Periasamy A, Booker CF, Day RN (2006) Monitoring dynamic protein interactions with photoquenching FRET. Nat Methods 3(7):519–524
152. Diaspro A, Testa I, Faretta M, Magrassi R, Barozzi S, Parazzoli D, Vicidomini G (2006) 3D localized photoactivation of pa-GFP in living cells using two-photon interactions. Conf Proc IEEE Eng Med Biol Soc 1:389–391
153. Martini J, Schmied K, Palmisano R, Toensing K, Anselmetti D, Merkle T (2007) Multifocal two-photon laser scanning microscopy combined with photo-activatable GFP for in vivo monitoring of intracellular protein dynamics in real time. J Struct Biol 158(3):401–409
154. Matsuda T, Miyawaki A, Nagai T (2008) Direct measurement of protein dynamics inside cells using a rationally designed photoconvertible protein. Nat Methods 5(4):339–345
155. Patterson GH, Lippincott-Schwartz J (2004) Selective photolabeling of proteins using photoactivatable GFP. Methods 32(4):445–450
156. Tulu US, Rusan NM, Wadsworth P (2003) Peripheral, non-centrosome-associated microtubules contribute to spindle formation in centrosome-containing cells. Curr Biol 13 (21):1894–1899
157. Subach FV, Patterson GH, Manley S, Gillette JM, Lippincott-Schwartz J, Verkhusha VV (2009) Photoactivatable mCherry for high-resolution two-color fluorescence microscopy. Nat Methods 6(2):153–159
158. Verkhusha VV, Sorkin A (2005) Conversion of the monomeric red fluorescent protein into a photoactivatable probe. Chem Biol 12(3):279–285
159. Subach FV, Malashkevich VN, Zencheck WD, Xiao H, Filonov GS, Almo SC, Verkhusha VV (2009) Photoactivation mechanism of PAmCherry based on crystal structures of the protein in the dark and fluorescent states. Proc Natl Acad Sci U S A 106(50):21097–21102

160. Pouwels LJ, Zhang L, Chan NH, Dorrestein PC, Wachter RM (2008) Kinetic isotope effect studies on the de novo rate of chromophore formation in fast- and slow-maturing GFP variants. Biochemistry 47(38):10111–10122
161. Gurskaya NG, Fradkov AF, Pounkova NI, Staroverov DB, Bulina ME, Yanushevich YG, Labas YA, Lukyanov S, Lukyanov KA (2003) A colourless green fluorescent protein homologue from the non-fluorescent hydromedusa Aequorea coerulescens and its fluorescent mutants. Biochem J 373(2):403–408
162. Chudakov DM, Verkhusha VV, Staroverov DB, Souslova EA, Lukyanov S, Lukyanov KA (2004) Photoswitchable cyan fluorescent protein for protein tracking. Nat Biotechnol 22 (11):1435–1439
163. Shroff H, Galbraith CG, Galbraith JA, White H, Gillette J, Olenych S, Davidson MW, Betzig E (2007) Dual-color superresolution imaging of genetically expressed probes within individual adhesion complexes. Proc Natl Acad Sci U S A 104(51):20308–20313
164. Cormack BP, Valdivia RH, Falkow S (1996) FACS-optimized mutants of the green fluorescent protein (GFP). Gene 173(1):33–38
165. Crameri A, Whitehorn EA, Tate E, Stemmer WP (1996) Improved green fluorescent protein by molecular evolution using DNA shuffling. Nat Biotechnol 14(3):315–319
166. Elowitz MB, Surette MG, Wolf PE, Stock J, Leibler S (1997) Photoactivation turns green fluorescent protein red. Curr Biol 7(10):809–812
167. Jakobs S, Schauss AC, Hell SW (2003) Photoconversion of matrix targeted GFP enables analysis of continuity and intermixing of the mitochondrial lumen. FEBS Lett 554 (1–2):194–200
168. Kiseleva Iu V, Mishin AS, Bogdanov AM, Labas Iu A, Luk'ianov KA (2008) The ability of green fluorescent proteins for photoconversion under oxygen-free conditions is determined by the chromophore structure rather than its amino acid environment]. Bioorg Khim 34(5):711–715
169. Bogdanov AM, Mishin AS, Yampolsky IV, Belousov VV, Chudakov DM, Subach FV, Verkhusha VV, Lukyanov S, Lukyanov KA (2009) Green fluorescent proteins are light-induced electron donors. Nat Chem Biol 5(7):459–461
170. Ando R, Hama H, Yamamoto-Hino M, Mizuno H, Miyawaki A (2002) An optical marker based on the UV-induced green-to-red photoconversion of a fluorescent protein. Proc Natl Acad Sci USA 99(20):12651–12656
171. Gurskaya NG, Verkhusha VV, Shcheglov AS, Staroverov DB, Chepurnykh TV, Fradkov AF, Lukyanov S, Lukyanov KA (2006) Engineering of a monomeric green-to-red photoactivatable fluorescent protein induced by blue light. Nat Biotechnol 24(4):461–465
172. Tsutsui H, Karasawa S, Shimizu H, Nukina N, Miyawaki A (2005) Semi-rational engineering of a coral fluorescent protein into an efficient highlighter. EMBO Rep 6(3):233–238
173. Wiedenmann J, Ivanchenko S, Oswald F, Schmitt F, Röcker C, Salih A, Spindler KD, Nienhaus GU (2004) EosFP, a fluorescent marker protein with UV-inducible green-to-red fluorescence conversion. Proc Natl Acad Sci U S A 101(45):15905–15910
174. Mizuno H, Mal TK, Tong KI, Ando R, Furuta T, Ikura M, Miyawaki A (2003) Photo-induced peptide cleavage in the green-to-red conversion of a fluorescent protein. Mol Cell 12 (4):1051–1058
175. Nienhaus K, Nienhaus GU, Wiedenmann J, Nar H (2005) Structural basis for photo-induced protein cleavage and green-to-red conversion of fluorescent protein EosFP. Proc Natl Acad Sci U S A 102(26):9156–9159
176. Hayashi I, Mizuno H, Tong KI, Furuta T, Tanaka F, Yoshimura M, Miyawaki A, Ikura M (2007) Crystallographic evidence for water-assisted photo-induced peptide cleavage in the stony coral fluorescent protein Kaede. J Mol Biol 372(4):918–926
177. Li X, Chung LW, Mizuno H, Miyawaki A, Morokuma K (2010) Competitive mechanistic pathways for green-to-red photoconversion in the fluorescent protein kaede: a computational study. J Phys Chem B 114(49):16666–16675
178. Lelimousin M, Adam V, Nienhaus GU, Bourgeois D, Field MJ (2009) Photoconversion of the fluorescent protein EosFP: a hybrid potential simulation study reveals intersystem crossings. J Am Chem Soc 131(46):16814–16823

179. Adam V, Nienhaus K, Bourgeois D, Nienhaus GU (2009) Structural basis of enhanced photoconversion yield in green fluorescent protein-like protein Dendra2. Biochemistry 48 (22):4905–4915
180. Chudakov DM, Lukyanov S, Lukyanov KA (2007) Tracking intracellular protein movements using photoswitchable fluorescent proteins PS-CFP2 and Dendra2. Nat Protoc 2 (8):2024–2032
181. Kedrin D, Gligorijevic B, Wyckoff J, Verkhusha VV, Condeelis J, Segall JE, van Rheenen J (2008) Intravital imaging of metastatic behavior through a mammary imaging window. Nat Methods 5(12):1019–1021
182. Wacker SA, Oswald F, Wiedenmann J, Knochel W (2007) A green to red photoconvertible protein as an analyzing tool for early vertebrate development. Dev Dyn 236(2):473–480
183. Wiedenmann J, Nienhaus GU (2006) Live-cell imaging with EosFP and other photoactivatable marker proteins of the GFP family. Expert Rev Proteomics 3(3):361–374
184. McKinney SA, Murphy CS, Hazelwood KL, Davidson MW, Looger LL (2009) A bright and photostable photoconvertible fluorescent protein. Nat Methods 6(2):131–133
185. Wiedenmann J, Gayda S, Adam V, Oswald F, Nienhaus K, Bourgeois D, Nienhaus GU (2011) From EosFP to mIrisFP: structure-based development of advanced photoactivatable marker proteins of the GFP-family. J Biophot 4:377–390
186. Wacker SA, Alvarado C, von Wichert G, Knippschild U, Wiedenmann J, Clauss K, Nienhaus GU, Hameister H, Baumann B, Borggrefe T, Knöchel W, Oswald F (2011) RITA, a novel modulator of Notch signalling, acts via nuclear export of RBP-J. EMBO J 30(1):43–56
187. Nowotschin S, Hadjantonakis AK (2009) Use of KikGR a photoconvertible green-to-red fluorescent protein for cell labeling and lineage analysis in ES cells and mouse embryos. BMC Dev Biol 9:49
188. Habuchi S, Tsutsui H, Kochaniak AB, Miyawaki A, van Oijen AM (2008) mKikGR, a monomeric photoswitchable fluorescent protein. PLoS ONE 3(12):e3944
189. Stark DA, Kulesa PM (2007) An in vivo comparison of photoactivatable fluorescent proteins in an avian embryo model. Dev Dyn 236(6):1583–1594
190. Dickson RM, Cubitt AB, Tsien RY, Moerner WE (1997) On/off blinking and switching behaviour of single molecules of green fluorescent protein. Nature 388(6640):355–358
191. Stiel AC, Trowitzsch S, Weber G, Andresen M, Eggeling C, Hell SW, Jakobs S, Wahl MC (2007) 1.8 A bright-state structure of the reversibly switchable fluorescent protein Dronpa guides the generation of fast switching variants. Biochem J 402(1):35–42
192. Habuchi S, Ando R, Dedecker P, Verheijen W, Mizuno H, Miyawaki A, Hofkens J (2005) Reversible single-molecule photoswitching in the GFP-like fluorescent protein Dronpa. Proc Natl Acad Sci U S A 102(27):9511–9516
193. Adam V, Lelimousin M, Boehme S, Desfonds G, Nienhaus K, Field MJ, Wiedenmann J, McSweeney S, Nienhaus GU, Bourgeois D (2008) Structural characterization of IrisFP, an optical highlighter undergoing multiple photo-induced transformations. Proc Natl Acad Sci U S A 105(47):18343–18348
194. Andresen M, Stiel AC, Trowitzsch S, Weber G, Eggeling C, Wahl MC, Hell SW, Jakobs S (2007) Structural basis for reversible photoswitching in Dronpa. Proc Natl Acad Sci U S A 104(32):13005–13009
195. Li X, Chung LW, Mizuno H, Miyawaki A, Morokuma K (2010) A theoretical study on the nature of on- and off-states of reversibly photoswitching fluorescent protein Dronpa: absorption, emission, protonation, and Raman. J Phys Chem B 114(2):1114–1126
196. Wilmann PG, Turcic K, Battad JM, Wilce MC, Devenish RJ, Prescott M, Rossjohn J (2006) The 1.7 A crystal structure of Dronpa: a photoswitchable green fluorescent protein. J Mol Biol 364(2):213–224
197. Abbruzzetti S, Bizzarri R, Luin S, Nifosi R, Storti B, Viappiani C, Beltram F (2010) Photoswitching of E222Q GFP mutants: "concerted" mechanism of chromophore isomerization and protonation. Photochem Photobiol Sci 9(10):1307–1319

198. Chudakov DM, Feofanov AV, Mudrik NN, Lukyanov S, Lukyanov KA (2003) Chromophore environment provides clue to "kindling fluorescent protein" riddle. J Biol Chem 278 (9):7215–7219
199. Schäfer LV, Groenhof G, Klingen AR, Ullmann GM, Boggio-Pasqua M, Robb MA, Grubmüller H (2007) Photoswitching of the fluorescent protein asFP595: mechanism, proton pathways, and absorption spectra. Angew Chem Int Ed Engl 46:530–536
200. Voliani V, Bizzarri R, Nifosi R, Abbruzzetti S, Grandi E, Viappiani C, Beltram F (2008) Cis-trans photoisomerization of fluorescent-protein chromophores. J Phys Chem B 112 (34):10714–10722
201. He X, Bell AF, Tonge PJ (2003) Ground state isomerization of a model green fluorescent protein chromophore. FEBS Lett 549(1–3):35–38
202. Stiel AC, Andresen M, Bock H, Hilbert M, Schilde J, Schonle A, Eggeling C, Egner A, Hell SW, Jakobs S (2008) Generation of monomeric reversibly switchable red fluorescent proteins for far-field fluorescence nanoscopy. Biophys J 95(6):2989–2997
203. Ando R, Mizuno H, Miyawaki A (2004) Regulated fast nucleocytoplasmic shuttling observed by reversible protein highlighting. Science 306(5700):1370–1373
204. Bock H, Geisler C, Wurm CA, von Middendorff C, Jakobs S, Schönle A, Egner A, Hell SW, Eggeling C (2007) Two-color far-field fluorescence nanoscopy based on photoswitchable emitters. Appl Phys B 88:161–165
205. Andresen M, Stiel AC, Folling J, Wenzel D, Schonle A, Egner A, Eggeling C, Hell SW, Jakobs S (2008) Photoswitchable fluorescent proteins enable monochromatic multilabel imaging and dual color fluorescence nanoscopy. Nat Biotechnol 26(9):1035–1040
206. Subach FV, Zhang L, Gadella TW, Gurskaya NG, Lukyanov KA, Verkhusha VV (2010) Red fluorescent protein with reversibly photoswitchable absorbance for photochromic FRET. Chem Biol 17(7):745–755
207. Chudakov DM, Belousov VV, Zaraisky AG, Novoselov VV, Staroverov DB, Zorov DB, Lukyanov S, Lukyanov KA (2003) Kindling fluorescent proteins for precise in vivo photolabeling. Nat Biotechnol 21(2):191–194
208. Henderson JN, Ai HW, Campbell RE, Remington SJ (2007) Structural basis for reversible photobleaching of a green fluorescent protein homologue. Proc Natl Acad Sci USA 104 (16):6672–6677
209. Shannon CE (1949) Communication in the presence of noise. Proceedings of the IRE 37:10–21
210. Westphal V, Rizzoli SO, Lauterbach MA, Kamin D, Jahn R, Hell SW (2008) Video-rate far-field optical nanoscopy dissects synaptic vesicle movement. Science 320(5873):246–249
211. Hein B, Willig KI, Hell SW (2008) Stimulated emission depletion (STED) nanoscopy of a fluorescent protein-labeled organelle inside a living cell. Proc Natl Acad Sci U S A 105 (38):14271–14276
212. Nägerl UV, Willig KI, Hein B, Hell SW, Bonhoeffer T (2008) Live-cell imaging of dendritic spines by STED microscopy. Proc Natl Acad Sci U S A 105(48):18982–18987
213. Strack RL, Hein B, Bhattacharyya D, Hell SW, Keenan RJ, Glick BS (2009) A rapidly maturing far-red derivative of DsRed-Express2 for whole-cell labeling. Biochemistry 48 (35):8279–8281
214. Klar TA, Jakobs S, Dyba M, Egner A, Hell SW (2000) Fluorescence microscopy with diffraction resolution barrier broken by stimulated emission. Proc Natl Acad Sci U S A 97 (15):8206–8210
215. Schwentker MA, Bock H, Hofmann M, Jakobs S, Bewersdorf J, Eggeling C, Hell SW (2007) Wide-field subdiffraction RESOLFT microscopy using fluorescent protein photoswitching. Microsc Res Tech 70(3):269–280
216. Bates M, Blosser TR, Zhuang X (2005) Short-range spectroscopic ruler based on a single-molecule optical switch. Phys Rev Lett 94(10):108101, 108104 pages
217. Bates M, Huang B, Dempsey GT, Zhuang X (2007) Multicolor super-resolution imaging with photo-switchable fluorescent probes. Science 317(5845):1749–1753

218. Hess ST, Gould TJ, Gudheti MV, Maas SA, Mills KD, Zimmerberg J (2007) Dynamic clustered distribution of hemagglutinin resolved at 40 nm in living cell membranes discriminates between raft theories. Proc Natl Acad Sci U S A 104(44):17370–17375
219. Shroff H, Galbraith CG, Galbraith JA, Betzig E (2008) Live-cell photoactivated localization microscopy of nanoscale adhesion dynamics. Nat Methods 5(5):417–423
220. Manley S, Gillette JM, Patterson GH, Shroff H, Hess HF, Betzig E, Lippincott-Schwartz J (2008) High-density mapping of single-molecule trajectories with photoactivated localization microscopy. Nat Methods 5(2):155–157
221. Niu L, Yu J (2008) Investigating intracellular dynamics of FtsZ cytoskeleton with photoactivation single-molecule tracking. Biophys J 95(4):2009–2016
222. Biteen JS, Thompson MA, Tselentis NK, Bowman GR, Shapiro L, Moerner WE (2008) Super-resolution imaging in live Caulobacter crescentus cells using photoswitchable EYFP. Nat Methods 5(11):947–949
223. Lillemeier B, Mörtelmaier M, Forstner M, Huppa J, Groves J, Davis M (2010) TCR and Lat are expressed on separate protein islands on T cell membranes and concatenate during activation. Nature Immunology 11(1):90–96
224. Schonle A, Hell SW (2007) Fluorescence nanoscopy goes multicolor. Nat Biotechnol 25 (11):1234–1235
225. van de Linde S, Endesfelder U, Mukherjee A, Schuttpelz M, Wiebusch G, Wolter S, Heilemann M, Sauer M (2009) Multicolor photoswitching microscopy for subdiffraction-resolution fluorescence imaging. Photochem Photobiol Sci 8(4):465–469
226. Sinnecker D, Voigt P, Hellwig N, Schaefer M (2005) Reversible photobleaching of enhanced green fluorescent proteins. Biochemistry 44(18):7085–7094
227. Hendrix J, Flors C, Dedecker P, Hofkens J, Engelborghs Y (2008) Dark states in monomeric red fluorescent proteins studied by fluorescence correlation and single molecule spectroscopy. Biophys J 94(10):4103–4113
228. Gunkel M, Erdel F, Rippe K, Lemmer P, Kaufmann R, Hormann C, Amberger R, Cremer C (2009) Dual color localization microscopy of cellular nanostructures. Biotechnol J 4 (6):927–938
229. Xia NS, Luo WX, Zhang J, Xie XY, Yang HJ, Li SW, Chen M, Ng MH (2002) Bioluminescence of Aequorea macrodactyla, a common jellyfish species in the East China Sea. Mar Biotechnol (NY) 4(2):155–162
230. Karasawa S, Araki T, Yamamoto-Hino M, Miyawaki A (2003) A green-emitting fluorescent protein from Galaxeidae coral and its monomeric version for use in fluorescent labeling. J Biol Chem 278(36):34167–34171
231. Shcherbo D, Merzlyak EM, Chepurnykh TV, Fradkov AF, Ermakova GV, Solovieva EA, Lukyanov KA, Bogdanova EA, Zaraisky AG, Lukyanov S, Chudakov DM (2007) Bright far-red fluorescent protein for whole-body imaging. Nat Methods 4(9):741–746

Tailoring Fluorescent Labels for Far-Field Nanoscopy

Dmytro A. Yushchenko and Marcel P. Bruchez

Abstract The choice of the fluorophore to be used in super-resolution far-field nanoscopy is an essential parameter that typically determines the quality of the resulting image. To overcome the diffraction limit, different super-resolution techniques exploit different optical and photochemical phenomena, imposing method-specific requirements for useful probes. The choice of the fluorophore is even more intimately tied to performance for super-resolution imaging in live cells, where both photophysical properties and target-specific labeling inside the cell are essential. In this chapter, we highlight the advances in fluorophore development for a range of existing super-resolution techniques. We discuss the requirements these distinct methods place on the fluorophores in order to achieve optimal resolution, particularly as these methods move toward imaging living cells beyond the diffraction limit.

Keywords Genetic targeting of fluorescent dyes · Live-cell imaging · Novel fluorophores · Super-resolution nanoscopy

Contents

D.A. Yushchenko and M.P. Bruchez (✉)
292 Mellon Institute, Molecular Biosensors and Imaging Center, Carnegie Mellon University, 4400 Fifth Avenue, Pittsburgh, PA 15213, USA
e-mail: bruchez@andrew.cmu.edu

P. Tinnefeld et al. (eds.), *Far-Field Optical Nanoscopy*,
Springer Ser Fluoresc (2015) 14: 159–188, DOI 10.1007/4243_2011_35,

1 Introduction

Development of super-resolution techniques opens new avenues in cell biology. It enables the visualization of labeled cellular features at biologically, as opposed to optically, relevant length scales and provides information related to molecular interaction and communication in live cells, the molecular details of life [1–5]. This sub-diffraction fluorescence imaging is not possible, however, without fluorophores.

The wide utilization of fluorescence imaging has ensured continued development of new fluorescent probes, yielding improvements in brightness, photostability, and available colors [6]. However, fluorophores for super-resolution have their own and in some cases very specific demands different from the conventional dyes. For example, while quantum dots are currently the brightest and the most photostable fluorophores, they have a very limited (yet) application in super-resolution imaging. Moving from static to dynamic super-resolution imposes additional demands, including targeting and brightness. Satisfying these requirements is a challenging task, but collaboration between method developers and chemists have produced a wide range of new probes for super-resolution imaging over the past 4 years.

We will begin this chapter by considering the requirements for dyes used in different super-resolution imaging techniques.

2 Fluorophore Properties for Super-Resolution Methods

As described in previous chapters of this book, the enhancement of spatial resolution in far-field optical imaging is possible due to fluorophore's transitions between a fluorescent ("on") state and a nonfluorescent ("off") state. The ability of the dye to occupy the fluorescent on state, while ensuring that its surrounding neighbors remain in the off state, allows the successive recording of features closer than the diffraction limit. All the super-resolution techniques described in this book rely on this on–off transition of the fluorophore, making it central requirement for any probe to be applied in super-resolution imaging. Super-resolution methods may be classified into several families depending on the way the fluorophore is switched and signal readout is implemented.

Historically, the first super-resolution method STED (Stimulated Emission Depletion) uses a pair of bright and dark states: the fluorescent singlet state S_1 (bright) and the ground state S_0 (dark). Excitation (from S_0 to S_1) makes the dye fluorescent, but applying a shaped red-shifted STED beam drives the probe to the ground state [3, 7]. The STED beam is usually designed to have a doughnut shape with zero intensity at the focal center and strong intensities at the periphery of the beam spot. If the STED beam is superimposed with excitation beam, only molecules that are close to the center of the STED beam are allowed to fluoresce, thus confining the emitting spot [8]. The same states are used in saturated structured illumination microscopy (SSIM) [9, 10]. The concept referred to as reversible saturable optical fluorescent transition (RESOLFT) [11] includes switching isomerization states and other optically bistable transitions in fluorophores as do the more recent stochastic approaches called (fluorescence) photoactivatable localization ((f)PALM) [12, 13] and stochastic optical reconstruction (STORM) [14]. PALM and STORM however differ from RESOLFT by the fact that the switching and readout are performed stochastically in space. In these concepts, wide-field illumination turns individual off-state markers into the on state such that within the diffraction range ($<$300 nm) less than a single marker is able to emit on average [1–3]. PALM and STORM differ only by the labeling approach. While PALM relies on genetically encoded proteins [2, 12], in STORM pairs of two photochromic dyes are used where one of them serves as an activator (switch-on facilitator) [1, 14]. Direct stochastic optical reconstruction (dSTORM) is a modified version of STORM that requires only one fluorophore. Here, a fluorescent singlet state with a long-lived photoreversible dark state of the dye is used for the on–off switch [15, 16]. Another very recent technique named super-resolution optical fluctuation imaging (SOFI) makes use of random temporal signal fluctuations of single emitters. In contrast to single-molecule switching methods here, many emitters can be on at the same time in a diffraction-limited volume and still contribute to enhanced resolution [17, 18]. Thus, due to the differences in the states, rates, and emitter densities required for these different methods, the demands to the fluorophores used in these super-resolution techniques are different. Below we describe the requirements for fluorophores used in each of these super-resolution techniques in more detail, with a focus on what properties can be refined to optimize the performance of the method.

3 Requirements for Spatially Patterned Super-Resolution Imaging

3.1 STED

In STED microscopy (Fig. 1a), the dyes are kept dark (off state) by treating them with red-shifted light, called the STED beam, which induces stimulated emission from their excited state, S_1, to their ground state, S_0. The occupation probability of

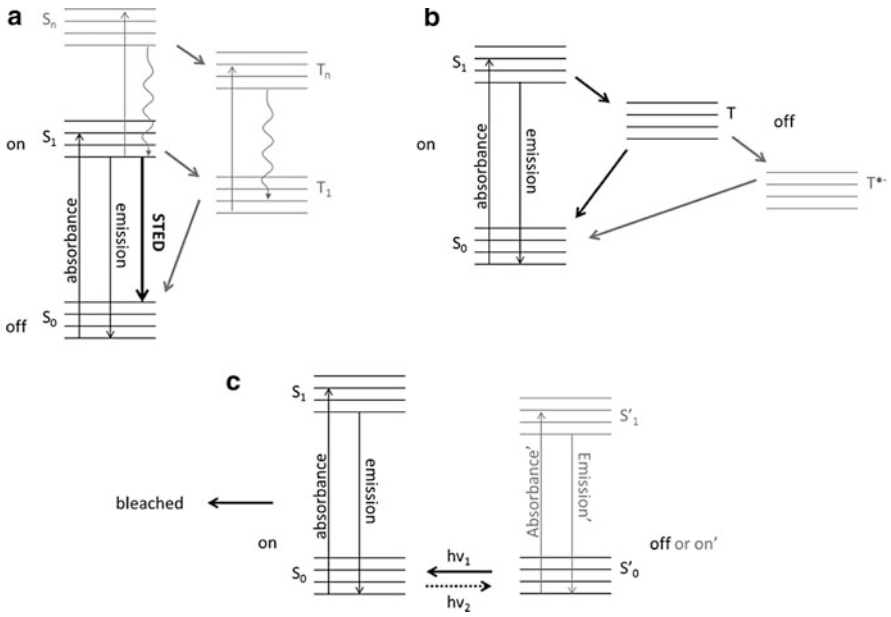

Fig. 1 Electronic energy level diagrams represent the bright and dark states of the fluorophores used in super-resolution imaging

the S_1 state decreases nearly exponentially with the intensity of the STED beam [3]. Applying the high intensity of the STED beam forces the dye to the nonemitting S_0 state, even if it was initially excited. Obviously, the fluorophores that had been kept dark by STED must instantly become bright when they fall into the donut minimum. But this is possible only if they have not been transferred to a long-lived dark state. The higher intensities of the STED beam increase the probability of the dye in the S_1 state to pass into such a long-lived dark state, or to be bleached [19]. In contrast, stimulated emission is reversible and almost any fluorophore can be transiently turned off by a STED beam [20]. Thus, if it were possible to minimize long-term darkening and bleaching, STED should provide nanoscale resolution with almost any fluorophore. Therefore, it is desirable to avoid any process that competes with stimulated emission. Tuning the STED beam wavelength to the red edge of the fluorescence spectrum helps to avoid excitation from the S_0 state, but transitions from excited states may still occur, such as crossing to the triplet states, T_1, as well as absorption to S_n and T_n states with $n > 1$ (Fig. 1a). Triplet states are involved in many bleaching pathways [21]. The higher S_n states can also lead to bleaching [22]. Both processes compete with favorable ultrafast nonradiative S_n to S_1 (or T_n to T_1) relaxation followed by spontaneous or stimulated emission [20].

Thereby the important requirement for dyes in STED microscopy is minimal depletion-beam induced absorption from the S_1 to S_n state and crossing to the triplet states T_n. This ensures maximal "cycles" between S_0 and S_1 and provides the

significant gain in resolution [19]. Thus, selection of ideal STED probes involves not only empirical characterization but also a detailed understanding of the photophysics and spectroscopy of the dye.

3.2 RESOLFT

Stimulated emission is not the only way to suppress undesired fluorescence emission in order to achieve improved resolution. RESOLFT is a more general scheme of super-resolution microscopy based on saturable depletion [3]. This scheme employs fluorescent probes that can be reversibly photoswitched between a fluorescent on state and a dark off state where the off state is often a dark isomer (Fig. 1c). Similar to STED, it uses a depletion laser to drive fluorophores at the periphery of the excitation into their dark state. In contrast to STED, which uses a high intensity depletion beam, an optical transition that has a low power requirement can be chosen for RESOLFT, allowing super-resolution imaging at much lower depletion laser intensity [23]. The important requirement for fluorophores used in RESOLFT is an efficient reversible transition between the on and off states. Because this method is essentially an oversampling of diffraction-limited images, each pixel represents an independent switching cycle. In this way, the gain of the resolution by these methods is proportional to the square root of the number of switching cycles (a resolution eight times beyond the diffraction limit would require 64 switching cycles). Switching fatigue is therefore the major limitation on achievable resolution for RESOLFT methods.

4 Requirements for Single-Molecule Localization Microscopy

(f)PALM and (d)STORM exploit molecular photoswitching to break the diffraction barrier based on stochastic activation. Here, the readout of the fluorescence and inactivation of isolated marker molecules are performed in a way that simultaneously emitting markers are further apart than the minimal distance resolved by the microscope [1–3], resulting in the confinement of the fluorescing spot to the size of a single molecule. Imaging the fluorescence signal from an individual marker produces a diffraction-limited spot whose centroid reveals the location of the emitter, with a precision that ideally scales inversely with the square root of the number of photons collected. After being recorded, the molecules must go back to a dark state to allow iteration of this process – activation, imaging, and deactivation. This process allows localization of many independently resolvable fluorophores and construction of super-resolution images from these found positions. The main advantage of such a single-molecule readout strategy relative to RESOLFT is that the marker molecules are not forced to undergo so many photoswitching cycles. In principle, one photoswitching cycle is enough for stochastic super-resolution imaging, as was shown in many (f)PALM experiments with photoactivatable FPs and

organic fluorophores [2]. From the practical point of view, however, reversible photoswitching may be advantageous since it is more suitable for continuous imaging of dynamic processes where de-novo synthesis and biological incorporation of previously bleached molecules is not fast enough. Reversibly photoswitchable fluorophores also enable combination of super-resolution imaging with other florescent techniques, for example, confocal microscopy that is especially useful in imaging of biological samples, and providing some microscopic context on which the super-resolution image can be superimposed.

The requirements for localization microscopy are quite different than those of RESOLFT methods. The fluorescent on state must yield enough photons to allow the precise calculation of the centroid. In addition, photoswitching properties should include spectral profiles for the active and inactive species that are sufficiently well separated and thermally stable so that spontaneous interconversion energies are very low compared with the light-controlled activation energy. Ideally, these probes should also exhibit high switching reliability and switching kinetics that can be controlled. In terms of photobleaching or photoswitching to a dark state, the best probes are those whose inactivation can be balanced with the activation rate to ensure that only a small population of molecules is activated (i.e., fluorescent) for readout, and that these activated molecules are separated by a distance greater than the resolution limits of the camera system. Both resolution and timescale in dynamic imaging are limited by the brightness of individual molecules and the number of locations that can be measured in a given time-window. Probes that can be switched on emit several thousand photons in a short frame (e.g., at the camera's maximum frame capture rate), and which bleach or switch off within 1–2 frames are ideal, as they achieve both high localization densities and high localization accuracy, the two critical factors for optimal resolution in localization imaging.

4.1 PALM

A wide variety of photoactivatable, photoconvertable, and photoswitchable FPs have been used in the PALM methodology [2]. Application of an FP is very convenient for biological studies since FP may be genetically encoded and fused to almost any protein of interest in the biological samples. The limitations of FPs, however, are related to the photophysical properties of their fluorophores, mainly brightness and photostability. The color variation (tuning) in FPs is also limited. Even though new FPs with improved photophysical properties have recently emerged [99], they still are inferior to organic fluorophores which are usually about twice as bright and substantially more photostable. Photoswitchable organic fluorophores are described in [100]. Here, we will highlight only the recently developed photoswitchable dyes for super-resolution microscopy. Many usable photoswitchable FPs and organic dyes display unspecific switching to the fluorescent state in the absence of specific activation light. This unspecific activation can be either spontaneous or induced by the imaging laser or the other lasers when used

in multicolor imaging. Taking into account the requirement of high localization density mentioned above, this unspecific activation could cause overlap and gradual reduction of single-molecule locations, preventing high-density, high-precision localization. Thus, photoswitchable fluorophores with more rigorously selectable activation properties are desirable to achieve the highest resolution with PALM.

4.2 STORM

As mentioned above, STORM and PALM are identical conceptually, but STORM makes use of reversible switching of various organic dyes. On the one hand, this may be more complicated since it requires the labeling of biological objects, typically with antibodies, but on the other hand gives wider range of labeling in respect to FPs. For example, the first application of STORM was shown on DNA labeled with cyanine dyes Cy3 and Cy5 [14]. Classical STORM requires at least two dyes. For example, when Cy5 is paired with Cy3, the same red laser that excites Cy5 is also used to switch the dye to a stable dark state. Subsequent exposure to green laser light converts Cy5 back to the fluorescent state, and this recovery rate depends on the close proximity of the secondary dye Cy3 (called the activator). Cy5 switching can also be facilitated by other activator fluorophores, such as Cy2 and Alexa Fluor 405 [24]. Furthermore, Cy3 was found to facilitate switching of other cyanines, such as Cy5.5 and Cy7. This finding greatly increases the palette of colors that are available for STORM imaging and has allowed simultaneous visualization of several different objects within the cell with 20–30 nm lateral resolution [24]. The requirement to have two chromophores in close apposition can be difficult to achieve especially in biological samples. Tandem dyes have been prepared to simplify this approach, and will be discussed further [24].

Advantageous to "classical" dye-pair STORM is a new STORM-type super-resolution microscopy that employs a single dye and is applicable to a broader range of fluorophores. This technology was reported independently and essentially contemporaneously in the groups of Hell, Sauer and Tinnefeld and were termed Ground-State Depletion followed by Individual Molecule return (GSDIM) [25], direct STORM (dSTORM) [26] and Blink Microscopy (BM) [27], respectively. Each of these techniques uses the generic transient dark states of the dye [28]. In case of GSDIM, it is a triplet or radical ion state, in dSTORM and BM it is long-lived a radical ion state (Fig. 1b). Similar to STORM, dSTORM and BM require the presence of reducing agents, often thiols, for the stabilization of the off states. The role of thiol depends on the nature of chromophores. In case of rhodamines and oxazines, it was shown that thiols (and other reducing agents) catalyze formation of a long-lived radical ion state (Fig. 1b) [29] while in the case of cyanines, the thiol may also form a covalent bond with the enamine moiety of the dye (Fig. 1c) [30]. In both cases, the process is reversible and the off state (radical ion or thiol conjugate) may be converted to the on state upon either UV (~405 nm) irradiation in case of

cyanines or reaction with oxidizer in case of cyanines and rhodamines. In this respect, the fundamental requirement for the dyes used in STORM, dSTORM and related techniques is their ability to generate a long-lived but reversible off state in controlled way. Recently, dSTORM and GSDIM were demonstrated in living cells using genetically expressed trimethoprim or SNAP tags [31–33].

4.3 SOFI

Similar to other super-resolution techniques, the dyes used in SOFI have to exhibit at least two distinct emission states. These states may be (and so far have been) fluorescent and nonfluorescent. In principle, any two or more states that are optically resolvable may work. Unlike PALM and STORM SOFI does not require activation of resolvable emitters, instead it relies on the independent stochastic fluctuations of the emitters [17]. However, the following conditions must be met: different emitters have to switch between states repeatedly and independently from each other in a stochastic way. They should have a high signal-to-noise or contrast ratio and high photostability. Ideally, the rate of switching has to be uniform. The last requirement will help to speed up the acquisition rate and ensure consistent image quality in SOFI [18].

5 Requirements for All Chromophores

5.1 Brightness

Although there are specific requirements for fluorophores used in the different super-resolution methods described above, the general desirable characteristics of fluorophores, brightness, and photostability are common across all techniques. Brightness is generally defined as the product of a fluorophore's extinction coefficient and quantum yield and represents the relative rate of photon emission by the fluorophore. It is an important characteristic of the dyes used in super-resolution since the brighter fluorophores emit more photons, making them easily detectable. This can speed up the acquisition, whether using patterned illumination or localization. This is especially important for the application of super-resolution techniques for dynamic live cell studies. Within the cell, biomolecules (proteins, nucleic acids, lipids), their complexes and even organelles are in constant dynamic movement [34, 35]. To visualize these structures with sub-diffraction resolution, the acquisition has to be fast (Fig. 2) so that the objects move less than the achievable localization accuracy during the acquisition. Brighter objects emit more photons per pixel over the same time, and can be localized to higher accuracy

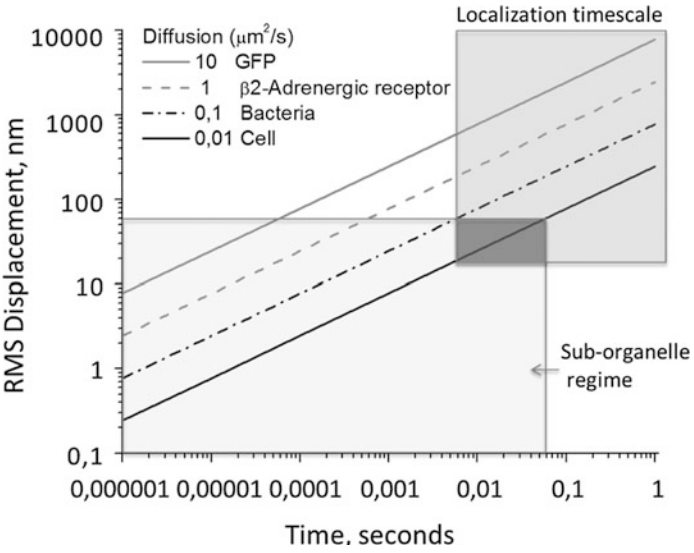

Fig. 2 Diffusion displacement of some cellular components as a function of time. The RMS displacement of free GFP protein in the cellular cytoplasm is ~7.5 nm in 1 μs. In living cells only relatively static structures (e.g., cytoskeleton) can produce significantly enhanced resolution because of the localization constraints (*overlapped*, *shaded region*)

in shorter imaging times. This leads to improved localization accuracy, a concept that has been described as "localization enhancement". In principle, this effect can be realized by increasing the brightness of the probes, or increasing the excitation laser power.

5.2 Excitation in the Red Region

Similar to conventional fluorescent microscopy, super-resolution techniques in biological applications favor fluorophores that absorb in the far-red or even the near-infrared optical region. Excitation at wavelengths longer than 600 nm minimizes the unwanted background signal originating from cellular autofluorescence, and minimizes excitation-based phototoxicity. This can be especially important when high powers are used for depletion or for rapid localization-based imaging approaches.

5.3 Targeting

Another important requirement for fluorophores used in any super-resolution technique is the ability to selectively label the object of interest. In this respect, the

obvious advantage in using fluorescent proteins for subdiffraction imaging of cellular structures is that they can be fused genetically to almost any protein of interest. Unfortunately, artifacts due to overexpression and the large size of FPs are also described in literature [36, 37]. As already mentioned, photoactivatable or photoswitchable FPs in general have a lower photon yield compared to organic fluorophores, limiting the improvement in resolution.

In fixed-cell super-resolution imaging, the most popular method for protein detection is immunofluorescence with labeled antibodies or fragments of antibodies that specifically bind to a target. A variety of antibodies and Fab fragments that are labeled with organic dyes is commercially available [4]. Immunofluorescence works best for permeabilized cells or extracellular or endocytosed proteins. One important limitation of immunolabeling arises from the relatively large size of antibodies. Their size affects the precision of object localization (due to uncertainty in the position of the fluorophore relative to the antigen) and the density of labeling. The labeling density limits the effective spatial resolution in any super-resolution technique. When the labeling efficiency of a sample or the underlying molecular density is not sufficient, artifacts can be observed in super-resolution images, for example, continuous structures appear discontinuous, or simply sparsely labeled. The effect of labeling density on the effective resolution can be quantified by the Nyquist–Shannon criterion [1, 2, 38]. It states that the minimal sampling density needed to capture information from the image is two fluorophores per resolution unit. According to this criterion, to achieve, for example, a 20 nm resolution a high labeling density of 10^4 dyes per μm^2 in general is required. With the heterogeneous distribution of the molecules in cells, appropriate application of such rules can be nonobvious.

Thus, improved techniques for labeling of biomolecules in the cell are desired. In this respect, the recent development of various expressed tag labeling strategies compatible with synthetic dyes is very promising and shows significant promise for applications in super-resolution imaging.

The types of fluorescent labels used in super-resolution techniques as well as the targets of improvement for these labels are summarized in Table 1.

6 Recent Advances in Fluorophore Development

6.1 STED

In principle, STED microscopy can use a wide range of organic dyes (http://www.mpibpc.mpg.de/groups/hell/STED_Dyes.html) but in practice the highest resolution may be achieved only with photostable dyes, for example, commercially available Alexa 488 and Atto 647N. Atto 647N was shown to have a minimal

Table 1 Super-resolution imaging methods and fluorophores used for their implementation

Method	Switching mechanism	Fluorescent label	Areas for improvement
STED and SSIM	Excitation and STED beam: $S_0 \rightarrow S_1 \rightarrow S_0$	Conventional dyes, FPs	Targeting, brightness, photostability, triplet depopulation
PALM	Violet and excitation beam: dark isomer → bright isomer → bleached product	Photoactivatable fluorescent proteins, caged dyes	Brightness, control of unspecific activation, low dark isomer emission
Reversible PALM and PALMIRA	Violet and visible beam (or thermal recovery) Photoconvertable: dark isomer → bright isomer → dark isomer Photoswitchable: bright isomer 1 → bright isomer 2 → bright isomer 1	Photoconvertable and photoswitchable fluorescent proteins, photoswitchable dyes	Brightness, photostability, control of isomerization (avoid unspecific isomerization), low dark isomer emission, targeting
STORM	Visible (often red) light (emission of activator) and excitation (in the presence of reduce agent) Cyanine dyes: dark product (e.g., thiol adduct) → bright dye → dark product Rhodamines and other: $T^{\bullet -} \rightarrow (S_0 \rightarrow S_1) \rightarrow T^{\bullet -}$	Pair of dyes: one is switchable between two states dye another is activator	Brightness, photostability, controlled reversible reaction with thiols or population and depopulation of stabilized triplet states, targeting
dSTORM, GSDIM and BM	Violet and visible beam, oxidation agent, excitation light and reducing agent: $T^{\bullet -} \rightarrow (S_0 \rightarrow S_1) \rightarrow T^{\bullet -}$	Conventional dyes able to switch between the long-lived radical ion and ground state	Brightness, photostability, well controlled population and depopulation of radical ion states, targeting
SOFI	Blinking or oxidation agent, excitation light and reducing agent: dark state → bright state → dark state	QDs or conventional dyes able to switch between the stable triplet state and ground state	Brightness, photostability, low dark state emission, uniform switching rate

S_1 to S_n absorption [19] and low ISC to the triplet state [39]. This near two-state behavior has made these dyes the most popular for STED applications. Recently, Belov and colleagues have developed a wide range of photostable, bright dyes with different colors based on rhodamine and carbopyronine chromophores similar to Alexa 488 and Atto 647N.

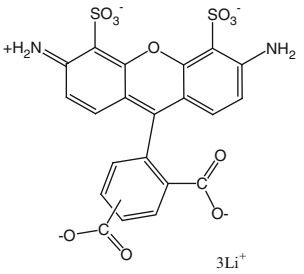

Alexa 488 (rhodamine)

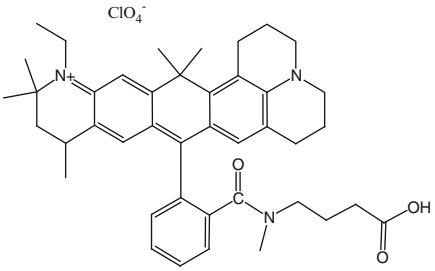

Atto 647N (carbopyronine)

A series of new fluorinated rhodamines for optical nanoscopy were synthesized in the work of Mitronova et al. [40]. The authors took advantage of knowledge that fluorination and sulfonation of the fluorophore may lead to increased photostability and brightness of the dye. They synthesized a range of these compounds with various combinations of fluorine and sulfo groups in the molecule 1 (R_1=H or F, R_2=H or SO_3H, R_3=H or CH_2CF_3, R_4=H or CO_2H).

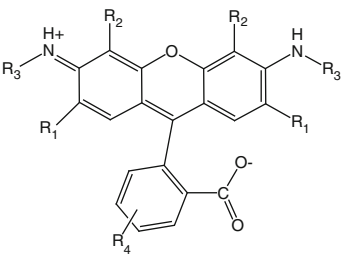

1

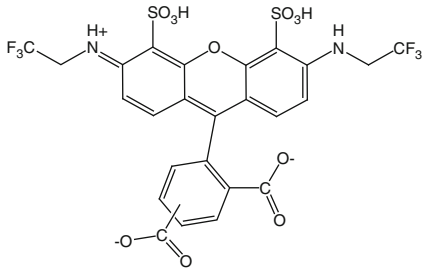

1h

Most of these dyes are highly fluorescent and all of them are photostable compounds in water, aqueous buffers, alcohols and typical mounting media used in standard fluorescence microscopy techniques, such as polyvinyl alcohol (PVA), or its mixtures with water and glycerol. They have absorption maxima between 480 and 515 nm with high extinction coefficients of up to $9 \times 10^4\ M^{-1}\ cm^{-1}$ and emit in the 510–535 nm region with fluorescence quantum yields of up to 0.95. The compounds are far more stable than the common dyes excitable at 488 nm, such as

Fluorescein and Oregon Green 488 and have similar or better (molecule 1h) performance than Rhodamine Green or Alexa Fluor 488. They may also be easily modified to reactive probes for specifically labeling molecules of interest. Sulfonation additionally makes these molecules highly water soluble, an essential requirement for most biological applications.

Kolmakov et al. [41] developed red-emitting rhodamines for fluorescence nanoscopy. These dyes have excitation maxima ~630 nm and emit at ~660 nm. Similar to the rhodamines described above, these dyes are very photostable and very bright and also show low intersystem crossing rates.

To redshift the excitation and emission of rhodamines, these authors introduced the fluorine atoms in the side aromatic ring of the molecule and extended the conjugation by introducing a six-membered ring with a double bond extending the xanthene heterocycle (molecule 2).

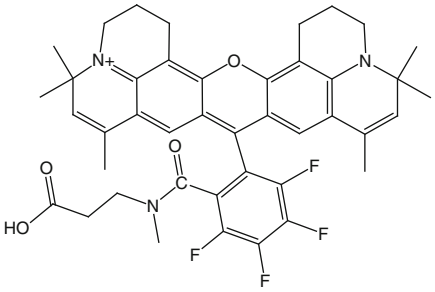

2

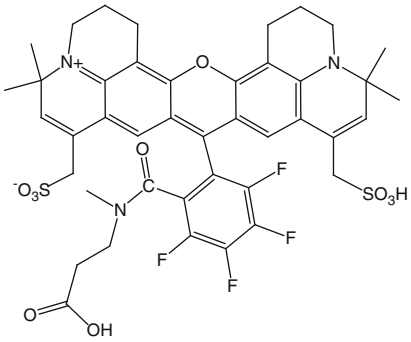

KK114

To obtain highly water-soluble derivative, molecule 2 was sulfonated. Apart from providing excellent solubility in water, sulfo groups prevent aggregation of the dye molecules in water and aqueous buffers. These modifications led to a surprising outcome, dye KK114 was observed to have very high quantum yield (~80%). As a result, these dyes are superior in many respects to Atto 647N. The polar hydrophilic KK114 does not integrate into biological membranes and can be used at high concentrations in labeling experiments. KK114 was used in STED microscopy for visualization of mitochondrial cristae of intact cells. The dyes without sulfonate groups are more hydrophobic and were used for lipid labeling in STED-FCS studies [41].

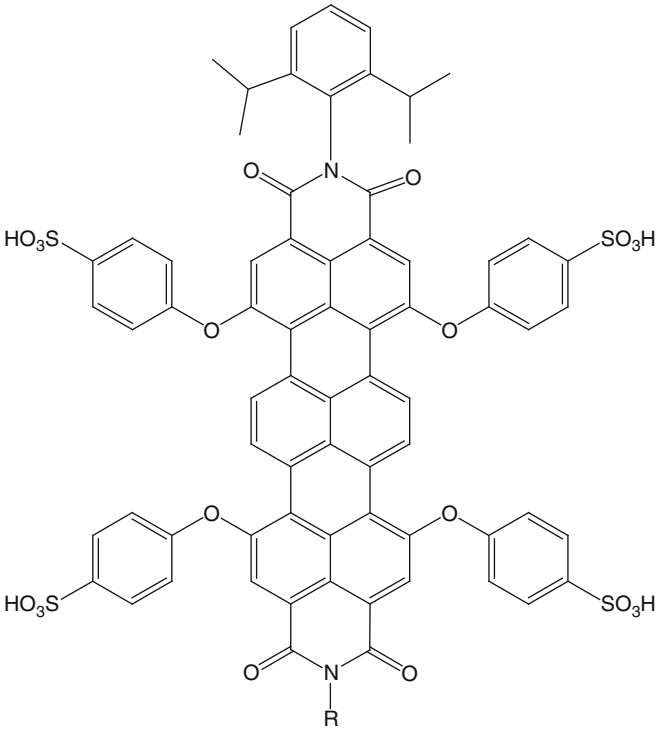

Carbopyronine dyes, such as Atto647N, are chemically very similar to the rhodamines, both of which are rigidized triarylmethane dyes. Compared to rhodamines, the oxygen atom at position 10 of the xanthene fragment is replaced by the geminal dimethyl group [$C(CH_3)_2$], introducing a large bathochromic shift in the absorption and emission bands of approximately 50 nm and changing the rate of triplet state formation. Until recently, the synthesis of this family of dyes was very poorly described in the literature. Recent work [39] demonstrated a general synthetic route to carbopyronines with variable functional groups. These dyes prepared with two methoxyethyl or hydroxyl groups are soluble in water and most organic solvents. In addition, sulfo derivatives of carbopyronines that are highly soluble in water were also synthesized. These dyes absorb around 640 nm and emit near 660 nm. They showed a low intersystem crossing rate and excellent properties for cellular imaging.

Another organic fluorophore that has potential for successful application in STED microscopy of biological samples is terylenediimide [19]. This is an extremely photostable fluorophore that found application in single-molecule studies due to its exceptional photostability. The main limitation for applications of this fluorophore in live cell imaging, its hydrophobicity, was overcome by introduction of four sulfonate groups in the core of the fluorophore [42, 43].

An alternative to organic dyes in STED microscopy may be fluorescent probes based on highly photostable inorganic nanocrystals. Among fluorescent inorganic nanocrystals, QDs are the most developed and adopted for biolabeling [44–46]. Unfortunately, the fact that the absorption band of most QDs overlaps with their emission along with the fact that QDs are not strictly singlet emitters and thus their dark state emission cannot be optically pumped has hampered QDs applicability to STED microscopy. In contrast, nitrogen-vacancy (NV) color centers in diamonds have recently turned out as excellent luminescence sources in STED microscopy, with no observable photobleaching [47, 48]. STED microscopy images of NV centers in diamond featured spatial resolution up to 6 nm in the focal plane. Presently, bioconjugation of NV nanodiamond to make them suitable probes for biological labeling is a challenging task and to our knowledge is still under development.

6.2 Localization Microscopy

There are several types of organic fluorophores that have a potential to be used in super-resolution localization microscopy. These are photoactivatable, photoconvertable, and photoswitchable molecules. While photoactivatable dyes can be switched only once from the dark (off) to bright (on) state, imaged and then bleached, photoswitchable molecules can undergo several (many) reversible switching cycles before photobleaching. Photoconvertable dyes may be considered as the particular case of photoactivatable dyes where both off and on states are fluorescent states but have different colors of fluorescence (Fig. 1c). The important advantage of the photoconvertable and photoswitchable fluorophores over photoactivatable is the ability to use them for super-resolution imaging of dynamic processes or for imaging by other fluorescent techniques simultaneously with super-resolution imaging. On the other hand, the advantage of photoactivatable fluorophores is their simplicity and quantitative capacity compared to photoconvertable and photoswitchable fluorophores.

The traditional method of preparation for photoactivatable dyes is based on the coupling of fluorophore and a quencher (often 2-nitrobenzyl derivative) that makes the fluorophore dark (off state). The irradiation of such molecule with (usually violet or UV) light triggers the release of the quencher and the fluorophore becomes bright (on state). An example of such photo-caged fluorophore is Q-rhodamine (Scheme 1a) [4, 49], which may be used in PALM imaging after immunolabeling [12] or other high-specificity intracellular protein labeling (see below).

A similar approach may be used for the synthesis of photoconvertable fluorophores. Johnsson et al. demonstrated a photoconvertable label based on Cy3–Cy5 pair linked with a photo-sensitive 2-nitrobenzyl linker (Scheme 1b) [50]. Before photo-activation, this Cy3–Cy5 probe excited at 500 nm emits at ~675 nm due to the FRET from Cy3 to Cy5 dye. After irradiation with UV light, however the emission shifts to ~575 nm due to release of Cy5 dye.

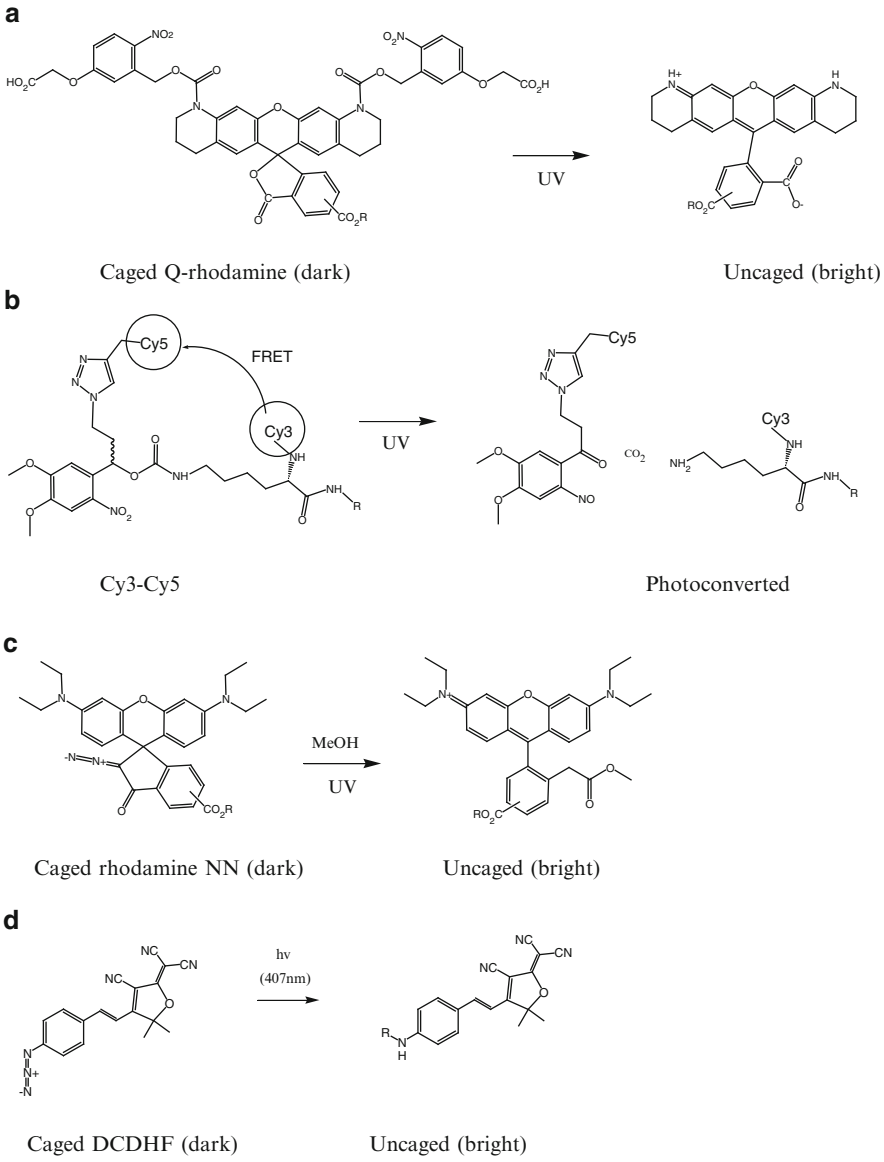

Scheme 1 Photoactivatable and photoconvertable fluorophores developed for super-resolution localization microscopy

A new method to create photo-caged rhodamines was recently presented by Belov et al. [51]. It is based on the incorporation of 2-diazoketone caging group into a spiro-9H-xanthene fragment of cyclized rhodamine molecule to give a so-called rhodamine NN dye (Scheme 1c). The caged rhodamine NN dyes undergo rapid

uncaging under standard irradiation conditions (with wavelengths <420 nm) forming highly fluorescent rhodamine derivatives. These dyes can be used in aqueous buffers, as well as in various embedding media utilized in imaging applications.

Another interesting approach for photo-caging was demonstrated by Moerner and Twieg labs on example of push–pull fluorophores containing an amine donor covalently linked to an electron acceptor group, such as dicyanomethylenedihydrofuran (DCDHF), by replacing the amine with an azide (Scheme 1d) [52, 53]. Unlike the amino group, the azido group is not a donor, so the azido derivative is dark under irradiation with long-wavelength light. Applying low-intensity activating violet light photo-chemically converts the azide to an amine, restoring the donor acceptor character, enhancing the red-shifted absorption and resulting in bright fluorescence emission.

Spiropyrans and diarylethenes are examples of reversibly photoswitchable molecules that could be used to develop photoswitchable fluorophores [54, 55]. Colorless spiropyrans undergo photo-induced ring-opening (photocycloreversion) under ultraviolet irradiation to yield their isomeric merocyanine forms, which have strong solvatochromic visible absorption bands in the range of 500–600 nm. The back-isomerization, i.e., photocyclization, from the mero to the spiro form, occurs thermally at relatively slow rates with half-life times in the order of 10^3 s. However, photocyclization can be substantially accelerated by irradiation with visible light [54]. Diarylethene derivatives exhibit superior fatigue resistant photochromic performance. They can be switched between the colored and colorless form upon irradiation with light of different wavelength more than 10^4 times and, in contrast to spiropyrans, the colored ring-closed isomers are extremely stable [56]. Unfortunately, both of these photochromic molecules are not fluorescent in water and have limited water solubility that restricts their application in biology [5]. To overcome these limitations, two approaches were recently proposed: (a) to use photochromic compounds as fluorescence resonance energy transfer (FRET) acceptors to reversibly switch the fluorescence of a donor fluorophore (e.g., rhodamine), Scheme 2; (b) to incorporate these molecules in water soluble nanoparticles that helps to overcome the problem of solubility in water.

A combination of these two approaches was implemented with a photochromic diarylethene and a rhodamine fluorescent dye. These covalently linked dyes were

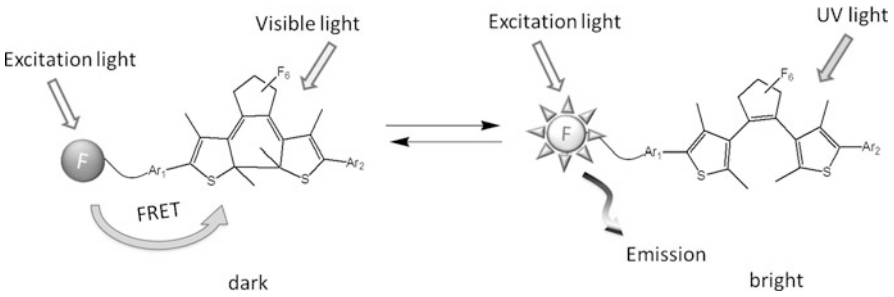

Scheme 2 Photoswitchable dyes based on the diarylethene photochromic molecule

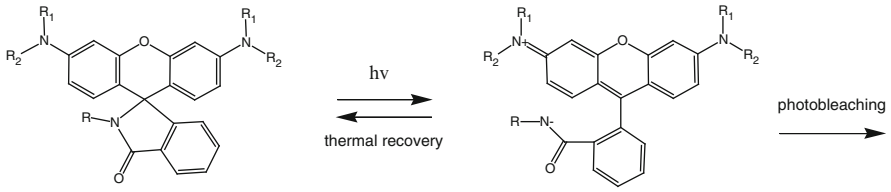

Scheme 3 Photoswitchable rhodamine spiroamides

incorporated in silica nanoparticles where they retained their properties, thereby allowing light-induced reversible high modulation of the fluorescence signal of a single particle for up to 60 cycles, before undergoing irreversible photobleaching [57]. In another example, QDs were used as energy donors and as a solubilization scaffold for diarylethenes [58]. This strategy creates photoswitchable, photostable NPs that are biocompatible and may be useful for super-resolution imaging.

Another type of photoswitchable fluorophore is based on rhodamine spiroamide (Scheme 3) [59, 60]. These molecules function similar to spiropyrans and diarylethenes by interconverting between two isomeric forms. The closed spiro form is transparent across the whole visible range of wavelengths. The photo-induced ring-opening reaction generates the rhodamine chromophore, which typically absorbs in the green region and emits in the red. Photoswitching between isomers may be realized by one-photon activation at 375 nm or two-photon activation at 747 nm. The open isomer returns to closed form with a characteristic lifetime of a few milliseconds (in polar environments). The open form of the spiroamide has all the advantages of rhodamines including a large number of emitted photons. Similar to rhodamines, the position of excitation and emission maxima of these compounds may be modulated by variation of substituents in xanthene heterocycle system. Due to these properties, rhodamine spiroamides found application in single-molecule switching microscopy including PALM with independent running acquisition (PALMIRA) [61].

6.3 STORM

In its initial implementation the STORM technique utilized a Cy3–Cy5 photoswitching system which additionally required thiol and oxygen scavenger. Due to a photomediated reaction with the thiol, Cy5 can enter the stable dark (off) state (Fig. 1c). Excitation of Cy3 induces recovery of the Cy5 fluorescent (on) state. The yield of Cy5 recovery may be controlled by the intensity and duration of Cy3 excitation. For the efficient switching on of Cy5 by Cy3 both dyes must be close enough (~2 nm). This is typically achieved by tandem-labeling of antibodies with both dyes. This probabilistic tandem-labeling results in probe heterogeneity, which can result in

undesirable heterogeneity in switching rates. To overcome this problem, Cy3–Cy5 heterodimers were synthesized that guarantee the homogeneous Cy3–Cy5 distribution and switching [62].

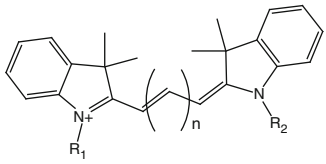

Cy3 (n=1) and Cy5 (n=3)

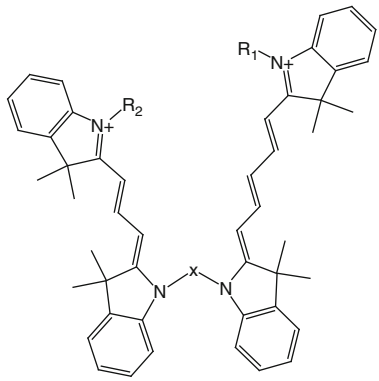

Cy3-Cy5

However, the presence of the activator fluorophore is not always necessary. Recently, it was shown that in specific conditions conventional dyes Cy5 and Alexa 647 can be switched reversibly between a fluorescent and dark state with high efficiency without the use of an activator fluorophore [15, 16]. Here, however, the required power of the green laser is about 200 times higher than when using an activating fluorophore. Because this approach requires only one fluorophore used in STORM, it was called "direct" STORM or dSTORM. The switching rate of the dye may be controlled by the variation of the power of the green and red laser since k_{on} and k_{off} activation rates have the linear dependence upon green and red laser power, respectively.

dSTORM and related GSDIM and BM techniques are not limited only to cyanine dyes. As was shown by van de Linde et al. [16], almost any dye based on rhodamine and oxazine fluorophores, including many commercially available Alexa and Atto dyes, can be reversibly switched between fluorescent and nonfluorescent states in the presence of thiol and oxygen. The thiol reacts with the triplet state of the dye, forming a radical anion and other reduced species of the fluorophore that are not fluorescent. Both radical anion and other reduced species are transferred efficiently to the fluorescent state upon reaction with oxygen. The fluorescence can be reversibly switched between on and off states many times and with minimal loss in fluorescent intensity after recovery [28].

Many conventional, bright, photostable and commercially available Alexa and Atto dyes were successfully applied in dSTORM conditions for super-resolution imaging, for example of the cytoskeleton network of fixed cells [29]. However, application of dSTORM for life cell imaging is more complicated since it requires presence of thiol in millimolar (better 100 mM) and oxygen in micromolar

concentrations. dSTORM imaging is possible in living cells using endogenous glutathione as the switching thiol, yet the distribution of thiols in the cell is not homogeneous and not all compartments have high thiol concentration. This fact potentially imposes some limits on the broad utility of dSTORM for live cell imaging.

7 Genetic Targeting of Fluorescent Dyes

Any fluorophore to be used for live cell super-resolution imaging must selectively and effectively label the molecules of interest within the cell. The FPs are very useful in this respect since they can be used for noninvasive labeling of intracellular targets by genetic fusion to the proteins of interest in the cell. However, the photophysical properties of the synthetic fluorophores are more advantageous in many super-resolution techniques compared to FPs. These probes have been traditionally targeted using antibody conjugation, although this has many disadvantages. Antibodies are not membrane permeable, and hence are not useful for intracellular labeling of living cells. Antibody staining also usually results in low labeling efficiency, a critical point for super-resolution imaging (see Nyquist criterion discussion above). Moreover the large size of antibodies adds uncertainty (~10 nm) to the spatial relationship between the label and its target. In recent years however, there has been significant progress in development of methods for specific targeting of synthetic fluorescent probes to biomolecules in living cells.

A proven approach for super-resolution imaging is a family of protein tags (typically small enzymes) that covalently react with an inhibitor-linked fluorophore (Fig. 3). Halo-tag [63] and the SNAP-tag [64] are probably the most famous representatives of this family. The advantages of these self-labeling proteins are their high speed and specificity, and the ability to employ various desirable synthetic fluorophores. Moreover, because these tags do not require the presence of additional factors (like enzymes), they are easy to use for intracellular labeling [65],

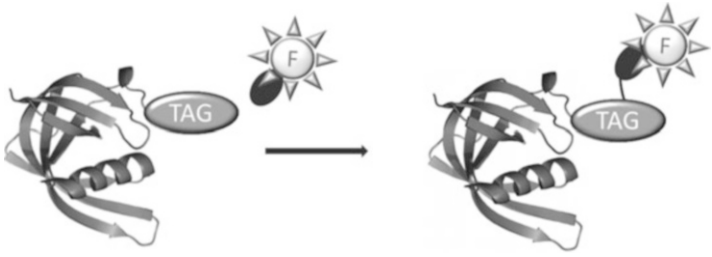

Fig. 3 Covalent tag-mediated labeling of proteins. Tag (recognition element, usually peptide or protein) is fused to the protein of interest (genetically). F is a fluorophore bound to a chemical moiety that mediates the covalent reaction with the Tag. This reaction may be either enzyme-mediated or may take place without enzyme (see text)

simply requiring that the inhibitor-linked fluorophore penetrate the cell to the labeling site. HaloTag and SNAP-tag work well within cells and also within subcellular compartments when cell-permeable substrates are used. For example, SNAP-tag labeling has been described not only for proteins in the cytosol, but also in the nucleus, mitochondria, endoplasmic reticulum, and golgi apparatus [66, 67]. It was successfully used for STED [68] and dSTORM [27] super-resolution imaging of live cells and STORM of fixed cells [69].

Another family of methods requires an enzyme in order to attach a label to a recognition sequence in the protein of interest. Among them is the well-established method based on phosphopantetheinyltransferase (PPTase)-mediated labeling. The natural substrate of these enzymes is CoA, but CoA derivatives linked to any label can also be accepted as substrates [70, 71]. The method is restricted to labeling cell surface proteins because intracellular CoA would interfere with labeling. An important advantage of this method is the ability to use a small peptide tag on the target. This approach is the most versatile choice for labeling extracellular proteins with arbitrary substrates.

For intracellular labeling, Biotin Ligase (BirA) and lipoic acid ligase found a broad application. BirA can be expressed within mammalian cells and used for the specific transfer of biotin and of a biotin isostere with a ketone functionality [72, 73]. Among the limitations of BirA labeling is the presence of other biotinylated proteins in cells and the fact that arbitrary labels such as fluorescent dyes cannot be transferred in one step. Lipoic acid ligase has been shown efficiently transfer labels containing reactive bromides, azides, and photocrosslinkers to tagged proteins in mammalian cells. An engineered lipoic acid ligase is able to accept the fluorescent dye coumarin as a substrate, enabling direct intracellular labeling [74, 75]. Currently, lipoic acid ligase does not allow a free choice of the fluorophore, because the introduced fluorophore has to fit into a cavity within the enzyme; new dyes therefore require a reengineering of lipoic acid ligase. However, this opens the possibility that orthogonal ligases that recognize distinct substrates could be developed, allowing small peptide tags inside the cell to be labeled with distinct fluorophores.

In some cases however the fusion of the tag to the protein of interest can significantly affect the function of this protein. This is especially the case for small proteins and peptides. In this respect, unnatural amino acid incorporation by genetic methods can be the less invasive method to obtain a labeled protein.

Direct incorporation of unnatural amino acids in the protein of interest using an expanded genetic code in living cells was developed by Schultz and co-workers [76]. They have created an in vivo system for site-specific mutagenesis of unnatural amino acids. It is based on the selection of orthogonal tRNA and aminoacyl-tRNA synthetases that recognized the amber stop codon and unnatural amino acid, respectively. Expression of the corresponding genes in a heterologous host together with the gene encoding the desired protein with the amber mutation produces the modified protein. Typically, the cell-culture media is supplemented with the unnatural amino acid. The extension of in vivo unnatural amino acid mutagenesis to yeast and mammalian cells has also been achieved. Many unnatural amino acids

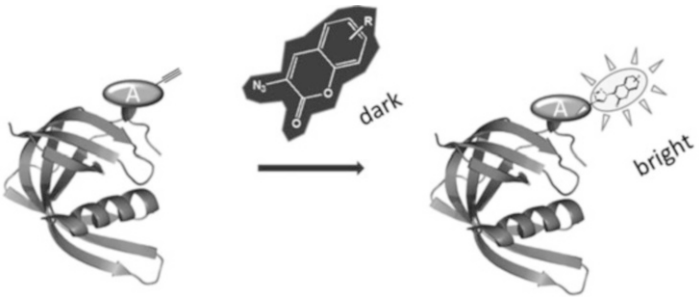

Fig. 4 Fluorogenic labeling of proteins using "click" chemistry. Unnatural amino acid A may be incorporated in the protein of interest by site-specific mutagenesis and genetic code expansion. Fluorogenic molecule is not essentially fluorescent until reaction with A. The bioorthogonal "click" reaction of the fluorogen with the unnatural amino acid leads to the formation of a covalent bond and activation of the fluorophore

including fluorescent analogs have been incorporated into proteins using this approach. Amino acids containing azides, alkynes, ketones, and alkenes have also been incorporated for further bioorthogonal reaction with fluorophores [77–79]. However, these chemistries must be carried out within the cell, inevitably resulting in issues of labeling efficiency and excess probe wash-out to achieve high signal-to-background labeling.

In this respect, an especially interesting advance is a fluorogenic "click" chemistry. The reaction of nonfluorescent alkynes and azides leads to the formation of highly fluorescent triazole adducts (Fig. 4). The obvious advantage of this approach is the low background level of the unreacted fluorophore and the resulting ability to skip a washing step of the labeled sample from the unreacted dye. Alkyne and azide derivatives of different fluorophores including coumarins [80, 81], naphtalimides [82], BODIPY dyes [83], etc. were shown to have such fluorogenic properties. Cu(I) catalyzed azide-alkyne cycloaddition reactions were used in vivo, for example, for labeling in mammalian cells newly synthesized proteins containing homopropargylglycine (alkyne) with membrane permeable 3-azido-7-hydroxycoumarin [84]. The toxicity of copper, however, raises concerns about the use of this method to label live cells. Copper-free azide-alkyne cycloaddition using cyclooctyne may provide a less-toxic alternative for live-cell labeling [85]. Cyclooctynes were already shown to be efficient targets for fluorogenic labeling of the membranes of live cells [86]. They were also used as tags for protein labeling in live cells [87], but copper-free fluorogenic labeling of proteins in live cells has yet to be implemented.

The first tag developed for specific covalent protein labeling was the tetracysteine tag, which exploits the large affinity of peptide sequences containing four cysteines toward fluorophores containing two arsenic atoms [88]. FlAsH and ReAsH, the most known biarsenical dyes, are cell permeable, making tetracysteine labeling a suitable method for the fluorescent labeling of small peptide tags within cells. The specificity of biarsenical labels for their tag, however, is not perfect. In order to reduce high

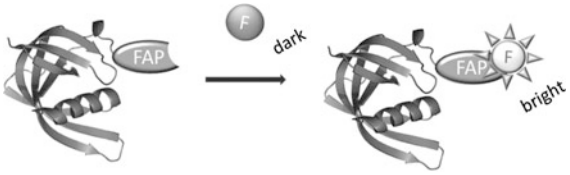

Fig. 5 Noncovalent labeling of proteins using Fluorogen Activating Peptide (FAP) tag. The FAP is genetically fused to the protein of interest. F is a fluorogenic dye that is essentially nonfluorescent while not bound to the FAP. Selective binding of fluorogen to FAP leads to the activation of fluorescence

background due to the reaction of biarsenical dyes with intracellular cysteines and glutathione, the labeling and washing procedures therefore have to be carried out in presence of a competing thiol reagent, which is cytotoxic [74]. Recently, a similar self-labeling tag was designed with the aim of eliminating thiol reagents. In this method, dyes derivatized with boronic acids are designed to react with a tetraserine tag, but more development is needed to selectivity label tagged proteins within the cell with this method [89]. Similar approaches based on His-tag [90], FLAG-tag [91], and N-terminal cysteines [92] for labeling with *N*-cyanobenzothiazole derivatives containing a label were developed. They were shown to be effective for labeling in cell lysates and on the surface of living cells; however, an intracellular labeling using these tags has not yet been demonstrated.

A good alternative to described above protein tags may be fluorogen-activating proteins (FAPs) fused to the protein of interest [93]. FAPs are designed to selectively bind specific nonrigid fluorophores that have very low level of fluorescence in the absence of FAP. The noncovalent binding of the fluorophore to the FAP leads to the activation of the fluorophore (fluorogen) fluorescence by hundreds-to-thousands fold due to the fluorophore constraint in the cavity of the FAP (Fig. 5). FAPs that bind derivatives of malachite green (MG) fluorophore displayed the greatest fluorogenic activation, up to 20,000-fold, primarily because of an extremely low unbound fluorescence in water [93]. The FAP–fluorogen interaction is noncovalent and reversible, leading to an equilibrium activation process with potentially tunable occupancy and intermittency. Several MG-binding clones were demonstrated with Kd values from low nM to near μM. Such variation may be useful for FAPs application in different super-resolution techniques. The tight binding (high affinity) may be useful in PALM-like application where bleaching of the dye after imaging is necessary. Instead reversible binding of FAPs with low affinity may be advantageous in SOFI technique where uniform switching between bright (bound) and dark (unbound) fluorophore states are required. Reversible binding may be also useful in STED imaging where photostability of the dye may be gained by the dye exchange.

FAPs also were developed for a range of fluorophores including Thiazole Orange (TO) [93] and Dimethyl Indole Red (DIR) [94], as well as a wide-range of DNA intercalating dyes [94]. For intracellular imaging, however MG-binding

FAPs are the most effective. Several MG derivatives were synthesized for selective cell labeling: MG-2p is a derivative of MG with polyethyleneglycol linker that does not penetrate through the cellular membrane and is used for the labeling of the proteins on the cell surface. In contrast, MG-ester derivative has a good penetration and is effective for labeling intracellular proteins. Similar to traditional FPs, FAPs may be genetically fused to the protein of interest within the cell for further labeling with fluorogenic dye. MG-binding FAPs have been employed in live and fixed-cell STED imaging of cytosolic FAP-β-actin using MG-ester [95].

8 Make Them Bright

As mentioned, the brightness of a probe can be expressed as the product of its extinction coefficient and quantum yield, a measure of the instantaneous emission rate of a probe under a given excitation power. Generally, the quantum yield of useful probes is between 0.2 and 0.8 [96], although some exceptional probes (phycoerythrin) have remarkable quantum yields approaching 1.0. While these differences may account for some variability in performance of probes, the gap between useful and perfect is not that great (~fivefold), so more significant variability of brightness comes from the differences in extinction coefficient for different probes.

Fluorescent proteins have extinction coefficients below $10^5\ M^{-1}\ cm^{-1}$, typically below $7 \times 10^4\ M^{-1}\ cm^{-1}$. Most dye molecules that are useful for cell imaging fall in the range of 7×10^4 to $2 \times 10^5\ M^{-1}\ cm^{-1}$. Given consistent quantum yields, this accounts for approximately two- to threefold difference in molecular brightness between dyes and fluorescent proteins. Far brighter, quantum dots and phycobiliproteins have maximum extinction coefficients $>10^6\ M^{-1}\ cm^{-1}$ [45, 97]. Both the quantum dots and phycobiliproteins achieve this high brightness by combining individual absorbing elements into a cohesive emitter. In the case of quantum dots, each unit cell contributes to the molar absorptivity for the particle, hence larger particles possess higher extinction coefficients per particle, the detectable unit. Similarly, B-phycoerythrin consists of a 240,000 MW protein decorated with 34 distinct bilin chromophores. Neither phycoerythrin nor quantum dots can be easily genetically targeted as expression proteins, which limits their use in cellular labeling, particularly for living cells. In addition, the size and multichromophore structure of these probes potentially broadens the location of the point emitter, limiting the achievable localization accuracy substantially relative to the number of photons collected.

We recently developed a new approach to target a multichromophore structure with a single localized emitter to a compact, genetically encoded structure [98]. Starting with the binding-mediated activation of Malachite Green fluorogen by a FAP, a number of donors were added to the fluorogen maintaining a single fluorogen per multichromophore structure. Because the fluorogen serves as an energy transfer acceptor, it is capable of quenching the fluorescence of the donors

(in this case Cy3), rendering the soluble multichromophore structure nonfluorescent. When bound to the FAP, the acceptor is activated for fluorescence by both direct and FRET-sensitized excitation. When multiple donors are used and the FRET-sensitized excitation is exploited, the extinction coefficients achieved with four donors are up to 5×10^5, approaching quantum dot extinction coefficients. The genetically expressed protein is ~25 kDa, and the multichromophore structure is 3 kDa, an overall fluorescent complex about the size of GFP, but nearly a factor of 10 brighter. Although unproven, we anticipate that the tight localization of the emitter in these structures may result in increased targeting precision, and improvements to the ultimate resolution achievable by super-resolution imaging.

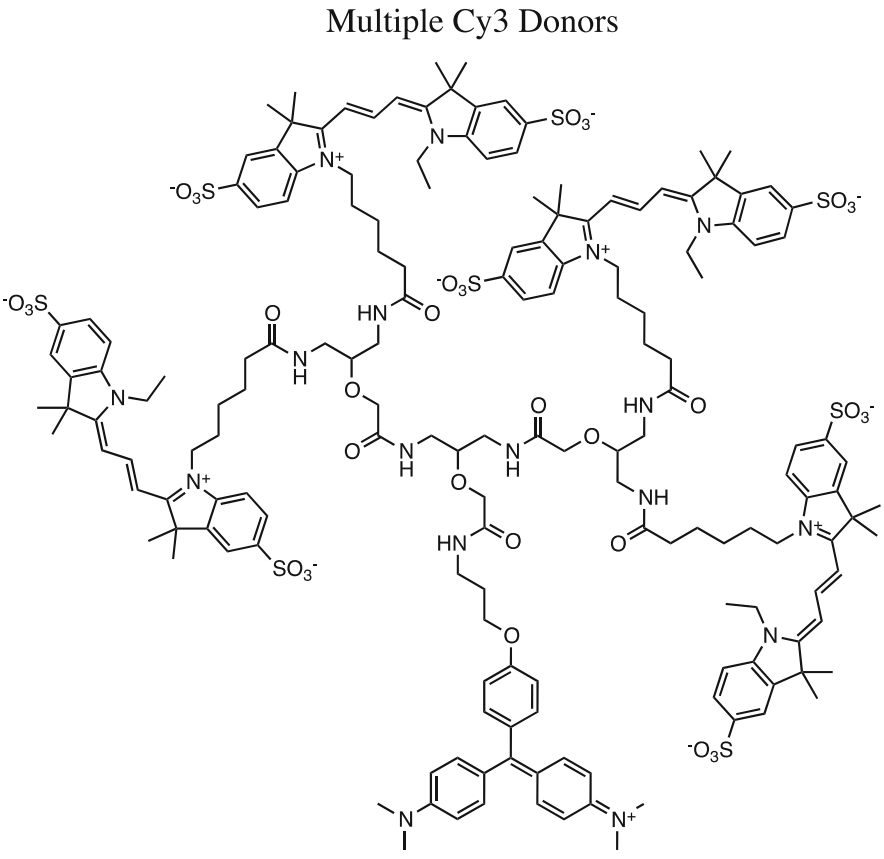

9 Conclusions

It is clear that super-resolution imaging approaches have benefited greatly from the availability of a wide range of fluorescent probes for conventional microscopy and the methods that have been developed for targeting these probes. Only recently, as chemists have teamed up with the method developers, have we started to see probe-development targeted to the requirements for distinct super-resolution methodologies. We have outlined here how different methodologies exploit distinct probe properties. As these efforts move forward, the synergy of new approaches, improved instrumentation, and targeted optimization of probe properties will yield improvements in resolution, speed, and accuracy of images at molecular length scales.

References

1. Huang B, Babcock H, Zhuang X (2010) Breaking the diffraction barrier: super-resolution imaging of cells. Cell 143(7):1047–1058
2. Patterson G et al (2010) Superresolution imaging using single-molecule localization. Annu Rev Phys Chem 61:345–367
3. Hell SW (2007) Far-field optical nanoscopy. Science 316(5828):1153–1158
4. Fernandez-Suarez M, Ting AY (2008) Fluorescent probes for super-resolution imaging in living cells. Nat Rev Mol Cell Biol 9(12):929–943
5. Heilemann M et al (2009) Photoswitches: key molecules for subdiffraction-resolution fluorescence imaging and molecular quantification. Laser Photon Rev 3(1–2):180–202
6. Haugland RP (2002) Handbook of Fluorescent Probes and Research Products, 9th ed.; Molecular Probes Inc: Eugene, OR
7. Hell SW, Wichmann J (1994) Breaking the diffraction resolution limit by stimulated emission: stimulated-emission-depletion fluorescence microscopy. Opt Lett 19(11):780–782
8. Hell SW (2009) Microscopy and its focal switch. Nat Methods 6(1):24–32
9. Heintzmann R, Jovin TM, Cremer C (2002) Saturated patterned excitation microscopy–a concept for optical resolution improvement. J Opt Soc Am A Opt Image Sci Vis 19 (8):1599–1609
10. Gustafsson MG (2005) Nonlinear structured-illumination microscopy: wide-field fluorescence imaging with theoretically unlimited resolution. Proc Natl Acad Sci U S A 102 (37):13081–13086
11. Hell SW (2003) Toward fluorescence nanoscopy. Nat Biotechnol 21(11):1347–1355
12. Betzig E et al (2006) Imaging intracellular fluorescent proteins at nanometer resolution. Science 313(5793):1642–1645
13. Hess ST, Girirajan TP, Mason MD (2006) Ultra-high resolution imaging by fluorescence photoactivation localization microscopy. Biophys J 91(11):4258–4272
14. Rust MJ, Bates M, Zhuang X (2006) Sub-diffraction-limit imaging by stochastic optical reconstruction microscopy (STORM). Nat Methods 3(10):793–795
15. Heilemann M et al (2008) Subdiffraction-resolution fluorescence imaging with conventional fluorescent probes. Angew Chem Int Ed Engl 47(33):6172–6176
16. van de Linde S et al (2009) Multicolor photoswitching microscopy for subdiffraction-resolution fluorescence imaging. Photochem Photobiol Sci 8(4):465–469

17. Dertinger T et al (2009) Fast, background-free, 3D super-resolution optical fluctuation imaging (SOFI). Proc Natl Acad Sci U S A 106(52):22287–22292
18. Dertinger T et al (2010) Superresolution optical fluctuation imaging with organic dyes. Angew Chem Int Ed Engl 49(49):9441–9443
19. Hotta J et al (2010) Spectroscopic rationale for efficient stimulated-emission depletion microscopy fluorophores. J Am Chem Soc 132(14):5021–5023
20. Westphal V et al (2007) Fluorescence depletion mechanisms in super-resolving STED microscopy. Chem Phys Lett 442(4–6):483–487
21. Donnert G et al (2006) Macromolecular-scale resolution in biological fluorescence microscopy. Proc Natl Acad Sci U S A 103(31):11440–11445
22. Tinnefeld P et al (2004) Higher-excited-state photophysical pathways in multichromophoric systems revealed by single-molecule fluorescence spectroscopy. Chemphyschem 5 (11):1786–1790
23. Hofmann M et al (2005) Breaking the diffraction barrier in fluorescence microscopy at low light intensities by using reversibly photoswitchable proteins. Proc Natl Acad Sci U S A 102 (49):17565–17569
24. Bates M et al (2007) Multicolor super-resolution imaging with photo-switchable fluorescent probes. Science 317(5845):1749–1753
25. Folling J et al (2008) Fluorescence nanoscopy by ground-state depletion and single-molecule return. Nat Methods 5(11):943–945
26. van de Linde S et al (2008) Photoswitching microscopy with standard fluorophores. Appl Phys B 93(4):725–731
27. Steinhauer C et al (2008) Superresolution microscopy on the basis of engineered dark states. J Am Chem Soc 130(50):16840–16841
28. Vogelsang J et al (2010) Make them blink: probes for super-resolution microscopy. Chemphyschem 11(12):2475–2490
29. Heilemann M et al (2009) Super-resolution imaging with small organic fluorophores. Angew Chem Int Ed 48(37):6903–6908
30. Dempsey GT et al (2009) Photoswitching mechanism of cyanine dyes. J Am Chem Soc 131 (51):18192–18193
31. Wombacher R et al (2010) Live-cell super-resolution imaging with trimethoprim conjugates. Nat Methods 7(9):717–719
32. Klein T et al (2011) Live-cell dSTORM with SNAP-tag fusion proteins. Nat Methods 8 (1):7–9
33. Testa I et al (2010) Multicolor fluorescence nanoscopy in fixed and living cells by exciting conventional fluorophores with a single wavelength. Biophys J 99(8):2686–2694
34. Izeddin I et al (2011) Super-resolution dynamic imaging of dendritic spines using a low-affinity photoconvertable actin probe. PLoS One 6(1):e 15611
35. Xie XS, Elf J, Li GW (2007) Probing transcription factor dynamics at the single-molecule level in a living cell. Science 316(5828):1191–1194
36. Moore I, Murphy A (2009) Validating the location of fluorescent protein fusions in the endomembrane system. Plant Cell 21(6):1632–1636
37. Shaner NC, Patterson GH, Davidson MW (2007) Advances in fluorescent protein technology. J Cell Sci 120(Pt 24):4247–4260
38. Shroff H et al (2008) Live-cell photoactivated localization microscopy of nanoscale adhesion dynamics. Nat Methods 5(5):417–423
39. Kolmakov K et al (2010) A versatile route to red-emitting carbopyronine dyes for optical microscopy and nanoscopy. European J Org Chem 19:3593–3610
40. Mitronova GY et al (2010) New fluorinated rhodamines for optical microscopy and nanoscopy. Chem Eur J 16(15):4477–4488
41. Kolmakov K et al (2010) Red-emitting rhodamine dyes for fluorescence microscopy and nanoscopy. Chem Eur J 16(1):158–166

42. Peneva K et al (2008) Water-soluble monofunctional perylene and terrylene dyes: powerful labels for single-enzyme tracking. Angew Chem Int Ed Engl 47(18):3372–3375
43. Jung C et al (2009) Photophysics of New water-soluble terrylenediimide derivatives and applications in biology. Chemphyschem 10(1):180–190
44. Howarth M et al (2008) Monovalent, reduced-size quantum dots for imaging receptors on living cells. Nat Methods 5(5):397–399
45. Alivisatos AP, Gu W, Larabell C (2005) Quantum dots as cellular probes. Annu Rev Biomed Eng 7:55–76
46. Ballou B et al (2004) Noninvasive imaging of quantum dots in mice. Bioconjug Chem 15 (1):79–86
47. Rittweger E et al (2009) STED microscopy reveals crystal colour centres with nanometric resolution. Nat Photonics 3(3):144–147
48. Han KY et al (2009) Three-dimensional stimulated emission depletion microscopy of nitrogen-vacancy centers in diamond using continuous-wave light. Nano Lett 9 (9):3323–3329
49. Gee KR, Weinberg ES, Kozlowski DJ (2001) Caged Q-rhodamine dextran: a new photoactivated fluorescent tracer. Bioorg Med Chem Lett 11(16):2181–2183
50. Maurel D et al (2010) Photoactivatable and photoconvertable fluorescent probes for protein labeling. ACS Chem Biol 5(5):507–516
51. Belov VN et al (2010) Rhodamines NN: a novel class of caged fluorescent dyes. Angew Chem Int Ed Engl 49(20):3520–3523
52. Lord SJ et al (2010) Azido push-pull fluorogens photoactivate to produce bright fluorescent labels. J Phys Chem B 114(45):14157–14167
53. Lord SJ et al (2008) A photoactivatable push-pull fluorophore for single-molecule imaging in live cells. J Am Chem Soc 130(29):9204–9205
54. Minkin VI (2004) Photo-, thermo-, solvato-, and electrochromic spiroheterocyclic compounds. Chem Rev 104(5):2751–2776
55. Irie M et al (2002) Organic chemistry: a digital fluorescent molecular photoswitch. Nature 420(6917):759–760
56. Takami S et al (2003) Extraordinarily high thermal stability of the closed-ring isomer of 1,2-bis(5-methyl-2-phenylthiazol-4-yl)perfluorocyclopentene. Chem Lett 32(10):892–893
57. Folling J et al (2008) Synthesis and characterization of photoswitchable fluorescent silica nanoparticles. Small 4(1):134–142
58. Diaz SA et al (2011) Photoswitchable water-soluble quantum dots: pcFRET based on amphiphilic photochromic polymer coating. ACS Nano 5(4):2795–2805
59. Folling J et al (2007) Photochromic rhodamines provide nanoscopy with optical sectioning. Angew Chem Int Ed Engl 46(33):6266–6270
60. Belov VN et al (2009) Rhodamine spiroamides for multicolor single-molecule switching fluorescent nanoscopy. Chem Eur J 15(41):10762–10776
61. Bossi M et al (2008) Multicolor far-field fluorescence nanoscopy through isolated detection of distinct molecular species. Nano Lett 8(8):2463–2468
62. Conley NR, Biteen JS, Moerner WE (2008) Cy3-Cy5 covalent heterodimers for single-molecule photoswitching. J Phys Chem B 112(38):11878–11880
63. Los GV et al (2005) The HaloTag (TM): a novel technology for cellular analysis. J Neurochem 94:15
64. Keppler A et al (2003) A general method for the covalent labeling of fusion proteins with small molecules in vivo. Nat Biotechnol 21(1):86–89
65. Hinner MJ, Johnsson K (2010) How to obtain labeled proteins and what to do with them. Curr Opin Biotechnol 21(6):766–776
66. Srikun D et al (2010) Organelle-targetable fluorescent probes for imaging hydrogen peroxide in living cells via SNAP-Tag protein labeling. J Am Chem Soc 132(12):4455–4465
67. Lippard SJ et al (2008) Organelle-specific zinc detection using zinpyr-labeled fusion proteins in live cells. J Am Chem Soc 130(47):15776

68. Hein B et al (2010) Stimulated emission depletion nanoscopy of living cells using SNAP-tag fusion proteins. Biophys J 98(1):158–163
69. Dellagiacoma C et al (2010) Targeted photoswitchable probe for nanoscopy of biological structures. Chembiochem 11(10):1361–1363
70. George N et al (2004) Specific labeling of cell surface proteins with chemically diverse compounds. J Am Chem Soc 126(29):8896–8897
71. Zhou Z et al (2008) An eight residue fragment of an acyl carrier protein suffices for post-translational introduction of fluorescent pantetheinyl arms in protein modification in vitro and in vivo. J Am Chem Soc 130(30):9925–9930
72. Slavoff SA et al (2008) Expanding the substrate tolerance of biotin ligase through exploration of enzymes from diverse species. J Am Chem Soc 130(4):1160–1162
73. de Boer E et al (2003) Efficient biotinylation and single-step purification of tagged transcription factors in mammalian cells and transgenic mice. Proc Natl Acad Sci U S A 100 (13):7480–7485
74. Uttamapinant C et al (2010) A fluorophore ligase for site-specific protein labeling inside living cells. Proc Natl Acad Sci U S A 107(24):10914–10919
75. Fernandez-Suarez M et al (2007) Redirecting lipoic acid ligase for cell surface protein labeling with small-molecule probes. Nat Biotechnol 25(12):1483–1487
76. Wang L, Schultz PG (2004) Expanding the genetic code. Angew Chem Int Ed Engl 44 (1):34–66
77. Deiters A, Schultz PG (2005) In vivo incorporation of an alkyne into proteins in Escherichia coli. Bioorg Med Chem Lett 15(5):1521–1524
78. Summerer D et al (2006) A genetically encoded fluorescent amino acid. Proc Natl Acad Sci U S A 103(26):9785–9789
79. Wang J, Xie J, Schultz PG (2006) A genetically encoded fluorescent amino acid. J Am Chem Soc 128(27):8738–8739
80. Sivakumar K et al (2004) A fluorogenic 1,3-dipolar cycloaddition reaction of 3-azidocoumarins and acetylenes. Org Lett 6(24):4603–4606
81. Zhou Z, Fahrni CJ (2004) A fluorogenic probe for the copper(I)-catalyzed azide-alkyne ligation reaction: modulation of the fluorescence emission via 3(n, pi)-1(pi, pi) inversion. J Am Chem Soc 126(29):8862–8863
82. Sawa M et al (2006) Glycoproteomic probes for fluorescent imaging of fucosylated glycans in vivo. Proc Natl Acad Sci U S A 103(33):12371–12376
83. Le Droumaguet C, Wang C, Wang Q (2010) Fluorogenic click reaction. Chem Soc Rev 39 (4):1233–1239
84. Beatty KE et al (2006) Fluorescence visualization of newly synthesized proteins in mammalian cells. Angew Chem Int Ed Engl 45(44):7364–7367
85. Jewett JC, Bertozzi CR (2010) Cu-free click cycloaddition reactions in chemical biology. Chem Soc Rev 39(4):1272–1279
86. Neef AB, Schultz C (2009) Selective fluorescence labeling of lipids in living cells. Angew Chem Int Ed Engl 48(8):1498–1500
87. Beatty KE et al (2010) Live-cell imaging of cellular proteins by a strain-promoted azide-alkyne cycloaddition. Chembiochem 11(15):2092–2095
88. Griffin BA, Adams SR, Tsien RY (1998) Specific covalent labeling of recombinant protein molecules inside live cells. Science 281(5374):269–272
89. Halo TL et al (2009) Selective recognition of protein tetraserine motifs with a cell-permeable, pro-fluorescent bis-boronic acid. J Am Chem Soc 131(2):438–439
90. Uchinomiya SH et al (2009) Site-specific covalent labeling of His-tag fused proteins with a reactive Ni(II)-NTA probe. Chem Commun (Camb) 39:5880–5882
91. Nonaka H et al (2009) FLAG-tag selective covalent protein labeling via a binding-induced acyl-transfer reaction. Bioorg Med Chem Lett 19(23):6696–6699
92. Ren H et al (2009) A biocompatible condensation reaction for the labeling of terminal cysteine residues on proteins. Angew Chem Int Ed Engl 48(51):9658–9662

93. Szent-Gyorgyi C et al (2008) Fluorogen-activating single-chain antibodies for imaging cell surface proteins. Nat Biotechnol 26(2):235–240
94. Zanotti KJ et al (2011) Blue fluorescent dye-protein complexes based on fluorogenic cyanine dyes and single chain antibody fragments. Org Biomol Chem 9(4):1012–1020
95. Fitzpatrick JA et al (2009) STED nanoscopy in living cells using fluorogen activating proteins. Bioconjug Chem 20(10):1843–1847
96. Lakowicz JR (2006) Principles of fluorescence spectroscopy. Springer Science, New York
97. Loos D et al (2004) Single-molecule spectroscopy selectively probes donor and acceptor chromophores in the phycobiliprotein allophycocyanin. Biophys J 87(4):2598–2608
98. Szent-Gyorgyi C et al (2010) Fluorogenic dendrons with multiple donor chromophores as bright genetically targeted and activated probes. J Am Chem Soc 132(32):11103–11109
99. Gayda S, Hedde PN, Nienhaus K (2011) Probes for nanoscopy: fluorescent proteins. Springer Ser Fluoresc. doi:10.1007/4243_2011_34
100. Aramendía PF, Bossi ML (2012) Probes for nanoscopy: photoswitchable fluorophores. Springer Ser Fluoresc. doi:10.1007/4243_2012_39

Probes for Nanoscopy: Photoswitchable Fluorophores

Pedro F. Aramendía and Mariano L. Bossi

Abstract In recent years, new concepts have emerged for imaging in a far-field fluorescence microscope with resolution under the diffraction limit. All these concepts bear in common the use of molecular states of the probe to switch its signal between a fluorescent and a dark state. So far, in these techniques different kinds of molecular switches have been applied, whose photochemical features become a crucial fact for the success. In this chapter, we will discuss how the two isomeric forms of a photochromic system can be used to design a fluorescent switch for that purpose. We will focus on the photochemical and photophysical relevant properties for these systems to fulfill the requirements of a suitable probe for the different strategies currently used in fluorescence nanoscopy. Examples containing diverse photochromes and their application in super-resolution fluorescence imaging will be described.

Keywords Imaging · Microscopy · Photomodulation · Photochromism · Photoswitching

Contents

P.F. Aramendía and M.L. Bossi (✉)
INQUIMAE—Departamento de Química Inorgánica, Analítica y Química Física, FCEN, Universidad de Buenos Aires, Pabellón 2, Ciudad Universitaria, C1428EHA Buenos Aires, Argentina

MLB and PFA are research staff from Carrera del Investigador Científico from CONICET (Consejo Nacional de Investigaciones Científicas y Técnicas, Argentina)
e-mail: mariano@qi.fcen.uba.ar

P. Tinnefeld et al. (eds.), *Far-Field Optical Nanoscopy*,
Springer Ser Fluoresc (2015) 14: 189–214, DOI 10.1007/4243_2012_39,

1 Introduction

Fluorescence microscopy is an essential tool in life sciences, in particular to determine the localization and supramolecular organization of biomolecules, and in the study of many relevant biological pathways and processes. Unlike most of other imaging techniques (e.g., electron microscopy or near-field techniques), far-field techniques are noninvasive which, along with the transparency of cells and tissues to visible light, allows for example the three-dimensional observation of organelles in the interior of a live cell, and tracking with excellent temporal resolution. In addition, combined with specific labeling techniques, selectivity of up to a single (bio)molecule can be achieved, even with more than one constituent being imaged simultaneously. However, cells can be as small as 1 μm (e.g., bacteria); so a detailed observation of the interior of a cell requires the ability to discern objects that are far much closer than a micrometer. For instance typical sizes of proteins are less than 15 nm, and organelles can be as small as 40 nm in diameter. Thus, the main limitation of conventional far-field fluorescent microscopy has been its relatively poor spatial resolution, posed by the wavelength of the light employed (λ) and the numerical aperture of commercial objective lenses (NA, normally 0.6–1.5). For visible light in the focal plane, the resolution is λ/(2.NA) ~200 nm [1]. This limitation, usually known as the diffraction barrier or Abbe's limit, has challenged fluorescence microscopy and has precluded the observation of many crucial processes at the subcellular level for over a century. The emergence of modern concepts based on the use of the molecular states of the fluorescent markers made it possible to circumvent the mentioned barrier while still using far-field optical arrays [2, 3].

Grouped under *Targeted Readout* and *Stochastic Readout* techniques [4], all the different variants bear a cunning but simple concept in common: switching the markers on and off between an emissive and a dark state (E $\leftrightarrow$ D). This signal switching renders a temporal discrimination of subdiffraction separated objects, i.e., several features or objects within a diffraction-limited spot of the sample are time-sequentially imaged. Even though the two groups have different requirements with respect to the switching conditions and the number of emitted (and detected) photons, the key role of the probe in all the fluorescence nanoscopies is evident, in particular, when it comes to its photophysical and photochemical properties as well as the mechanism responsible for the on/off signal modulation.

In general, different photoswitchable probes are commonly used in fluorescence nanoscopies. A possible classification is according to the following types: (1) photoswitchable and photochromic organic dyes (small molecules), (2) photoswitchable fluorescent proteins, and (3) inorganic nanoparticles (i.e., quantum dots or NV color centers in nanodiamonds). In addition, several mechanisms can be responsible for the switching, such as isomerization, population of a triplet state, a protonated or radical state, excited state redox reactions, or reversible binding. In this chapter, we will focus on the switching properties of organic dyes presenting two thermally stable states, or one long-lived metastable state ($\tau > \mu s$), with distinct emissive properties, and whose conversion is achieved by light absorption.

2 Photoswitchable Dyes: Why Using Long-Lived States?

Photochromism is defined as a reversible transformation between two chemical species having different absorption spectra, induced by light in one or both directions [5–7]. Changes in chemical and physical properties (such as spectral changes) are related to modifications of the molecular geometry and electronic distribution. A molecular switch is a molecule that is thermally stable in two different forms (i.e., is bistable), and can be interconverted by means of an external stimulus [8]. In a photoswitch, the stimulus is light (Fig. 1). The main difference between a molecular photoswitch and a photochromic compound is that bistability and bidirectional photoinduced paths are not the required conditions for the latter. Purely photochromic compounds (those who do not display thermal reactions) meet all the requirements for a photoswitch. However, a thermal reaction slow enough compared with the characteristic time of the experiment may render the system equally useful. Therefore, such quasi-bistable photochromic compounds can also be regarded or used as photoswitches in many applications. In particular, photochromic systems that present thermal reactions with long characteristic times (e.g., seconds), compared with typically on–off switching times required in nanoscopy applications, will be regarded through the following sections as quasi-bistable compounds. For those applications they are, in practice, similar to the fully bistable systems i.e., those that have a complete lack of thermal reactions.

Targeted Readout strategies are characterized by performing a switching-off process with a spatially modulated distribution of light intensity featuring at least one nodal point [9]. Only at this nodal point will all the fluorophores remain in the emitting state. Outside the node, a suitable light intensity must be applied to ensure that the transition of the markers from the emitting to the dark state is saturated. In the ideal case, the conversion to the dark state should be complete (i.e., the emitting state is fully depleted). This is achieved if the intensity is considerably larger than the saturation intensity (I_{SAT}), a characteristic property of the molecular states of the switchable marker, and defined as the intensity at which the population of the D state takes place at the same speed as its spontaneous depopulation. The achievable spatial resolution is $\Delta r \approx \lambda \Big/ 2n \sin\alpha \sqrt{1 + I/I_{\mathrm{SAT}}}$ [10], where λ is the

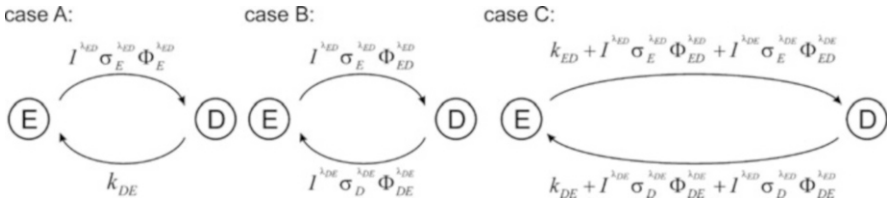

Fig. 1 States and transitions involved in a two-state molecular photoswitch. E and D represent the emissive and the dark state, respectively. Parameters: k are rate constants for thermal (dark) process, I is incident light intensity, σ are absorption cross-sections, and Φ are quantum efficiencies of photoinduced processes. The subscripts indicate the absorbing state (σ) or the initial and final states of a process (k and Φ), and the superscripts indicate the irradiation wavelength λ

wavelength of the light and ($2n \sin \alpha$) is the numerical aperture of the focusing lens. This resolution can be attained irrespective of the spatial distribution of the incident light around the nodal point. Moreover, an unlimited resolution can be achieved, provided enough intensity can be applied in practice. However, high intensities are usually undesirable for several reasons, such as to avoid photoinduced damage of the samples (particularly when imaging living organisms) and photobleaching of the fluorophores, or they may be unachievable, for example, by instrumental limitations imposed by the optics or light sources available. Since I_{SAT} is characteristic of the molecular states, the intensity to achieve a desired resolution can be reduced only and solely by changing the switchable marker. Different markers involving the same kind of transition (states) usually would render only small changes in I_{SAT}, while reduction of orders of magnitude can be achieved by changing the switching mechanism or the molecular states involved.

For example, let us consider the hypothetical transition between an emissive and a dark state E $\leftrightarrow$ D, where the direct (E $\rightarrow$ D) transition is photoinduced (Fig. 1, case A, where σ_E and Φ_{ED} are the cross-section and the quantum yield at the irradiation wavelength λ_{ED}) and the reverse one (E $\leftarrow$ D) is only spontaneous (with a rate constant equal to the inverse of the lifetime of the dark state, $k_{DE} = \tau_D^{-1}$). By definition, the saturation intensity in this case is $I_{SAT} = k_{DE}/\Phi_{ED}\,\sigma_E = (\tau_D\,\Phi_{ED}\,\sigma_E)^{-1}$. The inverse dependence of I_{SAT} with τ_D spans its value from over nine orders of magnitude. As an example, E and D in STED are the first excited singlet and the ground state, respectively (S_1 and S_0, $\Phi_{ED} = 1$; $\tau_D \approx 1$ ns); typical σ_E of visible dyes render I_{SAT} values on the order of tens to hundreds of MW cm^{-2}. These values can be reduced by six orders of magnitude if a metastable state D with a lifetime of a millisecond is used. In fact, I_{SAT} can be brought to zero, if a bistable compound is used (i.e., the thermal barrier for the spontaneous E $\leftarrow$ D transition is considerable higher than kT, rendering $k_{DE} \approx 0$). In this case, the reversibility condition, necessary for the targeted strategies, imposes the need of a photochemical path for the reverse transition, with a cross-section σ_D at a wavelength λ_{DE} (Fig. 1, case B).

In practice, some modifications must be considered to accurately describe actual systems (Fig. 1, case C). First, both reactions can be photoinduced and thermally induced. Second, due to the large width of regular absorption bands of organic dyes (ca. 50–100 nm), a cross talk in both directions must be considered: the E $\rightarrow$ D transition can be effected with λ_{DE} and the E $\leftarrow$ D transition at λ_{ED}. In the rate for each transition considered in Fig. 1 (case C), the first term is the spontaneous (thermal) rate, the second is the photoinduced one, and the third is the undesirable cross talk. This situation is often found in reversible photoisomerization reactions. In this case, the saturation intensity scales inversely with the lifetime of both states, so both E and D should be long lived in order to obtain a low I_{SAT}. If neither of the terms can be neglected, both D and E can be present at the saturation condition. However, note the difference in the lifetime of the states that must be considered as a thermal competing reaction: in an isomerization transition, if the D state is the metastable *cis* photoisomer, the lifetime that determines the value of I_{SAT} is that of a ground state of an isomer (*cis*-S_0), compared to the lifetime of a singlet excited state (e.g., S_1 in STED microscopy) that spontaneously decays much faster to the

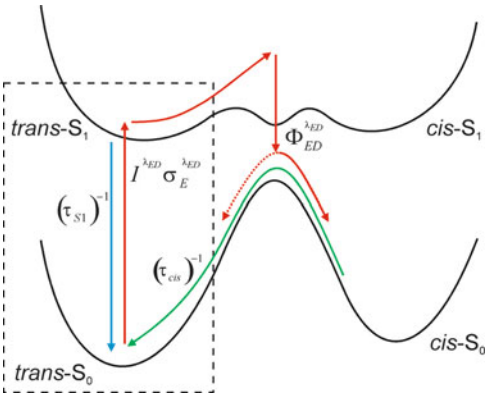

Fig. 2 Schematic representation of the states and energies of a photochromic compound with a *cis–trans* isomerization. The path for the *trans* → *cis* photoinduced isomerization is represented with *red lines*. Absorption to the excited *trans-S1* state is followed by a nuclear rearrangement and a decay to the ground state potential energy surface to render the *cis-S0* state. The quantum efficiency of the global process is Φ_{ED}. Alternatively, the molecule can spontaneously decay from the *trans-S1* state to the *trans-S0* ground state (*blue line*). τ_{S1} is the lifetime of the *trans-S1* state. The thermal back isomerization from the *cis-S0* to the *trans-S0* state is shown with a *green line*. The photoinduced back isomerization (path not shown) is also possible. Application of the switch for STED microscopy requires the use of only the *trans* states, as the D and E states, provided the *trans-S1* state is emissive. Alternatively, the ground states of the photochromic systems can be used in a targeted or stochastic technique

ground state. A photoisomerizable system, with an emitting stable isomer and a dark one, can thus be potentially used for resolution enhancement in two ways: *trans*-S_0 and *trans*-S_1, and *trans* S_1 and *cis*-S_0. The photophysics of the system explaining the two paths is depicted in Fig. 2. Note that when τ_E and/or $\tau_D \rightarrow \infty$, a drastic reduction in I_{SAT}, and thus in the applied intensity necessary to surpass the diffraction barrier, is obtained. In the limit of a bistable compound, the intensities to be used are only determined by practical factors such as image recording times. Regarding the cross-talk terms, it is desirable to keep them to a minimum; so when photoswitchable dyes are used in targeted techniques, ideally the absorption band of each state should not overlap or the cross-talk isomerization quantum yields should be negligible.

Stochastic Readout strategies are characterized by the repetitive localization with high precision of single probes in the E state that are sparsely distributed within a crowed of probes in the D state [11, 12]. Switching is essential to maintain a low and sparse population distribution of the probe in the emissive state at any time, and to refresh the probes to be localized (i.e., switch-off the probes already imaged, switch-on new ones, and repeat the process). In the absence of background, localization precision (Δx) is determined by the number of photons emitted by a fluorophore during an incursion to the emissive state (N_{PH}) to a value of $\Delta x \approx \lambda/2n \sin\alpha\sqrt{N_{PH}}$. [13]. Nonetheless, other factors must also be taken into account in order to translate this precision into a spatial resolution, in particular, the labeling

density and the contribution from the residual background fluorescence of the molecules in the nonemissive state. Let us consider, to illustrate this fact, that the D state has a brightness ($\varepsilon_{\lambda EX}\ \Phi_{FLUO}$) of 10^{-5} times the one of the emissive state. Such a state is obviously considered "nonemissive" for most purposes. A resolution of ca. 10 nm in the focal plane requires a labeling density $\geq 10^4$ probes/μm^2 (total probes in the E and D state) [14]. To reasonably avoid double event detection (i.e., two fluorophores erroneously assigned as a single one), only one probe in the E state must be in an area of 5 × 5 times the size of the diffraction-limited spot (also termed point spread function, PSF). Assuming a value of 200 nm for the PSF, the labeling density indicates that at least 10^4 molecules must be in the D state in that 5 × 5 PSF area. If the brightness contrast is 10^{-5}, we can estimate the background coming from the probes in the D state to be ≈10% of the average expected signal of the only molecule in the E state. Thus, a 10 nm resolution can only be achieved with systems with a brightness contrast of $\approx 10^{-5}$. In addition, the photophysics of the molecular switch should allow reaching the 10^4 D/E population ratio under practical measurement conditions. If reversible photoswitchable compounds are to be applied in stochastic techniques, these two requirements have to be considered. That means, conversions over 99.99% in the E → D direction (Fig. 2) must be achievable to drive the ensemble of probes in the imaging area almost completely to the nonemissive state. In the opposite direction, conversions of ~0.01% are in theory sufficient. The brightness contrast usually does not pose a problem since it is commonly possible to find at least a wavelength where only one of the photochromic isomers absorbs. However, with such demanding photochemical parameters, thermal reactions and cross talk should be more carefully regarded, since they are responsible for incomplete conversions (i.e., below 98%).

Despite the fact that reversibility of the switching process is not a necessary condition for *Stochastic Readout* strategies [4, 11] (switching-off can be replaced, for example, by irreversible photobleaching), it does have some inherent advantages. First, each marker can be localized several times. This is particularly useful for dynamic experiments in which several images must be acquired sequentially [15]. In addition, if for some reason the marker was rejected in an incursion to the E state (e.g., because fewer photons than a preset threshold were detected or another marker was in the E state at a distance shorter than the resolution of the microscope), it can be switched off and on again and localized successfully. Moreover, since the labeling density remains constant over time, there is no need to adjust instrumental variables, such as the intensity of the activating laser, to keep an approximately constant number of markers in the E state per frame, to avoid long (or irregular) recording times. Second, even though the spatial resolution of a *Stochastic Readout* does not depend directly on the applied intensity, lower intensities are also desirable for the same reasons as in the targeted techniques (avoiding sample photodamage). Thus *Stochastic* and *Targeted* strategies can benefit from long-lived dark states in a similar manner: with inefficient or noncompetitive thermal reactions, lower light intensity is needed to perform switching in one or both

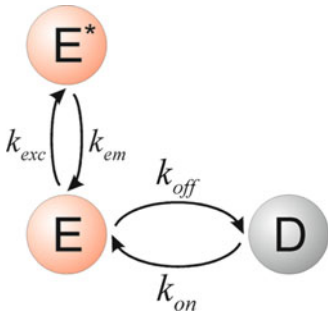

Fig. 3 Main processes involved in the switching and detection of a photochromic fluorescent switch. Targeted readout strategies demand many on/off cycles, while stochastic ones require a large number of photons from excitation/emission cycles

directions, either to assure a sparse distribution of probes in the E state or to saturate the E → D transition.

A switching mechanism based on photoinduced isomerizations has the advantage of a very versatile control of the E and D states of the probe. The parameters in Fig. 2, including the selection of the irradiation wavelengths, can be tuned in principle independently from one another, by chemical modifications of the dyes. For instance, if the thermal processes can be eliminated and cross-talk terms can be turned down to virtually zero, then the population in the E and D states can be controlled at will with the wavelength and intensity of the light used. Combined with the characteristic isomerization times in the excited state in the picoseconds range, this allows the custom setting of the population distribution of the probe from the emissive and the dark state, in theory to any desirable value in time and space. Furthermore, the product $\sigma\,\Phi$ of the photoinduced isomerization in both directions for common photochromic dyes is such that it allows enforcing this control with very low light intensities.

Two different aspects of the photochemical stability of a bistable, or a quasi-bistable compound, must be considered when applied in fluorescence nanoscopies (Fig. 3). On one hand, targeted strategies require the probe to be repeatedly cycled between the E and D state for a large number of times, while fewer E/E* cycles are sufficient. Thus, the critical fatigue resistance is measured as the number of switch-off/switch-on cycles before permanent photodamage of the dye molecule. This requires minimizing competitive secondary reactions, particularly from the excited states of both isomers. On the other hand, stochastic approaches require the extraction of many photons when the probe is at the E state. Then, only few (or even one) E/D cycles are required, and fatigue resistance is assessed as the maximum number of E/E* cycles attainable (i.e., the ground and excited singlet states of the emissive isomer). This requires a remarkable photostability only for the E states (ground and excited), in addition to a high brightness. The ability of a dye to produce enough number of either kind of cycles (E/D or E/E*) will determine its applicability and performance in each imaging approach.

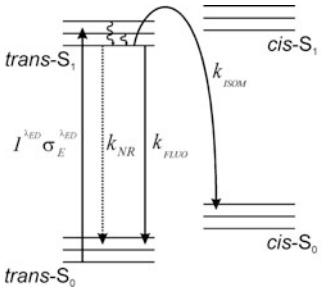

$$\Phi_{FLUO} = \frac{k_{FLUO}}{k_{FLUO} + k_{ISOM} + k_{NR}}$$

$$\Phi_{ISOM} = \frac{k_{ISOM}}{k_{FLUO} + k_{ISOM} + k_{NR}}$$

Fig. 4 Simplified Jablonsky diagram of a photochromic switch. The quantum efficiency of the fluorescence emission and isomerization processes, competing to depopulate the excited state of the *trans* isomer are shown in the *right*

3 Photoswitching, Photochromism, and Fluorescence

In general, most fluorescent compounds are not photochromic and the most common photochromic families of compounds are not fluorescent. This can be understood from the state diagram exemplified in Fig. 4. After the dye is excited and a fast thermal relaxation populates the lowest excited singlet state, S_1, three depopulation paths are common to any excited molecule: a nonradiative one (k_{NR}), a radiative one (k_{FLUO}) responsible for the fluorescence emission, and an isomerization path (k_{ISOM}) through any allowed channel in the potential energy surface (PES) of the excited state leading to the PES of the ground state of the isomer. This path usually involves some conformational changes and thus they evolve through a molecular coordinate, such as the flipping or rotation around a double bond (e.g., for a *cis–trans* isomerization), the breaking of a bond (e.g., of a spiro carbon), or a cyclization reaction.[1] The photoinduced reverse reaction proceeds through the excited state of the thermodynamically less stable isomer in a similar way. An interesting characteristic of photoisomerizations is that as the states involved in the primary light absorption step are the ground and first excited singlets of a regular organic dye, a two-photon absorption process is usually possible, and it has indeed been demonstrated for several photochromic dyes suitable for fluorescence nanoscopies [16–20].

The efficiency of the two key processes (Fig. 4), fluorescence emission and isomerization, add up to $1 - \Phi_{NR}$. Being two processes competing to depopulate the same excited state, one will grow at the expense of the other. Thus a fairly fluorescent dye with a $\Phi_{FLUO} \to 1$ usually has a poor isomerization efficiency. Conversely, photochromic reactions are known to be completed in a few

[1] Absorption to higher excited states does not change the picture since, according to Kasha's rule, relaxation to the lowest vibrational state of S_1 is very fast, so this is the departing state for the considered reactions at any excitation wavelength.

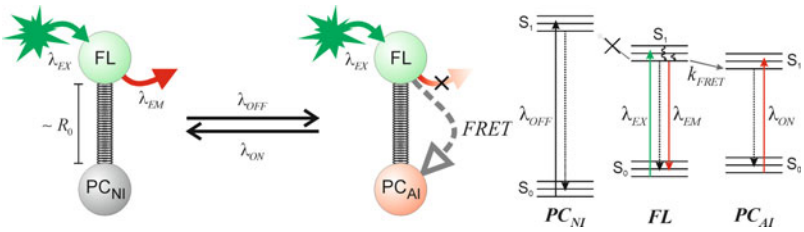

Fig. 5 Working principle of the dyads containing a photochromic compound (*PC*) and a fluorophore (*FL*) linked by a spacer. The photochromic reaction is driven by λ_{OFF} and λ_{ON}, while the emission of the fluorophore is excited at λ_{EX} and detected at λ_{EM}. The dyads are designed in such a way that energy transfer (*FRET*) is only possible between *FL* and one of the isomers *PC-AI* (the accepting isomer). This is achieved by: (1) maximizing the overlap between the emission of *FL* and the absorption of *PC-AI*, (2) minimizing the overlap between the emission of *FL* with the absorption of the neutral isomer (*PC-NI*), and (3) selecting the spacer to provide an average distance *FL–PC* on the order of the Förster radius (R_0) of the PC-AI/FL pair

picoseconds ($k_{ISOM.} \approx 10^{12}$ s^{-1}) [21]. Regular emission rates are much slower ($k_{FLUO.} \approx 10^{9}$ s^{-1}), leaving no chance for the molecule to emit light in the short time it remains in S_1 before isomerizing. As a result, relatively few photochromic compounds display emission in (at least) one of the isomers [17, 22–25].

A popular solution to bypass this problem and to convert almost any photochromic compound into a fluorescent switch is to combine in one molecule a photoswitchable and a fluorescent chromophore (Fig. 5). The two moieties are linked in a close proximity by a flexible or rigid spacer [26–32]. Although other mechanisms are possible (e.g., electron transfer [33–35] and electronic effects [36]), the preferred mechanism by which the photochromic reaction is transferred into a fluorescence modulation is usually Förster resonance energy transfer (FRET) [37], with the fluorophore (FL) acting as a donor and the two forms of the photochrome playing the role of a selective energy acceptor. The optimum situation for a good fluorescent switch is that only one of the isomers of the photochromic moiety acts as an efficient acceptor (acceptor isomer, AI), while the other is a poor one (neutral isomer, NI). This condition is obtained when the former has an absorption band overlapping the emission band of the fluorophore, and the latter does not. In other words, the spectroscopic differences between the two isomers result in a distinct overlap integral, and thus in a drastic change in the critical transfer distance (Förster radius, R_0). The linker should provide an average distance shorter than the value of R_0 (typically a few nanometers) of the pair FL-AI, but larger that the one for the pair FL-NI. In addition, the linker should be not too short in order to avoid quenching effects by a nonresonant mechanism [31]. Examples of fluorescent switchable dyads operating under this principle can be found in the literature combining a large variety of conventional fluorophores and different kinds of photochromic dyes, such as fulgides [26], diheteroarylethenes [29, 30], azobenzenes [38, 39], and spyropirans [40, 41].

A common problem of such photochrome-fluorophore dyads is encountered when the sample is interrogated in the dark state. The photons are absorbed by

the fluorophore and then the energy transfer process renders the markers in the excited state of the AI. If this moiety relaxes nonradiatively to AI-S_0, as depicted in Fig. 5, then excess energy is released as heat to the environment. However, if the path leading to NI-S_0 is followed, an "erasing effect" occurs (i.e., the sample changes in an undesirable manner its state while being probed by light). It should be noted that this path may not be very efficient, but at the irradiance level that the markers are subjected in the focal point of a microscope, the effect can become relevant. Although the dyads have two distinct chromophores (the photochrome and the fluorophore) with well-defined and separated electronic states, the erasing effect arises from the underlying problem that there is a common state for the two key processes: switching-on and energy transfer.

Dynamics of the excited states of each chromophore precludes a solution to the problem for FRET-based two dyes assemblies mentioned in the previous paragraph. The evident alternative to bypass this problem is to design similar adducts where the interaction between the chromophores occurs due to stereoelectronic effects in the ground state. Unlike the previous examples where the two blocks are electronically isolated for both isomeric states of the photochrome, the probes are designed in such a way that an electronic communication between the blocks is only possible in one of the isomers. Typically, this results in a large (bathochromic) shift in the absorption of the fluorophore from a wavelength λ_1 to λ_2. Thus, interrogation of the sample by excitation at λ_2 will only result in a signal output when the probe is in the isomeric form absorbing at this wavelength. Moreover, the chromophores are not unnecessarily forced through their excited states when the probe is interrogated in the off state, decreasing photobleaching rates. An interesting and potentially advantageous characteristic of this strategy is that both states could be emissive and with well-separated wavelengths (the emission shift should be similar to the absorption one, if there is not a dramatic modification on the Stokes shift). Nevertheless, any readout strategy requires only one bright isomer. Rhodamine spiroamides (RSAs) [17, 42, 43] and adducts containing a fluorophore and [1,3]-oxazines [44] or diheteroarylethenes [36] are examples of this kind of fluorescent switches.

4 Applications of Photoswitchable Dyes in *Targeted* and *Stochastic Readout* Strategies

The first application of a photochromic compound to switch fluorescence in fluorescence nanoscopies was performed in a system containing the photochrome, a fulgide, as a FRET acceptor, and a fluorescent coumarin dye. The moieties were two separated molecules, without a chemical bond between them, mixed in a polymer film [45]. The working principle is outlined in Fig. 6. Fulgides are derivatives of dimethylene succinic anhydrides that present photochromic behavior when at least one of the substituents is an aryl group (a furyl group in the present

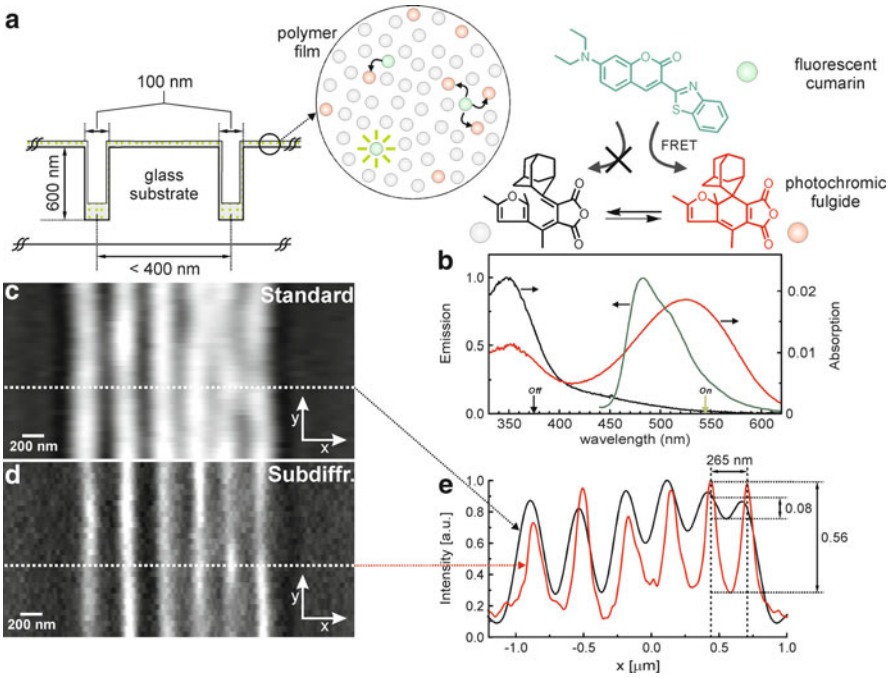

Fig. 6 Super-resolution (RESOLFT) imaging with the fulgide–coumarin system. (**a**) Chemical structure of the dyes, working principle of the system, and a representation of the object imaged. The dyes were mixed in a PMMA film, casted onto a coverslip with nanosized grooves produced by ion beam etching. (**b**) Absorption spectra of the open (*black line*) and closed isomer (*red line*) of the fulgide, and emission spectra of the coumarin (*green line*). (**c**–**e**) Images of a set of grooves with an average width of 90 nm and decreasing intergroove distance from left to right. (**c** and **d**) Standard and subdiffraction RESOLFT images, respectively. (**e**) Normalized line profile along the marked area of the images (*black line*: standard image; *red line*: RESOLFT image), showing the resolution increase. Adapted from [45]

example). The thermodynamically more stable open isomer is typically colorless, with an active absorption band in the near UV (~350 nm). The isomerization reaction is a photoinduced electrocyclic ring closure to yield the closed isomer, a 1,8a-dihydronaphthalene, which presents an absorption band at ~540 nm due to extended conjugation of the molecule through the double bonds. Irradiation of the closed isomer in the absorption band in the visible region (~540 nm) results in the ring-opening back isomerization to recover the initial open isomer. Most fulgides are quasi-bistable, i.e., have a very slow thermal recover (closed → open isomer), or are bistable as is the case of the adamantyl-furyl fulgide used in this application. Coumarin 6 was selected as the fluorescent component based on its photophysical properties. First, the emission band of the coumarin has a considerable overlap with the absorption band of the closed isomer of the fulgide; second, the lowest energy absorption band of the coumarin is centered at a minimum in the absorption of the FRET-accepting closed isomer of the fulgide. This latter feature

allows keeping the cross talk to a minimum between fluorophore excitation and the isomerization. The photochrome and the fluorophore were mixed in a polymer matrix (Poly(methyl methacrylate), PMMA) at concentrations that ensure that every coumarin has at least one fulgide at a distance in the order of the Förster radius of the donor–acceptor pair. In this way, the emission of the coumarin (excited a 405 nm) was modulated with 375 nm (off-switching) and 543 nm (on-switching). This approach with a high acceptor-to-donor ratio has two important advantages. Because multiple acceptors are present for each donor, the switching process is very efficient. In addition, the switching process remains operative even after some percent of the photochromes have been photobleached.

This simple approach was used in a targeted readout strategy (RESOLFT microscopy) to achieve subdiffraction resolutions with only a few hundred W cm^{-2} [45]. While this system was suitable as a proof of principle, combining the two functions in one molecule provides controllable location and the use of drastically lower quencher concentrations.

Diarylethenes (DAEs) are one of the most utilized photochromes in the last decades to build molecular photoswitches, because of their high fatigue resistance. Some DAEs have proved to endure the largest number of isomerization cycles reported so far for a photochromic dye ($>10^4$) [24]. In particular, diarylperfluorocyclopentenes with heterocyclic aryl groups (e.g., thiophenes in Fig. 7) are among the most photostable. In addition, the electron withdrawing character of the perfluoro substituent promotes the cyclization reaction, and the presence of heteroaryl groups makes both isomers thermally stable (the thiophenes in this example provide the bistability) [24]. The photochromism of diarylethenes, alike the one in fulgides, involves a reversible electrocyclic reaction between an open- and a closed-ring isomer. In the latter, delocalization of the π-electrons along the whole molecule is responsible for a long-wavelength absorption band. This band is absent in the open isomer, which behaves roughly as two separate chromophores. Since DAEs are rarely emissive, fluorescence modulation has been achieved by an appended fluorophore, commonly working as a FRET donor of the closed isomer [29]. With this strategy, fluorescent switching was even observed at the SM level [30]. However, because of the erasing effect while reading the off state of the dyad (DAE-fluorophore), the use of this system in a stochastic strategy is only possible if the quantum yield for the switch-on isomerization (CI → OI) is lower than 10^{-2} [46].

An important drawback of DAEs is the position of the first absorption band in the spectrum of the open isomer. The OI of perfluorocyclopentene derivatives normally absorbs below 300 nm, and thus photocyclization should be performed at short wavelengths which are generally unsuitable for conventional optics and laser power sources. Based on the fact that the absorption properties of both isomers depend on the substituents on the aryl groups, rational chemical modifications have rendered compounds that can be cycled and opened at 375 nm and 650 nm, respectively [31]. The modifications were chosen also to achieve nearly complete conversions on the photostationary state. Therefore, dyads formed with a DAE and a bridged rhodamine fluorophore (Fig. 7) present

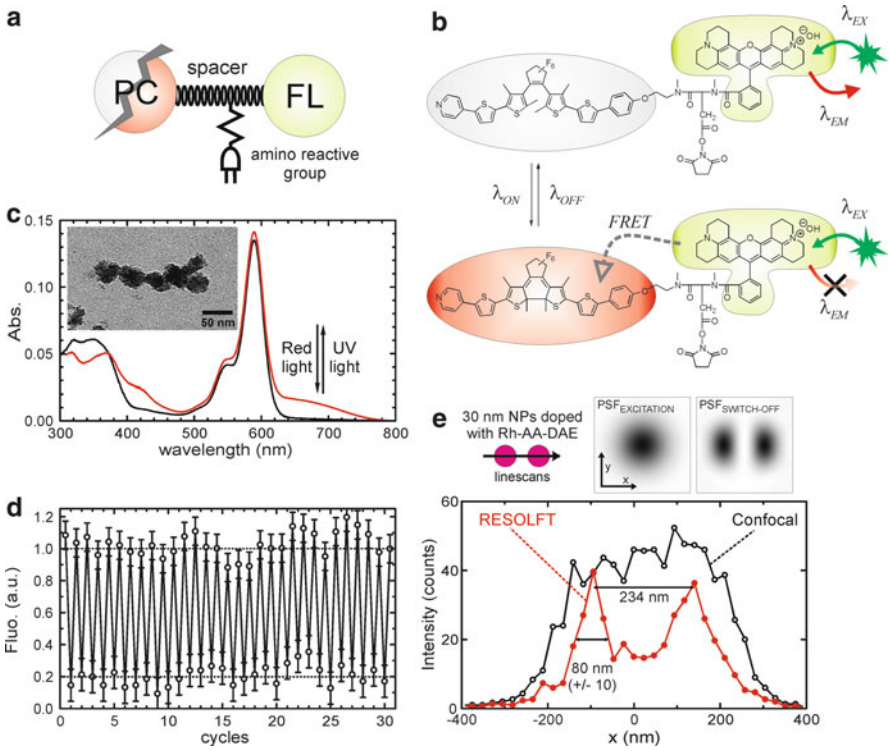

Fig. 7 (**a**, **b**) Cartoon representation and chemical structure of a photochromic fluorescent molecular switch based on a DAE (*gray*: open isomer; *red*: closed isomer) and a rhodamine linked by a flexible spacer, functionalized with an amino reactive group (succinimide ester). (**c**) Absorption spectra of an ethanolic suspension of ~30 nm silica nanoparticles stained with the probe in the open isomeric form (*black line*) and the closed one (*red line*); the *inset* shows a TEM image of the nanoparticles. (**d**) A series of 30 successive complete irradiation cycles (UV/red light) performed on a single silica particle in a confocal microscope. (**e**) RESOLFT microscopy of the switchable nanoparticles. Line scans along the *x* direction over two neighboring particles measured with a microscope in a conventional confocal mode (*black line*), and with the enhanced capabilities (*red line*, RESOLFT). The excitation PSF (543 nm) used in both measurements and the switch-off PSF (375 nm) used in the RESOLFT mode are also shown. Adapted from [47]

an efficient and high contrast fluorescence switching, i.e., over 95% of the signal could be switched off.

Super-resolution images of silica nanoparticles, tagged with one of these probes, were obtained by fluorescence microscopy (Fig. 7) [47]. A three cw-lasers setup was used, similar to the one used with the fulgide/coumarin mixtures, but with different excitation wavelengths. The photochromic system was switched on and off with 375 and 671 nm, respectively, while the rhodamine was excited at 543 nm. Despite the fact that the fluorescence of the doped nanoparticles in solution could be virtually completely depleted, the system displays the excitation/erasing problem described before when observed in the microscope. In fact, low excitation intensities improved

signal modulation to values close to those obtained in solution, but it resulted in very noisy data. Thus, a compromised situation was used to achieve images with an acceptable signal-to-noise ratio, resulting in an average switching-off ratio of 20%. This exemplifies how critical these erasing effects are and how they scale up when going from bulk measurements to nanosized objects in the focal plane of a microscope. Nevertheless, super-resolution images were obtained based in the DAE-rhodamine dyads, with a targeted strategy (RESOLFT). Resolution improvement as shown in Fig. 7 was obtained in one direction. Attempts to extend these results to two dimensions showed poor results due to low fatigue resistance of the photochromic building block. Signal modulation measurements over several nanoparticles indicated that after 60 on/off cycles, approximately 10% of the modulation ratio (signal in the off state/signal in the on state) was lost. This was evidenced by an increase in the off-level signal, with the on-level signal unaltered, indicating that the photochromic chromophore underwent irreversible photodamage.

The number of complete on/off cycles of the photochrome must be considerably improved if similar probes are to be successfully implemented in practical applications. A possible explanation for the relatively low number of cycles endured by this probe is the environment of the silica matrix. To rule out this effect, an alternative strategy was considered. An amino reactive adduct of the probe was tagged to a secondary antibody through standard procedures, and fixed cells were immunostained. While fluorescence was observed, and conventional (confocal) images could be recorded, no switching was possible under conditions similar to those used with the silica nanoparticles, described previously. This is a common drawback of the DAEs to be solved; while most of the outstanding performances were observed in apolar organic solvents, very few examples were reported in water [48–54]. Development of diarylperfluorocyclopentenes with improved solubility and photochromism in aqueous environments could overcome these drawbacks [55].

RSAs (Fig. 8) [56] are a family of photochromic compounds with a switching mechanism based on ground state electronic differences between the isomers. Unlike fulgides and diarylethenes, one of the isomers is fluorescent and thus there is no need to bridge a FRET donor. RSAs are formed by derivatization of the free carboxyl group of a rhodamine with an aromatic or aliphatic primary amine, followed by cyclization to a thermally stable isomer containing a five-membered ring. This form is called the closed isomer. The formation of this ring breaks the extended conjugation in the three condensed cycles and results in the disappearance of the characteristic rhodamine absorption in the visible range (and, of course, also emission). The closed isomer has its first absorption band at ~313 nm; irradiation in this band breaks the C–N spiro bond and opens the five-membered ring, to render the open isomer with the subsequent restoration of the rhodamine chromophore. The colored and brightly fluorescent OI has the characteristic photophysical properties of the parent rhodamine (i.e., absorption and fluorescence wavelengths, absorption coefficient, emission lifetime, and quantum yield). The first absorption band of the OI is found in the visible region (in the green to red ranges depending on the substitution pattern) [43]. This band is not photo-active for the back

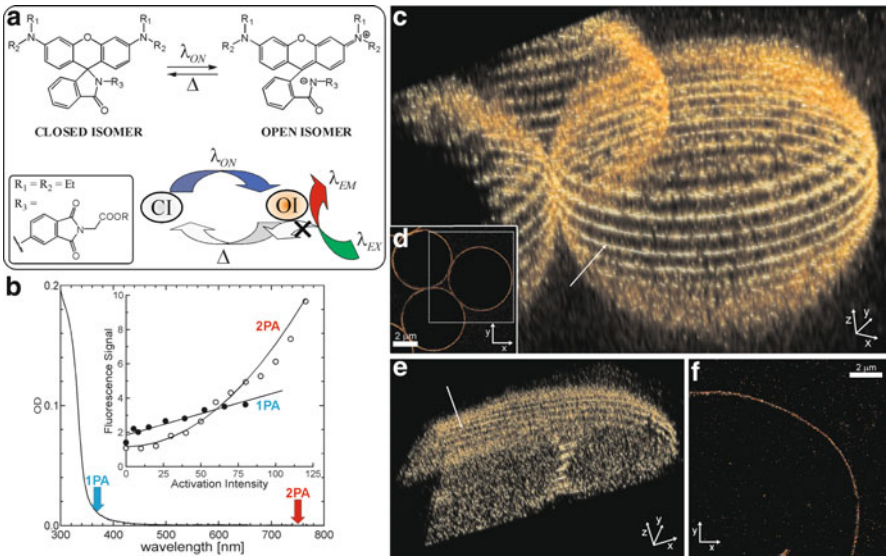

Fig. 8 (**a**) Photochromic reaction of RSAs and working principle of these photoswitches (the *inset* shows the substituents of the RSA used to record the images shown here). (**b**) Absorption spectra of the closed (dark) isomer; the *inset* shows the switch-on signal as a function of the intensity of the excitation light at 375 nm (1PA, one-photon absorption) and 747 nm (2PA, two-photon absorption). (**c**–**f**) Super-resolution 3D imaging with a probe using a stochastic SM activation and detection method (PALMIRA), with a 2PA switch-on process. (**c**) 3D reconstructed images of 5 μm silica beads, surface-stained with an amino reactive derivative of the probe. (**d**) An equatorial slice is shown (*arrow* in (**c**)). (**e**) 3D reconstructed images of lamin of a U373MG cell, immunostained with a secondary antibody tagged with an amino reactive derivative of the probe. (**f**) Equatorial slice (*arrow* in (**e**)). Adapted from [17]

isomerization (OI → CI). Thus, irradiation in the visible absorption band of the OI results in efficient fluorescence emission but does not result in the regeneration of the CI, allowing a readout of the system (by its emission signal) without an undesired erasing effect (Fig. 8). The back reaction proceeds only via a thermal pathway, with a characteristic time that is strongly dependent on the polarity of the environment: in the millisecond range in polar solvents and becoming much larger in apolar ones [56, 57].

The mechanism involving the creation and rupture of the typical rhodamine chromophore endows RSAs with two important advantages: a virtually infinite signal contrast between the two states, and the outstanding and well-known photostability of rhodamines that made them widely useful as fluorescent markers in biological systems and exploited in single molecule experiments since early times [58, 59]. Their poor ring-opening quantum yield makes them unsuitable for targeted techniques but is sufficient for stochastic ones. Therefore, RSA have been exclusively used as probes in SM localization microscopies.

Different chemical modifications have also been performed to red-shift the absorption band of the CI and to improve the isomerization efficiency, either initiated

by a one-photon or a two-photon absorption process [18]. The latter excitation process enabled optical sectioning in the switch-on process and allows to image thick samples (e.g., whole cells) without a TIRF illumination geometry, and maintaining an excellent localization precision in each *z*-section (Fig. 8) [17, 60]. In such experiments, there is an important amount of probes in out-of-focus planes. Remaining in the nonemissive form, their contribution to the background is unappreciable. This demonstrates the outstanding contrast between the dark and bright states, and the reliable control of the switching process offered by this family of photochromic compounds.

An interesting property of RSAs is that their photophysical properties, in particular absorption and emission wavelengths, can be easily tuned by changing the nature and position of different functional groups based on a well-known chemistry. More precisely, a color palette of RSA has been developed (Fig. 9) [43] and used in stochastic nanoscopies producing excellent localization precision [17, 42, 43, 60, 61]. Targeting of biomolecules or other molecules of interest has been achieved with the aid of selective chemical binding through amino or thiol reactive groups. These functional groups have been usually incorporated at the other end of the substituent group pending from the amide (group R_5 in Fig. 9), but it can be tailored in other positions of the photochrome (e.g., R_1 or X). Multicolor applications have also been performed, with the advantage that only one laser is needed for switching-on all the different probes, and another laser is used for excitation. Combined with a single molecule-based spectral analysis, up to three different RSA compounds were simultaneously imaged in the same sample [42], avoiding dedicated wavelengths for each marker or a sequential switching/detection scheme.

Spiropyrans (SP) is a family of photochromic compounds that encounters extensive applications to phototrigger a change in a secondary property, based on a large charge distribution and shape difference between the two isomers [62]. In particular, a well-known example is 6-NO_2-BIPS (SP in Fig. 10). Isomerization proceeds via a photoinduced homolytic cleavage of the C–O bond, followed by *cis* → *trans* isomerizations in the open form. The spiro center in the CI forces an orthogonal distribution of both halves of the molecule, preventing their electronic conjugation. In contrast, an extended conjugation is possible in the OI, resulting in a strong absorption band ($\varepsilon \sim 8 \times 10^4\ M^{-1}\ cm^{-1}$) in the 500–600 nm range. This isomer is called a photomerocyanine. The colored isomer reverts to the closed one via a thermal ($\tau \sim 10$–100 s) and a photoinduced pathway (with visible light irradiation), the latter with relatively low quantum efficiency. Photostability of 6-NO_2-BIPS is rather poor, because the triplet state is involved in the photoisomerization pathway. The merocyanine isomer is rarely fluorescent unless it is embedded in apolar environments. Thus, many reported examples of fluorescent switches are based in a 6-NO_2-BIPS used as a FRET-modulator of the fluorescent signal of a bridged fluorophore (e.g., Lucifer Yellow [40], rhodamines [41], BODIPY [63], or QDs [64]). A slow thermal reaction constant (slow switching-on) and poor fatigue resistance are probably the reasons why these dyads have not found yet applications in fluorescence nanoscopy [41].

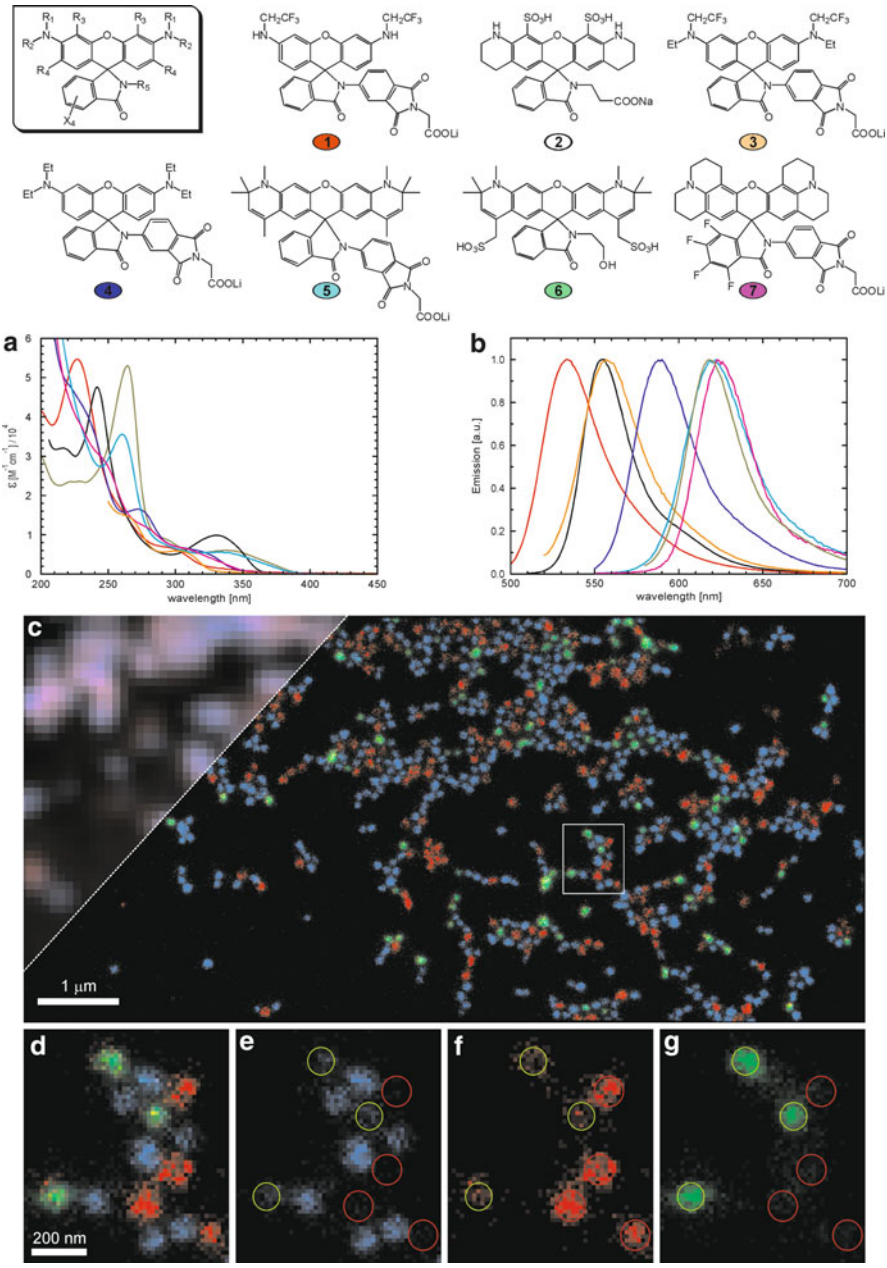

Fig. 9 Color palette of RSAs for fluorescence nanoscopies. (*A*, *B*) Absorption spectra of the CI isomer (D isomer), and fluorescence emission of the OI (E isomer) of the dyes, respectively. (*C*–*G*) Multicolor SM switching-based nanoscopy image of mixtures of silica beads each stained with one of three different photoswitchable markers (compounds 3, 5, and 6). (*C*) Overview. The *upper left triangle* shows the image obtained from classical diffraction-limited two-color imaging. No details can be discerned. (*D*) Enlarged section marked by the white rectangle in the overview and (*E*–*G*) *blue*, *red*, and *green* components. Adapted from [42, 43]

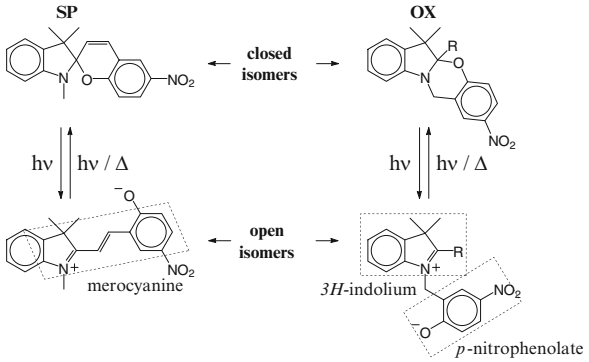

Fig. 10 Photochromic reaction of a spiropyran (*left*) and a [1,3]-oxazine (*right*). Thermodynamically more stable isomers are shown at the top (closed isomers). The chromophores in the metastable open isomers are highlighted

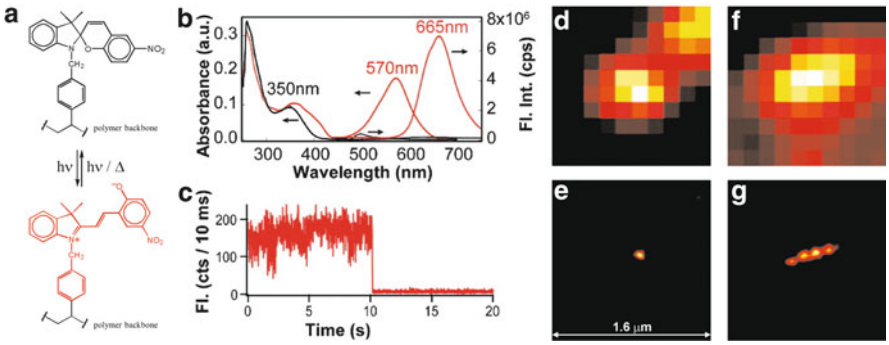

Fig. 11 (**a**) Chemical structure of the photochromic spiropyran polymerized into the hydrophobic cores of polymer nanoparticles. (**b**) Absorption (*left axes*) and fluorescence emission spectra (*right axes*) of the closed isomer (*black curves*) and open isomer (*red curves*). (**c**) A typical SM intensity trajectory of the dye in its emissive state, in a polymer nanoparticle. (**d**–**g**) Super-resolution imaging of 70-nm nanoparticles recorded with a SM switching stochastic approach (**e**, **g**). Conventional images are shown on top (**d**, **f**). The same scale was used in the four images. Adapted from [65]

The direct fluorescence of the merocyanine has recently been exploited for imaging beyond the diffraction limit using a stochastic approach [65], by embedding the probe in hydrophobic cavities of polymeric nanoparticles (Fig. 11). The increased fluorescence quantum yield ($\Phi_{\text{Fluo}} = 0.24$) and photostability provided by this environment allowed SM switching and localization with this system. The improvements were obtained at the expense of the photoswitching performance of the photochromic dye (i.e., lower $\Phi_{\text{CI}\rightarrow\text{OI}}$ and slower thermal recovery) [66], limiting the acquisition speed of the method. In addition, the absorption band of the OI is active for the reverse isomerization which competes with fluorescence emission. Moreover, although the number of detected photons per molecule

predicts a localization precision of a few nanometers, the resolution of the approach is limited by the size of the nanoparticle to about 40 nm [65]. Nevertheless, the possibility to switch-on and excite the merocyanine via two-photon absorption processes [19], and novel parent compounds that can switch the emission color from green to red (instead of off/on) [67], may lead this kind of compounds to interesting applications in fluorescence nanoscopy in the future.

A related family of photochromic compounds overcomes two of the most important disadvantages of SPs: fatigue resistance and slow thermal recovery. [1,3]-oxazines (OX, Fig. 10) have a similar photochromic mechanism as spiropyrans but a different molecular structure [68, 69]. In particular, the lack of the central double bond is responsible for a much shorter metastable isomer lifetime ($\tau = 22$ ns in acetonitrile, R = phenyl), by avoiding the need of a *trans* → *cis* isomerization in the thermal back reaction. Unlike SPs, the zwitterions OI of OXs do not have merocyanine chromophores. Instead, a 3*H*-indolium and a *p*-nitrophenolate, both nonemissive chromophores, are built up upon ring opening. The *p*-nitrophenolate moiety is responsible for an absorption band at around 440 nm. An interesting feature is that the choice of the substituent at the chiral center of the [1,3]oxazine ring (−R) can be used to tune the properties of the OI. For instance, its lifetime can be extended more than two orders of magnitude, and the absorption can be red-shifted over 100 nm (R = 2-(4-dimethylaminophenyl)-ethylene) [70]. Moreover, the emission of a coumarin fluorophore attached to this same position can be modulated through the photochromic reaction of an OX chromophore [44], based on ground state stereoelectronic properties of the isomers. The switching of this dye has been detected at the SM level, making this family of compounds promising candidates for stochastic readout strategies [71].

5 Comparing Photochromism with Other Switching Mechanisms

Photoswitchable (reversible) proteins usually display a switching mechanism involving a *cis–trans* isomerization of the central chromophore [72–74]. Therefore, they share similar photophysical properties as those involved in the fluorescence switching described in this chapter. Fluorescent proteins have the unique advantage of being genetically encoded, avoiding the need for a targeting strategy. However, organic photochromic and fluorescent dyes have two important advantages. First, they are usually brighter and more photostable than photoswitchable proteins. Second, organic photochromic dyes are much smaller in size (typically 500–1,000 Da as opposed to 27 kDa of a GFP). The latter feature is becoming more and more relevant at the current resolution level attainable: the molecular size of the label may become a limiting factor [15]. Thus, provided there is a reliable and specific labeling method which forms an adduct (probe-recognition tag) with a smaller size than a fused fluorescent protein, small photochromic dyes could even outperform their

genetically encoded counterparts. Most successful labeling methods require the generation of a chimera of the target protein by introducing a genetically encoded recognition tag, e.g., a small directing peptide sequence [75]. However, a remaining and quite relevant issue concerning the chemical properties of the probe must not be ignored when targeting intracellular structures in a living cell: the probe is required to be membrane-permeable and soluble in aqueous environments.

Non-photochromic small dyes have been successfully used in fluorescence nanoscopies based on other photoinduced reversible mechanisms, in particular optical shelving of the probe in the triplet state or in other generic long-lived dark states. For instance, GSD, GSDIM, STORM, or BM microscopies have exploited the blinking of carbocyanine, oxazine, or xanthenic dyes, such as Rhodamine 6G, Cy5, Cy7, and some Alexa and Atto dyes [76–82]. At a first glance, a clear advantage appears when these switching mechanisms are used. Triplet and generic radical-ion long-lived states are common to virtually all fluorophores. Thus, many commercial dyes can be accordingly used for imaging beyond the diffraction barrier, provided their brightness, switching wavelengths and rates, and other relevant physical parameters meet the conditions for the desired super-resolution technique. Another advantage is that usually only two or even one laser wavelength is used. In contrast, purely photochromic compounds need at least two, but in many cases they need three different excitation wavelengths for switching-on, switching-off, and fluorescence excitation. However, blinking strategies rely on the efficient population of dark states often populated through the triplet state (provided T_1 itself is not the aimed dark state). This brings about a few disadvantages compared to bistable compounds. On one hand, usually higher intensities ($\approx$100 kW cm^{-2}) [76, 83] are required to manipulate the population distribution of excited states. On the other hand, the triplet state is known to be one of the main components in the bleaching pathway of chromophores, challenging the number of switching cycles attainable by a fluorophore. Carbocyanines, for instance, can be switched up to 100 times under particular conditions regulating the population and depopulation rates of T_1 and other dark states [84]. Although this is on the same order as the number of switching cycles obtained with a photochromic switch in a microscope [47], diarylethenes [24] or other photochromic compounds [69] can endure, under certain conditions, a larger number of cycles. Moreover, when the bleaching mechanism is known (e.g., a proton migration), rational chemical modifications can be applied to improve fatigue resistance.

However, perhaps the most striking difference is that the regulation of the rates between the excited and radical/ionic dark states always needs additional external chemical species not always compatible with the sample or the conditions of the experiment. A second nearby chromophore acting as a blinking facilitator (the activator), oxygen scavengers (enzymes, polyvinyl alcohol), thiols, and redox active species (e.g., ascorbic acid, methyl viologen) are examples of them [85]. In addition, the switching mechanism and the dark states involved have not been fully elucidated in some cases. Summarizing, while blinking is a property already incorporated in every fluorophore accounting for the generality of this switching mechanism, photochromism may provide a more rational and easy control of the rates and state populations. Meanwhile, the fatigue resistance of the probes used up to date is similar, irrespective of the switching mechanism.

6 Concluding Remarks

The probes discussed in this chapter bear in common their (quasi)bistable nature in two states with distinct photochemistry and great contrast in brightness. The photochemical interconversion between those states provides the molecular switching mechanism necessary to achieve temporal discernment of objects closer than the diffraction-limited spot of a far-field microscope. Examples of successful imaging of nanosized objects have been described based on molecular systems containing a spiropyran, a fulgide, a diarylethene, or an RSA photochromic skeleton, with or without an auxiliary fluorescent moiety. Their particular photochemical features in combination with the requirements of the targeted and stochastic strategies determine how they have been used and their success.

Fulgides and diarylethenes photochromes were used as switchable FRET acceptors with a bound fluorophore as the donor. Examples with high energy transfer efficiency and a nearly complete conversion in the photostationary state were designed. Because the bright isomer is the thermodynamically stable state, the maximum D/E population ratio achievable is enough for targeted strategies, but insufficient for stochastic ones. So far, they have only found applications in targeted RESOLFT microscopy. To make them useful for a stochastic SM-based application, systems with the stable isomer as the dark one would be required. This seems unlikely in the frame of the FRET strategy, on the grounds of the spectroscopic properties presented by both isomers of most fulgides and DAEs known. On the other side, spiropyrans and RSAs with the dark state as the more stable one do not need an additional fluorescent moiety. While the relatively low number of on/off cycles they can perform has prevented their use in targeted approaches, their outstanding brightness and photochemical stability of the emissive state are suitable to detect and localize SMs of these probes with high precision. For this reason, they have found their application in stochastic approaches. SPs need a low polarity environment to reach the required brightness for SM detection, and so they have been used and included into polymer nanoparticles. RSAs have the advantage of their extraordinary performance in aqueous environments, for example they directly bind to antibodies.

A global comparison of the examples presented here renders the conclusion that photochromic compounds have been more effective in stochastic nanoscopies. The main reason is the higher success in obtaining molecular systems achieving a large number of E/E^* cycles rather than cycles between the two photoisomers (E/D), at least under the irradiation conditions required in the microscope. Undoubtedly, the prospects of photochromic organic dyes in targeted strategies are bound to the development of new compounds or families with higher cyclability. In addition, further advances on these molecular switches leading to improvements of their chemical and physical properties, such as chemical stability, enhanced performance in aqueous environments, or cell permeability will surely benefit both approaches, and lead to new and exciting applications.

References

1. Abbe E (1873) Beiträge zur Theorie des Mikroskops und der mikroskopischen Wahrnehmung. Arch Mikr Anat 9:413–468
2. Hell SW, Wichmann J (1994) Breaking the diffraction resolution limit by stimulated emission: stimulated-emission-depletion fluorescence microscopy. Opt Lett 19(11):780–782
3. Hell SW, Kroug M (1995) Ground-state-depletion fluorscence microscopy: a concept for breaking the diffraction resolution limit. Appl Phys B 60(5):495–497
4. Hell SW (2009) Microscopy and its focal switch. Nat Methods 6(1):24–32
5. Crano JC, Guglielmetti RJ (eds) (1999) Organic photochromic and thermochromic compounds. Topics in applied chemistry, vol 1. Plenum, New York, p 376
6. Bouas-Laurent H, Düurr H (2001) Organic photochromism (IUPAC technical report). Pure Appl Chem 73(4):639–665
7. Braslavsky S (2007) Glossary of terms used in photochemistry 3rd edition. Pure Appl Chem 79(3):293–465
8. Feringa BL, van Delden RA, Koumura N, Geertsema EM (2000) Chiroptical molecular switches. Chem Rev 100(5):1789–1816
9. Hell SW (2004) Strategy for far-field optical imaging and writing without diffraction limit. Phys Lett A 326(1–2):140–145
10. Westphal V, Hell SW (2005) Nanoscale resolution in the focal plane of an optical microscope. Phys Rev Lett 94(14):143903
11. Betzig E, Patterson GH, Sougrat R, Lindwasser OW, Olenych S, Bonifacino JS, Davidson MW, Lippincott-Schwartz J, Hess HF (2006) Imaging intracellular fluorescent proteins at nanometer resolution. Science 313(5793):1642–16455
12. Rust MJ, Bates M, Zhuang X (2006) Sub-diffraction-limit imaging by stochastic optical reconstruction microscopy (STORM). Nat Methods 3(10):793–795
13. Thompson RE, Larson DR, Webb WW (2002) Precise nanometer localization analysis for individual fluorescent probes. Biophys J 82(5):2775–2783
14. Huang B, Bates M, Zhuang X (2009) Super-resolution fluorescence microscopy. Annu Rev Biochem 78:993–1016
15. Shroff H, Galbraith CG, Galbraith JA, Betzig E (2008) Live-cell photoactivated localization microscopy of nanoscale adhesion dynamics. Nat Methods 5(5):417–423
16. Belfield KD, Liu Y, Negres RA, Fan M, Pan G, Hagan DJ, Hernandez FE (2002) Two-photon photochromism of an organic material for holographic recording. Chem Mater 14(9): 3663–3667
17. Folling J, Belov V, Kunetsky R, Medda R, Schonle A, Egner A, Eggeling C, Bossi M, Hell SW (2007) Photochromic rhodamines provide nanoscopy with optical sectioning. Angew Chem Int Ed 46(33):6266–6270
18. Folling J, Belov V, Riedel D, Schonle A, Egner A, Eggeling C, Bossi M, Hell SW (2008) Fluorescence nanoscopy with optical sectioning by two-photon induced molecular switching using continuous-wave lasers. ChemPhysChem 9(2):321–326
19. Zhu M-Q, Zhang G-F, Li C, Aldred MP, Chang E, Drezek RA, Li ADQ (2011) Reversible two-photon photoswitching and two-photon imaging of immunofunctionalized nanoparticles targeted to cancer cells. J Am Chem Soc 133(2):365–372
20. Miyasaka H, Murakami M, Itaya A, Guillaumont D, Nakamura S, Irie M (2001) Multiphoton gated photochromic reaction in a diarylethene derivative. J Am Chem Soc 123(4):753–754
21. Tamai N, Miyasaka H (2000) Ultrafast dynamics of photochromic systems. Chem Rev 100(5): 1875–1890
22. Takahashi T, Taniguchi Y, Umetani K, Yokouchi H, Hashimoto M, Kano T (1985) Cis-trans photoisomerization of perinaphthothioindigo for use as a photo-imaging sensor using fluorescence under He-Ne laser excitation. Jpn J Appl Phys 24(2):173–176
23. Tsivgoulis GM, Lehn J-M (1997) Multiplexing optical systems: multicolor-bifluorescent-biredox photochromic mixtures. Adv Mater 9(8):627–630

24. Irie M (2000) Diarylethenes for memories and switches. Chem Rev 100(5):1685–1716
25. Liang Y, Dvornikov AS, Rentzepis PM (2000) Synthesis and photochemistry of photochromic fluorescing indol-2-ylfulgimides. J Mater Chem 10(11):2477–2482
26. Walz J, Ulrich K, Port H, Wolf HC, Wonner J, Effenberger F (1993) Fulgides as switches for intramolecular energy transfer. Chem Phys Lett 213(3–4):321–324
27. Daub J, Beck M, Knorr A, Spreitzer H (1996) New molecular systems for functional dye-based molecular switching of luminescence. Pure Appl Chem 68(7):1399–1404
28. Bahr JL, Kodis G, de la Garza L, Lin S, Moore AL, Moore TA, Gust D (2001) Photoswitched singlet energy transfer in a porphyrin-spiropyran dyad. J Am Chem Soc 123(29):7124–7133
29. Giordano L, Jovin TM, Irie M, Jares-Erijman EA (2002) Diheteroarylethenes as thermally stable photoswitchable acceptors in photochromic fluorescence resonance energy transfer (pcFRET). J Am Chem Soc 124(25):7481–7489
30. Irie M, Fukaminato T, Sasaki T, Tamai N, Kawai T (2002) A digital fluorescent molecular photoswitch. Nature 420(6917):759–760
31. Bossi M, Belov V, Polyakova S, Hell SW (2006) Reversible red fluorescent molecular switches. Angew Chem Int Ed 45(44):7462–7465
32. de Meijere A, Zhao L, Belov VN, Bossi M, Noltemeyer M, Hell SW (2007) 1,3-bicyclo[1.1.1] pentanediyl: the shortest rigid linear connector of phenylated photochromic units and a 1,5-dimethoxy-9,10-di(phenylethynyl)anthracene fluorophore. Chem Eur J 13(9):2503–2516
33. Tsuchiya S (1998) Intramolecular electron transfer of diporphyrins comprised of electron-deficient porphyrin and electron-rich porphyrin with photocontrolled isomerization. J Am Chem Soc 121(1):48–53
34. Myles AJ, Branda NR (2000) Porphyrinic phenoxynaphthacenequinones. Tetrahedron Lett 41(20):3785–3788
35. Fukaminato T, Doi T, Tamaoki N, Okuno K, Ishibashi Y, Miyasaka H, Irie M (2011) Single-molecule fluorescence photoswitching of a diarylethene-perylenebisimide dyad: non-destructive fluorescence readout. J Am Chem Soc 133(13):4984–4990
36. Yan SF, Belov VN, Bossi ML, Hell SW (2008) Switchable fluorescent and solvatochromic molecular probes based on 4-amino-N-methylphthalimide and a photochromic diarylethene. Eur J Org Chem 2008(15):2531–2538
37. Clegg RM (1995) Fluorescence resonance energy transfer. Curr Opin Biotechnol 6(1): 103–110
38. Jin M, Lu R, Bao CY, Xu TH, Zhao YY (2004) Fluorescence modulation in azobenzene-substituted triphenyl pyrazoline derivative. Opt Mater 26(1):85–88
39. Harbron EJ, Vicente DA, Hoyt MT (2004) Fluorescence modulation via isomer-dependent energy transfer in an azobenzene-functionalized poly(phenylenevinylene) derivative. J Phys Chem B 108(49):18789–18792
40. Song L, Jares-Erijman EA, Jovin TM (2002) A photochromic acceptor as a reversible light-driven switch in fluorescence resonance energy transfer (FRET). J Photochem Photobiol A 150(1–3):177–185
41. Seefeldt B, Kasper R, Beining M, Mattay J, Arden-Jacob J, Kemnitzer N, Drexhage KH, Heilemann M, Sauer M (2010) Spiropyrans as molecular optical switches. Photochem Photobiol Sci 9(2):213–220
42. Bossi M, Folling J, Belov VN, Boyarskiy VP, Medda R, Egner A, Eggeling C, Schonle A, Hell SW (2008) Multicolor far-field fluorescence nanoscopy through isolated detection of distinct molecular species. Nano Lett 8(8):2463–2468
43. Belov VN, Bossi ML, Folling J, Boyarskiy VP, Hell SW (2009) Rhodamine spiroamides for multicolor single-molecule switching fluorescent nanoscopy. Chem Eur J 15(41):10762–10776
44. Deniz E, Sortino S, Raymo FM (2010) Fluorescence switching with a photochromic auxochrome. J Phys Chem Lett 1(24):3506–3509
45. Bossi M, Folling J, Dyba M, Westphal V, Hell SW (2006) Breaking the diffraction resolution barrier in far-field microscopy by molecular optical bistability. New J Phys 8:275

46. Fukaminato T, Sasaki T, Kawai T, Tamai N, Irie M (2004) Digital photoswitching of fluorescence based on the photochromism of diarylethene derivatives at a single-molecule level. J Am Chem Soc 126(45):14843–14849
47. Folling J, Polyakova S, Belov V, van Blaaderen A, Bossi ML, Hell SW (2008) Synthesis and characterization of photoswitchable fluorescent silica nanoparticles. Small 4(1):134–142
48. Takeshita M, Irie M (1997) Enhancement of the photocyclization quantum yield of 2,2[prime or minute]-dimethyl-3,3[prime or minute]-(perfluorocyclopentene-1,2-diyl)bis(benzo[b]- thiophene-6-sulfonate) by inclusion in a cyclodextrin cavity. Chem Commun (23):2265–2266
49. Soh N, Yoshida K, Nakajima H, Nakano K, Imato T, Fukaminato T, Irie M (2007) A fluorescent photochromic compound for labeling biomolecules. Chem Commun (48):5206–5208
50. Hirose T, Irie M, Matsuda K (2008) Temperature-light dual control of clouding behavior of an oligo(ethylene glycol)-diarylethene hybrid system. Adv Mater 20(11):2137–2141
51. Hirose T, Matsuda K, Irie M (2006) Self-assembly of photochromic diarylethenes with amphiphilic side chains: reversible thermal and photochemical control. J Org Chem 71(20): 7499–7508
52. Piao X, Zou Y, Wu J, Li C, Yi T (2009) Multiresponsive switchable diarylethene and its application in bioimaging. Org Lett 11(17):3818–3821
53. Zou Y, Yi T, Xiao SZ, Li FY, Li CY, Gao X, Wu JC, Yu MX, Huang CH (2008) Amphiphilic diarylethene as a photoswitchable probe for imaging living cells. J Am Chem Soc 130(47): 15750–15751
54. Zhou X, Duan Y, Yan S, Liu Z, Zhang C, Yao L, Cui G (2011) Optical modulation of supramolecular assembly of amphiphilic photochromic diarylethene: from nanofiber to nanosphere. Chem Commun 47(24):6876–6878
55. Polyakova S, Belov VN, Bossi ML, Hell SW (2011) Synthesis of photochromic compounds for aqueous solutions and focusable light. Eur J Org Chem 2011(18):3301–3312
56. Knauer KH, Gleiter R (1977) Photochromism of rhodarnine derivatives. Angew Chem Int Ed 16(2):113
57. Willwohl H, Wolfrum J, Gleiter R (1989) Kinetics and mechanism of the photochromism of N-phenyl-rhodaminelactame. Laser Chem 10(2):63–72
58. Kummer S, Dickson RM, Moerner WE (1998) Probing single molecules in polyacrylamide gels. Proc Soc Photo-Opt Instrum Eng 3272:165–173
59. Zondervan R, Kulzer F, Orlinskii SB, Orrit M (2003) Photoblinking of rhodamine 6G in poly (vinyl alcohol): radical dark state formed through the triplet. J Phys Chem A 107(35): 6770–6776
60. Foiling J, Belov V, Riedel D, Schonle A, Egner A, Eggeling C, Bossi M, Hell SW (2008) Fluorescence nanoscopy with optical sectioning by two- photon induced molecular switching using continuous- wave lasers. ChemPhysChem 9(2):321–326
61. Testa I, Schonle A, Middendorff CV, Geisler C, Medda R, Wurm CA, Stiel AC, Jakobs S, Bossi M, Eggeling C, Hell SW, Egner A (2008) Nanoscale separation of molecular species based on their rotational mobility. Opt Express 16(25):21093–21104
62. Guglielmetti R (1990) 4n + 2 Systems: spiropyrans. In: Dürr H, Bouas-Laurent H (eds) Photochromism: molecules and systems, 1st edn. Elsevier, Amsterdam, pp 314–466
63. Tomasulo M, Deniz E, Alvarado RJ, Raymo FM (2008) Photoswitchable fluorescent assemblies based on hydrophilic BODIPY-spiropyran conjugates. J Phys Chem C 112(21): 8038–8045
64. Medintz IL, Trammell SA, Mattoussi H, Mauro JM (2003) Reversible modulation of quantum dot photoluminescence using a protein- bound photochromic fluorescence resonance energy transfer acceptor. J Am Chem Soc 126(1):30–31
65. Hu DH, Tian ZY, Wu WW, Wan W, Li ADQ (2008) Photoswitchable nanoparticles enable high-resolution cell imaging: PULSAR microscopy. J Am Chem Soc 130(46):15279–15281
66. Zhu M-Q, Zhu L, Han JJ, Wu W, Hurst JK, Li ADQ (2006) Spiropyran-based photochromic polymer nanoparticles with optically switchable luminescence. J Am Chem Soc 128(13):4303–4309

67. Tian Z, Wu W, Wan W, Li ADQ (2009) Single-chromophore-based photoswitchable nanoparticles enable dual-alternating-color fluorescence for unambiguous live cell imaging. J Am Chem Soc 131(12):4245–4252
68. Tomasulo M, Sortino S, Raymo FM (2005) A fast and stable photochromic switch based on the opening and closing of an oxazine ring. Org Lett 7(6):1109–1112
69. Tomasulo M, Sortino S, White AJP, Raymo FM (2005) Fast and stable photochromic oxazines. J Org Chem 70(20):8180–8189
70. Deniz E, Tomasulo M, Sortino S, Raymo FM (2009) Substituent effects on the photochromism of bichromophoric oxazines. J Phys Chem C 113(19):8491–8497
71. Deniz E, Tomasulo M, Cusido J, Yildiz I, Petriella M, Sortino S, Bossi ML, Sortino S, Raymo FM (2012) Photoactivatable Fluorophores for Super-Resolution Imaging Based on Oxazine Auxochromes. J Phys Chem C 116(10), 6058–6068
72. Andresen M, Wahl MC, Stiel AC, Grater F, Schafer LV, Trowitzsch S, Weber G, Eggeling C, Grubmuller H, Hell SW, Jakobs S (2005) Structure and mechanism of the reversible photoswitch of a fluorescent protein. Proc Natl Acad Sci USA 102(37):13070–13074
73. Brakemann T, Weber G, Andresen M, Groenhof G, Stiel AC, Trowitzsch S, Eggeling C, Grubmüller H, Hell SW, Wahl MC, Jakobs S (2010) Molecular basis of the light-driven switching of the photochromic fluorescent protein Padron. J Biol Chem 285(19):14603–14609
74. Chudakov DM, Feofanov AV, Mudrik NN, Lukyanov S, Lukyanov KA (2003) Chromophore environment provides clue to "kindling fluorescent protein" riddle. J Biol Chem 278(9): 7215–7219
75. Fernandez-Suarez M, Ting AY (2008) Fluorescent probes for super-resolution imaging in living cells. Nat Rev Mol Cell Biol 9(12):929–943
76. Bretschneider S, Eggeling C, Hell SW (2007) Breaking the diffraction barrier in fluorescence microscopy by optical shelving. Phys Rev Lett 98(21):218103
77. Folling J, Bossi M, Bock H, Medda R, Wurm CA, Hein B, Jakobs S, Eggeling C, Hell SW (2008) Fluorescence nanoscopy by ground-state depletion and single-molecule return. Nat Methods 5(11):943–945
78. Heilemann M, van de Linde S, Schuttpelz M, Kasper R, Seefeldt B, Mukherjee A, Tinnefeld P, Sauer M (2008) Subdiffraction-resolution fluorescence imaging with conventional fluorescent probes. Angew Chem Int Ed 47(33):6172–6176
79. Vogelsang J, Kasper R, Steinhauer C, Person B, Heilemann M, Sauer M, Tinnefeld P (2008) A reducing and oxidizing system minimizes photobleaching and blinking of fluorescent dyes. Angew Chem Int Ed 47(29):5465–5469
80. Heilemann M, van de Linde S, Mukherjee A, Sauer M (2009) Super-resolution imaging with small organic fluorophores. Angew Chem Int Ed 48(37):6903–6908
81. Vogelsang J, Cordes T, Forthmann C, Steinhauer C, Tinnefeld P (2009) Controlling the fluorescence of ordinary oxazine dyes for single-molecule switching and superresolution microscopy. Proc Natl Acad Sci USA 106(20):8107–8112
82. Dertinger T, Heilemann M, Vogel R, Sauer M, Weiss S (2010) Superresolution optical fluctuation imaging with organic dyes. Angew Chem Int Ed 49(49):9441–9443
83. Gensch T, Böhmer M, Aramendía PF (2005) Single molecule blinking and photobleaching separated by wide-field fluorescence microscopy. J Phys Chem A 109(30):6652–6658
84. Heilemann M, Dedecker P, Hofkens J, Sauer M (2009) Photoswitches: key molecules for subdiffraction-resolution fluorescence imaging and molecular quantification. Laser Photonics Rev 3(1–2):180–202
85. Vogelsang J, Steinhauer C, Forthmann C, Stein IH, Person-Skegro B, Cordes T, Tinnefeld P (2010) Make them blink: probes for super-resolution microscopy. ChemPhysChem 11(12): 2475–2490

Far-Field Nanoscopy with Conventional Fluorophores: Photostability, Photophysics, and Transient Binding

Thorben Cordes, Jan Vogelsang, Christian Steinhauer, Ingo H. Stein, Carsten Forthmann, Andreas Gietl, Jürgen J. Schmied, Guillermo P. Acuna, Sebastian Laurien, Birka Lalkens, and Philip Tinnefeld

Abstract In several aspects, conventional organic fluorophores are the first choice for super-resolution microscopy. These fluorophores are well developed with respect to their photophysics and labeling chemistry. Their small size indicates minimal invasiveness. This chapter focuses on the use of conventional organic fluorophores for localization-based super-resolution imaging.

We argue that the number of possible fluorophore excitations, which is limited by photobleaching, determines the absolute resolution limit for super-resolution microscopy in general. Strategies for photostabilization are therefore discussed. For super-resolution imaging, conventional fluorophores can be used by exploiting generic dark states or transient binding of fluorophores to the target structure. We finally present several examples of super-resolution imaging with conventional fluorophores including protein aggregation and bottom-up produced calibration structures made of DNA origami.

T. Cordes (✉)
Molecular Microscopy Research Group & Single-Molecule Biophysics, Zernike Institute for Advanced Materials, University of Groningen, Nijenborgh 4, 9747 AG Groningen, The Netherlands
e-mail: t.m.cordes@rug.nl

J. Vogelsang
Institut für Experimentelle und Angewandte Physik, Universität Regensburg, Universitätsstrasse 31, 93053 Regensburg, Germany

C. Steinhauer, and I.H. Stein
Angewandte Physik – Biophysik & Center for NanoScience, Ludwig-Maximilians-Universität, Amalienstraße 54, 80799 Munich, Germany

C. Forthmann, A. Gietl, J.J. Schmied, G.P. Acuna, S. Laurien, B. Lalkens, and P. Tinnefeld (✉)
Institute of Physical and Theoretical Chemistry – NanoBioSciences, TU Braunschweig, Hans-Sommer-Str. 10, 38106 Braunschweig, Germany
e-mail: p.tinnefeld@tu-braunschweig.de

P. Tinnefeld et al. (eds.), *Far-Field Optical Nanoscopy*,
Springer Ser Fluoresc (2015) 14: 215–242, DOI 10.1007/4243_2012_40,

Keywords Organic fluorophores · Photostability · Single-molecule photophysics · Super-resolution microscopy

Contents

1 Introduction to "Conventional Fluorophores"

Two experimental realizations of far-field fluorescence microscopy are currently revolutionizing the way of looking at nanoscopic structures and allow optical imaging with sub-diffraction resolution or "super-resolution." One uses a spatial confinement of fluorescence in a scanning approach whereas the other is based on subsequent single-molecule localizations in a wide-field/total internal reflection fluorescence (TIRF) microscope [1–7]. Interestingly, both approaches can use the same type of fluorophores although the photophysical requirements for super-resolution imaging are considerably different.

Organic fluorophores are the primary choice for many applications in super-resolution imaging as they show intense luminescence in the visible or near-infrared spectral range. Furthermore, their structure is relatively small (i.e., on the order of only 1–2 nm) and does not involve large protein barrels [as for example the green fluorescent protein (GFP) and derivatives] or the assembly of even larger inorganic nanoparticles; both of the latter have considerable size (3–4 nm for monomeric fluorescent proteins (FPs) and up to several 10 nm for nanoparticles), a fact that obviously increases their potential to interfere with biological function or to alter natural morphology.

Another important advantage of organic fluorophores is the existence of generic dark states that have recently been shown to work as "switchable" off-states for several types of super-resolution techniques [8–10]. This reduces the demand for marker advancement with sophisticated and often sensitive photochromic groups.

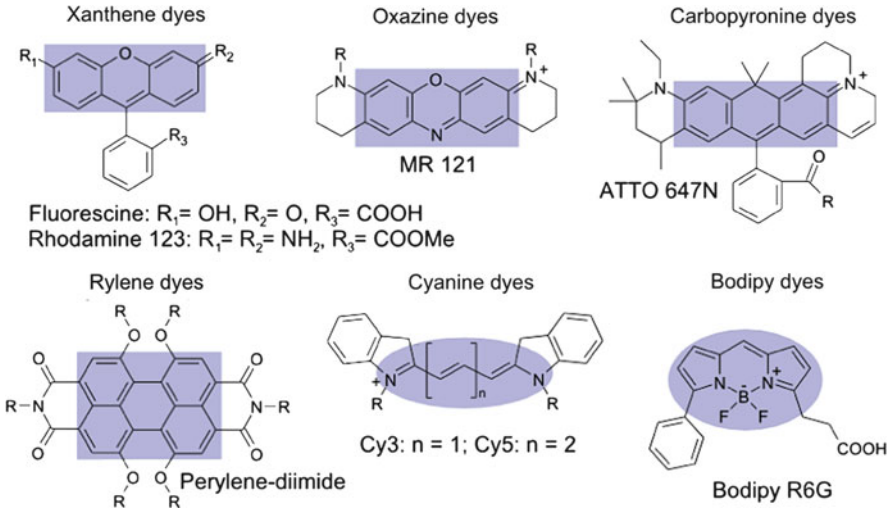

Fig. 1 Basic chemical structures of dyes from the classes of xanthenes (rhodamine, fluorescein), carbopyronines, oxazines, cyanines, bodipy's, and rylenes

Hence, organic fluorophores or "conventional fluorophores" (as they are denoted throughout this chapter), like (carbo)rhodamines, oxazines, cyanines, bodipy, and rylenes, are a primary choice for super-resolution imaging when both good photophysical performance and small size are required. Figure 1 provides an overview of some of the most frequently used basic fluorophore structures. Blue-shadowed areas mark the chromophore structure common to dyes from a specific class. Conventional organic fluorophores offer several unique advantages with respect to FPs or nanoparticles (quantum dots or nano-diamonds) other than their small size of only a few nanometers. They have gone through a long development with evolutionary advancement selecting for properties such as brightness (high extinction coefficient at the excitation wavelength, high fluorescence quantum yield) and photostability. They are easily modified chemically to meet requirements such as (water-)solubility or to tune their affinity for specific environments inside cells (e.g., dyes with high membrane affinity or preferred binding to double-stranded DNA). It is also straightforward to attach reactive groups that allow linking them to other (bio-)molecules of interest. These advantages have induced a new quest for selective in vivo labeling strategies with conventional organic fluorophores that have the clear potential to replace fluorescent proteins (see chapters by A. Yushchenko and M.P. Bruchez [76] and S. Gayda et al. [77] in this volume).

This chapter discusses how different conventional organic fluorophores can be used for a variety of super-resolution microscopy techniques. For this purpose, we show in Sect. 2 that the photostability of the fluorophores ultimately limits the achievable resolution for both super-resolution approaches, i.e., targeted switching and readout ("targeted readout," e.g., stimulated emission depletion (STED) [1],

ground state depletion (GSD) [11], saturated structured illumination microscopy (SSIM) [12, 13]) and stochastic switching and readout ("stochastic readout," e.g. photoactivated localization microscopy (PALM) [2], fluorescence photoactivation localization microscopy (fPALM) [14], statistical optical reconstruction microscopy (STORM) [15]). Due to this central role of photostability, we present different strategies to stabilize fluorophores by modifications of the chemical structure and by chemical additives (Sect. 3). Here, we also describe a recently developed concept to achieve high photostability based on a reducing and oxidizing system ("ROXS"). In Sect. 4, we focus on the manipulation of conventional fluorophores so that they can be used for stochastic readout approaches, which imply that the major fraction of fluorophores is prepared in an off-state throughout the measurement and the positions of a subpopulation of fluorophores are read out during each image frame. In this context, we differentiate between photo-induced, thermal (Sect. 4) and diffusion-based processes (Sect. 5). In the final section (Sect. 6), an approach for super-resolution calibration using structures created by DNA nanotechnology is discussed. Such structures are generally required to answer the question whether imaging problems are related to the setup or to the sample studied.

2 Photostability Limits Super-Resolution

Nowadays far-field super-resolution imaging is either based on spatial "fluorescence confinement" through targeted switching (e.g. STED [1], GSD [11], and SSIM [12]; see respective chapters in this book), or utilizes stochastic switching for subsequent localization of single fluorescent probes realized in "fluorescence localization" (e.g., PALM [2], fluorescence photoactivation localization microscopy (fPALM) [14], statistical optical reconstruction microscopy (STORM) [15], and variations thereof, e.g., direct statistical reconstruction microscopy (dSTORM), GSD and individual molecule return (GSDIM), and blink microscopy.

There are, however, different equations describing the maximal achievable resolution with different crucial parameters for the two approaches [see (2) and (3)]. Supported by a number of studies [2, 16–19], it has become clear that the key elements for the achievable resolution are (a) the photostability of the fluorescent probe and (b) the possibility to prepare it in two distinct states, i.e., a bright (denoted as on-state) and a dark state (denoted as off-state) [20]. In this section, we reconsider the factors that are actually responsible for the maximal achievable resolution of both super-resolution approaches, targeted switching and stochastic switching.

2.1 Determination of the Probe Position by "Fluorescence Localization"

It has been known for several decades that a single fluorescent point source can be localized in any fluorescence far-field microscope with nanometer precision using two-dimensional Gaussian fitting [16, 21]. In an ideal situation (no background, 100% detection efficiency), the achievable resolution d for the fluorescence localization approach is as follows:

$$d = \frac{\mathrm{FWHM}}{\sqrt{n}} \tag{1}$$

FWHM denotes here the full width at half maximum of the point spread function (*PSF*), and n the number of emitted photons. Certainly, nanometer precise single-molecule localization does not automatically result in sub-diffraction resolution images, i.e., the localization method is not per se a super-resolution imaging technique. Resolution beyond Abbe's limit can only be achieved by temporally separating the emission of all labels, summing up their positions and reconstructing an image. This ensures that only one fluorescent molecule is emitting within a diffraction-limited area at any given time. Though the photophysical parameters of fluorophores (e.g., average duration of on/off times) are known to influence resolution in STORM-type imaging, they do not dictate the physical limit of resolution. Equation (1) describes the "super-resolution limit" for fluorescence localization-based super-resolution imaging techniques with the crucial parameter n. From a photophysical point of view, this simply means that the resolution in fluorescence localization is ultimately limited to the number of emitted photons n, per localization of the emitter.

2.2 Determination of the Probe Position by "Spatial Fluorescence Confinement"

Alternatively, the photons of the conventional fluorophore can be spatially restricted to originate from an area much smaller than the FWHM of the PSF yielding sub-diffraction resolution [22]. The most common approaches to fluorescence confinement in a confocal scanning microscope concurrently use two different light beams for the spatial restriction: an excitation beam populates the fluorescent state of the fluorophore and a "switching" or "depletion" beam with a light intensity distribution that spatially suppresses out-of-focus fluorescence by depletion of the bright state. In principle, this spatial off-switching can be accomplished by any photo-induced transition into a nonfluorescent dark state (as described in detail in other chapters of this volume). By applying an appropriate spatial intensity distribution to the depleting beam, e.g., a doughnut, fluorescence is

only observed from the very center of the excitation volume. Here, the area from where fluorescence can be detected depends on the intensity I_{DEP} of the depletion beam and the photophysical properties of the emitter. Accordingly, the intensity I_{SAT}, at which $1/e$ of the emitters are depleted from the excited state, describes the intensity dependence of the switching mechanism. The relationship of these two intensities and their influence on resolution has been quantified by Hell [23]:

$$d = \frac{\text{FWHM}}{\sqrt{1 + (I_{DEP}/I_{SAT})}} \tag{2}$$

This relationship, derived from the wave nature of light and the photophysical properties of the involved states [1], describes the achievable imaging resolution of "fluorescence confinement" techniques for idealized emitters with basically an unlimited number of switching cycles c, between an on- and off-state.

Inspection of various publications based on fluorescence confinement, however, reveals that the resolution for reversible saturable optical fluorescence transitions (RESOLFT)-type experiments could not be decreased to an arbitrarily low value although higher I_{DEP} laser intensities would have been available [3]. In all cases, with the exception of [18], where other limiting factors such as imperfect optics and setup stability come into play, the main limiting factor was c and not the available intensity of the depletion beam I_{DEP} [17–19]. Neglecting other factors in biological applications such as the mobility/thermal motion of the fluorophores, it becomes clear that the Achilles' heel of the RESOLFT concept is the finite number of c as has been recognized before [3].

Focusing on the specific case of STED, c is directly related to the number of excitation/de-excitation cycles, since the fluorescing S_1 state is considered the on-state and S_0 the off-state [3]. This means that exactly one excitation/de-excitation process (no matter if it results in the emission of a photon) represents one switching cycle in the case of STED. As a consequence, the resolution in STED-based super-resolution microscopy is again directly limited by the photostability. This statement is supported by comparing the following studies: (a) STED performed with fluorescent proteins, which are known for their moderate photostability resulted in a resolution of ~50–100 nm [17]. (b) Organic fluorophores in combination with a photostabilizing buffer (ROXS) [24] enabled a significantly higher resolution of about 26 nm even for single molecules [19]. (c) Using nitrogen vacancy centers in diamond, which are practically unbleachable, a resolution down to 6 nm was demonstrated [18]. Although a decreasing motion of the fluorophores within these experiments from (a) to (c) has to be taken into account, the general trend points out that the number of switching cycles (= photostability) is linked with the achievable resolution.

The former considerations allow quantifying the achievable resolution of fluorescence confinement techniques by the number of achievable switching cycles c, between an on- and off-state in the case of two dimensions. For optimal resolution, the increment or step size of the scanning unit is directly adjusted to the area of the

fluorescence confinement, i.e., to I_{DEP} and the achievable resolution according to (2) [1]. Ideally, the fluorescence of the emitter is confined in a way that for each step of the scanning unit one switching cycle is conducted. At each pixel it is probed whether there is a molecule in the confined region. For nearly all pixels, the emitter is prepared in an off-state.

Only in the confined region at the very center of the fluorophore location it is prepared in an on-state. Thus, essentially one on-state (one photon) is enough to localize the fluorophore since the confinement provides the position intrinsically. As a consequence, the increment and hence the achievable resolution in the case of fluorescence confinement are limited by the number of switching cycles the emitter can undergo.

These considerations allow a direct comparison between fluorescence localization and fluorescence confinement for the two-dimensional case. As shown in Fig. 2, we assume a simple scenario for the localization precision of a single molecule for localization-based approaches. For an exemplary PSF with a FWHM of 300 nm, the emitter can be assigned to an area with a size that only depends on the number of detected photons: 100×100 nm^2 for 9 photons, 60×60 nm^2 for 25 photons, and 33×33 nm^2 for 81 photons (marked as red-hatched area in Fig. 2a).

In the confinement case (Fig. 2b), resolution beyond the diffraction limit is realized by switching the emitter into an off-state and a sequential detection of the remaining photons. The achievable confinement is presented for c switching cycles with the somewhat simplified view that one cycle is carried out per pixel with $c = 9$, 25 and 81, respectively. In the majority of cycles, the emitter is switched off (i.e., $(c - 1)$-off cycles) and only for the central pixel, the emitter is on (one on cycle) (Fig. 2b). The simplification of one cycle per pixel is a good approximation since the lower probability of excitation in the outer parts of the excitation focus (indicated as gray scale pixels in Fig. 2b) is roughly compensated by the requirement to cycle more than once in the central part of the focus to account for the Poissonian probability distribution of excitation. Accordingly, fluorescence of the emitter can be confined to an area of 100×100 nm^2 for $c = 9$ cycles, 60×60 nm^2 for $c = 25$ cycles, and 33×33 nm^2 for $c = 81$ cycles, which is graphically depicted in Fig. 1b for an equal pixel size over the diffraction-limited area.

This leads to the same functional behavior regarding the absolute resolution limit, by substituting the parameter n by c and assuming a unity fluorescence quantum yield.

$$d = \frac{\mathrm{FWHM}}{\sqrt{c}} \tag{3}$$

Considering now that one switching cycle between the S_1 and S_0 state has to be conducted to extract one photon, the parameters c and n are the same in the case of fluorescence localization.

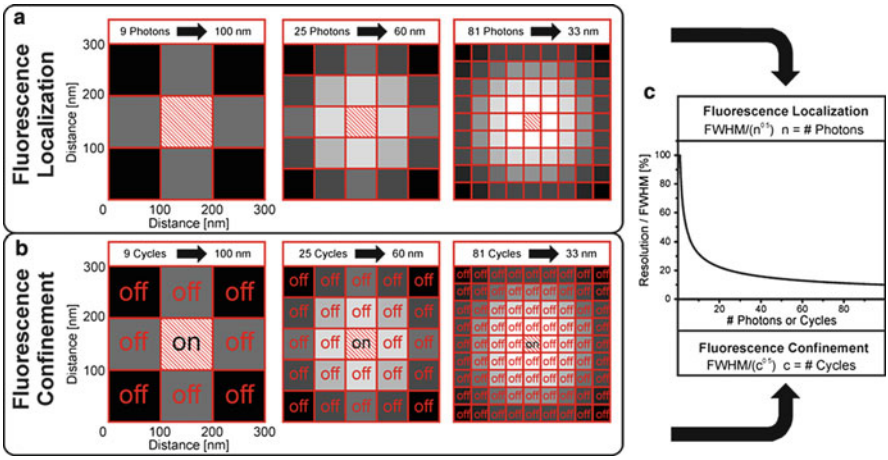

Fig. 2 The scheme shows the super-resolution limit of light-microscopy techniques with sub-diffraction resolution based on "fluorescence localization" and "fluorescence confinement." (**a**) Idealized intensity distribution of wide-field fluorescence images of a single fluorescent probe emitting 9, 25, and 81 photons, respectively. Here, *brighter squares* correspond to a higher number of photons detected in this area; please note that the *squares* in the figure do not correspond to the actual pixel size of the camera. Due to the resolution given by FWHM/($n \times 0.5$), the position of the molecule can be determined using two-dimensional Gaussian fitting to the intensity distribution. This allows to assign the position of the molecule to the red-hatched area of 100×100 nm^2 ($n = 9$ photons), 60×60 nm^2 ($n = 25$ photons), and 33×33 nm^2 ($n = 81$ photons). (**b**) Idealized fluorescence images of a single fluorescent probe as obtained by confocal scanning, where the molecule can be cycled 9, 25, and 81 times. Here, one "cycle" is equivalent to exactly one switching cycle between an on- and off-state. The gray scale value indicates the switching probability. Due to the confinement of the fluorescence, i.e., suppression of emission [see panel (**b**), off-squares], the position of the molecule can be assigned to an area of 100×100 nm^2 that corresponds to $c = 9$ cycles involving 1 cycle per pixel, 60×60 nm^2 with $c = 25$ cycles and 33×33 nm^2 with $c = 81$ cycles for an equally distributed pixel size over the diffraction-limited area. (**c**) The dependency of the achievable super-resolution is shown with respect to the number of emitted photons and excitation/de-excitation cycles, respectively

It should be noted that the square root dependence has different origins for the two approaches. In fluorescence localization, it is related to the standard error of a repetitive measurement with each detected photon representing an independent measurement of a molecule's position. In fluorescence confinement, the square root has geometric origin.

Interestingly, the limited repeatability of the measurement in photobleaching-limited super-resolution induces a different scaling law with respect to dimensionality. Equation (1) is independent of dimensionality, assuming that one photon is enough to localize an emitter in all three dimensions, whereas fluorescence confinement requires more cycles with increasing dimensionality if resolution is limited by c.

In conclusion, all upper considerations in combination with Fig. 2 clarify that the number of switching cycles for a single emitter commonly is the limiting factor for

both types of super-resolution approaches. In the two-dimensional case, a quantitative relation exists between the number of on cycles that are needed for the localization of a single molecule in fluorescence localization and the number of off cycles (and one on cycle) required to determine fluorophore positions in fluorescence confinement. Treating only the optimal case neglecting, e.g., background and detection sensitivity, these arguments yield a fundamental "super-resolution" limit and have to be adapted for practical purposes and to the details of the experimental realization. In cases where the resolution of fluorescence confinement depends on the limited number of switching cycles, Hell's equation [(2)] together with (3) could be used to adjust the intensity of the depletion beam at optimized pixel size in two dimensions (FWHM^2/c) yielding $I_{\mathrm{DEP}} = I_{\mathrm{SAT}} \cdot (c - 1) \approx I_{\mathrm{SAT}} \cdot c$ for $c \gg 1$. Similar considerations can be applied to other super-resolution techniques using saturation. SSIM, for example, is a highly paralleled scanning microscopy technique based on "inverse" fluorescence confinement [12]. There is another notion about the two discussed super-resolution approaches: super-resolution microscopy based on fluorescence confinement is realized via targeted switching of a certain subset of molecules [3, 20]. This targeted nature of switching could advantageously be used to adapt the scanning procedure and to even reduce the cycle-limited resolution in a structure-dependent way [25]. Accordingly, (3) applies to an arbitrary complex structure such as a grid-like point pattern, with a minimal point-to-point distance of two times the resolution d. In other cases, adapted sampling of pixels could improve the economy of cycling. Adapting I_{DEP} dynamically and starting at low I_{DEP} intensity, one would only have to further study pixels that exhibited fluorescence. This could significantly reduce the number of required cycles in structures with varying fluorophore density. Equation (3) is the limiting case for a structure of maximum complexity. This intelligent scanning scheme expands on the improvement of controlled light-exposure microscopy [26], by also adapting illumination dose of the depletion beam and pixel size to the measured structure.

3 Stable Fluorophores and Making Fluorophores Stable

The preceding section has clearly identified the photostability of fluorescent labels as one of the most crucial parameters for super-resolution imaging. Fortunately, owing to the long experience with fluorescent dyes in different research fields (e.g., dye lasers and fluorescence microscopy), a large pool of fluorescent dyes with all kinds of properties is available (see, e.g., [27]). Their absorbance and fluorescence spectra span a wide range from the UV to the IR, and they show different solubility in water or organic solvents, varying chemical functionalities, and they can be attached to almost any molecule of interest, even inside living cells. Despite these strengths, there are no dyes yet that do not undergo photobleaching under intense laser illumination and conditions relevant for life sciences. The question arises whether photobleaching, the sudden disappearance of fluorescence from a single dye molecule due to an irreversible photochemical reaction, is a universal feature of

organic dye molecules. If photobleaching is a generic feature of dye molecules, what are the potential sources and mechanisms, and can the quest for the "ultra-stable" fluorophores be successful in the end?

In the following, we discuss the mechanisms of photobleaching and their possible prevention. While the specific pathways that cause photobleaching are often less well understood, it is clear that it is always a specific chemical reaction that leads to irreversible degradation of a fluorescent dye. Product identification should consequently allow to identify the sensitive groups in the fluorophores and help to suppress these unwanted reactions by changing the fluorophore structure, i.e., by chemical modifications that weaken the reactivity of chemically active groups or that change redox properties. It is also known that steric shielding of the chromophore can enhance photostability. Such strategies are quite obvious from a chemist's perspective and have been discussed, for example, for pyrromethene dyes (Bodipy derivatives) and rhodamine derivatives [28, 29]. Using stabilizing substitutions on the fluorophore, it should be possible to block all degradation pathways and to create ultra-stable fluorophores (also see chapter by A. Yushchenko and M.P. Bruchez in this volume [76]). On the other hand, quantum mechanics has taught that even very unlikely reactions can occur with nonzero probability, meaning that even in apparently nonreactive fluorophores some degree of photobleaching will prevail.

The above considerations are supported by the huge variation of photostability observed for different classes of conventional fluorophores. While, for example, less than one photon is detected for a single tryptophan residue [30], single organic fluorophores can emit more than 10^8 photons before photodestruction even in aqueous buffers [4, 24].

Such strong variations in fluorophore performance are also observed for the same fluorophore under different environmental conditions. A single dicarbocyanine dye (Cy5) was found to emit less than 15,000 photons when being attached to dsDNA in water. Removing oxygen and depopulating reactive intermediate states using a buffer system described below, the photostability was increased by a factor of ~5,000 leading to the emission of ~10^8 photons [24].

This impressive example paves the way to a second strategy that allows reducing photobleaching and that is discussed in more detail below: by adapting the chemical environment of the fluorophore, specific degradation reactions can be effectively suppressed.

3.1 Photostabilization Using Additives

Chemical additives have been used for decades in fluorescence microscopy but always in an empirical fashion. Just a short time ago, studies with a rational photophysical model have resulted in improved formulas providing ultra-stable dyes. Accordingly, photobleaching pathways can be grouped into two classes [24, 31, 32]. The pathways either involve (a) reactive long-lived metastable states of the fluorophore (e.g., triplet or radical ion states) or (b) photobleaching occurs as

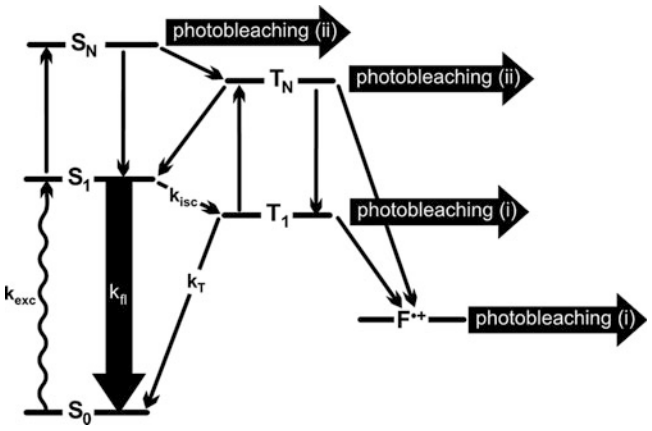

Fig. 3 Jablonski diagram indicating processes that can lead to irreversible destruction (photobleaching). Shown are the fluorophore's singlet ground state (S_0), the fluorescent first excited state (S_1) and higher excited states (S_N). The probability to enter the dark triplet state (T_1) with its inverse lifetime k_T is given by the rate constant of intersystem crossing (k_{isc}); higher triplet states are denoted as T_N. Photooxidation by ionization may also lead to radical cations ($F^{\bullet+}$) which are further possible intermediates of photobleaching

the result of absorption of a second photon yielding highly excited singlet or triplet states (see Fig. 3). Using additives, pathway (a) can be significantly influenced since metastable intermediate states, such as triplet and radical ion states, commonly have a lifetime considerably longer than the lifetime of the excited singlet state S_1 making them accessible to diffusion-controlled reactions. On the other hand, it is also not desired to depopulate the first excited singlet states with additives since this would simultaneously reduce the brightness of the fluorophore.

If, however, the first excited singlet/triplet state shows absorbance at the excitation wavelength (or another light wavelength used in the respective setup such as a STED depletion beam), it could be shelved to higher excited singlet or triplet states that both have a comparatively high reactivity and high probability to undergo photobleaching according to mechanism (b) (see Fig. 3). Such a mechanism can explain the recently observed different behavior of rylene dyes by comparing excited state spectra of these dyes with their photostability in STED measurements [33]. Perylene derivatives, whose excited states exhibit absorption at the depletion wavelength, performed much worse than terrylene derivatives with negligible excited state absorbance in the mentioned spectral range.

It has also been noticed that the energy of the $S_0 \rightarrow S_1$ absorption plays a major role for the photostability of fluorophores. Longer wavelength excitation (i.e., more red-shifted absorption/emission) seems to be favorable for the number of detected photons as observed in a series of, e.g., cyanine dyes: the number of detected photon increases from Cy2 < Cy3 < Cy5 under identical buffer conditions (see [34]). This observation is also supported by studies using simultaneous long- and short-wavelength excitation for fluorophores in FRET applications. Here, a strongly

increased tendency for photobleaching is observed when blue/green light is applied in addition to red excitation light for Cy5 or Alexa 647-fluorophores [31, 35]. A major problem with photobleaching caused by pathway (b) is that there is no unified strategy to prevent it other than using fluorophores in the red or near-infrared spectral region. An excitation wavelength-dependent analysis of the photobleaching lifetime of fluorophores in the presence and absence of ROXS will allow determining the relative contributions of both photobleaching pathways (a)/(b).

For many dyes, however, photobleaching can be efficiently reduced by considering long-lived intermediate states [according to pathway (a), see Fig. 3] such as the triplet state T_1, which has long been viewed as the primary candidate on the photobleaching pathway. Owing to its longer lifetime (μs to ms), competing reactions to ground state return via spin relaxation (with rate constant k_T) can easily occur. In most life science applications, molecular oxygen is present at upper micromolar concentrations. This causes, on the one hand, quenching of the triplet state T_1 and shortening of its lifetime ($1/k_T$); a fact that is beneficial for the average brightness of the fluorophore. Unfortunately, the result of this triplet–triplet annihilation process is a highly reactive singlet-oxygen species that can irreversibly react with the fluorescent dye.

This is why molecular oxygen is removed in demanding applications using, for example, enzymatic oxygen scavenging systems [36, 37]. The disadvantage of working in deoxygenated environment is, however, an increase of the triplet state lifetime. It is also not generally applicable such as in living aerobic cells. Long-lived triplet states cause a decrease in the fluorophore brightness and appear as transient dark states ("blinking") in single-molecule intensity transients. In addition, the long lifetime and the high reactivity of the triplet state allow other follow-up reactions to be effective even if they exhibit very low rate constants.

To deal with all these problems and also to suppress the formation of photo-oxidized states (Fig. 3), researchers started to use chemical additives [38]. From these efforts a number of substances emerged, some of which are commercially available. Especially reductants such as ascorbic acid (AA), 6-hydroxy-2,5,7,8-tetramethylchroman-2-carboxylic acid (Trolox, TX), 9,10 *p*-phenylenediamine (PPD, used in the commercial product called Vectashield), 1,4-diazabicyclo [2.2.2]octane (DABCO, used in a commercial product called Ibidi-MM), *n*-propyl gallate and β-mercaptoethylamine (MEA or cysteamine) [39–42], and triplet-quenchers such as cyclooctatetraene [43] are known to improve the photostability of fluorophores for a variety of applications [44, 45].

Generally, no common working principle, which explains the antifading capabilities of the substances on a molecular level, of the agents could be established.

The triplet state, which can be considered as one of the main sources of photobleaching, can be quenched by different processes: (a) Dexter transfer, e.g., triplet–triplet annihilation by oxygen or other substances (see [46]); (b) photo-induced electron transfer by using a reductant/oxidant to convert the triplet into a radical anion/cation.

So far, Dexter transfer could not be used efficiently (see the discussion about problems with oxygen above). Other substances used for triplet quenching (cyclooctatetraene and diphenylhexatriene [43, 46]) are not well soluble in water and are hence not suitable for most life science applications. Method (b), on the other hand, produces radical states, which may show high reactivity and therefore needs further consideration [47].

The success of triplet quenching by photo-induced redox reactions with the aim of increasing the photostability or brightness of a fluorophore depends on the properties of the formed radical ion, i.e., whether this species is sensitive to subsequent reactions or not. In some cases, reductants were found to strongly increase photostability and brightness, whereas for other dyes both properties are decreased using the same compounds (see, e.g., [32] and references therein). The lifetime and reactivity of radical ions are commonly related to the redox potentials of the dye as well as to the presence of reductants and oxidants. A dye with high electron affinity might form a less reactive but long-lived radical anion, while other fluorophores with lower electron affinity might be very reactive in their radical anionic state for the same environment.

For a general strategy, all long-lived intermediates and not only the triplet state have to be rapidly depopulated to restore the singlet manifold. Rapid depopulation of all reactive intermediates without creating other reactive particles (as in the case of oxygen) should therefore be a general strategy to improve photostability. To this end, it was shown that the lifetime of radical ions, formed e.g., by electron transfer quenching of triplet states, could themselves be quenched by the addition of a complementary redox compound [24]. It was shown that the simultaneous addition of reductant and oxidant in combination with oxygen removal results in ultra-stable fluorophores, i.e., ~5,000 times increased photon numbers for some dyes (with respect to PBS buffer) without observable intensity fluctuations due to triplet or radical states (Fig. 4c). The addition of either oxidant (Fig. 4a) or reductant (Fig. 4b) leads to a smaller increase in photon numbers, i.e., ~200 times for reductant and ≈10 times for the oxidant compared to pure PBS buffer. This increase for addition of only reductant or oxidant is further accompanied by intensity fluctuations of the observed fluorescence signals (blinking, Fig. 4b, c).

This somewhat “unintuitive” procedure, i.e., the addition of both reductant and oxidant in order to obtain stable fluorophores, can be rationalized on a molecular basis. Provided that reductant and oxidant do not undergo a one-electron transfer in their electronic ground states (the added compounds in [24] ascorbic acid (AA) and methylviologen (MV) exhibit redox potentials that do not allow a one-electron transfer to occur according to thermodynamic considerations), electron transfer can only occur after absorption of a photon by the fluorescent molecule. As these photocatalytic redox reactions between dye molecule and reductant/oxidant are diffusion controlled, the triplet state is the main precursor for the two possible radical ion states. In the presence of both reagents, and in the absence of oxygen, both radical states are formed with rate constants that depend on the concentration of the redox reagents and the energetic driving force between the triplet- and corresponding radical state (Fig. 5). The resulting radical ion is then depopulated

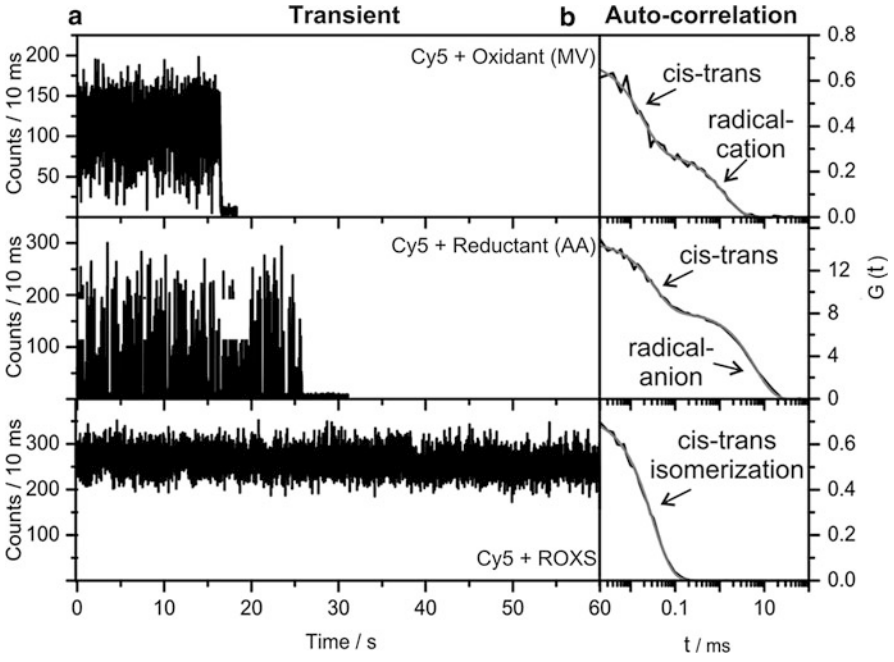

Fig. 4 Fluorescence intensity transients (**a**) and autocorrelation functions (**b**) measured with a confocal microscope. Excitation was carried out at 640 nm, time binning is 10 ms. The different panels are representative for different buffer conditions: *top*, oxygen removal and 100 μM methylviologen (MV); *middle*, oxygen removal and 100 μM ascorbic acid (AA); *bottom*, oxygen removal, 100 μM MV and 100 μM AA (reducing and oxidizing system, ROXS). Reprinted with permission from [4]. Copyright 2010 John Wiley and Sons

through the complementary electron transfer reaction with either reductant or oxidant. This is schematically shown in Fig. 5. In principle, both pathways, that is, a reduction step followed by an oxidation as well as an oxidation followed by a reduction, are possible. In all cases, the driving force of the reaction originates from the absorbed photon of the dye molecule which thereby returns to the singlet ground state.

The driving force of a photo-induced one-electron transfer reaction can be qualitatively estimated by comparing the redox potentials of the involved states (i.e., the triplet and each of the ionized states) with the redox properties of the added substances (AA/MV in our case). The Gibbs energy (ΔG_{et}) for the individual electron transfer processes (see Fig. 5) can be estimated by the Rehm–Weller equation

$$\Delta G_{et} = e \cdot \left[E_{ox} - E_{red}\right] - E_{0,0} + C$$

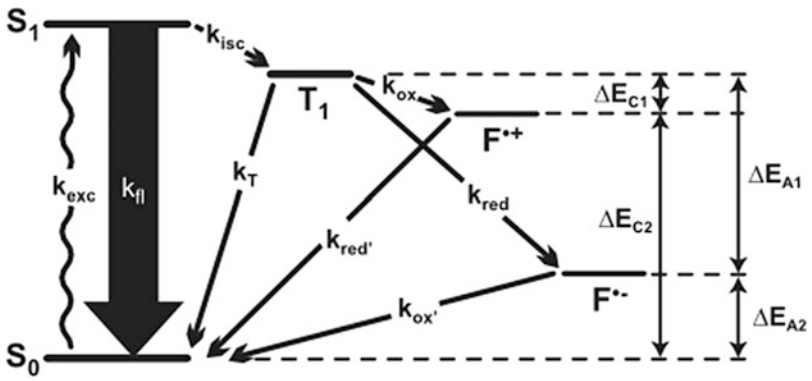

Fig. 5 Jablonski diagram according to the ROXS concept for a fluorophore with high electron affinity (e.g., oxazines or perylenes); note that the potential energy of reduced/oxidized states are specific for one fluorophore A single fluorophore is cycled between its singlet ground state (S_0) and the fluorescent first excited state (S_1) with the excitation rate k_{exc} emitting a characteristic number of photons. The probability to enter the dark triplet state (T_1) with its inverse lifetime k_T is given by the rate constant of intersystem crossing (k_{isc}). As the high reactivity of the triplet state can cause irreversible destruction of the fluorophore, it is rapidly depleted with rates $k_{red'/ox}$ by oxidizing or reducing agents forming a radical cation or anion ($F^{\bullet+/-}$), respectively. Each of the ionized states is depleted by the complementary redox reaction with rate constants $k_{red'/ox'}$ recovering the electronic ground state. Reprinted with permission from [48]. Copyright 2010 American Chemical Society

with e being the elementary electric charge, $E_{ox/red}$ the first-electron oxidation and reduction potential of the fluorophore, respectively, and $E_{0,0}$ the energy of the $S_0 \rightarrow S_1$ transition [49]. Considering the polar environment of water, the Coulombic interactions C can be neglected. In the case of Cy5, the absorption spectra provides the $E_{0,0}$ of 1.88 V. Since the triplet has ≈0.28 V less energy than S_1 [50], the energy $E_{0,0}$ to be used in the Rehm–Weller equation is 1.6 V for Cy5. $E_{ox/red}$ are obtained by cyclic voltametry with E_{red} (Cy5 vs. SCE) = −0.84 V and E_{ox} (Cy5 vs. SCE) = +0.97 V. The potentials for AA and MV are also found in the literature [51]: E_{red} (MV vs. SCE) = −0.69 V and E_{red} (AA vs. SCE) = +0.06 V. The free enthalpy for the charge separation processes accordingly is $\Delta G_{ox} = +0.06$ V and $\Delta G_{red} = -0.7$ V. Charge recombination is exergonic for both reactions with $\Delta G_{ox'} = -0.15$ V and $\Delta G_{red'} = -0.91$ V. Considering that the rate constant for each of the four processes (compare Fig. 5) is proportional to the concentration of the redox agents and exponentially related to the Gibbs enthalpy, the rate constant for oxidizing the triplet state is expected to be smaller than that for reduction. The rates for charge recombination also show that the radical cation will be more instable compared to the radical anion.

Similar considerations can be carried out for fluorophores with a low lying reduction potential (e.g., oxazines such as ATTO655) where we find that the Gibbs energy for the formation of the radical anion is highly exergonic ($\Delta G_{red} = -1.08$ eV), while the oxidation process is strongly endergonic ($\Delta G_{ox} = +0.44$ eV). Consequently, also the charge recombination process are changed to $\Delta G_{ox'} = +0.27$ eV

and $\Delta G_{red'} = -1.25$ eV indicating that the radical cation, if populated, will be very short lived due to the strong driving force, while the radical anion requires a strong oxidant to be efficiently recovered to the electronic ground state. As is shown in the following sections, this property of electron affine fluorophores can be used to switch single molecules between dark and bright states and to use them for localization-based super-resolution imaging.

4 Creating Dark States for Stochastic Switching and Readout

Conventional fluorophores (i.e., non-photochromic or photoactivatable) offer different possibilities to use them in localization-based super-resolution microscopy. When attaching a probe permanently to a structure of interest, it is necessary to prepare most of the labels in a nonfluorescent off-state to localize single emitters in different camera images. In STORM/PALM-type imaging, Gaussian fitting in single camera frames is used to determine the position of single emitters with nanometer precision. Superposition of all emitter positions allows reconstructing the structure of interest. Figure 6 shows the principle of localization-based super-resolution microscopy with conventional fluorophores. In the diffraction-limited TIRF image (Fig. 6, left), all fluorescent labels are active at the same time. Intermittent fluorescence of the labels allows subsequent localization of fluorophore subsets with nanometer precision (Fig. 6, middle images). Finally, the reconstructed image of all fluorophore positions allows obtaining images with sub-diffraction resolution on the order of 20 nm (Fig. 6, smiley on the right). Data are taken from [52].

One can use generic dark states that every fluorophores exhibits (e.g., the triplet state or radical states), provided that their lifetime is sufficiently long to allow temporal separation of all labels. Alternatively, reversible chemical reactions (e.g., as described in Sect. 3) can be exploited but have to occur on the time scale of the required switching. Conformational fluctuations in biomolecules in combination with fluorophore quenching (via, e.g., Förster resonance energy transfer or contact-induced quenching) which modulate the emission of a fluorophore can also be used [4].

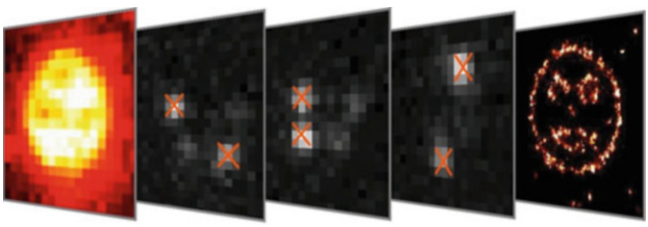

Fig. 6 Localization-based super-resolution microscopy: diffraction-limited TIRF image of 1.5 μm smiley (*left*) produced by single-molecule cut-and-paste [52]. Selection of 3 of 8,000 camera images used for reconstruction of the artificial super-resolution image (*right*)

4.1 Intrinsic Dark States

The triplet state or radical ion states are generic dark states of fluorophores and can hence be exploited to temporarily switch molecules off. The short lifetime of the triplet state (<15 ms for Cy5 in oxygen depleted aqueous buffer, 200 μs for PDI, <1 μs for ATTO655) limits its applicability for localization-based super-resolution techniques. For targeted readout, e.g., GSD, the feasibility of triplet states was already demonstrated [53]. In this case, the excitation intensity I_{exc} and the intersystem crossing rate constant k_{isc} define the kinetics for switching the fluorophore into the nonfluorescent triplet state. The on-switching is only determined by the rate constant k_T, which is the inverse of the triplet state lifetime. It hence determines the speed of acquisition. After switching the majority of the fluorophores into the nonfluorescent state, the remaining fluorophores are read out. Besides the short lifetime of the triplet state, its photochemical instability limits the number of possible switching cycles.

4.2 Electron-Transfer-Induced Dark States

Radical ion states, on the other hand, are well suited for stochastic readout super-resolution microscopy due to their much longer lifetimes. Using specific buffers or mounting media, and taking into account the photophysics according to the ROXS model, we and other groups could intentionally induce dark states that often can be ascribed to radical ion states for super-resolution imaging. These techniques have been termed blink microscopy (BM) [10], GSD and single-molecule return (GSDIM) [8] or dSTORM [9, 54]. The required long off-states are especially promoted for fluorophores with high electron affinity [48, 51, 54, 55]. The radical anion is comparably stable and it is easily formed through reduction of the triplet state (compare Fig. 5). In some cases (e.g., ATTO655), the radical cation is not accessible due to its high energy so that these fluorophores can be simply described by a two-state system as depicted in Fig. 7 (lower panel). Under reducing conditions, continuous excitation of a single fluorophore results in the stochastic switching between dark ("off") and bright periods ("on"); Fig. 7. The average on/off times are dictated by the concentration of the redox-active substances (which are AA and MV in the presented example), their redox properties and the fluorophore itself. It is hence possible to adjust the off/on-time ratio by changing the concentration of reductant/oxidant over a wide range (milliseconds to seconds). This range can even be extended by using different fluorophores with differing redox properties.

Interestingly, a similar behavior of continuous switching of single fluorophores (Fig. 7, upper panel) was also demonstrated for dyes from the classes of rhodamines, oxazines, and perylenes using reducing thiol components in an oxygenated environment [10, 48, 54, 57]. The applicability of thiol compounds seems to be very

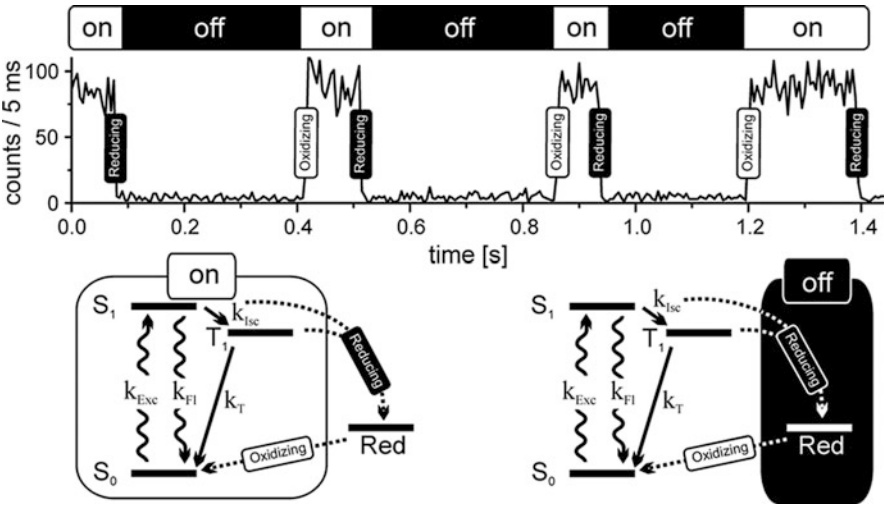

Fig. 7 Fluorescent transient of a single ATTO655 molecule in the presence of reductants and oxidants. Stochastic switching between fluorescent ("on") and nonfluorescent periods ("off") are seen in the figure corresponding to reducing and oxidizing steps. The lower part of the figure shows the Jablonski diagrams highlighting the two different states: The bright state corresponds to the fluorophore being in either the singlet ground- or the excited state and additionally the first triplet state. The dark off-state is the reduced form of the fluorophore. Reprinted with permission from [56]. Copyright 2009 Royal Society of Chemistry

general, but the switching process may rely on the same principles as shown in Fig. 7. The reducing species thereby is the deprotonated thiolate so that thiol compounds are commonly applied at higher concentrations (e.g., 100 mM) to provide sufficient concentration greater than micromolar of reducing thiolate. The high thiol concentration can have the additional benefit to quickly absorb reactive oxygen species. Due to the presence of reducing thiol components (e.g., glutathione) and oxygen in various cell compartments, a living cell provides all necessary components for "redox-blinking" and hence super-resolution imaging. It is just necessary to identify dyes such as TMR and ATTO655 that show the desired blinking properties under the specific biological conditions [4, 55, 57]. Different concentrations of gluthathione (e.g., in the cytoplasm or the mitochondria) may raise the need to identify different fluorophores for super-resolution imaging for different cell organelles.

4.3 Applications of Blink Microscopy

Recent applications of blink microscopy used the blinking of ATTO655 under reducing conditions to image globular and fibrillar aggregates formed by huntingtin (Htt) proteins, a protein that plays a major role in neurodegenerative disorders such

as Alzheimer's, Parkinson's, and Huntington's diseases [58]. The authors studied aggregates with fluorescently labeled and unlabelled Htt at a ratio of 1:100 that were adsorbed on glass coverslips (Fig. 8). The figure shows a typical fluorescence sum image (Fig. 8a) of an Htt aggregate together with a reconstructed image (Fig. 8b, c) from molecules with 43–48 nm localization precision. A comparison of the blink microscopy images (Fig. 8b, c) with an atomic-force-microscope image (Fig. 8e) is shown in Fig. 8d, nicely demonstrating the gain in optical resolution and the agreement of both techniques. These results present the first sub-diffraction fluorescence investigation of amyloid protein aggregates and demonstrate the power of localization-based super-resolution imaging using electron-transfer-induced dark states.

4.4 Fluorophore Dark States Induced by Chemical Reactions

Recently, it was also suggested and successfully demonstrated to use chemical reactions to modulate the fluorescent signal of a probe used for labeling. Here, the transition between a bright and a dark state was achieved by transient binding of a copper ion to bipiridinium ligands close to the fluorescent probe (TMR). Bright periods of the TMR fluorescence ("on") were interrupted by binding of the copper and a resulting quenching of the TMR probe ("off"). This strategy was successfully used to obtain super-resolution images of actin filaments and has the distinct advantages that the on-time can be easily varied by changing the copper concentration [59]. The off-time, on the other hand, may be modified by variations of the ligand that facilitates copper binding or varying the type of metal used for the quenching of TMR. While this scheme also relies on electron transfer, quenching the factors determining the on and off times are substantially different to blink microscopy since the off-state depends on the proximity of the complexed metal ion.

In contrast to this mechanism, there can also be direct chemical modifications of the fluorophore. A famous example is the switching of Cy5 as used for the original STORM/dSTORM publications, where the conjugation in the chromophore is directly disrupted by photoaddition of a thiol component [15, 60, 61].

Other chemical mechanisms may be the stochastic activation process of nonfluorescent substrates by chemical reactions or enzymatic processes [4]. In this case, nonfluorescent dyes with a specific target within a cell convert to a fluorescent species at their labeling target. This idea has also been used to beautifully image heterogeneous catalysis [62].

Recently, Pinaud and coworkers introduced a novel approach to activate fluorescent proteins using specific targeting of individual biomolecules in living cells with nanometer accuracy [63]. The fluorescent tag was based on a dark split-fluorescent protein that can be activated to a bright fluorescent state by complementation of small synthetic peptides. Next to single-molecule tracking to record the diffusion dynamics of extracellular and intracellular proteins, the authors

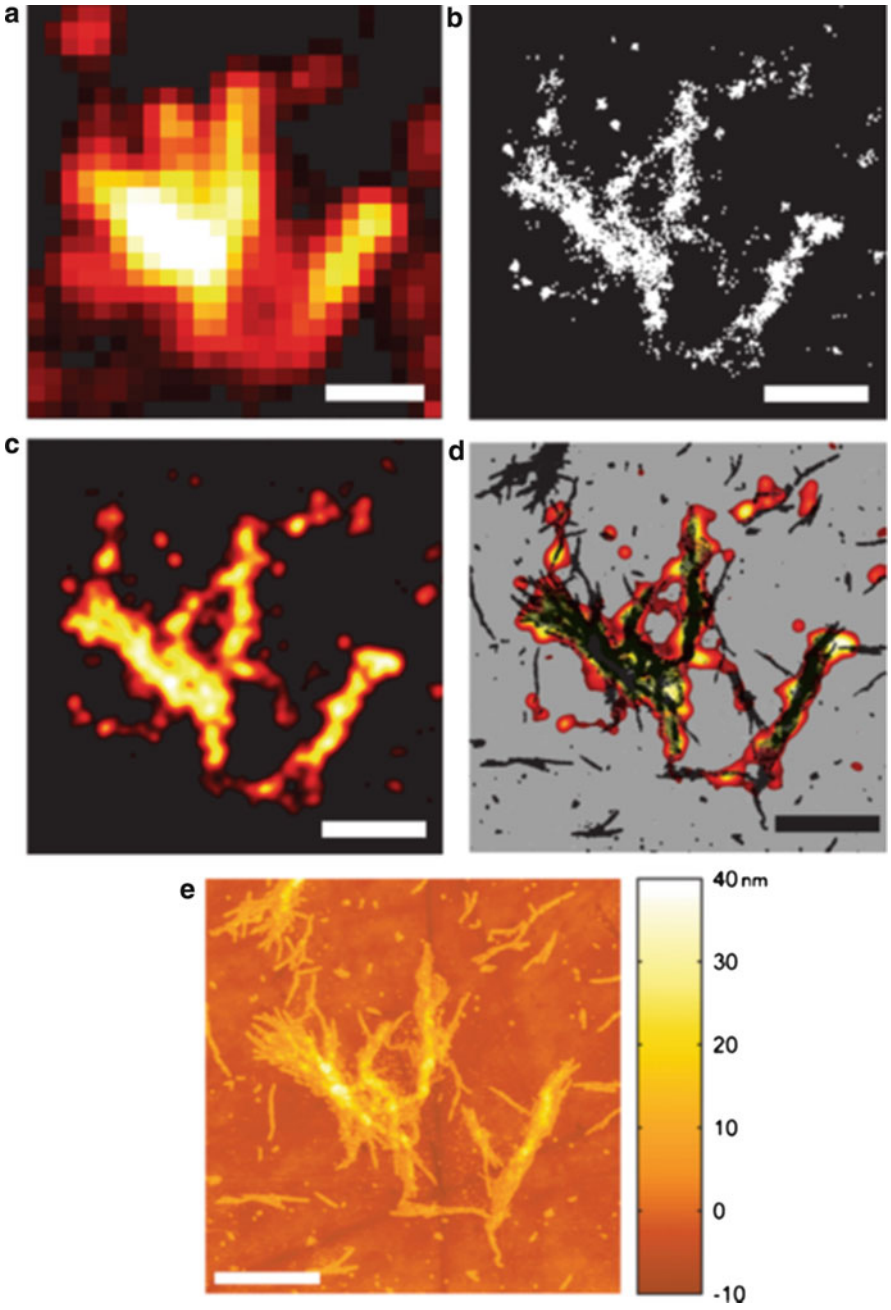

Fig. 8 Sub-diffraction images of an Htt aggregate: (**a**) sum of movie frames that were processed to create the SR reconstruction. (**b**) Points representing the centers of the single-molecule fits. (**c**) SR image displayed with color scale (fit density increases from black to red through to white). (**d**) AFM (black) and SR overlay image displayed on a gray background. (**e**) AFM image of aggregate. Scale bars: 1 μm. Figure reprint from [58] with permission of Wiley and Sons

showed that they can even combine their technique with single-pair FRET approaches in living cells. This allowed tracking single proteins independently of their expression level up to micromolar concentrations. The combination of genetically encoded probes with light-independent activation provides a unique tool that allows to target, image, and track single proteins at the posttranslational level.

5 Super-Resolution by Transient Binding: PAINT Your Structure

A simple but efficient method to generate fluctuating emission is the use of transient binding of fluorescently labeled molecules that specifically bind to the target structure. Instead of on–off switching of the fluorophore itself, the required low concentration of active fluorophores is achieved by a small fraction of reversibly bound molecules to the structure of interest. Over time, all binding positions on the structure are sampled and the accumulated localizations of binding sites result in the super-resolved image. This idea was first demonstrated by the Hochstrasser group and termed PAINT ("point accumulation for imaging in nanoscale topology") [64]. They showed that supported lipid bilayer topography could be imaged with resolution beyond the diffraction limit. Diffusing nile red fluorophores and their fluorescence increase when bound to lipids were used to determine the shape and distribution of large unilamellar vesicles (LUVs) and supported bilayers [64].

The idea was then extended in different variants that create contrast by different means such as metal quenching or enhancement [65, 66]. The Cognet group imaged cell membrane proteins and recorded diffusion transients upon binding [67]. This method is based on continuously and stochastically labeling membrane biomolecules with fluorescent ligands in solution while imaging the sample with oblique illumination [67].

We have recently used transient hybridization of short DNA strands (imager strands) to short single-stranded regions in the target structure (docking strands) for super-resolution imaging of DNA nanostructures (DNA-PAINT [68]). When a fluorophore-labeled oligonucleotide binds to a short DNA strand attached to the target structure, a fluorescent spot is observed that is localized with high precision. Subsequent localization of all docking strands in the structure of interest provides super-resolution images of the target structure. The main difference to photophysical or photochemical switching of fluorescent dyes is that the target structure is labeled with a short DNA sequence (the docking strands) instead of a fluorescent dye. The elegance of this approach is the precise control of binding strengths and hence lifetime of the dsDNA/fluorophore complexes by varying the length of the complementary DNA sequence. This lifetime increases from 0.63 s for nine complementary bases to 5 s for ten complementary bases [68]. On the other hand, the on-binding time depends on the concentration of labeled oligonucleotides in solution which makes it possible to extend the off-time at will. The somewhat

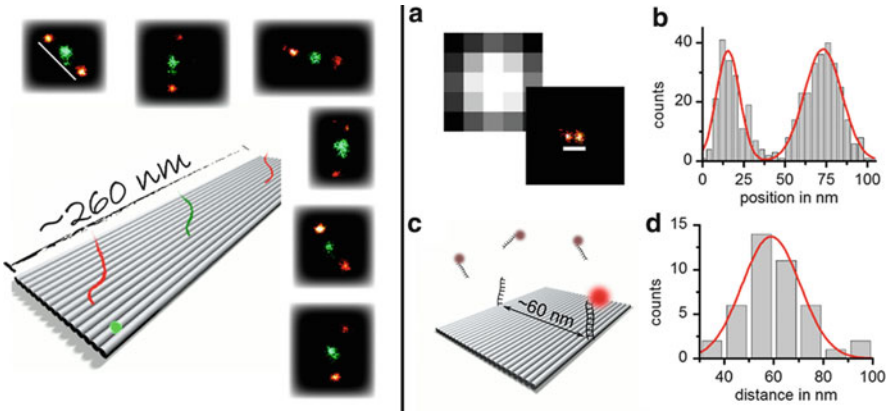

Fig. 9 *Left panel*: Long rectangular DNA origami modified with two different docking strands for imaging with *red* or *green* labeled imager strands is depicted to demonstrate the capabilities of DNA-PAINT. Overlays of two-color SR data generated with DNA-PAINT are shown on *top* and on the *right* (scale bars are 260 nm). *Right panel*: DNA nanostructures for use as nanoscale yardsticks for SR microscopes are shown: (**a**) comparison of diffraction-limited and SR images of two dyes placed at a distance of 60 nm. (**b**) Histogram of single-molecule localizations along the horizontal of the SR image. (**c**) Sketch of the nanoscale yardstick and the principle of DNA-PAINT. (**d**) Distribution of measured distances for many individual structures

higher background due to diffusing labeled oligonucleotides can be handled by the microscopy technique (e.g., TIRF microscopy reduces the effective excitation volume), by reducing the concentration (at the cost that the measurement time increases) or by the development of fluorogenic oligonucleotides that emit stronger upon binding. In a first approach, the fluorescence of the bound oligo increases by 70% due to the removal of photo-induced electron transfer from guanosine bases to the reporter fluorophore ATTO655 (see, e.g., [68, 69]).

PAINT offers several distinct advantages since the fluorescent label is not firmly attached to the target. Undesired changes of the sample morphology by introducing permanent labels such as rather large antibodies are minimized. Most importantly, no label positions are missed due to premature photobleaching or inactive fluorophore populations. Sampling of all possible labeling positions is becoming highly desirable since resolution in many cases is rather limited by the density of labeling than by the localization accuracy of a single fluorophore. Using DNA labeling, for example, on and off times are easily controlled and the technique works with essentially any single-molecule compatible fluorescent dye. An interesting approach for multiplexing is the combination of different recognition sequences that are either images subsequently or with different colored dyes. Figure 9 shows the combination of DNA-PAINT on DNA origami structures with ATTO655 (red) and Cy3B (green).

The PAINT idea might be generalized further since many biological interactions are intrinsically weak. Such interactions have not yet been amenable for single-

molecule studies because of the short lifetime and fraction of bound species. Such interactions might, however, be ideal for stochastic super-resolution imaging by transient binding.

6 DNA-Based Super-Resolution Standards

This volume shows a variety of different super-resolution techniques realizing different approaches such as those based on targeted readout and those based on stochastic readout. Especially, the stochastic readout realization has evolved into a large number of similar techniques that distinguish themselves in the way on- and off-switching is achieved. In addition, most super-resolution techniques are demonstrated by the precision of single-molecule localizations and by imaging of cytoskeleton filaments. All techniques certainly require simple and portable samples to compare the methods, to check for hardware alignment, and to answer specific questions such as the fraction of labeling positions that is actually sampled. How many of the possible fluorophore labeling positions really show up in the stochastically assembled super-resolution image? Such samples will also be able to answer the question of the actual resolution, limited not only by the localization accuracy but also by the density of imaged labels (see the discussion of the Nyquist sampling criterion in previous chapters).

We have recently introduced samples produced by DNA nanotechnology that have a defined number of fluorophores at defined distances [70, 71]. These so-called nanoscopic rulers are easily produced using the DNAorigami technique [72, 73]. Production involves folding of a long single-stranded DNA scaffold with short DNA staple strands that bind at particular locations along the ~8-kb long scaffold. Large numbers of identical structures are assembled in a single experiment by heating to ~90°C and cooling slowly. Excess staple strands are removed by gel electrophoresis or filtering. The origami technique can be used to assemble two- and three-dimensional objects [72, 74]. While two-dimensional structures allow bending of the DNA sheet, 3D origami can be very stiff and can be viewed as molecular bricks [70, 75]. With appropriate immobilization, e.g., via several biotins or on the basis of many electrostatic interactions, DNA structures are flatly attached to a surface and the designed distance is measured. So far, we have been able to resolve nanoscopic rulers with dye distances between 40 and 260 nm using blink microscopy, dSTORM (Cy5 thiol-related photochromism), DNA-PAINT and STED microscopy [68, 71]. Figure 9 shows a rectangular DNA origami in combination with blink microscopy images.

We anticipate that DNA origami-based nanoscopic rulers might become standard tools for all kinds of super-resolution microscopes similar to the stage micrometer available for common optical microscopes. An extension to 3D, a key challenge for super-resolution microscopy, could also be realized.

7 Conclusion

Conventional organic fluorophores are the premier choice for many fluorescence applications and also enter live-cell applications using new labeling schemes. In this chapter, different ways to use organic dyes for super-resolution imaging are discussed. From a theoretical perspective, we argue that the photostability is the key parameter of super-resolution techniques both for targeted readout and for stochastic readout. Photobleaching pathways are discussed and we demonstrate that photobleaching pathways with long-lived intermediates can be blocked with the aid of additives such as a combination of reducing and oxidizing compounds. We then show how dyes can be used for stochastic readout super-resolution microscopy using generic dark states or by transient binding. Finally, the need for super-resolution calibration structures led to the development of nanoscale rulers made of DNA that are produced using DNA nanotechnology (specifically DNA origami). The advantages of organic dyes and the simplicity of super-resolution imaging with these dyes are the basis that organic dyes will remain the labels of choice for many applications. Finally, it is anticipated that the availability of calibration standards for different super-resolution techniques will help to evaluate the different approaches. Moreover, we believe that such samples and the evaluation process will be a key to make super-resolution microscopy a standard and routine tool in biological laboratories.

Acknowledgments T. Cordes was supported by the Centre of Synthetic Biology (University of Groningen) and the Center for NanoScience (CeNS Munich). P. Tinnefeld was supported by the Biophotonics program of the German Ministry of Research and Education (BMBF/VDI) and the Nanosystems Initiative Munich (NIM).

References

1. Hell SW, Wichmann J (1994) Breaking the diffraction resolution limit by stimulated emission: stimulated-emission-depletion fluorescence microscopy. Opt Lett 19(11):780–782
2. Betzig E, Patterson GH, Sougrat R, Lindwasser OW, Olenych S, Bonifacino JS, Davidson MW, Lippincott-Schwartz J, Hess HF (2006) Imaging intracellular fluorescent proteins at nanometer resolution. Science 313(5793):1642–1645
3. Hell SW (2007) Far-field optical nanoscopy. Science 316(5828):1153–1158
4. Vogelsang J, Steinhauer C, Forthmann C, Stein IH, Person-Skegro B, Cordes T, Tinnefeld P (2010) Make them blink: probes for super-resolution microscopy. Chemphyschem. doi:10.1002/cphc.201000189
5. Huang B, Bates M, Zhuang X (2009) Super-resolution fluorescence microscopy. Annu Rev Biochem 78:993–1016
6. Schermelleh L, Heintzmann R, Leonhardt H (2010) A guide to super-resolution fluorescence microscopy. J Cell Biol 190(2):165–175. doi:jcb.201002018 [pii] 10.1083/jcb.201002018
7. Heilemann M, Dedecker P, Hofkens J, Sauer M (2009) Photoswitches: key molecules for subdiffraction-resolution fluorescence imaging and molecular quantification. Laser Photon Rev 3(1–2):180–202

8. Folling J, Bossi M, Bock H, Medda R, Wurm CA, Hein B, Jakobs S, Eggeling C, Hell SW (2008) Fluorescence nanoscopy by ground-state depletion and single-molecule return. Nat Methods 5(11):943–945
9. van de Linde S, Kasper R, Heilemann M, Sauer M (2008) Photoswitching microscopy with standard fluorophores. Appl Phys B Laser Optic 93(4):725–731
10. Steinhauer C, Forthmann C, Vogelsang J, Tinnefeld P (2008) Superresolution microscopy on the basis of engineered dark states. J Am Chem Soc 130(50):16840–16841
11. Hell SW, Kroug M (1995) Ground-state-depletion fluorscence microscopy: a concept for breaking the diffraction resolution limit. Appl Phys B Laser Optic 60(5):495–497
12. Gustafsson MG (2005) Nonlinear structured-illumination microscopy: wide-field fluorescence imaging with theoretically unlimited resolution. Proc Natl Acad Sci USA 102(37): 13081–13086
13. Heintzmann R, Jovin TM, Cremer C (2002) Saturated patterned excitation microscopy: a concept for optical resolution improvement. J Opt Soc Am A 19(8):1599–1609
14. Hess ST, Girirajan TP, Mason MD (2006) Ultra-high resolution imaging by fluorescence photoactivation localization microscopy. Biophys J 91(11):4258–4272
15. Rust MJ, Bates M, Zhuang X (2006) Sub-diffraction-limit imaging by stochastic optical reconstruction microscopy (storm). Nat Methods 3(10):793–795
16. Thompson RE, Larson DR, Webb WW (2002) Precise nanometer localization analysis for individual fluorescent probes. Biophys J 82(5):2775–2783
17. Willig KI, Kellner RR, Medda R, Hein B, Jakobs S, Hell SW (2006) Nanoscale resolution in gfp-based microscopy. Nat Methods 3(9):721–723
18. Rittweger E, Han KY, Irvine SE, Eggeling C, Hell SW (2009) Sted microscopy reveals crystal colour centres with nanometric resolution. Nat Photon 3(3):144–147
19. Kasper R, Harke B, Forthmann C, Tinnefeld P, Hell SW, Sauer M (2010) Single-molecule sted microscopy with photostable organic fluorophores. Small 6(13):1379–1384. doi:10.1002/smll.201000203
20. Hell SW (2009) Microscopy and its focal switch. Nat Methods 6(1):24–32
21. Bobroff N (1986) Position measurement with a resolution and noise-limited instrument. Rev Sci Instrum 57(6):1152–1157
22. Hell SW, Dyba M, Jakobs S (2004) Concepts for nanoscale resolution in fluorescence microscopy. Curr Opin Neurobiol 14(5):599–609
23. Hell SW (2004) Strategy for far-field optical imaging and writing without diffraction limit. Phys Lett A 326(1–2):140–145
24. Vogelsang J, Kasper R, Steinhauer C, Person B, Heilemann M, Sauer M, Tinnefeld P (2008) A reducing and oxidizing system minimizes photobleaching and blinking of fluorescent dyes. Angew Chem Int Ed 47:5465–5469
25. Staudt T, Engler A, Rittweger E, Harke B, Engelhardt J, Hell SW (2011) Far-field optical nanoscopy with reduced number of state transition cycles. Opt Express 19(6):5644–5657
26. Hoebe RA, Van Oven CH, Gadella TW Jr, Dhonukshe PB, Van Noorden CJ, Manders EM (2007) Controlled light-exposure microscopy reduces photobleaching and phototoxicity in fluorescence live-cell imaging. Nat Biotechnol 25(2):249–253
27. Drexhage KH (1973) Structure and properties of laser dyes. In: Schäfer FP (ed) Topics in applied physics, vol 1. Springer, Berlin, pp 144–178
28. Mula S, Ray AK, Banerjee M, Chaudhuri T, Dasgupta K, Chattopadhyay S (2008) Design and development of a new pyrromethene dye with improved photostability and lasing efficiency: theoretical rationalization of photophysical and photochemical properties. J Org Chem 73 (6):2146–2154. doi:10.1021/jo702346s
29. Kolmakov K, Belov VN, Bierwagen J, Ringemann C, Muller V, Eggeling C, Hell SW (2010) Red-emitting rhodamine dyes for fluorescence microscopy and nanoscopy. Chemistry 16(1):158–166. doi:10.1002/chem.200902309
30. Lippitz M, Erker W, Decker H, van Holde KE, Basche T (2002) Two-photon excitation microscopy of tryptophan-containing proteins. Proc Natl Acad Sci USA 99(5):2772–2777

31. Kong X, Nir E, Hamadani K, Weiss S (2007) Photobleaching pathways in single-molecule fret experiments. J Am Chem Soc 129(15):4643–4654
32. Widengren J, Chmyrov A, Eggeling C, Lofdahl PA, Seidel CAM (2007) Strategies to improve photostabilities in ultrasensitive fluorescence spectroscopy. J Phys Chem A 111(3):429–440
33. Hotta J, Fron E, Dedecker P, Janssen KP, Li C, Mullen K, Harke B, Buckers J, Hell SW, Hofkens J (2010) Spectroscopic rationale for efficient stimulated-emission depletion microscopy fluorophores. J Am Chem Soc 132(14):5021–5023. doi:10.1021/ja100079w
34. Lee J, Lee S, Ragunathan K, Joo C, Ha T, Hohng S (2010) Single-molecule four-color fret. Angewandte Chemie 122(51):10118–10121. doi:10.1002/ange.201005402
35. Eggeling C, Widengren J, Brand L, Schaffer J, Felekyan S, Seidel CAM (2006) Analysis of photobleaching in single-molecule multicolor excitation and Forster resonance energy transfer measurement. J Phys Chem A 110(9):2979–2995
36. Harada Y, Sakurada K, Aoki T, Thomas DD, Yanagida T (1990) Mechanochemical coupling in actomyosin energy transduction studied by in vitro movement assay. J Mol Biol 216(1):49–68
37. Aitken CE, Marshall RA, Puglisi JD (2008) An oxygen scavenging system for improvement of dye stability in single-molecule fluorescence experiments. Biophys J 94(5):1826–1835
38. Ha T (2001) Single-molecule fluorescence resonance energy transfer. Methods 25(1):78–86
39. Giloh H, Sedat JW (1982) Fluorescence microscopy: reduced photobleaching of rhodamine and fluorescein protein conjugates by n-propyl gallate. Science 217(4566):1252–1255
40. Longin A, Souchier C, Ffrench M, Bryon PA (1993) Comparison of anti-fading agents used in fluorescence microscopy: image analysis and laser confocal microscopy study. J Histochem Cytochem 41(12):1833–1840. doi:10.1177/41.12.8245431
41. Ono M, Murakami T, Kudo A, Isshiki M, Sawada H, Segawa A (2001) Quantitative comparison of anti-fading mounting media for confocal laser scanning microscopy. J Histochem Cytochem 49(3):305–311. doi:10.1177/002215540104900304
42. Yanagida T, Nakase M, Nishiyama K, Oosawa F (1984) Direct observation of motion of single f-actin filaments in the presence of myosin. Nature 307(5946):58–60
43. Dave R, Terry DS, Munro JB, Blanchard SC (2009) Mitigating unwanted photophysical processes for improved single-molecule fluorescence imaging. Biophys J 96(6):2371–2381
44. Rasnik I, McKinney SA, Ha T (2006) Nonblinking and long-lasting single-molecule fluorescence imaging. Nat Methods 3(11):891–893
45. Cordes T, Maiser A, Steinhauer C, Schermelleh L, Tinnefeld P (2011) Mechanisms and advancement of antifading agents for fluorescence microscopy and single-molecule spectroscopy. Phys Chem Chem Phys 13(14):6699–6709. doi:10.1039/c0cp01919d
46. Pfiffi D, Bier BA, Marian CM, Schaper K, Seidel CA (2010) Diphenylhexatrienes as photoprotective agents for ultrasensitive fluorescence detection. J Phys Chem A 114 (12):4099–4108. doi:10.1021/jp909033x
47. Doose S, Neuweiler H, Sauer M (2009) Fluorescence quenching by photoinduced electron transfer: a reporter for conformational dynamics of macromolecules. Chemphyschem 10 (9–10):1389–1398. doi:10.1002/cphc.200900238
48. Cordes T, Vogelsang J, Anaya M, Spagnuolo C, Gietl A, Summerer W, Herrmann A, Mullen K, Tinnefeld P (2010) Single-molecule redox blinking of perylene diimide derivatives in water. J Am Chem Soc 132(7):2404–2409
49. Rehm D, Weller A (1970) Kinetics of fluorescence quenching by electron and hydrogen-atom transfer. Isr J Chem 8(2):259–271
50. Huang Z, Ji D, Xia A, Koberling F, Patting M, Erdmann R (2005) Direct observation of delayed fluorescence from a remarkable back-isomerization in cy5. J Am Chem Soc 127 (22):8064–8066
51. Vogelsang J, Cordes T, Forthmann C, Steinhauer C, Tinnefeld P (2009) Controlling the fluorescence of ordinary oxazine dyes for single-molecule switching and superresolution microscopy. Proc Natl Acad Sci USA 106(20):8107–8112

52. Cordes T, Strackharn M, Stahl SW, Summerer W, Steinhauer C, Forthmann C, Puchner EM, Vogelsang J, Gaub HE, Tinnefeld P (2010) Resolving single-molecule assembled patterns with superresolution blink-microscopy. Nano Lett 10(2):645–651
53. Bretschneider S, Eggeling C, Hell SW (2007) Breaking the diffraction barrier in fluorescence microscopy by optical shelving. Phys Rev Lett 98(21):218103
54. van de Linde S, Loschberger A, Klein T, Heidbreder M, Wolter S, Heilemann M, Sauer M (2011) Direct stochastic optical reconstruction microscopy with standard fluorescent probes. Nat Protoc 6(7):991–1009. doi:nprot.2011.336 [pii] 10.1038/nprot.2011.336
55. Testa I, Wurm CA, Medda R, Rothermel E, von Middendorf C, Folling J, Jakobs S, Schonle A, Hell SW, Eggeling C (2010) Multicolor fluorescence nanoscopy in fixed and living cells by exciting conventional fluorophores with a single wavelength. Biophys J 99(8):2686–2694. doi:S0006-3495(10)00980-X [pii] 10.1016/j.bpj.2010.08.012
56. Vogelsang J, Cordes T, Tinnefeld P (2009) Single-molecule photophysics of oxazines on DNA and its application in a fret switch. Photochem Photobiol Sci 8(4):486–496
57. Wombacher R, Heidbreder M, van de Linde S, Sheetz MP, Heilemann M, Cornish VW, Sauer M (2010) Live-cell super-resolution imaging with trimethoprim conjugates. Nat Methods 7(9):717–719. doi:nmeth.1489 [pii] 10.1038/nmeth.1489
58. Duim WC, Chen B, Frydman J, Moerner WE (2011) Sub-diffraction imaging of huntingtin protein aggregates by fluorescence blink-microscopy and atomic force microscopy. Chemphyschem 12(13):2387–2390. doi:10.1002/cphc.201100392
59. Schwering M, Kiel A, Kurz A, Lymperopoulos K, Sprodefeld A, Kramer R, Herten DP (2011) Far-field nanoscopy with reversible chemical reactions. Angew Chem Int Ed Engl 50(13):2940–2945. doi:10.1002/anie.201006013
60. Heilemann M, Margeat E, Kasper R, Sauer M, Tinnefeld P (2005) Carbocyanine dyes as efficient reversible single-molecule optical switch. J Am Chem Soc 127(11):3801–3806
61. Dempsey GT, Bates M, Kowtoniuk WE, Liu DR, Tsien RY, Zhuang X (2009) Photoswitching mechanism of cyanine dyes. J Am Chem Soc 131:18192–18193
62. Roeffaers MB, De Cremer G, Libeert J, Ameloot R, Dedecker P, Bons AJ, Buckins M, Martens JA, Sels BF, De Vos DE, Hofkens J (2009) Super-resolution reactivity mapping of nanostructured catalyst particles. Angew Chem Int Ed Engl 48(49):9285–9289. doi:10.1002/anie.200904944
63. Pinaud F, Dahan M (2011) PNAS plus: targeting and imaging single biomolecules in living cells by complementation-activated light microscopy with split-fluorescent proteins. Proc Natl Acad Sci USA 108(24):E201–210. doi:1101929108 [pii] 10.1073/pnas.1101929108
64. Sharonov A, Hochstrasser RM (2006) Wide-field subdiffraction imaging by accumulated binding of diffusing probes. Proc Natl Acad Sci USA 103(50):18911–18916
65. Wu D, Liu Z, Sun C, Zhang X (2008) Super-resolution imaging by random adsorbed molecule probes. Nano Lett 8(4):1159–1162. doi:10.1021/nl0733280
66. Cang H, Labno A, Lu CG, Yin XB, Liu M, Gladden C, Liu YM, Zhang XA (2011) Probing the electromagnetic field of a 15-nanometre hotspot by single molecule imaging. Nature 469 (7330):385–388. doi:10.1038/nature09698
67. Giannone G, Hosy E, Levet F, Constals A, Schulze K, Sobolevsky AI, Rosconi MP, Gouaux E, Tampe R, Choquet D, Cognet L (2010) Dynamic superresolution imaging of endogenous proteins on living cells at ultra-high density. Biophys J 99(4):1303–1310. doi:10.1016/j.bpj.2010.06.005
68. Jungmann R, Steinhauer C, Scheible M, Kuzyk A, Tinnefeld P, Simmel FC (2010) Single-molecule kinetics and super-resolution microscopy by fluorescence imaging of transient binding on DNA origami. Nano Lett 10:4756–4761. doi:10.1021/nl103427w
69. Heinlein T, Knemeyer J-P, Piestert O, Sauer M (2003) Photoinduced electron transfer between fluorescent dyes and guanosine residues in DNA-hairpins. J Phys Chem B 107(31):7957–7964
70. Stein IH, Schuller V, Bohm P, Tinnefeld P, Liedl T (2011) Single-molecule fret ruler based on rigid DNA origami blocks. Chemphyschem 12(3):689–695. doi:10.1002/cphc.201000781

71. Steinhauer C, Jungmann R, Sobey TL, Simmel FC, Tinnefeld P (2009) DNA origami as a nanoscopic ruler for super-resolution microscopy. Angew Chem Int Ed Engl 48(47): 8870–8873
72. Rothemund PW (2006) Folding DNA to create nanoscale shapes and patterns. Nature 440(7082):297–302
73. Torring T, Voigt NV, Nangreave J, Yan H, Gothelf KV (2011) DNA origami: a quantum leap for self-assembly of complex structures. Chem Soc Rev. doi:10.1039/c1cs15057j
74. Douglas SM, Dietz H, Liedl T, Hogberg B, Graf F, Shih WM (2009) Self-assembly of DNA into nanoscale three-dimensional shapes. Nature 459(7245):414–418
75. Dietz H, Douglas SM, Shih WM (2009) Folding DNA into twisted and curved nanoscale shapes. Science 325(5941):725–730. doi:325/5941/725 [pii] 10.1126/science.1174251
76. Yushchenko DA, Bruchez MP (2012) Tailoring Fluorescent Labels for Far-Field Nanoscopy. Springer Ser Fluoresc. doi:10.1007/4243_2011_35
77. Gayda S, Hedde PN, Nienhaus K, Nienhaus DU (2011) Probes for Nanoscopy: Fluorescent Proteins. Springer Ser Fluoresc. DOI 10.1007/4243_2011_34

Part III
Developments and Applications of Optical Nanoscopy

NASCA Microscopy: Super-Resolution Mapping of Chemical Reaction Centers

Gert De Cremer, Bert F. Sels, Dirk E. De Vos, Johan Hofkens, and Maarten B.J. Roeffaers

Abstract Recently fluorescence microscopy has been introduced in the field of catalysis to study their dynamic molecular processes under in situ conditions with high spatial and temporal resolution. Because of the unique sensitivity down to the single molecule level, fluorescence microscopy allows to observe and localize chemical transformations with a subdiffraction-limited resolution. This chapter describes the use of fluorogenic probe molecules to visualize single chemical conversions using fluorescence microscopy. Special attention is paid to how visualization of single chemical conversions can yield super-resolution images beyond the diffraction limit.

Keywords Fluorogenic substrate · Heterogeneous catalysis · Single catalytic turnover counting · Wide-field fluorescence microscopy

G. De Cremer, B.F. Sels, and D.E. De Vos
Center for Surface Chemistry and Catalysis, Katholieke Universiteit Leuven, 3001 Heverlee, Belgium

J. Hofkens
Laboratory for Photochemistry and Spectroscopy, Katholieke Universiteit Leuven, 3001 Heverlee, Belgium

M.B.J. Roeffaers (✉)
Center for Surface Chemistry and Catalysis, Katholieke Universiteit Leuven, 3001 Heverlee, Belgium

Laboratory for Photochemistry and Spectroscopy, Katholieke Universiteit Leuven, 3001 Heverlee, Belgium
e-mail: maarten.roeffaers@biw.kuleuven.be

P. Tinnefeld et al. (eds.), *Far-Field Optical Nanoscopy*,
Springer Ser Fluoresc (2015) 14: 245–262, DOI 10.1007/4243_2011_33,

Contents

Abbreviations

BODIPY	4,4-Difluoro-4-bora-3a,4a-diaza-s-indacene
GSDIM	Ground-state depletion and single molecule return
LDH	Layered double hydroxide
MRI	Magnetic resonance imaging
NASCA	Nanometer accuracy by stochastic chemical reactions
PALM	Photo-activated localization microscopy
PET	Photo-induced electron transfer
PSF	Point-spread-function
STED	Stimulated emission depletion microscopy
STORM	Stochastic optical reconstruction microscopy
TIRF	Total internal reflection fluorescence

1 Introduction

The performance of a catalytic particle is determined by its chemical composition, the structure at the atomic scale, and the accessibility [1]. In order to better predict and understand the influence of these parameters on the catalytic performance, a broad range of physicochemical characterization techniques has been developed [1, 2]. In general, such in-depth characterizations focus on determining the catalysts' structure and chemical composition, preferentially at the atomic scale and under catalytically relevant conditions. For instance, detailed structural characterization of catalyst particles is routinely accessible via electron microscopy. Furthermore, it has recently become possible to obtain compositional and structural information on the catalyst particle using scanning probe [3] and X-ray microscopy [4].

In stark contrast to these detailed structural and chemical pictures of (inorganic) catalytic surfaces, insight into the organic chemical transformations at these surfaces is mostly limited to bulk analysis of reaction mixtures by, for example, chromatographic or mass spectrometric analysis. At best these conversions can be

observed with sub-millimeter spatial resolution using vibrational spectroscopy or MRI [5, 6]. This discrepancy in resolution and sensitivity hampers a one-to-one linking of catalytic activity to local catalyst properties.

To overcome this lacuna, microscopic techniques that combine an excellent spatial and temporal resolution with an exceptional sensitivity for organic compounds are necessary [7–9]. Similar requirements apply when studying biomedical samples in detail, and for such studies the use of fluorescence microscopy has proven to be a major advance. The field of fluorescence microscopy has witnessed strong technical and practical developments over the past decade, many of these advances aiming for improved sensitivity and enhanced spatial resolution. As a result, single molecule sensitivity has become widely available, and various diffraction-unlimited or super-resolution imaging schemes have been reported [10, 11]. While biomedical super-resolution imaging schemes such as PALM, STORM, and STED rely on the photostimulated switching of molecules between an emissive and a non-emissive state, diffraction-unlimited imaging of heterogeneous catalysts in NASCA microscopy, or Nanometer Accuracy by Stochastic Chemical reActions microscopy, uses the isolated signals of individual converted fluorogenic probe molecules [9]. In this approach, visualization and accurate localization of individual catalytic turnovers, occurring stochastically,

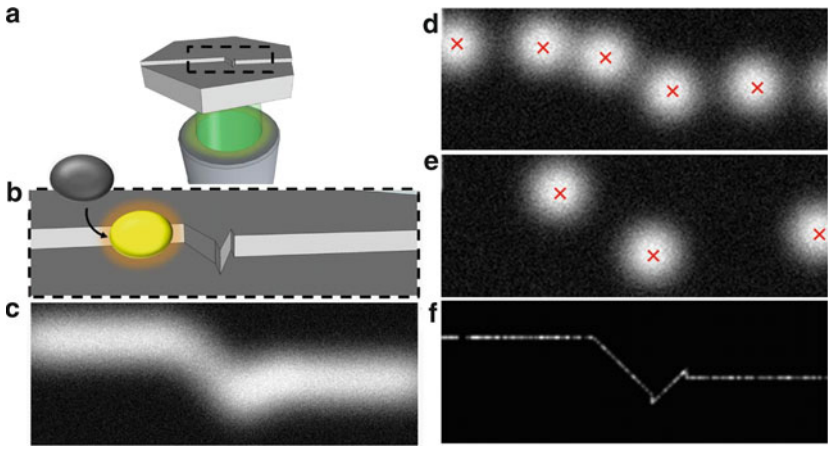

Fig. 1 Nanometer Accuracy by Stochastic Chemical reActions (NASCA) microscopy. (**a**) Catalytic materials contain a wide range of different facets and defects on which chemical reactions take place. (**b**) Fluorogenic substrates allow visualizing chemical conversions down to the single molecule level. (**c**) The resolution of traditional optical microscopy is limited to a few hundred nanometers. As a consequence, chemical events occurring on nanometer-sized features like this crystal edge are projected as broad zones of activity. (**d**, **e**) NASCA microscopy relies on recording the stochastic catalytic conversions of fluorogenic substrates at the single turnover level in real time. The exact location of each of these individual chemical reactions can be approximated with nanometer precision (*red crosses*) by mathematical fitting of the diffraction-limited point-spread-function (PSF). (**f**) Accumulation of these approximated reaction positions over consecutive frames allows reconstructing a high resolution optical image

allow reconstructing high resolution images of the active domains of the material under study [12, 13].

This chapter highlights this novel high resolution optical microscopy method based on localization of individual catalytic conversions of fluorogenic and chromogenic substrates. Next to reconstructing super-resolution images, elegant applications are illustrated such as quantification of the catalytic activity with preservation of spatial information at the nanometer scale. NASCA microscopy is technically simple since only one excitation wavelength is required avoiding the need for spatiotemporal overlap between different light sources, as is required in most other super-resolution fluorescence microscopy approaches. Figure 1 graphically explains the concept of NASCA microscopy. In this figure, it is obvious that accumulation of the approximated position of all the visualized individual chemical reactions allows reconstruction of a much more detailed image (Fig. 1f) than the traditional diffraction-limited one (Fig. 1c).

2 Concepts of Visualizing Catalytic Activity

The chemical conversion of nonfluorescent probes into strongly fluorescent reaction products is an ideal strategy to visualize and locate catalytic conversions inside (porous) materials. Such substrates are called fluorogenic and chromogenic compounds. Chromogenic substrates are noncolored species and only after their conversion they are able to absorb visible light. A fluorogenic reagent is a nonfluorescent chemical compound that can be chemically converted into a strongly fluorescent product molecule. Such compounds have been widely used to assess enzymatic activity [14]. Recently a few of such reagents have found their application in the characterization of catalyst particles using fluorescence microscopy [9, 15, 16]. In this context, the names fluorogenic and chromogenic are defined in a very broad sense: they also encompass molecules which as a result of a chemical transformation show a dramatic shift in their absorption spectrum and/or a drastic change in fluorescence quantum yield. This shift in photophysical properties results in a clear switch between a non-emissive and an emissive state at a selected excitation and detection wavelength. Simplified the molecule is converted from a non-detectable to a detectable state. Under the right conditions, the latter state can be visualized preferentially with single molecule sensitivity.

The first fluorogenic reagent described in literature to visualize individual chemical turnovers at a solid catalyst particle is the nonfluorescent acetic ester of fluorescein. Cleaving off the acetate groups, for example, according to base-catalyzed hydrolysis and transesterification reactions, yields the brightly emissive fluorescein (Fig. 2a), which can easily be detected at the single molecule level with current top-end fluorescence microscopes [17]. Fluorescein esters were already well known from biomedical research where they are used, for example, as cell viability probe reporting on the activity of intracellular esterases. Next to fluorogenic esters of fluorescein, there are many derivatives like ethers, amides, etc. of xanthene

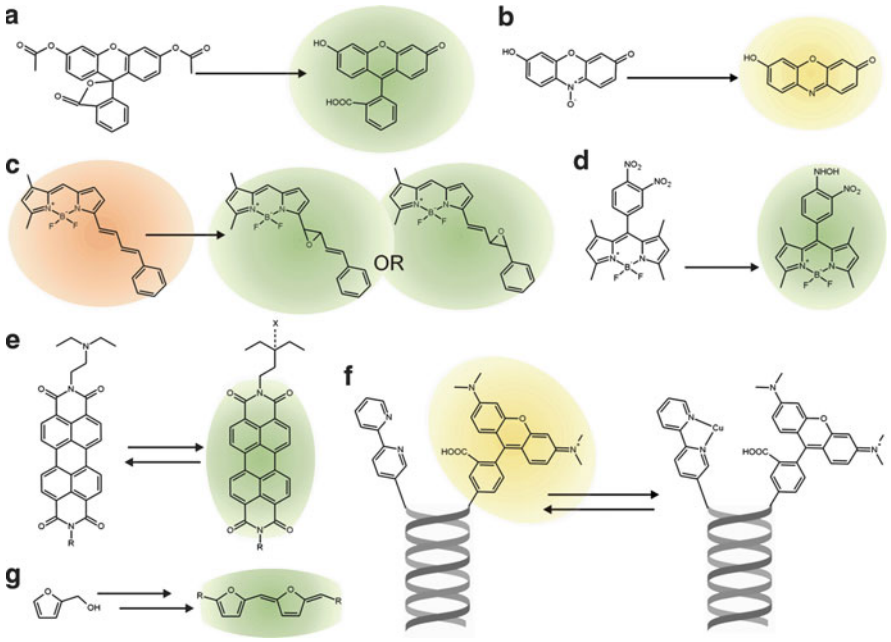

Fig. 2 Examples of fluorogenic probe reactions for NASCA microscopy [9, 12, 13]. (**a**) Formation of fluorescein from the fluorogenic substrate fluorescein diacetate [17]. (**b**) Reduction of the fluorogenic resazurin to the yellow fluorescent resorufin [18]. (**c**) Conversion of the red fluorescent phenylbutadiene-BODIPY to the green fluorescent epoxidized product [12, 13]. (**d**) Photocatalytic reduction of the fluorogenic dinitrophenyl-BODIPY yields a green fluorescent product [19]. (**e**) An amine in the unbound state quenches the fluorescence of a perylene diimide (PDI) chromophore via photo-induced electron transfer (PET). This process is inhibited when the free electron pair of the amine binds a proton or a metal ion, which is indicated by *X*, thereby restoring the fluorescence of PDI [20]. (**f**) Fluorescence quenching by Cu(II) complexation on a nearby bipyridine group [21–23]. (**g**) Catalytic oligomerization of furfuryl alcohol results in strongly fluorescent reaction products [13, 24, 25]

dyes known. This wide variety of fluorogenic substrates is further extended with nonfluorescent oxidized or reduced versions of chromophores. Well-known examples of such chromophores are rhodamine and its reduced version dihydrorhodamine and resorufin and the oxidized form resazurin (Fig. 2b) [18], etc. The commercial availability of many of these dyes enables to target acid and base as well as redox-type catalytic reactions.

Recent reports have also shown that an intelligent derivatization and functionalization of well-known chromophores can also be used to generate reaction-specific fluorogenic reagents. De Cremer et al. reported on monitoring individual epoxidation reactions using a phenylbutadiene-functionalized BODIPY dye (Fig. 2c) [12, 26]. The addition of this phenylbutadiene-conjugated system to the central chromophore induces a red shift of about 80 nm in both the absorption and fluorescence spectrum compared to the original dye [27]. Selective epoxidation of

the butadiene bridge of this substituted dye shifts the absorption and fluorescence maximum back toward the original chromophore. Excitation near the absorption maximum of these products and fluorescence detection around its emission maximum allows the detection of individual reaction products even in the presence of a large excess of phenylbutadiene-functionalized BODIPY reagents in the surrounding solution.

Majima and coworkers also used BODIPY dye as a starting point to generate a reduction sensitive probe molecule (Fig. 2d) [19]. Addition of a 3,4-dinitrophenyl group quenches the fluorescence of the chromophore by photo-induced electron transfer (PET) from the excited chromophore to the dinitrophenyl moiety. Reduction of one nitro group to a hydroxylamine makes this intramolecular electron transfer unfavorable, hence restoring the fluorescence of the BODIPY chromophore. This makes the 3,4-dinitrophenyl functionalized BODIPY an excellent fluorogenic substrate to study the exact location of, for example, photocatalytic reductions.

Electron or energy transfer processes can also be used to monitor reversible binding and unbinding reactions with single molecule sensitivity. One such example is the protonation–deprotonation of amines (Fig. 2e) [20]. While amines with a free electron pair can quench the fluorescence of an excited chromophore in the vicinity via a PET process, protonation of the amine hinders this process, hence restoring the fluorescence intensity. Ions like Cu(II) can also quench the fluorescence of nearby chromophores. Functionalization of a strong chromophore with a copper-binding group like a bipyridine ligand results in a reversible fluorescent switch in which the fluorescence emission is determined by the binding or unbinding of Cu(II) ions (Fig. 2f) [23]. Thus a wide variety of fluorogenic chromophores can be thought of and designed starting from existing chromophores.

Next to these fluorogenic derivatives of well-known chromophores, a series of probe reactions has been described based on small organic molecules, like furfuryl alcohol [8, 13, 24, 28], styrenes [29, 30], thiophenes [31], etc., which via catalytic action are converted into extended conjugated systems (Fig. 2g). These oligomers are very efficient to probe, for example, acid-catalyzed conversions in the nanopores of zeolites. Stabilization of the oligomer by tight confinement in the pores enhances the fluorescence emission. Even though these reactions have shown their power as catalytic activity reporters at the single catalytic particle level, almost all studies average out the fluorescence intensity over a multitude of product molecules located within a diffraction-limited area. So far only one of these reactions was successfully monitored at the single molecule level [13]. The acid-catalyzed furfuryl alcohol condensation yields fluorescent oligomers which are sufficiently bright to detect individual reaction products.

In conclusion, the use of fluorogenic substrates makes it possible to visualize individual catalytic turnovers and approximate the exact position of this conversion with nanometer precision (see Fig. 1). Tuning the substrate concentration and balancing its conversion rate with the speed of disappearance of the fluorescent products due to photobleaching or diffusion allow mapping out and even quantifying local reaction rates at the single conversion level.

When no suitable chromogenic reactant can be found, one can still rely on the use of a spectator fluorophore bound to the reagent. This is for instance demonstrated by the group of Blum for a BODIPY-bound platinum complex [32–35]. By imaging the fluorescence in total internal reflection mode, TIRF microscopy, only species physi- and/or chemisorbed in close distance (few tens of nanometers) to the cover glass–liquid interface can be detected. Although this approach is thus not suitable to monitor reactions deep inside catalytic materials, it provides a useful alternative to the use of chromogenic substances when interested in surface processes.

3 Pinpointing Individual Catalytic Turnovers with Nanometer Precision at Catalytic Surfaces

The influence of structural features of solid catalyst particles on their local catalytic activity was for the first time directly observed on layered double hydroxide (LDH) crystals [17]. The LDH crystals used in this study consist of sheets of aluminum hydroxides in which aluminum(III) occupies two of three octahedrons. Introduction of lithium in the residual octahedrons results in positively charged layers which gives the material an interesting anion exchange capacity. Presence of hydroxide ions in the galleries between the sheets gives solid base catalyst functionality to the structure, illustrating its catalytic potential [36]. Clearly the crystals have different crystal facets, being the (large) basal plane and the lateral faces, with their own specific environments and a varying accessibility which will unavoidably lead to differences in local catalytic activity.

The base-catalyzed conversion of the fluorogenic fluorescein ester (Fig. 2a) was carried out in two different solvents that also act as reagent for the conversion into the strongly emissive fluorescein. When operated in an aqueous environment, the fluorogenic ester is hydrolyzed into fluorescein and free acetate, whereas in an *n*-butanol the same fluorescein is formed together with the corresponding acetic ester in a transesterification reaction. The strongly fluorescent reaction product allows the observation of both reactions with single turnover sensitivity. Interestingly, for the hydrolysis reaction catalytic turnovers were mainly observed at the crystal's lateral faces, whereas for the transesterification in *n*-butanol the whole outer surface participated in the catalytic conversion. The reconstructed NASCA images clearly show this difference between both reactions (Fig. 3).

Next to reconstructing such activity maps, NASCA microscopy (see also Fig. 1) also allows the quantification of the local catalytic rates and this by simple counting of the amount of turnovers for a selected area during a certain time interval. The transesterification reaction showed a homogeneously distributed activity over the whole outer surface (Fig. 3a–c). This catalytic activity increases linearly with an increased substrate concentration. On the other hand, the hydrolysis activity was for 85% confined to the lateral crystal faces (Fig. 3d–f). During these experiments, the diffusion of the fluorescein product over the catalyst surface could also be observed.

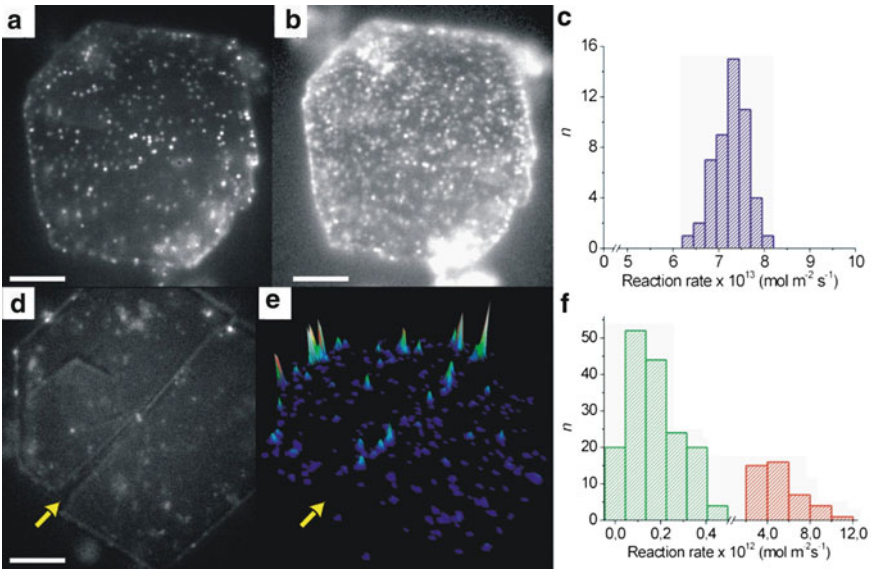

Fig. 3 (**a**, **b**) Fluorescence image during the transesterification of the fluorogenic fluorescein diacetate ester with *n*-butanol by a LDH, 40 nM (**a**) and 700 nM (**b**) substrate concentration. The *bright spots* correspond to single catalytic reaction products at the LDH outer surface. (**c**) Quantification of the initial transesterification rates for 1 μm^2 domains. (**d**) Fluorescence image of a LDH crystal during hydrolysis of 600 nM C-FDA. (**e**) Accumulated intensity on the same crystal over 256 consecutive images, highlighting the higher contribution of the lateral faces to the total hydrolysis activity. (**f**) Quantification of the initial hydrolysis rates for 1 μm^2 domains. The fast subpopulation (*red*) corresponds to active domains located at lateral faces, whereas the basal planes are responsible for the slow population (*green*). Scaling bars: 5 μm. Reproduced with permission from [17]. Copyright 2006, Nature Publishing Group

A large fraction of the molecules (90%) showed a high surface mobility ($D = 3 \times 10^{-14}$ m^2 s^{-1}), whereas for 10% of the molecules the observed displacements are smaller than the experimental error.

A second example where NASCA microscopy was exploited is in the field of electrocatalysis [18]. Here, single electrocatalytic reductions by single-walled carbon nanotubes (SWNT) were observed with a wide-field fluorescence microscope using the conversion of the fluorogenic resazurin into the strongly fluorescent resorufin (see Fig. 2b). By localizing and counting these conversions on the long nanotubes (length of a few micrometer), NASCA microscopy revealed that the reactions are concentrated in areas of about 20 nm diameter, which equals the accuracy limit of this study. From this result it was thus concluded that the electrocatalytic reductions occur at discrete reaction sites with a nanometer-size dimension that are present along the SWNTs. Moreover, careful analysis of the kinetics of the reaction process revealed a large heterogeneity in reactivity among these reactive sites reflecting the heterogeneity in electronic properties.

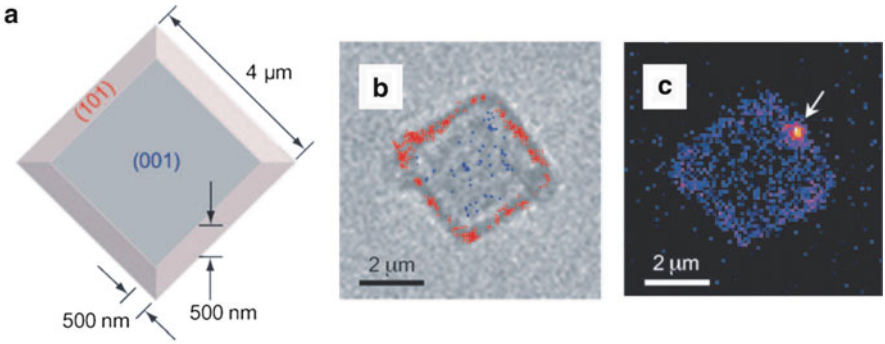

Fig. 4 (**a**) Schematic of a single micrometer-sized anatase TiO_2 crystal with preferential (001) facets. (**b**) Optical transmission image of a single TiO_2 crystal, and (**c**) fluorescence image of the same crystal in an argon saturated 2.0 mM dinitrophenyl-BODIPY solution under 488 nm laser and UV irradiation. The *red* and *blue* dots in image (**b**) indicate photocatalytic turnovers located on the (101) and (001) surfaces, respectively, observed during 3 min of irradiation. The fluorescent products were localized by mathematical fitting of the PSF. The *arrow* in (**c**) indicates an individual reaction product. Copyright Wiley-VCH Verlag GmbH & Co. KGaA. Reproduced with permission from [19]

Majima and coworkers also used this single catalytic turnover detection scheme to precisely map redox reactions at the outer surface of individual photocatalyst particles [19, 37, 38]. As fluorogenic probe molecule they used the 3,4-dinitrophenyl-substituted BODIPY dye, where the fluorescence of the excited chromophore is quenched by an intramolecular PET to the 3,4-dinitrophenyl moiety (Fig. 2d). Photocatalytic reduction of one of the nitro's to a hydroxylamine restores the chromophore's emissive properties (Fig. 2d). These photocatalytic events can be selectively visualized on individual micrometer-sized anatase particles (Fig. 4) [19]. By pinpointing the different turnovers on top of the optical transmission image, it becomes clear that the majority of the photocatalytic conversions takes place on the (101) plane. Quantification of these conversions learns that the photocatalytic reduction of this probe at the (101) plane is about three times more efficient than at the (001) plane (Fig. 4b). This observation is linked to the spatially selective migration of photogenerated electrons and holes.

4 Nanoscale Activity Mapping Inside 3D Nanoporous Catalysts

The previous examples nicely demonstrate the strength of NASCA microscopy for observing individual catalytic events and quantifying the surface activity. However, many heterogeneous catalysts have complex three-dimensional structures often with a complex intracrystalline nanoporous network to maximize the catalytically active surface. Because of size restrictions, these nanopores cannot accommodate the well-known polycyclic aromatic chromophores commonly used in single

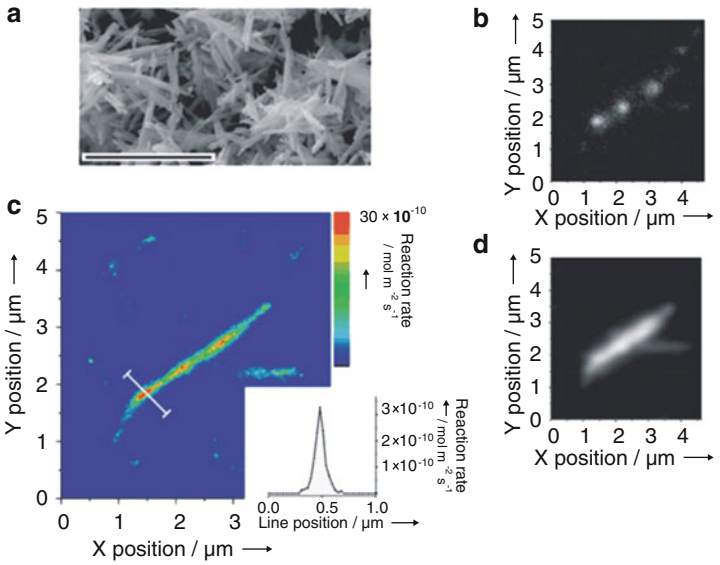

Fig. 5 (**a**) SEM image of needle-like ZSM-22 crystallites (average particle width: 120 nm; scale bar: 5 µm). (**b**) Individual catalytic conversions of furfuryl alcohol on ZSM-22 crystallite. (**c**) Diffraction-limited image resulting from accumulation of all fluorescence observed during 1,000 s of reaction. (**d**) NASCA map showing catalytic reactivity for 20 × 20 nm^2 pixels. The intensity of the bins is determined by the amount of reactions localized in each bin using the high resolution scheme. *Inset*: local reaction rate as measured along the white line. A width of about 100 nm is obtained, corresponding to the real width of the imaged structure. Copyright Wiley-VCH Verlag GmbH & Co. KGaA. Reproduced with permission from [13]

molecule fluorescence studies. As a result, observation of single catalytic turnovers in these porous networks critically depends on the identification of small reagent molecules that are converted into sufficiently bright fluorescent product molecules that can be distinguished from the background noise. Surprisingly, furfuryl alcohol is such a reagent. Roeffaers et al. have shown that the pore-entrapped reaction products of an acid-catalyzed oligomerization reaction are sufficiently bright to enable single molecule observations in a wide-field fluorescence microscope [13].

First, the catalytic conversion of furfuryl alcohol inside the pores of needle-shaped H-ZSM-22 crystallites was observed (Fig. 5). In every frame, bright emissive spots originating from individual oligomeric reaction products were observed (Fig. 5b). Using the single molecule localization techniques, these reaction sites were accumulated over 10,000 frames (1,000 s). The resulting NASCA microscopy image projects the catalyst particle with its real width of approximately 100 nm (Fig. 5c). In contrast, a normal diffraction-limited fluorescence image transforms these 100 nm thin catalytic rods as approximately 500 nm wide objects (Fig. 5d).

Furthermore, NASCA microscopy makes it possible to quantify the local catalytic activity at the nanometer scale. Such reactivity maps clearly uncover zones with different reactivity within an individual ZSM-22 needle. NASCA microscopy

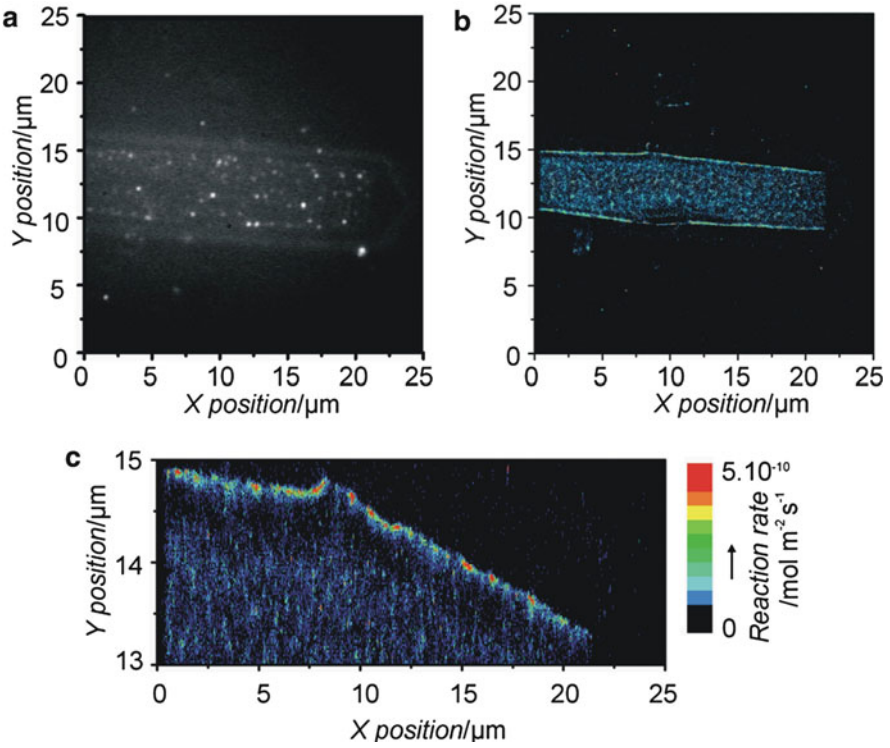

Fig. 6 (**a**) Individual fluorescent product molecules on a ZSM-5 crystal. The contours of the crystal are vaguely visible because of a small amount of unfiltered scattered light. (**b**) NASCA map showing catalytic reactivity for 20 × 20 nm^2 pixels. (**c**) Details of the edge of the crystals intergrowth where a nanometer-sized edge is present which shows a tenfold enhanced reactivity. Copyright Wiley-VCH Verlag GmbH & Co. KGaA. Reproduced with permission from [13]

is the first technique that gives access to local, nanoscale catalytic reactivity inside porous structures, making it the true organic counterpart of high resolution inorganic imaging techniques like electron microscopy.

This same furfuryl alcohol oligomerization reaction was also used to visualize nanoscale reactivity profiles of the large hexagonal facets of ZSM-5 (Fig. 6). Such NASCA micrographs reveal a strongly enhanced catalytic reactivity in a central zone in the middle of these facets. Furthermore, zooming in on these super-resolution NASCA maps uncovers the presence of a very narrow zone with tenfold increased activity, lining the highly active central zone. The origin of this enhanced catalytic activity was revealed in a detailed electron microscopic study: the central zone with elevated activity overlapped with the 90° intergrowths present in the main crystal body. These intergrowths are also outlined by distinct 50–100 nm high steps in which fresh furfuryl alcohol reagent can diffuse into the catalyst porous network from two perpendicular directions. This enhanced supply of reagents at the edges of the intergrowth may explain the local increase in turnover event frequency (Fig. 6).

The pore-entrapped reaction products rapidly accumulate near the outer surface of the zeolite particles; this restricts current studies to the observation of catalytic reactivity to the initial stages of the process. Use of reactions in which the formed product can freely diffuse away would solve this problem, enabling observation of the catalytic activity during steady-state conditions as is shown in the following part.

5 NASCA Microscopy Reveals the Effect of Intraparticle Diffusion Limitations on the Catalytic Activity

The above-mentioned NASCA approach was recently applied to evaluate the catalytic performance of a Ti-MCM-41 epoxidation catalyst in the presence of tert-butyl hydroperoxide [12, 26]. This catalyst consists of micrometer-sized particles with parallel mesoporous channels of about 2.5 nm in diameter. As a probe reaction, a phenylbutadienyl-substitued BODIPY dye (PBD-BODIPY) was used. This red fluorescent dye undergoes a strong blue-shift upon epoxidation (Fig. 2c). Thus, by spectral selection one can selectively monitor the formation of individual PBD-BODIPY molecules inside the catalytic particles. Figure 7 shows a representative picture of individual reaction positions, obtained by the NASCA approach, overlaid with a transmission image of the corresponding catalyst particle. Surprisingly, the NASCA image reveals that the reaction turnovers are almost exclusively confined to the outer few hundred nanometers of the catalyst particles. These results were interpreted in terms of diffusion limitations: the influx of PBD-BODIPY molecules cannot keep up with the fast rate of conversion of these molecules. As a result, a steep concentration gradient throughout the particle is observed, even in steady-state conditions. In the case of a first-order reaction, the

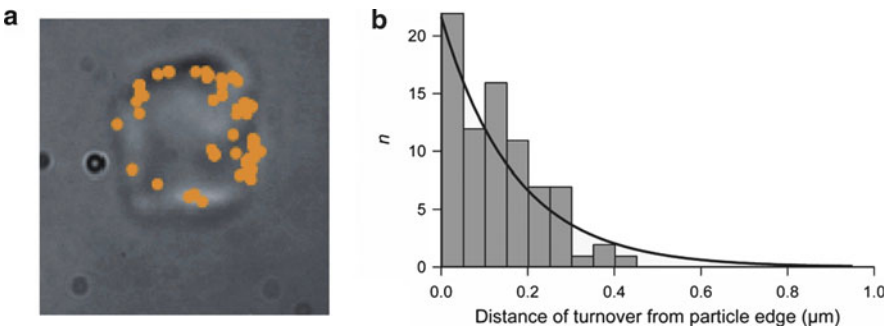

Fig. 7 (**a**) High-accuracy localized reaction positions inside an individual Ti-MCM-41 particle (particle dimension: ± 3 μm). (**b**) The histogram of the distances between the fitted position and the particle's edge directly reflects the reagent concentration profile inside the particles and can thus be directly related to the degree of diffusion limitation. Adapted with permission from [12, 26]

spatial distribution of detected reaction events, that is, the NASCA map, directly reflects this concentration gradient (Fig. 7b) [12, 26]. Therefore, from the NASCA map, the degree of diffusion limitation can be directly quantified, as demonstrated by De Cremer et al. The catalyst was found to work at only 30–40% of its maximum capacity due to diffusion limitation. Moreover, as the single molecule approach for activity monitoring yields an absolute number of reaction events per unit of time, the reaction rate constant could be calculated, and together with the spatial distribution of the reactivity, an absolute value of the intraparticle diffusion coefficient could be obtained as well. Such values are extremely hard to obtain by the traditional "ensemble-averaged" experiments.

Thus, one NASCA microscopy experiment yields enough information to directly map and quantify the local reaction rates, and to determine effective diffusion coefficients, rate constants, and reactions efficiencies of individual catalyst particles even in steady-state conditions.

6 Extending NASCA Microscopy into Biology

Reaction cycles containing a fluorescent species can also be used to visualize and localize biological structures. Schwering et al. used the reversible Cu(II) complexation reaction (Fig. 2f) to switch the fluorescence of a nearby chromophore between

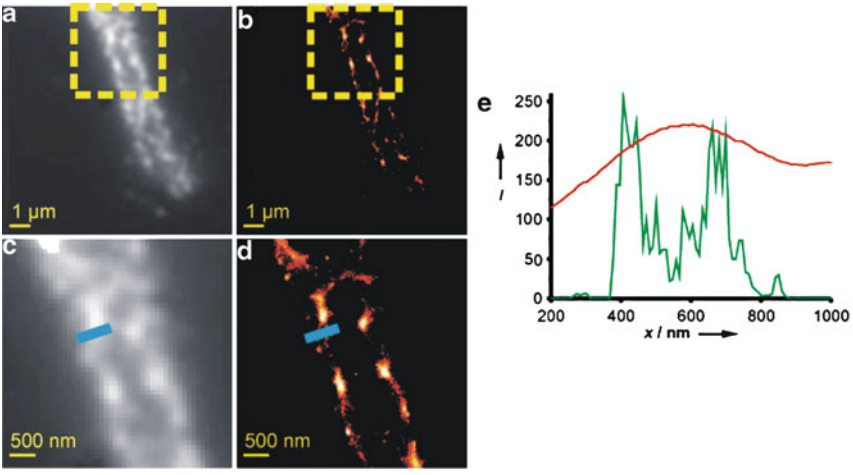

Fig. 8 Fluorescence microscopy-based imaging of labeled microtubules in fixed mouse fibroblasts. (**a**) Normal diffraction-limited fluorescence micrograph (accumulation of 8,000 frames). (**b**) Super-resolution image, reconstructed from localization of individual chromophore from the 8,000 frames in (**a**). (**c**, **d**) Zooming in on selected regions of, respectively, (**a**) and (**b**) clearly shows the difference in resolution. (**e**) Line profile showing the fluorescence intensity for the diffraction-limited (*red*) and the super-resolution image (*green*). Copyright Wiley-VCH Verlag GmbH & Co. KGaA. Reproduced with permission from [23]

an ON and an OFF state. Attaching such a chemical switch to a tubulin-antibody enables the visualization of microtubules within fibroblast cells. While many details are lost in the traditional diffraction-limited fluorescence image, localization of individual switching molecules enabled the authors to reconstruct a more detailed picture (Fig. 8). This approach has some advantages over PALM microscopy, since only one excitation source is required which is similar to GSDIM or dSTORM experiments [39, 40]. The authors indicate that the advantage over GSDIM or dSTORM is the independence of the ON–OFF switching on the excitation power. The fluorescent state of the probe can be controlled by the Cu(II) content in the cell.

While the use of Cu(II) ions in cells is not always desirable, a more general solution might come from probes from which the fluorescence emission is, for example, based on the binding of protons [20]. Loading chromophores with the right pK_a would allow to probe biological structures with a NASCA microscopy imaging scheme.

7 Conclusion and Perspectives

This chapter summarizes the power of NASCA microscopy as a super-resolution optical technique. NASCA microscopy exploits the possibility of current fluorescence microscopes to observe individual chemical transformations of fluorogenic substrates. These conversions are recorded as diffraction-limited intensity profiles by a sensitive CCD camera. Mathematical fitting of this PSFs and this for many consecutive frames allows the reconstruction of high resolution images. Such NASCA micrographs reveal nanoscale features that would otherwise be lost in a diffraction-limited study. An obvious application of NASCA microscopy is the study of catalytic materials. Here not only high resolution activity mapping is possible; NASCA microscopy also allows quantification of local reactivity rates. Also in biological systems NASCA microscopy could reveal new information. Using fluorogenic substrates local enzymatic activity could be probed or structures of interest labeled with an enzyme could be targeted. Such an approach would be advantageous over other types of diffraction-unlimited optical microscopy since only one laser is required to visualize the products, and since bleaching of the attached chromophore does not occur, an enzyme-labeled structure can be targeted for many consecutive frames. On the other hand, probe molecules that switch between a fluorescent ON and OFF state when binding by analytes could also be envisioned. Chemical binding and unbinding of such biological substances like small molecules, proteins, etc. or even just protons could also give the necessary temporary signals necessary to allow a precise localization. Binding and unbinding events can also be directly monitored on very thin samples or on flat surfaces by using dye-bound reagents in combination with TIRF microscopy [32–35]. This eliminates the need for chromogenic reagents, and thus a wealth of different surface-related reactions can be assessed with this approach.

References

1. Niemantsverdriet JW (2007) Spectroscopy in catalysis: An introduction. 3rd, Completely Revised and Enlarged Edition edn. Wiley-VCH, Weinheim
2. Weckhuysen BM (2009) Chemical imaging of spatial heterogeneities in catalytic solids at different length and time scales. Angew Chem Int Edit 48(27):4910–4943
3. Hulsken B, Van Hameren R, Gerritsen JW, Khoury T, Thordarson P, Crossley MJ, Rowan AE, Nolte RJM, Elemans J, Speller S (2007) Real-time single-molecule imaging of oxidation catalysis at a liquid–solid interface. Nat Nanotechnol 2(5):285–289. doi:10.1038/nnano.2007.106
4. de Smit E, Swart I, Creemer JF, Hoveling GH, Gilles MK, Tyliszczak T, Kooyman PJ, Zandbergen HW, Morin C, Weckhuysen BM, de Groot FMF (2008) Nanoscale chemical imaging of a working catalyst by scanning transmission x-ray microscopy. Nature 456 (7219):222–225
5. Urakawa A, Baiker A (2009) Space-resolved profiling relevant in heterogeneous catalysis. Top Catal 52(10):1312–1322. doi:10.1007/s11244-009-9312-3
6. Bergwerff JA, Lysova AA, Alonso LE, Koptyug IV, Weckhuysen BM (2007) Probing the transport of paramagnetic complexes inside catalyst bodies in a quantitative manner by magnetic resonance imaging. Angew Chem Int Edit 46:7224–7227. doi:10.1002/anie.200701399
7. Roeffaers MBJ, De Cremer G, Uji-i H, Muls B, Sels BF, Jacobs PA, De Schryver FC, De Vos DE, Hofkens J (2007) Single-molecule fluorescence spectroscopy in (bio)catalysis. P Natl Acad Sci USA 104(31):12603–12609
8. Roeffaers MBJ, Hofkens J, De Cremer G, De Schryver FC, Jacobs PA, De Vos DE, Sels BF (2007) Fluorescence microscopy: Bridging the phase gap in catalysis. Catal Today 126 (1–2):44–53
9. De Cremer G, Sels BF, De Vos DE, Hofkens J, Roeffaers MBJ (2010) Fluorescence micro (spectro)scopy as a tool to study catalytic materials in action. Chem Soc Rev 39(12):4703–4717
10. Hell SW (2009) Microscopy and its focal switch. Nat Methods 6(1):24–32. doi:10.1038/nmeth.1291
11. Hell SW (2007) Far-field optical nanoscopy. Science 316(5828):1153–1158. doi:10.1126/science.1137395
12. De Cremer G, Roeffaers MBJ, Bartholomeeusen E, Lin K, Dedecker P, Pescarmona PP, Jacobs PA, De Vos DE, Hofkens J, Sels BF (2010) High-resolution single-turnover mapping reveals intraparticle diffusion limitation in ti-mcm-41 catalyzed epoxidation. Angew Chem Int Edit 49(5):908–911
13. Roeffaers MBJ, De Cremer G, Libeert J, Ameloot R, Dedecker P, Bons A-J, Bückins M, Martens J, Sels BF, De Vos DE, Hofkens J (2009) Super-resolution reactivity mapping of nanostructured catalyst particles. Angew Chem Int Edit 48(49):9285–9289
14. Smiley RD, Hammes GG (2006) Single molecule studies of enzyme mechanisms. Chem Rev 106(8):3080–3094
15. Tachikawa T, Majima T (2010) Single-molecule, single-particle fluorescence imaging of tio2-based photocatalytic reactions. Chem Soc Rev 39(12):4802–4819. doi:10.1039/b919698f
16. Chen P, Zhou XC, Shen H, Andoy NM, Choudhary E, Han KS, Liu GK, Meng WL (2010) Single-molecule fluorescence imaging of nanocatalytic processes. Chem Soc Rev 39 (12):4560–4570. doi:10.1039/b909052p
17. Roeffaers MBJ, Sels BF, Uji-i H, De Schryver FC, Jacobs PA, De Vos DE, Hofkens J (2006) Spatially resolved observation of crystal-face-dependent catalysis by single turnover counting. Nature 439(7076):572–575
18. Xu WL, Shen H, Kim YJ, Zhou XC, Liu GK, Park J, Chen P (2009) Single-molecule electrocatalysis by single-walled carbon nanotubes. Nano Lett 9(12):3968–3973. doi:10.1021/nl900988f
19. Tachikawa T, Wang N, Yamashita S, Cui SC, Majima T (2010) Design of a highly sensitive fluorescent probe for interfacial electron transfer on a tio2 surface. Angew Chem Int Edit 49 (46):8593–8597. doi:10.1002/anie.201004976

20. Ameloot R, Roeffaers MBJ, Baruah M, De Cremer G, Sels BF, De Vos DE, Hofkens J (2009) Towards direct monitoring of discrete events in a catalytic cycle at the single molecule level. Photochem Photobiol Sci 8(4):453–456
21. Kiel A, Jarve A, Kovacs J, Mokhir A, Kramer R, Herten DP (2007) Single-molecule studies on individual metal complexes. Proc of SPIE 6,444
22. Kiel A, Kovacs J, Mokhir A, Kramer R, Herten DP (2007) Direct monitoring of formation and dissociation of individual metal complexes by single-molecule fluorescence spectroscopy. Angew Chem Int Edit 46(18):3363–3366
23. Schwering M, Kiel A, Kurz A, Lymperopoulos K, Sprodefeld A, Kramer R, Herten DP (2011) Far-field nanoscopy with reversible chemical reactions. Angew Chem Int Edit 50 (13):2940–2945. doi:10.1002/anie.201006013
24. Roeffaers MBJ, Sels BF, Uji-i H, Blanpain B, L'Hoest P, Jacobs PA, De Schryver FC, Hofkens J, De Vos DE (2007) Space- and time-resolved visualization of acid catalysis in zsm-5 crystals by fluorescence microscopy. Angew Chem Int Edit 46(10):1706–1709
25. Roeffaers MBJ, Ameloot R, Bons A-J, Mortier W, De Cremer G, de Kloe R, Hofkens J, De Vos DE, Sels BF (2008) Relating pore structure to activity at the subcrystal level for zsm-5: An electron backscattering diffraction and fluorescence microscopy study. J Am Chem Soc 130(41):13516–13517
26. De Cremer G, Bartholomeeusen E, Pescarmona PP, Lin K, De Vos DE, Hofkens J, Roeffaers MBJ, Sels BF (2010) The influence of diffusion phenomena on catalysis: A study at the single particle level using fluorescence microscopy. Catal Today 157:236–242
27. Pap EHW, Drummen GPC, Winter VJ, Kooij TWA, Rijken P, Wirtz KWA, Op den Kamp JAF, Hage WJ, Post JA (1999) Ratio-fluorescence microscopy of lipid oxidation in living cells using c11-bodipy581/591. FEBS Lett 453(3):278–282
28. Roeffaers MBJ, Sels BF, De Schryver FC, Jacobs PA, Hofkens J, De Vos DE (2007) In situ filming of reactions inside individual zeolite crystals using fluorescence microscopy. Stud Surf Sci Catal 170:717–723
29. Kox MHF, Stavitski E, Weckhuysen BM (2007) Nonuniform catalytic behavior of zeolite crystals as revealed by in situ optical microspectroscopy. Angew Chem Int Edit 46 (20):3652–3655
30. Stavitski E, Kox MHF, Weckhuysen BM (2007) Revealing shape selectivity and catalytic activity trends within the pores of h-zsm-5 crystals by time- and space-resolved optical and fluorescence microspectroscopy. Chem-Eur J 13(25):7057–7065
31. Kox MHF, Domke KF, Day JPR, Rago G, Stavitski E, Bonn M, Weckhuysen BM (2009) Label-free chemical imaging of catalytic solids by coherent anti-stokes raman scattering and synchrotron-based infrared microscopy. Angew Chem Int Edit 48(47):8990–8994. doi:10.1002/anie.200904282
32. Canham SM, Bass JY, Navarro O, Lim SG, Das N, Blum SA (2008) Toward the single-molecule investigation of organometallic reaction mechanisms: single-molecule imaging of fluorophore-tagged palladium(ii) complexes. Organometallics 27(10):2172–2175. doi:10.1021/om800228v
33. Lim SG, Blum SA (2009) A general fluorescence resonance energy transfer (fret) method for observation and quantification of organometallic complexes under reaction conditions. Organometallics 28(16):4643–4645. doi:10.1021/om900629s
34. Esfandiari NM, Wang Y, Bass JY, Cornell TP, Otte DAL, Cheng MH, Hemminger JC, McIntire TM, Mandelshtam VA, Blum SA (2010) Single-molecule imaging of platinum ligand exchange reaction reveals reactivity distribution. J Am Chem Soc 132(43):15167–15169. doi:10.1021/ja105517d
35. Esfandiari NM, Wang Y, McIntire TM, Blum SA (2011) Real-time imaging of platinum-sulfur ligand exchange reactions at the single-molecule level via a general chemical technique. Organometallics 30(11):2901–2907. doi:10.1021/om100911n
36. Sels BF, De Vos DE, Jacobs PA (2001) Hydrotalcite-like anionic clays in catalytic organic reactions. Catal Rev 43(4):443–488

37. Tachikawa T, Yamashita S, Majima T (2011) Evidence for crystal-face-dependent tio2 photocatalysis from single-molecule imaging and kinetic analysis. J Am Chem Soc 133 (18):7197–7204. doi:10.1021/ja201415j
38. Wang N, Tachikawa T, Majima T (2011) Single-molecule, single-particle observation of size-dependent photocatalytic activity in au/tio2 nanocomposites. J Chem Sci 2(5):891–900. doi:10.1039/c0sc00648c
39. Heilemann M, van de Linde S, Schuttpelz M, Kasper R, Seefeldt B, Mukherjee A, Tinnefeld P, Sauer M (2008) Subdiffraction-resolution fluorescence imaging with conventional fluorescent probes. Angew Chem Int Edit 47(33):6172–6176. doi:10.1002/anie.200802376
40. Folling J, Bossi M, Bock H, Medda R, Wurm CA, Hein B, Jakobs S, Eggeling C, Hell SW (2008) Fluorescence nanoscopy by ground-state depletion and single-molecule return. Nat Methods 5(11):943–945. doi:10.1038/nmeth.1257

Counting Molecules: Toward Quantitative Imaging

Maximilian H. Ulbrich

Abstract In this chapter, we describe how single-molecule fluorescence can be used to analyze protein–protein interactions by enabling the direct visualization of protein complexes and the number and species of their constituent subunits. The prerequisites for this visualization are a low protein density, facilitating the discrimination of individual fluorescent complexes, and high labeling efficiency and specificity to allow for quantitative measurements of protein interactions. We describe three experimental realizations of quantitative imaging techniques made possible by the single-molecule approach: counting the photobleaching steps of fluorescent complexes, the analysis of a histogram of measured spot intensities, and the colocalization of fluorescent tags of multiple colors. Applications of this approach range from the determination of a protein's oligomerization state to the analysis of the subunit content of large protein assemblies containing multiple subunit types. We describe the minimal setup required for these experiments and present several examples of this approach applied to current biological questions.

Keywords Single-molecule imaging, Subunit counting, TIRF microscopy, Protein multimerization, Membrane protein assembly, Intensity distribution analysis

Contents

M.H. Ulbrich (✉)
Centre for Biological Signalling Studies (BIOSS) and Institute for Physiology at the Department of Medicine, Albert-Ludwigs-University Freiburg, 79104 Freiburg im Breisgau, Germany
e-mail: max.ulbrich@bioss.uni-freiburg.de

P. Tinnefeld et al. (eds.), *Far-Field Optical Nanoscopy*,
Springer Ser Fluoresc (2015) 14: 263–292, DOI 10.1007/4243_2011_36,

1 Introduction

Single-molecule experiments can provide valuable information that goes beyond that derived from bulk experiments. In particular, the elimination of ensemble averaging reveals the full distribution of states assumed by a population of molecules, whereas bulk measurements can only deliver a single average value. Depending on the experimental design, information on different state parameters can be measured for each individual molecule over time. Using fluorescence as a readout, these parameters are usually restricted to the position of the molecule and the intensity and wavelength spectrum of the emitted fluorescence.

When observing biological samples such as living cells, the positions of single molecules and their movements over time can be used to calculate their diffusion coefficients and to determine their associations with other molecules. With the use of a suitably designed probe, changes in function lead to changes in fluorescence intensity or shifts in the emission spectrum. In this chapter, we focus on the case where a fluorescent probe is merely used as a marker to tag a protein of interest, and the information is gained from the colocalization of interacting molecules and the intensity distribution of the fluorescent protein complexes in time and space. When different protein species are tagged with multiple, spectrally distinguishable fluorophores, colocalization of the different markers can be related to the association of the different proteins (Fig. 1a). When only one fluorescent protein is used, the intensity emitted from a single fluorescent spot allows for the deduction of the multimerization state of the protein because each of the associating subunits carries one fluorescent tag that contributes to the total intensity (Fig. 1b). In addition, by observing photobleaching steps from single fluorescent spots, the number of multimerized protein subunits can be counted with high fidelity (Fig. 1c).

A fundamental condition for detecting protein interactions via the colocalization of multiple fluorescent tags is the complete but exclusive labeling of the proteins

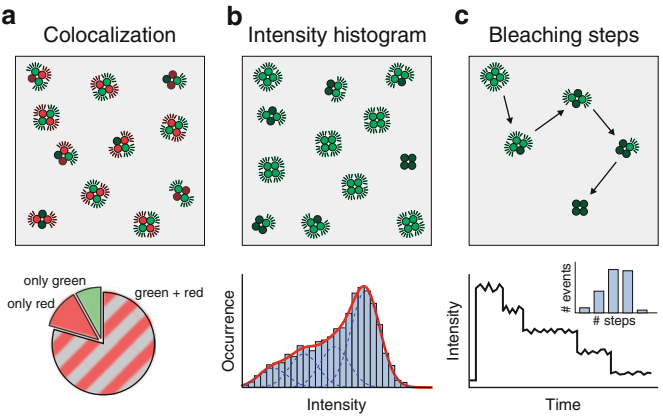

Fig. 1 Schemes for quantitative single-molecule imaging of protein complexes. (**a**) Colocalization of *red* and *green* fluorescence allows for the assessment of the interaction of differentially labeled subunits. To obtain a valid representation of the interaction, the majority of fluorescent tags must be functional. (**b**) When the protomers of a homomultimeric protein are fluorescently labeled, the fluorescence intensity from single complexes is a multiple of the unitary fluorescence from a single tag. Due to noise, the intensity levels are broadened (*bottom*; *blue dashed lines* indicate distributions for complexes with 1, 2, 3, and 4 functional tags) and result in a complex intensity distribution (*red solid line*). From this distribution of emission intensities and its changes during photobleaching, the multimerization state of the protein can be deduced. (**c**) If it is possible to track the fluorescence intensity of single complexes from the onset of illumination until photobleaching, bleaching steps can be identified (*bottom*). The number of bleaching steps relates to the multimerization state of the protein

of interest. When only a small fraction of the target protein is successfully labeled, the few fluorescent molecules present will be associated with nonfluorescent molecules, and interactions will be missed; conversely, if nontarget proteins or the background are labeled, they can be misinterpreted as the target protein, again introducing a mismatch between the real and observed degrees of interaction. Therefore, particular care must be taken to ensure proper labeling, and appropriate corrections may need to be applied during postprocessing.

The analysis of protein interactions and multimer formation by imaging single fluorescent molecules requires that the molecules are sufficiently spatially separated so as to enable their resolution as individual fluorescent spots and that their movement is slow. These conditions are not met in many systems; in particular, for most soluble intracellular proteins, their concentrations are far too high, and their diffusion is fast. Suitable proteins include membrane proteins, which diffuse slowly and can be expressed at very low densities, large proteins that are present only in a single or very few copies per cell, such as bacterial DNA replication machinery, or soluble proteins after purification and immobilization to the coverslip.

In Sect. 2, we discuss the different paradigms for the formation of protein multimers, ranging from obligatory interactions that define the elementary function

of the protein complex to optional interactions that modulate or regulate its function. Section 3 deals with the experimental details and instrumentation of the imaging setup required for quantitative single-molecule imaging. In Sect. 4, several explicit examples are provided to demonstrate how protein interactions can be quantified. Finally, the challenges, difficulties, and future prospects of the techniques are discussed.

2 Multimeric Protein Assemblies

Interactions between proteins play a pivotal role in virtually all biological processes. Protein–protein interactions can be classified into different categories based on their functions. For some proteins, these functions arise through their multimerization, as for cytoskeletal proteins, rotary motors, and ion channels. Other proteins form larger assemblies consisting of different factors that share various tasks in a highly complex process, as in DNA replication or the exocytosis of vesicles. In many cases, the function of a core protein is regulated by optional interactions with auxiliary subunits that can either modulate core protein functionality, as with the beta subunits of many ion channels, or confer new properties on the core proteins, e.g., calmodulin interacts with a variety of proteins to impart Ca^{2+} dependence.

2.1 New Properties Emerging from Homomultimerization

The assembly of multiple, often identical building blocks to create larger structures with emergent properties is a common theme in nature. Protein homomultimerization, i.e., the formation of multimers from identical monomers, is frequently observed in proteins involved in structural support, rotary motion, the enclosure of specific contents, or the transport of substances through a central pore.

The filamentous cytoskeletal proteins actin and tubulin form chains containing up to thousands of monomers and are used not only for mechanical support of the cell but also as scaffolds for the directed motion of the cargo-carrying proteins myosin, kinesin, and dynein [1, 2]. Spherical structures are used for the enclosure of various contents or the generation of subcellular compartments. Examples include the protein envelope of many viruses and phages and the clathrin coats that form pits on the cytosolic side of cell membranes to assist in the formation of small vesicles during endocytosis and intracellular trafficking [3, 4].

Ring-shaped multimeric proteins are commonly assembled from a small and defined number of monomers, and their functions are often the transport of compounds through their central pore. Typical homomultimeric membrane proteins include ion channels and transporters, which usually consist of 2–6 monomers and transport ions or small molecules across the cell membrane, either passively, driven

by the electrochemical gradient, or actively, by the cotransport of other ions, ATP hydrolysis, or proton flux. The tetrameric Shaker potassium channel is one of the most studied proteins in this class, but many trimeric (e.g., P2X receptors), pentameric (acetylcholine receptors), hexameric (connexins), and even higher-order multimers are also known [5–8]. In a wider sense, members of this class also include heteromultimeric proteins, wherein the different subunits contribute equally to the central pore and only differ in small respects (e.g., heterotetrameric NMDA receptors) [9].

The rotary motor proteins are another class of ring-shaped multimeric proteins. The most important rotary protein is the F_0F_1-ATPase, which couples a trimeric ATP-synthesizing rotor to a ring of 9–14 peptides that is driven by transmembrane proton flux [10, 11]. Another example of a rotary motor is the bacterial flagellar motor, which enables these microbes to move rapidly by driving the rotation of the flagellum at speeds of up to hundreds of rotations per second [12]. The motor uses the energy from an electrochemical ion gradient to generate torque that is transmitted through the membrane and cell wall to the flagellum by several rotor and stator rings that each consist of different but defined numbers of subunits. Viral DNA packaging motors and helicases, which promote DNA strand separation, combine rotation with simultaneous linear motion along the DNA or RNA passing through the central aperture of the ring [13, 14].

2.2 *Larger Protein Assemblies for Complex Actions*

Most biological processes are too complicated to be performed by a single protein but instead consist of a multitude of simple tasks that are integrated into a multistep process, for example, a signaling cascade. Although many of these processes are distributed across different subcellular locations (e.g., chemotaxis and the generation of action potentials in nerve cells), some are carried out by a single complex of molecular machinery comprising tens of components. In only a few cases is this molecular machine sufficiently compact to be amenable to X-ray crystallography (e.g., ribosomes); more often, flexible parts, weak binding, and variable component stoichiometries impede purification and crystal formation (as with exocytosis machinery, the nuclear pore complex, the DNA replisome, and the flagellar motor) [12, 15–17]. The application of a subunit-counting approach for the analysis of DNA replication machinery is discussed in Sect. 4.2.

2.3 *Auxiliary Proteins Modulate Functions*

The functions of many proteins are modulated by cofactors that associate with the core proteins and modify their functions. Signaling cascades of the immune system, the cell cycle, apoptosis, and many other cellular processes depend on protein phosphorylation

and dephosphorylation by kinases and phosphatases that transiently bind to the proteins to add or remove phosphate groups. Another prominent modulator is calmodulin, which confers calcium sensitivity to proteins that do not have calcium-binding domains [18]. Because these soluble modulatory proteins usually have dissociation constants in the nano- to micromolar ranges, single-molecule approaches are rendered difficult due to background emission from unbound molecules in the cytoplasm when their concentrations exceed approximately 1 nM.

However, certain regulatory proteins, i.e., those having a high affinity and specificity for the core protein, particularly when bound to or associated with the plasma membrane, are more amenable to single-molecule imaging with subunit counting. Many ion channels in the brain and other tissues undergo modulation by one or more auxiliary subunits that are developmentally regulated or differentially expressed in various tissues. Examples include the modulation of the KCNQ potassium channels by KCNE, AMPA receptors by TARPs (transmembrane AMPA receptor regulatory proteins), and ClC chloride channels by Barttin. The stoichiometry of the KCNQ1/KCNE1 complex has recently been analyzed using the single-molecule subunit-counting approach, and work on AMPA receptors and ClC channels is currently in progress [19].

3 Instrumentation and Techniques

To obtain quantitative information from single-molecule data with the highest possible quality, care must be taken to select the proper equipment. For the discrimination of photobleaching steps, the separation of adjacent fluorescence peaks, and the tracking of single molecules, measures must be taken to reduce the fraction of events that must be excluded from the evaluation due to insufficient reliability of the intensity trace or space trajectory: these are the maximization of the number of collected photons from the signal and decreasing the noise and background levels. For the applications described in this chapter, the equipment of choice is usually a standard inverted microscope equipped with a high-numerical-aperture (NA) objective (1.45 or more), a back-illuminated EMCCD (electron-multiplying CCD) camera, high-quality emission filter sets, and a laser-based illumination system. In the following, we briefly discuss the advantages over alternative components and explain in further detail how to design a laser illumination system suitable for single-molecule imaging. When set up correctly, this system should enable the researcher to directly observe fluorescence and bleaching steps of single molecules of bright fluorescent proteins (GFP, YFP) and organic dyes (Alexa, Cy dyes) without filtering or postprocessing. Care should be taken when using other system designs, e.g., confocal microscopes. Not all of them have the photon yield, time resolution, signal-to-noise ratio, etc. to observe bleaching steps or establish intensity histograms. Unless the methods development is the focus of the work, we recommend to rely on microscope setups that have been proven their ability to deliver results on subunit counting. An overview of popular single-molecule fluorescence setup designs is given in [20].

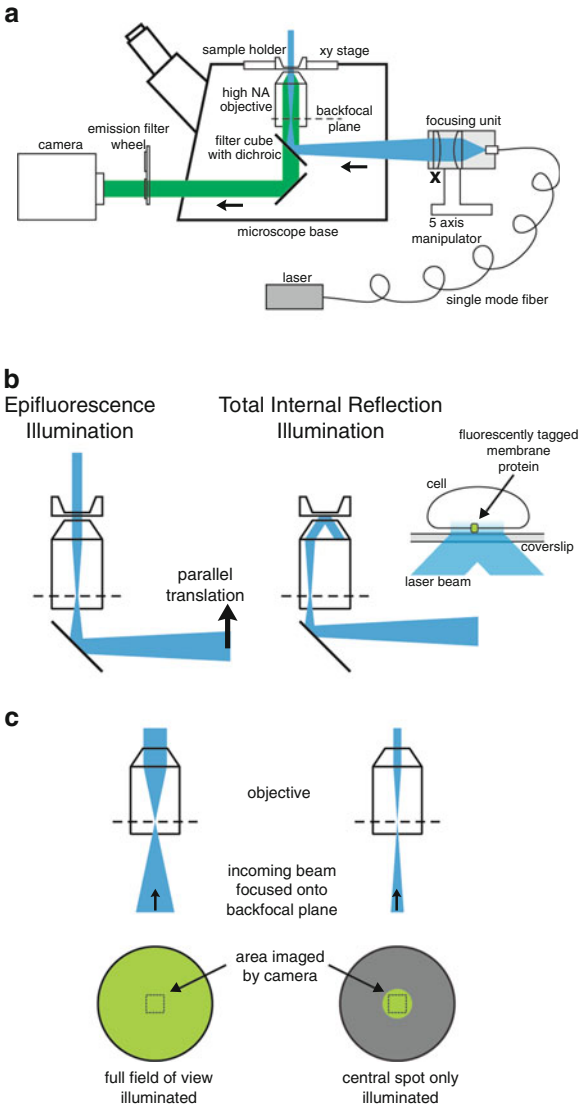

Fig. 2 Microscope setup for single-molecule TIRF and epifluorescence imaging. (**a**) The essential components for a single-molecule imaging setup are a high-NA objective, high power density at the sample, and an EMCCD camera. (**b**) Switching between epifluorescence and TIR illumination can easily be accomplished by parallel translation of the light beam that is focused onto the back-focal plane. When the incident angle of the beam at the coverslip exceeds the critical angle, the light is reflected, but the evanescent wave can still excite fluorescently tagged proteins in the membrane of an attached cell (*inset*). (**c**) Reducing the angle of the incoming beam yields higher power density at the sample and at the same time prevents photobleaching of sample regions that are not being imaged by the camera

3.1 Microscope

In many single-molecule imaging experiments, the sample consists of fluorescent molecules attached directly to a coverslip surface in an aqueous environment or cells growing on the coverslip and expressing the protein(s) of interest. Although other settings are also possible, an inverted microscope capable of fluorescence excitation through the lens is usually the simplest configuration for this purpose (Fig. 2a). To prevent premature photobleaching of the sample, it may be necessary to select the area to be imaged with the illumination switched off. Therefore, it is helpful to equip the microscope with a motorized stage because it facilitates small, controlled movements in the *x*–*y* plane. The use of a motorized focus control can also avoid small changes of the focal plane, in the range of 100 nm, that readily introduce visible distortions of the imaged fluorescent molecules. To further reduce influences that might compromise the quality of acquired video recordings, vibrations should be reduced by mounting the microscope on an optical table.

3.2 High-NA Objective Lens

Because the aperture of the objective lens is directly related to the amount of emitted fluorescent light that is directed toward the camera, a high-NA objective is required to collect as many photons as possible. For many applications with live cells, total internal reflection (TIR) illumination is desired; this is also only possible with an NA that is considerably larger than the refractive index of water (approximately 1.33). Some available TIR objectives have an NA of 1.45, and several companies offer NA 1.49 objectives; even NA 1.57 and NA 1.65 objectives are available. However, the latter two require special coverslips that are very expensive ($50 or more each); therefore, due consideration should be given to the necessity of their use.

3.3 EMCCD Camera

In the last decade, several camera types with built-in signal amplification have become commercially available. The EMCCD design has proven to be the best for detecting low numbers of photons, in the range of <100 per pixel, with moderate frame rates of <100 Hz, while the level of noise introduced by the camera remains negligible. A new generation of cameras, termed sCMOS (scientific complementary metal oxide semiconductor) has recently been introduced; however, preliminary tests in our laboratory showed that their performance in single-molecule experiments is inferior to that of EMCCD cameras.

Many companies offer back-illuminated versions of EMCCD cameras. Instead of sending the incoming light to the front face of the sensor, where thin layers of metal wiring partially cover the imaging area and thereby impede the collection of light, in the back-illuminated version, the sensor is flipped, and a large part of the substrate is etched away, allowing exposure of the light-sensitive layer from the back, where no wiring structures block the incoming light. Compared with standard front-illuminated technology that achieves approximately 50% quantum efficiency, back-illuminated devices reach quantum efficiencies of more than 90%, thereby yielding an increased signal/noise (S/N) ratio and better discrimination of separate events.

3.4 Small-Angle Laser Beam Illumination

The configuration of the light source for an experiment involving the tracking and/or photobleaching of single fluorescent molecules depends on the type of sample to be imaged. Many samples display relatively strong background fluorescence from intracellular compartments. In this case, a total internal reflection fluorescence (TIRF) configuration should be considered; here, incident light is restricted to the parts of the sample lying within a very thin layer (approximately 100 nm) near the coverslip surface (Fig. 2b). This is achieved by directing a collimated light beam, usually from a laser, at the interface between the coverslip and the sample space at a very low angle, thereby preventing the light from passing from the material with the higher refractive index (glass) into that with the lower refractive index (water, or the sample in aqueous environment). Although it is reflected back into the glass, the incoming beam is still able to penetrate into the sample space with an exponentially decaying intensity and a penetration depth on the order of the wavelength, and thus it can excite parts of the sample within this area (the membrane of an attached cell). For some types of experiments, TIR illumination is not necessary, e.g., when working with cell-free systems such as purified protein attached to the coverslip.

Most commercially available epifluorescence and TIRF condensers are designed to illuminate the full visible field of view. However, for single-molecule experiments, it can be advantageous to reduce the size of the illuminated sample area to a diameter of a few tens of microns, for two reasons. First, a good S/N ratio requires a high illumination power; to obtain the flux of 10,000 photons per second or more from a single GFP molecule required to achieve sufficient localization accuracy in each 30-ms frame of an acquired movie, the illumination power density must be in the range of 1 kW/cm^2, equivalent to 1 mW over a 10 μm $\times$ 10 μm area. Most standard laser sources available for the life sciences are limited to power outputs of approximately 10–50 mW. Therefore, it is not possible to illuminate the full visible field of view (approximately 200 μm in diameter) with a sufficiently

high power density, which means that the condenser must be modified or custom-built. The second reason to restrict the illumination to a small area is the rapid photobleaching of the fluorophores when illuminated at very high power (typically occurring in 5 s to 1 min, depending on the fluorophore) and the need to acquire images from an area of the sample that has not been photobleached during previous acquisitions. If the full visible field of view is simultaneously illuminated, a large area of the sample will be bleached and thus unusable for successive experiments. Because the area imaged by the camera in single-molecule experiments is usually only 10–20 μm wide, it is sufficient to expose this area during acquisition and leave the rest of the visible field of view unilluminated (Fig. 2c).

The illuminated area of the sample can be reduced to a small spot by decreasing the total angle covered by the light beam that reaches the objective back-focal plane (Fig. 2c). The angle α can be calculated from the desired spot radius r_s at the sample plane, the tube length l_t (Zeiss, 165 mm; Olympus, 180 mm; Leica and Nikon, 200 mm), and the magnification m of the objective as $\alpha = 2\tan^{-1} r_s m / l_t$. Accordingly, when using a convex lens of focal length f (labeled "X" in Fig. 2a) to focus a collimated laser beam onto the back-focal plane, the beam radius r_b striking the lens should be $r_b = f r_s m / l_t$. A simple design for this purpose can be realized by fiber coupling the laser and using a commercial or custom-built collimator to create a parallel beam with a larger diameter (5–10 mm); then, using a lens with a focal length of approximately 200 mm, this larger beam is focused through the back port of the microscope via the dichroic in the filter cube and onto the back-focal plane. Mounting the focusing unit on a five-axis manipulator stage allows the user to adjust the focused beam to the point of the back-focal plane where the light exiting the objective front lens illuminates the sample in either TIRF or epifluorescence configurations.

3.5 Alternative System Designs

We shortly want to introduce two alternative microscope designs that have been demonstrated to work well for single molecule subunit counting. They have certain advantages and allow to analyze samples that might be impossible to use by an objective-based TIR setup, but are more difficult to build than the objective-based TIR setup.

The first is the prism-based TIR configuration. The excitation laser is approaching the coverslip from the back surface, but the objective is imaging the sample from the front side. To enable the laser to hit the coverslip–water interface with a low angle, a prism is attached to the back of the coverslip by a thin layer of immersion oil. The sample can either be imaged by a water objective in the solution or, in case a flow chamber is used, through the lid of the chamber. The advantage of prism over objective-based TIR microscopy lies in the higher mechanical stability of the coverslip due to the support by the prism, allowing the exchange or flow of solutions during the experiment without deformation of the coverslip that leads to a

focus change and concomitant loss of the image. This microscope design was used recently for subunit counting of soluble and membrane proteins. Without prior purification, GFP-labeled proteins were immobilized directly from cell lysates by binding to specific antibodies attached to the coverslip [21]. Subunit counting was successfully applied to the soluble enzyme protein kinase A, to the β_2 adrenergic receptor, and the mitochondrial antiviral signaling protein.

Another alternative microscope design that was used for single-molecule subunit counting of a soluble protein is based on an electrokinetic trap to keep a fluorescently labeled protein molecule in the focal volume of the microscope [22]. Diffusion of the molecule away from the center can be sensed by a beam, spinning around the molecule, and will be compensated by a feedback loop that applies a voltage to the trap electrodes to pull the molecule back into the focus. Due to the difference in their diffusion constant, large single molecules like enzymes will be trapped, but small unbound dye molecules can escape the trap. While the molecule is trapped, the dye molecules attached to each of its subunits are bleaching and can be counted. This approach had been used to determine cooperative behavior of ATP binding and hydrolysis at the mammalian chaperonin TRiC [22].

4 Experimental Approaches

Several single-molecule approaches have recently been developed in efforts to decipher the multimerization states and the stoichiometry of protein complexes by subunit counting. The underlying principle common to all is the identification of individual protein complexes as fluorescent spots in an image (Fig. 3a) and the elaboration of an intensity distribution or a histogram of photobleaching steps, as outlined in the introduction. Because of the differences in cell types and the variability of protein properties in their native environment, it is difficult to describe a standard approach that is suitable for any given biological question. Therefore, we herein provide an overview of different methodologies that have recently been successfully applied and can be adapted to specific problems.

4.1 Counting Bleaching Steps

Upon prolonged high-intensity illumination of fluorescent proteins or organic dyes, the molecules undergo a destruction or alteration of their chemical structure that leads to an irreversible loss of fluorescence, a phenomenon called photobleaching. Photobleaching is a stochastic process which, under normal imaging conditions, occurs with a low and constant probability for each excitation–emission cycle. When working with a large number of fluorescent molecules, photobleaching is perceived as an exponential decay of sample intensity; however, on a single-

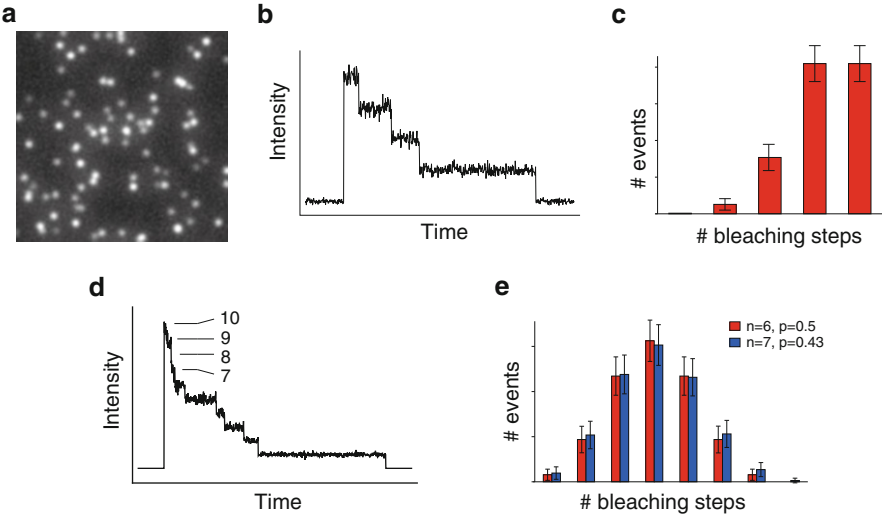

Fig. 3 Determination of the oligomerization state by counting bleaching steps (simulated data). (**a**) Single fluorescently labeled protein complexes must be identified in the image. (**b**) For each spot, the fluorescence is recorded, and the number of steps until complete photobleaching are counted. (**c**) The histogram of bleaching-step numbers should display a binomial distribution that can be fitted with the probability of a fluorophore being functional and the degree of oligomerization as free parameters. Because only a limited number of events can be evaluated, the histogram will display deviations from its expectation value. (**d**) With an increasing number of subunits, bleaching at the beginning of the photobleaching process happens faster and noise increases, making the counting of steps impossible. (**e**) With an increasing degree of oligomerization, it becomes more difficult to distinguish between n and $n + 1$ subunits, in particular, when the probability p of a fluorophore being functional is low, as exemplified for two distributions with different pairs of n and p values (expected standard deviation for 100 events)

molecule level, a sudden and complete loss of emission from each individual fluorescent molecule can be observed.

Although it is undesirable in most biological fluorescence applications, the photobleaching process can be exploited in single-molecule experiments because the stepwise bleaching allows for the identification and counting of multiple fluorescent tags, even those lying within a diffraction-limited spot. When a protein of a fixed oligomerization state is labeled with a fluorescent tag, counting the bleaching steps in single protein complexes provides a method for counting the subunits of the protein (as illustrated in Fig. 3a–c).

However, a high degree of multimerization complicates the counting of bleaching steps for two technical reasons: (1) usually, a certain fraction of fluorophores is not functional, and this causes a mismatch between the observed number of bleaching steps and the number of protein subunits; and (2) the gap between consecutive steps becomes shorter, and noise from multiple fluorophores accumulates, thereby "washing out" the individual steps.

4.1.1 Masking of Bleaching Steps by Noise

When counting a larger number of subunits, the noise intrinsic to the emission process complicates the discrimination of adjacent bleaching steps in two ways. First, the average time between steps becomes shorter because the frequency of bleaching events is proportional to the number of fluorophores that are still functional. Therefore, there is a higher chance that two steps will occur within a few consecutive frames and may thus be mistaken for a single step (Fig. 3d). Second, noise increases with the number of fluorophores and can become large enough to mask the bleaching steps at the beginning of the exposure, when all the fluorophores are still functional.

Together, these two effects limit the number of bleaching steps that can be reliably identified from a single trace; the particulars depend on the fluorophore used for labeling. With organic dyes that display low noise, high intensity and slow photobleaching, up to seven bleaching steps can be reliably counted, as demonstrated in one study [23]. When using GFP tags genetically fused to the protein of interest, the inherent noise usually limits the number of distinct bleaching steps to four or five [24]. In many cases, it is possible to determine the number of bleaching steps manually. There are also some algorithms that can extract stepwise changes from noisy data. These algorithms allow an unbiased processing of the intensity traces from fluorescent spots. In the ideal case, an algorithm would extract the bleaching steps from noisy data based on the information that (1) step changes occur always from higher to lower intensity, (2) step sizes are equal, and (3) noise levels are correlated to emission intensity. However, algorithms like the one designed by Watkins and Yang [25] or Chung and Kennedy [26] are limited to the extraction of any step-like changes from noisy data, but do not take into account these restrictions that are unique to the bleaching step situation. Therefore, often the manual identification of bleaching steps works more reliable. Nevertheless, when the quality of the data permits it, these algorithms work well for counting bleaching steps [23].

4.1.2 Nonfluorescent Fraction

Most fluorescent proteins contain a sizeable fraction of nonfluorescent molecules, resulting in a decrease in the number of bleaching steps counted from some of the protein complexes and an underestimation of the actual extent of multimerization; when using an organic dye, the same problem can occur due to nonoptimal labeling of the protein of interest. By counting the bleaching steps of many individual protein complexes in the observed area, a histogram can be constructed, with the number of events evidencing a certain number of bleaching steps. Here, we assume that the nonfluorescent tags are evenly distributed across the whole population of protein molecules, resulting in a binomial distribution if the protein resides exclusively in a defined multimerization state (Fig. 3c). The unknown fraction of nonfluorescent protomers appears as a free parameter in the binomial distribution

and can be obtained from the best fit of the theoretical distribution to the measured histogram.

The reliable determination of a protein's multimerization state is only possible when the theoretical distributions for n and $n + 1$ subunits are well distinguishable. With an increasing fraction of nonfunctional tags and an increasing degree of multimerization, the binomial distributions for n and $n + 1$ become more similar (Fig. 3e). An estimate of the possible achievable accuracy of a binomial fit to the measured histogram can be made by calculating the deviation from the expectation value that an experiment will bear. A few examples should clarify this important issue: e.g., when the fraction of functional tags is 80% and the protein is a tetramer, 41% of the complexes are expected to bleach in four steps. If bleaching steps from 100 complexes are counted, it is unlikely to observe exactly 41 events with four steps. By means of statistics, one can calculate that the standard deviation of this value is about 5% of the total events, i.e., in most cases, between 36 and 46 events with four steps will be counted. The same calculations apply to events with 1, 2, and 3 bleaching steps (error bars in Fig. 3c). In this example, distributions for trimers or pentamers will always be very different from the tetramer distribution. However, when comparing a hexamer and heptamer and fractions of 50% and 43% of functional tags as in the example of Fig. 3e, the difference between the two distributions is not significant when evaluating 100 events.

In practice, it is more difficult to specify definite values for the maximum fraction of nonfunctional tags allowed when a certain degree of multimerization should be reliably deduced from the measured histograms. The main reason for this is that the experimental result deviates in important aspects from the theoretical predictions. The deviation usually depends on the specific design of the experiment and the setup, e.g., in theory, it should be impossible to obtain five bleaching steps from a pure tetramer when all complexes can be spatially discriminated, and therefore, a single event with five bleaching steps would exclude the possibility that the observed protein is a tetramer. However, in practice one will always observe a small fraction of events with a larger number of bleaching steps than the protein actually has subunits. This could be caused by two complexes "sticking" to each other, a misassembled protein with an extra subunit, or by a small movement of the protein that changes its position, which can introduce changes of the emission as explained below.

A rough estimation combining theoretical and practical aspects yields the following values for the minimum fraction p of functional tags when analyzing a protein with subunit number n in order to determine its multimerization state with high reliability:

$n = 1$	$p = 40\%$
$n = 2$	$p = 65\%$
$n = 3$	$p = 70\%$
$n = 4$–5	$p = 75\%$
$n = 6$–8	$p = 80\%$

4.1.3 Mobility of Fluorophores

The movement of fluorophores during imaging introduces additional noise into the recorded intensity. When the TIR microscopy configuration is used, variations in the distance of the protein from the coverslip translate into changes in illumination intensity experienced by the fluorophore due to the exponential decay of the evanescent field with distance from the coverslip, with a length constant on the order of 100 nm. Therefore, when the cell membrane is not completely flat, proteins that are diffusing laterally in the membrane display larger fluctuations in observed emission intensity than immobile proteins. To date, the counting of bleaching steps to determine the multimerization state of a protein has only been successfully applied to immobilized proteins [19, 24, 27–34].

4.1.4 Examples

Following the validation of the subunit-counting approach with different well-characterized proteins of known, fixed multimerization states, the technique has been used by our group and others to analyze a variety of new proteins with previously unknown subunit numbers. We next present examples of subunit counting for proteins labeled with organic dyes *in vitro* and for GFP-labeled proteins in living cells.

Pore-forming toxins, mainly produced by bacteria, are transmembrane proteins that, when integrated into the plasma membrane of a target cell, form oligomeric assemblies with a central pore; examples include hemolysin, gramicidin, and anthrax toxin. However, the number of monomers necessary to form a ring has not been determined with certainty for all of them. In a study by Hagan Bayley and coworkers, the single-molecule subunit-counting approach was successfully applied to the β-barrel-forming toxins α-hemolysin, which forms a homomer, and leukocidin, which is a heteromer of the two subunits LukF and LukS [23]. For both proteins, the exact number of subunits in each complex was unclear, but they were known to range between six and eight. Oligomerization of the α-hemolysin and leukocidin subunits was induced by mixing them with membranes, and the assembled multimers were subsequently purified by washing out the membrane fraction and separating the multimers from the remaining monomers by electrophoresis. Prior to oligomerization, the monomers were labeled with Alexa-647 maleimide by reaction with an artificially introduced cysteine residue, yielding a labeling efficiency of over 90% as estimated by gel electrophoresis with subsequent analysis of the unlabeled and labeled protein fractions.

For imaging, the proteins were adsorbed onto a coverslip and washed with a buffer containing oxygen scavengers to prevent blinking and premature photobleaching of the dye molecules. Because a cell-free system was used, the epifluorescence configuration was applied, using a laser power density of 3 kW/cm^2 and a 14.4 μm × 14.4 μm imaging area. Fluorescently labeled α-hemolysin

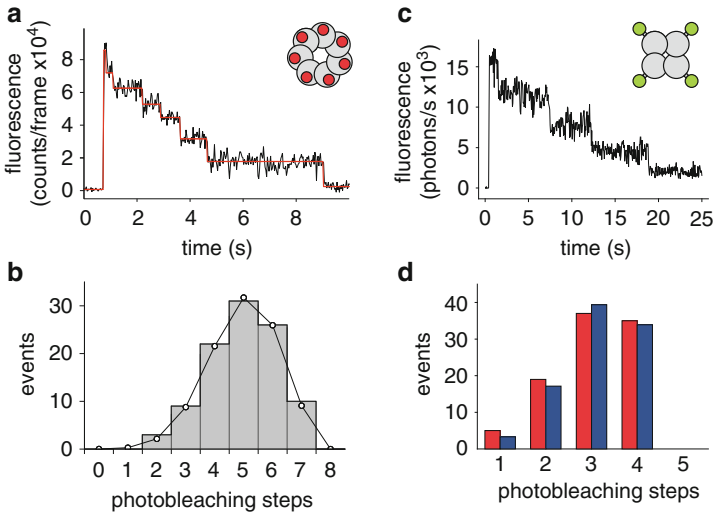

Fig. 4 Counting bleaching steps of proteins labeled with organic dyes and FPs. (**a**) Bleaching steps from the heptameric Alexa 647-labeled α-hemolysin and (**b**) the histogram of bleaching-step numbers (*gray bars*) together with the fitted binomial distribution, showing a labeling efficiency of 71% (adapted from Das et al. [23]). (**c**) Bleaching steps from the tetrameric mEGFP-labeled CNG channel and (d) the histogram of bleaching-step numbers (*red bars*) together with the fitted binomial distribution (*blue bars*), showing a 77% probability of the GFP tag being functional (adapted from Ulbrich and Isacoff [24])

displayed up to seven bleaching steps, and the resulting intensity histogram, constructed from approximately 100 fluorescent spots, gave a good fit to the binomial distribution for seven subunits, with a fitted labeling efficiency of 71% (Fig. 4a, b). For leukocidin, in each of two experiments, only one of the two subunits, either LukF or LukS, was labeled while the other subunit was unlabeled. In both cases, up to four bleaching steps were detected. The bleaching-step histograms were well fitted by binomial distributions with fluorescent subunit fractions of 74% and 64%, respectively. The conclusion was that there were eight subunits in the assembled leukocidin multimer, with a LukF/LukS stoichiometry of 4:4. The discrepancy between the 90% labeling efficiency as determined by biochemical analysis and the 74% or 64% of fluorescent subunits as determined by the binomial fit can be explained by the presence of nonfluorescent dye molecules.

The applicability of the subunit-counting approach to membrane proteins expressed in living cells was first demonstrated in the laboratory of Ehud Isacoff, using several well-known protein complexes with one, two, or four subunits [24]. In these experiments, we used *Xenopus laevis* (African clawed frog) oocytes, a well-established system for membrane protein expression. In this system, RNA obtained by *in vitro* transcription is directly injected into the cells; thus, the expression level of the target protein can easily be regulated by diluting the RNA, even down to the level of individual molecules. In *Xenopus* oocytes, diffusion within the membrane

is suppressed for many proteins, possibly due to interactions of intracellular domains with the dense cytoskeleton or the binding of extracellular domains to the coverslip. In contrast, most membrane proteins show considerable lateral diffusion in mammalian cell lines such as HEK293, COS-7, or CHO cells.

To ensure that the reference proteins were pure populations of monomers, dimers, and tetramers, neuronal ion channels were used, as these proteins pass a thorough quality-control checkpoint in the ER before being transported to the plasma membrane. The CNG channel was selected as a prototypical tetrameric protein bearing homology to the tetrameric potassium channels of the *Shaker* type (Fig. 4c). A monomeric EGFP tag was fused to the C-terminus via a flexible linker composed of 17 amino acids. To represent a dimeric protein, the GFP tag was fused to either the NR1 or NR2 subunit of the NMDA receptor, which assembles in a strict 2:2 stoichiometry. The α subunit of the voltage-gated Ca^{2+} channel was chosen as a typical monomeric ion channel.

After RNA injection and expression for approximately 24 h, the vitelline membrane, a protective protein layer enclosing the oocytes, was removed to enable close contact of the plasma membrane with the coverslip. Additional treatment with a mixture of hyaluronidase and neuraminidase improved cellular attachment to the coverslip. Due to the high autofluorescence from within the cell, TIR illumination was employed at power densities ranging from 0.5 to 1 kW/cm^2, with an image size of 13 μm × 13 μm. Despite some background signal from intracellular proteins, clear bleaching steps were identified for the majority of spots, and the histograms of bleaching-step numbers followed the binomial distribution calculated for a 75–85% probability of each GFP tag being fluorescent (Fig. 4d).

Both examples demonstrate that for the case of immobilized proteins that form obligatory multimeric assemblies with fixed stoichiometry, the counting of photobleaching steps is a straightforward and efficient method for determining the oligomerization state. In the following section, we present an approach for subunit counting that does not require the identification of bleaching steps.

4.2 Intensity Distribution Analysis

The identification of bleaching steps is only possible when the noise is reasonably low and the time between steps is sufficiently long (Fig. 3d). In many cases, excessive noise, caused either by diffusion of the molecules or intracellular background fluorescence, hampers the discrimination of distinct intensity levels during the bleaching of a single molecule, and the counting of bleaching steps becomes impossible. Nevertheless, the emission intensities of the multimeric GFP-tagged proteins are quantized, and the intensity levels, corresponding to complexes with 1, 2, 3, 4 . . . *n* GFP-tagged subunits, are evenly spaced, despite the signal broadening due to noise (e.g., the intensity histogram shown in Fig. 1b can be fitted with four distributions with evenly spaced peaks). If a sufficiently large number of events are collected, the average intensity levels, representing the distinct numbers of

fluorescent tags and their occupancies, can be extracted from the histogram of the measured emission intensities. The only condition required for this quantitation is that all GFP tags experience the same excitation intensity, which necessitates either homogeneous illumination across the imaged area or correction for inhomogeneous excitation during postprocessing. Because perfectly even illumination is more difficult to achieve in the TIRF configuration and fluctuations in the distance of the fluorophore from the coverslip change the experienced excitation intensity, epifluorescence illumination is often used.

4.2.1 Examples

Recently, a group led by Gerhard Schütz developed an approach to deduce the multimerization state of Orai, an essential part of the calcium release-activated calcium channel, which freely diffuses in the cell membrane when expressed in most mammalian cell lines [35]. Previous attempts to determine its multimerization state by counting the bleaching steps in the resting and activated states led to contradictory results [28, 30]. The new approach was based on a concept termed "thinning out clusters while conserving the stoichiometry of labeling" (TOCCSL), as outlined in Fig. 5.

Here, stably transfected T24 cells were used as an expression system based on their good signal-to-noise ratio in this application. A common problem in single-molecule imaging when transfecting plasmid DNA into mammalian cells is the overexpression of the protein of interest, resulting in a membrane density too high to discriminate individual fluorescent molecules. This issue was resolved by first completely photobleaching the imaging area with a high-intensity pulse (Fig. 5a, 1–2) and then waiting for unbleached Orai complexes in the surrounding membrane to repopulate the photobleached area by lateral diffusion from the edges (Fig. 5a, 3). Using epifluorescence illumination, intracellular membrane compartments in the imaging area were also bleached, which prevented unbleached molecules inside the cell from appearing at the cell membrane during the subsequent course of the experiment.

After a recovery time of 30–90 s, the acquisition of single-molecule fluorescence traces has begun because at this point, a sufficient number of unbleached Orai complexes had diffused from outside the bleached region back into the previously bleached part, but the population remained sparse enough to allow for sufficient separation (Fig. 5a, 4). Initially, the fluorescence of the Orai complexes was recorded in their unbleached state. After a few frames, a short photobleaching pulse was delivered, with an intensity strong enough to bleach a sizeable fraction of the GFP tags but not all of them; this left many complexes with one or two functional GFP tags but only a few with three or four (Fig. 5a, 5). The acquisition was continued to record the fluorescence of the Orai complexes in this partially bleached state.

Histograms of single-molecule emission intensities were constructed at various time points during the acquisition. The intensity distribution for the first frame

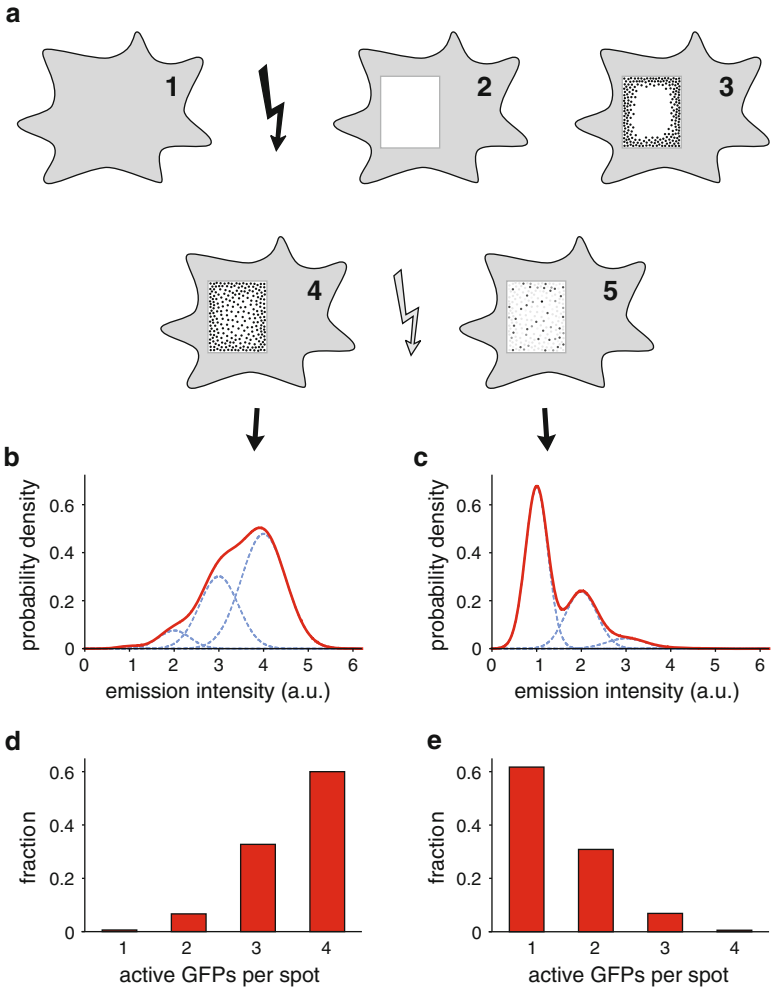

Fig. 5 Principle of intensity histogram analysis after TOCCSL (thinning out clusters while conserving the stoichiometry of labeling), as described in Madl et al. [35]. (**a**) *1*. Cells express the GFP-labeled membrane protein of interest at high density. *2*. With an intense photobleaching pulse, all GFP tags in the imaging area are photobleached. *3*. Unbleached proteins start to diffuse into the bleached area from the edges. *4*. After a recovery time, the imaging area is repopulated by unbleached protein. *5*. A short, weaker photobleaching pulse partially bleaches the GFP tags, leaving complexes with a low number of functional tags. (**b**) Intensity histograms are constructed from spots recorded directly after the recovery period and (**c**) after the photobleaching pulse. (**d**, **e**) Fitting the histograms with common intensity levels yields the number of functional GFP tags

acquired showed the highest average intensity, and the distribution for the last acquired period after the photobleaching pulse had the lowest. The histograms were then fitted with the sums of normal distributions around distinct intensity levels that

reflected different numbers of fluorescent GFP tags in the Orai complex (Fig. 5b, c). The assumption of four intensity levels best matched the measured distributions, given the expectations that intensity levels should be almost equidistant and their half-widths should follow a square-root function. The fitted weights in fact yielded histograms that displayed binomial distributions (Fig. 5d, e). The intensity histogram and the changes in the distributions due to photobleaching strongly suggest a tetrameric assembly of Orai under the conditions used. This work effectively demonstrated that intensity histogram analysis with subsequent photobleaching can be used to reveal the multimerization state of a GFP-tagged protein, even when diffusion in the cell membrane prohibits the detection of defined bleaching steps.

A very different approach based on the analysis of the intensity histogram was devised by Mark Leake and coworkers [36, 37]. The goal here was to determine the stoichiometry of the components in the DNA replication machinery of the bacterium *Escherichia coli* (Fig. 6a). In contrast to the proteins discussed above, the

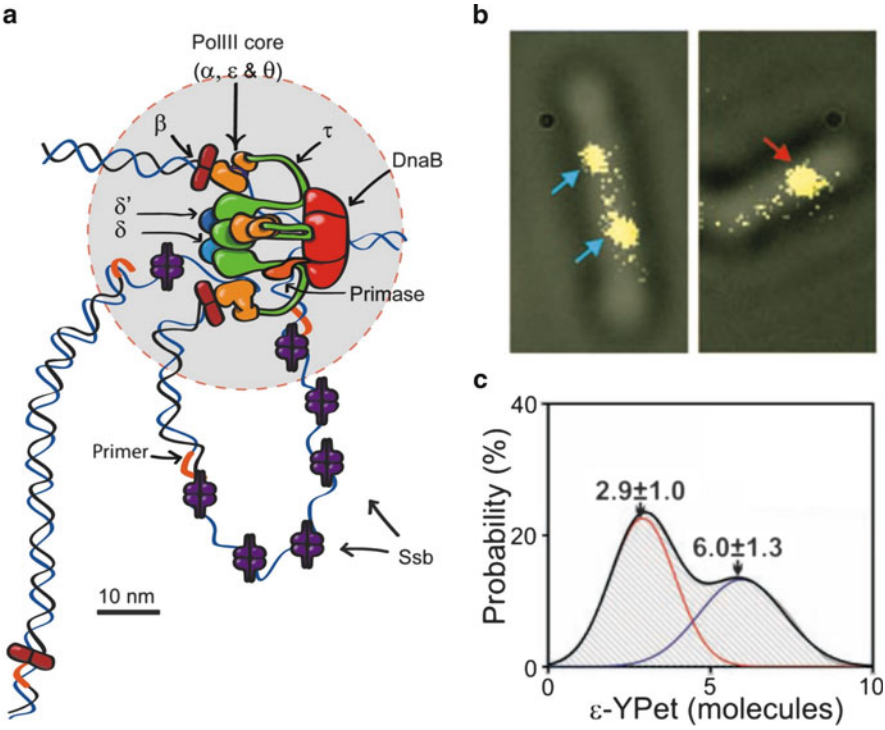

Fig. 6 Subunit composition of the DNA replication machinery (adapted from Reyes-Lamothe et al. [36]). (**a**) Arrangement of Pol III core as deduced by subunit counting. (**b**) DIC image of *E. coli* bacteria carrying YPet-labeled Pol III ε subunits overlaid with fluorescence images, showing two separated fluorescent spots or one central spot containing both replication forks. (**c**) Intensity histogram (*gray shaded*) obtained from ε-YPet strain (the *x*-axis is normalized to the fluorescence of a single YPet molecule). The fit with two Gaussians for three (*red*) and six (*blue*) ε-YPet molecules suggests that there are three ε subunits in the Pol III core

replication machinery is composed of complexes of more than ten cytoplasmic components and displays only slow diffusion due to its large size and association with the chromosomal DNA. Although more copies of the proteins of interest may be present in a cell, only those participating in DNA replication are localized to the complex and therefore visible as an immobile spot when tagged with an FP, whereas emission from the remaining fraction, rapidly diffusing in the cytoplasm, is blurred over the whole cell. Each cell contains a maximum of only two replication machinery complexes; therefore, either two fluorescent spots are observed when the two replication forks are separated by more than approximately 200 nm, or there is only one spot when the two forks are too close to be resolved optically (Fig. 6b).

To determine the copy numbers of the different proteins participating in the replication machinery, each subunit was individually tagged with the yellow fluorescent protein YPet and used to construct a unique bacterial strain with the corresponding gene replaced with its tagged version. The effect of slow diffusion was eliminated by reducing the total imaging time to 90 ms using high laser power density. A high frame rate of >300 fps was achieved with a low-resolution (128 × 128 pixels) EMCCD camera, allowing for faster acquisition than the more popular 512 × 512-pixel cameras. For each acquisition, only a single *E. coli* cell was illuminated with a laser focused onto a small spot (with a 7 μm half-width) in epifluorescence configuration. Initial emission intensities were estimated from exponential fits to the photobleaching curves of individual spots, and intensity histograms were constructed from up to 50 acquisitions for each of the labeled replication-fork proteins. Gaussian fits to the histograms revealed bimodal distributions, with the higher-intensity peak originating from cells with only one fluorescent spot containing two replication forks and the lower-intensity peak reflecting bacteria with two spots, each containing one fork (Fig. 6b, c). The intensity of a single YPet molecule was determined by a Fourier spectral approach that the authors had developed previously for a similar work on the bacterial flagellar motor [37]. By comparison of the intensities, the authors deduced the multiplicity of each of the replication fork components. It is remarkable that the fraction of nonfluorescent YPet molecules in the *E. coli* expression system appeared to be very low, as no additional peaks corresponding to submaximal bleaching step numbers were observed.

The last example shows that it is possible to deduce the composition of a multiple-protein complex by counting the number of each subunit type individually while keeping all other parts of the complex unlabeled. This is only possible when the stoichiometry is fixed. If subpopulations of different stoichiometries are present, the use of multiple colors is an advantage.

4.3 Colocalization of Multiple Colors

When the proteins of interest can assemble in variable stoichiometries, two or more subpopulations of complexes will appear, and it becomes difficult to decipher their

assembly patterns using only one type of fluorescent tag. If two or more tags are available, the different subpopulations can more easily be discriminated based on the presence, number of bleaching steps, or differential emission intensity of the tags. Additionally, the use of multiple colors facilitates the characterization of a purely homogeneous population of protein complexes (Fig. 1a).

Obviously, a requisite condition for the analysis of interactions by the colocalization of two colors is a high probability that both tags are functional or, when using organic dyes, that the proteins of interest are all labeled. Nonspecific labeling of other proteins and dye binding to the coverslip and the membrane must also be minimized. Unfortunately, to date, it has only been possible to utilize FPs in the green/yellow range for counting bleaching steps because red FPs photobleach too quickly and are also less likely to be functional. Because green and yellow fluorophores are spectrally too similar to be separated in dual-color single-molecule imaging, colocalization with the simultaneous counting of subunit numbers for both components is not possible using only these tags. However, subunit counting of a GFP-labeled protein and colocalization with a red-labeled protein (without counting subunits) can be realized.

4.3.1 Example

Using the same microscope setup as described above for subunit counting with GFP-labeled, immobilized membrane proteins in *Xenopus* oocytes, we modified the subunit-counting technique to colocalize green- and red-labeled subunits of the NMDA receptor to elucidate its assembly [38]. The classical NMDA receptor consists of NR1 and NR2 subunits with a fixed 2:2 stoichiometry. Similarly, the NR3 subunit assembles with NR1 in an obligatory 2:2 composition. However, it remained unclear whether NR1, NR2, and NR3 follow a stoichiometric, random or exclusive assembly pattern when coexpressed (see Fig. 7a).

In pilot experiments, we discovered that the probability of fluorescence and the total number of photons emitted before photobleaching were significantly lower for red fluorescent proteins than for GFP, yielding reduced colocalization of green and red fluorescence. Therefore, we used the orange-red FP Tomato to construct a tandem tetrameric tag (ttTomato), which we estimated has a probability of approximately 80% of carrying at least one functional FP (Fig. 7b). With the NR1:NR3 receptor serving as a reference for an obligatory heteromer, we validated the colocalization approach by coexpressing NR1-ttTomato and NR3-mEGFP, resulting in a nearly complete overlap of red and green fluorescence (Fig. 7c, left). To determine whether NR2 and NR3 coassemble with NR1 within the same receptor, we coexpressed unlabeled NR1 with NR2-mEGFP and NR3-ttTomato. Very little overlap of red and green fluorescence was observed, suggesting that NR2 and NR3 do not assemble into the same receptor but rather form separate populations of NR1:NR2-mEGFP and NR1:NR3-ttTomato (Fig. 7c, right).

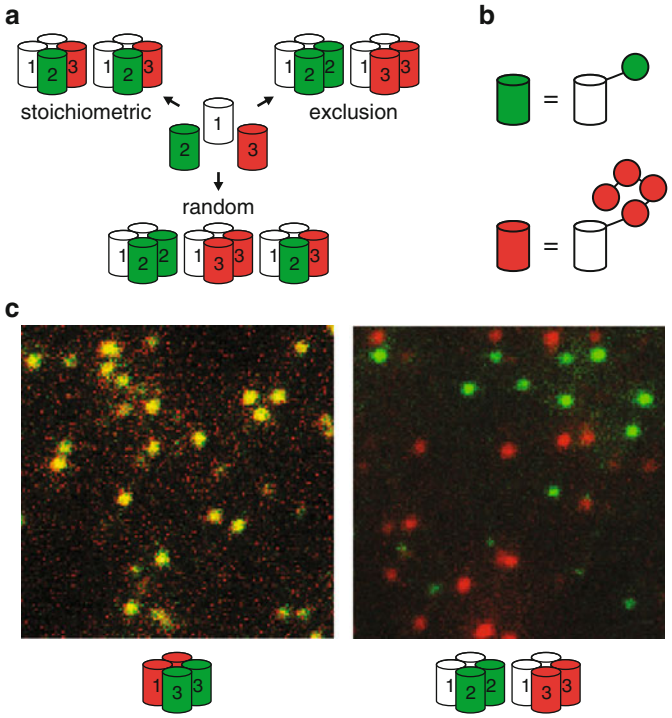

Fig. 7 Colocalization of *red* and *green* FP labeled NMDA receptor subunits, as described in Ulbrich and Isacoff [38]. (**a**) Stoichiometric, random, and exclusive assembly rules for NR2 and NR3 with two obligatory NR1 subunits would result in different degrees of *red*/*green* fluorescence overlap. (**b**) For *green* fluorescence, a C-terminal GFP tag was used; for *red* fluorescence, a tandem tetrameric Tomato (ttTomato) tag was used to maximize the probability that at least one FP was functional. (**c**) Obligatory assembly of the NR1-ttTomato:NR3-GFP subunit combination yielded almost complete overlap (*left*). NR1/NR2-GFP/NR3-ttTomato coexpression yielded either *red* or *green* but no yellow spots, indicating an exclusion rule

5 Caveats

Before choosing a strategy and an expression system for single-molecule subunit counting with a given protein, a few important factors should be considered to minimize the chances of obtaining disappointing or incorrect results.

5.1 Expression Systems

In the studies to date, *Xenopus* oocytes, mammalian cell lines, and *E. coli* bacteria have been used for subunit counting; each presents advantages and disadvantages. *Xenopus* oocytes allow for the simultaneous expression of multiple proteins over a

wide range of densities because expression levels can be individually adjusted for each protein by changing the concentration of injected RNA. In contrast, the expression of multiple proteins in mammalian cell lines at defined concentrations is more difficult because transient DNA transfections usually result in widely varying expression levels. To obtain reproducible protein densities, the time-consuming generation of stably transfected cell lines may be necessary.

A disadvantage of *Xenopus* oocytes is the complex topology of the plasma membrane, displaying many small membrane projections called microvilli; at 1–2-μm long and 200-nm wide, these projections force membrane proteins to follow complex paths in all dimensions during diffusion. Due to the exponentially decaying excitation light intensity in TIR microscopy and the small focal range of only $\approx$ 100 nm when using high-NA objectives, the emission intensities of the fluorescent tags vary rapidly and continuously unless the proteins are immobilized. During the course of our studies, we found that some proteins are naturally immobile in *Xenopus* oocytes (e.g., NMDA and AMPA receptors and CNG and K^+ channels), whereas others display high mobility (e.g., TARPs, some GPCRs, Ci-VSP, and Hv1).

In the case of diffusing membrane proteins, or when transient protein interactions are being studied, mammalian cell lines may be the better choice because their membranes are flat and maintain a constant distance from the coverslip across the attached area of the cell, yielding long, continuous traces. We found that many proteins that remain immobile in *Xenopus* oocytes move by diffusion in the membranes of mammalian cells. Unfortunately, with diffusing proteins, it is impossible to directly observe the bleaching steps for a sufficiently large fraction of molecules so as to enable a reliable statistical analysis, as described in Sect. 4.1. In this case, the more complicated approach of intensity distribution analysis must be employed (see Sect. 4.2).

So far, the *E. coli* system has only been used for the analysis of larger protein assemblies such as the flagellar motor or the DNA replisome, which are specific to this organism. It remains an open question whether single-molecule subunit counting is feasible or even possible in *E. coli* cells for exogenous membrane proteins such as eukaryotic ion channels.

5.2 Choice of Fluorophore

In the studies discussed above and in other subunit-counting work, only GFP-/YFP-based tags or bright organic fluorophores such as the Cy dyes have been used. In preliminary testing, we evaluated several other orange- and red-shifted fluorescent proteins that proved to be inferior in several ways to FPs in the green/yellow range. A major shortcoming of these FPs is their low probability of forming functional fluorophores, in the range of 30% for some red FPs. Thus, even small numbers of subunits cannot be counted reliably. Furthermore, the total number of emitted photons before photobleaching is smaller for FPs in the orange/red range than for

GFP or YFP, making the counting of bleaching steps difficult. Therefore, we only used orange/red FPs for certain purposes in which the low fraction of functional tags and fast photobleaching was acceptable, e.g., for labeling a tetrameric channel while counting the number of auxiliary subunits. We recommend using FPs in the green/yellow range; where two or more different colors are needed, multiple experiments can be performed in which the colors are swapped.

5.3 *Endogenous Unlabeled Protein*

All cell membranes contain proteins that typically constitute as much as 50% of the total membrane area. When a protein of interest is endogenously expressed by the selected cell type, it may outnumber the exogenously expressed, fluorescently labeled protein by a large factor in a single-molecule experiment, and the tagged subunits may coassemble with the excess untagged molecules. When the multimerization state is then assessed by counting bleaching steps or measuring the intensity of fluorescent complexes, the protein may be mistaken for a monomer despite its actual oligomeric assembly. Interference by endogenous unlabeled protein can be avoided by choosing a cell type that does not express the protein of interest endogenously, by suppressing endogenous expression (e.g., using knockout strains or RNA silencing) or by thinning out clusters while conserving the stoichiometry of labeling (TOCSSL), as described in Sect. 4.2 [35, 39, 40].

5.4 *Contamination with Unbound Dye, Nonspecific Labeling, and Dirt*

The low density of fluorescent tags necessary for the subunit-counting approach, typically 1–10 tags/μm^2, requires an even lower density of unwanted background labels. Here, there are three primary sources of contamination: fluorescent particles on the coverslip that were present before the experiment, either from the production process, cell culture, or earlier experiments; unbound fluorescent molecules that diffuse in the solution and bind to the coverslip or the cell membrane; and nonspecific labeling when working with organic dyes.

An effective measure to reduce contamination from glassware is the repeated use of the same tools with careful washing before and after each experiment. The mixing of chambers and tools used for organic dye labeling and FP experiments can also cause cross-contamination. When working with *Xenopus* oocytes, care should be taken to keep the plasma membrane of the cells completely intact because the leakage of intracellular organelles carrying tagged proteins into the extracellular

solution distorts the measured distributions. In general, clean working conditions are absolutely necessary to avoid contamination with unwanted fluorescent debris.

6 Outlook

We presented several examples demonstrating how the subunit content and stoichiometry of multimeric protein complexes can be determined either by counting bleaching steps from the onset of illumination to the fully bleached state or, if the fluorescence traces recorded from individual protein complexes are too noisy or too short, by fitting the intensity histogram of many observed fluorescent spots using multiple, equally spaced Gaussians. The colocalization of several colors can provide additional information on more complex assembly patterns.

Limitations on the maximum number of subunits that can be reliably counted, and on the complexity of heteromeric proteins that can be analyzed in this way are imposed by the fraction of subunits that do not carry a functional, i.e., fluorescent, tag, and by the average number of photons a single fluorophore emits before photobleaching occurs. To date, few researchers reporting the development of novel fluorophores have measured their single-molecule properties, perhaps because no high-throughput assay has been available. However, studies comparing the fluorescence probabilities of existing green/yellow FPs and those exploring alternative red FPs suitable for single-molecule subunit counting are in progress.

The potential of organic dyes for quantitative single-molecule studies could be better realized by the optimization of protocols for labeling proteins in living cells. For this purpose, enzymatic labeling approaches, e.g., the SNAP-tag, HALO-tag, and the biotin ligase systems, offer high efficiency and specificity [41–43]. Other designs could involve fluorogen-activating proteins or the incorporation of fluorescent unnatural amino acids into the proteins [44, 45].

Unfortunately, the power densities supplied by today's commercially available TIRF illuminators are too low (by a factor of 10–100) for the observation of single molecules with low noise and their bleaching within 30 s or less. Application of the single-molecule subunit-counting technique is therefore restricted to microscopes with custom-built TIRF illuminators that achieve a high power density at the sample by reducing the illuminated area while keeping the total beam power constant, as described in Sect. 3. Hopefully, microscopy companies will soon market this type of TIRF illuminator and so enable scientists in many more laboratories to take advantage of these single-molecule techniques.

The engineering of new fluorescent proteins and organic dyes has continually produced new fluorophores with brighter and more photostable emission. With labels in multiple wavelength ranges, it will soon be possible to quickly analyze complex protein interactions and determine a protein's multimerization state with high fidelity. Brighter fluorophores will also enable the development of easier assays that can be applied by scientists not experienced in microscopy or that can

even be automated and will help further advance single-molecule techniques into live-cell applications.

References

1. Fletcher DA, Mullins D (2010) Cell mechanics and the cytoskeleton. Nature 463:485–492
2. Vale RD (2003) The molecular motor toolbox for intracellular transport. Cell 112:467–480
3. Rux JJ, Burnett RM (1998) Spherical viruses. Curr Opin Struct Biol 8:142–149
4. Strauss JH, Strauss EG (2001) Virus evolution: how does an enveloped virus make a regular structure? Cell 105:5–8
5. Cooper E, Couturier S, Ballivet M (1991) Pentameric structure and subunit stoichiometry of a neuronal nicotinic acetylcholine receptor. Nature 350:235–238
6. MacKinnon R (1991) Determination of the subunit stoichiometry of a voltage-activated potassium channel. Nature 350:232–235
7. Nicke A, Baumert HG, Rettinger J, Eichele A, Lambrecht G, Mutschler E, Schmalzing G (1998) $P2X_1$ and $P2X_3$ receptors form stable trimers: a novel structural motif of ligand-gated ion channels. EMBO J 17:3016–3028
8. Stauffer KA, Kumar NM, Gilula NB, Unwin N (1991) Isolation and purification of gap junction channels. J Cell Biol 115:141–150
9. Laube B, Kuhse J, Betz H (1998) Evidence for a tetrameric structure of recombinant NMDA receptors. J Neurosci 18:2954–2961
10. Bianchet M, Ysern X, Hullihen J, Pedersen PL, Amzel LM (1991) Mitochondrial ATP synthase – a quaternary structure of the F1 moiety at 3.6 Å determined by X-ray-diffraction analysis. J Biol Chem 266:21197–21201
11. Stahlberg H, Muller DJ, Suda K, Fotiadis D, Engel A, Meier T, Matthey U, Dimroth P (2001) Bacterial Na^+-ATP synthase has an undecameric rotor. EMBO Rep 2:229–233
12. Sowa Y, Berry RM (2008) Bacterial flagellar motor. Q Rev Biophys 41:103–132
13. Patel SS, Picha KM (2000) Structure and function of hexameric helicases. Annu Rev Biochem 69:651–697
14. Rao VB, Feiss M (2008) The bacteriophage DNA packaging motor. Annu Rev Genet 42: 647–681
15. Chapman ER (2002) Synaptotagmin: a Ca^{2+} sensor that triggers exocytosis? Nat Rev Mol Cell Biol 3:498–508
16. Johnson A, O'Donnell M (2005) Cellular DNA replicases: Components and dynamics at the replication fork. Annu Rev Biochem 74:283–315
17. Suntharalingam M, Wente SR (2003) Peering through the pore: nuclear pore complex structure, assembly, and function. Dev Cell 4:775–789
18. Hoeflich KP, Ikura M (2002) Calmodulin in action: diversity in target recognition and activation mechanisms. Cell 108:739–742
19. Nakajo K, Ulbrich MH, Kubo Y, Isacoff EY (2010) Stoichiometry of the KCNQ1-KCNE1 ion channel complex. Proc Natl Acad Sci USA 107:18862–18867
20. Moerner WE, Fromm DP (2003) Methods of single-molecule fluorescence spectroscopy and microscopy. Rev Sci Instrum 74:3597–3619
21. Jain A, Liu RJ, Ramani B, Arauz E, Ishitsuka Y, Ragunathan K, Park J, Chen J, Xiang YK, Ha T (2011) Probing cellular protein complexes using single-molecule pull-down. Nature 473:484–488
22. Jiang Y, Douglas NR, Conley NR, Miller EJ, Frydman J, Moerner WE (2011) Sensing cooperativity in ATP hydrolysis for single multisubunit enzymes in solution. Proc Natl Acad Sci USA 108:16962–16967

23. Das SK, Darshi M, Cheley S, Wallace MI, Bayley H (2007) Membrane protein stoichiometry determined from the step-wise photobleaching of dye-labelled subunits. ChemBioChem 8: 994–999
24. Ulbrich MH, Isacoff EY (2007) Subunit counting in membrane-bound proteins. Nat Methods 4:319–321
25. Watkins LP, Yang H (2005) Detection of intensity change points in time-resolved single-molecule measurements. J Phys Chem B 109:617–628
26. Chung SH, Kennedy RA (1991) Forward-backward nonlinear filtering technique for extracting small biological signals from noise. J Neurosci Methods 40:71–86
27. Haggie PM, Verkman AS (2008) Monomeric CFTR in plasma membranes in live cells revealed by single molecule fluorescence imaging. J Biol Chem 283:23510–23513
28. Ji W, Xu PY, Li ZZ, Lu JZ, Liu L, Zhan Y, Chen Y, Hille B, Xu T, Chen LY (2008) Functional stoichiometry of the unitary calcium-release-activated calcium channel. Proc Natl Acad Sci USA 105:13668–13673
29. Kohout SC, Ulbrich MH, Bell SC, Isacoff EY (2008) Subunit organization and functional transitions in Ci-VSP. Nat Struct Mol Biol 15:106–108
30. Penna A, Demuro A, Yeromin AV, Zhang SYL, Safrina O, Parker I, Cahalan MD (2008) The CRAC channel consists of a tetramer formed by Stim-induced dimerization of Orai dimers. Nature 456:116–120
31. Plant LD, Dementieva IS, Kollewe A, Olikara S, Marks JD, Goldstein SAN (2010) One SUMO is sufficient to silence the dimeric potassium channel K2P1. Proc Natl Acad Sci USA 107: 10743–10748
32. Tombola F, Ulbrich MH, Isacoff EY (2008) The voltage-gated proton channel Hv1 has two pores, each controlled by one voltage sensor. Neuron 58:546–556
33. Yu Y, Ulbrich MH, Li MH, Buraei Z, Chen XZ, Ong ACM, Tong L, Isacoff EY, Yang J (2009) Structural and molecular basis of the assembly of the TRPP2/PKD1 complex. Proc Natl Acad Sci USA 106:11558–11563
34. Zhang W, Jiang YX, Wang Q, Ma XY, Xiao ZY, Zuo W, Fang XH, Chen G (2009) Single-molecule imaging reveals transforming growth factor-β-induced type II receptor dimerization. Proc Natl Acad Sci USA 106:15679–15683
35. Madl J, Weghuber J, Fritsch R, Derler I, Fahrner M, Frischauf I, Lackner B, Romanin C, Schütz GJ (2010) Resting state Orai1 diffuses as homotetramer in the plasma membrane of live mammalian cells. J Biol Chem 285:41135–41142
36. Reyes-Lamothe R, Sherratt DJ, Leake MC (2010) Stoichiometry and architecture of active DNA replication machinery in Escherichia coli. Science 328:498–501
37. Leake MC, Chandler JH, Wadhams GH, Bai F, Berry RM, Armitage JP (2006) Stoichiometry and turnover in single, functioning membrane protein complexes. Nature 443:355–358
38. Ulbrich MH, Isacoff EY (2008) Rules of engagement for NMDA receptor subunits. Proc Natl Acad Sci USA 105:14163–14168
39. Moertelmaier M, Brameshuber M, Linimeier M, Schütz GJ, Stockinger H (2005) Thinning out clusters while conserving stoichiometry of labeling. Appl Phys Lett 87:263903
40. Ruprecht V, Brameshuber M, Schütz GJ (2010) Two-color single molecule tracking combined with photobleaching for the detection of rare molecular interactions in fluid biomembranes. Soft Matter 6:568–581
41. Chen I, Howarth M, Lin WY, Ting AY (2005) Site-specific labeling of cell surface proteins with biophysical probes using biotin ligase. Nat Methods 2:99–104
42. Keppler A, Gendreizig S, Gronemeyer T, Pick H, Vogel H, Johnsson K (2003) A general method for the covalent labeling of fusion proteins with small molecules in vivo. Nat Biotechnol 21:86–89
43. Los GV, Encell LP, McDougall MG, Hartzell DD, Karassina N, Zimprich C, Wood MG, Learish R, Ohane RF, Urh M, Simpson D, Mendez J, Zimmerman K, Otto P, Vidugiris G, Zhu J, Darzins A, Klaubert DH, Bulleit RF, Wood KV (2008) HaloTag: a novel protein labeling technology for cell imaging and protein analysis. ACS Chem Biol 3:373–382

44. Pantoja R, Rodriguez EA, Dibas MI, Dougherty DA, Lester HA (2009) Single-molecule imaging of a fluorescent unnatural amino acid incorporated into nicotinic receptors. Biophys J 96:226–237
45. Szent-Gyorgyi C, Schmidt BA, Creeger Y, Fisher GW, Zakel KL, Adler S, Fitzpatrick JAJ, Woolford CA, Yan Q, Vasilev KV, Berget PB, Bruchez MP, Jarvik JW, Waggoner A (2008) Fluorogen-activating single-chain antibodies for imaging cell surface proteins. Nat Biotechnol 26:235–240

In Vivo Tracking of Single Biomolecules: What Trajectories Tell Us About the Acting Forces

Mario Brameshuber and Gerhard J. Schütz

Abstract It would be the dream of many experimental scientists in cell biology to be able to follow the life of a protein molecule over time, to watch its encounters with other proteins, to record its conformational fluctuations, and from that data to understand its functionality. Indeed, technology is now at hand to detect the signal of a single molecule in a live cell context. In particular, researchers have been employing single molecule tracking to recover the forces that act on biomolecules: active transport can be discriminated from free or confined diffusion, and nanoscopic details within the molecular paths can be investigated. In the first part of this chapter, we provide an overview over typical diffusion models for biomolecular motion. Yet, experiment, data analysis, and interpretation are not that simple: trajectories are frequently too short, the data are too noisy, and only a vanishingly small fraction of proteins is actually visible. In the second part of this chapter, we therefore delineate how diffusion models can be implemented for data analysis. As a showcase, we discuss recent single molecule data obtained on Lck, an important kinase in T cell signaling.

Keywords Active transport · Diffusion · Fick's law · Fokker–Planck equation · Lck · Localization precision · Single molecule microscopy · Single molecule tracking

M. Brameshuber and G.J. Schütz (✉)
Institute of Applied Physics, Vienna University of Technology, Wiedner Hauptstraße 8-10, A-1040 Wien, Austria

Biophysics Institute, Johannes Kepler University Linz, Altenbergerstr. 69, A-4040 Linz, Austria
e-mail: schuetz@iap.tuwien.ac.at

P. Tinnefeld et al. (eds.), *Far-Field Optical Nanoscopy*,
Springer Ser Fluoresc (2015) 14: 293–330, DOI 10.1007/4243_2011_38,

Contents

1 Introduction

A biological cell is one of the most fantastic objects a physicist can approach: it is extremely complex, containing more than 100,000 different proteins (including those that are posttranslationally modified), more than 10,000 types of lipids, thousands of microRNAs, not to name all the small molecular weight compounds and ions; it is highly dynamic, with characteristic time constants ranging from microseconds for conformational fluctuations of proteins, up to minutes for gene

expression, migration, or cell division; it is stable and can be grown outside of its physiological environment in the body; and it is of key importance: an understanding of the cell will ultimately lead us toward an understanding of the whole organism.

From the beginning of cell biology, the possibility to visualize structures paved the way for new insights and hypothesis, making microscopy the key technology. The investigated structures were getting smaller and smaller, leading us down to the ultimate limit, the individual molecule. Now, we are not far from being able to determine – at least for a set of a few immobile proteins – the exact position of any molecule within a given cell with nanometer accuracy. We can image stable structures like microtubules or small organelles, we can identify molecular clusters, and we can relate the location of different types of proteins.

1.1 The Alien and the City

Consider – as a metaphor – a city, with thousands of people moving or resting, interacting or staying alone, working or waiting. Consider the impression an alien gets from this city. Being *per se* ignorant, it would not know the function of the city and it wouldn't understand the actions of its inhabitants. What would be the best way to get an understanding of what is going on?

- As a first approach, the alien could take a photograph and determine a map of all the people. It would discriminate areas with high population density from areas with low density. By recording a movie, it will even see changes in the local densities with time. This is the microscopist's approach.
- Secondly, the alien may group the people according to the specific characteristics, for example, their jobs, their hobbies, their clothes, their gender. Each individual may be part of multiple groups, as they are not mutually exclusive. We may call this the molecular biologist's approach.
- Next, the alien may actively interfere with the system. For example, it could selectively remove a specific group of people and watch the consequences on the rest of the system. This would be the geneticist's approach.
- The alien could further disassemble the whole city by removing all buildings, streets, etc., extract all the people and chase them through an obstacle course. Then, it may measure the speed, and it may analyze which people stay together. We may call the alien now a biochemist.
- Having the people now isolated from their native environment, the alien chemist may confront them with various substrates to see whether they get modified by the people, or the alien physicist may try to reconstitute the city from scratch again.

- Finally, the alien could follow each individual person and join him/her through his/her daily life. It will monitor each encounter with other people, measure the consequences, and try to determine the driving forces for all the actions. Our alien acts now as a single molecule researcher.

This is of course by far not a comprehensive list. Optimally, our alien researcher would try to combine all approaches in order to obtain a holistic picture. Going back to the origin of our metaphor – the cell – we would like to argue in the following that the single molecule approach has a high potential for substantial advancements in our understanding of cellular processes.

1.2 How Do We Perceive a Cell?

It is interesting – but not surprising – that the metaphor works: over the hundreds of years, social systems have created the terminologies that are now applied in the natural sciences. Consequentially, we essentially see what we can denominate: trafficking, pathways, transport, and migration are exemplary terms in cell biology. To some extent, we thereby create the image of a cell.

Growing up in stable and structured environments, we tend to get biased toward seeing structures. Indeed, proteins, lipids, and nucleic acids can be assembled in complex stable structures. Such structures have become subject to a plethora of studies, which aim at an understanding of the generation, role, and purpose of the molecular assembly.

Many molecules in a cell, however, become only transiently part of an assembly, which may or may not modulate their functionality. In this case, being part of a specific structure is only one aspect of the description of the molecule, among many others.

1.3 Lck: An Example for the Diversified Life of a Protein

Let us consider as an example Lck, a tyrosine kinase relevant in early T cell signaling [1, 2] (Fig. 1). Lck can be reversibly acylated with palmitic chains on two cysteines, thereby switching between a cytosolic and a membrane-anchored version [3, 4] (*i*). When located on the plasma membrane of a CD4-positive T cell, Lck will associate with the transmembrane protein CD4 [5–10] (*ii*). CD4-binding is crucial for bringing the kinase to its substrate, the T cell receptor [11] (*iii*). In addition, Lck itself can be switched on and off by phosphorylation of two tyrosines [2], which is regulated by the balance of the kinase Csk and the phosphatase CD45 (*iv*). The large ectodomain of CD45 leads to its exclusion from the close contact region between a T cell and an antigen-presenting cell, so that Lck activity ultimately depends on the location within the plasma membrane [12, 13]. Upon T cell activation, Lck associates with lipid nanodomains, so-called rafts [8] (*v*).

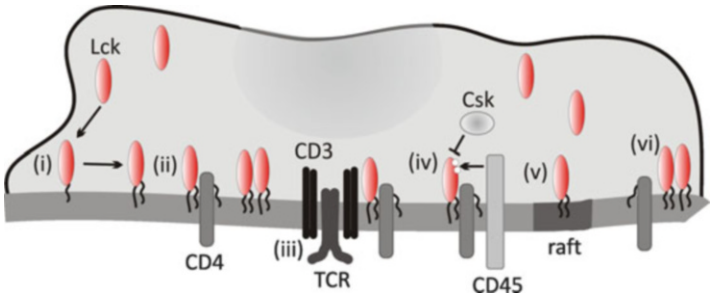

Fig. 1 The diversified life of the tyrosine kinase Lck (*red ellipse*). Upon reversible acylation with palmitic chains *Lck* can switch from a cytosolic to a membrane-anchored form (*i*). If located in the plasma membrane of a CD4-positive T cell, *Lck* will associate with the transmembrane protein *CD4* (*ii*). This binding is the crucial step for bringing the kinase to the T cell receptor (*TCR*), enabling the phosphorylation of tyrosine residues on this substrate (*iii*). The activity of Lck is regulated by phosphorylation of two tyrosines, controlled by the balance of the kinase *Csk* and the phosphatase *CD45* (*iv*). Upon T cell activation *Lck* was described to associate with lipid rafts (*v*). *Lck* can be present in different oligomeric states, e.g. a dimer (*vi*)

Finally, Lck can homodimerize or form even larger oligomeric complexes [10, 14–17] (*vi*).

Note that the described model for Lck function is far from being proven. Nobody has ever observed the sequence of events which leads to the phosphorylation of the T cell receptor. It is the compendium of hundreds of rather indirect studies which indicate that this model may actually be true. The dream experiment would be to follow the Lck molecule over time, watch its encounters with other enzymes that add or remove palmitic acids or phosphate groups, monitor the chemical modifications of Lck, and ultimately detect its function – the phosphorylation of tyrosines on the T cell receptor. We would thus like to track the chemical state over time.

Moreover, chemical modifications and stable interactions will change the affinity of Lck to other structures in the cell. Attraction or repulsion influences the interaction likelihood. Therefore, a comprehensive map of the forces the molecule experiences during its excursions is of key relevance for understanding the regulation mechanisms.

1.4 Forces and Chemistry

Our Lck example can be generalized: a mechanistic understanding of cell biology requires the knowledge of the molecular force fields and chemistry over time. From the forces we can predict the paths; from the chemical state we can predict the function. While the chemical state of a molecule is still difficult to track over time, the force fields are getting accessible.

Which forces act on a biomolecule in a cell?

- Thermal forces. Biomolecules are constantly subject to collisions with each other, which generate a random Brownian motion. Thermal forces are not directional, the energy comes from $k_B T$, where k_B is Boltzmann's constant and T the absolute temperature.
- Electrostatic forces. Many biomolecules are charged and thereby attract or repel each other. Electrostatic interactions are to some extent shielded in the salt solution of a cell.
- Steric hindrance. Biomolecules such as proteins, nucleic acids, or lipids are rather bulky objects that cannot access every point in space due to size exclusion.
- Solubility differences. There are biomolecules with preferential solubility in polar versus nonpolar environments, rendering the molecule attracted to the polar aqueous phase (hydrophilic molecules) or to nonpolar lipid membranes, lipid droplets, or lipoprotein particles (hydrophobic molecules).
- Direct binding. A multitude of protein domains is known, which mediates direct protein interaction.
- Chemical forces. ATP hydrolysis allows for conformational changes that can be translated into directed movements of biomolecules.

1.5 From Single Molecule Trajectories, We Get Insights into Structures Below the Diffraction Limit

Forces generate movements, and objects move because of forces. It is thus plausible to analyze movements in order to study forces. A straightforward approach would be to make use of the random nondirectional collisions exerted onto a diffusing particle by its liquid environment. They generate the Brownian motion, which is the standard mode of locomotion of biomolecules. Additional forces essentially add directionality to the diffusional paths, and modify the overall shape of the trajectories (in the limit of strong friction – which is generally the case in the highly viscous media of a cell – we can neglect acceleration).

Experimental progress in the last years indeed enabled the observation and tracking of single biomolecules in living cells [18, 19]; for a recent review, see [20]. In each image, the position of the biomolecules can be determined to extremely high precision.

While there may be distortions for fixed dipoles, the signal distribution of a freely rotating dye is well approximated by a Gaussian function [21, 22]. Background and readout noise as well as Poisson fluctuations of the signal itself, however, render the determination of the maximum of the Gaussian profile prone to errors. Still, it is possible to determine the position even of a weak emitter like a single dye molecule to an accuracy that is substantially less than the actual signal width [23–25]; for a high signal to noise ratio an impressive subnanometer precision was reported [25].

The positions obtained on consecutive frames can be connected, yielding single molecule trajectories [26–28]: for each trajectory, a data set is obtained with $\{\vec{r}_i\}$ denoting the single molecule positions, and $\{\vec{\sigma}_i\}$ the localization errors; i specifies the frame index.

How can we make use of the trajectories in order to obtain insights into the forces that act on a biomolecule? The answer depends on the acting forces. Think as an example of a cargo that is carried by molecular motors along cytoskeletal filaments. The tight linkage renders diffusion of the cargo negligible, so that the shape of the trajectory resembles precisely the structure of the filament [29, 30]; subdiffraction localization precision can be directly converted into a superresolution image of the transport pathways and structures (Fig. 2).

When diffusion cannot be neglected, the situation gets more complicated. It is very difficult to decide – based on the observation of a single biomolecule – whether a trajectory is the result of pure Brownian motion, or whether additional forces are

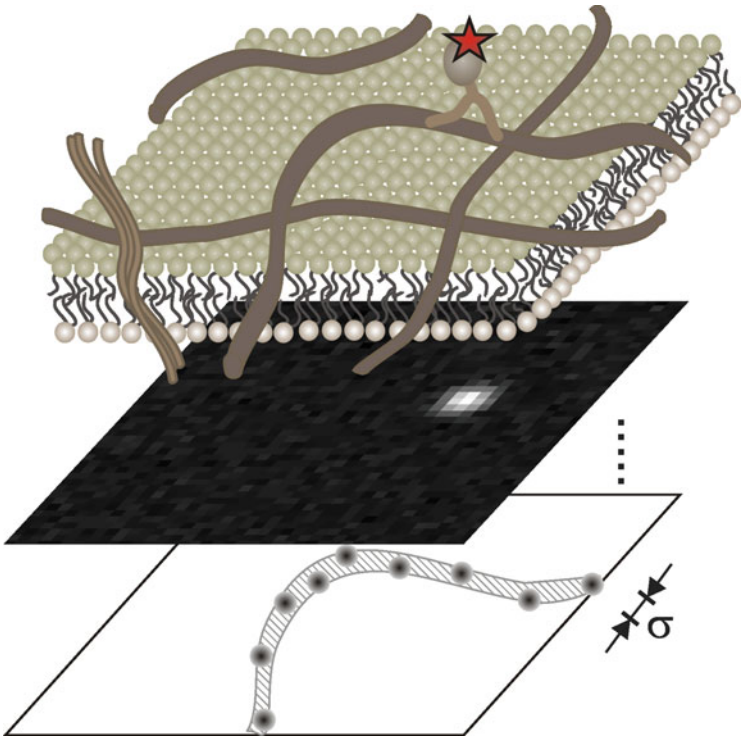

Fig. 2 Single particle trajectories allow for mapping structural elements at superresolution. As an example, molecular motors transport cargo vesicles along cytoskeletal filaments. When imaged onto a CCD chip the position of the fluoresecent marker located on the cargo molecule can be localized down to the subdiffraction localization precision σ. Following the trajectory of the moving molecules by recording a time lapse of images allows for generating a superresolution image of transport pathways and structures

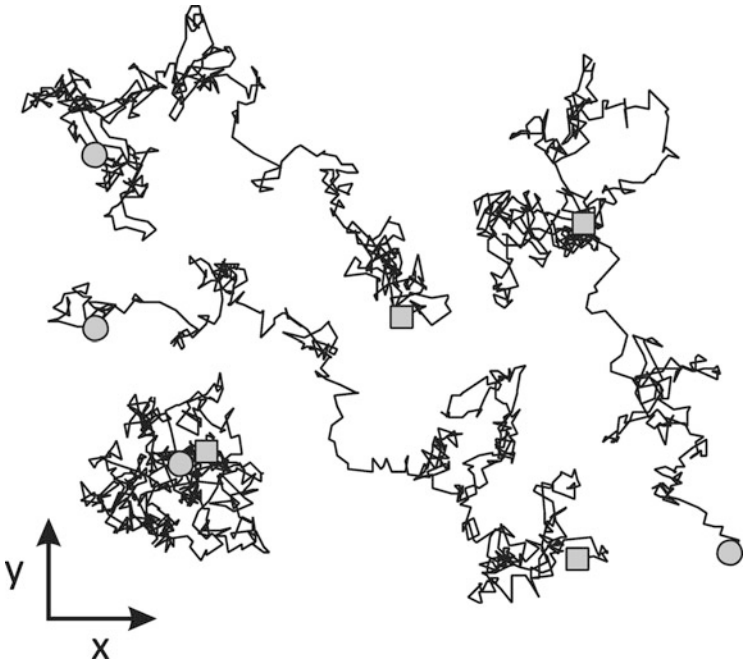

Fig. 3 Typical trajectories are asymmetric. Shown are four randomly simulated trajectories of free diffusion, each consisting of 500 steps. The start (*circle*) and end points (*square*) of the respective trajectories are marked in the image. Only one trajectory has a spherical shape (bottom left), while the others show substantial asymmetry

involved. In a seminal paper, Rudnick and Gaspari characterized the shapes of random walks; they showed that free diffusion results in trajectories that are far from being spherical, but instead show substantial asymmetry [31]. The analysis of large statistical data sets is therefore usually necessary to claim peculiarities in the diffusional motion [32] (Fig. 3).

2 The Diffusing Biomolecule: In Theory

In the following, we give a brief introduction into biomolecular diffusion phenomena. Detailed discussions can be found, e.g., in [26, 33–35]. Let us start by discussing briefly the case of free diffusion.

2.1 Free Diffusion in a Homogeneous Medium

In case of free diffusion, Fick's law relates the time evolution of the probability density of a particle's position $p(\vec{r}, t)$ to its spatial profile.

$$\frac{\mathrm{d}}{\mathrm{d}t}p(\vec{r},t) = D\nabla^2 p(\vec{r},t)$$

with D denoting the diffusion constant. D is connected via the fluctuation–dissipation theorem to the dissipative frictional force the particle would experience if it was dragged through the sample, $D = k_\mathrm{B}Tb$, where b is the mobility defined as the ratio of velocity over frictional force. For a sphere of radius R in a fluid of viscosity μ this relation is well known, $b = (6\pi\mu R)^{-1}$; however, in more complicated environments the situation is less clear. For example, the size dependence of the diffusion constant describing the diffusion of proteins [36–42] and lipids [43–45] in membranes is currently heavily debated. The diffusion of rather small proteins with $R \lesssim 7$ nm has been described by the Saffman–Delbrück theory, yielding $b = \dfrac{\ln(h\mu_\mathrm{m}/R\mu_\mathrm{f}) - \gamma}{4\pi\mu_\mathrm{m}h}$, with h the membrane thickness, $\gamma = 0.5772$ Euler's constant, and μ_m, μ_f the viscosities of the membrane and the surrounding fluid, respectively [37]. For larger proteins, $b \propto 1/R^2$ was found using computer simulations [42], whereas experiments yielded a $1/R$ dependence [36]. Together, it is currently not advisable to try to determine the size of a diffusing object based solely on its mobility.

For a particle diffusing in n dimensions and starting at the origin at time zero, $p(\vec{r}, t = 0) = \delta(\vec{r})$, the solution to Fick's law is given by a Gaussian profile:

$$p(\vec{r},t)\mathrm{d}\,\vec{r} = (4\pi Dt)^{-\frac{n}{2}}\exp\left(-\frac{r^2}{4Dt}\right)\mathrm{d}\,\vec{r}.$$

The maximum of the Gaussian profile does not change with time, so that the average position of the particle remains at the origin: $\langle\vec{r}\rangle = \int_{-\infty}^{\infty}\vec{r}p(\vec{r},t)\mathrm{d}\,\vec{r} = \vec{0}$. The average distance covered by the particle, however, increases with time t according to

$$\langle r^2\rangle = \int_{-\infty}^{\infty} r^2 p(\vec{r},t)\mathrm{d}\,\vec{r} = 2nDt.$$

$\langle r^2\rangle$ is termed mean square displacement (msd). The time-dependence of msd is currently the most commonly used relation for analyzing transport mechanisms by single particle tracking.

2.2 Barriers and Confined Diffusion

In a cell, there may be (im)permeable barriers to the movements of biomolecules. Let us first consider briefly the effect of a single reflecting wall that constrains the motion of the particle in one dimension (without loss of generality denoted x); the wall shall be located at $x = 0$, the particle shall start at time $t = 0$ at position

$x = -x_0$ ($p(x, t = 0) = \delta(x + x_0)$). Then, the probability density function is described by a sum of two Gaussians: the first is equal to the case the wall was not there; the second follows the path of the molecules mirror image:

$$p(x,t)_{\text{imperm}}\mathrm{d}x = (4\pi Dt)^{-\frac{1}{2}}\left[\exp\left(-\frac{(x_0-x)^2}{4Dt}\right)+\exp\left(-\frac{(x_0+x)^2}{4Dt}\right)\right]\mathrm{d}x.$$

In consequence, the tracer's average position gets shifted away from the barrier. Powles et al. generalized the impermeable wall scenario by calculating the effect of a single permeable barrier with permeability P ($P = 0$ denotes the impermeable barrier, $P \to \infty$ the fully permeable barrier) [34]

$$p(x,t)_{\text{perm}} = p(x,t)_{\text{imperm}} - (4\pi Dt)^{-\frac{1}{2}}\int_0^\infty \mathrm{d}x' 2P\exp(-2Px')\exp\left(-\frac{(x_0-x+x')^2}{4Dt}\right)$$

for $x < 0$

and

$$p(x,t)_{\text{perm}} = (4\pi Dt)^{-\frac{1}{2}}\int_0^\infty \mathrm{d}x'\, 2P\exp(-2Px')\exp\left(-\frac{(x_0+x+x')^2}{4Dt}\right) \quad \text{for } x > 0.$$

Barriers may be assembled such that they confine the tracer to a finite space. In biology, this scenario turned out to be interesting, in particular when considering the mobility of a tracer in a membrane [46]. Analytical solutions to $p(\vec{r}, t)\mathrm{d}\vec{r}$, however, are cumbersome: Powles et al. calculated a formula for the probability distribution of a one-dimensional tracer which is confined between two barriers, starting in the center [34], yet it has become more useful to determine the msd: one may consider a square with side-length L, yielding

$$\langle r^2\rangle_{\text{square}} = \frac{L^2}{3} - \frac{32L^2}{\pi^4}\sum_{k=1(\text{odd})}^{\infty}\frac{1}{k^4}\exp[-\left(\frac{k\pi}{L}\right)^2 Dt]$$

[34, 46],

or a circle with radius R, yielding

$$\langle r^2\rangle_{\text{circle}} = R^2\left[1-\exp\left(-\frac{4Dt}{R^2}\right)\right]$$

[32, 35].

We have recently provided an approximation for confined diffusion in a permeable meshwork of squares [47].

$$\langle r^2\rangle_{\text{perm square}} = \alpha\left\{\frac{\alpha L^2}{3} - \frac{32\alpha L^2}{\pi^4}\sum_{k=1(\text{odd})}^{\infty}\frac{1}{k^4}\exp\left[-\frac{(k\pi)^2}{\alpha L^2}Dt\right]\right\} + 4(1-\alpha)Dt.$$

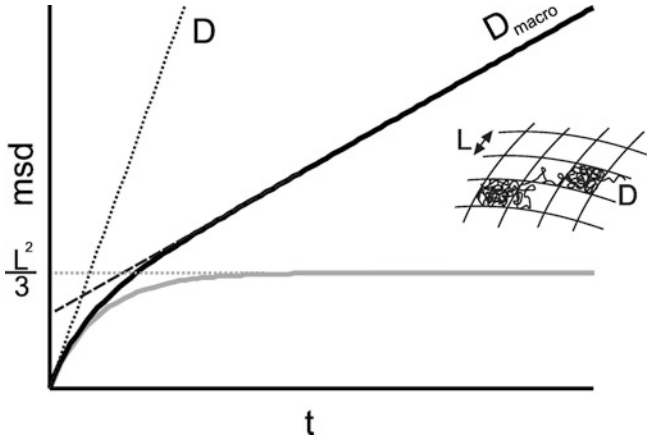

Fig. 4 Confined diffusion. The mean square displacement as a function of time is shown for partially (*black full line*) and fully (*gray line*) confined diffusion. For short times the motion can be described by free diffusion (*black dotted line*), for long times the motion approximates again free diffusion but with a reduced diffusion constant D_{macro} (*black dashed line*). For fully confined diffusion the motion stalls on long time scales and reaches a value given by $L^2/3$ (*gray dotted line*), with L the size of the confinement

On short times, the motion approaches free diffusion with diffusion constant D; on long times, the motion gets again Brownian but with a reduced diffusion constant $D_{\text{macro}} = (1 - \alpha)D$ (Fig. 4).

2.3 Diffusion with External Force Fields

When external potentials V (or force fields $\vec{F} = -\vec{\nabla}V$) are present, Fick's law must be generalized to the Fokker–Planck equation

$$\frac{\mathrm{d}}{\mathrm{d}t}p(\vec{r},t) = \left(\nabla^2 D - \frac{\vec{\nabla}\cdot\vec{F}}{\gamma}\right)p(\vec{r},t),$$

where γ denotes the friction coefficient. For conservative forces (i.e., zero curl $\vec{\nabla}\times\vec{F} = 0$), the system will approach a stationary Boltzmann distribution $p(\vec{r},t) \propto \exp\left(-\frac{V(\vec{r})}{k_B T}\right)$. Jin et al. simulated the impact of various conservative force fields on single particle-tracking data [48], which could be discriminated based on the direct analysis of the probability density function.

Dissipative forces are more difficult to analyze. A special and simple case arises when the external force is exerted by a constant viscous drag $\vec{F} = \gamma\vec{v}$, yielding the Galilei-invariant diffusion–advection equation $\frac{\mathrm{d}}{\mathrm{d}t}p(\vec{r},t) = (\nabla^2 D - \vec{v}\cdot\vec{\nabla})p(\vec{r},t)$, which is solved by

$$p(\vec{r},t)\mathrm{d}\,\vec{r} = (4\pi Dt)^{-\frac{n}{2}} \exp\left(-\frac{(\vec{r}-\vec{v}t)^2}{4Dt}\right)\mathrm{d}\,\vec{r}.$$

Essentially, diffusion and transport are uncoupled. The drift affects both first and second moment of the distribution: $\langle\vec{r}\rangle = \vec{v}t$, and $\langle r^2\rangle = 4Dt + v^2t^2$.

2.4 *Diffusion in a Percolated System*

What would be the effect of excluded volume on the lateral mobility of a tracer? In a series of papers, Michael Saxton calculated the influence of mobile or immobile obstacles on the two-dimensional diffusion behavior of a random walker [32, 49–51]. Essentially, mobile obstacles reduce the lateral diffusion constant without further affecting the mode of motion [49, 50]. However, obstacles may also be immobile or diffuse much slower than the tracer. With increasing density of immobile obstacles the diffusional space becomes increasingly fragmented into separated vacancies containing the tracer, which can be well described by percolation theory [49, 50]. In this case, long-range diffusion is hindered, and the mean square displacement scales with a fractional power of time $\langle r^2\rangle \propto t^{\alpha}$, with $\alpha < 1$; the phenomenon was termed anomalous subdiffusion. In obstructed space, the coefficient α depends on the obstacle density and the tracer size [50].

3 The Diffusing Biomolecule: In Practice

Since the 1980s, single particle or single molecule tracking have enjoyed increasing popularity among bioscientists for studying biomolecular diffusion. Upon labeling with a fluorescent or light-scattering particle, the biomolecule of interest gets detectable and can be followed in time (for reviews see, e.g., [26, 35, 52, 53]). In this section, we discuss practical issues a researcher may encounter when studying two-dimensional biomolecular diffusion.

3.1 *Localization Errors Increase the MSD*

In practice, a fluorescent dye cannot be located to infinite accuracy; thus, the shape of trajectories gets distorted. From the errors in localizing the molecule in x and y direction, σ_{xy}, we can calculate the average virtual distance of the detected from the real position, $\sigma = \frac{\sigma_{xy}}{\sqrt{2}}$. If the localization errors follow a normal distribution, the influence on the obtained diffusion data is as if they originated from a time-independent additional movement:

$$p(\vec{r},t)\mathrm{d}\,\vec{r} = (4\pi Dt)^{-\frac{n}{2}} \exp\left(-\frac{r^2}{4Dt+\Delta}\right)\mathrm{d}\,\vec{r},$$

where $\Delta = 4\sigma_{xy}^2$ specifies the effect of the localization errors [47]. Accordingly, msd increases by a constant offset $\langle r^2\rangle = 4Dt + \Delta$. The reason for the increase can be made intuitively clear. Consider the distance measurement between two points separated by $\sqrt{4Dt}$; for simplicity, the position of the first point is assumed to be known precisely, the second point shall be shifted by a fixed value σ toward an arbitrary direction (specified by polar angle ϑ). Then, the average of the virtual square distance b^2 is given by $b^2 = \langle 4Dt + \sigma^2 + 2\left(\sqrt{4Dt}\right)\sigma\cos\vartheta\rangle_\vartheta = 4Dt + \sigma^2$. If we allow for shifts of the first location as well, we obtain $b^2 = 4Dt + 2\sigma^2 = 4Dt + 4\sigma_{xy}^2$.

The localization errors have to be considered particularly when researchers attempt to infer the mobility from the time dependence of the msd: in this case, finite localization precision may be misinterpreted as indication for anomalous subdiffusion [54]. It should be noted that one may invert the above relation to infer σ_{xy} from the offset of an msd analysis, for example, to get a robust estimate for localization errors in superresolution microscopy.

3.2 *Diffusion During the Illumination Reduces the* MSD

What is actually the position of a moving biomolecule? In practice, the experimentalist applies nonzero integration time in order to obtain sufficient photons from the point emitter for high accuracy localization. Therefore, the recorded signal distribution reflects the path of the molecule during its illumination; the measured position is given by the average position of the molecule during its illumination. In order to reduce this effect, many research groups prefer the usage of stroboscopic illumination, so that the illumination time can be adjusted independently of the delay between two consecutive images.

The effect of finite illumination times t_{ill} on the msd of a freely diffusing particle in 2D has been calculated already 10 years ago in a paper that was hardly noticed by the community [55]. Essentially, the measured msd is reduced according to

$$\langle r^2\rangle = 4Dt - \frac{4}{3}Dt_{\mathrm{ill}}.$$

The reason is intuitively clear: the average position of the tracer is shifted toward the continuation of its path in the next frame, making the distance shorter; in other words, the trajectory appears slightly smoothened.

The effect of finite illumination time gets more pronounced for confined diffusion. The centroids of trajectories with a length comparable to the domain size will not be equally distributed over the domain, but shifted toward the domain center [47, 56, 57]. Therefore, the domain size and the diffusion constant appear reduced.

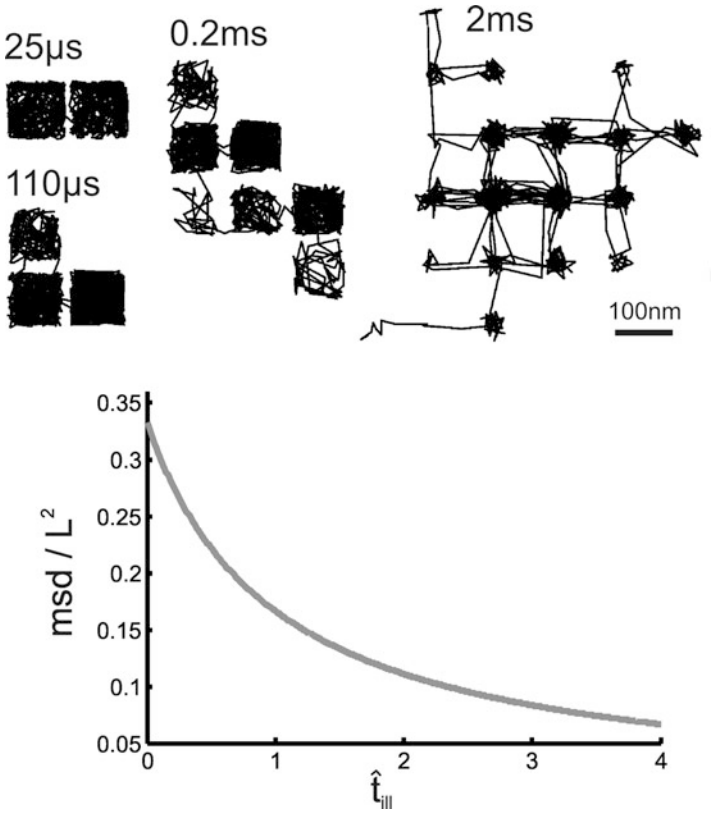

Fig. 5 Illumination time effect. The *upper panel* shows the effect of the illumination time on the apparent confinement size. With increasing time the detected points of the trajectories within a compartment become more centralized due to the averaging during the illumination time. Note that more hops between adjacent compartments can be detected with a higher illumination time (right trajectory), but the size of the confinements are dramatically under-estimated. The *lower panel* shows msd/L^2 as a function of the normalized illumination time. Only for an illumination time of zero the theoretical dependence of the confinement size on the msd, msd $= L^2/3$, can be evaluated (compare Fig. 4). For higher illumination times the correction term $\frac{1}{3}\frac{1}{1+\hat{t}_{\mathrm{ill}}}$ has to be applied (*gray line*). Parts of the figure were reprinted from Ritchie et al. [56], with permission from Elsevier

$$\langle r^2 \rangle_{\text{perm square}} = \alpha \left\{ \frac{\alpha L^2}{3} - \frac{32\alpha L^2}{\pi^4} \sum_{k=1(\text{odd})}^{\infty} \frac{1}{k^4} \exp\left[-\frac{(k\pi)^2}{\alpha L^2} Dt \right] \right\} \frac{1}{1+\hat{t}_{\mathrm{ill}}} + 4(1-\alpha)\, D\left(t - \frac{1}{3} t_{\mathrm{ill}} \right),$$

where $\hat{t}_{\mathrm{ill}} = \frac{4D}{L^2} t_{\mathrm{ill}}$ denotes the illumination time normalized to the transit time of the particle through the domain (Fig. 5).

3.3 Geometry Issues

Analysis and interpretation of probe mobility in membranes typically imply that the probe molecules move in a flat plane. Yet, even on a model membrane undulations or fluctuations on a length scale close to the localization precision can be absolutely expected. In a cell membrane, the probe molecule may well enter even more complex, highly curved three-dimensional structures such as caveolae, clathrin-coated pits, or membrane tubules. Rugged topology may affect the analysis of mobility and association state [58].

In case of mobility analysis, the projection of the movement onto the focal plane is measured. Ruffled surfaces or thermal membrane fluctuations will essentially reduce the effective two-dimensional diffusion constant [58–60]. However, there are membrane systems which deviate more strongly from a flat two-dimensional surface, thereby massively altering the apparent mobility [58]. As an example, we have recently calculated and measured the mobility of membrane proteins diffusing along the circumference of tunneling nanotubules (TNTs) [61], cylindrical structures with a radius $R \sim 130$ nm which interconnect different cells for membrane and organelle exchange [62]. Since the molecules are tied to the cylindrical surface of the TNT, msd for transverse motion saturates at R^2 for long time lags. For short time-lags, the mobility can be approximated by $\langle r^2 \rangle \approx D_\perp t$, concomitant with a reduction of the apparent mobility by a factor of 2.

3.4 Anomalous Subdiffusion

Experimentalists frequently observe diffusion laws that deviate from the linear time dependence of the msd but instead follow a sublinear relation $\langle r^2 \rangle \propto t^\alpha$, with $\alpha < 1$ [63–66]; this behavior has been termed anomalous subdiffusion. Anomalous subdiffusion is a rather descriptive term and does not provide a priori mechanistic information on the diffusion process itself [67]. Various scenarios may result in subdiffusive phenomena:

- Diffusion in a percolated matrix near the percolation threshold [50]
- Rugged topologies which confine the tracer [58]
- Heavy-tailed waiting time distributions on binding sites [67]
- Oligomerization of the tracer to a linear polymer yields anomalous diffusion on short time scales [68]
- Also hop diffusion between slightly different compartments will yield anomalous diffusion [26].

Finally, care should be taken in data interpretation since the label may also affect the measured mobility [69].

4 How to Analyze the Data?

Having collected tens to hundreds of single molecule trajectories, the experimentalist needs to extract the relevant information. It turned out that this challenge is highly nontrivial and resulted in a manifold of proposed methods.

4.1 MSD Analysis

A straightforward way for data analysis is to study the time dependence of the msd. Four major cases can be discriminated (Fig. 6):

- Free diffusion: $\langle r^2 \rangle = 4Dt + \text{offset}$
- Diffusion with flow: $\langle r^2 \rangle = 4Dt + v^2t^2 + \text{offset}$
- Anomalous subdiffusion: $\langle r^2 \rangle = D_\alpha t^\alpha + \text{offset}$
- Immobilization: $\langle r^2 \rangle = \text{offset}$

When plotting $\langle r^2 \rangle$ versus time, the curvature of the data thus provides information on the transport mechanism: positive curvature indicates drift or flow, while free diffusion results in a straight line of nonzero slope; zero slope indicates the immobilization of the particle. Negative curvature, in contrast, may have several reasons (see discussion above for anomalous subdiffusion).

Recently, Tejedor et al. pointed out that analyzing the mean maximal excursion provides better estimates than the msd for the anomalous diffusion exponent [70].

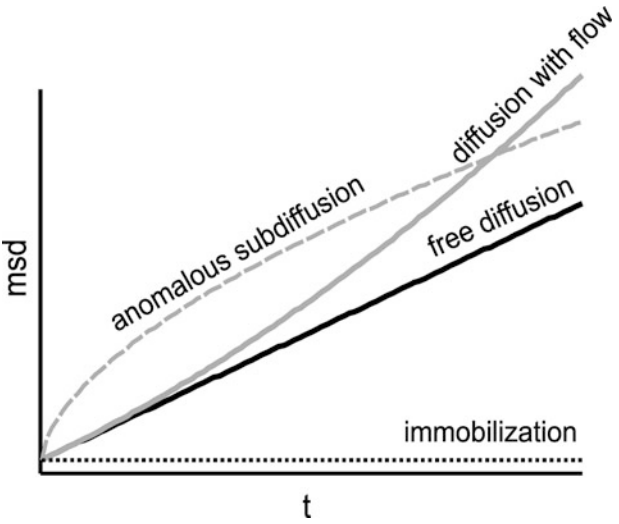

Fig. 6 Time-dependence of the mean square displacement (*msd*). Four characteristic classes of transport mechanisms are shown and can be discriminated by their specific curvature or slope

4.2 Intrinsic Fluctuations in MSD Analysis

The large intrinsic fluctuations in the displacements of a diffusing particle are of interest for an experimentalist. For free diffusion, the standard deviation of r^2 is given by $\sqrt{\langle r^4 - \langle r^2 \rangle^2 \rangle} = \sqrt{2n} \cdot 2Dt$; in two dimensions, the standard deviation of r^2 is thus equal to its mean! That means, when measuring mobilities we need to record large data sets in order to obtain robust results.

A typical single molecule tracking study is based on the measurement of the average square step-size for a given time lag. A single trajectory of length N provides N independent measures of the frame-to-frame square displacement $(\vec{r}_{i+1} - \vec{r}_i)^2{}_{i=0\ldots N-1}$, or in general $N - n + 1$ measures of the distance traveled during n frames $(\vec{r}_{i+n} - \vec{r}_i)^2{}_{i=0\ldots N-n}$. The variable n can be interpreted as dimensionless time-lag. Importantly, in contrast to $n = 1$ the data obtained for $n > 1$ are not independent. Qian et al. [71] calculated the errors in the msd obtained from the trajectory of a single, two-dimensional random walker:

$$\text{var} = \frac{(4Dn\Delta T)^2(2n^2+1)}{3n(N-n+1)}$$

with ΔT the time delay between two consecutive recordings and N the number of steps contained in the trajectory; $n = t_{\text{lag}}/\Delta T$ denotes the time lag in units of frames. The variance significantly exceeds the respective value for independent data, $\text{var} = \frac{(4Dn\Delta T)^2}{(N-n+1)}$. The equation is also well suited for analyzing multiple trajectories in a single msd-plot if N is replaced by $N \cdot \#_{\text{traces}}$, with $\#_{\text{traces}}$ the total number of traces included in the analysis.

We recently discussed the quality of a mobility estimate, based on the analysis of the time dependence of the msd [26]. Interestingly, the best estimate can be achieved when selecting only the first two data points for the fit; including additional data points may seem to improve the fit quality (in particular when the plots are visually inspected), yet the fit converges to the wrong value. This result is a consequence of the fact that the msd values calculated at different time lags are mutually dependent [71]: for example, if the recorded trajectories show by chance a step-size smaller than the expectation value for $n = 1$, the occurrence of a smaller step-size at $n > 1$ will also be more likely. The curves thus appear incorrectly too smooth. The quality of the estimate could be improved only if data from independent experiments would be included. An analogues estimate for single trajectories can be found in a paper by Saxton [72].

4.3 Analysis of the Probability Distributions

Naturally, probability distributions contain substantially more information than the moments. Yet the mathematics becomes typically more involved. We thus discuss here just a few rather simple cases.

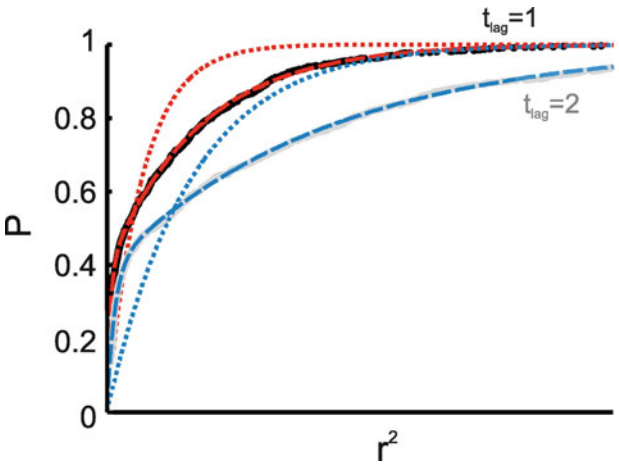

Fig. 7 Step-size distribution analysis. The probability of finding a square displacement smaller than r^2 is plotted for the case of free diffusion. Two different time-lags (*black* and *gray data points*) are included. The fits show clearly that the distributions can only be described by a mix of two different exponential components (*dashed lines*). A mono-exponential fit yields poor results (*dotted lines*). From the bi-exponential fit the two different mobilities and the fractions of the diffusing species can be extracted

Jin et al. analyzed the residual fluctuations of molecules trapped in an attractive potential [48]. Following Boltzmann's distribution, the radial pattern of positions provides information on the confining potential via $p(r) = p(0)\exp(-\frac{V(r)}{k_B T})$.

Multiple diffusing fractions can be discriminated by analyzing the step-size distribution [73]. Assuming pure Brownian motion, the probability of finding a square displacement smaller than r^2 is given by $P = 1 - \exp(-\frac{r^2}{4Dt})$. A mixture of two different fractions β with mobility D_1 and D_2 can be identified as different exponential components $P = 1 - \beta \cdot \exp(-\frac{r^2}{r_1^2(t)}) - (1-\beta)\cdot\exp(-\frac{r^2}{r_2^2(t)})$ (Fig. 7). The time dependence of the characteristic decay lengths $r_i(t)$ can then be further analyzed; for example, freely diffusing subfractions would yield $r_i^2(t) = 4D_i t$. This approach has been successfully applied to identify subfractions of distinct mobility in model systems [65, 73] and living cells [74, 75].

The reconstruction of the trajectories is actually not required for the analysis of the square displacements' probability distribution; Semrau et al. have shown that the images containing the single molecule positions can be correlated directly, without the need for single molecule tracking [76]. Their idea was based on image correlation microscopy, but instead of taking the original data for correlation they suggested to use the superresolution images obtained after fitting the particle positions. The cumulative correlation function is then given by $C_{\mathrm{cum}}(r^2, t) = P(r^2, t) + c\pi r^2$, with c denoting the particle concentration. One can thus easily extract the cumulative probability function of the diffusion process from the measured correlation function $P(r^2, t) = C_{\mathrm{cum}}(r^2, t) - c\pi r^2$.

Usually, a closed analytical theory for diffusion is only available for the simplest models; extensions to more realistic scenarios that account for complex diffusion processes or that include experimental constraints are still difficult to tackle. We therefore introduced recently a general method for global analysis of single molecule tracking data for cases where no analytical description of the diffusion process is available [77]. The idea is to simulate the potential outcome of an experiment, Y, on the computer assuming a specific diffusion model, and compare the simulation results with the experimental data X. Quantitative comparison is performed using statistical testing. As an output the test yields the *p*-value, which is a measure of the statistical difference between the two distributions X and Y (Fig. 8).

4.4 Transitions Within Trajectories

A biomolecule will in general encounter transitions between different mobility states. An example could be that a molecule switches between a fast and a slow diffusion state (D_1 versus D_2) with characteristic rate constants k_{12} and k_{21}. Matsuoka et al. provided an interesting framework for identifying such transitions, based on the behavior of the square displacements' autocorrelation [78]; see also [79]. For free diffusion, they calculated

$$\langle x^2(t)x^2(t')\rangle = \begin{cases} 4D^2\Delta t^2, t \neq t' \\ 12D^2\Delta t^2, t = t' \end{cases}$$

which is gives a delta peak at $t - t' = 0$, indicating the absence of correlation. In contrast, if transitions are present in the traces the persistence in one mobility state leads to a smooth (exponential) change of the autocorrelation function

$$\langle x^2(t)x^2(t')\rangle = \begin{cases} f_1 \exp(-k[t - t']) + \text{offset}, t \neq t' \\ f_1 + \text{offset} + f_2, t = t' \end{cases},$$

where f_1, f_2, and *offset* depend on D_1, D_2, k_{12}, and k_{21}; the characteristic time constant of the exponential decay depends on the transition rate constants as $k = k_{12} + k_{21}$.

4.5 Local Analysis

Ideally, researchers would like to spot all encounters that affect the mobility of the tracer, without a priori assumptions. A first attempt for local analysis – i.e. for identifying transient confinements within a single trajectory – was reported by Saxton [32], who calculated the probability for a random walker with mobility

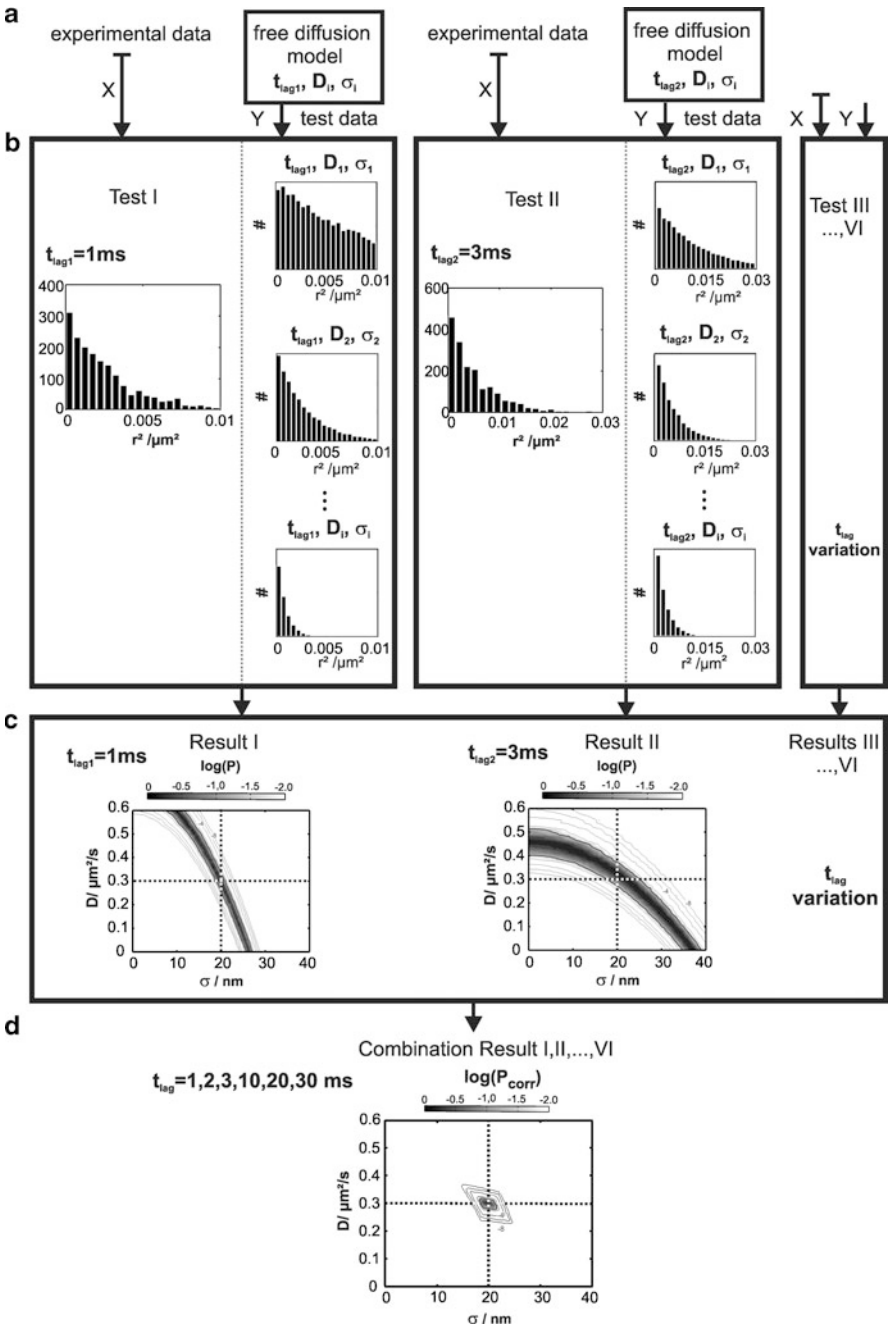

Fig. 8 Tests for free diffusion, performed at different time-lags. (*A*) Two input data sets are required for each time-lag: Firstly, experimental data sets *X*, which were here generated virtually on the computer with a set-point of $D_0 = 0.3\ \mu m^2/s$ and $\sigma_0 = 20$ nm; secondly, probe data sets *Y*,

D to be accidentally confined for a time t within a circle of radius R: $\log \psi = 0.2048 - 2.5117 \frac{Dt}{R^2}$. Simson et al. used this formula to determine probability profiles for transient confinements characterized by the parameter $L = -\log(\psi) - 1$ [80]. Segments within the trajectory above a certain threshold ($L > 3.16$) for a specific minimum duration (typically $t_c = 2.7$s) were classified as confined, the rest of the trajectory as freely diffusing. This strategy has been employed afterward also by other groups [27, 81]. The algorithm is comparably robust against the detection of false positive events, yet confinements are easily missed [82]. More recently, Montiel et al. introduced a test-based approach for identifying transition points between two different diffusion constants [83]. Finally, segmenting the trajectory allows for local msd analysis on each segment to identify, for example, regions of confined diffusion [84].

4.6 Comparing Time and Ensemble Average to Check for Ergodicity

An interesting result was reported recently: when investigating the mobility of the Kv2.1 potassium channel in the live cell plasma membrane, the time average of single molecule square displacements turned out to be substantially different from the ensemble average, indicating nonergodic behavior [66]. Weigel et al. calculated histograms of square displacements in two ways: (1) they determined the average square displacement of each trajectory $\langle r^2 \rangle_{\text{trajectory}}$, and constructed a histogram over all trajectories ("time average"); (2) they determined the average square displacement at each time point $\langle r^2(t) \rangle$, and constructed a histogram over all time points ("ensemble average"). They found that the time average yielded substantially broader histograms than the ensemble average, indicating that there was heterogeneity of the diffusion behavior within the measured population.

4.7 Direct Imaging of Structures by Tracking Multiple Molecules

There may be regions in the cell, in which the mobility of a molecule is slower or faster, in which barriers reflect the molecule, or in which confinements affect the

Fig. 8 (continued) which were simulated at the according experimental t_{lag} in the parameter range D = 0–0.6 μm^2/s, σ=0–40 nm. (*B*) We used multiple experimental data sets *X*, obtained at different time-lags t_{lag}, and compared each with multiple probe data sets *Y*. Two examples for $t_{lag} = 1$ ms and $t_{lag} = 3$ ms are shown. The corresponding test results are plotted as contour graphs in (*C*). (*D*) When combining t_{lag} values for $t_{lag} = 1, 2, 3, 10, 20$, and 30 ms the confidence region gets substantially restricted and the set-point can be precisely extracted. Parts of the figure were reprinted from Wieser et al. [77], with permission from Elsevier

mobility. Using a global analysis, all regions of a cell would be averaged out, thereby losing information on lateral heterogeneities. Local analysis of single trajectories, however, typically does not provide sufficient data to reconstruct a map. Ideally, thousands of trajectories should be recorded and analyzed; the obtained data could then be combined into a spatially resolved map of single molecule motions. If the density of trajectories was high enough, even subdiffraction features could be visualized.

The first experimental realization of this idea was done by live cell photoactivation microscopy combined with single molecule tracking [85]. Serge et al. provided an algorithm for tracking single particles at high density, so that confinement regions could be mapped [27]. In some cases, structures could be even directly observed by overlaying all recorded trajectories. For example, CD36 was found to diffuse freely along linear tracks in the plasma membrane; the linear structures were shown to be created by the cortical cytoskeleton [86]. Similar effects were observed for the diffusion of the Fcε receptor [87].

Still, the challenge of imaging a dynamic object at high spatial resolution tools is huge, as we pointed out in a comment recently [88]. Consider a slowly moving cellular structure described by a diffusion constant of 10^{-3} μm^2/s. For imaging at 200 nm resolution, a total recording time of ~10s is sufficient to virtually freeze the motion of the structure. Resolution of 20 nm – as achievable with single molecule techniques – demands for a recording time of only ~100 ms. This demand is still incommensurable with the overall recording time of tens of seconds required to obtain a single photoactivation microscopy image [89].

5 How Shall the Experiment Be Performed?

5.1 Time Resolution

Cell biology itself defines the requirements for a successful implementation of single molecule microscopy. Active transport in living cells occurs at speeds of several micrometers per second [90]; Brownian motion of cell components ranges from diffusion constants of ~100 μm^2/s for proteins in solution, over ~1 μm^2/s for lipids in lipid bilayers, down to values smaller than 10^{-4} μm^2/s as found for immobilized membrane proteins [35]. In these cases, millisecond time resolution is required for resolving submicrometer displacements.

What would be the consequences of choosing a long illumination time?

- For freely diffusing molecules each image would look blurred, since it contains the average path of the molecule during the illumination. As a rule of thumb, one may claim that the average distance the particle moves during its illumination remains smaller than the diffraction-limited spot size. In two dimensions, this is given by $4Dt_{\mathrm{ill}} \lesssim \left(\frac{0.6\lambda}{NA}\right)^2$. As example, a protein diffusing at $D = 1$ μm^2/s would require illumination times $t_{\mathrm{ill}} \lesssim 15$ms.

- When tracking freely diffusing single molecules, the msd yields a negative offset and the trajectories appear smoothened (see discussion above). The effect scales with $\langle r^2(t=0)\rangle \sim \frac{4}{3} D t_{\mathrm{ill}}$.
- The detected motion of confined molecules is strongly affected, because the detected average path of the trajectory collapses in the domain center (see discussion above). In consequence, the detected domain size in the msd analysis is reduced according to $L \rightarrow \frac{L}{\sqrt{1+\hat{t}_{\mathrm{ill}}}}$, $\hat{t}_{\mathrm{ill}} = \frac{4D}{L^2} t_{\mathrm{ill}}$. Assuming a diffusion constant of $D = 1\ \mu\mathrm{m}^2/\mathrm{s}$ and an actual domain size of 100 nm, illumination for 30 ms would yield an apparent reduction in the domain size by a factor of 3.5!
- Moreover, also the trajectories themselves look different. Hop diffusion between adjacent compartments would appear as jumps between sites of immobilization [56].

There are two main limitations to the obtainable speed of the single molecule imaging system, the camera readout time and the obtainable illumination time:

1. *Camera readout***.** The image quality depends critically on the noise levels of the detector, which are essentially determined by the dark signal and by the readout noise. Dark noise can be eliminated by cooling the chip. Low read-out noise, however, is difficult to achieve and only possible at very low digitization rates (typically 50–100 kHz), rendering such devices rather slow. Still, cooled slow-scan CCD cameras were the first camera-based systems for the detection of single dye molecules [91, 92]. Systems are available with a read-out noise of ~2 electrons per pixel at 50 kHz read-out rate, which is negligible compared to sample background noise.

With low digitization speed below 100 kHz, full-frame read out would require several seconds. Even read out of a subregion of 100 × 100 pixels, sufficient for imaging a single small cell, would take at least 200 ms. Although this time resolution is high enough to observe, e.g., intracellular transport, reorganization processes on a molecular level typically happen on a much faster timescale. In order to resolve such rapid kinetics, some manufacturers offer a special operation mode based on multiple frame transfer. In this mode, only a small subregion of the chip is used for observation. Upon illumination, this subregion is shifted into a masked area of the chip very rapidly, where it is temporarily stored; the readout process is performed subsequently after several illumination/shifting-cycles and independently from this timing protocol.

Continuous rapid imaging has been enabled by the use of image-intensified cameras that operate at ~ MHz digitization speeds, but which have the disadvantages of lower quantum efficiency, worse resolution, and additional spontaneous intensifier noise. Recently introduced electron-multiplying CCD (EM-CCD) cameras make use of on-chip electron amplification before fast read out. A 5 MHz chip may be run at a readout noise of 50 electrons per pixel, thus for typically applied gains G ~ 1,000 this noise term will vanish (effective readout noise $\ll 1e^-$ per pixel), and the device is operated in the shot noise limit. The advantage compared to nonamplified CCDs is the option to run the chip at extremely high frame rates (1,000 frames per second of a 50 × 50 pixel subregion is absolutely possible) and low readout noise.

Note, however, that compared to a slow-scan CCD, the image quality will be slightly deteriorated due to the additional amplification noise.

For single molecule tracking, it is actually not required to record an image on a camera: three pixels were found to be sufficient to determine the position to accuracy of a few nanometers. Sahl et al. used three avalanche photodiodes combined with confocal microscopy to follow the diffusion of fluorescent lipids in the live cell plasma membrane [93]. The three point detectors were arranged such that their projection back into sample space formed a triangle with overlapping point spread functions, which allowed for recording the single molecule transits at extremely fast time resolution below 1 ms.

2. *illumination time***.** On the one hand, many researchers attempt to keep the illumination as short as possible to virtually freeze the motions of the molecule. On the other hand, sufficient photons need to be collected during the illumination time to enable single fluorophore localization at high accuracy. That means, the fluorophore has to be sufficiently bright, and the background signal sufficiently low.

In general, fluorescence brightness can be modeled by assuming a two- or three-level system: the single molecule brightness is then given by $F = \frac{f_\infty t_{ill}}{(1+\frac{I_s}{I})}$, where $f_\infty t_{ill}$ denotes the brightness at infinite excitation intensity I, and I_s the saturation intensity [92, 94]. Ideally, fluorophores should thus be selected which show high photon emission rate f_∞.

In addition, if high power light sources are available a high saturation intensity of the fluorophore may also be exploited for reducing the illumination time. At illumination intensities $I \ll I_s$, we can expect the dye molecule to reside in its ground state at the time that the excitation photon hits the dye. The single molecule brightness is then mainly determined by the absorption properties; it scales linearly with I and t_{ill}. In this regime, a reduction of the illumination time can be exactly compensated by increasing the excitation intensity.

Unfortunately, this strategy does not work for $I \gg I_s$. Since the signal saturates in this regime, a reduction in t_{ill} can only be compensated by increasing the excitation intensity disproportionately. Yet, also unspecific background contributes to the overall signal. Such background signals typically do not show saturation and thus increase linearly with increasing excitation. In consequence, the contrast for single molecule detection decreases with increasing I.

As examples, rhodamine shows a saturation intensity of $I_S \sim 7$ kW/cm^2 [92], Alexa647 a saturation intensity of $I_s \sim 19$ kW/cm^2 [47]. Good organic fluorophores have an excitation rate of ~10^6 s^{-1} at $I = 1$ kW/cm^2.

5.2 *Photobleaching and Blinking*

Ideally, the molecule should not only be observable rapidly but the observation should also persist over long periods of time. Yet, photobleaching limits the amount of excitation/emission cycles of a fluorophore. Metaphorically speaking, there is a global photon budget that cannot be exceeded. One can spend the budget for

generating just a few very bright images, thereby yielding high localization accuracy at the expense of short trajectory lengths or vice versa. Using stroboscopic illumination allows us to extend the time range independent of photobleaching effects. An excellent overview of the literature can be found in Diaspro et al [95]. We will discuss here only briefly some implications for single molecule tracking in live cells.

There is not a single process that accounts for the termination of a dye's fluorescence emission. Chemically, a photobleached fluorophore may have become destroyed (photolysis) or bonded to a nearby molecule. Processes leading to photobleaching may involve the presence of oxygen, and the optical excitation of multiple excited states [96–98].

Consequentially, there are two main routes toward minimizing photobleaching: (1) addition of chemicals. One may use triplet quenchers to reduce the triplet state occupancy, or oxygen scavengers to remove reactive oxygen. Reducing agents, however, are toxic to cells when applied at the required high concentration [95]. (2) reducing the excitation intensity, while keeping the overall dose of light constant. Indeed, the GFP photobleaching rate could be significantly reduced (and the brightness increased) by reducing the excitation intensity [98].

Furthermore, some fluorophores show photoinduced blinking [99]. In the case of GFP, the probability for detecting it in the on-state decreases with increasing excitation intensity: equal on- and off-times were found for intensities around 1.5 kW/cm^2. The dark-state lifetime is independent from the excitation intensity and rather long lived, with typical off-times of ~1.6 s [100]. Photoinduced blinking affects tracking, as it is difficult to re-identify mobile molecules after a dark period (see, e.g., [27]); again, low excitation power keeps the population of the dark state unlikely and thus enhances the trackability. For some fluorophores, permanent photobleaching is preceded by blinking periods [101].

Besides the termination of a trajectory, there may be more detrimental effects on the cell. Heinze et al. have shown for example that protein interactions may be released by photobleaching one of the interaction partners [102].

5.3 Thinning Out the Labeled Species

Although there is hardly any limit to the precision with which we can localize a single molecule [25], the distance to the nearest neighbor molecule still needs to be substantially larger than the width of the point-spread function so that the two molecules can be discriminated and followed in time [27]. Let us assume a protein with a medium expression level of 10^4 copies per cell, and let us consider the situation of a T cell with 5 μm diameter. In this case, on average 130 protein molecules would be located in one μm^2 of the plasma membrane. This is about 1,000-fold too dense for resolving single molecules!

In order to dilute the fluorescent species, researchers frequently photobleach the sample [103], or label [104, 105] or photoactivate [85] only a minor subfraction of

the target molecule. While this approach is fine for single molecule tracking, it prevents the extraction of information such as the oligomeric state of the observed structure; random photobleaching reduces also the number of active dyes per protein cluster, so that information about the stoichiometry is lost.

We have recently devised a new methodology to thin out clusters in biomembranes without altering the stoichiometry of the label (Thinning Out Clusters while Conserving Stoichiometry of Labeling (TOCCSL) [106]). In conjunction with single molecule brightness analysis [107], TOCCSL allows for the quantification of the oligomeric state of mobile membrane constituents at essentially arbitrary expression levels. Figure 9 shows the principle of the method: by photobleaching a small area of the membrane, all fluorophores within this area are switched off while the fluorophores in the remaining regions of the plasma membrane remain active. Thereby, oligomers become either dark or retain their brightness. Brownian motion leads to recovery of the fluorescence signal; at the onset of this recovery process, the individual entities can be resolved as well-separated diffraction-limited signals. The brightness of each signal can be quantified and, upon comparison to the brightness of a single dye molecule, the oligomeric state can be inferred. We have used this method to quantify the homoassociation of fluorescent lipids or proteins [10, 108] in the live cell plasma

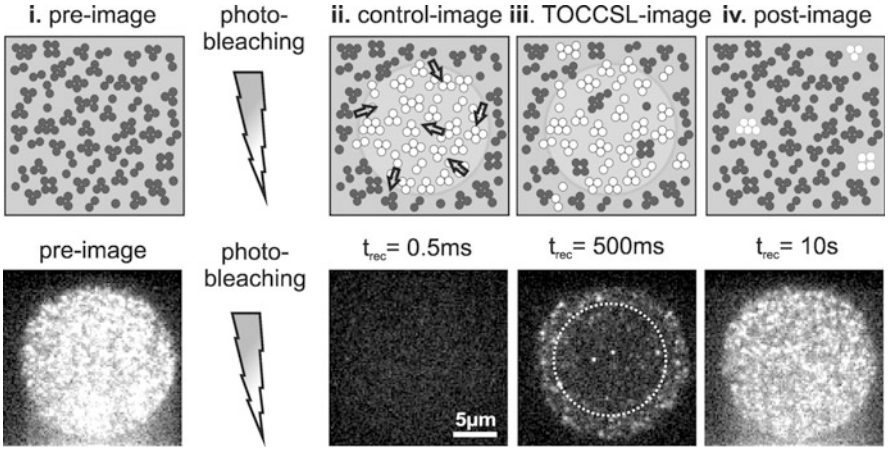

Fig. 9 Principle of TOCCSL. The *top row* presents a sketch of the TOCCSL procedure, the *bottom row* the effect on fluorescently labeled artificial clusters (FITC-labeled antibodies) diffusing freely in a supported lipid bilayer. (*i*) represents the initial situation, where the surface density is too high to resolve single fluorescence-labeled clusters. The analysis region is defined by imaging a round diaphragm onto the object plane. Immediately after photo-bleaching of the analysis region the sample is totally devoid of any fluorescence signal (*ii*). At the onset of the recovery process due to Brownian motion single fluorescein-antibody conjugates can be observed as well separated spots within the analysis region (*iii*). By comparing the brightness of the recovered signals with the brightness of single dye-molecules the degree of clustering can be determined. After a longer recovery time the system reaches the equilibrated state again (*iv*), similar to the pre-bleach image, and the TOCCSL procedure can be repeated. Parts of this figure were reprinted with permission from Moertelmaier et al. [106]. Copyright 2005, American Institute of Physics

membrane, and the oligomeric state of an ion channel [109]. But the approach allows for going beyond pure brightness analysis: when combined with two-color microscopy, complexes can be directly imaged and the distances of the associated molecules can be measured [110].

6 Applications on the Exemplary Case of Lck

We have briefly presented Lck and its eminent role for T cell signaling in the introduction subsection. Substantial insights into the Lck behavior came from different single molecule studies, which shall be discussed in this subsection as exemplary applications of single molecule tracking. We start by giving a brief overview over T cell activation.

6.1 T Cell Activation

The activation of a T cell by an antigen-presenting cell involves the formation of a stable and highly structured interface termed immunological synapse [111–113]. Within the first few minutes upon contact, proteins become segregated into a central cluster (central Supramolecular Activation Cluster, cSMAC) containing for example the T cell receptor (TCR) and a peripheral ring (pSMAC) containing, for example, integrins like LFA-1[111].

The decisive element of T cell activation is the transinteraction of peptide-loaded MHC (pMHC) on an antigen-presenting cell with the TCR on the T cell [114]. This interaction is rather short lived: even strong binders show a lifetime of just a few hundred milliseconds [115]. MHC can further interact with CD4, yet with even lower affinity [116]. CD4 binding does not depend on the presented peptide, and it does not interfere with the pMHC–TCR interaction. Importantly, CD4 is assumed to be stably associated with Lck via a zinc clasp structure [5, 9]. CD4 recruitment to the TCR is thus believed to be central for T cell activation, as it enables the phosphorylation of specific tyrosines – so called immunoreceptor tyrosine-based activation motifs (ITAMs) – on the TCR by Lck [11].

Details of the immune synapse formation were obtained using reconstituted systems, in which the antigen-presenting cell was replaced by either surfaces coated with stimulating antibodies [103, 117, 118], or by fluid-supported lipid bilayers functionalized with stimulating proteins [112]. Although those systems do not represent the in vivo situation of T cell activation, they provide several technological advantages; they are suitable for Total Internal Reflection (TIR) fluorescence microscopy, thereby eliminating intracellular fluorescence background; they allow for specific manipulation and variation of features that may also be expected on the antigen-presenting cell; finally, the two-dimensional interface facilitates single molecule investigations. Using TIR microscopy on reconstituted systems, TCR microclusters were discovered in the synapse. Such microclusters form in the

periphery of the synapse as signaling units and are actively transported to the cSMAC for TCR endocytosis and degradation [119, 120].

6.2 Lck Diffusion Varies Within the T Cell Synapse

Together with many other proteins, cortical filamentous actin was shown to be reorganized during synapse formation [117]; moreover, actin is involved in the transport of the TCR microcluster to the cSMAC [121]. It thus appeared natural to investigate the effect of actin on the mobility of important T cell signaling molecules.

Ike et al. measured the impact of actin reorganization on Lck movements in Jurkat T cells [118]. To activate the T cells, surfaces were coated with fluorescent aggregates of stimulating CD3 antibody, and cells were centrifuged onto the functionalized cover slips; activation sites could thereby be directly visualized. As probe molecules Ike et al. used GFP-fusion constructs of full-length Lck (Lck-GFP), and of the first 10 N-terminal amino-acids of Lck (Lck-N10-GFP); the latter construct contains essentially the membrane-anchoring motif only, and lacks all known protein interaction sites.

In their experiments, single Lck molecules were tracked and the mobility was determined as a function of the position relative to the stimulation site. The effect was quite dramatic: Lck-GFP and Lck-N10-GFP diffusion increased with increasing distance twofold and fourfold, respectively. The effect showed actin dependence: first, actin was concentrated around the activation cluster, as shown by expression of actin-GFP; second, when the actin membrane skeleton was degraded, the mobility of both constructs increased dramatically.

Formally, the results show that D is not constant but a function of the position within the synapse $D \rightarrow D(\vec{r})$. There may be at least two mechanisms that could explain such an effect: (1) The viscosity of the plasma membrane may vary. In particular, if Lck was diffusing as part of nanoscopic platforms, an increased presence of immobile obstacles close to the activation site would reduce the mobility. This mechanism would affect the mobility of both Lck-GFP and Lck-N10-GFP in the same way. (2) the accessible volume close to the plasma membrane may vary. In this case, the effect will depend on the shape and flexibility of the protein, and may well be different for Lck-GFP compared to Lck-N10-GFP.

6.3 Lck Mobility Depends on Protein Clusters in the T Cell Plasma Membrane

A similar study was performed by Douglass and Vale [103]: Jurkat T cells were plated on glass cover slips coated with specific CD3 antibodies (activating surface) or nonspecific IgGs (nonactivating surface). This study focused on the

interaction of Lck with CD2, a coreceptor in T cell signaling. CD2 clustered at the interface with the activating surface, and the clusters remained stable over time. Strong colocalization was observed with the TCR and with Lck-GFP, but not with Lck-N10-GFP. Photobleaching studies were performed to measure the exchange rate within clusters: while the TCR remained stable, there was full recovery of Lck on a seconds time scale, and of CD2 on a minutes time scale.

Using two-color microscopy, the behavior of Lck-GFP and Lck-N10-GFP could be measured relative to the CD2 clusters. Interestingly, the diffusion coefficient of Lck-GFP was significantly reduced inside CD2 clusters compared to outside, whereas Lck-N10-GFP did not show any difference in the mobility. Moreover, Lck-GFP, but not Lck-N10-GFP, was frequently observed to halt transiently at CD2 clusters. The lack of any effect on Lck-N10-GFP indicates that protein interactions are responsible for the transient recruitment of Lck to CD2.

The question remained, by which mechanism the observed CD2 clusters were formed. Douglass and Vale did not observe any influence of actin: CD2 clusters did not colocalize with F-actin, which was located preferentially at the peripheral lamellipodia of the cells. Also degradation of actin had no effect on CD2 clusters once they were formed.

At first glance, the results appear to be inconsistent with the study of Ike et al. discussed above [118]. There are, however, two main differences in the experimental approaches between the two studies: first, Jurkat cells were activated homogeneously (Douglass) or with an antibody cluster (Ike). It may well be that the generation of a single activation site induces stronger structural changes of the membrane skeleton than the rather homogeneous activation. Second, actin was removed after synapse formation (Douglass) or before (Ike). Douglass and Vale used Latrunculin, which binds free actin monomers and thereby hinders the growth of filaments [122, 123]. Preformed filaments, however, may well have lower turnover rates, thus being rather insusceptible to the drug application; it remains questionable whether Latrunculin indeed removed actin from CD2 clusters.

6.4 The Lck Membrane Anchor Shows Predominantly Free Diffusion in the Plasma Membrane

Lommerse et al. studied the mobility of Lck-N10-YFP in 3T3 cells (a mouse fibroblast cell line) [124]. They analyzed the mobility based on the square displacements' cumulative probability, yielding two fractions. The majority of molecules (85%) belonged to the fast fraction, which showed free diffusion. The remaining 15% were classified as "slow"; this population could be best fitted by a confined diffusion model; confinement sizes of $L \sim 200$ nm were estimated.

6.5 Lck Shows Homoassociation

Lck consists of consecutive SH4, SH3, SH2, and tyrosine kinase (SH1) domains, with the N-terminal membrane-proximal SH4 domain being myristoylated and double-palmitoylated. First indications for Lck homo-association arose from crystallographic studies on Lck SH3–SH2 domains, where the SH2 domain of one protein was found to bind to the SH3 domain of the second protein and *vice versa*, creating a "head to tail" interaction of two molecules [14]. Interaction between isolated SH2 and SH3 domains was also shown biochemically [15], and zinc-dependent homodimerization was reported for Lck SH3-domains in solution [16]. Moreover, glutathione S-transferase (GST)-pull down assays revealed association of SH2–SH3 domains with endogenous full-length Lck from Jurkat T cell lysates [17].

In a recent study on interaction mechanisms between CD4 and Lck, we determined Lck–GFP homoassociation in a T24 cell line [10]. We used our TOCCSL method for reducing the surface density of active label without altering the brightness of potential aggregates. Indeed, we found that compared to the distribution of single YFP molecules the histogram of Lck–YFP showed broadening particularly not only toward double fluorescence intensity but also to larger brightness values; analysis of the stoichiometric composition yielded 38 $\pm$ 5% monomers, 45 $\pm$ 7% dimers, and 17 $\pm$ 6% higher order oligomers. Thus, Lck moves preferentially as small associates – monomers, dimers, and higher order oligomers – in the plasma membrane.

6.6 Measuring the Lck Exchange Kinetics Between Cytosol and Plasma Membrane

At the inner leaflet of the plasma membrane there is a continuous exchange of peripheral proteins that interact with lipids, proteins, or insert transiently by reversible acylation/deacylation. Our knowledge on exchange between cytosolic and membrane-associated fractions of proteins, however, is still rather poor, mainly due to difficulties in determining the turnover rates. In particular, detecting the few association events of peripheral proteins with the plasma membrane is difficult, considering the vast excess of proteins already present there.

We used our TOCCSL method to photobleach a small region in the plasma membrane using TIR excitation. Unbleached fluorescent proteins in the cytosol can then rapidly traverse the evanescent field of ~100 nm and enter the analysis region directly from the top, whereas the movement of membrane-bound proteins from the edges takes much longer. After a short recovery time, we recorded single molecule trajectories and determined the diffusion constant, which allowed us to discriminate membrane-inserted proteins from the cytoplasmic pool. This TOCCSL variant was used for studying exchange kinetics of Lck–YFP [4].

With increasing recovery time from 1 ms up to 80 ms we observed an increasing fraction of molecules with lower mobility that matched the diffusion constant of membrane-inserted Lck; apparently, these molecules have inserted into the membrane during the recovery time, most likely via mono- or double-palmitoylation. We estimated an association rate constant of ~2.6 s^{-1}; the reciprocal value of 400 ms can be interpreted as the time a membrane proximal Lck molecule needs to associate with the plasma membrane. From steady-state analysis, we could further estimate the lifetime in the plasma membrane, yielding ~50s. With $D = 0.26\ \mu m^2/s$, this time is sufficient to reach the opposite side of a T cell via Brownian motion before dissociation. Therefore, Lck may shuttle between the plasma membrane and the cytosol. It would be interesting now to study if this shuttling process is linked to the functional state of the kinase.

7 The Next Steps to Do

In summary, the question is not whether we should use single molecule tracking but how we should use it. Even if we accept current technological limitations, a plethora of variants most likely has not even been though about yet. Thus, we are convinced that experimental creativity is the most valuable lab equipment. Still, there are multiple constraints that need to be addressed:

- *The dye*. Current dyes are not good enough. In order to improve time resolution, we need dyes that are brighter and more photostable. Fluorescent proteins suffer from rather poor spectroscopic properties; selecting two different fluorescent proteins for two color microscopy at the single molecule level is barely possible.
- *The detector*. Camera detectors provide photon counts at sufficient quality: (1) nearly every photon is counted; (2) the read-out speed matches the required illumination times for single molecule detection; (3) in live cell experiments, noise is mainly dominated by the fluctuations of the specific signal and the background. A lot of information, however, regarding the arrival time, the color, and the polarization of the photons cannot be recorded.
- *The labeling*. By adding a label, we change the system. GFP is a 27 kD protein containing 238 amino acids, which substantially increases the size of the protein it is fused to. Even more so, we may dramatically change the expression level, the trafficking, and the regulation of posttranslational modifications of the studied protein. Small organic dyes lack the inherent specificity to target the protein of interest. Antibodies allow for highly specific labeling; however, their size of around 150 kD may severely impact the molecular behavior. Also the size of quantum dots may influence the molecular motion of the biomolecule it is linked to [69].
- *The experimental system*. For convenience, most microscopic studies of cells are currently performed on tumor cell lines in buffer at room temperature on glass surfaces. We should approach the physiological situations by studying primary cells in medium at physiological temperature in the physiological matrix.

Acknowledgments This work was supported by the Austrian Science Fund (FWF project Y250-B03) and the GEN-AU project of the Austrian Federal Ministry for Science and Research.

References

1. Davis MM, Krogsgaard M, Huse M, Huppa J, Lillemeier BF, Li QJ (2007) T cells as a self-referential, sensory organ. Annu Rev Immunol 25:681–695
2. Boggon TJ, Eck MJ (2004) Structure and regulation of src family kinases. Oncogene 23(48):7918–7927
3. Kabouridis PS, Magee AI, Ley SC (1997) S-acylation of lck protein tyrosine kinase is essential for its signalling function in t lymphocytes. EMBO J 16(16):4983–4998
4. Zimmermann L, Paster W, Weghuber J, Eckerstorfer P, Stockinger H, Schütz GJ (2010) Direct observation and quantitative analysis of lck-exchange between plasma membrane and cytosol in living t cells. J Biol Chem 285(9):6063–6070
5. Veillette A, Bookman MA, Horak EM, Bolen JB (1988) The cd4 and cd8 t cell surface antigens are associated with the internal membrane tyrosine-protein kinase p56lck. Cell 55 (2):301–308
6. Shaw AS, Chalupny J, Whitney JA, Hammond C, Amrein KE, Kavathas P, Sefton BM, Rose JK (1990) Short related sequences in the cytoplasmic domains of cd4 and cd8 mediate binding to the amino-terminal domain of the p56lck tyrosine protein kinase. Mol Cell Biol 10(5):1853–1862
7. Turner JM, Brodsky MH, Irving BA, Levin SD, Perlmutter RM, Littman DR (1990) Interaction of the unique n-terminal region of tyrosine kinase p56lck with cytoplasmic domains of cd4 and cd8 is mediated by cysteine motifs. Cell 60(5):755–765
8. Filipp D, Leung BL, Zhang J, Veillette A, Julius M (2004) Enrichment of lck in lipid rafts regulates colocalized fyn activation and the initiation of proximal signals through tcr alpha beta. J Immunol 172(7):4266–4274
9. Kim PW, Sun ZY, Blacklow SC, Wagner G, Eck MJ (2003) A zinc clasp structure tethers lck to t cell coreceptors cd4 and cd8. Science 301(5640):1725–1728
10. Schwarzenbacher M, Kaltenbrunner M, Brameshuber M, Hesch C, Paster W, Weghuber J, Heise B, Sonnleitner A, Stockinger H, Schütz GJ (2008) Micropatterning for quantitative analysis of protein-protein interactions in living cells. Nat Methods 5(12):1053–1060
11. Li QJ, Dinner AR, Qi S, Irvine DJ, Huppa JB, Davis MM, Chakraborty AK (2004) Cd4 enhances t cell sensitivity to antigen by coordinating lck accumulation at the immunological synapse. Nat Immunol 5(8):791–799
12. Choudhuri K, Wiseman D, Brown MH, Gould K, van der Merwe PA (2005) T-cell receptor triggering is critically dependent on the dimensions of its peptide-mhc ligand. Nature 436(7050):578–582
13. Irles C, Symons A, Michel F, Bakker TR, van der Merwe PA, Acuto O (2003) Cd45 ectodomain controls interaction with gems and lck activity for optimal tcr signaling. Nat Immunol 4(2):189–197
14. Eck MJ, Atwell SK, Shoelson SE, Harrison SC (1994) Structure of the regulatory domains of the src-family tyrosine kinase lck. Nature 368(6473):764–769
15. Panchamoorthy G, Fukazawa T, Stolz L, Payne G, Reedquist K, Shoelson S, Songyang Z, Cantley L, Walsh C, Band H (1994) Physical and functional interactions between sh2 and sh3 domains of the src family protein tyrosine kinase p59fyn. Mol Cell Biol 14(9):6372–6385
16. Romir J, Lilie H, Egerer-Sieber C, Bauer F, Sticht H, Muller YA (2007) Crystal structure analysis and solution studies of human lck-sh3; zinc-induced homodimerization competes with the binding of proline-rich motifs. J Mol Biol 365(5):1417–1428

17. Lee-Fruman KK, Collins TL, Burakoff SJ (1996) Role of the lck src homology 2 and 3 domains in protein tyrosine phosphorylation. J Biol Chem 271(40):25003–25010
18. Schütz GJ, Kada G, Pastushenko VP, Schindler H (2000) Properties of lipid microdomains in a muscle cell membrane visualized by single molecule microscopy. EMBO J 19(5):892–901
19. Sako Y, Minoghchi S, Yanagida T (2000) Single-molecule imaging of egfr signalling on the surface of living cells. Nat Cell Biol 2(3):168–172
20. Lord SJ, Lee HL, Moerner WE (2010) Single-molecule spectroscopy and imaging of biomolecules in living cells. Anal Chem 82(6):2192–2203
21. Mortensen KI, Churchman LS, Spudich JA, Flyvbjerg H (2010) Optimized localization analysis for single-molecule tracking and super-resolution microscopy. Nat Methods 7(5):377–381
22. Stallinga S, Rieger B (2010) Accuracy of the gaussian point spread function model in 2d localization microscopy. Opt Express 18(24):24461–24476
23. Schmidt T, Schütz GJ, Baumgartner W, Gruber HJ, Schindler H (1996) Imaging of single molecule diffusion. Proc Natl Acad Sci USA 93(7):2926–2929
24. Yildiz A, Forkey JN, McKinney SA, Ha T, Goldman YE, Selvin PR (2003) Myosin v walks hand-over-hand: single fluorophore imaging with 1.5-nm localization. Science 300 (5628):2061–2065
25. Pertsinidis A, Zhang Y, Chu S (2010) Subnanometre single-molecule localization, registration and distance measurements. Nature 466(7306):647–651
26. Wieser S, Schütz GJ (2008) Tracking single molecules in the live cell plasma membrane-do's and don't's. Methods 46(2):131–140
27. Serge A, Bertaux N, Rigneault H, Marguet D (2008) Dynamic multiple-target tracing to probe spatiotemporal cartography of cell membranes. Nat Methods 5(8):687–694
28. Jaqaman K, Loerke D, Mettlen M, Kuwata H, Grinstein S, Schmid SL, Danuser G (2008) Robust single-particle tracking in live-cell time-lapse sequences. Nat Methods 5(8):695–702
29. Schutz GJ, Axmann M, Freudenthaler S, Schindler H, Kandror K, Roder JC, Jeromin A (2004) Visualization of vesicle transport along and between distinct pathways in neurites of living cells. Microsc Res Tech 63(3):159–167
30. Mudrakola HV, Zhang K, Cui B (2009) Optically resolving individual microtubules in live axons. Structure 17(11):1433–1441
31. Rudnick J, Gaspari G (1987) The shapes of random walks. Science 237:384–389
32. Saxton MJ (1993) Lateral diffusion in an archipelago. Single-particle diffusion. Biophys J 64(6):1766–1780
33. Metzler R, Klafter J (2000) The random walk's guide to anomalous diffusion: a fractional dynamics approach. Phys Rep 339(1):1–77
34. Powles JG, Mallett MJD, Rickayzen G, Evans WAB (1992) Exact analytic solutions for diffusion impeded by an infinite array of partially permeable barriers. Proc R Soc Lond A 436(1897):391–403
35. Saxton MJ, Jacobson K (1997) Single-particle tracking: applications to membrane dynamics. Annu Rev Biophys Biomol Struct 26:373–399
36. Gambin Y, Lopez-Esparza R, Reffay M, Sierecki E, Gov NS, Genest M, Hodges RS, Urbach W (2006) Lateral mobility of proteins in liquid membranes revisited. Proc Natl Acad Sci USA 103(7):2098–2102
37. Saffman PG, Delbruck M (1975) Brownian motion in biological membranes. Proc Natl Acad Sci USA 72(8):3111–3113
38. Hughes BD, Pailthorpe BA, White LR, Sawyer WH (1982) Extraction of membrane microviscosity from translational and rotational diffusion coefficients. Biophys J 37(3):673–676
39. Hughes BD, Pailthorpe BA, White LR (1981) The translational and rotational drag on a cylinder moving in a membrane. J Fluid Mech 110:349–372
40. Petrov EP, Schwille P (2008) Translational diffusion in lipid membranes beyond the saffman-delbruck approximation. Biophys J 94(5):L41–L43

41. Kumar M, Mommer MS, Sourjik V (2010) Mobility of cytoplasmic, membrane, and DNA-binding proteins in escherichia coli. Biophys J 98(4):552–559
42. Guigas G, Weiss M (2006) Size-dependent diffusion of membrane inclusions. Biophys J 91(7):2393–2398
43. Falck E, Patra M, Karttunen M, Hyvonen MT, Vattulainen I (2005) Response to comment by almeida et al.: free area theories for lipid bilayers–predictive or not? Biophys J 89(1):745–752
44. Falck E, Patra M, Karttunen M, Hyvonen MT, Vattulainen I (2004) Lessons of slicing membranes: interplay of packing, free area, and lateral diffusion in phospholipid/cholesterol bilayers. Biophys J 87(2):1076–1091
45. Almeida PF, Vaz WL, Thompson TE (2005) Lipid diffusion, free area, and molecular dynamics simulations. Biophys J 88(6):4434–4438
46. Kusumi A, Sako Y, Yamamoto M (1993) Confined lateral diffusion of membrane receptors as studied by single particle tracking (nanovid microscopy). Effects of calcium-induced differentiation in cultured epithelial cells. Biophys J 65(5):2021–2040
47. Wieser S, Moertelmaier M, Fuertbauer E, Stockinger H, Schütz GJ (2007) (un)confined diffusion of cd59 in the plasma membrane determined by high-resolution single molecule microscopy. Biophys J 92(10):3719–3728
48. Jin S, Haggie PM, Verkman AS (2007) Single-particle tracking of membrane protein diffusion in a potential: simulation, detection, and application to confined diffusion of cftr cl- channels. Biophys J 93(3):1079–1088
49. Saxton MJ (1987) Lateral diffusion in an archipelago. The effect of mobile obstacles. Biophys J 52(6):989–997
50. Saxton MJ (1994) Anomalous diffusion due to obstacles: a monte carlo study. Biophys J 66(2 Pt 1):394–401
51. Saxton MJ (1993) Lateral diffusion in an archipelago. Dependence on tracer size. Biophys J 64(4):1053–1062
52. Michalet X, Pinaud FF, Bentolila LA, Tsay JM, Doose S, Li JJ, Sundaresan G, Wu AM, Gambhir SS, Weiss S (2005) Quantum dots for live cells, in vivo imaging, and diagnostics. Science 307(5709):538–544
53. Pinaud F, Clarke S, Sittner A, Dahan M (2010) Probing cellular events, one quantum dot at a time. Nat Methods 7(4):275–285
54. Martin DS, Forstner MB, Kas JA (2002) Apparent subdiffusion inherent to single particle tracking. Biophys J 83(4):2109–2117
55. Goulian M, Simon SM (2000) Tracking single proteins within cells. Biophys J 79(4):2188–2198
56. Ritchie K, Shan XY, Kondo J, Iwasawa K, Fujiwara T, Kusumi A (2005) Detection of non-brownian diffusion in the cell membrane in single molecule tracking. Biophys J 88(3):2266–2277
57. Destainville N, Salome L (2006) Quantification and correction of systematic errors due to detector time-averaging in single-molecule tracking experiments. Biophys J 90(2):L17–L19
58. Adler J, Shevchuk AI, Novak P, Korchev YE, Parmryd I (2010) Plasma membrane topography and interpretation of single-particle tracks. Nat Methods 7(3):170–171
59. King MR (2004) Apparent 2-d diffusivity in a ruffled cell membrane. J Theor Biol 227 (3):323–326
60. Reister E, Seifert U (2005) Lateral diffusion of a protein on a fluctuating membrane. Europhys Lett 71(5):859–865
61. Wieser S, Schütz GJ, Cooper ME, Stockinger H (2007) Single molecule diffusion analysis on cellular nanotubules: implications on plasma membrane structure below the diffraction limit. Appl Phys Lett 91(23):233901
62. Rustom A, Saffrich R, Markovic I, Walther P, Gerdes HH (2004) Nanotubular highways for intercellular organelle transport. Science 303(5660):1007–1010
63. Smith PR, Morrison IE, Wilson KM, Fernandez N, Cherry RJ (1999) Anomalous diffusion of major histocompatibility complex class i molecules on hela cells determined by single particle tracking. Biophys J 76(6):3331–3344

64. Horton MR, Hofling F, Radler JO, Franosch T (2010) Development of anomalous diffusion among crowding proteins. Soft Matter 6(12):2648–2656
65. Deverall MA, Gindl E, Sinner EK, Besir H, Ruehe J, Saxton MJ, Naumann CA (2005) Membrane lateral mobility obstructed by polymer-tethered lipids studied at the single molecule level. Biophys J 88(3):1875–1886
66. Weigel AV, Simon B, Tamkun MM, Krapf D (2011) Ergodic and nonergodic processes coexist in the plasma membrane as observed by single-molecule tracking. Proc Natl Acad Sci USA 108(16):6438–6443
67. Condamin S, Tejedor V, Voituriez R, Benichou O, Klafter J (2008) Probing microscopic origins of confined subdiffusion by first-passage observables. Proc Natl Acad Sci USA 105 (15):5675–5680
68. Schmidt U, Weiss M (2011) Anomalous diffusion of oligomerized transmembrane proteins. J Chem Phys 134(16):165101
69. Nechyporuk-Zloy V, Dieterich P, Oberleithner H, Stock C, Schwab A (2008) Dynamics of single potassium channel proteins in the plasma membrane of migrating cells. Am J Physiol Cell Physiol 294(4):C1096–C1102
70. Tejedor V, Benichou O, Voituriez R, Jungmann R, Simmel F, Selhuber-Unkel C, Oddershede LB, Metzler R (2010) Quantitative analysis of single particle trajectories: mean maximal excursion method. Biophys J 98(7):1364–1372
71. Qian H, Sheetz MP, Elson EL (1991) Single particle tracking. Analysis of diffusion and flow in two-dimensional systems. Biophys J 60(4):910–921
72. Saxton MJ (1997) Single-particle tracking: the distribution of diffusion coefficients. Biophys J 72(4):1744–1753
73. Schütz GJ, Schindler H, Schmidt T (1997) Single-molecule microscopy on model membranes reveals anomalous diffusion. Biophys J 73(2):1073–1080
74. Lommerse PH, Blab GA, Cognet L, Harms GS, Snaar-Jagalska BE, Spaink HP, Schmidt T (2004) Single-molecule imaging of the h-ras membrane-anchor reveals domains in the cytoplasmic leaflet of the cell membrane. Biophys J 86(1):609–616
75. Pinaud F, Michalet X, Iyer G, Margeat E, Moore HP, Weiss S (2009) Dynamic partitioning of a glycosyl-phosphatidylinositol-anchored protein in glycosphingolipid-rich microdomains imaged by single-quantum dot tracking. Traffic 10(6):691–712
76. Semrau S, Schmidt T (2007) Particle image correlation spectroscopy (pics) retrieving nanometer-scale correlations from high-density single-molecule position data. Biophys J 92 (2):613–621
77. Wieser S, Axmann M, Schütz GJ (2008) Versatile analysis of single-molecule tracking data by comprehensive testing against monte carlo simulations. Biophys J 95(12):5988–6001
78. Matsuoka S, Shibata T, Ueda M (2009) Statistical analysis of lateral diffusion and multistate kinetics in single-molecule imaging. Biophys J 97(4):1115–1124
79. Ying W, Huerta G, Steinberg S, Zuniga M (2009) Time series analysis of particle tracking data for molecular motion on the cell membrane. Bull Math Biol 71(8):1967–2024
80. Simson R, Sheets ED, Jacobson K (1995) Detection of temporary lateral confinement of membrane proteins using single-particle tracking analysis. Biophys J 69(3):989–993
81. Meier J, Vannier C, Serge A, Triller A, Choquet D (2001) Fast and reversible trapping of surface glycine receptors by gephyrin. Nat Neurosci 4(3):253–260
82. Meilhac N, Le Guyader L, Salome L, Destainville N (2006) Detection of confinement and jumps in single-molecule membrane trajectories. Phys Rev E 73(1):011915
83. Montiel D, Cang H, Yang H (2006) Quantitative characterization of changes in dynamical behavior for single-particle tracking studies. J Phys Chem B 110(40):19763–19770
84. Huet S, Karatekin E, Tran VS, Fanget I, Cribier S, Henry JP (2006) Analysis of transient behavior in complex trajectories: application to secretory vesicle dynamics. Biophys J 91 (9):3542–3559
85. Manley S, Gillette JM, Patterson GH, Shroff H, Hess HF, Betzig E, Lippincott-Schwartz J (2008) High-density mapping of single-molecule trajectories with photoactivated localization microscopy. Nat Methods 5(2):155–157

86. Jaqaman K, Kuwata H, Touret N, Collins R, Trimble William S, Danuser G, Grinstein S (2011) Cytoskeletal control of cd36 diffusion promotes its receptor and signaling function. Cell 146(4):593–606
87. Andrews NL, Lidke KA, Pfeiffer JR, Burns AR, Wilson BS, Oliver JM, Lidke DS (2008) Actin restricts fcepsilonri diffusion and facilitates antigen-induced receptor immobilization. Nat Cell Biol 10(8):955–963
88. Brameshuber M, Schutz GJ (2008) How the sum of its parts gets greater than the whole. Nat Methods 5(2):133–134
89. Lillemeier BF, Mortelmaier MA, Forstner MB, Huppa JB, Groves JT, Davis MM (2010) Tcr and lat are expressed on separate protein islands on t cell membranes and concatenate during activation. Nat Immunol 11(1):90–96
90. Howard J (2001) Mechanics of motor proteins and the cytoskeleton. Sinauer Assoc, Sunderland
91. Funatsu T, Harada Y, Tokunaga M, Saito K, Yanagida T (1995) Imaging of single fluorescent molecules and individual atp turnovers by single myosin molecules in aqueous-solution. Nature 374(6522):555–559
92. Schmidt T, Schütz GJ, Baumgartner W, Gruber HJ, Schindler H (1995) Characterization of photophysics and mobility of single molecules in a fluid lipid membrane. J Phys Chem 99:17662–17668
93. Sahl SJ, Leutenegger M, Hilbert M, Hell SW, Eggeling C (2010) Fast molecular tracking maps nanoscale dynamics of plasma membrane lipids. Proc Natl Acad Sci USA 107(15):6829–6834
94. Demtröder W (2003) Laser spectroscopy, 3rd edn. Springer, Berlin
95. Diaspro A, Chirico G, Usai C, Ramoino P, Dobrucki JW (2006) Photobleaching. In: Pawley JB (ed) Handbook of biological confocal microscopy, 3rd edn. Springer Science + Business Media, New York
96. Zondervan R, Kulzer F, Kol'chenko MA, Orrit M (2004) Photobleaching of rhodamine 6 g in poly(vinyl alcohol) at the ensemble and single-molecule levels. J Phys Chem A 108:1657–1665
97. Deschenes LA, Vanden Bout DA (2002) Single molecule photobleaching: increasing photon yield and survival time through suppression of two-step photolysis. Chem Phys Lett 365:387–395
98. Bernas T, Zarebski M, Dobrucki JW, Cook PR (2004) Minimizing photobleaching during confocal microscopy of fluorescent probes bound to chromatin: role of anoxia and photon flux. J Microsc 215(Pt 3):281–296
99. Dickson RM, Cubitt AB, Tsien RY, Moerner WE (1997) On/off blinking and switching behaviour of single molecules of green fluorescent protein. Nature 388(6640):355–358
100. Garcia-Parajo MF, Segers-Nolten GM, Veerman JA, Greve J, van Hulst NF (2000) Real-time light-driven dynamics of the fluorescence emission in single green fluorescent protein molecules. Proc Natl Acad Sci USA 97(13):7237–7242
101. Annibale P, Vanni S, Scarselli M, Rothlisberger U, Radenovic A (2011) Identification of clustering artifacts in photoactivated localization microscopy. Nat Methods 8:527–528
102. Heinze KG, Costantino S, De Koninck P, Wiseman PW (2009) Beyond photobleaching, laser illumination unbinds fluorescent proteins. J Phys Chem B 113(15):5225–5233
103. Douglass AD, Vale RD (2005) Single-molecule microscopy reveals plasma membrane microdomains created by protein-protein networks that exclude or trap signaling molecules in t cells. Cell 121(6):937–950
104. Vrljic M, Nishimura SY, Brasselet S, Moerner WE, McConnell HM (2002) Translational diffusion of individual class ii mhc membrane proteins in cells. Biophys J 83(5):2681–2692
105. Drbal K, Moertelmaier M, Holzhauser C, Muhammad A, Fuertbauer E, Howorka S, Hinterberger M, Stockinger H, Schütz GJ (2007) Single-molecule microscopy reveals heterogeneous dynamics of lipid raft components upon tcr engagement. Int Immunol 19(5):675–684

106. Moertelmaier M, Brameshuber M, Linimeier M, Schütz GJ, Stockinger H (2005) Thinning out clusters while conserving stoichiometry of labeling. Appl Phys Lett 87:263903
107. Schmidt T, Schütz GJ, Gruber HJ, Schindler H (1996) Local stoichiometries determined by counting individual molecules. Anal Chem 68(24):4397–4401
108. Brameshuber M, Weghuber J, Ruprecht V, Gombos I, Horvath I, Vigh L, Eckerstorfer P, Kiss E, Stockinger H, Schutz GJ (2010) Imaging of mobile long-lived nanoplatforms in the live cell plasma membrane. J Biol Chem 285(53):41765–41771
109. Madl J, Weghuber J, Fritsch R, Derler I, Fahrner M, Frischauf I, Lackner B, Romanin C, Schutz GJ (2010) Resting state orai1 diffuses as homotetramer in the plasma membrane of live mammalian cells. J Biol Chem 285(52):41135–41142
110. Ruprecht V, Brameshuber M, Schütz GJ (2010) Two-color single molecule tracking combined with photobleaching for the detection of rare molecular interactions in fluid biomembranes. Soft Matter 6(3):568–581
111. Monks CR, Freiberg BA, Kupfer H, Sciaky N, Kupfer A (1998) Three-dimensional segregation of supramolecular activation clusters in t cells. Nature 395(6697):82–86
112. Grakoui A, Bromley SK, Sumen C, Davis MM, Shaw AS, Allen PM, Dustin ML (1999) The immunological synapse: a molecular machine controlling t cell activation. Science 285(5425):221–227
113. Bromley SK, Burack WR, Johnson KG, Somersalo K, Sims TN, Sumen C, Davis MM, Shaw AS, Allen PM, Dustin ML (2001) The immunological synapse. Annu Rev Immunol 19:375–396
114. Krogsgaard M, Davis MM (2005) How t cells 'see' antigen. Nat Immunol 6(3):239–245
115. Huppa JB, Axmann M, Mortelmaier MA, Lillemeier BF, Newell EW, Brameshuber M, Klein LO, Schütz GJ, Davis MM (2010) Tcr-peptide-mhc interactions in situ show accelerated kinetics and increased affinity. Nature 463(7283):963–967
116. Xiong Y, Kern P, Chang H, Reinherz E (2001) T cell receptor binding to a pmhcii ligand is kinetically distinct from and independent of cd4. J Biol Chem 276(8):5659–5667
117. Bunnell SC, Kapoor V, Trible RP, Zhang W, Samelson LE (2001) Dynamic actin polymerization drives t cell receptor-induced spreading: a role for the signal transduction adaptor lat. Immunity 14(3):315–329
118. Ike H, Kosugi A, Kato A, Iino R, Hirano H, Fujiwara T, Ritchie K, Kusumi A (2003) Mechanism of lck recruitment to the t-cell receptor cluster as studied by single-molecule-fluorescence video imaging. Chemphyschem 4(6):620–626
119. Campi G, Varma R, Dustin ML (2005) Actin and agonist mhc-peptide complex-dependent t cell receptor microclusters as scaffolds for signaling. J Exp Med 202(8):1031–1036
120. Saito T, Yokosuka T, Hashimoto-Tane A (2010) Dynamic regulation of t cell activation and co-stimulation through tcr-microclusters. FEBS Lett 584(24):4865–4871
121. Demond AL, Mossman KD, Starr T, Dustin ML, Groves JT (2008) T cell receptor microcluster transport through molecular mazes reveals mechanism of translocation. Biophys J 94:3286–3292
122. Morton WM, Ayscough KR, McLaughlin PJ (2000) Latrunculin alters the actin-monomer subunit interface to prevent polymerization. Nat Cell Biol 2(6):376–378
123. Wakatsuki T, Schwab B, Thompson NC, Elson EL (2001) Effects of cytochalasin d and latrunculin b on mechanical properties of cells. J Cell Sci 114(Pt 5):1025–1036
124. Lommerse PH, Vastenhoud K, Pirinen NJ, Magee AI, Spaink HP, Schmidt T (2006) Single-molecule diffusion reveals similar mobility for the lck, h-ras, and k-ras membrane anchors. Biophys J 91(3):1090–1097

Index

P. Tinnefeld et al. (eds.), *Far-Field Optical Nanoscopy*,
Springer Ser Fluoresc (2015) 14: 331–336, DOI 10.1007/4243_2014,